Thick-target neutron yields for intermediate-energy heavy ion experiments at NSRL

A Dissertation Presented for the

Doctor of Philosophy

Degree

The University of Tennessee, Knoxville

Hunter Nathaniel Ratliff

December 2018

© by Hunter Nathaniel Ratliff, 2018
All Rights Reserved.

Acknowledgments

This work was supported by NASA grants NNX17Al10A and NNX15AD89A. Additionally, I was supported by The University of Tennessee Chancellor's Distinguished Graduate Fellowship.

I would like to thank Dr. Lawrence Heilbronn for serving as my graduate advisor for the past four years and for the guidance provided in all of my research endeavors in graduate school.

I am grateful to Dr. Lawrence Townsend, Dr. Steven Skutnik, and Dr. Jeffrey Moersch for serving on my committee and for providing advice and feedback on this work.

I would also like to thank Dr. Michael Sivertz, Dr. Adam Rusek, Ms. Rory Rosselot, Mr. Charlie Pearson, and Dr. Chiara La Tessa at the NASA Space Radiation Laboratory; Dr. Martha Clowdsley, Dr. Tony Slaba, Dr. Matthew Beach, and Dr. Steve Blattnig from the NASA Langley Research Center; and Dr. Cary Zeitlin from Wyle Laboratories who were vital to the design, setup, and execution of these experiments.

I am remarkably grateful to Dr. Natalie McGirl and Dr. Luis Castellanos for teaching me about some of the analysis techniques used in this work and how to use ROOT for analyzing data.

I would also like to thank Hui-Chen Wang for collaborating in the experiments and for providing the PHITS simulations whose results are presented in this work.

I would like to provide additional thanks to Dr. Ondrej Chvala for granting assistance with, access to, and troubleshooting of the NE computing cluster.

Abstract

Recently published NASA simulations emulating an enclosed spacecraft exposed to galactic cosmic rays (GCRs) have shown that an optimal shielding wall thickness beyond which astronaut dose equivalent rises is present when using aluminum walls, though not with polyethylene walls [1]. Neutrons produced in the back wall of the spacecraft were shown to be primarily responsible for the rise in dose for thicknesses beyond the optimal thickness. The NASA research also demonstrated a large variance in dose predictions between the various standard particle transport codes which appeared to be predominately attributable to discrepancies in how the codes handle neutron and complex light ion production in these GCR primary and secondary interactions in the shielding materials.

To test these predictions and provide data against which the particle transport codes can be benchmarked, particle beams characteristic of GCRs were accelerated into two thick targets of aluminum and/or polyethylene (materials common to space radiation shielding), emulating the walls of a spacecraft, across three experiments conducted at the NASA Space Radiation Laboratory. In these experiments, double-differential neutron yields from the upstream target were measured at six different angles and characterized using time-of-flight techniques. Additionally, neutrons from background, room scattering, and the downstream target were characterized using a technique developed in this work involving deconvolution of collected pulse height spectra with a response function. Monte Carlo simulations emulating the experiment using MCNP and PHITS were conducted to provide a comparison to the collected data and to bring any discrepancies in the models to light.

This work seeks to both provide a detailed look at where the particle transport codes poorly predict the experimental results as well as provide insight to spacecraft shielding design as it pertains to minimizing neutron dose.

Table of Contents

1 Introduction **1**

1.1 Overview and goals 1

1.2 Original contribution 2

1.2.1 Scientifically novel facets of this work 3

1.2.2 Unique efforts relative to other analyses of these experiments 4

1.3 Outline 6

2 Background **9**

2.1 Space radiation 9

2.2 Collision mechanics 12

2.3 Motivation for these experiments 14

2.4 NASA's goals for this project 15

2.5 Light production in organic liquid scintillators 17

3 Experiment **21**

3.1 Structure of the experiment 21

3.2 Data acquisition system and logic 28

3.3 Special beam considerations and exceptions 31

4 Upstream target neutron data analysis **34**

4.1 General approach to the analysis 35

4.2 Data filtering in ROOT 37

4.2.1 "Self-time" cuts 37

4.2.2 "Veto" cuts . . . 38
4.2.3 "Good beam" graphical cuts . . . 39
4.2.4 Neutron/photon discrimination graphical cuts . . . 40
4.3 Calibrations . . . 48
4.3.1 Time calibrations . . . 49
4.3.2 Charge calibrations . . . 50
4.4 Normalizing and combining data . . . 54
4.5 Characterizing the prompt gamma peak . . . 55
4.5.1 Extrapolation to zero target thickness . . . 59
4.6 Performing neutron time-of-flight calculations . . . 60
4.6.1 Time-of-flight calculation methodology . . . 60
4.6.2 Time-of-flight data analysis . . . 61
4.7 Solid angle normalization . . . 63
4.8 Detector efficiency corrections and SCINFUL-QMD . . . 65
4.9 Neutron production point corrections . . . 66
4.9.1 Effective production point and target thickness calculations . . . 67
4.9.2 Application of production corrections to ToF calculations . . . 77
4.10 Correcting undershadowed data: a higher Q_{total} cut . . . 86
4.11 Rebinning . . . 88
4.11.1 Interpolate edges and redistribute bin contents . . . 88
4.11.2 Preserve original bin edges and contents . . . 90
4.11.3 Specific rebinning algorithm for time-of-flight neutrons . . . 90

5 Uncertainty quantification for upstream target neutron data 98
5.1 Fundamental approach to error propagation . . . 98
5.2 Statistical Uncertainties (y-axis) . . . 100
5.3 Systematic Uncertainties (y-axis) . . . 101
5.3.1 Solid angle uncertainty . . . 102
5.3.2 Graphical cut uncertainty . . . 108
5.4 Energy Resolution (x-axis) . . . 112

6 Downstream target and room scattered neutron data analysis 114
6.1 Theory of extracting energy spectra from QDC data . . . 115
6.2 Exporting QDC spectra from ROOT . . . 117
6.3 Experimental PHS rebinning . . . 120
6.4 Generating response matrices . . . 120
6.4.1 Preparing the response matrix for deconvolution . . . 124
6.5 Deconvolution . . . 125
6.5.1 Normalization of deconvoluted results . . . 129
6.6 Uncertainty quantification of deconvolution . . . 131
6.7 Validation of the deconvoluted results . . . 134

7 Monte Carlo full-room simulations 143
7.1 Modeled room geometry . . . 144
7.2 MCNP simulations . . . 147
7.2.1 MCNP tally methodology . . . 147
7.2.2 MCNP results rebinning and remaining normalizations . . . 154
7.3 PHITS simulations . . . 154

8 Results and trends 156
8.1 Yield spectra . . . 156
8.1.1 Double-differential upstream target neutron yields . . . 157
8.1.2 Energy-dependent differential downstream target neutron yields . . . 174
8.1.3 Energy-dependent differential combined neutron yields . . . 183
8.2 Performance of Monte Carlo results against the data . . . 187
8.2.1 Monte Carlo vs. data: Upstream target results . . . 187
8.2.2 Monte Carlo vs. data: Downstream target results . . . 195
8.2.3 PHITS vs. MCNP: Upstream target results . . . 203
8.2.4 PHITS vs. MCNP: Downstream target results . . . 210
8.2.5 Summary of the performance of PHITS and MCNP . . . 216
8.3 Effective dose calculations . . . 219
8.3.1 Compilation of a hybrid GCR-like effective dose . . . 221

9 Data availability **243**

9.1 NASA and UT data repositories 244

9.2 SHAEDIT online tool 245

9.2.1 SHAEDIT usage walk-through 246

10 Conclusions **253**

Bibliography **257**

Appendices **266**

A Equipment **267**

B Production point correction plots **268**

B.1 Condensed plots 268

B.2 All individual plots 271

C Yield spectra plots **307**

C.1 Upstream target plots 307

C.2 Downstream target plots 349

D Effective dose tables **395**

D.1 Upstream target effective doses 395

D.2 Total effective doses (without solid angle normalization) 401

E Data repository structure **432**

Vita **436**

List of Tables

2.1 Light response parameterization coefficients 19

3.1 NSRL thick-target experiment schedule 22
3.2 Shadow bar configurations 24
3.3 Stopping location of all beam projectiles 27
3.4 Trigger logical diagram initialisms and abbreviations 30

4.1 Q_{total} threshold cut channels 48
4.2 Higher Q_{total} pulse height threshold cuts 48
4.3 QDC channel to light yield fitting parameters for Equation 4.5 53
4.4 Shadow bar configuration for 400 MeV/n C on 20 g/cm^2 Al 57
4.5 Prompt gamma peak fitting parameters for 400 MeV/n C on Al (units in `s1.tdc` channels) 59
4.6 Mean solid angle for each detector 64
4.7 All applied Q_{total} pulse height threshold cuts (November 2016 values) 87
4.8 Explanations of logical conditions in Equation 4.26 89

5.1 Min/max solid angle for each detector for a single production point 103
5.2 General coordinates for detector edges. 105
5.3 Minimum and maximum solid angles for each detector for the 60 g/cm^2 HDPE upstream target 107

6.1 QDC channel to light yield fitting parameters for Equation 6.3 118
6.2 Actual QDC spectra MeVee bounds 119

7.1 Possible track lengths and flux-to-yield conversion values 153

8.1 Upstream target neutron overall results comparison to Monte Carlo 189
8.2 Downstream target neutron overall results comparison to Monte Carlo . . . 197
8.3 Upstream target neutron overall comparison of PHITS vs. MCNP 204
8.4 Downstream target neutron overall comparison of PHITS vs. MCNP 211
8.5 Experimentally calculated effective dose for C projectiles at 10° 225
8.6 GCR relative abundances of experimentally sampled ions ($W = 80$) 226
8.7 Sampled GCR relative abundances with $W = 10$ (solar minimum) 227
8.8 Sampled GCR relative abundances with $W = 140$ (solar maximum) 227

9.1 SHAEDIT links 245

A.1 List of logic units and their manufacturers 267

D.1 Upstream target effective dose for H projectiles 396
D.2 Upstream target effective dose for He projectiles 397
D.3 Upstream target effective dose for C projectiles 398
D.4 Upstream target effective dose for Si projectiles 399
D.5 Upstream target effective dose for Fe projectiles 400
D.6 Total effective dose for H projectiles at 10° 402
D.7 Total effective dose for He projectiles at 10° 403
D.8 Total effective dose for C projectiles at 10° 404
D.9 Total effective dose for Si projectiles at 10° 405
D.10 Total effective dose for Fe projectiles at 10° 406
D.11 Total effective dose for H projectiles at 30° 407
D.12 Total effective dose for He projectiles at 30° 408
D.13 Total effective dose for C projectiles at 30° 409
D.14 Total effective dose for Si projectiles at 30° 410
D.15 Total effective dose for Fe projectiles at 30° 411
D.16 Total effective dose for H projectiles at 45° 412
D.17 Total effective dose for He projectiles at 45° 413

D.18 Total effective dose for C projectiles at 45° 414
D.19 Total effective dose for Si projectiles at 45° 415
D.20 Total effective dose for Fe projectiles at 45° 416
D.21 Total effective dose for H projectiles at 60° 417
D.22 Total effective dose for He projectiles at 60° 418
D.23 Total effective dose for C projectiles at 60° 419
D.24 Total effective dose for Si projectiles at 60° 420
D.25 Total effective dose for Fe projectiles at 60° 421
D.26 Total effective dose for H projectiles at 80° 422
D.27 Total effective dose for He projectiles at 80° 423
D.28 Total effective dose for C projectiles at 80° 424
D.29 Total effective dose for Si projectiles at 80° 425
D.30 Total effective dose for Fe projectiles at 80° 426
D.31 Total effective dose for H projectiles at 135° 427
D.32 Total effective dose for He projectiles at 135° 428
D.33 Total effective dose for C projectiles at 135° 429
D.34 Total effective dose for Si projectiles at 135° 430
D.35 Total effective dose for Fe projectiles at 135° 431

E.1 Columns in upstream target secondary particle text files 434
E.2 Columns in measured downstream target neutron text files 435

List of Figures

2.1 GCR elemental abundances for Z $\geq$ 2 and their contributions to dose equivalent on the lunar surface [9] 10
2.2 GCR fluxes for ions of various charges during the 1977 solar minimum [11] . 11
2.3 Stages of the abrasion-ablation model [14] 12
2.4 Visualization of the relative kinetic energies (from bottom left to top right) of the projectile fragment, fireball, target/target fragment, and pre-collision projectile [16] 13
2.5 Simulated dose equivalent inside of a water slab sandwiched between two slabs of varying thicknesses of aluminum or polyethylene being bombarded by GCRs [1] 15

3.1 Closeup of the 30° detector, N2, with its various components labeled 23
3.2 Experiment room at NSRL with important features relevant to this work labeled. (The OLS labels are placed at the base of the stand for each detector.) 23
3.3 Shadow bars in arrangement B (concealing 10° and 60° detectors) 25
3.4 Pictured are all 8 upstream targets employed to-scale with dashed lines indicating their mass centers. 25
3.5 Pictured is a to-scale schematic of the beam/detector/target system. In red is the largest target, 60 g/cm^2 HDPE, and in blue is the smallest target, 20 g/cm^2 Al. 27
3.6 Pictured is the electronic logic map of the data acquisition system. 29
3.7 Physics / data acquisition room at NSRL with logic equipment shown . . . 30

3.8 Illustration of acquisition gate and trigger being set by a coincidence between OLS/CS **and** a coincidence in both start scintillators [2] 31

4.1 Example N1 TDC spectrum (zoomed in) 37
4.2 Example N1V1 QDC spectrum 38
4.3 1500 MeV/n C on Al `s1.qdc:s2.qdc` good beam plot after making a cut . . 39
4.4 400 MeV/n C on Al `n1.h_qdc:n1.t_qdc` n/γ plot with pileup 41
4.5 400 MeV/n C on Al `n1.h_qdc:n1.t_qdc` n/γ plot 42
4.6 400 MeV/n C on Al `n1.h_qdc:n1.t_qdc` n/γ plot 42
4.7 400 MeV/n C on Al `n1.ha_qdc:n1.ta_qdc` attenuated n/γ plot 43
4.8 All runs `n4.ha_qdc:n4.ta_qdc` attenuated n/γ plot 44
4.9 All runs `n4.ha_qdc:n4.ta_qdc` attenuated n/γ plot with cuts 44
4.10 400 MeV/n C on Al `n4.h_qdc:n4.t_qdc` unattenuated n/γ plot 45
4.11 Y-Projection of N4 Q_{tot} channel 185 projected on the Q_{head} axis with Gaussian fits for each peak 47
4.12 Time calibration curve of `s1.tdc` 49
4.13 QDC calibration spectra for N3 52
4.14 Calibration curve translating channel number to light produced in keVee for N1 (10°) in the November 2016 experiments 53
4.15 Normalized γ TDC spectrum for 400 MeV/n C on 20 g/cm^2 Al for N1 . . . 57
4.16 Normalized γ ToF spectrum for 400 MeV/n C on 20 g/cm^2 Al for N4 57
4.17 Normalized γ TDC spectra in N4 with Gaussian fits for 400 MeV/n C incident on Al targets 58
4.18 Normalized γ TDC spectrum in N1 with a Gaussian fit for 400 MeV/n C incident on 60 g/cm^2 Al 58
4.19 Mean solid angle 64
4.20 Sample output efficiency spectrum from SCINFUL-QMD 66
4.21 Neutron production in 60 g/cm^2 Al front target for 400 MeV/n C 67
4.22 Neutron production in 60 g/cm^2 Al front target for 400 MeV/n C with 80% line 68

4.23 Discontinuities are created by discrete production point correction regions. . 70
4.24 Neutron production in 40 g/cm^2 Al front target for 400 MeV/n C 72
4.25 Neutron production in 20 g/cm^2 HDPE front target for 1463 MeV/n Fe . . 72
4.26 Mean and median production point as a function of position in target with 80% production band shown as vertical error bars on the median curve and one standard deviation as the error bars on the mean curve 74
4.27 Same as Figure 4.26 except with the addition of the minimum-width 80% production band as red error bars 75
4.28 Neutron production in 20 g/cm^2 Al front target for 1500 MeV/n C 76
4.29 Effect of neutron energy shift 79
4.30 Neutron production in 60 g/cm^2 HDPE front target for 400 MeV/n Fe . . . 81
4.31 ToF spectra with no production point or effective target thickness corrections 82
4.32 x-axis energy shift from production point correction 82
4.33 ToF spectrum after applying production point correction 83
4.34 ToF spectrum with production point and effective target thickness corrections 83
4.35 ToF plot using "minimum-width band" for effective target boundaries 84
4.36 The three plots show how the x-axis uncertainty is reduced by choosing the effective front target boundaries less conservatively. 85
4.37 Rebinning method which generates new bin boundaries and redistributes old bin content to new bins 88
4.38 Rebinning method which preserves old bin boundaries by just stacking together old bins to generate new ones 90
4.39 Demonstration that a universal statistical uncertainty per bin is not ideal . 91
4.40 Rebinning logic map/flowchart 94

5.1 Variance in the solid angle 102
5.2 Variance in the solid angle including varying production points 103
5.3 Finding coordinates of A and B 104
5.4 Pictured is an illustration of the solid angle extremes for upstream versus downstream detectors. 106

5.5 Pictured is a to-scale schematic of the beam/detector/target system. In red is the largest target, 60 g/cm^2 HDPE, and in blue is the smallest target, 20 g/cm^2 Al. 108
5.6 Pictured is the percentage of bins of all of the November 2016 upstream target neutron yield spectra with given percent graphical cut uncertainties. 110
5.7 Pictured is a similar plot to Figure 5.6 but integrated such that each bin shows the percentage of data points with a percentage graphical cut uncertainty greater than that on the x-axis. 110
5.8 Pictured is the percentage of bins of all of the November 2016 upstream target neutron yield spectra with given percentage $\varepsilon_{\mathrm{GC}(\sigma_Y)}$. 111
5.9 Pictured is a similar plot to Figure 5.8 but integrated such that each bin shows the percentage of data points with a percentage $\varepsilon_{\mathrm{GC}(\sigma_Y)}$ greater than that on the x-axis. 111

6.1 Viable combinations for deconvolution (blue=viable, red = not viable) . . . 121
6.2 Pictured is an example response matrix from SCINFUL-QMD. 122
6.3 The finer response matrix from SCINFUL-QMD used before rebinning . . . 123
6.4 This figure highlights the individual steps of the deconvolution process. . . . 128
6.5 Shadowed neutrons detected at 10° from the NNLS deconvolution for 800 MeV H incident on the 60° HDPE upstream target followed by the 60 g/cm^2 HDPE downstream target 130
6.6 Shadowed neutrons detected at 10° from Tikhonov regularization followed by L-curve analysis for 800 MeV H incident on the 60° HDPE upstream target followed by the 60 g/cm^2 HDPE downstream target 131
6.7 Shadowed neutrons detected at 10° for 800 MeV H incident on the 60° HDPE upstream target followed by the 60 g/cm^2 HDPE downstream target (Tikhonov exact and MC average results overlap.) 132
6.8 The L-curve and its curvature for shadowed neutrons detected at 10° for 800 MeV H incident on the 60° HDPE upstream target followed by the 60 g/cm^2 HDPE downstream target 134

6.9 Comparison of time-of-flight and deconvolution methods for neutrons detected at 10° for 400 MeV/n C incident on the 20 g/cm^2 Al upstream target 135
6.10 Comparison of time-of-flight and deconvolution methods for neutrons detected at 30° for 400 MeV/n C incident on the 20 g/cm^2 Al upstream target 136
6.11 Comparison of time-of-flight and deconvolution methods for neutrons detected at 60° and 80° for 400 MeV/n C incident on the 20 g/cm^2 Al upstream target 136
6.12 Comparison of time-of-flight and deconvolution methods for neutrons detected at all angles for 1500 MeV/n He incident on the 60 g/cm^2 Al upstream target 139
6.13 Comparison of time-of-flight and deconvolution methods for neutrons detected at all angles for 400 MeV H incident on the 20 g/cm^2 Al upstream target 140
6.14 Comparison of time-of-flight and deconvolution methods for neutrons detected at all angles for 400 MeV/n Si incident on the 20 g/cm^2 HDPE upstream target 141
6.15 Comparison of time-of-flight and deconvolution methods for neutrons detected at all angles for 800 MeV/n Si incident on the 60 g/cm^2 AlPE upstream target 142

7.1 3D render of the modeled geometry using the `[T-3Dshow]` tally in PHITS . 145
7.2 Horizontal slice of room geometry at detector height in 60 g/cm^2 AlPE configuration 145
7.3 Pictured is the described coordinate system for the cylinder with an eye symbol denoting the viewing perspective used for two-dimensional areal projections. 152

8.1 Explanation of each plotted energy bin 157
8.2 Neutrons detected at 10° from all 400 MeV/n projectile species incident on the 20 g/cm^2 AlPE upstream target 158

8.3 Neutrons detected at 10° from all 400 MeV/n projectile species incident on the 60 g/cm^2 AlPE upstream target 159
8.4 Neutrons detected at 10° from all 400 MeV/n projectile species incident on the 20 g/cm^2 AlPE upstream target alongside Monte Carlo simulated results 160
8.5 Neutrons detected at all angles from all 400 MeV/n Si incident on the 20 g/cm^2 HDPE upstream target 161
8.6 Neutrons detected at all angles (spaced apart by powers of 10) from all 400 MeV/n Si incident on the 20 g/cm^2 HDPE upstream target with Monte Carlo code results included 162
8.7 Neutrons detected at 10° from 400 MeV/n Si projectiles incident on the 20 g/cm^2 HDPE upstream target alongside Monte Carlo simulated results . . . 163
8.8 Neutrons detected at 10° from 800 and 1500 MeV/n Si projectiles incident on the 20 g/cm^2 HDPE upstream target alongside Monte Carlo simulated results 164
8.9 Neutrons detected at 45° from 1500 MeV/n Si projectiles incident on the 20 g/cm^2 HDPE upstream target alongside Monte Carlo simulated results . . . 165
8.10 Neutrons detected at 10° from C projectiles incident on the 20 g/cm^2 and 60 g/cm^2 Al upstream targets 165
8.11 Neutrons detected at 10° from 400 MeV/n C projectiles incident on the three materials of each upstream target for the 20 g/cm^2 and 60 g/cm^2 thicknesses 167
8.12 Neutrons detected at 10° from projectiles incident on the 20 g/cm^2 upstream targets 167
8.13 Neutrons detected at 10° from 400 MeV/n C projectiles incident on the three thicknesses of each pure upstream target 168
8.14 Neutrons detected at 10° from 800 MeV/n Si projectiles incident on the three thicknesses of each pure upstream target 168
8.15 Neutrons detected at 10° from 400 MeV/n Si projectiles incident on the three thicknesses of each pure upstream target 169
8.16 Neutrons detected at 10° from 400 MeV/n C projectiles incident on the 20 g/cm^2 and 60 g/cm^2 Al and HDPE upstream targets alongside Monte Carlo simulated results 170

8.17 Neutrons detected at 80° and 135° from 400 MeV/n Si projectiles incident on the 20 g/cm^2 Al upstream target alongside Monte Carlo simulated results 170
8.18 Neutrons detected at 10° from 2500 MeV H projectiles incident on the three thicknesses of each pure upstream target (spaced apart by powers of 100) alongside Monte Carlo simulated results 171
8.19 Neutrons detected at 10° from 800 MeV/n projectiles (spaced apart by powers of 100) incident on the 60 g/cm^2 HDPE upstream targets alongside Monte Carlo simulated results 172
8.20 Neutrons detected at 30° from C projectiles and at 60° for Si projectiles incident on the 60 g/cm^2 AlPE upstream targets alongside Monte Carlo simulated results 173
8.21 Neutrons detected at 10°, 30°, and 45° (spaced apart by powers of 10) from 400 MeV/n Fe projectiles incident on the 20 g/cm^2 and 60 g/cm^2 AlPE upstream targets alongside Monte Carlo simulated results 173
8.22 Shadowed neutrons detected at 10° from all 400 MeV/n projectile species incident on the 20 g/cm^2 AlPE upstream target 176
8.23 Shadowed neutrons detected at 10° from all 1500 MeV/n projectile species (2500 MeV H) incident on the 20 g/cm^2 AlPE upstream target followed by the 60 g/cm^2 HDPE downstream target 176
8.24 Shadowed neutrons detected at each detector angle from all 800 MeV/n He projectiles incident on the 20 g/cm^2 AlPE upstream target followed by the 60 g/cm^2 HDPE downstream target 178
8.25 Shadowed neutrons detected at 10° from C projectiles incident on the 20 g/cm^2 and 60 g/cm^2 Al upstream targets followed by the 60 g/cm^2 Al downstream target 178
8.26 Shadowed neutrons detected at 10° from 800 MeV/n He projectiles incident on the 20 g/cm^2 and 60 g/cm^2 thicknesses of each upstream material composition targets followed by the 60 g/cm^2 downstream target of the same material 179

8.27 Shadowed neutrons detected at 10° from 800 MeV/n Fe projectiles incident on the 20 g/cm^2 and 60 g/cm^2 thicknesses of each upstream material composition targets followed by the 60 g/cm^2 downstream target of the same material . 179
8.28 Shadowed neutrons detected at 10° from 1500 MeV/n He and 400 MeV/n Si projectiles incident on the three thicknesses of each pure upstream target material followed by the 60 g/cm^2 downstream target of the same material . 180
8.29 Shadowed neutrons detected at 10° from all 1500 MeV/n projectile species (2500 MeV H) incident on the 20 g/cm^2 AlPE upstream target followed by the 60 g/cm^2 HDPE downstream target alongside Monte Carlo simulated results 181
8.30 Shadowed neutrons detected at each detector angle (spaced apart by powers of 10) from 800 MeV/n He projectiles incident on the 20 g/cm^2 AlPE upstream target followed by the 60 g/cm^2 HDPE downstream target alongside Monte Carlo simulated results 182
8.31 Shadowed neutrons detected at 10° from C projectiles incident on the 20 g/cm^2 Al upstream target followed by the 60 g/cm^2 Al downstream target alongside Monte Carlo simulated results 182
8.32 Downstream target-produced and room scattered neutrons detected at 10° from 400 MeV/n C projectiles incident on the 20 g/cm^2 Al and HDPE upstream targets followed by the 60 g/cm^2 downstream target of the same material alongside Monte Carlo simulated results 183
8.33 All neutrons detected at 10° from 400 MeV/n C projectiles incident on the 20 g/cm^2 AlPE upstream target followed by the 60 g/cm^2 HDPE downstream target 184
8.34 All neutrons detected at 10° from 2500 MeV H projectiles incident on the 20 g/cm^2 and 60 g/cm^2 Al and HDPE upstream targets followed by the 60 g/cm^2 downstream target of the same material 184
8.35 All neutrons detected at 10° from 2500 MeV H projectiles incident on all 60 g/cm^2 upstream target combinations 185

8.36 All neutrons detected at 10° from 400 MeV/n Fe projectiles incident on all 20 g/cm^2 and 60 g/cm^2 upstream targets followed by the 60 g/cm^2 downstream target of the same material 186
8.37 Ratio of Monte Carlo results to experimental results for every data point from the upstream target neutron dataset 188
8.38 Components of Figure 8.37 for each front target 190
8.39 Components of Figure 8.37 for each detector angle 191
8.40 Components of Figure 8.37 for each projectile species 192
8.41 Components of Figure 8.37 for each projectile energy 193
8.42 Ratio of Monte Carlo results to experimental results for every data point from the downstream target neutron dataset 196
8.43 Components of Figure 8.42 for each front target 198
8.44 Components of Figure 8.42 for each detector angle 199
8.45 Components of Figure 8.42 for each projectile species 200
8.46 Components of Figure 8.42 for each projectile energy 201
8.47 Ratio of PHITS results to MCNP results for every data point from the upstream target neutron dataset 203
8.48 Components of Figure 8.47 for each front target 205
8.49 Components of Figure 8.47 for each detector angle 206
8.50 Components of Figure 8.47 for each projectile species 207
8.51 Components of Figure 8.47 for each projectile energy 208
8.52 Ratio of PHITS results to MCNP results for every data point from the downstream target neutron dataset 210
8.53 Components of Figure 8.52 for each front target 212
8.54 Components of Figure 8.52 for each detector angle 213
8.55 Components of Figure 8.52 for each projectile species 214
8.56 Components of Figure 8.52 for each projectile energy 215
8.57 Effective dose versus projectile mass for all systems 222
8.58 Effective dose versus detector angle for all systems 223
8.59 Pictured is the impact of solar cycle on GCR flux. 227

8.60 Total GCR effective dose E_{GCR} at 10° 229
8.61 GCR effective dose for W=80 in each detector 231
8.62 Upstream contribution to total GCR effective dose E_{GCR} at 10° 232
8.63 Downstream contribution to total GCR effective dose E_{GCR} at 10° 233
8.64 Total GCR effective dose E_{GCR} at 10° by source ion 233
8.65 GCR effective dose originating from the upstream target for W=80 in each detector broken down by source ion species contribution 234
8.66 GCR effective dose originating from the downstream target and room scattering for W=80 in each detector broken down by source ion species contribution 235
8.67 Total GCR effective dose for W=80 in each detector broken down by source ion species contribution 236
8.68 Total GCR effective dose E_{GCR} at 10° for various W 239
8.69 Effective dose per GCR source particle for whole range of W values in each detector 240
8.70 Total GCR effective dose E_{GCR} at 10° for various W but normalized to abundances associated with W=0 241
8.71 Relative effective dose per W=0 GCR source particle for whole range of W values in each detector 242

9.1 Binder loading screen 247
9.2 Binder repository directory 247
9.3 Initial SHAEDIT page 248
9.4 Mandatory initial prompts for running SHAEDIT 248
9.5 SHAEDIT plot construction options 250
9.6 SHAEDIT example plot and other options 251
9.7 SHAEDIT interface for viewing text files of plotted spectra 252

B.1 Production point (median) and effective target thickness (minimum thickness containing 80% of neutrons produced in a given energy bin) for all systems measured in the November 2016 experiment. 269

B.2 Production point (median) and effective target thickness (minimum thickness containing 80% of neutrons produced in a given energy bin) for all systems measured in the November 2017 experiment. 270
B.3 Neutron production corrections for 400 MeV H on 20 g/cm^2 Al 271
B.4 Neutron production corrections for 400 MeV H on 20 g/cm^2 HDPE 271
B.5 Neutron production corrections for 400 MeV H on 40 g/cm^2 HDPE 272
B.6 Neutron production corrections for 400 MeV H on 60 g/cm^2 HDPE 272
B.7 Neutron production corrections for 400 MeV H on 20 g/cm^2 AlPE 272
B.8 Neutron production corrections for 400 MeV H on 60 g/cm^2 AlPE 273
B.9 Neutron production corrections for 800 MeV H on 20 g/cm^2 HDPE 273
B.10 Neutron production corrections for 800 MeV H on 40 g/cm^2 HDPE 273
B.11 Neutron production corrections for 800 MeV H on 60 g/cm^2 HDPE 274
B.12 Neutron production corrections for 800 MeV H on 20 g/cm^2 AlPE 274
B.13 Neutron production corrections for 800 MeV H on 60 g/cm^2 AlPE 274
B.14 Neutron production corrections for 2500 MeV H on 20 g/cm^2 Al 275
B.15 Neutron production corrections for 2500 MeV H on 40 g/cm^2 Al 275
B.16 Neutron production corrections for 2500 MeV H on 60 g/cm^2 Al 275
B.17 Neutron production corrections for 2500 MeV H on 20 g/cm^2 HDPE 276
B.18 Neutron production corrections for 2500 MeV H on 40 g/cm^2 HDPE 276
B.19 Neutron production corrections for 2500 MeV H on 60 g/cm^2 HDPE 276
B.20 Neutron production corrections for 2500 MeV H on 20 g/cm^2 AlPE 277
B.21 Neutron production corrections for 2500 MeV H on 60 g/cm^2 AlPE 277
B.22 Neutron production corrections for 400 MeV/n He on 20 g/cm^2 HDPE . . . 277
B.23 Neutron production corrections for 400 MeV/n He on 40 g/cm^2 HDPE . . . 278
B.24 Neutron production corrections for 400 MeV/n He on 60 g/cm^2 HDPE . . . 278
B.25 Neutron production corrections for 400 MeV/n He on 20 g/cm^2 AlPE 278
B.26 Neutron production corrections for 400 MeV/n He on 60 g/cm^2 AlPE 279
B.27 Neutron production corrections for 800 MeV/n He on 20 g/cm^2 Al 279
B.28 Neutron production corrections for 800 MeV/n He on 40 g/cm^2 Al 279
B.29 Neutron production corrections for 800 MeV/n He on 60 g/cm^2 Al 280

B.30 Neutron production corrections for 800 MeV/n He on 20 g/cm^2 HDPE . . . 280
B.31 Neutron production corrections for 800 MeV/n He on 40 g/cm^2 HDPE . . . 280
B.32 Neutron production corrections for 800 MeV/n He on 60 g/cm^2 HDPE . . . 281
B.33 Neutron production corrections for 800 MeV/n He on 20 g/cm^2 AlPE 281
B.34 Neutron production corrections for 800 MeV/n He on 60 g/cm^2 AlPE 281
B.35 Neutron production corrections for 1500 MeV/n He on 20 g/cm^2 Al 282
B.36 Neutron production corrections for 1500 MeV/n He on 40 g/cm^2 Al 282
B.37 Neutron production corrections for 1500 MeV/n He on 60 g/cm^2 Al 282
B.38 Neutron production corrections for 1500 MeV/n He on 20 g/cm^2 HDPE . . 283
B.39 Neutron production corrections for 1500 MeV/n He on 40 g/cm^2 HDPE . . 283
B.40 Neutron production corrections for 1500 MeV/n He on 60 g/cm^2 HDPE . . 283
B.41 Neutron production corrections for 1500 MeV/n He on 20 g/cm^2 AlPE . . . 284
B.42 Neutron production corrections for 1500 MeV/n He on 60 g/cm^2 AlPE . . . 284
B.43 Neutron production corrections for 400 MeV/n C on 20 g/cm^2 Al 284
B.44 Neutron production corrections for 400 MeV/n C on 40 g/cm^2 Al 285
B.45 Neutron production corrections for 400 MeV/n C on 60 g/cm^2 Al 285
B.46 Neutron production corrections for 400 MeV/n C on 20 g/cm^2 HDPE 285
B.47 Neutron production corrections for 400 MeV/n C on 40 g/cm^2 HDPE 286
B.48 Neutron production corrections for 400 MeV/n C on 60 g/cm^2 HDPE 286
B.49 Neutron production corrections for 400 MeV/n C on 20 g/cm^2 AlPE 286
B.50 Neutron production corrections for 400 MeV/n C on 60 g/cm^2 AlPE 287
B.51 Neutron production corrections for 800 MeV/n C on 20 g/cm^2 Al 287
B.52 Neutron production corrections for 800 MeV/n C on 40 g/cm^2 Al 287
B.53 Neutron production corrections for 800 MeV/n C on 60 g/cm^2 Al 288
B.54 Neutron production corrections for 800 MeV/n C on 20 g/cm^2 HDPE 288
B.55 Neutron production corrections for 800 MeV/n C on 40 g/cm^2 HDPE 288
B.56 Neutron production corrections for 800 MeV/n C on 60 g/cm^2 HDPE 289
B.57 Neutron production corrections for 800 MeV/n C on 20 g/cm^2 AlPE 289
B.58 Neutron production corrections for 800 MeV/n C on 60 g/cm^2 AlPE 289
B.59 Neutron production corrections for 1500 MeV/n C on 20 g/cm^2 Al 290

B.60 Neutron production corrections for 1500 MeV/n C on 40 g/cm^2 Al 290
B.61 Neutron production corrections for 1500 MeV/n C on 60 g/cm^2 Al 290
B.62 Neutron production corrections for 1500 MeV/n C on 20 g/cm^2 HDPE . . . 291
B.63 Neutron production corrections for 1500 MeV/n C on 40 g/cm^2 HDPE . . . 291
B.64 Neutron production corrections for 1500 MeV/n C on 60 g/cm^2 HDPE . . . 291
B.65 Neutron production corrections for 1500 MeV/n C on 20 g/cm^2 AlPE 292
B.66 Neutron production corrections for 1500 MeV/n C on 60 g/cm^2 AlPE 292
B.67 Neutron production corrections for 400 MeV/n Si on 20 g/cm^2 Al 292
B.68 Neutron production corrections for 400 MeV/n Si on 40 g/cm^2 Al 293
B.69 Neutron production corrections for 400 MeV/n Si on 60 g/cm^2 Al 293
B.70 Neutron production corrections for 400 MeV/n Si on 20 g/cm^2 HDPE . . . 293
B.71 Neutron production corrections for 400 MeV/n Si on 40 g/cm^2 HDPE . . . 294
B.72 Neutron production corrections for 400 MeV/n Si on 60 g/cm^2 HDPE . . . 294
B.73 Neutron production corrections for 400 MeV/n Si on 20 g/cm^2 AlPE 294
B.74 Neutron production corrections for 400 MeV/n Si on 60 g/cm^2 AlPE 295
B.75 Neutron production corrections for 800 MeV/n Si on 20 g/cm^2 Al 295
B.76 Neutron production corrections for 800 MeV/n Si on 40 g/cm^2 Al 295
B.77 Neutron production corrections for 800 MeV/n Si on 60 g/cm^2 Al 296
B.78 Neutron production corrections for 800 MeV/n Si on 20 g/cm^2 HDPE . . . 296
B.79 Neutron production corrections for 800 MeV/n Si on 40 g/cm^2 HDPE . . . 296
B.80 Neutron production corrections for 800 MeV/n Si on 60 g/cm^2 HDPE . . . 297
B.81 Neutron production corrections for 800 MeV/n Si on 20 g/cm^2 AlPE 297
B.82 Neutron production corrections for 800 MeV/n Si on 60 g/cm^2 AlPE 297
B.83 Neutron production corrections for 1500 MeV/n Si on 20 g/cm^2 Al 298
B.84 Neutron production corrections for 1500 MeV/n Si on 40 g/cm^2 Al 298
B.85 Neutron production corrections for 1500 MeV/n Si on 60 g/cm^2 Al 298
B.86 Neutron production corrections for 1500 MeV/n Si on 20 g/cm^2 HDPE . . . 299
B.87 Neutron production corrections for 1500 MeV/n Si on 40 g/cm^2 HDPE . . . 299
B.88 Neutron production corrections for 1500 MeV/n Si on 60 g/cm^2 HDPE . . . 299
B.89 Neutron production corrections for 1500 MeV/n Si on 20 g/cm^2 AlPE . . . 300

B.90 Neutron production corrections for 1500 MeV/n Si on 60 g/cm^2 AlPE . . . 300
B.91 Neutron production corrections for 400 MeV/n Fe on 20 g/cm^2 HDPE . . . 300
B.92 Neutron production corrections for 400 MeV/n Fe on 40 g/cm^2 HDPE . . . 301
B.93 Neutron production corrections for 400 MeV/n Fe on 60 g/cm^2 HDPE . . . 301
B.94 Neutron production corrections for 400 MeV/n Fe on 20 g/cm^2 AlPE 301
B.95 Neutron production corrections for 400 MeV/n Fe on 60 g/cm^2 AlPE 302
B.96 Neutron production corrections for 800 MeV/n Fe on 20 g/cm^2 HDPE . . . 302
B.97 Neutron production corrections for 800 MeV/n Fe on 40 g/cm^2 HDPE . . . 302
B.98 Neutron production corrections for 800 MeV/n Fe on 60 g/cm^2 HDPE . . . 303
B.99 Neutron production corrections for 800 MeV/n Fe on 20 g/cm^2 AlPE 303
B.100 Neutron production corrections for 800 MeV/n Fe on 60 g/cm^2 AlPE 303
B.101 Neutron production corrections for 1500 MeV/n Fe on 20 g/cm^2 Al 304
B.102 Neutron production corrections for 1500 MeV/n Fe on 40 g/cm^2 Al 304
B.103 Neutron production corrections for 1500 MeV/n Fe on 60 g/cm^2 Al 304
B.104 Neutron production corrections for 1500 MeV/n Fe on 20 g/cm^2 HDPE . . . 305
B.105 Neutron production corrections for 1500 MeV/n Fe on 40 g/cm^2 HDPE . . . 305
B.106 Neutron production corrections for 1500 MeV/n Fe on 60 g/cm^2 HDPE . . . 305
B.107 Neutron production corrections for 1500 MeV/n Fe on 20 g/cm^2 AlPE . . . 306
B.108 Neutron production corrections for 1500 MeV/n Fe on 60 g/cm^2 AlPE . . . 306

C.1 Upstream target neutrons from 400 MeV/n H incident on Al targets 308
C.2 Upstream target neutrons from 400 MeV/n H incident on HDPE targets . . 309
C.3 Upstream target neutrons from 400 MeV/n H incident on AlPE targets . . . 310
C.4 Upstream target neutrons from 800 MeV/n H incident on HDPE targets . . 311
C.5 Upstream target neutrons from 800 MeV/n H incident on AlPE targets . . . 312
C.6 Upstream target neutrons from 2500 MeV/n H incident on Al targets 313
C.7 Upstream target neutrons from 2500 MeV/n H incident on HDPE targets . 314
C.8 Upstream target neutrons from 2500 MeV/n H incident on AlPE targets . . 315
C.9 Upstream target neutrons from 400 MeV/n He incident on HDPE targets . 316
C.10 Upstream target neutrons from 400 MeV/n He incident on AlPE targets . . 317

C.11 Upstream target neutrons from 800 MeV/n He incident on Al targets 318
C.12 Upstream target neutrons from 800 MeV/n He incident on HDPE targets . 319
C.13 Upstream target neutrons from 800 MeV/n He incident on AlPE targets . . 320
C.14 Upstream target neutrons from 1500 MeV/n He incident on Al targets . . . 321
C.15 Upstream target neutrons from 1500 MeV/n He incident on HDPE targets . 322
C.16 Upstream target neutrons from 1500 MeV/n He incident on AlPE targets . 323
C.17 Upstream target neutrons from 400 MeV/n C incident on Al targets 324
C.18 Upstream target neutrons from 400 MeV/n C incident on HDPE targets . . 325
C.19 Upstream target neutrons from 400 MeV/n C incident on AlPE targets . . . 326
C.20 Upstream target neutrons from 800 MeV/n C incident on Al targets 327
C.21 Upstream target neutrons from 800 MeV/n C incident on HDPE targets . . 328
C.22 Upstream target neutrons from 800 MeV/n C incident on AlPE targets . . . 329
C.23 Upstream target neutrons from 1500 MeV/n C incident on Al targets 330
C.24 Upstream target neutrons from 1400 MeV/n C incident on HDPE targets . 331
C.25 Upstream target neutrons from 1400 MeV/n C incident on AlPE targets . . 332
C.26 Upstream target neutrons from 400 MeV/n Si incident on Al targets 333
C.27 Upstream target neutrons from 400 MeV/n Si incident on HDPE targets . . 334
C.28 Upstream target neutrons from 400 MeV/n Si incident on AlPE targets . . 335
C.29 Upstream target neutrons from 800 MeV/n Si incident on Al targets 336
C.30 Upstream target neutrons from 800 MeV/n Si incident on HDPE targets . . 337
C.31 Upstream target neutrons from 800 MeV/n Si incident on AlPE targets . . 338
C.32 Upstream target neutrons from 1470 MeV/n Si incident on Al targets 339
C.33 Upstream target neutrons from 1500 MeV/n Si incident on HDPE targets . 340
C.34 Upstream target neutrons from 1500 MeV/n Si incident on AlPE targets . . 341
C.35 Upstream target neutrons from 400 MeV/n Fe incident on HDPE targets . . 342
C.36 Upstream target neutrons from 400 MeV/n Fe incident on AlPE targets . . 343
C.37 Upstream target neutrons from 800 MeV/n Fe incident on HDPE targets . . 344
C.38 Upstream target neutrons from 800 MeV/n Fe incident on AlPE targets . . 345
C.39 Upstream target neutrons from 1470 MeV/n Fe incident on Al targets . . . 346
C.40 Upstream target neutrons from 1463 MeV/n Fe incident on HDPE targets . 347

C.41 Upstream target neutrons from 1500 MeV/n Fe incident on AlPE targets . . 348
C.42 Downstream target neutrons from 400 MeV/n H incident on Al targets . . . 350
C.43 Downstream target neutrons from 400 MeV/n H incident on HDPE targets 351
C.44 Downstream target neutrons from 400 MeV/n H incident on AlPE targets . 352
C.45 Downstream target neutrons from 800 MeV/n H incident on Al targets . . . 353
C.46 Downstream target neutrons from 800 MeV/n H incident on HDPE targets 354
C.47 Downstream target neutrons from 800 MeV/n H incident on AlPE targets . 355
C.48 Downstream target neutrons from 2500 MeV/n H incident on Al targets . . 356
C.49 Downstream target neutrons from 2500 MeV/n H incident on HDPE targets 357
C.50 Downstream target neutrons from 2500 MeV/n H incident on AlPE targets 358
C.51 Downstream target neutrons from 400 MeV/n He incident on Al targets . . 359
C.52 Downstream target neutrons from 400 MeV/n He incident on HDPE targets 360
C.53 Downstream target neutrons from 400 MeV/n He incident on AlPE targets 361
C.54 Downstream target neutrons from 800 MeV/n He incident on Al targets . . 362
C.55 Downstream target neutrons from 800 MeV/n He incident on HDPE targets 363
C.56 Downstream target neutrons from 800 MeV/n He incident on AlPE targets 364
C.57 Downstream target neutrons from 1500 MeV/n He incident on Al targets . . 365
C.58 Downstream target neutrons from 1500 MeV/n He incident on HDPE targets 366
C.59 Downstream target neutrons from 1500 MeV/n He incident on AlPE targets 367
C.60 Downstream target neutrons from 400 MeV/n C incident on Al targets . . . 368
C.61 Downstream target neutrons from 400 MeV/n C incident on HDPE targets 369
C.62 Downstream target neutrons from 400 MeV/n C incident on AlPE targets . 370
C.63 Downstream target neutrons from 800 MeV/n C incident on Al targets . . . 371
C.64 Downstream target neutrons from 800 MeV/n C incident on HDPE targets 372
C.65 Downstream target neutrons from 800 MeV/n C incident on AlPE targets . 373
C.66 Downstream target neutrons from 1500 MeV/n C incident on Al targets . . 374
C.67 Downstream target neutrons from 1400 MeV/n C incident on HDPE targets 375
C.68 Downstream target neutrons from 1400 MeV/n C incident on AlPE targets 376
C.69 Downstream target neutrons from 400 MeV/n Si incident on Al targets . . . 377
C.70 Downstream target neutrons from 400 MeV/n Si incident on HDPE targets 378

C.71 Downstream target neutrons from 400 MeV/n Si incident on AlPE targets . 379
C.72 Downstream target neutrons from 800 MeV/n Si incident on Al targets . . . 380
C.73 Downstream target neutrons from 800 MeV/n Si incident on HDPE targets 381
C.74 Downstream target neutrons from 800 MeV/n Si incident on AlPE targets . 382
C.75 Downstream target neutrons from 1470 MeV/n Si incident on Al targets . . 383
C.76 Downstream target neutrons from 1500 MeV/n Si incident on HDPE targets 384
C.77 Downstream target neutrons from 1500 MeV/n Si incident on AlPE targets 385
C.78 Downstream target neutrons from 400 MeV/n Fe incident on Al targets . . 386
C.79 Downstream target neutrons from 400 MeV/n Fe incident on HDPE targets 387
C.80 Downstream target neutrons from 400 MeV/n Fe incident on AlPE targets . 388
C.81 Downstream target neutrons from 800 MeV/n Fe incident on Al targets . . 389
C.82 Downstream target neutrons from 800 MeV/n Fe incident on HDPE targets 390
C.83 Downstream target neutrons from 800 MeV/n Fe incident on AlPE targets . 391
C.84 Downstream target neutrons from 1470 MeV/n Fe incident on Al targets . . 392
C.85 Downstream target neutrons from 1463 MeV/n Fe incident on HDPE targets 393
C.86 Downstream target neutrons from 1500 MeV/n Fe incident on AlPE targets 394

Chapter 1

Introduction

1.1 Overview and goals

This work involves the characterization of neutron yield spectra in an experiment where five ion species (H, He, C, Si, and Fe) each at three different energies (400, 800, and 1500-2500 MeV/n) characteristic of galactic cosmic rays (GCRs) were accelerated into two thick targets composed of materials used for shielding in outer space (aluminum and polyethylene). Both targets were placed along the beam axis to emulate the walls of an enclosed spacecraft. The secondary particles produced were then detected in six organic liquid scintillators placed at different angles (spanning 10° to 135°) with respect to a primary target and beamline. All detected neutrons were either produced in the primary upstream target directly or produced/scattered in/from the downstream target or elsewhere in the room to then strike the detectors. All tested beam and target combinations totaled 500 hours of beam time.

In addition to the analysis techniques required to process the raw data into energy spectra, the substantial quantity of data brings about additional engineering challenges. If handled manually, this type of analysis is extremely prone to individual errors going unnoticed in addition to consuming a substantial amount of time. Thus, a large focus of this work involves automating the analysis steps wherever possible. The immense amount of data produced at the end of this analysis is also difficult for an individual to fully digest at once, so another focus of this work is to determine a number of ways that the final results of this experiment can be visually represented in a concise fashion.

So, this project has substantial components in both methodology development and implementation as well as more general engineering challenges associated with massive datasets such as assuring data quality and consistency and representing the data succinctly. The distinct goals of this research work are enumerated below.

1. Generate time-of-flight double-differential neutron yield spectra for neutrons produced in the thick upstream target
2. Develop and implement a pulse height deconvolution methodology to characterize the energy spectra of downstream target and room scattered neutrons striking the detectors
3. Optimize the analysis work flow as much as possible to make processing such a large volume of data feasible and consistently accurate
4. Engineer ways to concisely visualize these results in a digestible fashion
5. Characterize trends of where Monte Carlo simulated results are in disagreement with experimental results
6. Compile and host the final data in a way that is accessible to any future scientist

1.2 Original contribution

Put briefly, this work's original contributions are:

1. Generalization, upscaling, and automation of existing time-of-flight methodologies utilized by prior work [2]
2. Development of production point and effective target thickness corrections used to improve the accuracy of the time-of-flight-derived upstream target yield spectra
3. Development of a robust and automated deconvolution algorithm used to characterize the neutrons produced in the downstream target
4. Building, execution, and post-processing of MCNP6 simulations emulating the experiment

5. Writing and post-processing neutron tallies for PHITS simulations of the experiment
6. Performing a systematic analysis to identify locations of consistent disagreement between the simulated and experimental results
7. Consolidation of the large volume of neutron data to a more digestible and engineering-focused form through an effective dose analysis
8. Development of an online data viewing tool for all results (simulated and experimental) pertaining to this experiment

Providing additional context, the original portions of this work can be broken into a more broad discussion of what about the experiment and analyses presented in this work are scientifically unique (Section 1.2.1) and a more specific discussion detailing what portions of this work were developed and performed by me versus that accomplished by other individuals also involved with these experiments (Section 1.2.2).

1.2.1 Scientifically novel facets of this work

- The measurement of double-differential neutron yields at the six off-axis angles in this experiment from the tested projectile beams incident on thick aluminum, polyethylene, and hybrid targets of the thicknesses used in this work had never been performed before (detailed in Reference 2).
- The inclusion of a second thick target to emulate a back wall which serves as a secondary neutron production zone appears to be completely novel, and this work specifically focuses on the characterization of these back target-produced neutrons.
- MCNP and PHITS calculations were performed to fully emulate all experimental measurements. This work includes a comprehensive comparison of these modeled results to the experimental data and discerns where they deviate, pointing toward areas of improvement in these codes and the physics models within them.
- The results of this work serve as a benchmark dataset against which other models can also be compared.

- This work provides preliminary guidance on spacecraft shielding design and optimization for future deep-space missions.

1.2.2 Unique efforts relative to other analyses of these experiments

This section overviews my specific role in this experiment in the context of the other analysis efforts pertaining to this experiment. This section contains some specific details explained in future chapters but feels best suited for inclusion here in the introductory chapter.

The experimental campaign featured in this work took place across three experiments in March 2016, November 2016, and November 2017. The experiment was designed and had already undergone a commissioning run prior to my involvement in the project. Additionally, I was not involved with the collection or time-of-flight analysis of any data collected in the initial full experiment conducted in March 2016. Prior works are based on the design, execution, and analysis of this initial March 2016 experiment [2, 3, 4]. My work involved the characterization of upstream target-produced neutrons for the November 2016 and 2017 experiments and characterization of the downstream target-produced and room-scattered neutrons for all three experiments.

I was present for and actively involved in the experiment execution and data acquisition for the experiments which took place in November of 2016 and 2017 and comprised 400 of the total 500 hours of beam time involved in the measurement campaign. For both experiments, I assisted with reconfiguring the experiment room for each tested system, performed live analysis and diagnostics on the data acquisition computer to ensure the experiment was running smoothly, and made decisions relevant to running the experiment such as adjusting voltages of the start scintillators or changing the beam current to affect the good beam fraction and detector live time. Additionally, in the final November 2017 experiment, I took charge of managing the experimental schedule, making sure we had allotted enough time for each beam, sequenced the runs to minimize time spent reconfiguring the experiment room, and factored in downtime and the constraints imposed by the facility which provided us with each beam.

At its core, the time-of-flight analysis presented in this work is rooted in earlier work [2]. The majority of the data filtering analyses are relatively unchanged from what had been developed prior, barring the fixes necessary to correct for some of the minor experimental setbacks which occurred while collecting the data. The unique challenges posed to me for the data filtering portion of the analysis was generalizing and automating the existing procedures to accommodate the massive volume of data collected. Ultimately, this involved heavy amounts of scripting to automate every task not requiring direct human input or judgment.

In the later stages of the time-of-flight analysis where spectra of raw counts are normalized and converted to yield spectra, I implemented several major improvements. The most noteworthy of these is the development of a fully continuous production point correction which resolves inaccuracies attributable to the initial assumption that the neutrons produced in the upstream target are all produced at the target's center point. Related to that correction, I also developed an effective target thickness correction which provides a more realistic assumption about the distribution of neutron production along the length of the target, allowing for use of a reduced variance in flight path extremes which can notably reduce the energy resolution uncertainty in the final spectra. To handle the large volume of data and reduce the role of human judgment involved, I created a robust and generalized rebinning algorithm to meet numerous constraints; it also improved the prior bin midpoint methodology by determining a yield-weighted midpoint for each final bin. The uncertainty quantification efforts for the upstream target-produced neutron spectra in this work were also generalized and made to be specific for each data point within each spectrum rather than using more general, global uncertainty values as had been done in prior work [2].

As mentioned earlier, all analyses pertaining to the characterization and uncertainty quantification of downstream target-produced and room-scattered neutrons are original to this work, though some overlap in methodology is present in the data filtering processes.

My work also involved the construction, execution, and post-processing of MCNP simulations of the November 2016 and 2017 experiments, using the simulations conducted in prior work as a framework for the automated generation of these MCNP input files [3]. While the post-processing methodologies for upstream target-produced secondaries had been

created in prior work [3], I had to develop a methodology for extracting the downstream target-produced and room-scattered neutron contributions without creating a need to rerun the already completed simulations of the March 2016 experiment. My role in the PHITS simulations, which used a similar geometry to the MCNP simulations, pertained to the design and post-processing of the neutron tallies.

All results presented in this dissertation are original to this work. The individual upstream target neutron spectra showcased are only those from the November 2016 and 2017 experiments, but neutron results from all three experiments are included in the downstream target neutron spectra, the greater systematic assessment of the performance of the Monte Carlo codes, and the effective dose calculations.

After the final experiment, I took up the mantle of data curator between the various students at the University of Tennessee (UT) performing the analyses to convert raw experimental data to secondary particle yield spectra and the scientists at NASA who will ultimately be conducting extensive further analyses utilizing these spectra. While serving this role, I had convenient access to all of the experimental and simulated results, inspiring me to generate an online tool for the viewing of all spectral results of this experimental campaign.

So, in short, my original contributions to this work comprise the analysis of all back-target produced neutrons and the upstream target-produced neutrons from the November 2016 and 2017 experiments. The methodology for the downstream target-produced neutrons is original to this work. This work generalized, upscaled, and automated as much of the upstream target analysis as possible while also implementing several large improvements to the methods previously utilized. This work also contains a comprehensive and systematic look at the results and their trends, both in isolation of the experiment as well as in comparison with the Monte Carlo simulated results. Finally, I developed an online tool for convenient viewing of all collected and simulated experimental data.

1.3 Outline

The structure of the remaining dissertation is outlined in the list below.

- Chapter 2 details the background details relevant to this work. This includes information on the radiation in space, the reaction mechanisms most relevant to this work, studies which motivated these experiments, NASA's larger goals for this project of which this work is a part of, and the mechanisms of light production in scintillators.
- Chapter 3 details the experimental campaign conducted at NSRL.
- Chapter 4 details the analysis procedures relevant to the neutrons produced in the upstream targets which traveled directly to the neutron detectors and were characterized using time-of-flight techniques. This is broken down into steps of filtering neutron events from the upstream target from all other particles and background neutrons followed by then converting raw spectra of counts in channels to double-differential yield spectra.
- Chapter 5 details the statistical and systematic uncertainty quantification process for the neutrons produced in the upstream target.
- Chapter 6 contains discussion of all analysis and uncertainty quantification pertaining to the downstream target-produced and room-scattered neutrons, characterized using a deconvolution technique.
- Chapter 7 details the Monte Carlo simulations using MCNP6 and PHITS 2.88 to emulate the whole experimental campaign and it's full-room geometry [5, 6].
- Chapter 8 explores the results of this work. It is broken down into Section 8.1 which looks at individual spectra against each other and/or simulated spectra to observe general trends, Section 8.2 which performs a systematic analysis of the MCNP and PHITS simulations against experimental results and each other to discern overarching trends, and Section 8.3 which seeks to collapse the experimental axes present in the neutron data to make comparison of the various individual experimental axes, particularly target choice, more digestible.

- Chapter 9 discusses the public availability of this data and provides a walkthrough of an online tool developed in this work for the purpose of making exploration of this massive dataset as accessible as possible.
- Chapter 10 presents the conclusions drawn from this work.
- Appendix A contains a list of the equipment used in these experiments.
- Appendix B contains all of the plots relevant to the production point and effective target thickness corrections discussed in Section 4.9.
- Appendix C contains individual neutron yield plots alongside Monte Carlo results for every single spectrum analyzed in this work.
- Appendix D contains comprehensive effective dose tables corresponding to the analysis presented in Section 8.3.
- Appendix E details the UT/NASA data file repository structure and the formatting of the text files within it.

Chapter 2

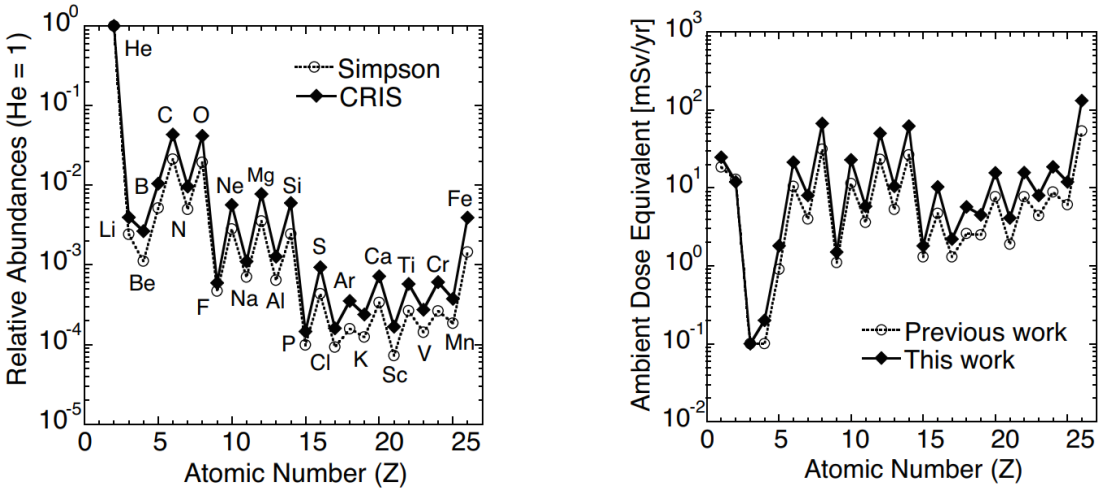
Background

This chapter seeks to outline the motivation for this work and provide the background information necessary to understand this motivation and some of the analysis presented.

2.1 Space radiation

The series of experiments whose results are presented in this work sought to emulate the galactic cosmic ray (GCR) induced radiation environment in an enclosed spacecraft. To understand why the beam projectiles utilized in this experiment were selected, it is worth briefly discussing the radiation environment in deep space.

Understanding the risk posed to astronauts by the radiation environment in space is imperative for planning long manned missions, including those to Mars. The radiation environment in deep space comes from two primary sources. The first is solar energetic particles (SEPs) which are primarily protons ejected from the sun during solar particle events (SPEs) such as flares and coronal mass ejections, lasting hours to days [7]. Due to the limited duration of SEP flux elevations, SEPs are generally viewed as an acute risk. Galactic cosmic rays (GCRs), which originate from outside of the solar system, are the second primary source of radiation in space and are roughly composed of 87% protons, 12% helium ions, and 1% heavier ions all the way up to uranium, though with decreasing abundances for higher masses [8]. Unlike SEP flux, GCR flux does not have impulsive fluctuations; it is fairly constant across time, though it does vary slightly with the 11-year solar cycle [8]. This makes GCR



(a) GCR relative elemental abundances

(b) Elemental dose contributions (lunar surface)

Figure 2.1: GCR elemental abundances for Z $\geq$ 2 and their contributions to dose equivalent on the lunar surface [9]

exposure a chronic radiation risk which must be mitigated constantly. As shown in Figure 2.1 for the GCR-induced radiation environment on the lunar surface, while the abundances of heavier ions diminish, their contribution to astronaut dose remains significant [9].

Dose is proportional to energy deposited by a particle which is proportional to the square of its charge, partially explaining the increased importance of the heavier GCR ions [10]. In a shielded environment, this effect is complicated by these incident GCR ions undergoing fragmentation/spallation reactions within the shielding material, creating secondaries with lower charge and thus greater penetrating power.

Due to the production and acceleration mechanisms of GCRs, the velocity distributions of each ion in the GCR spectrum are fairly similar; this is apparent when plotting their flux spectra against kinetic energy in MeV/nucleon. The kinetic energies of galactic cosmic rays span many decades, from very low energies up to 10^{20} eV [8], though the flux for each ion peaks between 100 MeV/n and 1 GeV/n as shown in Figure 2.2 [11]. This peak shifts to slightly higher energies during solar maximum, as will be highlighted later in Section 8.3.1. Thus, the selected beam energies of 400, 800, and 1500 MeV/n in this experiment seek to sample the most abundant regions of the GCR flux. For species selection, hydrogen and helium are fairly obvious choices given their overwhelming abundance in the GCR spectrum. To sample the heavier components, carbon, silicon, and iron beams were selected in part

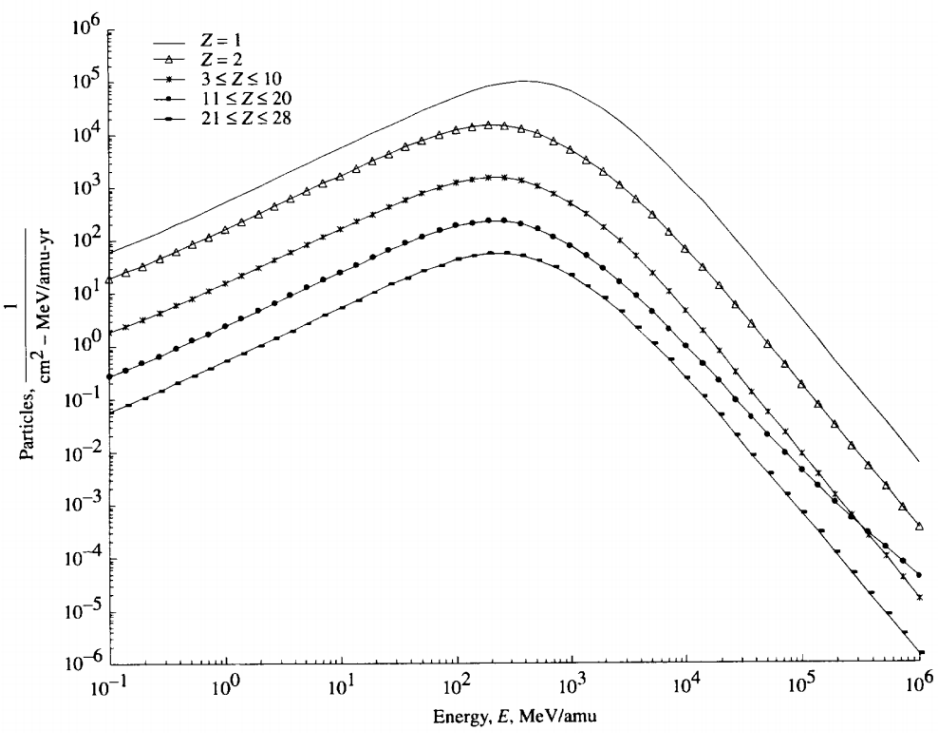


Figure 2.2: GCR fluxes for ions of various charges during the 1977 solar minimum [11]

because, relative to the other GCR ions of similar mass, they are the most abundant; this can be seen in Figure 2.1a. Additionally, these heavier nuclei were selected for a few physics reasons as well. ^{12}C, ^{28}Si, and ^{56}Fe are all even-even nuclei, and the population of the various nuclear shells and subshells in each affect their breakup. The increased nucleon clustering occurring in the breakup of the lighter nuclei, especially the alpha clustering of carbon breakup, are interesting physics this experiment desired to observe. Thus, these species spanning the range of various nuclear structure effects influencing breakup were selected.

In proximity to Earth, a third source of radiation exists: the trapped radiation belts. Earth is surrounded by belts of radiation trapped by the planet's magnetic field. For deep space missions, the effect of passing through the trapped radiation belts is marginal in comparison to the GCR and SPE contributions to the total effective dose over a whole mission. However, the trapped radiation belts are a strong driver of radiation risk for near-Earth missions, such as those onboard the International Space Station.

2.2 Collision mechanics

In this work, neutrons produced from the GCR-like beams incident on spacecraft-like shields/targets are studied. This section seeks to briefly detail what interaction mechanisms are at play to produce these neutrons.

As the beam projectile ions traverse the materials along the beamline, they lose energy through electronic collisions (ionizing target atoms while maintaining a straight-forward trajectory) and nuclear collisions. At lower energies, nuclear collisions often entail some form of elastic or inelastic scattering and deflection of the incident particle's trajectory while imparting some recoil energy onto the target nucleus. At the high, relativistic energies utilized in this experimental campaign, most nuclear reactions result in the fragmentation of the projectile and/or target nuclei. This process is typically described with the abrasion-ablation model, depicted in Figure 2.3 [12, 13, 14].

Phenomenologically, the abrasion-ablation process can be thought of as two distinct stages after the collision. In the first step, abrasion (or cascade), immediately following the collision, the excited projectile and target fragments leave behind a very excited "fireball" of nucleons (sometimes also referred to as the intermediate rapidity source) from the overlap region of the two nuclei during the collision. It is immediately followed by the ablation (or evaporation) stage where nucleons are ejected from the three agglomerates of nucleons undergoing nuclear deexcitation [14]. While peripheral collisions can result in only the shearing off of a few nucleons, more direct collisions can result in the complete destruction of the projectile and target nuclei.

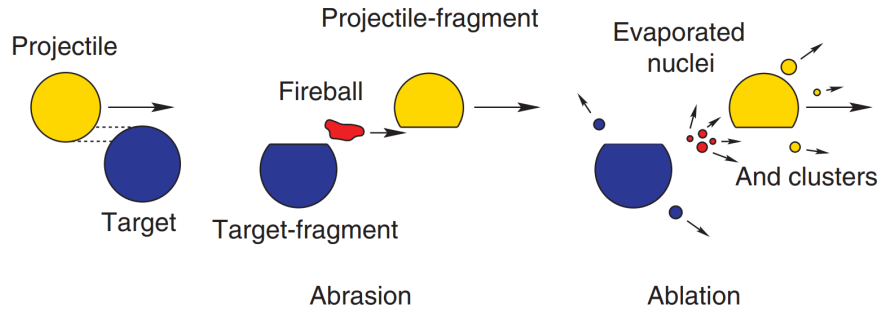


Figure 2.3: Stages of the abrasion-ablation model [14]

The mathematics describing the abundances of each secondary fragment produced (for heavy on heavy collisions) and their energy and angular distributions is rather complicated and is further detailed in References 12, 13, and 14. The most important takeaway for neutron production is to think of where neutrons are being produced and what their expected trajectories should be.

Generally, these collisions can be thought of as involving a target nucleus at rest in the lab frame and a projectile nucleus moving at the accelerated beam velocity. Upon collision, the projectile fragment retains most of its momentum, and the target fragment remains relatively at rest, though some momentum is exchanged between the two. The fireball of nucleons in the overlap region end up with momentum in the direction of the incident beam but with less magnitude, typically about one third to one half that of the projectile beam [15]. This is visualized in Figure 2.4 [16] (and can also be seen with the small arrows in Figure 2.3).

While evaporation is typically an isotropic process [16], in the lab frame, the evaporation-produced nucleons still must conserve the momentum of the fragment from which they are born. Thus, the neutrons measured in this work can be described as being characteristic of target fragment evaporation (typical of the neutrons at the lowest energies), projectile fragmentation (typical of the neutrons at the highest energies), and ablation of the fireball/intermediate rapidity (characteristic of neutrons between the two extremes).

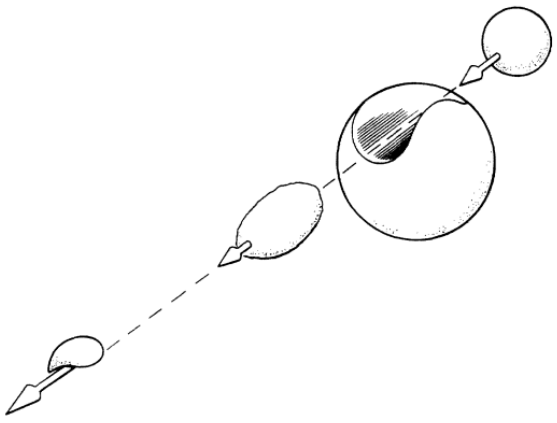


Figure 2.4: Visualization of the relative kinetic energies (from bottom left to top right) of the projectile fragment, fireball, target/target fragment, and pre-collision projectile [16]

Complex light ions (predominantly d, t, ^{3}He, and α) can be formed either through direct fragmentation or through the coalescence of neutrons, protons, and other lighter fragments which happen to lie in the same phase space as each other after a fragmentation reaction [16]. These complex light ions, as well as the liberated individual nucleons and the still-energetic projectile fragment, can go on to induce additional fragmentation reactions within the thick targets used in the experiments of this work, creating additional secondary particles.

2.3 Motivation for these experiments

Discrepancies exist between the various particle transport codes useful for modeling space radiation environments and the experimental data for these fragmentation cross sections [17], and these cross section discrepancies propagate into simulations employing realistic shielding materials and thicknesses, yielding sometimes stark differences in the production of neutrons and complex light ions in particular [18, 1].

This production of secondary particles from the fragmentation of projectile/target nuclei (which can then result in more fragmentation/spallation reactions) is even further complicated in an enclosed spacecraft environment: Radiation which penetrates the shielding and cabin can then undergo reactions while attempting to leave the spacecraft. Calculations by Dr. Tony Slaba et al. explored this effect along with the impacts of shielding thickness and the differences between transport codes; the most interesting results from that work are illustrated in Figure 2.5 [1]. In these simulations, a thin water slab in which dose equivalent was tallied was surrounded on both sides by either aluminum or polyethylene shields of variable thickness which were then bombarded with the GCR spectrum of ions. FLUKA, Geant4, MCNP6, and PHITS are well-known and widespread Monte Carlo transport codes, and 3DHZETRN is a deterministic transport code developed by NASA [19]. In Figure 2.5 two different physics model packages are utilized in Geant4, and three versions of 3DHZETRN with different angular resolutions are utilized where N=1 assumes all particles travel straight-ahead, N=2 allows for bi-directional neutron transport, and N=34 allows for particle transport in 34 different directions, effectively making it a decent approximation of full three-dimensional transport [1, 19]. The disagreement of the N=1

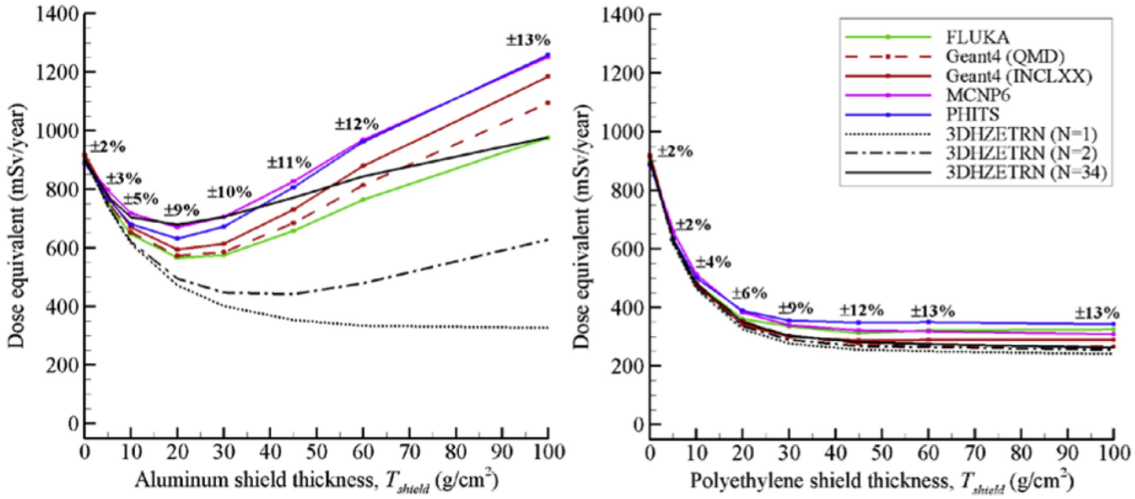


Figure 2.5: Simulated dose equivalent inside of a water slab sandwiched between two slabs of varying thicknesses of aluminum or polyethylene being bombarded by GCRs [1]

and N=2 versions of 3DHZETRN with the more physically realistic Monte Carlo codes and improved 3DHZETRN with propagation in more transverse directions emphasizes the significance of particles produced in the back wall of a spacecraft (or the downstream target in this work's experiment). While these results also depict the discrepancies between individual transport codes, the most noteworthy takeaway is that there seems to be an optimal shielding thickness when using aluminum.

Dr. Slaba's work illustrated that the majority (∼70%) of this buildup in dose equivalent at the higher thicknesses was from protons which in turn were produced in majority (∼75%) by neutron interactions [1]. The buildup of dose equivalent between two slabs of shielding material is the foundation of the series of experiments featured in this work where a similar scenario of an enclosed spacecraft being bombarded by GCRs was emulated experimentally at the NASA Space Radiation Laboratory.

2.4 NASA's goals for this project

This work is only a piece of a much larger project of NASA's; the title of the overarching project is "Thick Galactic Cosmic Rays (GCR) Shielding Project" and is under the Advanced Radiation Protection (ARP) project which is funded through NASA's Game Changing Development Program in NASA's Space Technology Mission Directorate. The Thick GCR

Shielding Project ultimately wishes to provide the information necessary to enable the design of passive GCR shielding in spacecraft. This overarching goal is broken into numerous discrete steps and substeps (and even more subdivisions) of which the work presented in this document is a part.*

The simulations which motivated this work, discussed in Section 2.3, identified that there is likely to be an optimal shielding thickness and also highlighted uncertainties in the available transport calculations. The experimental portion of the Thick GCR Shielding Project seeks to validate the existence of this optimal shielding thickness and assemble a benchmark dataset with quantified uncertainties against which the transport codes can be compared.

After the completion of the experimental measurements and the secondary particle yield analysis (and their uncertainty quantification), the portion of this project in which The University of Tennessee (UT) is involved, NASA plans to use the results for the following: First will be the development of a thick shield efficiency database (with accompanying uncertainties) containing dose, dose equivalent, and whole body effective dose as a function of shielding thickness for a variety of shielding materials. The development of this database will follow an extensive transport code benchmarking effort which should result in the identification and validation of an optimal shielding thickness. Following this will be substantial uncertainty quantification efforts seeking to estimate uncertainty in astronaut radiation exposure and risk calculations for spacecraft with thick shielding and to identify the largest uncertainties present in simulated transport of GCRs through thick shields.

The University of Tennessee's role in this project was in the design, execution, and data analysis of the thick-target experiments at NSRL. While the analysis of the raw experimental data was completed almost exclusively by UT, the design and execution of the experiment was a collaborative effort between UT, NASA, NSRL, and a few other individuals. The data analysis was separated into multiple categories based on when the measurements were made (experiments in March 2016, November/December 2016, or November 2017), detector type (organic liquid scintillator or NaI), secondary particles (neutrons or charged particles),

*The information presented in this section on the objectives of the Thick GCR Shielding Project is sourced from the 2014 grant proposal document which outlines the entire project but is not published or publicly available.

and, for neutrons only, production location (upstream target or downstream target). These analysis categories were split across six graduate students at UT and a postdoctoral fellow at NASA Langley Research Center. The analysis for which I was responsible and is presented in this work pertains to all neutrons detected in the organic liquid scintillation detectors, from both targets, for the second two experiments (conducted in November 2016 and 2017) and the neutrons from only the downstream target for the first experiment (conducted in March 2016). A more comprehensive outline of this division of labor which also includes the accompanying Monte Carlo simulations can be found in Section 1.2.2.

The "minimum success criteria" of the Thick GCR Shielding Project are (1) the completion of databases of experimental thick target beam measurements and transport code benchmarks and (2) the quantification of transport uncertainty in thick aluminum and polyethylene shields for a range of thicknesses. The work presented in this document slot into the first goal in providing neutron yield databases from the thick target experiments at NSRL. The neutron database and accompanying Monte Carlo simulations will assist in the larger benchmarking and uncertainty quantification efforts to be conducted at NASA. The goals for this dissertation project presented in Section 1.1 pertain to meeting the objectives set by NASA as well as performing additional work to discern trends in the experimental and simulated results and to promote exposure of this large dataset to other scientists in the field.

2.5 Light production in organic liquid scintillators

Understanding the production of light in organic liquid scintillators is vital to the methodology used to characterize the neutrons produced in the downstream target as detailed later in Chapter 6. The methodology relies on possessing knowledge of the light response of the used liquid scintillators to incident neutrons. Presenting a challenge, the neutron energies relevant to this work are well above the well-studied energy range of fission neutrons and above where purely mono-energetic neutron sources exist. As will be discussed in greater detail in Chapter 6, this work ultimately opts to use model-generated detector response functions. However, one must understand the physics of light production in

liquid scintillators to have confidence in these models and understand why the methodology outlined in Chapter 6 works (and appreciate the challenges associated with those methods).

When radiation deposits energy in a liquid scintillator, primarily composed of molecules of carbon and hydrogen, the electrons in the molecules of the scintillation fluid are elevated to higher energy levels, and light is produced as the molecules de-excite to lower states, primarily through prompt fluorescence. Since an elevated state can de-excite to a variety of different vibrational states of the ground state and quench through a variety of other non-light-producing mechanisms, the light production for two identical charged particles depositing energy in an organic scintillator will vary [20].

Introducing more variance into the light response is the fact that neutrons are indirectly ionizing radiation. To deposit energy in the scintillation fluid, neutrons must first strike one of the carbon or hydrogen nuclei, creating ionized particles which can then deposit energy through electronic stopping power and possibly additional nuclear collisions. Firstly, the collision and following reaction itself is stochastic. Proton recoil is the primary neutron reaction which causes light production in organic scintillators; however, neutrons can also strike the carbon nuclei, causing them to either simply recoil or undergo a 3-alpha breakup reaction ($n+^{12}C \rightarrow n' + 3\alpha$) or a number of other possible reactions. All of these resulting ions deposit energy (and, thus, produce light) differently from each other. Additionally, the energy imparted onto the scintillation fluid nuclei from a neutron collision is, itself, a stochastic process. Furthermore, in the realm of high energy neutrons such as in this experiment, it is possible (and, eventually, quite likely) to produce recoil protons which will escape the scintillation volume before depositing all of their energy. Thus, for even a mono-energetic neutron source, the light response of an organic liquid scintillator is distributed.

The light response of organic liquid scintillators has been studied extensively. Some studies have produced parameterized light response functions for total energy deposition of various charged particles in various scintillation materials [21, 22] while others provide a more detailed parameterization based on particle species, energy, and stopping power in various materials [23, 24]. These parameterizations typically are based upon fitting the extensive detector response data taken by V.V. Verbinski in 1968 in addition to other experimental measurements [25]. The parameterizations featured in Reference 22 are shown below in

Equations 2.1 and 2.2 using the parameters shown in Table 2.1; the light produced by a charged particle born in the scintillator with kinetic energy E_K which escapes with E_{Rem} kinetic energy remaining is characterized as the difference in the light production of the initial and escaping particles as shown in Equation 2.3. Light yield is often measured in units of "electron equivalent" as denoted by L_{ee} in the equations below and adopt the standard SI prefixes used for describing particle energies (1 MeV electron equivalent = 1 MeVee).

$$L(E_{particle}) = L_{ee} = a_1 E_{particle} - a_2[1 - exp(-a_3 E_{particle}^{a_4})] \tag{2.1}$$

$$L(E_{Be}) = L_{ee} = \frac{L(E_C)}{3} \quad , \quad L(E_{e^-}) = L_{ee} \tag{2.2}$$

$$L(\Delta E) = L(E_K) - L(E_{Rem}) \tag{2.3}$$

In this work, the Japan Atomic Energy Agency (JAEA) code SCINFUL-QMD is used to characterize the light response and efficiency of the scintillators used in this experiment to incident neutrons [26]. The SCINFUL-QMD code, as the name implies, builds upon the SCINFUL library and code developed by J.K. Dickens at Oak Ridge National Laboratory in 1988 which characterizes neutron response from 0.1 MeV up to 80 MeV [27]. In SCINFUL-QMD, cross section data from the SCINFUL library is extrapolated to 150 MeV, beyond which the quantum molecular dynamics plus statistical decay model (QMD+SDM) is employed to model nuclear reactions. The modeled light production process employed in SCINFUL-QMD is similar to the total energy deposition and scintillation material dependent parameterizations of References 21 and 22, based on the data present in the original SCINFUL library as well as more recent response measurements discussed in References 28, 29, and 30.

Table 2.1: Light response parameterization coefficients

Particle	a_1	a_2	a_3	a_4
Proton	0.66055	1.64456	0.37686	0.96652
Alpha	0.391	4.159	0.085	1.1
Carbon	0.138	75.786	0.001745	1.007

Equations and values from [22]

Thus, individual neutrons of the same energy produce variable light response when interacting in an organic liquid scintillator. This is because the reaction, energy transfer, secondary ion transport, excitation, and de-excitation processes which occur in the chain of events from a neutron entering a detector, interacting, and producing light are all stochastic in nature. Over a large number of incident neutrons at a given energy, a distribution of responses characteristic of that neutron energy will emerge. Since the experimentally measured light response is a convolution of many of these individual interactions except from neutrons of a variety of unknown energies of unknown intensities, a deconvolution methodology, like that presented later in Chapter 6, is necessary to characterize the neutron energy spectra from the measured pulse height spectra. Crucial to the deconvolution methodology is a response function that accurately represents the scintillator's light response to neutrons; in this work, the SCINFUL-QMD code is used to serve that purpose.

Chapter 3

Experiment

This experiment was completely designed and preliminarily tested before I had joined this research effort. This chapter will cover the experiment's design to the extent necessary to understand it and the rationale of some of the decisions made during the execution of the experiment while I was present, but it will not deeply cover the decisions made before. For a comprehensive discussion on the experiment's design, see References 2 and 3.

3.1 Structure of the experiment

The measurement campaign consisted of 500 hours of beam time spread across three separate experiments which took place in March 2016 (100 hours), November/December 2016 (200 hours), and November 2017 (200 hours) at the NASA Space Radiation Laboratory (NSRL) on the Brookhaven National Laboratory (BNL) campus. In this campaign, five different ion species were accelerated at three different intermediate energies into eight different thick targets composed of varying amounts of aluminum (Al) or high-density polyethylene (HDPE) or a combination of the two (AlPE). The run schedule for all of these combinations is shown in Table 3.1.

In the experiment room, six organic liquid scintillators (OLS) used for neutron and light ion detection were placed at different angles—10°, 30°, 45°, 60°, 80°, and 135°—with respect to the beamline and center of the upstream target. These six OLS detectors are sometimes denoted as N1, N2, N3, N4, N5, and N6. Additionally, each detector is surrounded by two

Table 3.1: NSRL thick-target experiment schedule

Beams	400 MeV/n			800 MeV/n			1500* MeV/n		
	Al	HDPE	AlPE	Al	HDPE	AlPE	Al	HDPE	AlPE
H	1/3†	2	3	1	2	3	2	2	3
He	1	2	3	2	2	3	2	2	3
C	2	3	3	2	3	3	2	3	3
Si	2	3	3	2	3	3	2	3	3
Fe	1	2	3	1	2	3	2	2	3

1 = March 2016, 2 = November/December 2016, and 3 = November 2017
*2500 MeV used instead of 1500 MeV/n for H beams; for heavier ions it was sometimes slightly below 1500.
†400 MeV H incident on 20 g/cm^2 Al was also repeated in November 2017.

veto detectors (n1v1, n1v2, n2v1, n2v2, n3v1, n3v2, n4v1, n4v2, n5v1, n5v2, n6v1, n6v2) for charged particle discrimination purposes, and two start scintillators (s1 and s2) are used to determine valid (uninteracted) particles striking the upstream target and initiate the event timing. Figure 3.1 shows how the veto paddles are arranged around each OLS, also denoting the detection volumes and photomultiplier tubes (PMTs).

Two types of liquid scintillator were used across the six detectors. The 10°, 30°, and 45° detectors were made of EJ-301 while the remaining 60°, 80°, and 135° detectors were made of EJ-309. These detectors were cylindrical with an active volume diameter of 12.7 cm (5") and a length of 12.7 cm (5"). The veto detectors (also referred to as veto paddles) were EJ-204 solid plastic scintillators. They were square with side lengths of 12.7 cm and a thickness of 0.635 cm. Both of the two start scintillators were EJ-228 solid plastic scintillators.

On the opposite side of the beamline, two sodium iodide (NaI) arrays were placed at -10° and -30°, each covered with three EJ-204 solid plastic scintillators (referred to as charged scintillator "CS" paddles) to provide finer angular resolution. However, these detectors were used exclusively for charged particle detection; thus, they will not be discussed in any more detail here. Reference 4 describes the charged particle analysis pertaining to the NaI arrays.

A panoramic photo of the experiment setup is shown in Figure 3.2; in this particular setup, a 60 g/cm^2 aluminum front target is in place.

Within the experiment room, the detectors are located at set distances from the center of the upstream target, a location which is held constant and referred to as the origin location of the experiment room. The six OLS detectors were placed at distances of 3 m (10°, 30°,

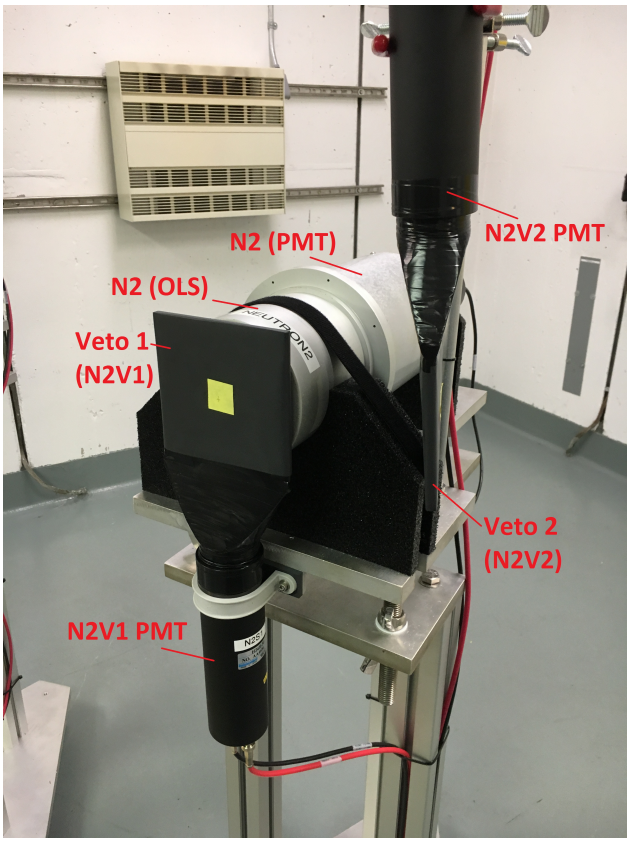


Figure 3.1: Closeup of the 30° detector, N2, with its various components labeled

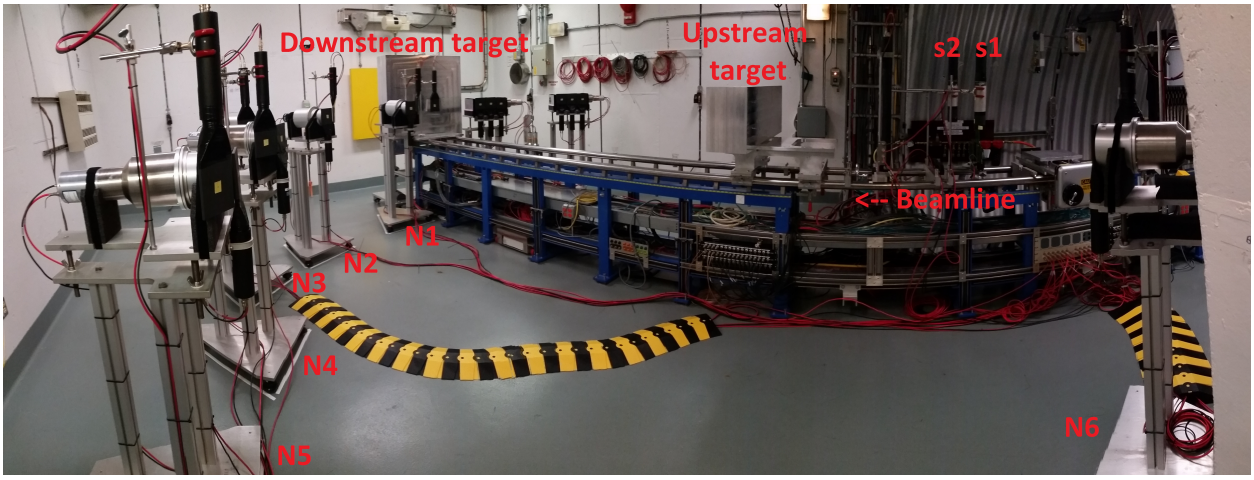


Figure 3.2: Experiment room at NSRL with important features relevant to this work labeled. (The OLS labels are placed at the base of the stand for each detector.)

and 45°), 2.5 m (60° and 80°), and 2 m (135°) from this origin point at their respective angles from the beamline axis.

To employ time-of-flight techniques, a method for separating neutrons produced in the upstream target which fly directly to the OLS detectors from all other neutrons is necessary. In this experiment, this is accomplished through a background subtraction by employing shadow bars. These "shadow bars" are iron poles of diameter equal to the OLS detectors' (12.7 cm) and of lengths 182 cm or 91 cm which are used to "shadow" detectors from neutrons produced in the upstream target. In a measurement where a shadow bar is placed between the upstream target and a detector, the neutrons seen in the covered detector are only those which are produced elsewhere in the room (predominantly in the downstream target) and/or scattered throughout the room before striking the detector. When unconcealed, the detector sees these neutrons plus those produced in the upstream target, allowing for a background subtraction after normalization, leaving only neutrons produced in the upstream target. Four different shadow bar configurations were utilized in the experiments as shown in Table 3.2. Figure 3.3 depicts shadow bar Setup B in the experiment room.

The eight upstream targets to-scale relative to each other are shown in Figure 3.4. The pure aluminum targets were always followed by a 60 g/cm^2 aluminum downstream target, and all of the polyethylene-containing targets were followed by a 60 g/cm^2 HDPE downstream target. The upstream targets always had their mass centers located at the origin point of the experiment room.

Table 3.2: Shadow bar configurations

Detector	Angle off beam axis	Setup A	Setup B	Setup C	Setup D
N1	10°	-	x_1	-	-
N2	30°	-	-	x_1	-
N3	45°	-	-	-	x_1
N4	60°	-	x_2	-	-
N5	80°	-	-	x_2	-
N6	135°	-	-	-	x_2

"x" indicates a detector covered by a shadow bar; "-" indicates a detector uncovered. x_1 denotes use of the 182 cm shadow bar while x_2 denotes use of the 91 cm shadow bar.

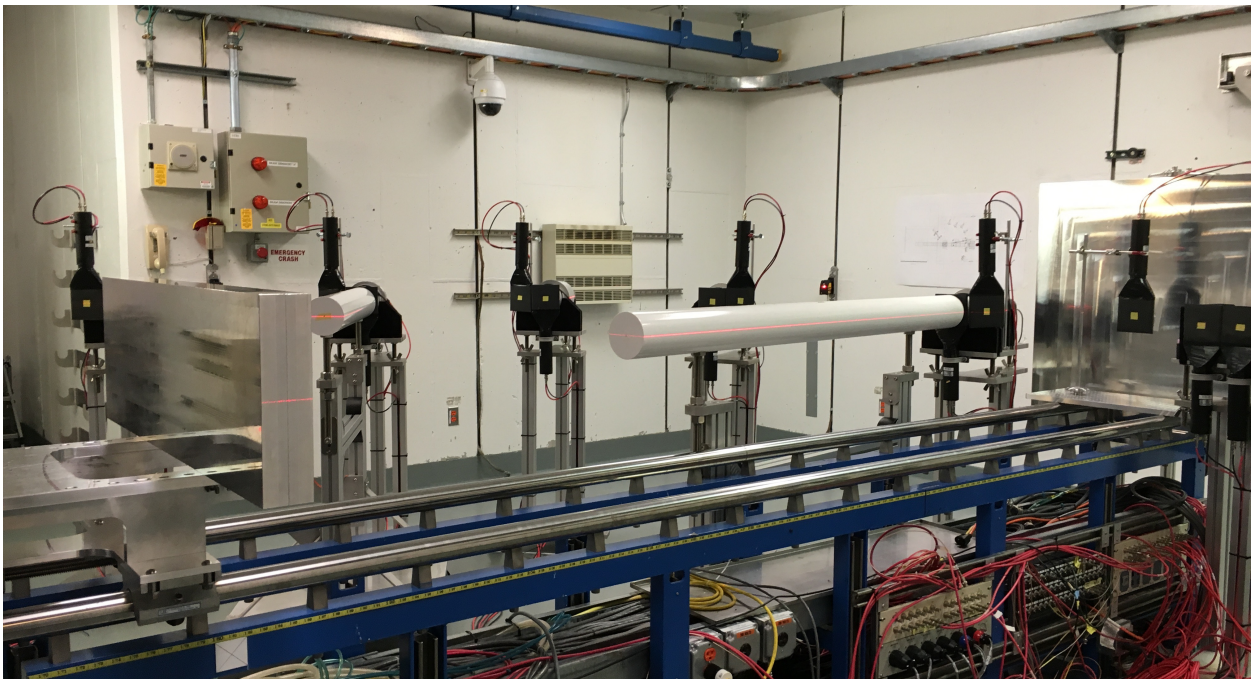


Figure 3.3: Shadow bars in arrangement B (concealing 10° and 60° detectors)

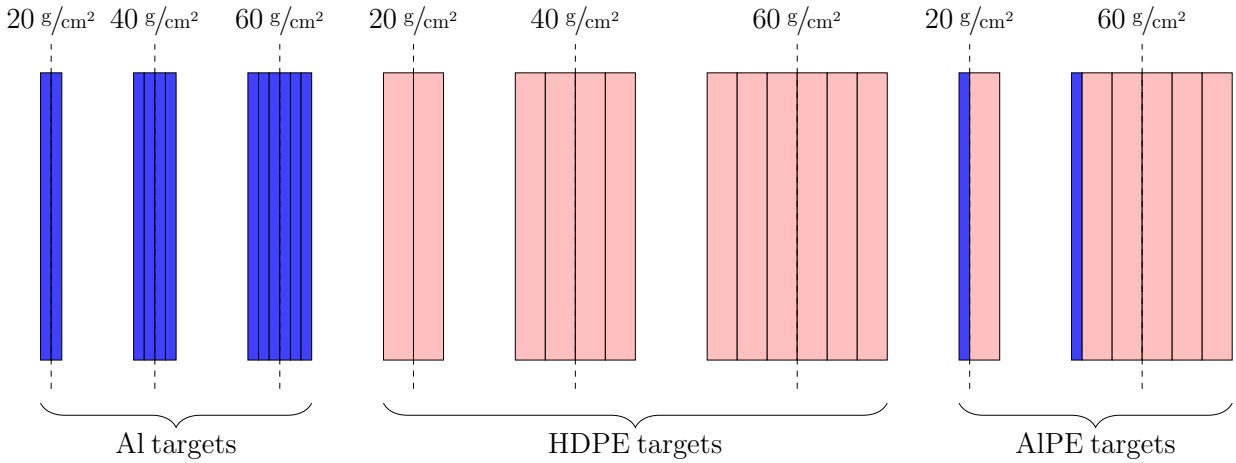


Figure 3.4: Pictured are all 8 upstream targets employed to-scale with dashed lines indicating their mass centers.

The end goal of this project was to test and characterize the secondary particles produced in every combination of the following:

- 5 different beam species (H, He, C, Si, and Fe)
- 3 different energies per species (400, 800, and 1500 MeV/n for Z>1 / 2500 MeV for H)
- 8 different upstream targets
  - 3 front target thickness for pure Al or pure HDPE targets (20, 40, and 60 g/cm^2)
  - 2 front target thickness for hybrid targets (10 g/cm^2 Al + 10 g/cm^2 HDPE and 10 g/cm^2 Al + 50 g/cm^2 HDPE where Al is always on the most upstream end)
- 4 different shadowbar configurations (A, B, C, and D)
- 6 different detector angles (10°, 30°, 45°, 60°, 80°, and 135°)

This results in a total of 120 unique beam/target combinations or 480 different run configurations once factoring in the shadow bar arrangements, and each run has numerous data channels for each detector. Figure 3.5 shows a to-scale image of the experiment (excluding shadowbars, walls, or any other features of the room geometry) which illustrates the detector layout and just how physically large the thinnest target (20 g/cm^2 Al) and thickest target (60 g/cm^2) actually are in comparison to the other experimental dimensions (size of the detectors and their distances from the targets).

Additionally, it is worth noting, for the sake of future discussions, where the beam will stop in each of these projectile/target combinations. This is shown below in Table 3.3 where UST denotes the beam stopping in the upstream target, DST denotes the beam penetrating the upstream target but stopping in the downstream target, and DMP denotes the beam penetrating both targets and stopping in the beam dump further downstream. Table 3.3 was generated using simple stopping power calculations utilizing the Bethe formula for stopping power [31].

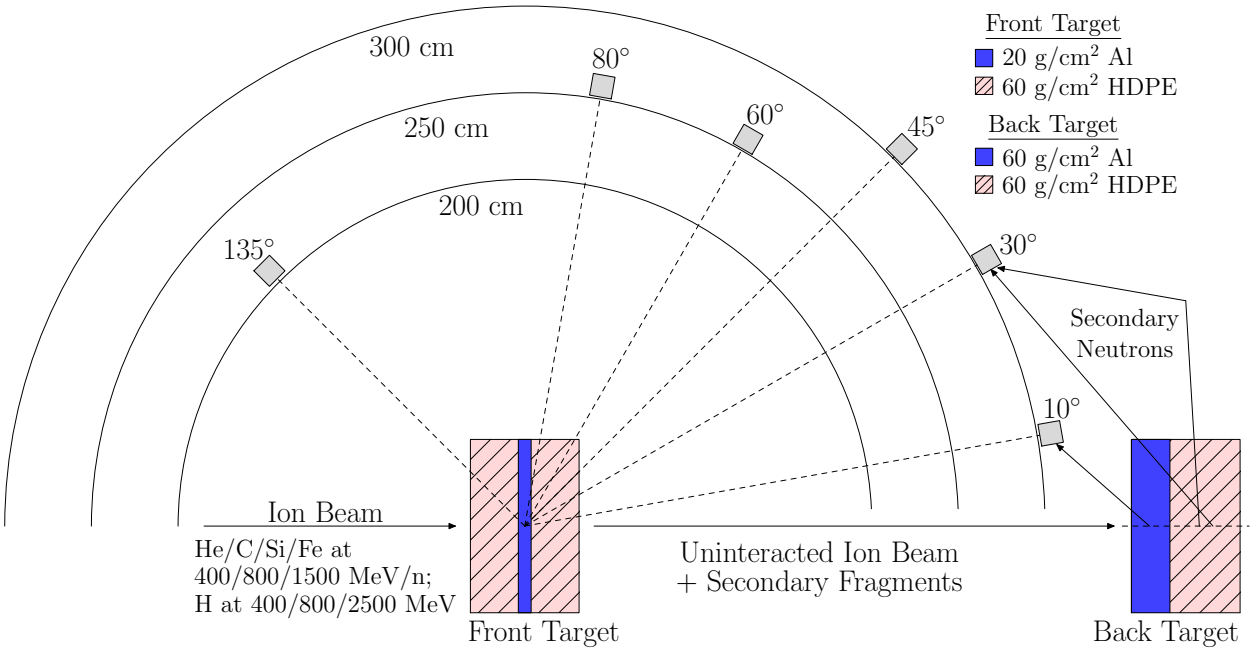


Figure 3.5: Pictured is a to-scale schematic of the beam/detector/target system. In red is the largest target, 60 g/cm^2 HDPE, and in blue is the smallest target, 20 g/cm^2 Al.

Table 3.3: Stopping location of all beam projectiles

Projectile		Upstream target material and thickness (in g/cm^2)							
Species	Energy (MeV/n)	Aluminum			HDPE			Al+HDPE	
		20	40	60	20	40	60	20	60
H	400	DMP	DMP	DST	DST	DST	DST	DST	DST
	800	DMP	DMP	DMP	DMP	DMP	DMP	DMP	DMP
	2500	DMP	DMP	DMP	DMP	DMP	DMP	DMP	DMP
He	400	DMP	DMP	DST	DST	DST	DST	DST	DST
	800	DMP	DMP	DMP	DMP	DMP	DMP	DMP	DMP
	1500	DMP	DMP	DMP	DMP	DMP	DMP	DMP	DMP
C	400	DST	UST	UST	DST	UST	UST	DST	UST
	800	DMP	DST	DST	DST	DST	DST	DST	DST
	1500*	DMP	DMP	DMP	DMP	DMP	DMP	DMP	DMP
Si	400	UST	UST	UST	UST	UST	UST	UST	UST
	800	DST	DST	UST	DST	UST	UST	DST	UST
	1500*	DMP	DMP	DST	DST	DST	DST	DST	DST
Fe	400	UST	UST	UST	UST	UST	UST	UST	UST
	800	DST	UST	UST	UST	UST	UST	DST	UST
	1500*	DST	DST	UST	DST	DST	UST	DST	UST

UST = upstream target, DST = downstream target, and DMP = beam dump

*Beam energy was sometimes slightly below 1500 MeV/n.

3.2 Data acquisition system and logic

The trigger logic used in this experiment was set up using the equipment listed in Appendix A arranged as shown in Figure 3.6 with some of the depicted initialisms and abbreviations listed in Table 3.4. A picture of what this diagram looks like with actual cables and equipment is shown in Figure 3.7, depicting the physics and data acquisition room at NSRL. The finer details of this setup and the rationale behind it can be found in Reference 2.

This describes how a pulse generated in any of the detectors ultimately impacts event timing and what information is recorded. The coincidence modules (COINC) and multiplicity logic units (MLU) function similarly to logical AND gates, triggering when any two or more of its inputs are valid. A dummy signal is constantly fed to the MLUs, forcing them to instead operate like OR gates, triggering when any OLS detector or CS paddle covering a NaI detector sees a signal. Note that only the start scintillators, OLS detectors, and CS paddles covering the NaI detectors are part of the trigger logic; the veto detectors and NaI arrays themselves do not play a role in event triggering/timing. Figure 3.8 shows an example of these required coincidence signals [2]. The first 200 ns gate and delay (G/D) generator is used to set the time window in which all signals are collected for a given triggered event. The second gate and delay generator is used to generate a much longer gate which feeds a "computer busy" signal to the main coincidence module; this is cut short if it receives an "event complete" signal from the CAMAC controller. Scaler modules were used throughout the electronic setup to track when each logical requirement is met. These are outputted digitally to files in the data acquisition computer as well as to visual displays (seen on the far left of Figure 3.7). All events entering the coincidence module contributed to the "RAW" event scalar, and those events which also were not blocked by the "computer busy" signal **and** set the 200 ns acquisition gate contributed to the "LIVE" event scalar. The quotient of these scalars (LIVE/RAW) is how detector live time was determined, accounting for the dead time of the system.

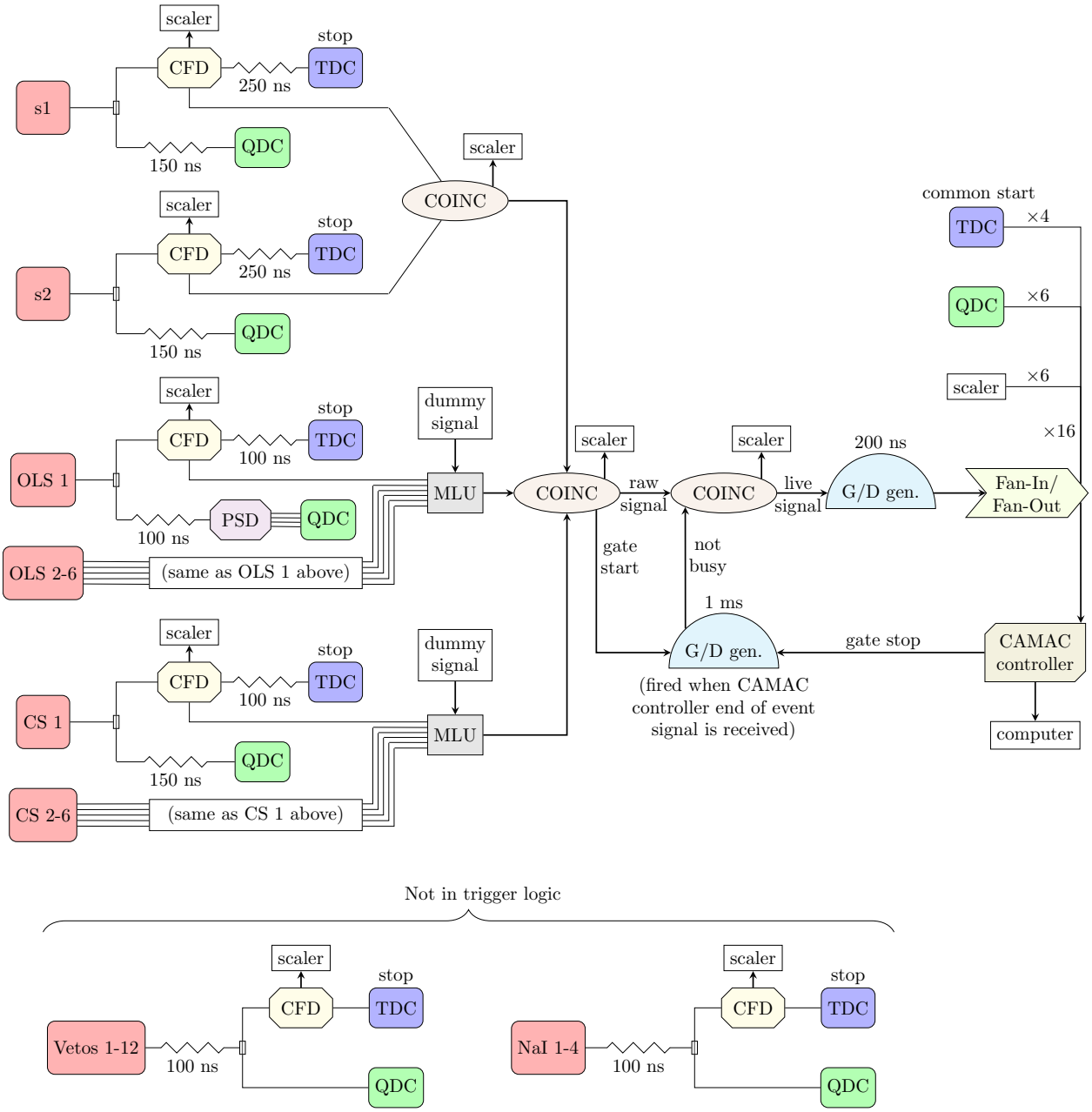


Figure 3.6: Pictured is the electronic logic map of the data acquisition system.

Table 3.4: Trigger logical diagram initialisms and abbreviations

Initialism	Meaning
TDC	time-to-digital converter unit
QDC	charge-to-digital converter unit
CFD	constant fraction discriminator
PSD	pulse shape discrimination module
COINC	coincidence module
MLU	multiplicity logic unit
G/D gen	gate and delay generator

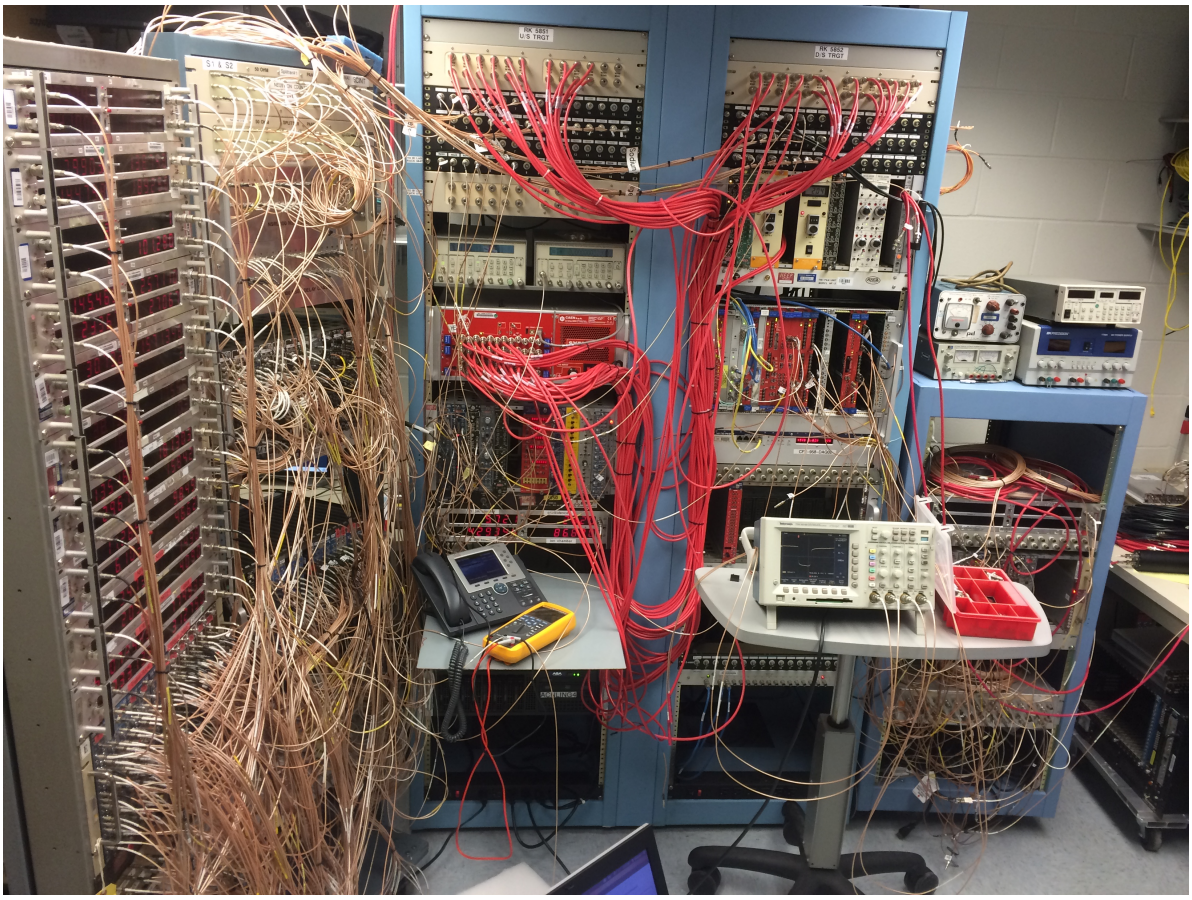


Figure 3.7: Physics / data acquisition room at NSRL with logic equipment shown

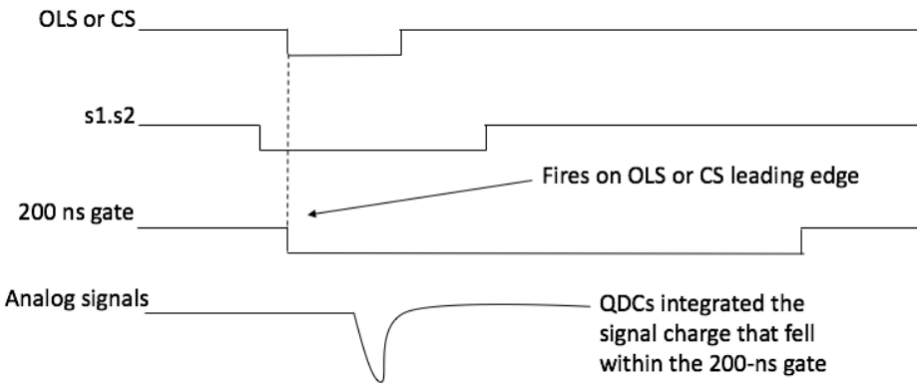


Figure 3.8: Illustration of acquisition gate and trigger being set by a coincidence between OLS/CS **and** a coincidence in both start scintillators [2]

QDC signals

The charge information from each pulse from the OLS detectors is binned into four separate charge QDC channels. The first major split divides the signal into a pulse being kept as-is (or "normal") and a pulse which is passed through attenuators (so, "attenuated"). Then, each of those two signals is split again. The first is the total charge integrated across the whole event; this is referred to as Q_{total} or just Q_{tot}. The second is each pulse's charge integrated over the first 30 ns (or "head") of the event, referred to as Q_{head}. These pulses which are integrated over different times are later used for applying pulse shape discrimination techniques to separate neutrons from photons, as detailed in later in Section 4.2.4. As will be seen in that section, the attenuated signals are necessary to characterize pulses which would otherwise be lost to a pileup peak in the highest unattenuated QDC channels. Additionally, as is shown in Section 4.3.2 and utilized in Section 6.2, the attenuated signal allows for a major extension of the maximum neutron energy whose pulse shape can be distinguished, a vital capability for characterizing the neutrons produced in the downstream target.

3.3 Special beam considerations and exceptions

One large goal sought throughout the experiment was maximization of the number of good events which are triggered in the detection system per unit time, since, ultimately, the experiment costs a set amount of money per hour of beam time used. This optimization

ended up becoming a balancing act where beam current was the primary knob which could be used to adjust the number of good events triggered. The two event loss/rejection mechanisms which hurt total efficiency are dead time and good beam fraction (fraction of beam particles which are uninteracted and not simultaneously accompanied by other particles when detected in the start scintillators, discussed in Section 4.2.3). When the beam current is very low, detector live time is very high, and good beam fraction is optimized since the number of double-hits (which are later filtered out) is minimized. However, the absolute quantity of events detected is low in this case. As the beam current is ramped up, the live time and good beam fraction decrease, though the absolute number of good events continues to rise. However, at some point additional increase in beam current actually decreases the total number of good triggered events due to a significant fraction of detected beam particles being double hits and the detector live time continuing to fall. For projectiles at higher energies or of higher mass, the increased particle yields also influence the detector live time. This optimization was performed constantly throughout the experiment by studying the scalers denoting the number of coincidences in the start scintillators and live time in conjunction with an estimate of the good beam fraction made on the data acquisition computer.

One of the most important optimizations conducted by the NSRL team was the lengthening of the beam spills. A spill is the period of time over which a "packet" of beam particles is delivered, and spills occur with some frequency. In an ideal world, spills are as even and long as possible with as little gap as possible between spills. Without going into any detail of the micro-structure of the beam spills, this can be seen essentially as a square wave which toggles the beam on/off. In this experiment, beam spills typically lasted on the order of two to three seconds and occurred about once every five seconds. The lengthening of the beam spills plays a significant role in influencing the total efficiency of the experiment. For a given number of beam particles delivered in a single spill, the number of good events detected is higher for a spill of three seconds than a spill of half of a second.

As was noted in the second footnote of Table 3.1, the maximum beam energy used at NSRL was not necessarily 1500 MeV/n for the heavier beams. One example of this is that 1400 MeV/n carbon beams were used in the November 2017 experiment rather than 1500 MeV/n. In this case, the carbon ions can be accelerated in either a 5+ or 6+ charge state.

At the 6+ charge state, carbon has the same magnetic rigidity as many components in the air (when also fully stripped), meaning contaminants will travel with the C^{6+} beam without being rejected at the bending stages. To avoid this, the carbon ions were accelerated at the 5+ charge state. This did come with a trade-off: Higher charge states allow for longer beam spills since less energy is required to accelerate and bend the higher-charged beams. This energy requirement (which manifests itself as heat in the accelerator's magnets) is one of the core limiting constraints. While NSRL has the capability of ramping a C^{5+} beam up from 1400 MeV/n to 1500 MeV/n, increasing the beam energy (while holding charge state constant) reduces the spill length since the amount of energy which can be dumped into the magnets per unit time is constant. Thus, as a compromise to maintain reasonably long spills with the C^{5+} beam, it was decided that reducing the beam energy from 1500 MeV/n to 1400 MeV/n was an acceptable trade-off.

The exceptions where an energy below 1500 MeV/n was utilized for the maximum beam energy are listed below.

- 1400 MeV/n C when incident on pure HDPE and hybrid AlPE upstream targets
- 1470 MeV/n Si when incident on pure aluminum upstream targets
- 1470 MeV/n Fe when incident on pure aluminum upstream targets
- 1463 MeV/n Fe when incident on pure HDPE upstream targets

In addition to these exceptions, the maximum proton beam energy utilized was 2500 MeV rather than 1500 MeV simply due to the higher energy being available. Beams heavier than protons were sourced from the Electron Beam Ion Source (EBIS) while the proton projectiles originated from the Tandem van de Graff, both feeding into BNL's Booster Synchrotron before being delivered to NSRL.

Chapter 4

Upstream target neutron data analysis

This work encompasses analysis of all neutron data from the November 2016 and November 2017 experiments, and limited analysis of the March 2016 neutron data. The collected neutron data falls into two distinct categories: neutrons produced in the upstream target and neutrons produced anywhere else (but predominately in the downstream target). The upstream target neutron data in this work comes only from the November 2016 and 2017 experiments while the back target and room scattered neutron data analysis was performed for all three experiments. Due to the presence of the shadow bars, the neutrons produced in the upstream target can be isolated from all of the others, and since the flight path to each detector is known, time-of-flight techniques used with the collected timing data can be utilized to determine the energy spectra of the incident neutrons. However, the flight paths are not known for the room scattered and downstream target-produced neutrons. For these neutrons, an energy spectrum must be extracted from the charge deposition (light production in the scintillator) data, which is a completely separate analysis technique. Thus, this work is divided into two portions: upstream target neutron data (this chapter) and downstream target plus room scattered neutron data (Chapter 6). Additionally, full-room geometry MCNP and PHITS simulations were conducted to provide a comparison to the experimentally collected data (Chapter 7).

4.1 General approach to the analysis

Due to the volume of data, a significant fraction of this work involved generalizing and automating the analysis; this will be discussed first due to its prolific nature.

At the top level, the analysis tasks can be broken down to two distinct categories: actions that require manual human input in ROOT [32] and actions which can be scripted using Python. In the analysis, ROOT is first used to sift the data (logic gates and graphical cuts) and apply some normalizations (live time and fraction of beam which strikes the front target uninteracted, a.k.a. good beam fraction). Once that process is complete, the time and charge channels are outputted from ROOT as text files. From there, Python is used to extract the data and fully automate each action which must be performed on every dataset.

While ROOT is a very powerful tool for data manipulation, it is important to use the most appropriate tool for each task. ROOT's strength lies in sorting and selecting data through 1D cuts/gates and 2D graphical cuts; this allows the extraction of important/usable/relevant data points for further analysis. While performing all of the analysis in ROOT and C++ is completely possible, Python 3 (along with its NumPy, SciPy, and a number of other libraries) is used for actual numerical manipulation due to being easier to code in and being an overall more versatile tool. Thus, the data analysis is split into two stages: filtering out data using ROOT and performing analysis of this data using Python.

The very repetitive tasks in ROOT are also made easier by automating much of the work as possible. ROOT can be completely operated using a command line interface, but scripts (called macros in ROOT) can be written to automate a series of commands. Since the series of commands is nearly identical for every dataset barring their run numbers and names, Python is used to generate all of the ROOT macros for every system at once. While this saves a substantial amount of time, it also prevents any lone human errors for a particular system from occurring. Any mistake made in the Python script generating the ROOT macros will be present across all systems and will become obvious very quickly.

This analysis can be broken down into the following steps:

1. Isolate properly timed events in each detector (self-time cuts)

2. Discriminate charged particle events from neutral particle events (veto cuts)

3. Filter out events for which the projectile had already undergone a nuclear interaction prior to striking the target and events where two or more beam particles struck the beam scintillators within a 200 ns window (good beam graphical cut)

4. Separate neutron events from photon events (neutron/gamma separation graphical cut)

5. Determine below what point neutrons and photons cannot be distinguished (Q_{total} pulse height threshold cuts)

6. Normalize counts to live time for each run and detector

7. Add normalized data for all unshadowed detectors for each system (and for all shadowed detectors if a given system had multiple runs where a detector was covered)

8. Normalize each set of shadowed and unshadowed counts for each detector and system to the total number of good beam particles for each combination

9. Subtract the normalized shadowed neutron data from the normalized unshadowed neutron data, yielding normalized counts for neutrons produced in the upstream target

10. Determine the average neutron flight path to each detector (and solid angle) for each beam/target combination

11. Using the time-of-flight data and flight distance, transform the time-binned axis to velocity and then to kinetic energy

12. Normalize the data to detector efficiency and solid angle

13. Rebin the data as a function of bin spacing, bin statistics, and energy resolution

14. Normalize the data to energy bin width

15. Save and plot the final results

This entire process is covered in more detail in the following sections. In addition to analysis of the collected experimental data, the full-room simulations conducted with MCNP required notable methodology development and analysis in order to recreate the yield values

being measured in this experiment. The MCNP simulations and the specific efforts required to extract front target neutron data are covered in Section 7.2.

4.2 Data filtering in ROOT

Steps 1 through 7 of the enumerated list in Section 4.1 are accomplished in ROOT, and they will be expanded upon in this section. These steps consist of setting up logical gates and filters which will be later applied to data histograms when outputting time spectra in order to separate the triggered events of interest from everything else.

4.2.1 "Self-time" cuts

The "self-time" cuts are made first. What this amounts to is finding the TDC channel for each of the six OLS detectors which is populated when an event is triggered in that detector. An example of this is shown in Figure 4.1 for the 10° detector N1. All events correctly timed in the N1 OLS are retrieved by filtering only events which meet the criteria of `"52<n1.tdc<63"`.

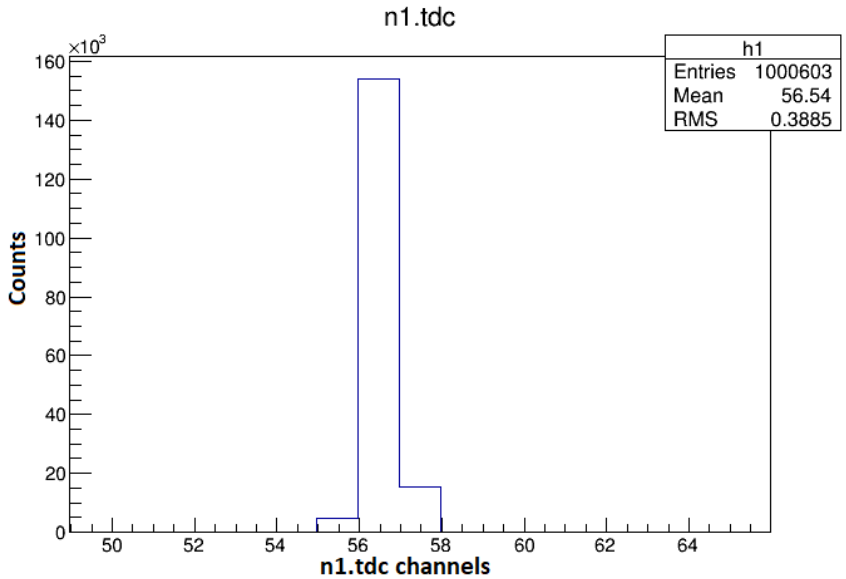
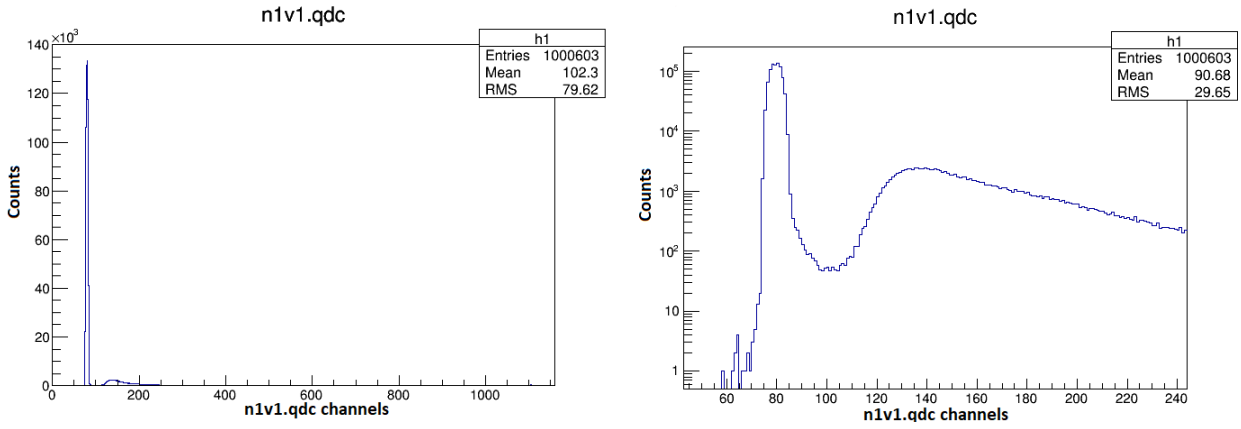


Figure 4.1: Example N1 TDC spectrum (zoomed in)

4.2.2 "Veto" cuts

Another gate referred to as a "veto cut" is created to discriminate charged particles from neutral particles. This is done by looking at the energy deposited (charge liberated) in the plastic scintillator veto paddles placed in front of each OLS detector. Charged particles will deposit energy in these veto paddles due to their electronic stopping power while the neutral particles, which almost never interact in the veto paddle detectors, typically will not. So, when plotting counts in the veto detector binned by charge deposited (QDC channels), a curve like what is shown in Figure 4.2 is obtained.

The linear scale of Figure 4.2a illustrates the prominence of neutral particle events, but more discussion can be had by looking at Figure 4.2b. The left peak corresponds with events depositing little to no charge in the veto paddles while the right peak and its following continuum corresponds to the charged particles. Thus, similar to the self-time cuts, a simple logical gate can be established to discriminate charged and neutral particles. In this specific example, channel 87 was decided to be the separation point, so a gate of `"n1v1.qdc<87"` in ROOT can now be applied. It is important that this cut is made quite close to the left peak to minimize the amount of low charge depositing charged particles falsely filtered as neutral particles. This process is then repeated for both of the veto paddles for each of the six OLS detectors.



(a) Zoomed out on linear y-scale

(b) Zoomed in on logarithmic y-scale

Figure 4.2: Example N1V1 QDC spectrum

4.2.3 "Good beam" graphical cuts

A "good beam graphical cut" is made to filter out events where the accelerated beam particle had undergone a nuclear reaction prior to striking the upstream target. In the experiment, two small "start scintillators" are located upstream of the front target. In addition to being used for the system timing and triggering, their charge deposition channels (QDC channels) are used to determine whether a beam particle has interacted or not prior to reaching the target. For example, Figure 4.3 is a three-dimensional plot showing the charge channels for each of the two start scintillators and counts as the z-axis (color) for a 1500 MeV/n C beam incident on aluminum targets. The bright spot in the middle is encompassed by a black oval shape which is the good beam graphical cut. This cut is drawn manually by the user in ROOT and can be saved for later use as a filter.

There are three main features to this plot. First, the spot in the middle is indicative of particles which deposit a consistent amount of energy in each start scintillator. Since one can assume that the majority of particles do not have nuclear interactions prior to reaching the target, this middle blob is characteristic of particles which are "good" (of known energy and species). Next, there is a horizontal line on the `s1.qdc` axis. This is indicative of scenarios

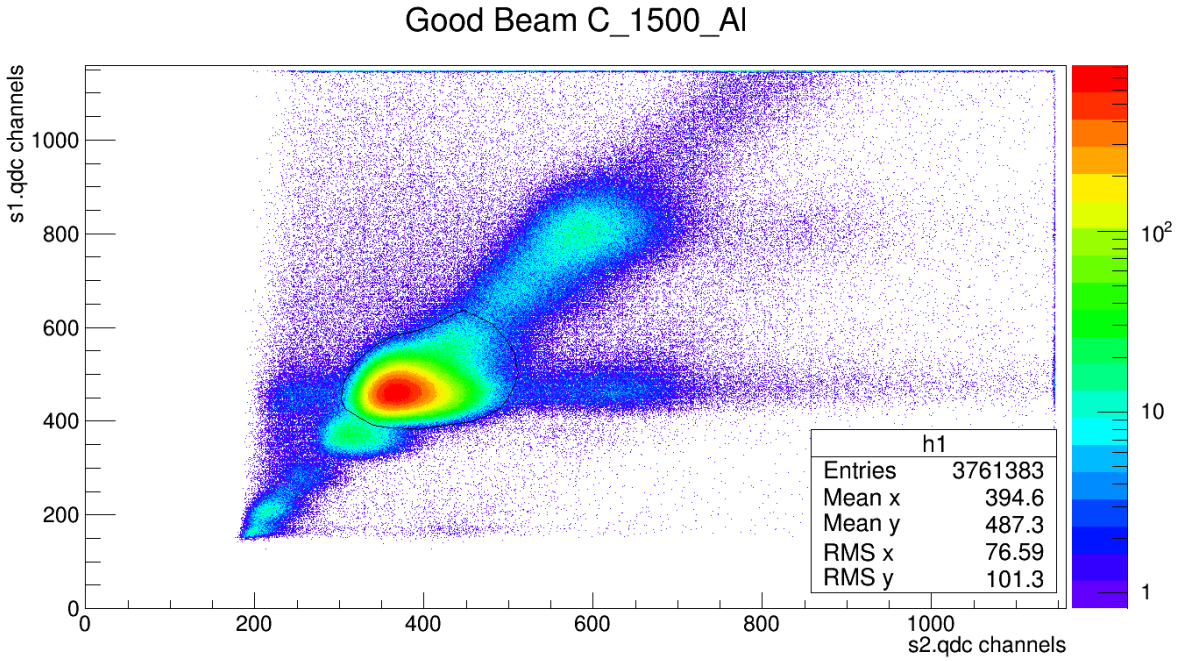


Figure 4.3: 1500 MeV/n C on Al `s1.qdc:s2.qdc` good beam plot after making a cut

where a beam particle deposits a consistent amount of energy in the first start scintillator but then fragments and/or scatters prior to reaching the second start scintillator, meaning these are no longer "good" beam particles. Lastly is the diagonal line which actually has two portions. These events are still those which deposit similar amounts of energy in each detector, but the upper portion represents events where two beam particles deposited energy in the start scintillators at nearly the same time (within the same trigger) while the lower portion is predominantly characteristic of beam particles which fragmented before reaching either start scintillator. Neither the already fragmented particles nor the double-hit events are desirable, so those are also filtered out with this good beam graphical cut. This good beam graphical cut is distinct and must be made for each different beam.

4.2.4 Neutron/photon discrimination graphical cuts

Once neutral events have been separated from charged particle events, neutron and photon events must be distinguished. This is done by looking at the time-dependence of charge deposited within the liquid scintillators. As was discussed in Section 3.2, each charge signal is split into the following four bins:

- Unattenuated whole signal ("normal" Q_{total} / $Q_{total}^{norm.}$)
- Unattenuated integration of the first 30 ns of signal ("normal" Q_{head} / $Q_{head}^{norm.}$)
- Attenuated whole signal ("attenuated" Q_{total} / $Q_{total}^{atten.}$)
- Attenuated integration of the first 30 ns of signal ("attenuated" Q_{head} / $Q_{head}^{atten.}$)

Interacting incident photons deposit charge more rapidly and thus produce a larger Q_{head} than neutrons, and this is the crux of neutron/gamma separation. Q_{head} and Q_{total} can be plotted against each other, and two distinct lines will appear, one for neutrons and one for photons.

This process only needed to be repeated once per OLS detector since the voltages were held constant throughout each experiment and the energy deposition of neutrons/photons in the scintillators is not dependent on the projectile or target.

Unattenuated signal

A plot of Q_{head} versus Q_{total} for the unattenuated signal for neutral particle data collected from 400 MeV/n C beams incident on all aluminum targets is shown for the 10° detector N1 in Figure 4.4.

There are two definite lines visible, though they are still close to each other. The bottom line consists of neutron events, and the top line consists of photon events. While the two lines are well separated at higher channels, the lines are very close and eventually merge at lower channels as shown in Figure 4.5.

Similar to what was done with the good beam graphical cuts, lines can be manually drawn in ROOT to designate regions of a plot containing desired data. A completed neutron/gamma cut is shown in Figure 4.6. Neutrons are all events within the lower triangle-like shape while photon events are all events which fall in the larger rectangle but not in the neutron triangle.

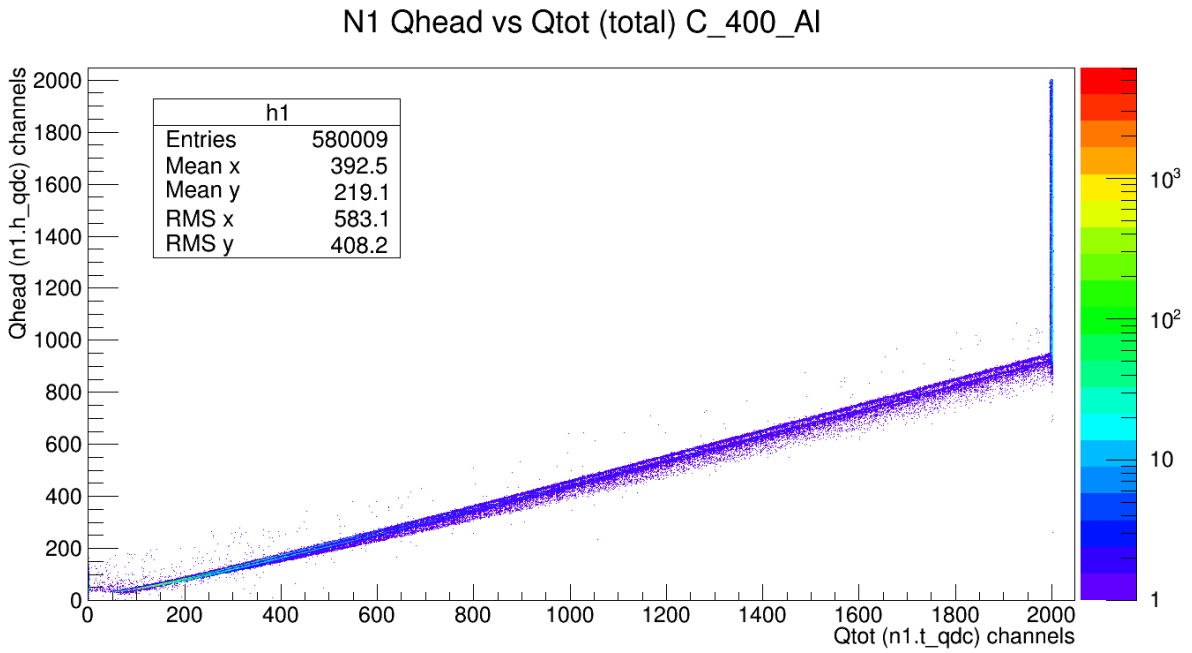


Figure 4.4: 400 MeV/n C on Al `n1.h_qdc:n1.t_qdc` n/γ plot with pileup

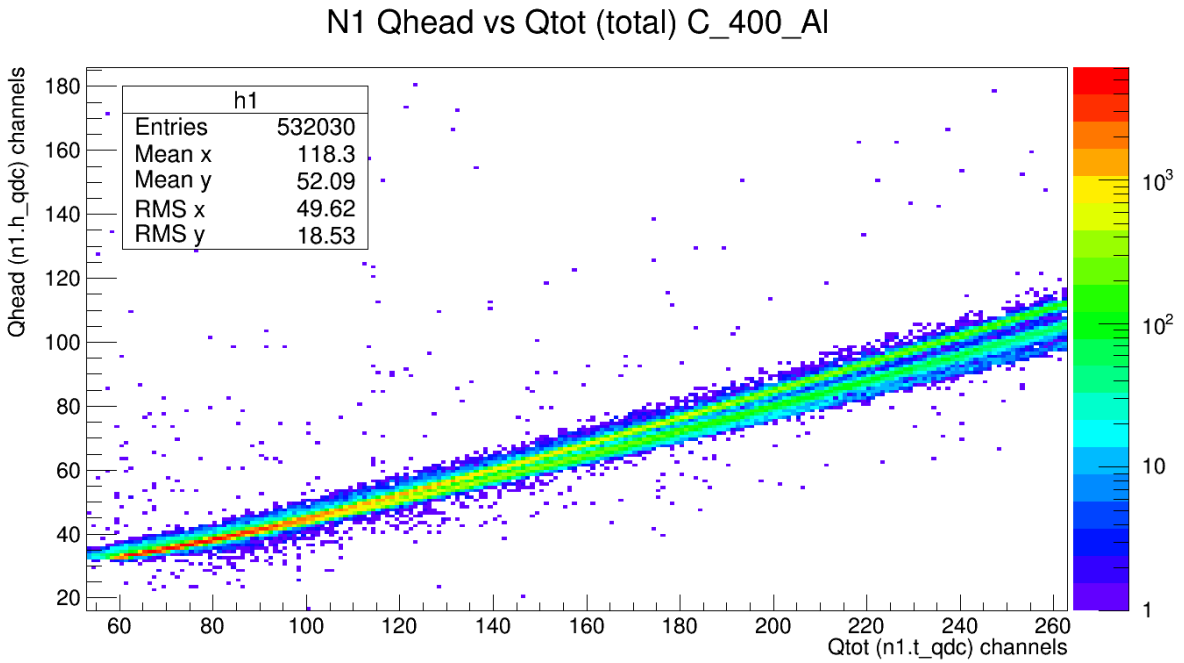


Figure 4.5: 400 MeV/n C on Al `n1.h_qdc:n1.t_qdc` n/γ plot

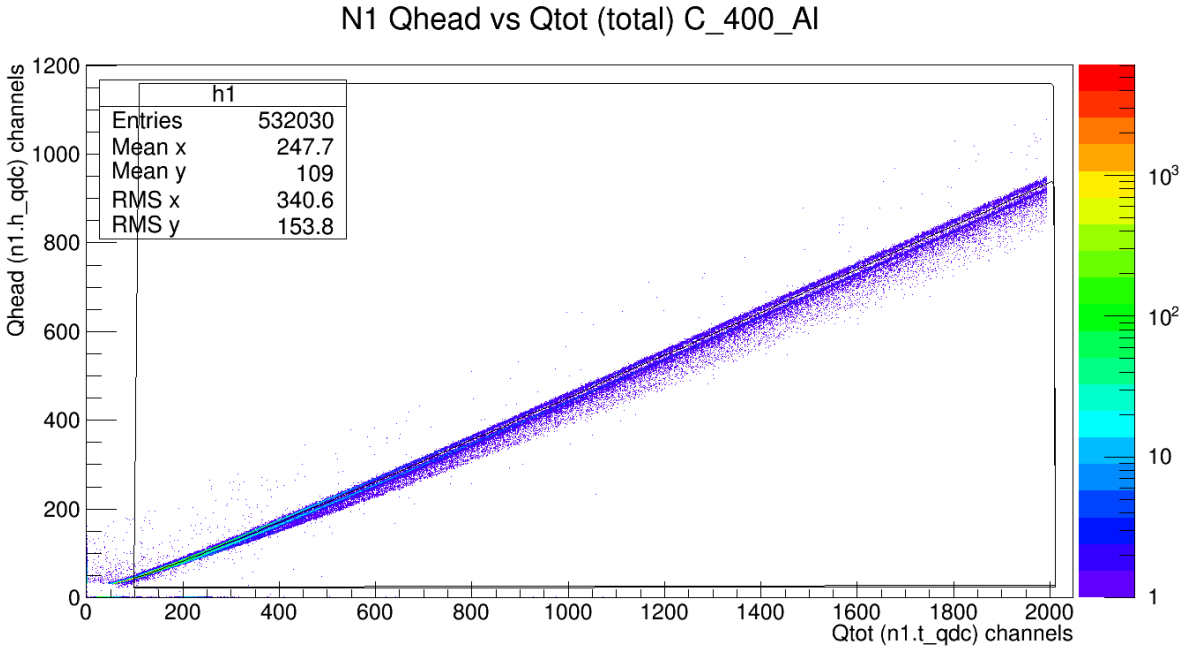


Figure 4.6: 400 MeV/n C on Al `n1.h_qdc:n1.t_qdc` n/γ plot

Attenuated signal

The plots in Figures 4.4 through 4.6 have been for the "normal" signal; the pileup peak on the far right of Figure 4.4 illustrates why an attenuated signal is also collected. Once attenuated, a pileup peak no longer exists on the far right. So, these same plots can be generated for the attenuated signal (though gating on the pileup peak which was excluded earlier as to not double count events), allowing for higher energy neutrons to be distinguished from photons while also keeping the minimum energy before the two lines merge as low as reasonably possible. Figure 4.7 shows this attenuated version of the same plot when gated on events within the pileup peak.

The top line eventually fades away, leaving only neutron events. This is best illustrated using one of the detectors being operated at a higher voltage and at one of the broader angles, such as N4 (60°). Additionally, since fewer counts end up in the pileup peak than not, making this graphical cut is easier when viewing this plot using all systems experimentally tested (all beam/target combinations). The attenuated signal neutron/photon separation plot is shown below in Figure 4.8.

A similar cut is made here, though the neutron cut is less of a triangle now that it includes all events beyond the point where the photon line fades away (Figure 4.9).

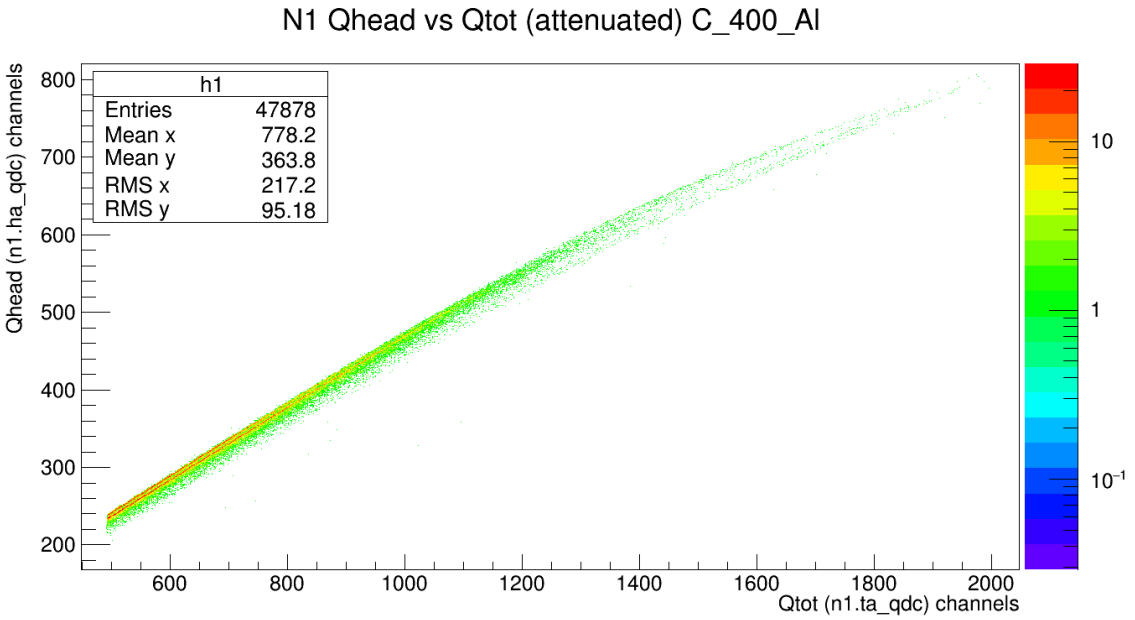


Figure 4.7: 400 MeV/n C on Al `n1.ha_qdc:n1.ta_qdc` attenuated n/γ plot

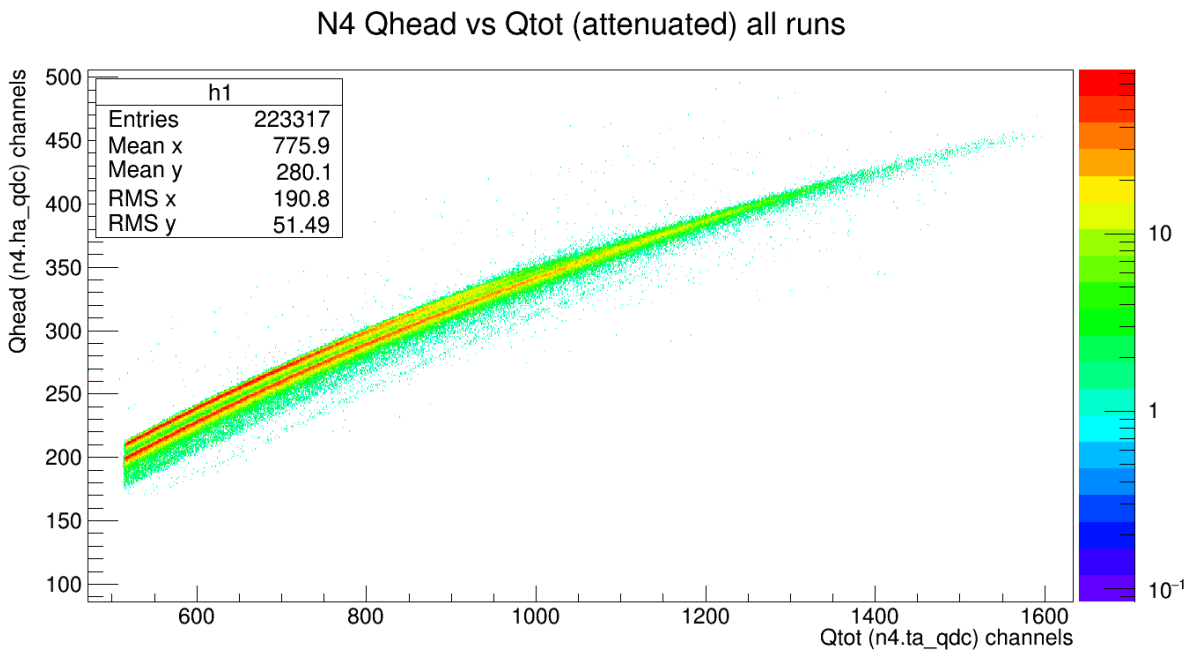


Figure 4.8: All runs `n4.ha_qdc:n4.ta_qdc` attenuated n/γ plot

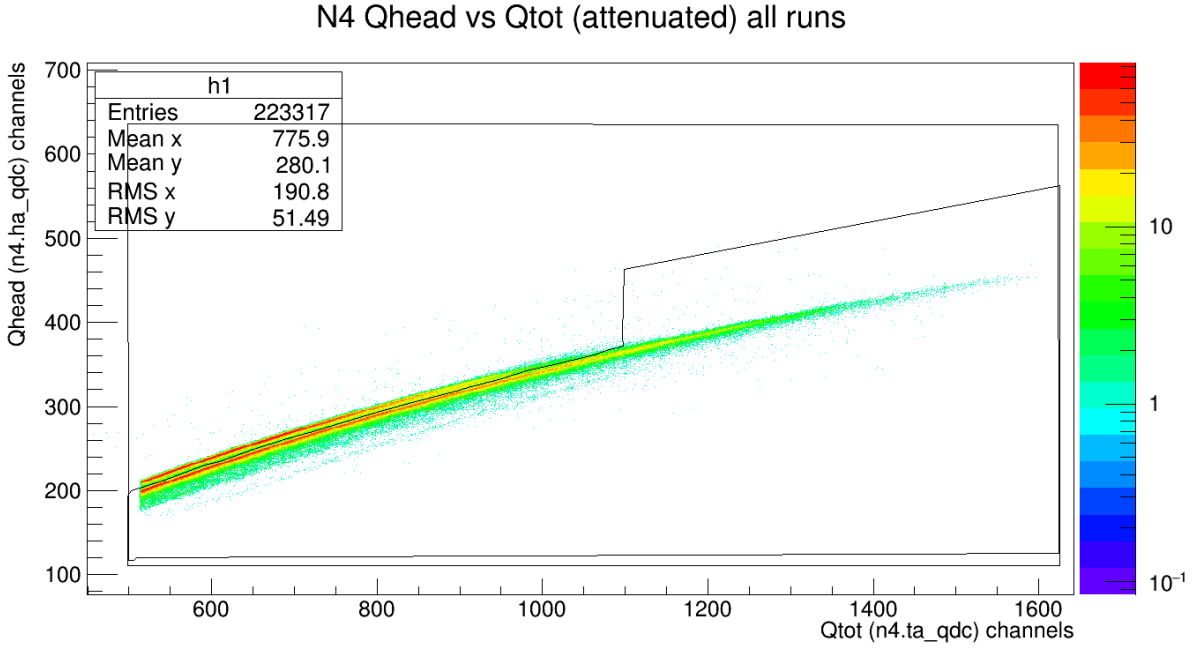


Figure 4.9: All runs `n4.ha_qdc:n4.ta_qdc` attenuated n/γ plot with cuts

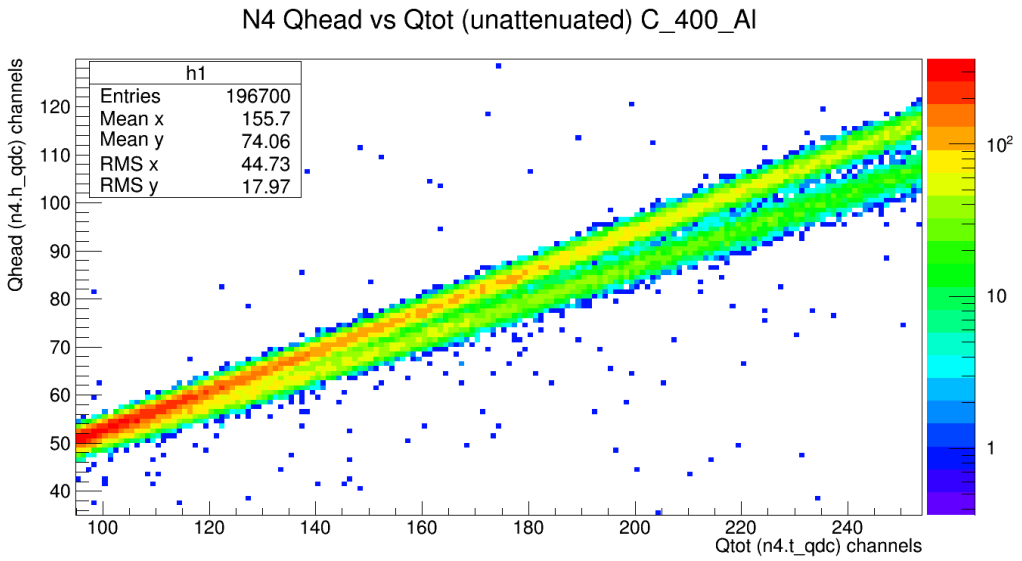


Figure 4.10: 400 MeV/n C on Al `n4.h_qdc:n4.t_qdc` unattenuated n/γ plot

Determining the lowest point of separation

The next step involves determining where neutrons and photons can no longer be distinguished from each other. Initially, the n/γ cuts were drawn to an arbitrarily low channel, much lower than the two lines can be reasonably separated. Now, a scientifically sound way of determining the cutoff point below which neutron events and photon events cannot be adequately separated is warranted, seeking to extend the range of neutron energies this methodology is sensitive to as low as justifiably possible.

This is accomplished by picking a Q_{total} channel where the curves are adequately separated, projecting this single channel slice onto the y-axis (Q_{head}), fitting a Gaussian to each of the two peaks which correspond to the neutron and gamma lines at that Q_{total} channel, and determining how many standard deviations apart the two are from each other. In this work, the standard was set at a separation of 2σ between the two curves. The ideal 2σ separation channel is then found iteratively. After picking a best first guess Q_{total} channel and finding the separation, a new higher or lower Q_{total} channel can be picked depending on whether the separation was less than or greater than 2σ. This is repeated until the Q_{total} channel corresponding to a 2σ separation is found.

As an example, Figure 4.10 shows the low-energy portion of the n/γ plot for 400 MeV/n C on Al in the N4 detector. It is obvious that the two lines are adequately separated on the

right edge of the plot and clearly merged on the left end of the plot; thus, the point of 2σ separation must lie within the shown window of QDC channels.

A Q_{total} channel is selected, the z-axis (counts) of the plot is projected onto the Q_{head} axis, and the two peaks are fitted with a Gaussian distribution, recording the mean $\bar{x}$ and standard deviation σ values for each peak. From that, a separation value is calculated (shown in Equation 4.1).

$$\text{Separation} = \bar{x_2} - \bar{x_1} \tag{4.1}$$

The objective is to make the separation equal to two standard deviations (2σ) as shown in Equation 4.2.

$$\text{Separation} = \bar{x_2} - \bar{x_1} = 2 \cdot (\sigma_1 + \sigma_2) \tag{4.2}$$

To make the manual iteration process easier, it is convenient to introduce a new value, ξ, which is the convergence criteria and is equal to the number of standard deviations separating the two curves (Equation 4.3). If ξ is above 2, a lower Q_{total} channel should be selected in the following iteration, and if ξ is below 2, a higher Q_{total} channel should be selected next.

$$\xi = \frac{\bar{x_2} - \bar{x_1}}{\sigma_1 + \sigma_2} \tag{4.3}$$

For this example at the 60° detector N4, the ideal amount of separation between the two peaks is shown in Figure 4.11. To be more conservative, this process was performed while looking at data from all projectile/target combinations at once rather than a specific combination.

Q_{total} pulse height threshold cuts

After finding the minimum point where neutrons and photons can be distinguished, an actual value must be selected on where to make this cutoff. This step is referred to as making Q_{total} pulse height threshold cuts.

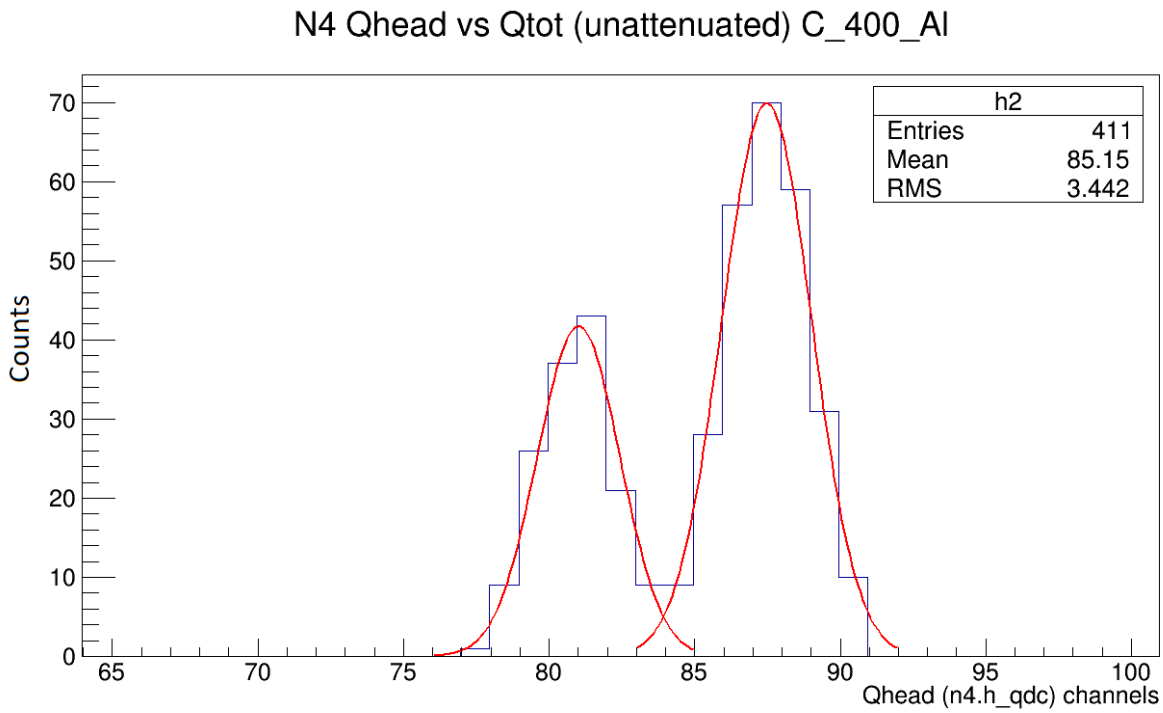


Figure 4.11: Y-Projection of N4 Q_{tot} channel 185 projected on the Q_{head} axis with Gaussian fits for each peak

Section 4.3.2 details the process of the QDC calibrations which serve as a way to translate QDC channels to units of MeV electron equivalent, or MeVee. The minimum separation MeVee values can be translated to a corresponding neutron energy with a code using the methods presented in Reference 25. The code is used to correlate the relationship between MeVee and the energy of a recoil proton (in MeV) resulting in the same pulse height. Then, that proton energy is taken to be the maximum-energy recoil proton from a neutron collision, meaning the kinetic energy of the neutron is equal to that of the recoil proton. For the sake of being conservative, the calculated minimum neutron energy is then rounded up to the nearest integer. Then, this process is done again in reverse. This new neutron energy is used to find the corresponding electron-equivalent energy using the same code as before. Then, the QDC calibration curves are used to translate this MeVee value back to a QDC channel which can be used now as a logical gate to exclude events below this minimum channel. Table 4.1 highlights this process for the analysis performed on the data collected in the November 2016 experiment. The values in the rightmost column, $Q_{tot,cut}$, are used to set the minimum charge deposited by neutrons required to be included in the analysis.

Table 4.1: Q_{total} threshold cut channels

Detector	$Q_{tot,min}$ (channel #)	L_{min} (MeVee)	$E_{n,min}$ (MeV)	$E_{n,cut}$ (MeV)	L_{cut} (MeVee)	$Q_{tot,cut}$ (channel #)
N1	143	1.74	4.69	5	1.895	154
N2	110	0.97	3.12	4	1.309	138
N3	123	1.29	3.79	4	1.309	125
N4	189	0.66	2.37	3	0.925	257
N5	168	0.39	1.67	2	0.510	215
N6	155	0.26	1.26	2	0.510	293

Table 4.2: Higher Q_{total} pulse height threshold cuts

Detector	$E_{n,cut}$ (MeV)	L_{cut} (MeVee)	$Q_{tot,cut}$ (channel #)
N1	20	11.505	812
N2	20	11.505	964
N3	20	11.505	911
N4	8	3.580	930
N5	6	2.430	941
N6	5	1.895	1051

Higher thresholds

While the previously discussed Q_{total} pulse height threshold cuts set the absolute minimum neutron energy this analysis is sensitive to, it is also useful to apply higher thresholds on the data filtered in this way, as will be discussed in greater detail in Section 4.10. It is the same process as just discussed except that now the higher initial threshold is arbitrarily selected rather than being derived. Table 4.2 shows a set of cuts determined for greater neutron energies for data taken in the November 2016 experiment.

4.3 Calibrations

Before delving further into the analysis, it is beneficial to first detail the experimental calibrations performed which are used to translate the collected channel-binned data into bins with some physical meaning.

4.3.1 Time calibrations

Since the crux of the time-of-flight method requires knowing the flight time of each detected particle, knowing the time-width of each TDC bin is vital to the analysis. This is achieved by performing time calibrations.

Initially, this was accomplished by feeding a pulser with no delay into the triggering system, producing a single peak in the `s1.tdc` spectrum. Then, various amounts of known delay can be added to shift this peak, providing a relationship between time (in ns) and TDC channel; this was achieved by adding cables (manufactured by Ramtronix Inc.) of known length (in ns) to the pulser. However, the initial timing calibrations yielded a conversion factor of about 0.225 ns/channel, which is notably lower than the expected 0.25 ns/channel.

At the very end of the November 2017 experiment, a different methodology was employed to perform this timing calibration. Instead of adding "known" delay with cables, a DG535 Digital Delay and Pulse Generator (manufactured by Stanford Research Systems, Inc.) was used to perform the same calibration methodology except with many more points sampled; this calibration curve is shown in Figure 4.12. The slope of this curve is the time-width of each TDC bin. Using this more rigorous method, the `s1.tdc` channels were determined to each be 0.251 ns wide, much closer to the expected value.

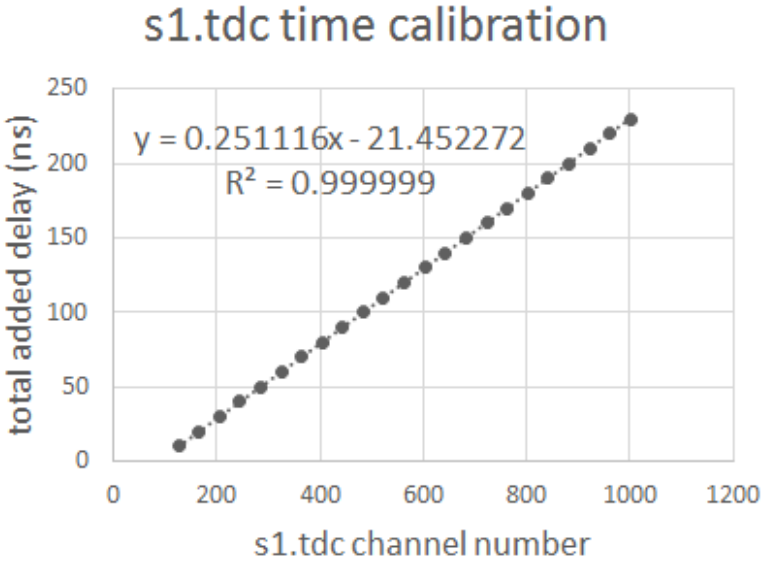


Figure 4.12: Time calibration curve of `s1.tdc`

This presents an interesting experimental and engineering discussion point: When two theoretically equivalent methods yield different results, which (if either) should be trusted? In this case, the original method involved performing a linear regression on three data points: no cable added, one "8 ns" cable added, and two "8 ns" cables added. The second method involved sampling 23 different delay values. This discrepancy is addressed by asking which is more trustworthy, the manufacturer-stated delay of the cables (stated to be accurate only to 10%) or the manufacturer-stated delay of the digital delay generator (stated to be accurate to 5 ps). It is obvious that results from the delay module are much more trustworthy, and the discrepancies in the advertised accuracy of each reinforce this. Using this more trustworthy channel-width value, it was calculated that the cables used in the initial calibrations were approximately 8.9 ns in length rather than the stated 8 ns.

Though the arguments for trusting the delay module over the cables are already strong, one would perform a third timing calibration using an entirely different method in an ideal world to avoid any confirmation bias. Due to time constraints, this was not done here. It felt sufficient to trust the manufacturer-stated delay of the delay module which yielded a time resolution in line with what the TDC signal processing manufacturer states.

4.3.2 Charge calibrations

The QDC calibration curves are used to convert the QDC spectra from channel number to units of light production, MeVee (or keVee), generating pulse height spectra. These are used in the analysis covered in Chapter 6 as well as when determining the Q_{total} pulse height threshold cuts discussed in Section 4.2.4. For each of the six liquid scintillators, total pulse height data is collected in two channels: an unattenuated signal (`nX.t_qdc`) and an attenuated signal (`nX.ta_qdc`). Additionally, there are the integrated "head" signals which were used when making the neutron/gamma discrimination graphical cuts, but they are not used here.

In order to convert the channel numbers to light production, calibration measurements whose light production is known are necessary. Since the unit of light yield used here, MeVee (MeV *electron equivalent*), is the amount of light deposited by an electron depositing that much energy, the most straightforward way of doing this is by measuring electrons of known

energies depositing energy into the OLS detectors. To avoid needing beta sources of relatively high energies and needing to account for particles slowing in the air and detector casing, the easiest way to make these measurements is with a photon source. The photons reach the detection volume with maximum energy, and the ones which interact will do so (most often) via Compton scattering, producing electrons of energies shown in Equation 4.4.

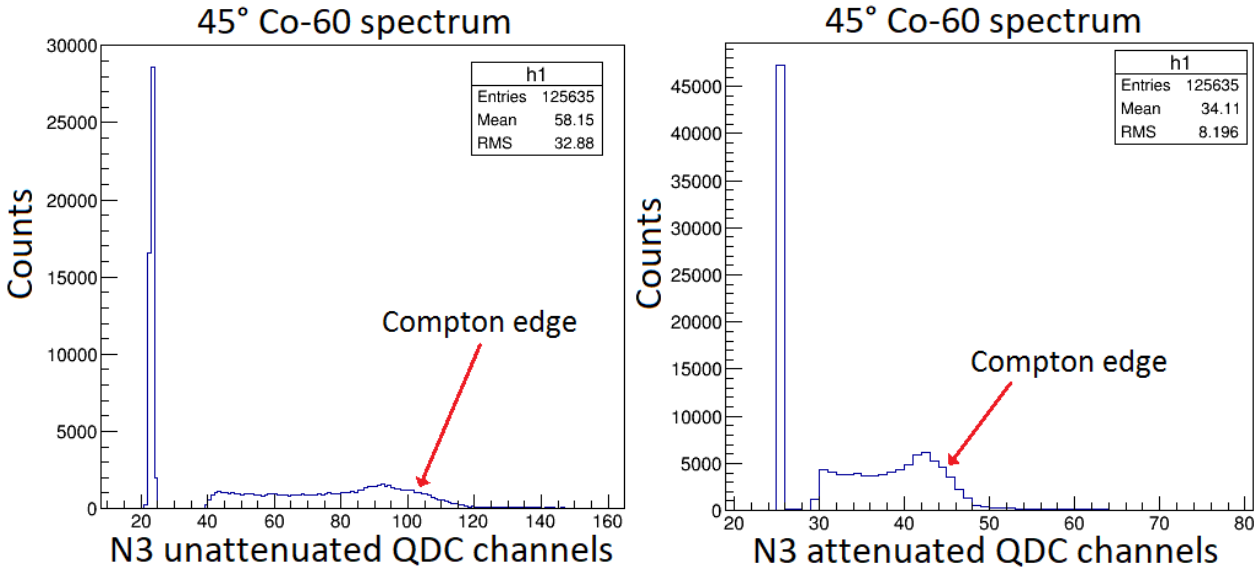
$$E_e = E_\gamma \left[1 - \left(1 + \frac{E_\gamma}{m_e c^2}(1 - \cos\theta) \right)^{-1} \right] = E_\gamma - E'_\gamma \tag{4.4}$$

Since the photon energies of the calibration photon sources are known and the maximum energy electron is created when $\theta = 180°$, the energy of the maximum recoil energy electron can be calculated. The photon sources used in the calibrations were ^{137}Cs and ^{60}Co. ^{137}Cs has a prominent photon energy of 661.62 keV (maximum recoil electron energy of 477.3 keV), but ^{60}Co has two prominent photons at 1332 keV and 1173 keV which appear as one single peak in the scintillators. The peak should be centered at the weighted average (by branching ratio) of these energies which is 1251.49 keV, resulting in a maximum recoil electron energy of 1039.31 keV. This provides two data points. In each QDC spectrum, there is a low channel pileup referred to as the "pedestal" which is taken to be the 0 keVee mark. These features can be seen in Figure 4.13.

Knowing the maximum electron energy, the channel corresponding to the Compton edge, which corresponds to 80% of the maximum recoil electron energy, can be selected [25]. So, the Compton edge channel can be identified by finding the counts in the peak channel, multiplying that value by 0.8, and finding the corresponding average channel value (not necessarily an integer) to the right of the peak that would have that bin value [2, 33].

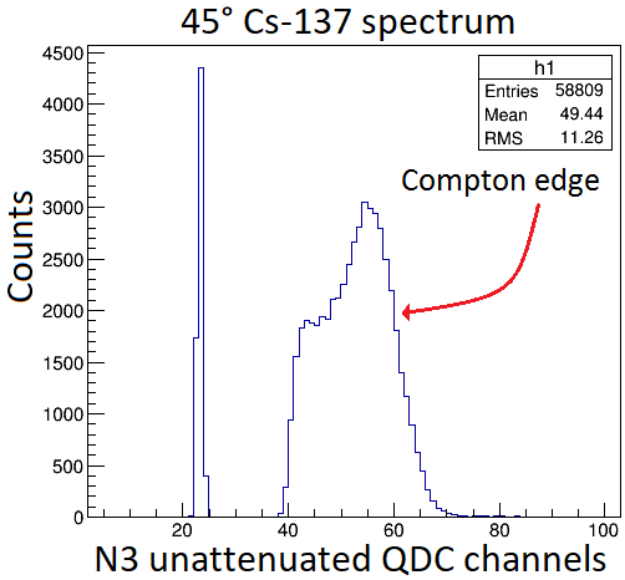
A linear regression fit (Equation 4.5) is then performed with channel number on the x-axis and the electron energies on the y-axis. The unattenuated QDC calibration curve for N1, the 10° detector, in the November 2016 experiment is shown plotted in Figure 4.14. This process is also completed for the attenuated spectra. All of the fitting parameters for the QDC calibrations of the November 2016 experiment are tabulated in Table 4.3.

$$y(\text{keVee}) = m \cdot x(\text{channel } \#) + b \tag{4.5}$$

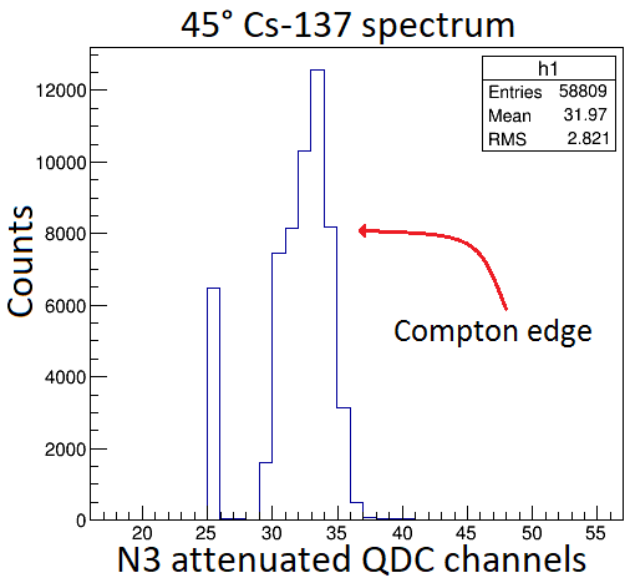


(a) Unattenuated ^{60}Co spectrum

(b) Attenuated ^{60}Co spectrum



(c) Unattenuated ^{137}Cs spectrum



(d) Attenuated ^{137}Cs spectrum

Figure 4.13: QDC calibration spectra for N3

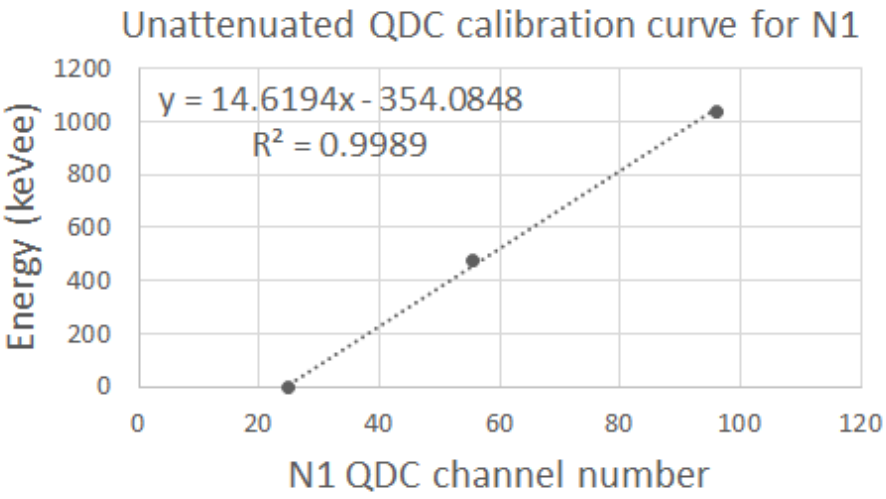


Figure 4.14: Calibration curve translating channel number to light produced in keVee for N1 (10°) in the November 2016 experiments

Table 4.3: QDC channel to light yield fitting parameters for Equation 4.5

Detector	Operating Voltage (V)	Unattenuated `NX.t_qdc` m (keVee/ch)	b (keVee)	R^2	Attenuated `NX.ta_qdc` m (keVee/ch)	b (keVee)	R^2
N1	1500	14.6194	-354.0848	0.9989	61.1630	-2878.8183	0.9998
N2	1400	12.3348	-382.1599	0.9987	54.7282	-1209.2806	0.9997
N3	1400	12.9661	-302.2524	0.9993	57.7672	-1506.6862	0.9998
N4	1800	3.9458	-87.3884	0.9995	17.1850	-432.7622	0.9999
N5	1800	2.6451	-56.9052	0.9988	11.2565	-279.4153	1.0000
N6	1900	1.8279	-24.8576	0.9988	7.9312	-188.4455	1.0000

4.4 Normalizing and combining data

Once all of the appropriate filters have been determined to isolate the good neutron events from everything else, time spectra can be generated. Since each measurement was made across multiple runs using different shadowbar configurations, each final time spectrum is the combination of several measurements. This section discusses how this combination of individual measurements is handled from a mathematical standpoint. When adding and/or subtracting runs, maintaining proper data normalization is critical.

Neutrons from the upstream target are isolated by subtracting the normalized counts observed when a detector is covered (shadowed) from the normalized counts observed when it is not concealed (unshadowed).

The normalized sum of M runs is calculated by Equation 4.6 where:

- s_i is the total number of incident beam particles of run i.
- g_i is the good beam fraction of run i.
- l_i/r_i is the fractional detector live-time of run i.
- E_i is the number of events in run i meeting the criteria of the desired gates and cuts.

$$\text{Normalized sum of M runs} = \left(\sum_i^M s_i g_i\right)^{-1} \cdot \sum_i^M \frac{E_i}{l_i/r_i} \tag{4.6}$$

The first term is the normalization to the total number of good beam particles striking the target ($s_i g_i$) across the runs being added. The second term converts the number of measured events E_i to the number of actual events by dividing by the live time correction (l_i/r_i).

Expanding Equation 4.6 to the case in this work, the normalized difference of M unshadowed runs and N shadowed runs is shown in Equation 4.7. The added terms and subtracted terms are treated separately in normalization prior to taking the difference.

$$\text{Normalized difference} = \left(\left(\sum_i^M s_i g_i\right)^{-1} \cdot \sum_i^M \frac{E_i}{l_i/r_i}\right) - \left(\left(\sum_j^N s_j g_j\right)^{-1} \cdot \sum_j^N \frac{E_j}{l_j/r_j}\right) \tag{4.7}$$

The normalization is what allows this subtraction to be made fairly. The end result of this process is a spectrum of neutrons produced in the front target alone normalized to the number of good source particles and compensated for detector live-time.

After isolation and normalization, neutron TDC spectra can be exported from ROOT. The TDC spectra, only normalized to detector live-time, are printed to text files with the normalization factor for the number of good beam particles printed at the end. For each beam/target/detector combination, two files are written: a summed and normalized spectrum for unshadowed runs and a summed and normalized spectrum for shadowed runs. These are then read by Python and stored in NumPy arrays for all further calculations, including the eventual background subtraction as depicted in Equation 4.7.

4.5 Characterizing the prompt gamma peak

Section 4.6.1 will discuss the time-of-flight methodology in more explicit detail, but the core idea is that the neutron flight times are not derived from the absolute TDC channel time. Instead, the neutron flight time is calculated relative to the flight time of photons produced in the upstream target. A prominent peak characteristic of photons produced in the upstream target, referred to as the "prompt gamma peak," is present in the photon time spectra and must be characterized.

Since photons travel at a constant velocity, their time spectra are characterized by a prominent peak which is only widened by the variance in possible production points (primarily due to the thickness of the targets) and variance in possible detection locations (due to the depth of the OLS detectors). The location of this peak is used for defining the relative neutron flight time, and the width of this peak is later used in the energy resolution calculation (Section 5.4). In Section 4.2.4, two cuts were made on the shown n/γ plots: one isolating neutrons and another encompassing all events. Normalized photon time spectra are composed in the exact same fashion as neutron time spectra except gating on events within the all-encompassing cut but not inside the neutron-exclusive graphical cut.

Since the position of this photon peak and its width will vary with each different beam and target, this process must be repeated for every single beam/target/detector combination.

Across the November 2016 and 2017 experiments, this process is repeated 630 times. This section will step through a brief example of this process for 400 MeV/n C incident on 20 g/cm^2 Al for the N1 and N4 detectors. Table 4.4 shows the relevant run numbers to this example and their shadowbar configurations. When looking at detectors N1 and N4 for example, runs 267, 272, and 278 are added and run 273 is subtracted in the normalization.

The importance of performing this normalization in identifying the prompt gamma peak is showcased in Figure 4.15 where the normalized counts prior to background subtraction are shown in black and the normalized counts after background subtraction are shown in blue.

The leftmost peak disappears almost entirely after subtracting out the shadowed runs, and the middle peak shows some depression. The right peak remains almost entirely unchanged. This illustrates that the rightmost peak is the prompt gamma peak since subtracting the shadowed runs should leave it unchanged (since no prompt gamma rays reach the detector when covered by a shadow bar). Removing the contamination from photons produced elsewhere (namely the back target for the lower-angled detectors but also from other room features) allows for the correct identification of which peak corresponds to photons produced in the front target. The difference is also stark when looking at the detectors at higher angles. For instance, Figure 4.16 shows this same plot for N4.

Once a method to identify which peak is the prompt gamma peak has been developed, its location and width need to be numerically quantified. The same Gaussian fitting techniques as used earlier in determining the minimum neutron/gamma separation channel are utilized here. Since the prompt gamma rays can be produced anywhere in the target, the variance in gamma times of flight should increase with increasing target thickness. For the sake of consistency, it is desirable to use the same minimum and maximum channels for fitting Gaussian curves for a given beam and detector, so it logically follows to first fit the widest peak, the one for 60 g/cm^2. Figure 4.17 shows the fitted prompt gamma peaks for photons from the 400 MeV/n C beam incident on the three thicknesses of aluminum targets for detector N4. This is then repeated for the remaining five OLS detectors. Figure 4.18 shows the fit for N1 with a target thickness of 60 g/cm^2.

Table 4.4: Shadow bar configuration for 400 MeV/n C on 20 g/cm^2 Al

Run	Shadowbar configuration	Uncovered detectors	Covered detectors
267	D	1,2,4,5	3,6
272	C	1,3,4,6	2,5
273	B	2,3,5,6	1,4
278	A	1,2,3,4,5,6	-

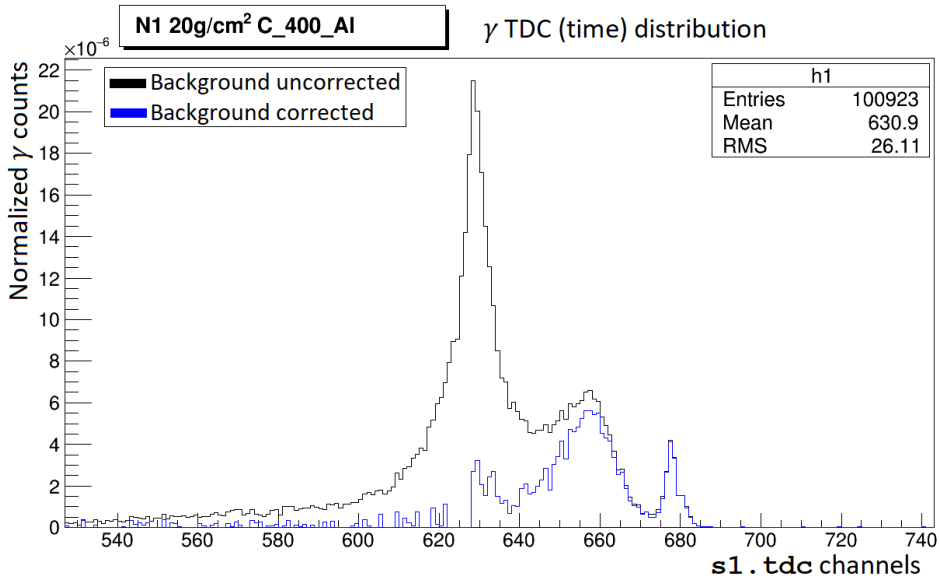


Figure 4.15: Normalized γ TDC spectrum for 400 MeV/n C on 20 g/cm^2 Al for N1

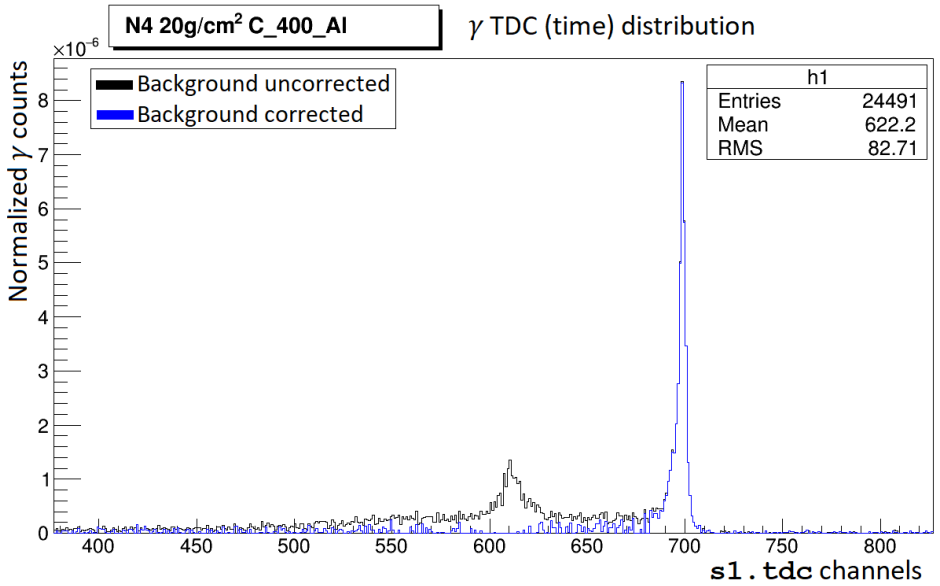
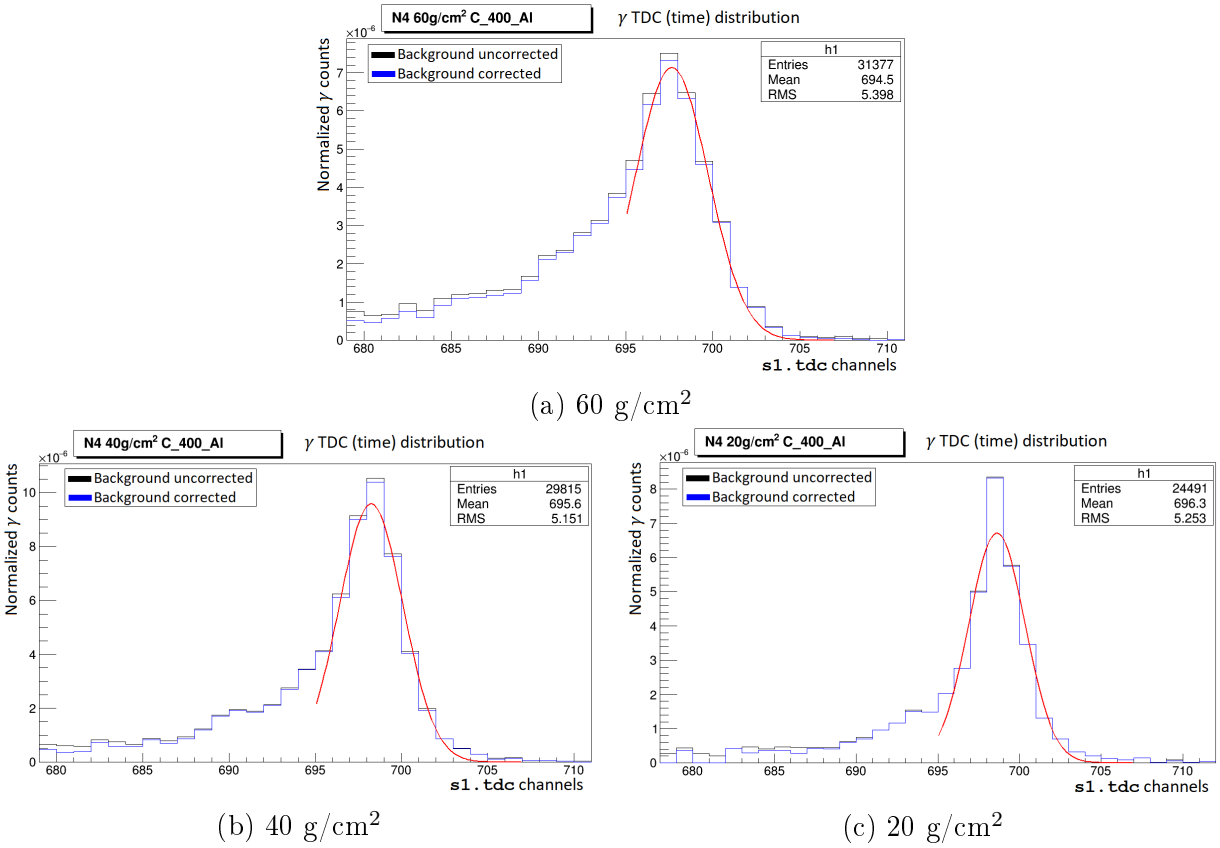


Figure 4.16: Normalized γ ToF spectrum for 400 MeV/n C on 20 g/cm^2 Al for N4



(a) 60 g/cm^2

(b) 40 g/cm^2

(c) 20 g/cm^2

Figure 4.17: Normalized γ TDC spectra in N4 with Gaussian fits for 400 MeV/n C incident on Al targets

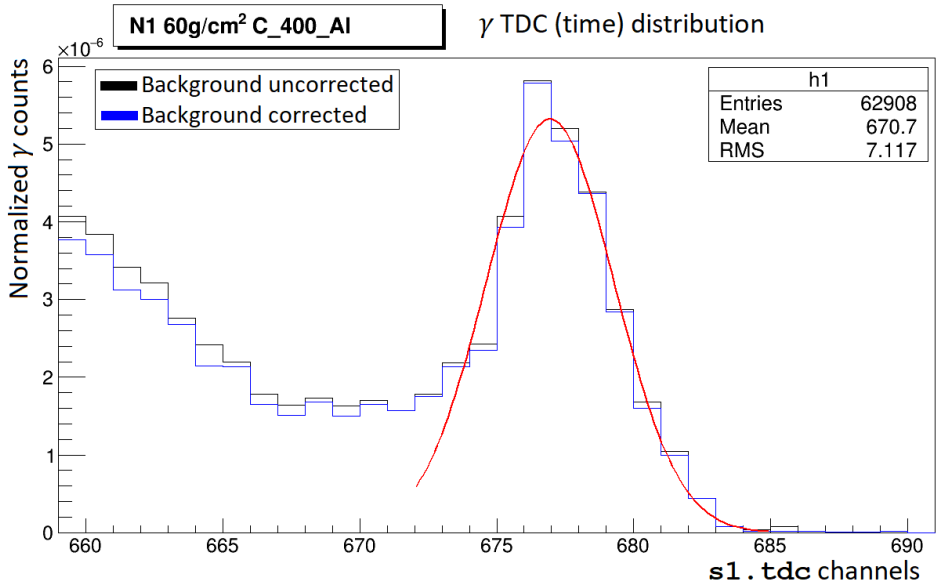


Figure 4.18: Normalized γ TDC spectrum in N1 with a Gaussian fit for 400 MeV/n C incident on 60 g/cm^2 Al

Table 4.5: Prompt gamma peak fitting parameters for 400 MeV/n C on Al (units in `s1.tdc` channels)

	N1	N2	N3	N4	N5	N6
P_{min}	672	666	666	695	687	704
P_{max}	685	678	678	707	700	716
$\bar{x}_{60}$	676.95	669.42	669.34	697.65	690.85	707.75
σ_{60}	2.34	2.12	2.16	2.09	2.70	2.45
$\bar{x}_{40}$	677.29	669.49	669.76	698.22	691.73	707.24
σ_{40}	2.25	1.86	1.97	1.83	2.23	2.28
$\bar{x}_{20}$	677.89	669.81	670.25	698.62	692.45	707.17
σ_{20}	2.13	1.82	1.78	1.73	2.16	1.83

Table 4.5 summarizes the channels used for fitting the Gaussian curve and resulting fitting parameters for each detector and target thickness in this example. P_{min} and P_{max} are the bounding channels used in each Gaussian fit. The peaks indeed become slimmer with decreasing target thickness, as indicated by the σ values.

This process concludes the analysis steps requiring use of ROOT.

4.5.1 Extrapolation to zero target thickness

Discussed in greater detail later in Section 5.4, timing resolution is a core component of the energy resolution uncertainty whose other core component is neutron flight path uncertainty. The width of the prompt gamma peak is used in the time resolution portion of this calculation. However, simply using the prompt gamma peak widths for each different target thickness would result in double counting the effect of the thickness of each target since it is already (and more naturally) folded into the flight path uncertainty calculation. Thus, a timing uncertainty completely decoupled from the target thickness is desired.

This is done by performing a linear regression of the full-width at half maximum (FWHM) values for the three target thicknesses (20/40/60 g/cm^2); the y-intercept would become the FWHM at an extrapolated target thickness of 0 g/cm^2. Ideally, this value should be constant for each of the six detectors. However, this is not the case; the fit yields slightly variable FWHM values for a zero thickness target when evaluated for different beam/target combinations. Rather than just picking a value from a single system to use universally or

using the changing value for each system, an average FWHM at 0 g/cm^2 was calculated using all fits which had an $R^2 \geq 0.95$ for each detector. This intrinsic timing resolution was found to be on the order of about 1.2 ns for each detector, ranging from 0.9 ns to 1.4 ns.

4.6 Performing neutron time-of-flight calculations

This section describes the time-of-flight calculation methodology in general and then discusses the actual analysis methods employed to perform these calculations on the experimental data.

4.6.1 Time-of-flight calculation methodology

A time-of-flight (ToF) energy spectrum can be generated for each detector, beam, target material, and target thickness combination. Fundamentally, this whole process is a matter of translating the x-axis from ROOT, `s1.tdc` channels, to neutron kinetic energy as shown below and is purely algebraic.

$$\text{TDC ch.} \rightarrow \text{TDC time } (ns) \rightarrow \text{flight time } (ns) \rightarrow \text{velocity } \left(\tfrac{cm}{ns}\right) \rightarrow \text{kinetic energy } (MeV)$$

The flight time of a neutron is described by Equation 4.8. Note that the timing is determined relative to the "prompt gamma" rays which are photons produced at an assumed location within the upstream target. The total neutron flight time is just the sum of traversal times through the different materials between the production and detection points for the prompt gamma rays plus the delay between the prompt gamma ray's arrival time and the neutron's arrival time.

$$t_{n_i} = \frac{d_n}{c} + \left((k_{TDC,p\gamma} - k_{TDC,n_i}) \cdot w_{ns/TDC-ch}\right) \tag{4.8}$$

- t_{n_i} - neutron flight time
- d_n - neutron (and prompt gamma ray) flight distance (Equation 4.9)
- c - speed of light

- $k_{TDC,p\gamma}$ - prompt gamma TDC channel
- k_{TDC,n_i} - each neutron TDC channel
- $w_{ns/TDC-ch}$ - conversion factor for ns per channel

The neutron's flight distance, d_n, is the sum of the distance of the production point in the front target to the veto paddle, the thickness of the veto paddle, the gap between the veto and the OLS detector, the thickness of the aluminum detector casing, and half of the active volume of the OLS detector. The detectors are 5"×5" (or 12.7 cm in length and diameter), and the aluminum casing is six hundredths of an inch thick.

$$d_n = d_{\text{target center to veto}} + \delta_{\text{veto}} + d_{\text{veto-detector gap}} + \delta_{\text{Al case}} + \delta_{\text{half detector length}} \tag{4.9}$$

Now knowing the distanced traveled by the neutron and its flight time, the velocity can be derived by dividing distance by time (Equation 4.10).

$$v_n = d_n/t_n \tag{4.10}$$

The velocity can be used to calculate the Lorentz variables β and γ which can be used to calculate the kinetic energy of the neutron, T_n, given its mass m_n (Equation 4.11).

$$T_n = (\gamma - 1)m_n c^2 = \left(\sqrt{\frac{1}{1-\beta^2}} - 1\right) m_n c^2 = \left(\sqrt{\frac{1}{1-(v_n/c)^2}} - 1\right) m_n c^2 \tag{4.11}$$

4.6.2 Time-of-flight data analysis

The same methodology is applied in the actual data analysis on the x-axis (time/energy) except with a few corrections. To be certain that no photons are polluting the neutron spectrum, all events that are triggered within some number of TDC channels of the prompt gamma peak are excluded. In this work, this distance is 3σ of the prompt gamma peak width. During the actual time-of-flight calculations, the x-axis undergoes several transformations as shown earlier.

After the time-of-flight calculations, no more needs to be done to the x-axis aside from rebinning (covered in Section 4.11.3). To save time and effort in the rebinning process later, the absolute statistical uncertainties σ_i associated with each y-axis bin are transformed to a new value, N_i, which is a function of fractional uncertainty; Section 5.1 contains more detailed discussion on this. Having converted the absolute uncertainties to a quantity related to the fractional uncertainty, the multiplicative corrections to the y-axis can be made without needing to constantly update the uncertainties too.

Once imported into Python, the first step taken is the background subtraction. As was discussed earlier, each beam/target/detector combination has two spectra associated with it: the unshadowed spectrum and the shadowed spectrum which will be subtracted from the unshadowed spectrum. The good beam (source particle) normalization is performed immediately followed by this background subtraction, yielding a single TDC spectrum. This process was done in Python rather than ROOT to maintain stronger control over the uncertainty analysis; Section 5.1 covers how the uncertainty N_i values are handled when combining the spectra.

The number of channels available in each collected spectrum is too much. There are too many channels with poor statistics, and the variance from data point to data point is high. To alleviate this, channels are combined into less fine bins in a rebinning process. Discussion of the rebinning process is left to Section 4.11.3. For now, the takeaway is that after rebinning each spectrum has its own number of bins which is likely different from the other spectra and is no longer constant.

The y-axis must undergo a series of normalizations to be converted from raw counts to the desired double-differential yield. The live-time and good beam fraction normalizations, which amount to normalizing the recorded data to the number of valid source particles incident on the target, occurred in the analysis performed with ROOT.

The remaining y-axis corrections are multiplicative in nature. First, detector efficiency must be accounted for. Using the efficiency curve results from SCINFUL-QMD (discussed in Section 4.8) for each detector, each energy bin is divided by the detector's efficiency at that energy. This is done by taking the midpoint of each energy bin and interpolating an efficiency value from the SCINFUL-QMD results at that energy.

Since the desired end units of yield are number per $MeV \cdot sr \cdot s.p.$ ($s.p.$ = source particle), bin width and solid angle normalizations are also made. The bin width correction is the division of each y-axis bin value by the x-axis bin width in MeV. The solid angle correction is also a division, but the process of calculating the solid angle itself is slightly more complex and will be covered in Section 4.7.

Each data point also possesses systematic uncertainties which are covered in greater depth in Chapter 5. The x-axis location of each point has some uncertainty due to energy resolution which is a function of the timing resolution and flight path uncertainty. On the y-axis, each data point is characterized by the statistical uncertainty derived from counting statistics and a systematic uncertainty. The systematic uncertainty is broken into three components: efficiency uncertainty, graphical cut uncertainty, and solid angle uncertainty.

4.7 Solid angle normalization

In addition to dividing by bin width, yield results are also divided by solid angle. Since the detectors lie different distances from the upstream target, the solid angle from the production point is different for each detector. Figure 4.19 shows an arbitrary upstream target / detector system looking down from above; the whole image is taken to be in the plane of the beam centerline. O is the center of the upstream target and is assumed to be the neutron production point. M, N, and Y lie at half of the detector's full length from the detector face.

The angle used in the solid angle calculation, θ, is equal to the angle of $\angle MOY$ or half of $\angle MON$. It can be solved for using Equation 4.12 where r_d is the radius of the detector (a constant equal to the length of $\overline{MY}$) and d_f is the neutron flight distance, $\overline{OY}$.

$$\theta = \tan^{-1}(r_d/d_f) \tag{4.12}$$

θ can then be plugged into the solid angle equation for a cone (since the detector's cross section perpendicular to the neutron flight path is circular), yielding Equation 4.13. The resulting mean solid angles for each detector are shown in Table 4.6.

$$\Omega = 2\pi(1 - \cos\theta) = 2\pi(1 - \cos(\tan^{-1}(r_d/d_f))) \tag{4.13}$$

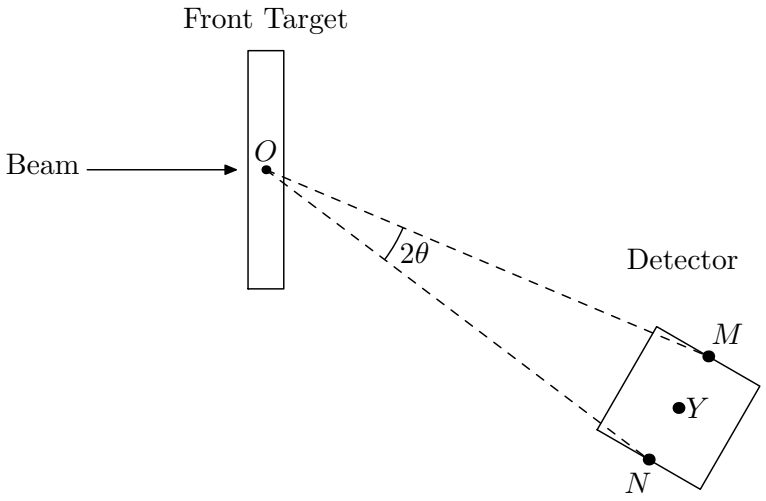


Figure 4.19: Mean solid angle

Table 4.6: Mean solid angle for each detector

Detector	Ω (sr)
N1	1.3343×10^{-3}
N2	1.3381×10^{-3}
N3	1.3376×10^{-3}
N4	1.9072×10^{-3}
N5	1.9066×10^{-3}
N6	2.9180×10^{-3}

However, in reality, all incident neutrons are not interacting with the detector at its midpoint; neutrons can also interact close to the front or back face of the detector, introducing a range of possible solid angles. This is how solid angle uncertainty is determined and is discussed further in Section 5.3.1.

Additionally, as discussed later in Section 4.9, the assumption that neutrons are produced in the center of the target is not accurate for a number of the beam/target configurations. When using a new effective neutron production point, a more representative solid angle Ω_{true} can be calculated for each data point. The methodology for calculating this new true solid angle is the same as is used in calculating the extreme values of the solid angle covered in Section 5.3.1, and the methodology for determining the new production point is covered in Section 4.9.

4.8 Detector efficiency corrections and SCINFUL-QMD

In addition to solid angle and bin width, the neutron data must also be corrected for the intrinsic detector efficiency, which is a function of neutron energy and pulse height threshold. The SCINFUL-QMD code is used to calculate efficiencies for each of the six detectors at a number of different bias threshold energies (determined by the Q_{total} pulse height threshold). In each simulation, detector efficiency for 104 different monoenergetic neutron energies ranging from 2 MeV to 2950 MeV is calculated at a variety of biases.

Each of these SCINFUL-QMD calculations is performed three times for the detector distances of 200 cm (N6), 250 cm (N4 and N5), and 300 cm (N1, N2, and N3). While the distance does not make a large difference, the three are still marginally different from each other. Figure 4.20 shows a sample output efficiency spectrum from SCINFUL-QMD.

These values are used in correcting the neutron spectra where every energy bin in the spectra is divided by a detector efficiency calculated in SCINFUL-QMD. Since the neutron energies simulated will not line up with the bin center neutron energies of the data, the curves generated by SCINFUL-QMD are interpolated for energies between data points.

Efficiency curves were generated for a variety of different bias thresholds for use with the multiple different Q_{total} threshold pulse height cuts as will be discussed in Section 4.10.

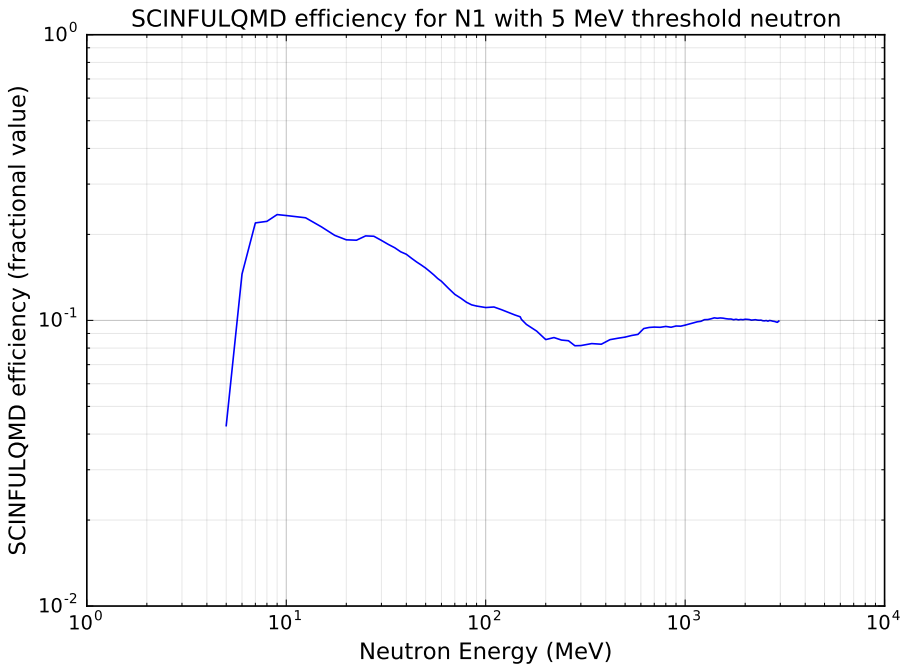


Figure 4.20: Sample output efficiency spectrum from SCINFUL-QMD

4.9 Neutron production point corrections

All time-of-flight calculations so far have assumed that every neutron is produced at the center of the upstream target. This, however, is not the case. For some projectile/target combinations, neutron production in a given energy range is quite localized. This allows for use of a new, more accurate, flight path with much less uncertainty. Approximating where in the upstream target neutrons are produced provides a new flight path for use in the time-of-flight calculations, a reduction in flight path uncertainty (reducing energy resolution uncertainty in x), and a reduction in solid angle uncertainty (reducing systematic uncertainty in y).

The new quantities to determine for every projectile/target combination as a function of energy are (1) a new effective neutron production point and (2) a new adjusted effective target thickness/location; these calculations are discussed in Section 4.9.1. After determining these values, incorporating them into the time-of-flight calculations is not straightforward; this is covered in detail in Section 4.9.2.

4.9.1 Effective production point and target thickness calculations

Initial methodology

In the prior work of Reference 2, a simple correction was developed to account for the uneven distribution of neutron production within the depth of the targets; it was primarily developed to improve x-axis uncertainty for high energy neutrons where $E_n \geq E_{beam[MeV/n]}$. This is done using the PHITS transport code's `[T-Product]` tally to determine high energy neutron production as a function of depth in target for every projectile/target combination. In that work, proton source particle runs were ignored since it is kinematically unlikely for neutrons with $E_n \geq E_{beam[MeV/n]}$ to be produced in great quantity, though characterization of production at lower energies is still desirable and was performed in this work.

Each of these original high-energy simulations only used four energy bins: 1 MeV to 20 MeV, 20 MeV to 100 MeV, 100 MeV to $E_{beam[MeV/n]}$, and $E_{beam[MeV/n]}$ to $(2E_{beam[MeV/n]}+100)$. This upper energy bound is somewhat arbitrary; it is just meant to exceed the beam energy by a significant amount. Figure 4.21 shows the results of one of these simulations for 400 MeV/n C incident on a 60 g/cm^2 Al front target.

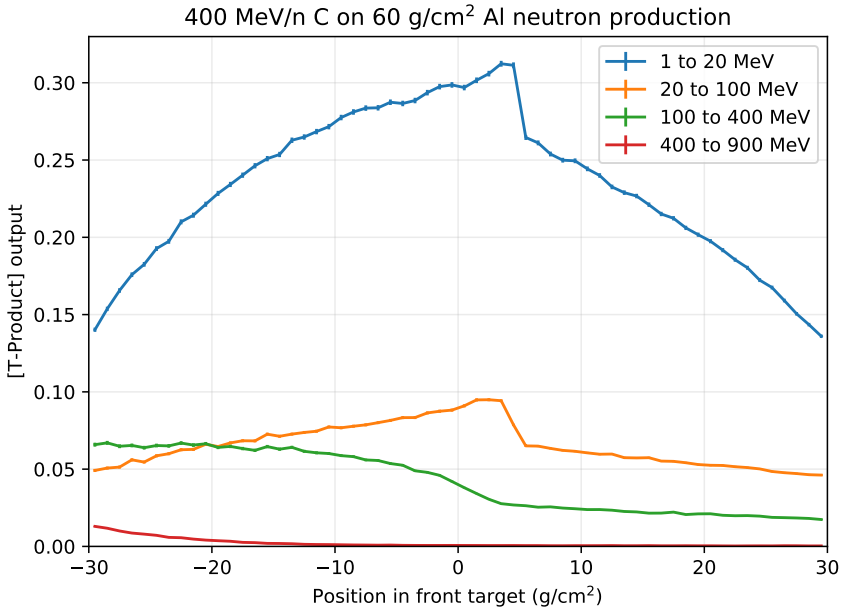


Figure 4.21: Neutron production in 60 g/cm^2 Al front target for 400 MeV/n C

Additionally, for each bin in the tallied `[T-Product]` output, the integral percentage neutron production yield is calculated in the analysis code using Equation 4.14 where N_T is the total number of positional bins the front target is divided into, N_j is the number of number of bins leading up to and including the present bin j ($N_j < N_T$), and A_i is the tally value of bin i. Since the target is being stepped through in 1 g/cm^2 steps in all simulations, there are 60 bins populated for the 60 g/cm^2 targets, 40 bins populated for the 40 g/cm^2 targets, and 20 bins populated for the 20 g/cm^2 targets.

$$P_{j,\text{ integral percentage produced}} = 100\% \times \left(\left(\sum_{i=1}^{N_j} A_i \right) \Big/ \left(\sum_{i=1}^{N_T} A_i \right) \right) \tag{4.14}$$

This calculation allows for quick determination of by what depth in the front target a certain percentage of neutrons in a given energy bin (the highest energy bin is the one of concern here) have been produced. Figure 4.22 shows the same plot as Figure 4.21 except with only the highest energy bin (400 MeV to 900 MeV in this case). Additionally, a vertical line has been drawn at the location in the target by which 80% of the neutrons in that energy bin have been produced. This effect is most exaggerated for the high atomic number projectiles.

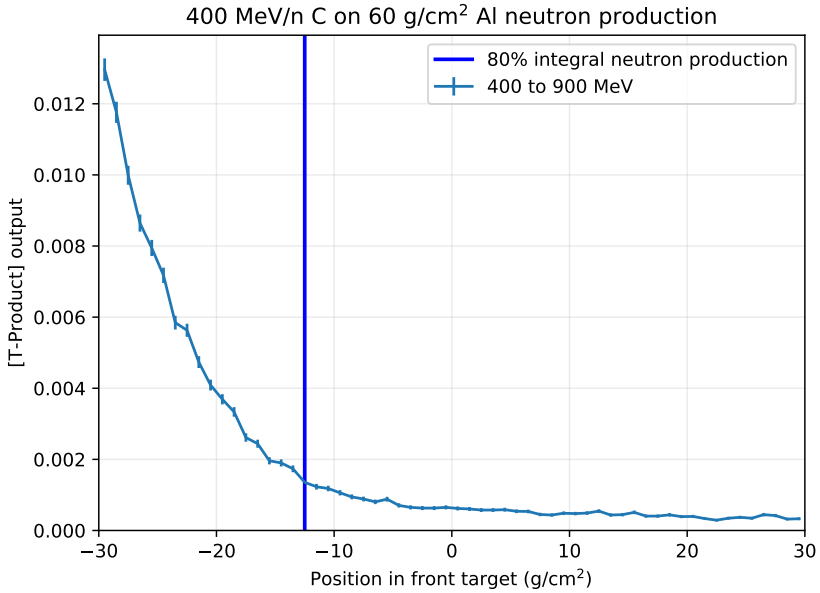


Figure 4.22: Neutron production in 60 g/cm^2 Al front target for 400 MeV/n C with 80% line

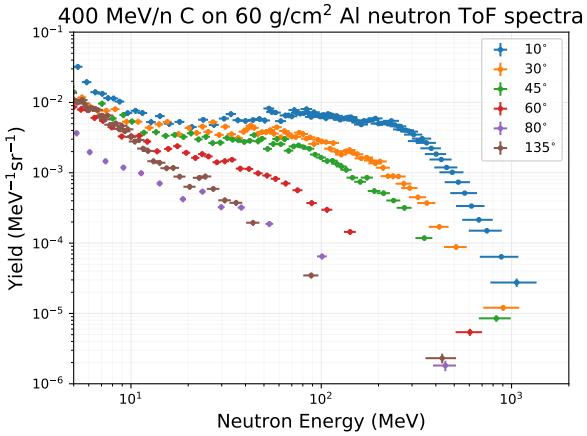
These PHITS calculations allow for use of a more accurate mean production point for these high energy neutrons as well as narrow down where in the target these neutrons are produced, allowing for the reduction of their solid angle and flight path uncertainties. However, this creates a notable discontinuity in the neutron energy spectra by producing a gap immediately after the beam energy due to the flight path suddenly changing. Additionally, this makes the one bin that bridges this gap become much wider than it should be, meaning it falls well below its surrounding points after dividing by bin width, further exacerbating this issue.

Figure 4.23a shows ToF spectra that have not had any production point corrections applied with error bars denoting statistical uncertainty in y and energy resolution uncertainty in x. Figure 4.23b shows this same spectrum but with the $E_n \geq E_{beam[MeV/n]}$ region shifted/corrected. The high energy x error bars do get smaller, and this effect is notably more pronounced for higher Z ions. However, a significant discontinuity appears at the beam energy, 400 MeV/n. In an attempt to make this gap less immense, this correction was also applied to the 100 MeV to $E_{beam[MeV/n]}$ region as seen in Figure 4.23c. While this does make the gap smaller, it spawns another shift discontinuity at 100 MeV with the point bridging the gap being notably depressed.

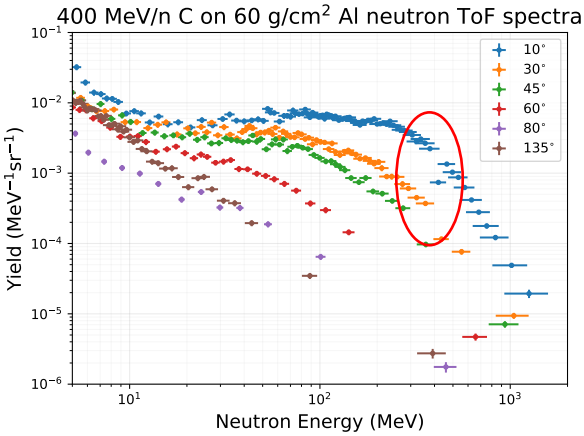
The crux of this issue is the sudden shift in flight path and neutron energy. By changing the flight path at a distinct threshold, a gap/discontinuity is spawned between the two. This problem should be alleviated if the flight path is instead represented as a continuous function of neutron energy. This begins the original work presented in this research which sought to iterate on, improve, and generalize the idea of using PHITS simulations to update neutron production point locations used in all time-of-flight-related calculations.

Creating a continuous production point

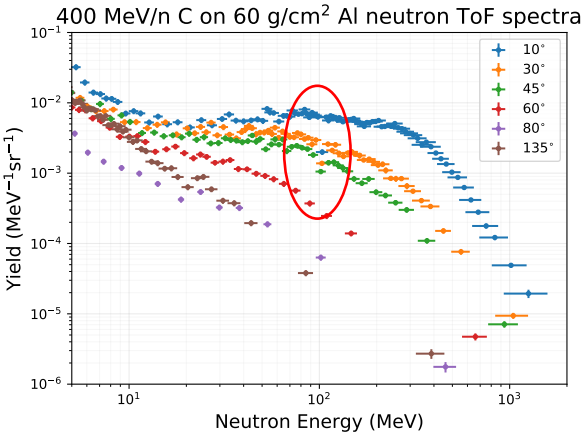
Additional PHITS simulations were conducted with more finely resolved energy bins in the intermediate energy regions. The new energy bins are: one bin from 1 MeV to 20 MeV, one bin from 20 MeV to 100 MeV, $(E_{beam[MeV/n]}/100) - 1$ bins each 100 MeV wide, and a final bin from $E_{beam[MeV/n]}$ to $(2E_{beam[MeV/n]} + 100)$. For each energy bin, a mean and median



(a) ToF spectrum with no production point correction



(b) Production point correction for $E_n > E_{beam}$



(c) Correction for $E_n > 100$ MeV

Figure 4.23: Discontinuities are created by discrete production point correction regions.

production point can be found. In these calculations, it is assumed that all events in each position bin are equally distributed across the 1 g/cm^2 depth steps.

The median production point is taken to be the first position bin in the integral production matrix, found earlier in Equation 4.14, exceeding 50% for each energy bin. To make the resolution of this position finer than 1 g/cm^2, the exact 50% product point, $\widetilde{x}$, is found by interpolating within the bin as shown in Equation 4.15. P_i is the integral percentage of neutrons produced by and including position bin i, i_m is the index of the position bin first exceeding 50% neutrons produced ($P_{i_m} > 50\%$), and x_i is the i^{th} position bin's left edge value (with x_{i+1} being the i^{th} position bin's right edge value).

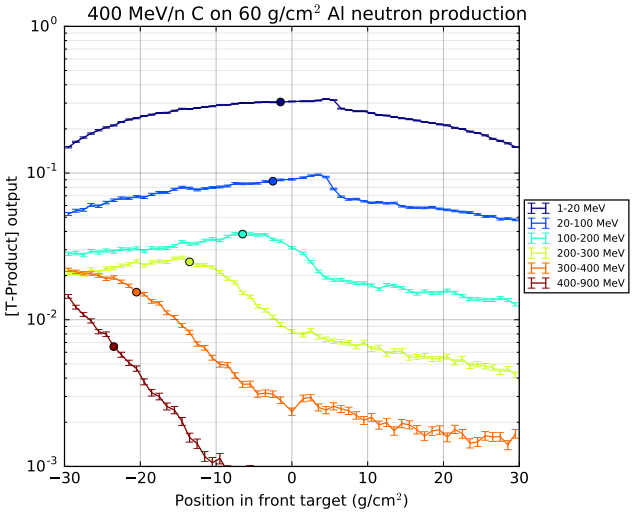
$$\widetilde{x} = \left(\frac{50\% - P_{i_m-1}}{P_{i_m} - P_{i_m-1}} \right) (x_{i_m+1} - x_{i_m}) + x_{i_m} \tag{4.15}$$

The mean production point is calculated using Equation 4.16 where M is the number of position (x-axis) bins along the thickness of the front target, X_i is the i^{th} position bin's midpoint value, and $T_{\text{prod},i}$ is the i^{th} `[T-Product]` bin value (or the number of events in that bin). This calculation is repeated for every energy bin. The `[T-Product]` tally value can be used directly, rather than using the number of events in the bin, since it is a normalized frequency distribution of events already.

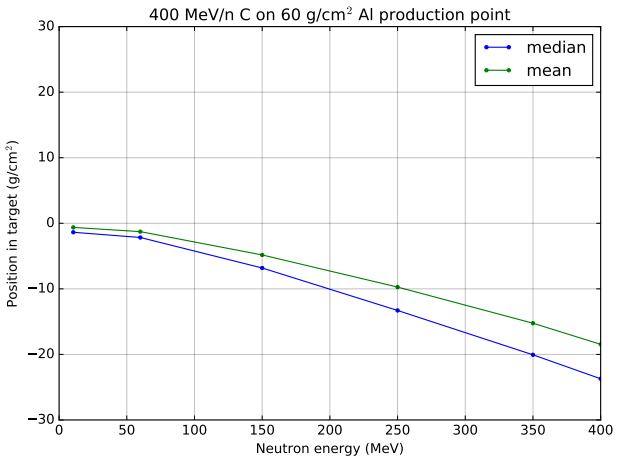
$$\bar{x} = \left(\sum_{i=1}^{M} X_i T_{\text{prod},i} \right) \Bigg/ \left(\sum_{i=1}^{M} T_{\text{prod},i} \right) \tag{4.16}$$

Figure 4.24a shows an updated version of Figure 4.21 but with more energy bins and the median production point plotted as a dot on each curve. Figure 4.24b shows how the mean and median production points change as a function of secondary neutron energy.

The higher energy beams with more energy bins better illustrate the production point's functionality of neutron energy. Figure 4.25a shows `[T-Product]` output as a function of position in target and energy bin for neutrons produced in the 20 g/cm^2 HDPE target being bombarded by the 1463 MeV/n Fe beam. Figure 4.25b shows how the mean and median production points change as a function of neutron energy in this case.

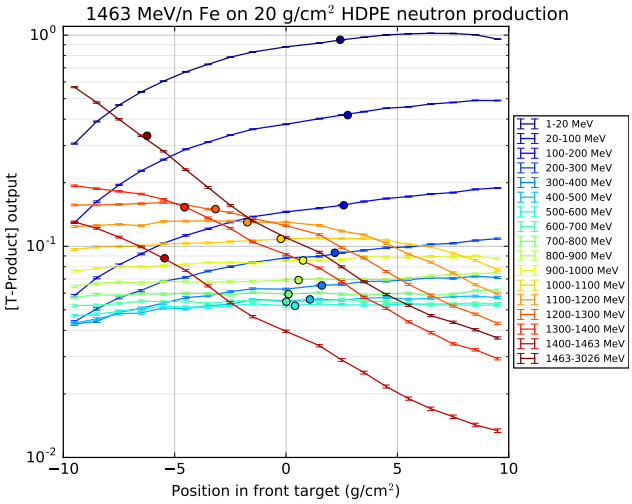


(a) `[T-Product]` distributions

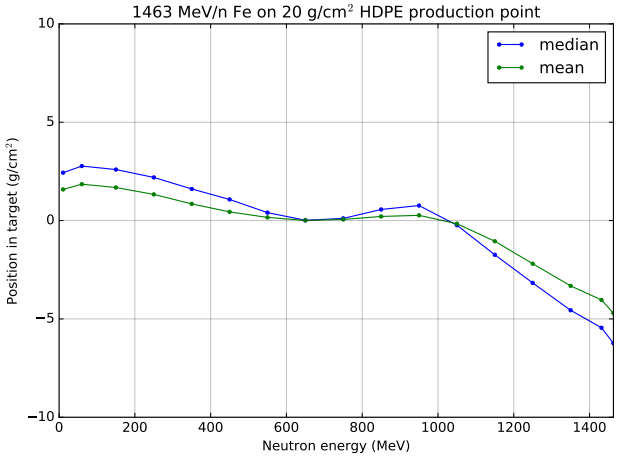


(b) Mean and median production points

Figure 4.24: Neutron production in 40 g/cm^2 Al front target for 400 MeV/n C



(a) `[T-Product]` distributions



(b) Mean and median production points

Figure 4.25: Neutron production in 20 g/cm^2 HDPE front target for 1463 MeV/n Fe

Incorporating the production distributions

Additionally, the variance σ^2 can also be approximated from this tally information. The approach to calculate the variance for a Monte Carlo simulation is shown in Equation 4.17.

$$\sigma^2 \approx \left(\sum_{n=1}^{N}(\hat{x}_n - \bar{x})^2\right) \Big/ (N-1) \tag{4.17}$$

Here, N is the total number of events tallied, $\hat{x}_n$ is the individual value of each tally, and $\bar{x}$ is the mean. Note that since the mean here, $\bar{x}$, is actually an approximation of the mean rather than the true mean, $N-1$ is used in the denominator rather than just N alone. This equation cannot be applied exactly as is since PHITS is not collecting a list of the exact x-coordinates for each neutron produced. Instead, since the number of counts in each position bin can be found from the fractional error (see Equation 5.4 from Section 5.1), one can conduct this calculation assuming every event tallied in a position bin occurs at its midpoint, $\hat{x}_{i,\text{mid}}$, as shown in Equation 4.18. N_i is the number of events tallied in the i^{th} of M position bins, and N_{total} is the number of events tallied across all M position bins.

$$\sigma^2 \approx \left(\sum_{i=1}^{M} N_i \times (\hat{x}_{i,\text{mid}} - \bar{x})^2\right) \Big/ (N_{\text{total}} - 1) \tag{4.18}$$

To make this more precise though, one can instead evenly sample $(\hat{x}_i - \bar{x})^2$ over the entire range of the position bin, x_i to x_{i+1}, and find its average value, $((\hat{x}_i - \bar{x})^2)_{avg}$ as shown in Equation 4.19.

$$\begin{aligned}((\hat{x}_i - \bar{x})^2)_{avg} &= \frac{1}{x_{i+1} - x_i}\int_{x_i}^{x_{i+1}} (x - \bar{x})^2 dx \\ &= \frac{1}{x_{i+1} - x_i}\left(\frac{1}{3}(x_{i+1}^3 - x_i^3) - \bar{x}(x_{i+1}^2 - x_i^2) + \bar{x}^2(x_{i+1} - x_i)\right)\end{aligned} \tag{4.19}$$

This can be substituted back into Equation 4.18, yielding Equation 4.20.

$$\sigma^2 \approx \left(\sum_{i=1}^{M} N_i \times \left((\hat{x}_i - \bar{x})^2\right)_{avg}\right) \Big/ (N_{\text{total}} - 1) \tag{4.20}$$

The standard deviation σ can be taken to just be the square root of the variance σ^2.

A similar quantity can be derived from the median. Since the median is located at the depth in the target where 50% of the neutrons in a certain energy bin are created, one can encompass the median in a band with an upper and lower bound which contains a certain percentage of the total neutrons produced. For instance, a band containing 80% of all neutrons could be drawn around the median with the lower bound located at the point at which 10% of all neutrons have been produced and the upper bound at the point at which 90% of all neutrons have been produced. Figure 4.26 shows an example of the new effective target location/thickness using these mean/standard deviation and median/median band techniques.

A perhaps even better approach to implementing this "integral percentage production band" could be to determine the band's lower and upper bounds by forcing the constraining factor to be the minimization of the distance between the lower and upper bounds rather than having an equal fraction of neutrons produced on each side of the median. While this method would not necessarily change the bounds for the more flat or center-peaked `[T-Product]` distributions, it could considerably shrink the effective thickness of the target

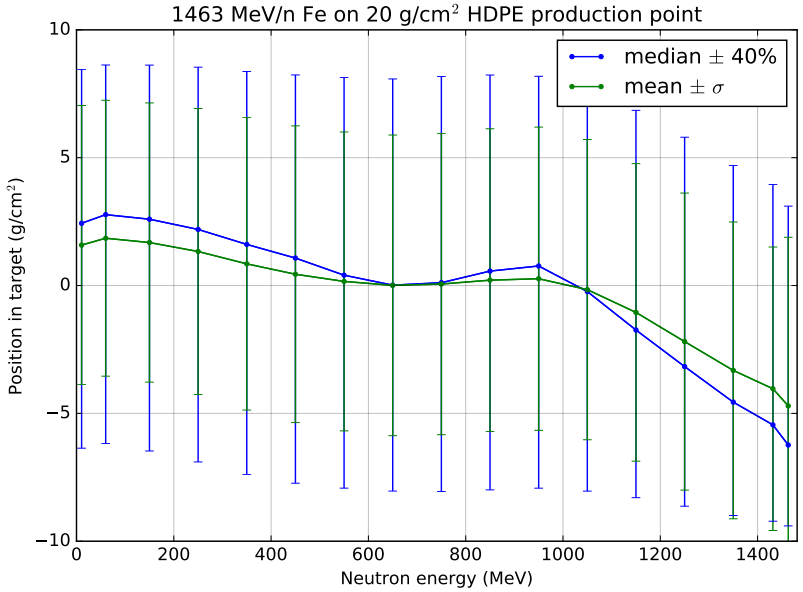


Figure 4.26: Mean and median production point as a function of position in target with 80% production band shown as vertical error bars on the median curve and one standard deviation as the error bars on the mean curve

for the production spectra heavily peaked toward one face of the target, namely the very high energy neutrons around and above the beam energy. This action is expressed mathematically in Equation 4.21 where x_{upper} and x_{lower} are the lower and upper bounds of the band, $T_{\text{prod}}(x)$ are the `[T-Product]` position bins for a given energy group, and $P_{\text{threshold}}$ is the desired threshold percentage of neutrons the band should contain.

$$\underset{x_{\text{lower}}}{\text{argmin}}(x_{\text{upper}} - x_{\text{lower}}) \text{ such that } \int_{x_{\text{lower}}}^{x_{\text{upper}}} T_{\text{prod}}(x)dx = P_{\text{threshold}} \tag{4.21}$$

By once again using the integral production array calculated earlier in Equation 4.14, represented as $P(x)$, this can be simplified to a much easier to calculate Equation 4.22.

$$\underset{x_{\text{lower}}}{\text{argmin}}(x_{\text{upper}} - x_{\text{lower}}) \text{ such that } P(x_{\text{upper}}) - P(x_{\text{lower}}) = P_{\text{threshold}} \tag{4.22}$$

From a coding perspective, the way to calculate these lower and upper bounds is to determine x_{upper} for every x_{lower} bin where $P(x_{\text{lower}}) \leq 100\% - P_{\text{threshold}}$, calculate the difference $(x_{\text{upper}} - x_{\text{lower}})$, and afterward select the bounds where this quantity is minimized. An updated version of Figure 4.26 including calculations using this "minimum-width band" method is shown in Figure 4.27.

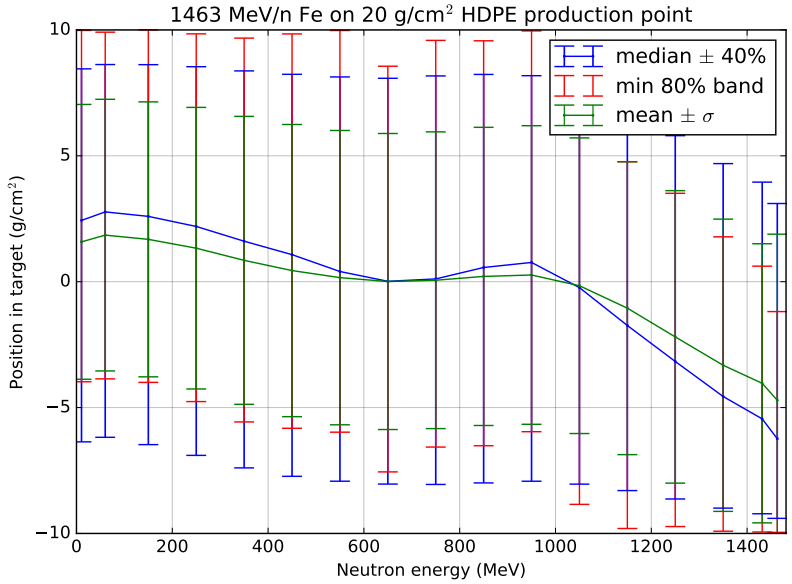
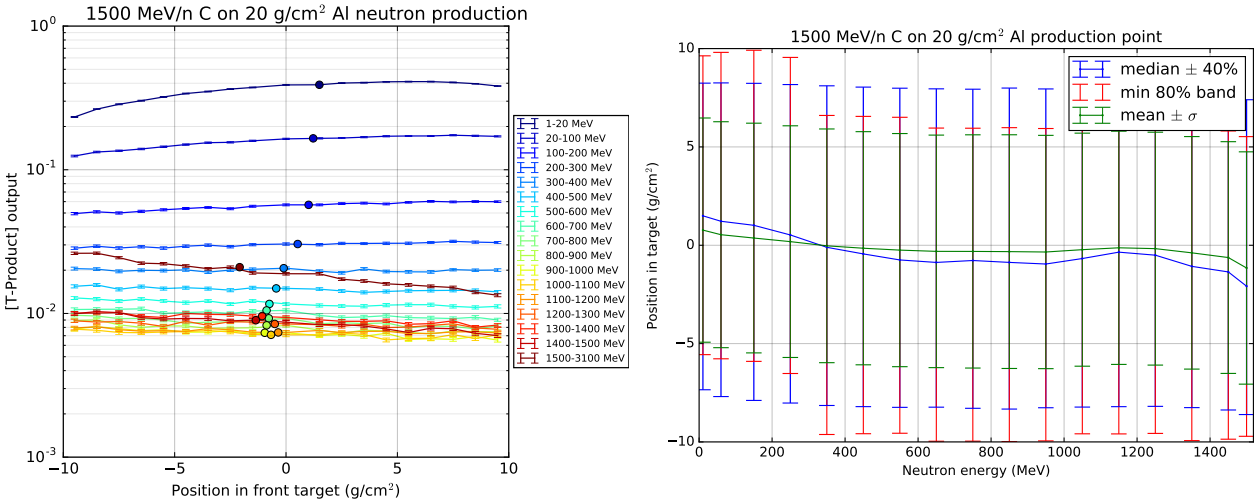


Figure 4.27: Same as Figure 4.26 except with the addition of the minimum-width 80% production band as red error bars

These calculations provide a convenient way to determine an adjusted effective target thickness and more precise production point. Now the choice must be made on which of these options to use. Since neutron production is not Gaussian distributed in the target, the median production point seems like a more natural approach to this task over the mean. Using the same reasoning for determining the effective target thickness, one can rule out use of the standard deviation methodology, leaving the "median band" and the "minimum-width band" methods.

Strong arguments can be made for the use of either of these two methods. The "minimum-width band" method best accomplishes the goal of minimizing flight path and solid angle uncertainties and is a strong choice especially for the cases where production in the target is highly localized toward one face of the target. However, its behavior is not as consistent as the "median band" method. For instance, in the case of 1500 MeV/n C incident on a 20 g/cm^2 Al front target where neutron production is fairly even throughout the target (Figure 4.28a), there is a sudden shift in the effective target location when using the "minimum-width band" method after 300 MeV (Figure 4.28b). Even in the case presented earlier in Figure 4.27, there are a handful of minor inconsistencies from energy bin to energy bin.

This inconsistency brings the validity of the "minimum-width band" method into question for such cases where neutron production is fairly uniform in the target. While this method



(a) `[T-Product]` distributions

(b) Mean and median production points

Figure 4.28: Neutron production in 20 g/cm^2 Al front target for 1500 MeV/n C

appears valid in extreme cases, it seems not to perform as desired here. However, since the median location is being used and the absolute effective target thickness (but not position) is continuous, the fractional change in the total flight path, which is the term used in the x-axis uncertainty term, across these discontinuous-looking jumps is actually continuous.

The "minimum-width band" method does produce notably finer results, especially for the more extreme cases. While the "median band" method has more consistency and feels more natural by having an even fraction of neutrons being produced in either section between the median production point and effective target boundary, the "minimum-width band" method was decided on for its objectively stronger performance in reducing the x-axis uncertainty.

4.9.2 Application of production corrections to ToF calculations

Applying all of this new information to the ToF calculations is not straightforward. One can notice some recursion occurring here in the proposed methodology. In the ToF energy calculation, the flight path must be known beforehand. It is assumed that the center of the target is the production point. This analysis proposes that then, given a certain energy is calculated, the ToF calculation is redone using a new production point deduced from the initial calculated energy. This leads to an iterative process where the calculation is redone until some convergence is reached.

Since the production point changes smoothly with energy (as seen in Figure 4.28b and the similar figures before it), the production point used in the ToF energy calculations can be interpolated from these plots. For any neutrons with energy greater than the beam energy, the production point value from the $E_{beam[MeV/n]}$ to $(2E_{beam[MeV/n]} + 100)$ bin is used. It is assumed that this behavior is consistent for all neutrons even further above the beam energy.

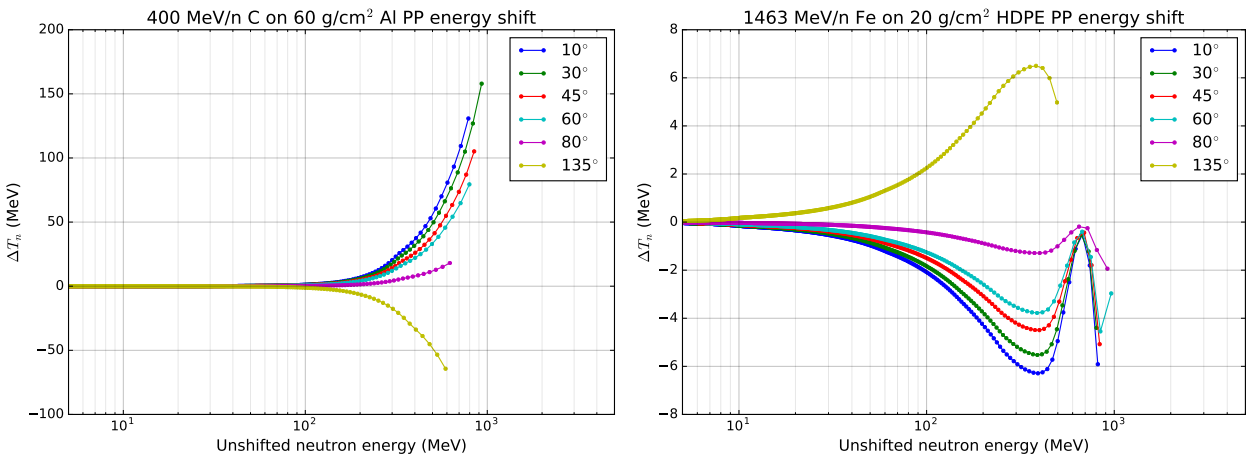
After first calculating an initial neutron kinetic energy T_n, the first step in this iterative process is to identify which energy bin, $E_{min,i}$ to $E_{max,i}$ (or $E_{min,i+1}$), of the PHITS-simulated results that T_n is in. Then, since the production points calculated with PHITS are for ranges of energies, not discrete energies, the midpoint of the energy bin $E_{\text{mid},i}$ and the midpoints of the surrounding energy bins $E_{\text{mid},i-1}$ and $E_{\text{mid},i+1}$ are calculated. The corresponding production points are referred to as $x_{\text{pp},i-1}$, $x_{\text{pp},i}$, and $x_{\text{pp},i+1}$. These are all then used to determine the interpolated production point $\hat{x}_{\text{pp}}(T_n)$ in Equation 4.23.

$$\hat{x}_{\mathrm{pp}}(T_n) = \begin{cases} \left(\dfrac{T_n - E_{\mathrm{mid},i-1}}{E_{\mathrm{mid},i} - E_{\mathrm{mid},i-1}}\right)(x_{\mathrm{pp},i} - x_{\mathrm{pp},i-1}) + x_{\mathrm{pp},i-1} & \text{, if } T_n < E_{\mathrm{mid},i} \\ x_{\mathrm{pp},i+1} - \left(\dfrac{E_{\mathrm{mid},i+1} - T_n}{E_{\mathrm{mid},i+1} - E_{\mathrm{mid},i}}\right)(x_{\mathrm{pp},i+1} - x_{\mathrm{pp},i}) & \text{, if } T_n > E_{\mathrm{mid},i} \end{cases} \tag{4.23}$$

Next, the new flight path which is taken to be the distance between this new production point and the assumed interaction point, taken to be the center of the detection volume, is calculated with the Cartesian distance formula (Equation 5.17). Section 5.3.1 covers the characterization of important spatial locations in the experiment room in Cartesian coordinates in detail. It is assumed that this shift in production point only occurs in the beamline axis; no positional shifting occurs in the plane perpendicular to the beam axis. After determining the new flight path distance d_n', velocity v_n' (Equation 4.10) and kinetic energy T_n' (Equation 4.11) are recalculated in the same fashion as discussed in Section 4.6.1. This process is repeated until the convergence criteria in Equation 4.24 is met where ϵ is set to a small value ($\epsilon = 0.0001$ was used here).

$$\left|\frac{T_n' - T_n}{T_n'}\right| < \epsilon \tag{4.24}$$

Once convergence is achieved and a new T_n' has been found, the new production point $\hat{x}_{\mathrm{pp}}$ is saved for use in calculating a corresponding new average solid angle and for energy resolution calculations later. Section 5.3.1 covers the general methodology employed to calculate solid angles in this experiment with production and interaction points using their spatial coordinates. The primary difference is that rather than using the front or back face of the detector as the interaction plane, the center plane of the detector ($\overline{MYN}$ in Figure 5.2) is used instead. This also implies that each bin will have its own slightly different solid angle correction rather than having one universal solid angle per detector. After this step, the spectra are rebinned as discussed in Section 4.11.3. The effect of this energy shift is depicted in Figures 4.29a and 4.29b where ΔT_n is the change in neutron energy by introducing this production point correction.



(a) 400 MeV/n C on 60 g/cm^2 Al (b) 1463 MeV/n Fe on 20 g/cm^2 HDPE

Figure 4.29: Effect of neutron energy shift

These figures illustrate how prominent or insignificant this correction can be. In the case of the high energy iron beam incident on a thin HDPE target where production is relatively even and fairly centered in the target, no point is shifted more than 10 MeV. However, in the case of the "low" energy carbon on the thick aluminum target, the high neutron energy points, where neutron production is extremely localized on the upstream face of the target, see a substantial shift in energy. Note that these curves depict exactly what one would expect to see when the production point is shifted. In the case of the carbon beam, the production point is shifted upstream over the whole energy domain (Figure 4.24b). The flight time remains constant, but the flight path increases for the downstream detectors (N1-N5), increasing velocity and kinetic energy, and decreases for the upstream detector (N6), decreasing velocity and kinetic energy. The reverse is seen in the iron beam where neutron production below about 1 GeV is actually centered slightly downstream from the center of the primary target (Figure 4.26).

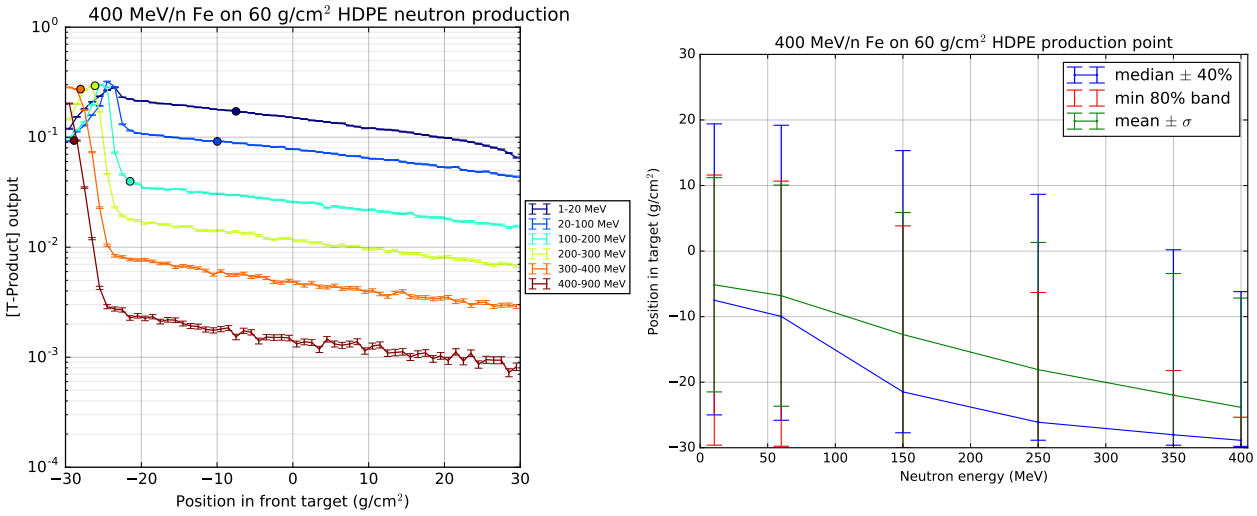
Several other corrections also employ a reduced target thickness. Most notably is the energy resolution calculation used to determine the x-axis error bars covered later in Section 5.4. Within Equation 5.23, the flight path length L and variance in flight paths ΔL terms are affected by these corrections. Since each bin of the rebinned spectra is some sum of the originally structured bins for which individual flight paths were calculated in the time-of-flight energy calculations, a weighted (by number of counts in each bin) average production

point can be determined for each new bin. This new mean production point is used to calculate the average flight path L for the bin.

The ΔL term is a function of the minimum and maximum possible flight paths, L_{min} and L_{max}. These flight path extremes are determined by the effective target thickness desired. The methodology utilizing the band of minimum width containing 80% of all neutrons produced is used here. First, as was done earlier, the average neutron energy for the bin, $T_{n,\text{avg}}$ is compared to the energy bins of the PHITS-simulated results to determine what energy bin of the median band should be used. Then, given the energy bin and the integral percentage of neutrons wished to be included in the effective target thickness, the minimum (most upstream) and maximum (most downstream) production points, $x_{\text{pp,min}}$ and $x_{\text{pp,max}}$, are extracted from the array those values were stored in when originally calculated. These extreme production points are then used to calculate the extreme flight paths. For the downstream detectors N1-N5, L_{min} is taken to be the distance from $x_{\text{pp,max}}$ to the center of the front face of the detector, and L_{max} is taken to be the distance from $x_{\text{pp,min}}$ to the center of the back face of the detector. For the upstream detector N6, L_{min} is the distance between $x_{\text{pp,min}}$ and N6's front face, and L_{max} is the distance between $x_{\text{pp,max}}$ and N6's back face.

Additionally, using the same information from the extreme production points and extreme flight paths, new extreme solid angles can be calculated. These calculations will not be covered in detail here since the method is the same as described in Section 5.3.1 except using $x_{\text{pp,min}}$ and $x_{\text{pp,max}}$ instead of the centers of the most upstream and downstream faces of the target (referred to as O_0 and O_2 in Section 5.3.1).

To conclude this section, a demonstration of how all of these corrections affect the original spectra will be shown. As noted earlier, the effects of these corrections are more pronounced in some spectra than in others. To best demonstrate the effect of the shifting production point, a system where this shift is extreme is desirable. Additionally, to showcase the increase in energy resolution (reduction in x-error), a case where production is very localized in the target should be picked. The 400 MeV/n Fe beam incident on the 60 g/cm^2 HDPE target configuration meets both of these criteria. How neutron production in the target changes as a function of energy is illustrated in Figures 4.30a and 4.30b for this example case.



(a) `[T-Product]` distributions

(b) Mean and median production points

Figure 4.30: Neutron production in 60 g/cm^2 HDPE front target for 400 MeV/n Fe

Neutron production over most energy ranges for this beam/target combination are concentrated toward the upstream face of the target. Additionally, production is very localized, especially at higher neutron energies where the effective target thickness becomes less than half of the actual thickness. Figure 4.31 shows this ToF neutron energy spectrum before any corrections have been applied. The spectra presented thus far have only undergone the background subtraction, the previously discussed normalizations, and a very rudimentary rebinning to 10% statistical uncertainty in each bin.

The effect of applying just the production point correction is studied first; Figure 4.32 shows the x-axis energy shift brought on by the correction. Note that this example is the most extreme case of this correction; the energy shift experienced by the other spectra is more minor since production is not nearly as concentrated on the upstream face in the other projectile/target configurations. Figure 4.33 shows the same spectrum as Figure 4.31 but with the production point correction applied. Note that the energies for N1-N5 are shifted up and for N6 are shifted down as discussed earlier.

Next, both the production point and effective target thickness corrections can be employed, yielding the results shown in Figure 4.34. Note that the shown effective target thickness correction employs the median band method with 80% of neutrons produced contained in the band (median ± 40%). Lastly, the energy resolution uncertainty (and

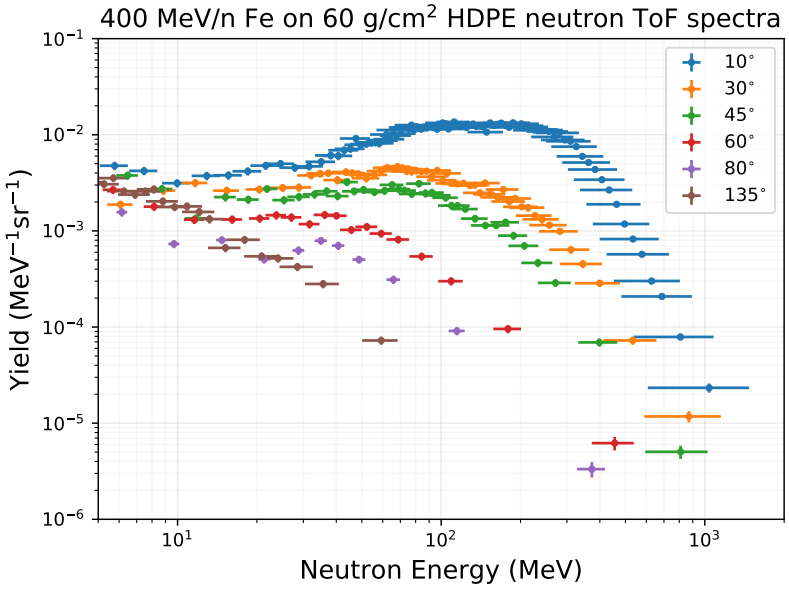


Figure 4.31: ToF spectra with no production point or effective target thickness corrections

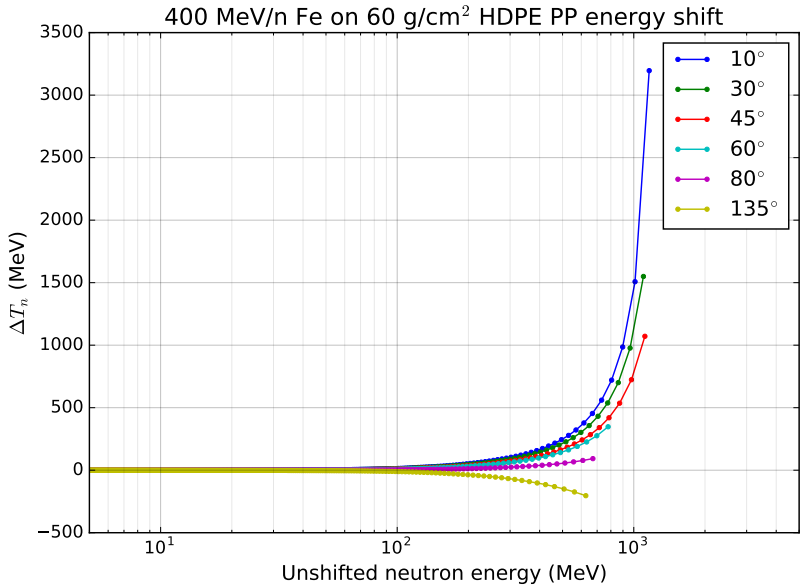


Figure 4.32: x-axis energy shift from production point correction

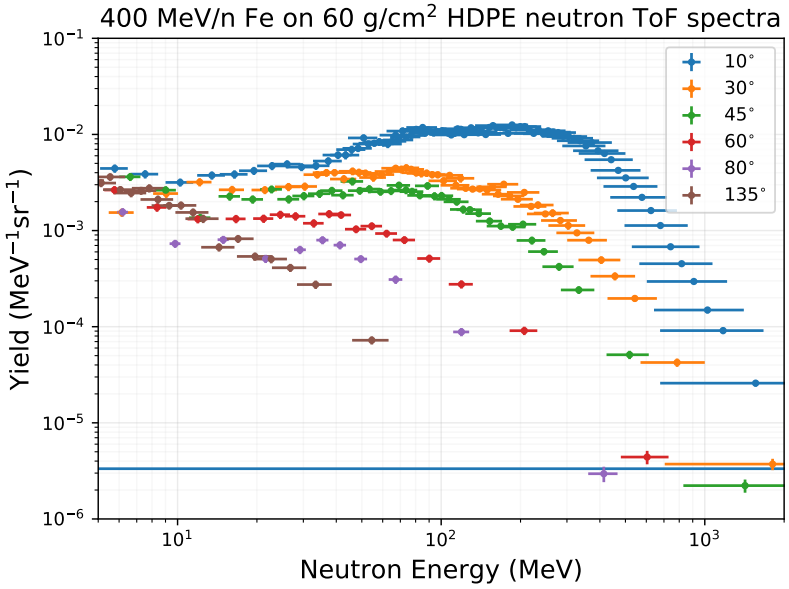


Figure 4.33: ToF spectrum after applying production point correction

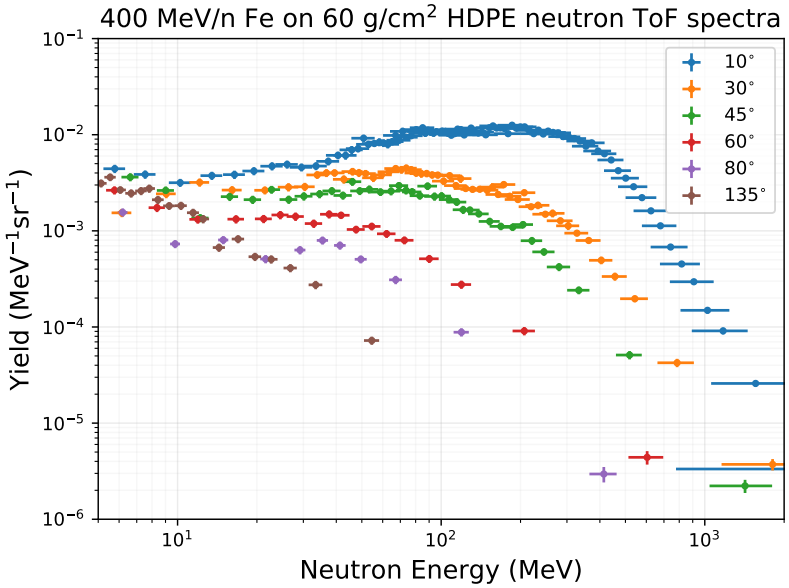


Figure 4.34: ToF spectrum with production point and effective target thickness corrections

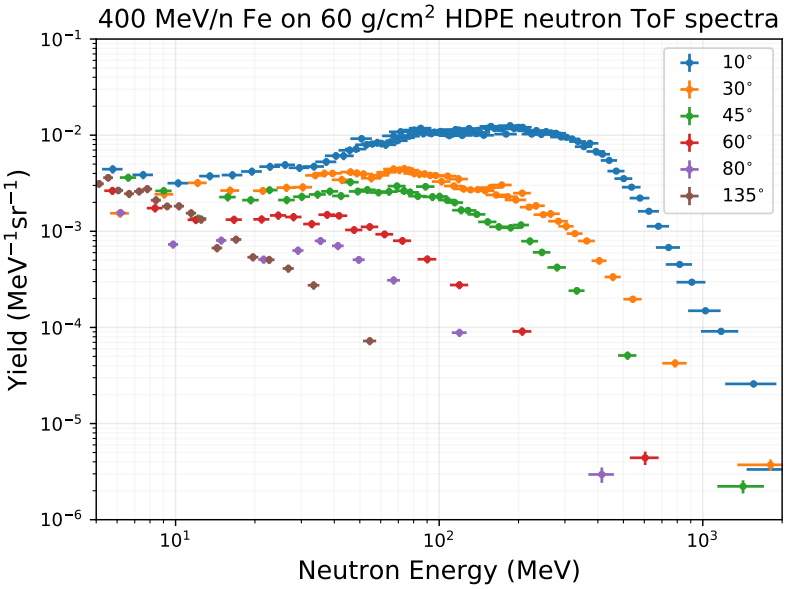
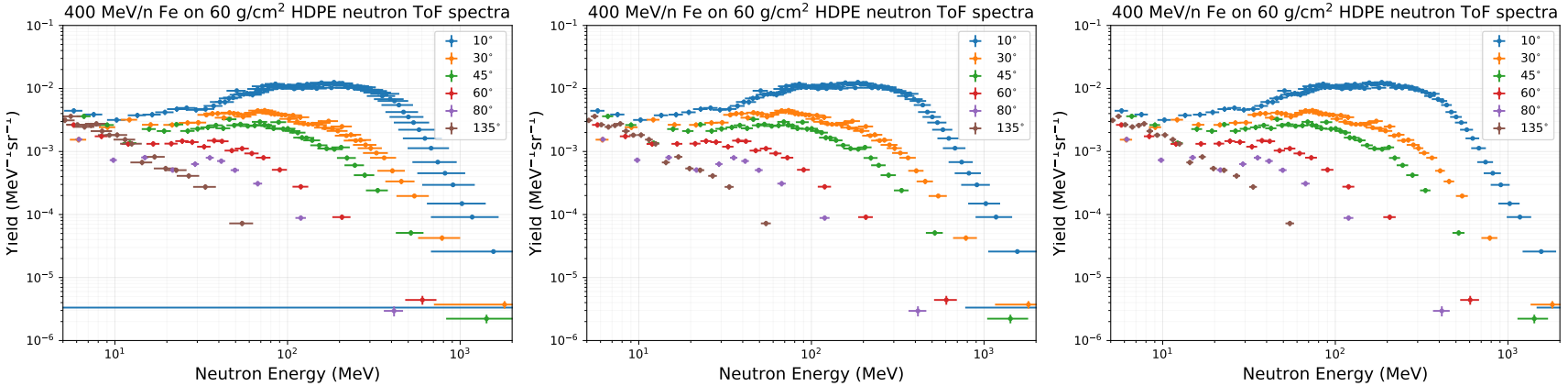


Figure 4.35: ToF plot using "minimum-width band" for effective target boundaries

solid angle uncertainty) can be recalculated using smallest target thickness containing 80% of the neutrons produced as shown in Figure 4.35.

The reduction in x-axis error is significant with either method, especially at higher energies; these previous three ToF plots (Figures 4.33, 4.34, and 4.35) are shown side-by-side in Figure 4.36 to illustrate this point.

In summary, the production point correction alone affects the neutron kinetic energy and average solid angle. The production point correction in conjunction with the effective target thickness correction affect the flight path uncertainty, a factor in the energy resolution x-axis uncertainty, and the solid angle uncertainty. These production point corrections yield more accurate neutron energy spectra (assuming PHITS accurately models this neutron production) with finer energy resolution uncertainty. The various plots showcased in this section illustrating the steps of the production point and effective target thickness corrections (PHITS `[T-Product]` distributions versus target depth, mean/median production points with effective thickness bands versus secondary neutron energy, and shift in neutron energy as a function of the original energy) can be found for all of the experimental systems to which they were applied in Appendix B.



(a) No correction (b) "median band" (c) "minimum-width band"

Figure 4.36: The three plots show how the x-axis uncertainty is reduced by choosing the effective front target boundaries less conservatively.

4.10 Correcting undershadowed data: a higher Q_{total} cut

Due to imperfections with the shadow bar background subtraction, sometimes low to intermediate energy neutrons produced from uninteracted beam or secondary fragments interacting in the back target or bouncing off the walls in a peculiar way can masquerade as higher energy neutrons with the time of flight methodology used. Additionally, in cases where the normalized counts in a given TDC bin were actually higher in the normalized shadowed runs than in the normalized unshadowed runs, bins with negative yield values exist. In an attempt to resolve this, an arbitrary breakpoint energy, for example 20 MeV, can be established above which new Q_{total} pulse height threshold cuts can be used. This allows for the regions above the cutoff to not be influenced by the abundance of lower energy particles potentially masquerading as higher energy ones. The end of Section 4.2.4 covers how these new cuts are calculated.

The methodology is to perform all of this analysis on multiple sets of data: once using data with the original Q_{total} cut values applied and again using additional new Q_{total} cut values at higher thresholds. Then, during the rebinning process in the time-of-flight calculations, which data is passed to the final array becomes a function of bin energy. If the bin is below a new threshold, data using the original Q_{total} cut values are used, and above/between new thresholds data using the new Q_{total} cut values are used. This allows for the stitching together of multiple sets.

Due to the higher voltages detectors N4-N6 were operated at, the previously mentioned higher threshold of 20 MeV light equivalent (11.5 MeVee), once converted to QDC channels, exceeds the maximum QDC bin in each of the three most upstream detectors. This is not a major issue since the more downstream detectors should be the ones suffering most from this issue in the first place. Since it takes little effort to enforce a new Q_{total} pulse height threshold cut on N4-N6 if it's already being done on N1-N3, lower thresholds for those detectors can just be picked at similar QDC channels. Generating spectra with this higher threshold is as simple as changing the Q_{total} pulse height threshold cuts in the ROOT macros and rerunning them to produce a new set of output text files.

Table 4.7: All applied Q_{total} pulse height threshold cuts (November 2016 values)

Det.	Original Q_{total}			Intermediate Q_{total}			High Q_{total}		
	$E_{n,cut}$ (MeV)	L_{cut} (MeVee)	$Q_{tot,cut}$ (ch #)	$E_{n,cut}$ (MeV)	L_{cut} (MeVee)	$Q_{tot,cut}$ (ch #)	$E_{n,cut}$ (MeV)	L_{cut} (MeVee)	$Q_{tot,cut}$ (ch #)
N1	5	1.895	154	10	4.795	353	20	11.505	812
N2	4	1.309	138	10	4.795	420	20	11.505	964
N3	4	1.309	125	10	4.795	394	20	11.505	911
N4	3	0.925	257	5	1.895	503	8	3.580	930
N5	2	0.510	215	4	1.390	548	6	2.430	941
N6	2	0.510	293	3	0.925	520	5	1.895	1051

In this work, each final TDC spectrum is formed from combining three spectra, each with a different Q_{total} pulse height threshold cut; they are denoted as Original Q_{total}, Intermediate Q_{total}, and High Q_{total} and are summarized in Table 4.7. These are the values used for the analysis of data collected in November 2016; the November 2017 values are slightly different but still very similar.

Next, these three spectra need to be stitched together into one. This is done before any rebinning but after the energy axis bins have been calculated. Initially, one may use each spectra in its corresponding energy range (for N1: "Original" to 10 MeV, "Intermediate" in 10-20 MeV, and "High" above 20 MeV), but a different method is employed instead. The spectra drop off as the threshold is approached from the right, so in the region just above 20 MeV, the spectra are artificially deflated when using a 20 MeV threshold cut. To circumvent this, the new threshold TDC spectra are only applied starting at energies slightly above the threshold value. For instance, for N1, the "Original" TDC spectra are used below 15 MeV, the "Intermediate" TDC spectra are then used up to 30 MeV, and the "High" TDC spectra are used beyond that.

Of important note, the efficiency for a spectrum with a 20 MeV threshold is much lower than that of a spectrum with a 5 MeV threshold. Thus, additional SCINFUL-QMD simulations were conducted to generate efficiency spectra for use in the regions where these different Q_{total} thresholds are enforced. If the correct efficiency values are not used, a major discontinuity will appear at the transition between the two Q_{total} thresholds.

Depending on when/how the detector efficiency correction is made, there are still minor discontinuities produced by this method. The detector efficiencies change significantly with the threshold bias value (Q_{total} cut location in MeVee), so, if not handled correctly, the sensitive transition region between Q_{total} cuts can form a discontinuity. These are alleviated by coding the efficiency value used in each final bin to be a weighted (by the N value, proportional to fractional uncertainty as discussed in Section 5.1) average of the efficiency values appropriate for the energies of the smaller bins composing each final bin.

4.11 Rebinning

Rebinning is crucial for expressing data with clarity. It allows for many bins with poor statistics to be condensed into few bins with acceptable statistics. There are a number of different approaches one can take with rebinning; two will be discussed here.

4.11.1 Interpolate edges and redistribute bin contents

The first involves the user creating entirely new bin boundaries that do not necessarily line up with the old bin boundaries. Figure 4.37 shows an example of this.

The bin widths do not need to be even like in this example; they could have arbitrary spacing using the same methodology. For an original set of M bins with bin values of y_i and bin boundaries of x_i and x_{i+1} being rebinned into N bins with new bin values of y'_j and new bin boundaries of x'_j and x'_{j+1}, the new bin values can be calculated with Equation 4.25.

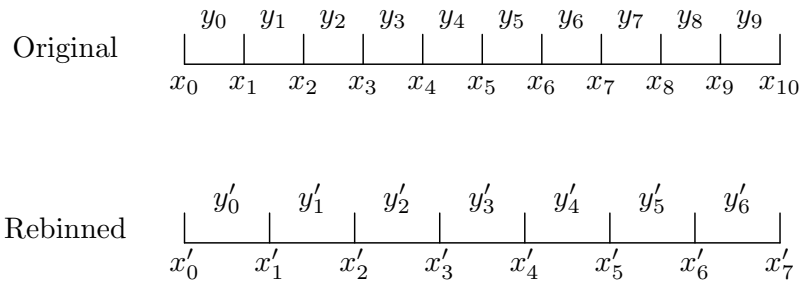


Figure 4.37: Rebinning method which generates new bin boundaries and redistributes old bin content to new bins

$$y'_j = \sum_{i=0}^{M} f_i y_i \tag{4.25}$$

The fraction of the old bin that overlaps with the new bin, f_i, is described in Equation 4.26 whose inequalities are explained in Table 4.8. This assumes that the content of a bin is evenly distributed between the minimum and maximum boundaries of a bin. These equations could be made more complicated if one wanted to use information from the surrounding bins to form a distribution of how content is spread within a single bin. But, this complication is typically not warranted since the process of rebinning usually entails combining smaller bins into larger ones, not creating smaller bins from larger ones.

$$f_i = \begin{cases} 0 & \text{, if } (x_i \geq x'_{j+1}) \text{ or } (x_{i+1} \leq x'_j) \\ \dfrac{x_{i+1} - x'_j}{x_{i+1} - x_i} & \text{, if } (x_i \leq x'_j) \text{ and } (x'_j < x_{i+1} < x'_{j+1}) \\ \dfrac{x'_{j+1} - x_i}{x_{i+1} - x_i} & \text{, if } (x'_j < x_i < x'_{j+1}) \text{ and } (x'_{j+1} \leq x_{i+1}) \\ \dfrac{x'_{j+1} - x'_j}{x_{i+1} - x_i} & \text{, if } (x_i < x'_j) \text{ and } (x_{i+1} > x'_{j+1}) \\ 1 & \text{, if } (x_i \geq x'_j) \text{ and } (x_{i+1} \leq x'_{j+1}) \end{cases} \tag{4.26}$$

This methodology is employed to rebin the simulated Monte Carlo results into energy bins matching those determined for the experimental results.

Table 4.8: Explanations of logical conditions in Equation 4.26

Condition	Meaning
$(x_i \geq x'_{j+1})$ or $(x_{i+1} \leq x'_j)$	bins do not overlap
$(x_i \leq x'_j)$ and $(x'_j < x_{i+1} < x'_{j+1})$	old bin overlaps with minimum of new bin
$(x'_j < x_i < x'_{j+1})$ and $(x'_{j+1} \leq x_{i+1})$	old bin overlaps with maximum of new bin
$(x_i < x'_j)$ and $(x_{i+1} > x'_{j+1})$	old bin entirely encompasses new bin
$(x_i \geq x'_j)$ and $(x_{i+1} \leq x'_{j+1})$	old bin entirely encompassed by new bin

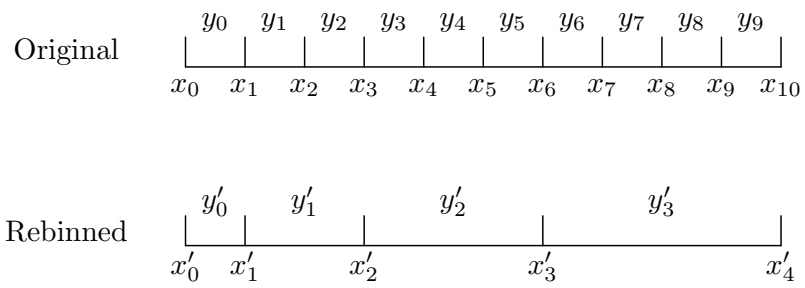


Figure 4.38: Rebinning method which preserves old bin boundaries by just stacking together old bins to generate new ones

4.11.2 Preserve original bin edges and contents

Since in this research the identity of the old bin boundaries need to be preserved for timing uncertainty reasons, a different approach to rebinning is needed. This other method involves just adding old bins together to create new bins, meaning the set of new bin edges will be entirely contained in the set of old bin edges. This can be done in such a way that old bins are stacked into a new bin until certain criteria are met before moving on to filling the next new bin. In the context of these experiments, it is useful to stack bins until some statistical threshold is met (such as 10% fractional uncertainty per bin). An example of this is illustrated in Figure 4.38.

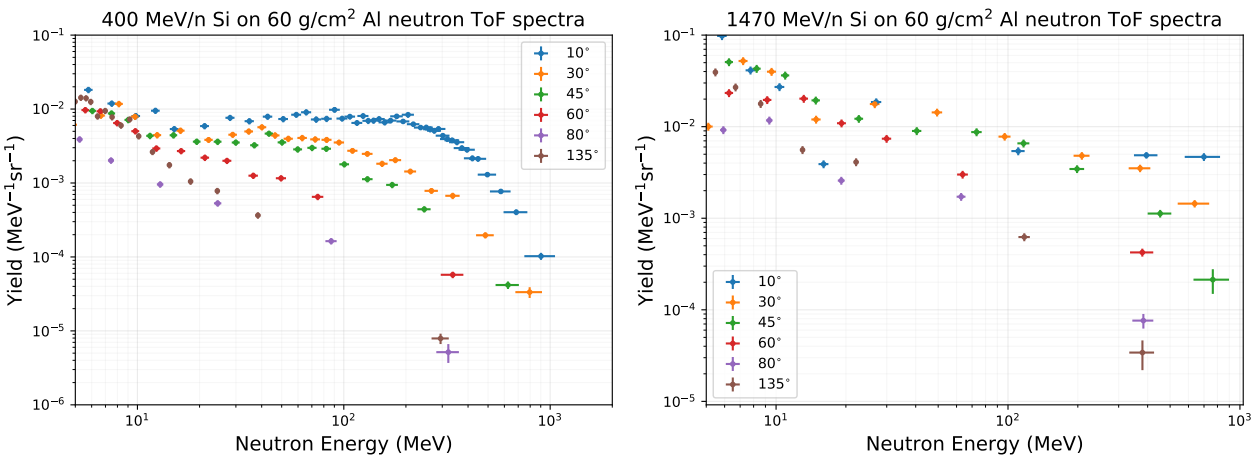
In this case, the math to determine the content of each new bin is much easier. Equation 4.25 still holds, but f_i is now calculated with the simpler Equation 4.27.

$$f_i = \begin{cases} 0 & \text{, if } \ (x_i \geq x'_{j+1}) \text{ or } (x_{i+1} \leq x'_j) \\ 1 & \text{, if } \ (x_i \geq x'_j) \text{ and } (x_{i+1} \leq x'_{j+1}) \end{cases} \tag{4.27}$$

This is the rebinning methodology employed in the neutron time-of-flight calculations discussed in Section 4.6.2.

4.11.3 Specific rebinning algorithm for time-of-flight neutrons

While the data can be rebinned to a set statistical fractional uncertainty alone, not all datasets are equal. When rebinned to 10% statistical uncertainty per bin, some datasets still have more points than are necessary and could be rebinned to tighter stastistical uncertainties



(a) Abundant data points

(b) Sparse data points

Figure 4.39: Demonstration that a universal statistical uncertainty per bin is not ideal

while others are more sparsely populated and would stand to gain more by accepting worse statistics per bin to gain an extra few data points. Figure 4.39 illustrates this point.

Though the normalized neutron yield is greater for the higher-energy beams, the statistics are considerably worse due to the maximum usable beam current (source ions per second) at NSRL being lower for higher energy species due to the experimental constraints discussed earlier in Section 3.3. Statistics are also poorer for thinner targets since the total interaction probability of each source ion scales with target thickness.

In addition to beam energy and target thickness, the abundance or sparseness of data points is also a function of detector angle. Note that in Figure 4.39a N1 (10°) has an abundance of data points, N2 and N3 (30° and 45°)—and to a lesser extent N4 and N6 (60° and 135°)—have a moderate number of points, and N5 (80°) is rather sparsely populated.

Furthermore, data point density (for bins of constant fractional error) is also a function of neutron energy, especially when above the beam energy. While it may be appropriate to rebin the intermediate energy range (about 80 MeV to 400 MeV) of Figure 4.39a to fewer bins for N1, the number of bins beyond 400 MeV should probably not be reduced. For the detectors at higher angles, this is more notable at even lower energies.

So, rebinning requires making trade-offs which can be subjective. One can increase the number of data points by sacrificing statistical certainty of each point's exact location (increasing error bars) or increase certainty of each point's location by lumping more data

into each bin, reducing the total number of data points. Thus, the objective is to strike a balance between the certainty of each point's location and having enough data points to determine the physical trends in the spectra.

There are several additional considerations that must also be made when rebinning. First, to ensure that the high energy neutron data is not contaminated with photons, one must exclude bins any closer than 3σ of the prompt gamma peak (or beyond it) on the fast end of the TDC time axis. On a similar note, bins below the original (lowest) Q_{total} cutoff energy on the TDC energy axis must also be excluded to prevent photon contamination of the low energy neutrons. These two constraints only affect the range of TDC bins available for rebinning. The actual widths of the final bins are influenced by three factors: statistical uncertainty, energy resolution uncertainty, and timing resolution requirements.

The first criterion to meet concerns the intrinsic timing resolution of the detection system. To enforce this, each final bin must be wider than the FWHM of the prompt gamma peak on the time axis. Next is the energy resolution uncertainty. This calculation is discussed in detail in Section 5.4, but it is effectively what will become the final x-axis energy uncertainty. For the sake of cleaner plots and avoiding concerns about data points overlapping on the x-axis, it is beneficial to ensure that the x-error, when plotted centered on each final bin's midpoint, is contained within the boundaries of the final bin. This leads to another decision that must be made: How will each final bin's midpoint be selected? The simplest approach would be to just average each bin's edges, but this results in an energy higher than it should be. An alternate approach is to use the bin's average velocity converted to energy as the midpoint. The truest approximation of the bin's average energy is to use the yield values of each constituent channel to determine a weighted average energy for the final bin; this is shown in Equation 4.28 where g is an index of the original TDC spectrum, i is the initial bin index of the original TDC spectrum for each final bin, N is the number of original TDC bins combined into each final bin, Y_g is the yield value associated with each original TDC bin, and $E_{g,\text{avg}}$ is the arithmetic average energy of each original TDC bin's energy boundaries.

$$E_{\text{bin,avg}} = \left(\sum_{g=i}^{i+N} Y_g E_{g,\text{avg}}\right) \Bigg/ \left(\sum_{g=i}^{i+N} Y_g\right) \tag{4.28}$$

Lastly, statistical uncertainty must be factored in while rebinning to ensure that each final bin meets a desired statistical criterion. As mentioned earlier, the statistical criteria (along with energy resolution) are coupled with the number of data points in the final rebinned spectra. Rather than picking a static statistical uncertainty to rebin to, a set of nested loops is employed to iteratively loosen the constraints on how many points are desired and what statistical uncertainty is allowable for each data point until a spectra striking an appropriate balance between number of points and uncertainty is achieved.

Other factors to consider include how negative yield values are handled and factoring in the minimum data point spacing desires discussed earlier. Due to the background subtraction, it is possible to have negative yield bins, even after trying to alleviate this with higher Q_{total} thresholds as was discussed in Section 4.10. These bins are typically concentrated at the lowest energies, and this work opts to drop negative yield bins which occur below 10 MeV. However, the handful of negative yield bins above 10 MeV are retained since these results are known to be statistically significant from the rebinning process, though non-physical. This was determined to be the best way to handle the presence of bins with negative yield values; selectively avoiding individual TDC bins of negative yield in the rebinning process would both be deceptive and result in inflated yield values.

To prevent the high-energy portion of the spectra from being too sparsely populated, an extra criterion is added to the rebinning process which allows for the criteria for individual bin statistics and minimum desired number of final bins to be iteratively loosened to more relaxed values, resulting in a greater number of bins in the more sparsely populated regions of each spectrum at the expense of individual bin statistics.

Since there are so many spectra to be generated and rebinned, a system of rules and logic loops to use for determining the binning of each spectrum was developed rather than making binning decisions (or even just exceptions) for every single spectrum. After factoring in the stated considerations and a few more exceptions to handle, a full rebinning algorithm was developed for these spectra which solved all cases of needing to individually treat yield spectra. A flowchart in Figure 4.40 displays the full logic of the rebinning process used with all of the variables within it defined below.

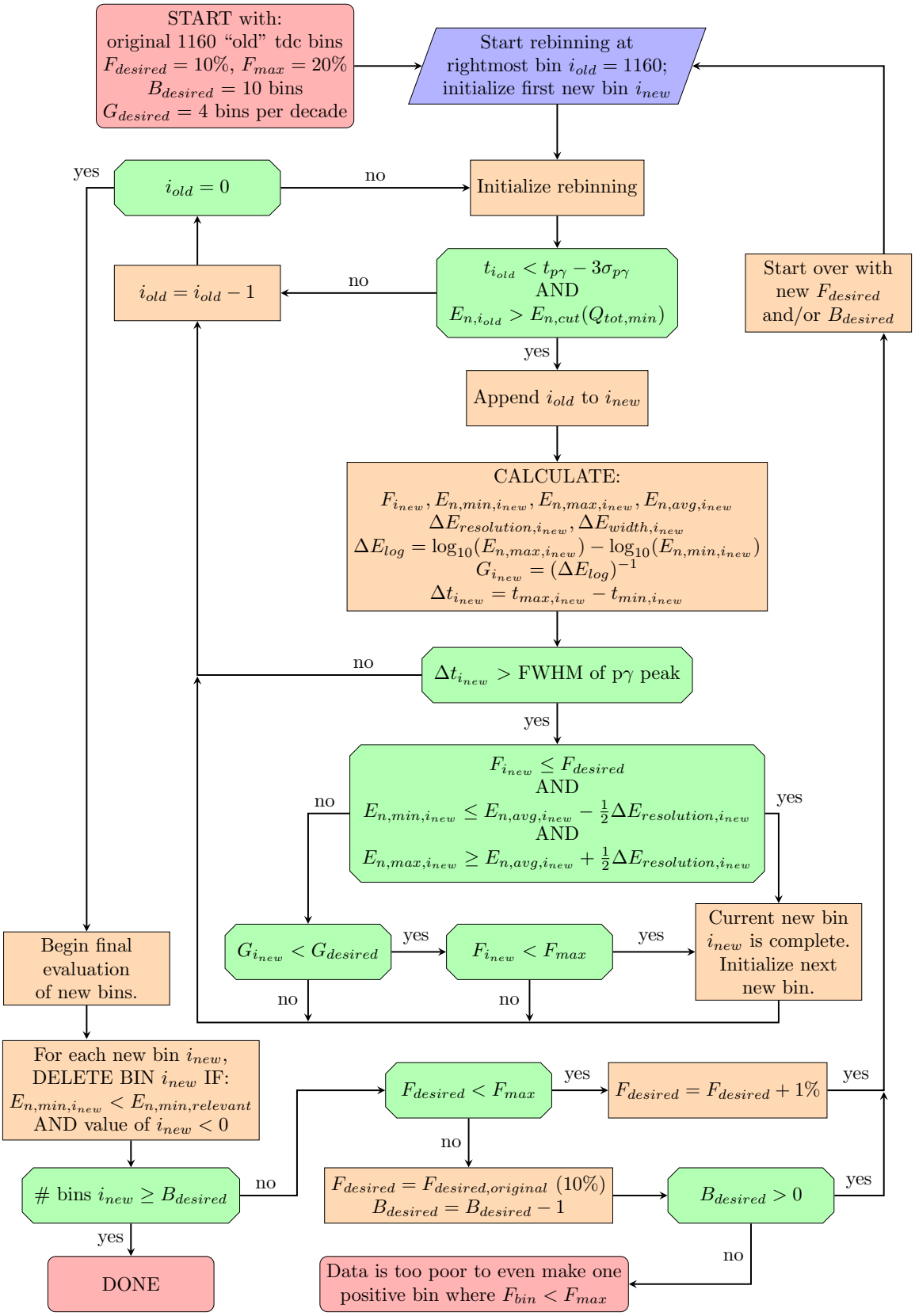


Figure 4.40: Rebinning logic map/flowchart

- $F_{desired} = 10\%$ — optimal desired maximum fractional statistical uncertainty per bin
- $F_{max} = 20\%$ — maximum allowable fractional statistical uncertainty per bin
- $B_{desired} = 10$ bins — optimal desired minimum number of bins in final spectrum
- $G_{desired} = 4$ bins per decade — optimal desired minimum number of bins per energy decade in final spectrum
- i_{old} — index of "old" bin from original unrebinned TDC spectrum
- i_{new} — index of "new" bin being generated in this algorithm
- $t_{i_{old}}$ — time axis value of old bin i_{old} in ns
- $t_{p\gamma}$ — time axis value of prompt gamma peak in ns
- $\sigma_{p\gamma}$ — standard deviation of prompt gamma peak in ns
- $E_{n,i_{old}}$ — energy axis value of old bin i_{old} in MeV
- $E_{n,cut}(Q_{tot,min})$ — energy axis value of the lowest used Q_{total} pulse height threshold cut in MeV
- $F_{i_{new}}$ — fractional statistical uncertainty in bin i_{new}
- $E_{n,min,i_{new}}$ — left bin edge energy axis value of new bin i_{new} in MeV
- $E_{n,max,i_{new}}$ — right bin edge energy axis value of new bin i_{new} in MeV
- $E_{n,avg,i_{new}}$ — bin midpoint energy axis value of new bin i_{new} in MeV (Equation 4.28)
- $\Delta E_{resolution,i_{new}}$ — energy resolution uncertainty of bin i_{new} calculated at $E_{n,avg,i_{new}}$ in MeV (see Equation 5.23 in Section 5.4)
- $\Delta E_{width,i_{new}} = E_{n,max,i_{new}} - E_{n,min,i_{new}}$ — energy axis width of bin i_{new} in MeV
- ΔE_{log} — fraction of energy axis decade occupied by bin i_{new}
- $G_{i_{new}}$ — number of i_{new} bin widths that would fill one energy decade

- $\Delta t_{i_{new}}$ — time axis width of bin i_{new} in ns
- $E_{n,min,relevant}$ = 10 MeV — cutoff energy in MeV below which negative yield bins are rejected

Additionally, a simplified written explanation of the rebinning process is provided below.

1. Initialize rebinning process by initializing very first "new" bin.
2. Start stacking "old" bins from the highest energy points, moving left (ensures statistics for high energy bins).
3. Make sure the time-axis value of each "old" bin is 3σ left of the prompt gamma peak.
4. Make sure the energy-axis value of each "old" bin is above the original (lowest) Q_{total} cutoff energy.
5. Append this "old" bin to the current "new" bin.
6. Calculate some values about the new bin.
    - Bin width (in energy and time domains)
    - Energy resolution
    - Fractional statistical uncertainty
7. Make sure the width of the bin on the time-axis is greater than the FWHM of the prompt gamma peak.
8. Check to see if the energy resolution (x-error) is smaller than the bin width and if the current "new" bin's fractional error is less than or equal to the desired fractional error (10%).
9. If not but the bin is already getting wider (on the log scale) than what is desired in order for points to not be spaced too far apart, see if the "new" bin's fractional error is less than the more lenient maximum allowable fractional error (20%).

10. If not, keep stacking "old" bins onto the "new" bin until its fractional error falls below the maximum allowable fractional error.

11. Current "new" bin is complete. Initialize another "new" bin and start over with the next "old" bin in line repeating instructions from line #2 above.

12. Purge all "new" bins with negative y-values and bin energies below some threshold beneath which neutron results are of less concern (10 MeV here).

13. See if the number of "new" bins is greater than or equal to the desired number of "new" bins (currently set to 10 bins).

14. If not, start over at step #1 except using a higher desired fractional uncertainty threshold (increase by 1% each iteration; 10%→11%).

15. If incrementing up the desired fractional uncertainty causes it to exceed the maximum allowed fractional uncertainty, instead reset the desired fractional uncertainty to its original value (10%) and decrease the desired number of "new" bins by one (10→9). Then start over at step #1 again.

16. After enough iterations, binning will be completed with this method unless there are not enough positive points in the dataset to form even a single bin meeting the absolute maximum fractional uncertainty criterion.

Chapter 5

Uncertainty quantification for upstream target neutron data

5.1 Fundamental approach to error propagation

Most values within this analysis have an associated statistical uncertainty bound to them, and streamlining the management of those uncertainties is important for their propagation. Generally, the absolute error of a sum (or difference) is the individual absolute errors summed in quadrature (Equations 5.1 and 5.2). Likewise, the fractional error of a product (or quotient) is the individual fractional errors summed in quadrature. While this is more complicated for other functions, most of the analysis performed here consist of the four basic algebraic operations. However, this analysis introduces one notable complication in the uncertainty analysis: the necessity of rebinning. While rebinning the actual contents of a bin is straightforward, how to split an error apart and then redistribute it is not.

$$(A \pm \sigma_A) + (B \pm \sigma_B) = (X \pm \sigma_X) \tag{5.1}$$

$$\sigma_X = \sqrt{\sigma_A^2 + \sigma_B^2} \tag{5.2}$$

Note that σ_A in these equations is only equal to $\sqrt{A}$ if A is still the original, unnormalized, number of counts in a bin. Earlier normalization performed in ROOT, which was all

multiplicative in nature, can be undone by looking at the fractional uncertainty (Equation 5.3). Any constants applied in the normalization will cancel out, leaving an expression of the pure number of counts in A, N_A (Equation 5.4).

$$\frac{\sigma_A}{A} = \frac{c_{constant} \times \sqrt{N_A}}{c_{constant} \times N_A} = \frac{1}{\sqrt{N_A}} \tag{5.3}$$

$$N_A = \left(\frac{\sigma_A}{A}\right)^{-2} \tag{5.4}$$

This serves a strong utility: N_A can be freely rebinned in the exact same fashion as A. This is analogous to rebinning a 2048 channel multi-channel analyzer's output into 512 channels by summing the counts in every 4 channels into each new bin. Since the counts are distributed continuously across bins as a spectrum, bins can be split into fractions when rebinning, allowing for fractional redistribution of a single bin's counts to numerous new bins if bin edges do not line up in the exact same locations as before. Uncertainty analysis would be considerably more complex without being able to do this.

Because of this utility for rebinning, the N value is toted along with each bin's content rather than the absolute error in the analysis post-processing codes used in this work. Additionally, these N values can be used in representing uncertainties and is also how uncertainty is handled when combining multiple datasets (namely unshadowbarred and shadowbarred datasets in this analysis) as seen in Equation 5.5.

$$\sigma_X = \sqrt{N_A^{-1}A^2 + N_B^{-1}B^2} \tag{5.5}$$

Converting σ_X back to a N_X value is the next logical step. This is done by reapplying Equation 5.4 and substituting in σ_X from Equation 5.5, yielding Equation 5.6. Note that this case is assuming addition of A and B. When subtracting, the $(A+B)$ terms should be replaced with $(A-B)$.

$$N_X = \left(\frac{\sigma_X}{X}\right)^{-2} = \left(\frac{\left(N_A^{-1}A^2 + N_B^{-1}B^2\right)^{1/2}}{(A+B)}\right)^{-2} = \frac{(A+B)^2}{N_A^{-1}A^2 + N_B^{-1}B^2} \tag{5.6}$$

In more general terms, N_X for a sum of M values $A_i \pm \sigma_{A_i}$ each already with their own N_{A_i} values calculated is expressed in Equation 5.7. Note that this equation's numerator assumes a sum. Subtraction with this method should be viewed as just addition with negative values.

$$N_X = \left(\sum_{i=1}^{M} A_i\right)^2 \Bigg/ \left(\sum_{i=1}^{M} N_{A_i}^{-1} A_i^2\right) \tag{5.7}$$

For the sake of completeness, it is interesting to note that the expression for the uncertainty of a product/quotient is even cleaner when using "N" values over absolute uncertainties (Equations 5.8 and 5.9).

$$(A \pm \sigma_A) \times (B \pm \sigma_B) = (Y \pm \sigma_Y) \tag{5.8}$$

$$\sigma_Y = (A \times B)\sqrt{\left(\frac{\sigma_A}{A}\right)^2 + \left(\frac{\sigma_B}{B}\right)^2} = (A \times B)\sqrt{N_A^{-1} + N_B^{-1}} \tag{5.9}$$

When adding or multiplying by scalars with some uncertainty, N can be easily converted back to absolute or fractional uncertainty in order to perform the operation the traditional way and then be converted back to N afterward. However, this can "contaminate" the value such that N is no longer representative of the number of counts contained in a bin but is rather just an abstract relation of the fractional error.

5.2 Statistical Uncertainties (y-axis)

The statistical uncertainties brought about by counting statistics are handled as discussed in Section 5.1. ROOT's `Sumw2()` function automatically handles statistics while the spectra are still in ROOT. Once the datasets are exported to Python, the absolute uncertainties are translated to N_X values. These N_X values are not affected by any of the normalizations or x-axis transformations that follow. When the shadowbarred spectra are subtracted from the unshadowbarred spectra, Equation 5.6 is used to calculate the new N_X values for the combined data. Afterward, the spectra are rebinned as discussed in Section 4.11 using

Equations 4.25 and 4.27. The N_X values are rebinned in exactly the same fashion as the bin's content (yield values).

The statistical uncertainties are taken to be the uncertainty inherent to the process being measured even with perfect acquisition and analysis techniques. This statistical uncertainty from a counting experiment, given sufficient counts in each bin, takes a Gaussian form and can be represented as a standard deviation. As it relates to the neutron yield, this statistical uncertainty (equal to one standard deviation) will be referred to as σ_Y.

5.3 Systematic Uncertainties (y-axis)

In this experiment and analysis, there are three sources of systematic uncertainty: detector efficiency (ε_η), solid angle ($^{\sigma_\Omega}/_{\Omega}$, Section 5.3.1), and graphical cuts ($\varepsilon_{\mathrm{GC}}$, Section 5.3.2). All three of these values are fractional uncertainties.

These three values are then combined into a single systematic uncertainty which is reported to NASA. This total systematic uncertainty ($\sigma_{\mathrm{sys,tot}}$) is calculated by taking the sum of the three constituent systematic fractional uncertainties (producing $\varepsilon_{\mathrm{sys,tot}}$) and multiplying by the y-axis values, normalized yield Y, (converting from fractional to absolute error at the end) as shown in Equations 5.10 and 5.11. Adding the fractional (rather than absolute) uncertainties makes sense since these corrections are multiplicative, not additive. Additionally, since these uncertainties, while independent, are not randomly distributed, they are added together normally rather than being added in quadrature.

$$\varepsilon_{\mathrm{sys,tot}} = \frac{\sigma_\Omega}{\Omega} + \varepsilon_\eta + \varepsilon_{\mathrm{GC}} \tag{5.10}$$

$$\sigma_{\mathrm{sys,tot}} = \varepsilon_{\mathrm{sys,tot}} \times Y_{\#/(MeV \cdot sr \cdot s.p.)} \tag{5.11}$$

The simplest of these values is the assumed systematic uncertainty in the detector efficiency correction. Based on calculations by Dr. Pi-En Tsai [33] (and confirmed by Dr. Natalie McGirl [2]) and previous studies [34, 26], a universal detector efficiency uncertainty

of roughly 10% is assumed for all bins (Equation 5.12). This can be thought of as a measure of how closely SCINFUL-QMD's modeling of detector response is estimated to reflect reality.

$$\varepsilon_\eta = 0.1019 \tag{5.12}$$

The remaining two components of the systematic uncertainty in yield are slightly more complicated and warrant more detailed discussions in the following two subsections.

5.3.1 Solid angle uncertainty

In reality, all incident neutrons are not interacting with the detector at its midpoint; neutrons can also interact close to the front or back face of the detector, introducing a range of possible solid angles (Figure 5.1). Here, the largest solid angle is produced from $2\theta = \angle AOB$ (in red), and the smallest solid angle is produced from $2\theta = \angle COD$ (in blue). The math to determine the solid angle remains the same (Equation 4.13) except the neutron flight distance d_f should be updated to $\overline{OX}$ or $\overline{OZ}$ depending on whether the maximum or minimum solid angle is being calculated. Table 5.1 contains these extreme solid angle values attributable to the detector depth alone.

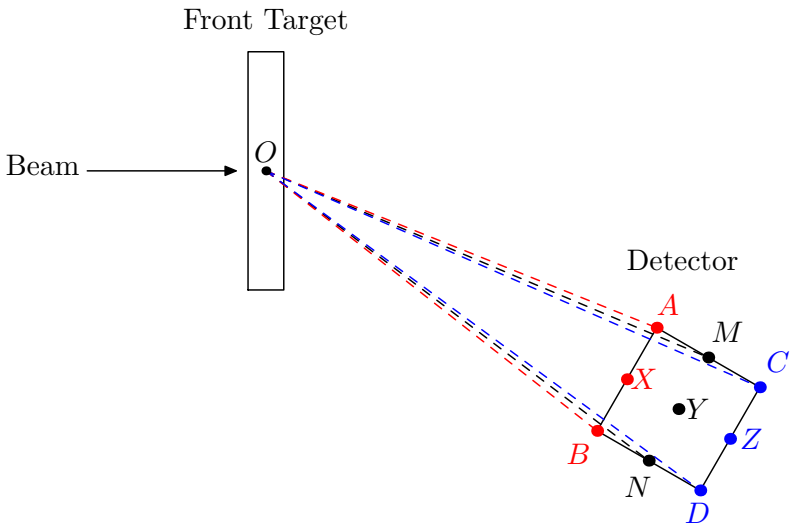


Figure 5.1: Variance in the solid angle

Table 5.1: Min/max solid angle for each detector for a single production point

Detector	Ω_{min} (sr)	Ω_{max} (sr)
N1	1.2809×10^{-3}	1.3910×10^{-3}
N2	1.2845×10^{-3}	1.3951×10^{-3}
N3	1.2841×10^{-3}	1.3946×10^{-3}
N4	1.8166×10^{-3}	2.0048×10^{-3}
N5	1.8160×10^{-3}	2.0041×10^{-3}
N6	2.7480×10^{-3}	3.1043×10^{-3}

Additionally, the fact that neutrons can be produced anywhere along the thickness of the front target (Figure 5.2) must be considered. Here, the largest solid angle is produced from $2\theta = \angle AO_2B$ (in red), and the smallest solid angle is produced from $2\theta = \angle CO_0D$ (in blue). The math for these angles and solid angles is complicated by the fact that the triangles formed are no longer right triangles.

Since the absolute locations and dimensions of everything in the experiment are known, coordinates can be assigned to each labeled point, and the distances can be calculated. To find the angle θ, the law of cosines is employed (Equation 5.13).

$$C^2 = A^2 + B^2 - 2AB\cos(\theta_c) \rightarrow \theta_c = \cos^{-1}\left(\frac{A^2 + B^2 - C^2}{2AB}\right) \tag{5.13}$$

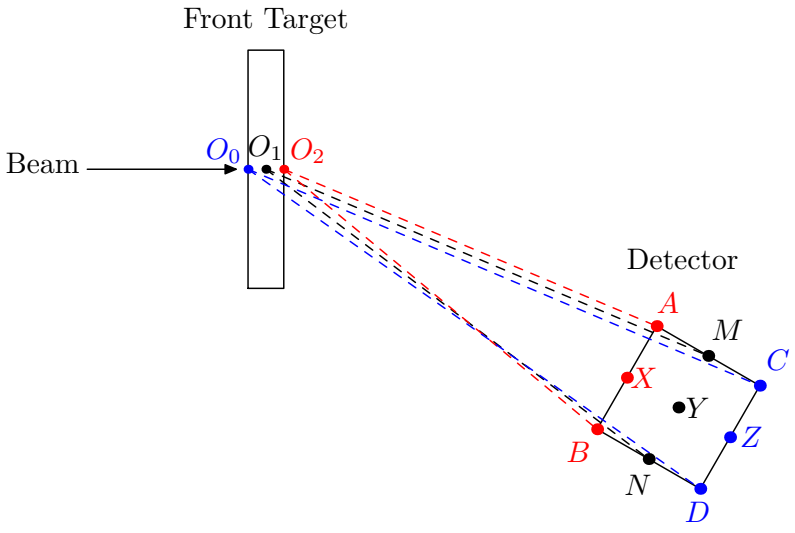


Figure 5.2: Variance in the solid angle including varying production points

In the context of this experiment, this becomes Equation 5.14 where $d_1 = \overline{O_2A}$ and $d_2 = \overline{O_2B}$ for the maximum solid angle and $d_1 = \overline{O_0C}$ and $d_2 = \overline{O_0D}$ for the minimum solid angle; additionally, r_d is the radius of the detector and is equal to $\overline{YM}$ (6.35 cm or 2.5").

$$2\theta = \cos^{-1}\left(\frac{d_1^2 + d_2^2 - (2r_d)^2}{2d_1d_2}\right) \tag{5.14}$$

The coordinate of the center of the target O_1 will be taken to be (0,0). Since the distance $\overline{O_1X}$ is what was measured at NSRL, the coordinates of A, B, C, and D need to be calculated in terms of that distance and the detector's physical dimensions. Let ϕ be the angle the detector is offset from the beamline axis. First, the coordinates of the center of the front and back faces of the detector, X and Z, can be calculated (Equation 5.15).

$$(x_\phi, y_\phi) = (d_f\cos(\phi), d_f\sin(\phi)) \tag{5.15}$$

For X, d_f is just the neutron flight path measured to the front face of the detector; for Z it is just this same distance plus the length of the detector. To find the coordinates of A and B, the X coordinate just needs to be shifted by a distance equal to the radius of the detector r_d (likewise with C and D by shifting Z by r_d). This is illustrated in Figure 5.3 with some extra lines drawn for convenience.

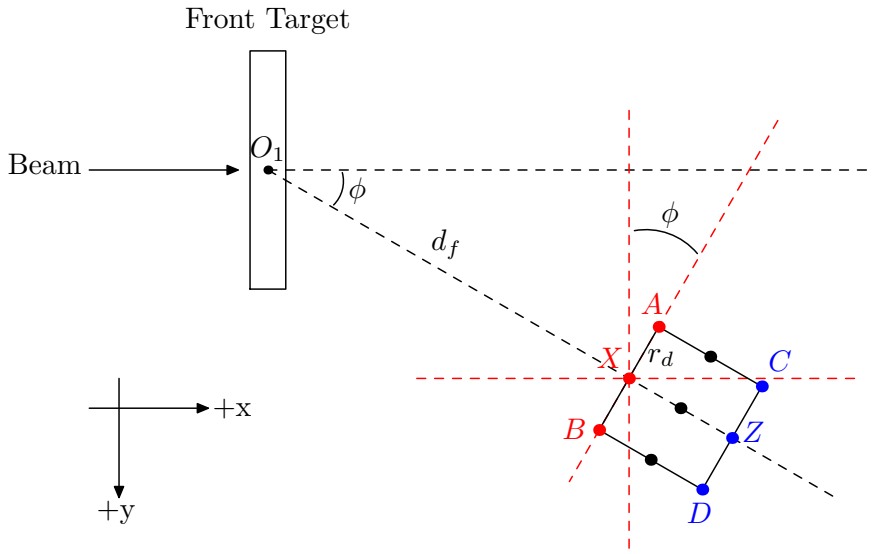


Figure 5.3: Finding coordinates of A and B

Table 5.2: General coordinates for detector edges.

Point	x_p	y_p
A	$d_f\cos(\phi) + r_d\sin(\phi)$	$d_f\sin(\phi) - r_d\cos(\phi)$
B	$d_f\cos(\phi) - r_d\sin(\phi)$	$d_f\sin(\phi) + r_d\cos(\phi)$
C	$(d_f + l_d)\cos(\phi) + r_d\sin(\phi)$	$(d_f + l_d)\sin(\phi) - r_d\cos(\phi)$
D	$(d_f + l_d)\cos(\phi) - r_d\sin(\phi)$	$(d_f + l_d)\sin(\phi) + r_d\cos(\phi)$

Trigonometry can once again be used to calculate how to shift X to find A (Equation 5.16). Note that in the coordinate system in Figure 5.3 the +y direction is pointing downward on the page.

$$\begin{aligned}(x_A, y_A) &= (x_X, y_X) + (r_d\sin(\phi), -r_d\cos(\phi)) \\ &= ((d_f\cos(\phi) + r_d\sin(\phi)), (d_f\sin(\phi) - r_d\cos(\phi)))\end{aligned} \tag{5.16}$$

The general equations for A, B, C, and D are tabulated in Table 5.2. Note that the term l_d is the length of the active volume of the scintillator. For these detectors, this length is equal to the diameter of the active detection volume ($l_d = \overline{XZ} = 2r_d$).

N1-N5 have angles less than 90°, but N6 has an angle of 135°. For the sake of solid angle calculations, this could be viewed as the N6 detector just being placed at 45° but with the front and back sides of the target flipped. Since O_0 and O_2 are the same x distance from O_1 though, the image would look the same as Figure 5.3. So, the calculation, if using $\phi = 135°$, would require switching the maximum solid angle 2θ to be $\angle AO_0B$ rather than $\angle AO_2B$. If the 135° detector is assumed to be placed at 45° instead, the calculations can be performed with the same coordinates used for the other five detectors to obtain the same minimum and maximum possible solid angles had it been done the more difficult way. Figure 5.4 highlights the differences in this calculation for the upstream detector versus the downstream detectors.

Now that the coordinates for A, B, C, and D have been determined, the distances in Equation 5.14 can be calculated with the Cartesian distance formula (Equation 5.17).

$$d_{12} = \sqrt{(x_1 - x_2)^2 + (y_1 - y_2)^2} \tag{5.17}$$

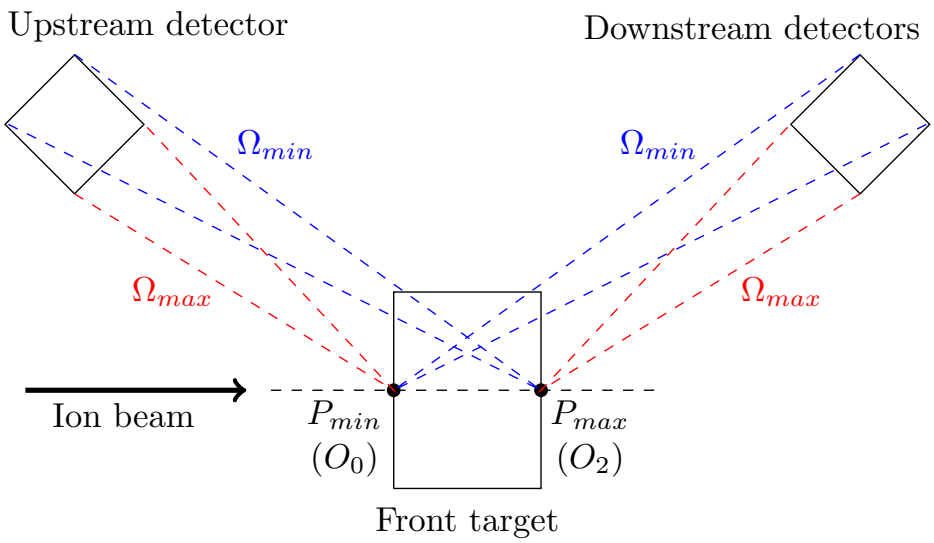


Figure 5.4: Pictured is an illustration of the solid angle extremes for upstream versus downstream detectors.

These distances can now be substituted back into Equation 5.14 to find the angle θ used in the solid angle equation (Equation 5.20). For the maximum solid angle, $2\theta = \angle AO_2B$, $d_1 = \overline{O_2A}$ and $d_2 = \overline{O_2B}$, and for the minimum solid angle, $2\theta = \angle CO_0D$, $d_1 = \overline{O_0C}$ and $d_2 = \overline{O_0D}$. Note that $O_0 = (\frac{-1}{2}t_{FT}, 0)$ and $O_2 = (\frac{1}{2}t_{FT}, 0)$ where t_{FT} is the thickness of the front target. Equations 5.18 and 5.19 show the maximum and minimum angles to be used in Equation 5.20 to calculate the minimum and maximum sold angles.

$$2\theta_{max} = \cos^{-1}\left(\frac{(d_{O_2A})^2 + (d_{O_2B})^2 - (2r_d)^2}{2(d_{O_2A})(d_{O_2B})}\right) \tag{5.18}$$

$$2\theta_{min} = \cos^{-1}\left(\frac{(d_{O_0C})^2 + (d_{O_0D})^2 - (2r_d)^2}{2(d_{O_0C})(d_{O_0D})}\right) \tag{5.19}$$

$$\Omega_{min/max} = 2\pi(1 - \cos(\theta_{min/max})) \tag{5.20}$$

For the sake of finding the maximum possible solid angles in the experiment here, the math using the 60 g/cm^2 HDPE target, which is 62.7 cm thick ($\rho_{HDPE} = 0.957$ g/cm^3), is shown below. This calculation is done for all eight front target physical thicknesses. The

Table 5.3: Minimum and maximum solid angles for each detector for the 60 g/cm^2 HDPE upstream target

Detector	Ω_{min} (sr)	Ω_{max} (sr)
N1	1.0617×10^{-3}	1.7247×10^{-3}
N2	1.0837×10^{-3}	1.6740×10^{-3}
N3	1.1107×10^{-3}	1.6045×10^{-3}
N4	1.5887×10^{-3}	2.2209×10^{-3}
N5	1.6986×10^{-3}	2.0294×10^{-3}
N6	2.2189×10^{-3}	3.8001×10^{-3}

minimum and maximum solid angle values calculated from this method with this target are shown in Table 5.3.

Table 5.3 highlights that solid angle can be quite sensitive to where the neutron is produced and where it interacts in the detector. Pictured in Figure 5.5 is a to-scale model of the detector/target system. In the light red is the 60 g/cm^2 HDPE front target and in light blue is the 20 g/cm^2 Al target. It illustrates just how much solid angle variance is possible with the varying target thicknesses.

As noted in Section 4.9, when correcting for effective target thickness and neutron production point, these extreme solid angle calculations are later repeated for every single data point except using $x_{\text{pp,min}}$ and $x_{\text{pp,max}}$ instead of the centers of the most upstream and downstream faces of the target (O_0 and O_2) to calculate the solid angle extreme values. Additionally, using the updated production point location, the new effective true solid angle Ω_{true} is calculated using the same methodology as outlined in this section; note that the actual Ω_{true} for each final bin is a weighted average of the individual Ω_{true} values for each smaller constituent bin before rebinning. Then, the fractional uncertainty of the solid angle is calculated using Equation 5.21.

$$\frac{\sigma_\Omega}{\Omega} = \frac{1}{2} \times \left(\frac{\Omega_{max} - \Omega_{min}}{\Omega_{true}} \right) \tag{5.21}$$

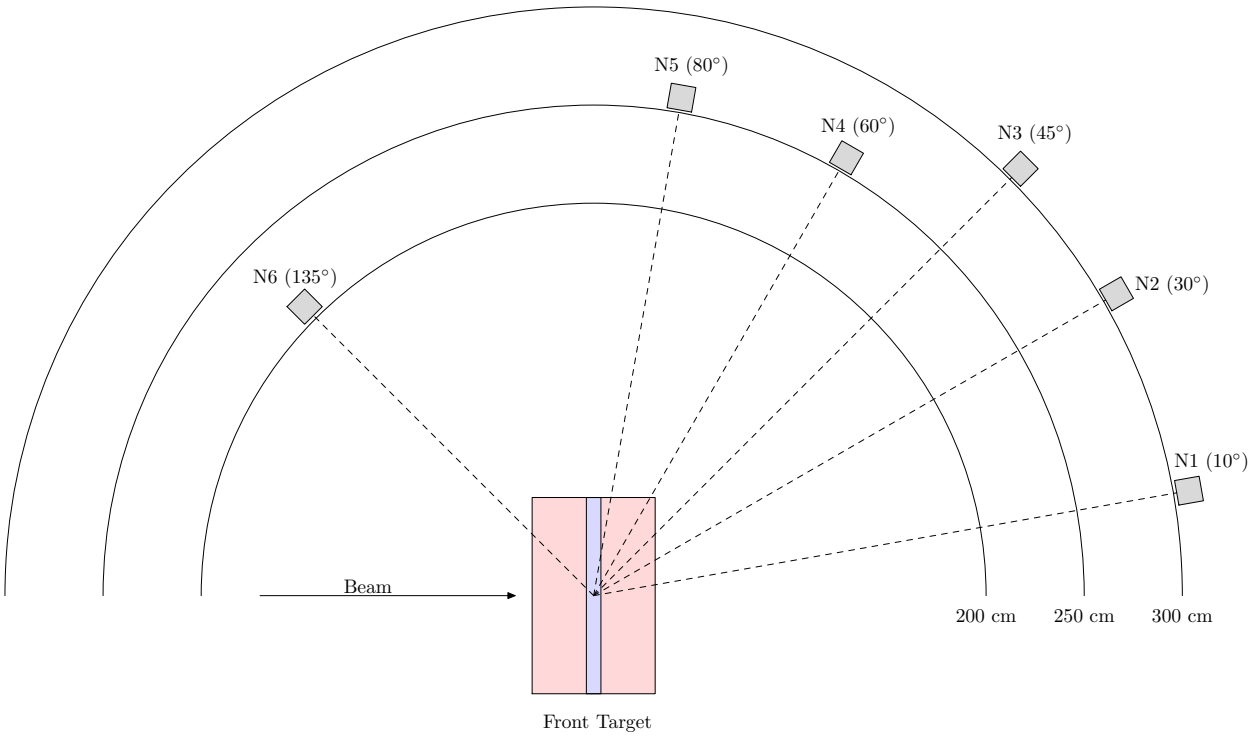


Figure 5.5: Pictured is a to-scale schematic of the beam/detector/target system. In red is the largest target, 60 g/cm^2 HDPE, and in blue is the smallest target, 20 g/cm^2 Al.

5.3.2 Graphical cut uncertainty

The graphical cut uncertainties are the final step of the uncertainty analysis to be applied. It entails redoing all of the graphical cuts (good beam cuts as detailed in Section 4.2.3 and neutron/gamma discrimination cuts as detailed in Section 4.2.4), redoing all of the analysis with the new graphical cuts, and taking the percent difference of each data point for the two different sets of calculations. While the first data set calculated is still to be used for everything mentioned already, this percent difference represents the systematic uncertainty of the graphical cut process for each data point.

After being exported from ROOT, read in by Python, and stored in a NumPy matrix, these new TDC values can undergo the same treatment as the original set of data in the ToF calculations. The x-axis conversions (TDC channels to MeV), however, do not need to be repeated since the channel numbers for both sets are the same. In this second pass, since data points were initially rebinned to statistics and other criteria, the original binning is copied regardless of statistics here to ensure that bin widths and locations are kept constant.

Before and throughout the rebinning process, it is important that all normalization that happens to the y-axis data happens to both the first and second pass data. Once all of the rebinning is complete, the fractional difference between the y-data of the two passes can be calculated and taken to be the fractional uncertainty of the graphical cut methodology ($\varepsilon_{\mathrm{GC}}$) used in calculating the total systematic uncertainty. Figures 5.6 and 5.7 show how the graphical cut uncertainty (represented as a percentage rather than a fractional value) is distributed across all of the upstream target neutron yield spectra data points for the November 2016 dataset. Note the logarithmic y-axis scale. These plots illustrate that the systematic uncertainty attributable to the graphical cuts is typically quite low, below 10% in almost 90% of all bins and below 40% in 98% of all bins.

The graphical cut uncertainty is the one form of systematic uncertainty that can also affect the statistical uncertainty since it impacts the number of counts being included in each bin. While the other systematic uncertainties could only shift the distribution of counts within a bin, the graphical cut uncertainty has the ability to change the mean number of counts and standard deviation of a bin, affecting the actual distribution. This uncertainty can be thought of as error bars that can be plotted on top of the statistical error bars. The uncertainty in the statistical uncertainty (σ_Y) introduced by the graphical cut systematic uncertainty will be denoted as $\varepsilon_{\mathrm{GC}(\sigma_Y)}$. The way one would adjust the statistical uncertainty to account for this is shown in Equation 5.22.

$$\sigma_{Y,\mathtt{total}} = \sigma_Y \times (1 \pm \varepsilon_{\mathrm{GC}(\sigma_Y)}) \tag{5.22}$$

In reality, if incorporating this value in a calculation, one would just use the upper bound to increase the standard deviation by a multiplicative factor of $(1 + \varepsilon_{\mathrm{GC}(\sigma_Y)})$. Note that combining the core statistical uncertainty σ_Y with this uncertainty introduced by the graphical cuts like this is not standard practice in reporting statistical uncertainties and should only be used if attempting to make a calculation using conservatively high yield values. Figures 5.8 and 5.9 show how $\varepsilon_{\mathrm{GC}(\sigma_Y)}$ (represented as a percentage rather than a fractional value) is distributed across all of the forward neutron yield spectra data points for the November 2016 dataset.

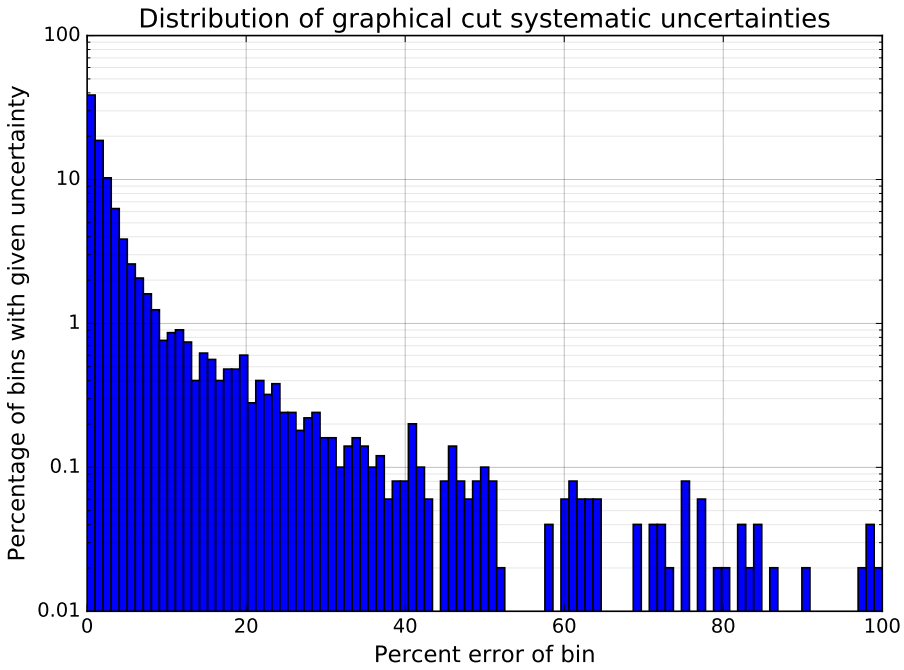


Figure 5.6: Pictured is the percentage of bins of all of the November 2016 upstream target neutron yield spectra with given percent graphical cut uncertainties.

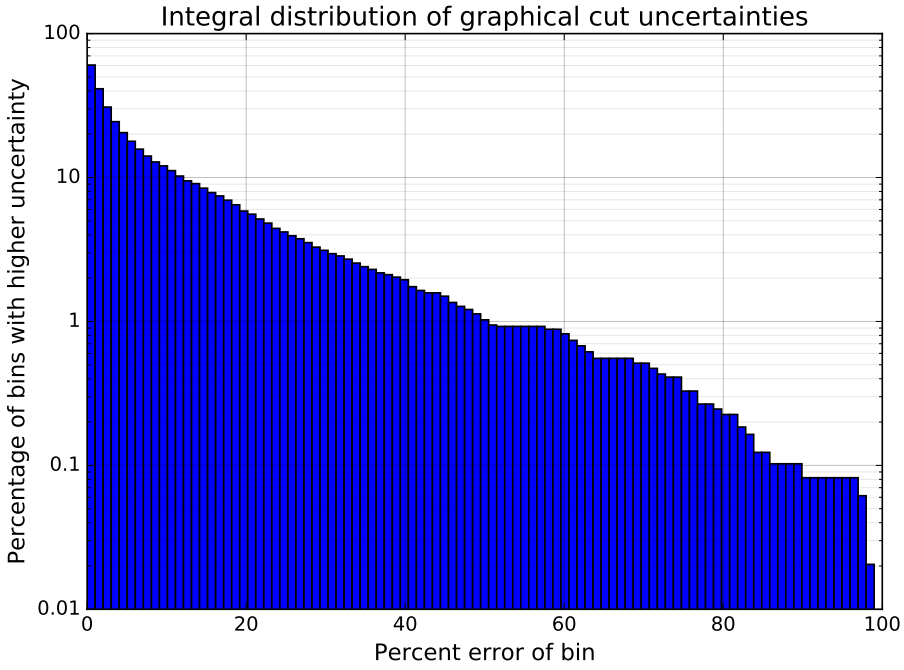


Figure 5.7: Pictured is a similar plot to Figure 5.6 but integrated such that each bin shows the percentage of data points with a percentage graphical cut uncertainty greater than that on the x-axis.

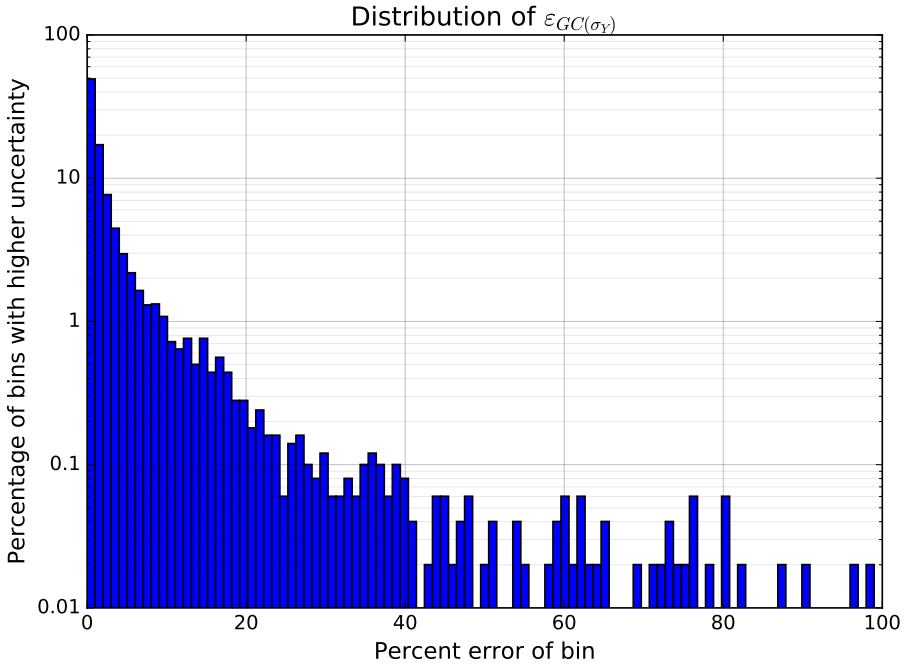


Figure 5.8: Pictured is the percentage of bins of all of the November 2016 upstream target neutron yield spectra with given percentage $\varepsilon_{\mathrm{GC}(\sigma_Y)}$.

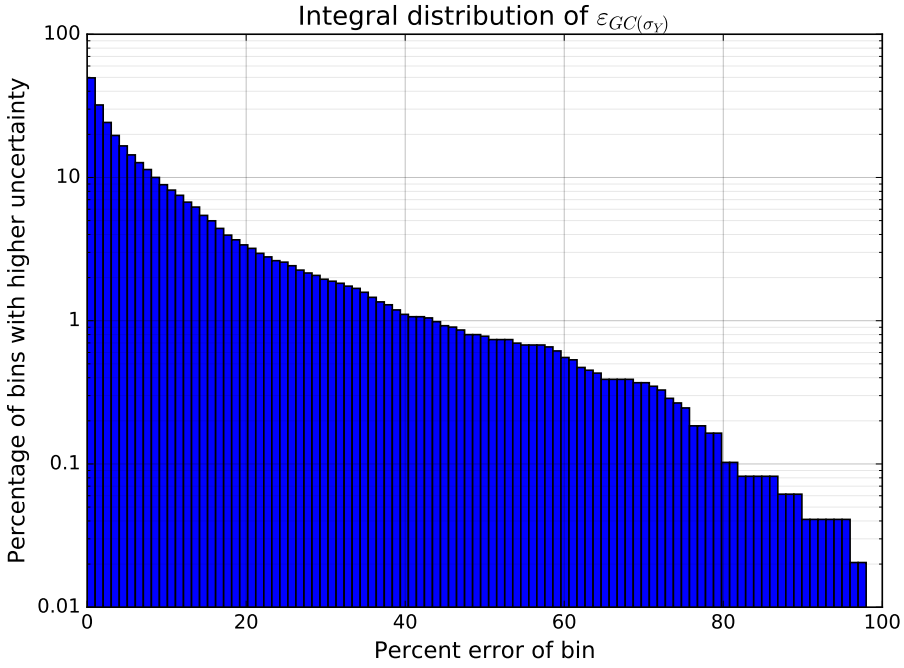


Figure 5.9: Pictured is a similar plot to Figure 5.8 but integrated such that each bin shows the percentage of data points with a percentage $\varepsilon_{\mathrm{GC}(\sigma_Y)}$ greater than that on the x-axis.

The plots illustrate that this systematic uncertainty in the statistical uncertainty incurred by making the graphical cuts, from a practical standpoint, is negligible. $\varepsilon_{\mathrm{GC}(\sigma_Y)}$ only exceeds 10% in 9% of all bins, and $\varepsilon_{\mathrm{GC}(\sigma_Y)} < 40\%$ in 99% of all bins. This means that in 9% of all bins, one could reasonably justify increasing the statistical uncertainty, which is already rebinned to at most 10% in a majority of bins (though up to 20% in a handful of bins), by 10% for a net effect of increasing the total statistical uncertainty by 1%. Thus, while an interesting and worthwhile point of exploration and verification, this additional component of systematic uncertainty to be factored into the statistical uncertainty is ignored.

5.4 Energy Resolution (x-axis)

The energy resolution of the time-of-flight spectra is calculated by Equation 5.23 [34]. This is essentially the fractional uncertainty of each bin's energy midpoint on the x-axis (neutron energy) and, so far in this document, has been visually represented as horizontal error bars.

$$\frac{\Delta E_n}{E_n} = \frac{E_n + m_n c^2}{E_n} \frac{\beta^2}{1-\beta^2} \sqrt{\left(\frac{\Delta L}{L}\right)^2 + \left(\frac{\Delta t}{t}\right)^2} \tag{5.23}$$

Where:

- E_n = individual neutron energy bin midpoint in MeV
- $\Delta E_n / E_n$ = fractional energy resolution per bin
- $m_n c^2$ = rest mass energy of the neutron = 939.565 MeV/c^2
- $\beta = v_n / c$ = fraction of the speed of light at which the neutron is traveling
- L = neutron flight path from production point* to center of detector
- $\Delta L = \frac{1}{2}(L_{max} - L_{min})$ = half of the maximum difference in possible flight paths

*The production point in the front target is calculated using PHITS simulations of each beam/target combination and is detailed in Section 4.9. Prior to implementing this calculation, the center of the target was taken to be the production point.

- L_{max} = maximum neutron flight path, distance from most upstream face[†] of front target to back face of detector
- L_{min} = minimum neutron flight path, distance from most downstream face[†] of front target to front face of detector

- t = individual neutron time of flight in ns for E_n
- $\Delta t = \frac{1}{2}FWHM_{p\gamma}$ = half of prompt gamma peak FWHM extrapolated to 0 g/cm^2 target thickness in ns (intrinsic timing resolution, discussed in Section 4.5.1)

The ΔL term is the only one here that warrants additional discussion; all other values have already been calculated (or can be easily calculated) by the time this correction is performed. Referring back to Figure 5.2 in Section 5.3.1, L_{max}, the longest flight path, is taken to be $\overline{O_0Z}$, and L_{min}, the shortest flight path, is taken to be $\overline{O_2X}$. The coordinates for all of these points were already calculated in order to determine the coordinates of the corners of the detector for use in the solid angle variance calculations. Thus, the distances can be easily found once again with the Cartesian distance formula (Equation 5.17).

Aside from that, this is a straightforward calculation and is the only uncertainty involving the energy axis of the neutron yield plots. This calculation must be performed for every single energy bin of every spectrum.

[†]Likewise, the effective target thickness calculations discussed in Section 4.9 are used to update the effective upstream and downstream bounds of the target to locations corresponding to the physically smallest dimensions containing 80% of all neutrons produced at a given energy.

Chapter 6

Downstream target and room scattered neutron data analysis

The previous two chapters discussed the analysis relevant to "forward" neutrons, the neutrons which traveled in a straight line from their production points in the upstream target to the detector in which they interacted. In the experiment, these "forward" neutrons were isolated using shadow bars to perform a background subtraction. However, to make the analysis complete, one should also attempt to gather information from these other neutrons which were produced outside of the upstream target or did not travel in a straight line from the upstream target to the detectors in which they interacted. Conveniently, the methodology for isolating the background component was already developed earlier when outputting the TDC spectra into text files for shadowed and unshadowed runs. Since the flight paths of these other neutrons are unknown, this TDC data is not of any use; though, the methods used to isolate the shadowed runs are. Instead, the QDC (charge collection / light production) spectra are utilized. Using the calibration curves found in Section 4.3.2, every QDC spectrum can be converted into a pulse height spectrum from which an energy spectrum can be extracted through the methods presented in this chapter.

6.1 Theory of extracting energy spectra from QDC data

The end goal of this research is to extract neutron energy spectra from pulse height distributions generated in liquid scintillation detectors. Specifically, the detectors of concern are 5" x 5" EJ-301/EJ-309 organic liquid scintillators. Due to the nature of energy deposition of neutrons in the scintillators (mainly through proton recoil and carbon interactions), a monoenergetic neutron source will still yield a distributed response. A more detailed discussion on the theory behind light production in liquid scintillators was covered earlier in Section 2.5. An unfolding/deconvolution procedure must be conducted to extract a neutron energy spectrum from a measured pulse height spectrum (PHS); however, this process is not straightforward. The main challenges are (1) generating an accurate response function for the detector and (2) then unfolding the measured pulse height spectra to extract the neutron energy spectra.

The total light response of a detector to an incident neutron flux should look like the sum of the individual pulse height spectra of the monoenergetic constituents of the incident neutron spectrum weighted by the intensity of each neutron energy present. The detector's characteristic light response function $\overline{\overline{R}}$ multiplied by the incident neutron spectrum $\vec{\Phi}$ should yield the measured pulse height distribution $\vec{L}$ (Equation 6.1) [35]. Note that since the response function is characteristic of a detector, it only needs to be calculated once for a detector.

$$\vec{L} = \overline{\overline{R}}\vec{\Phi} \tag{6.1}$$

Equation 6.1 can be rearranged to show the incident neutron spectrum in terms of the response function and PHS (Equation 6.2).

$$\vec{\Phi} = \overline{\overline{R}}^{-1}\vec{L} \tag{6.2}$$

However, this operation is not as simple as it looks. Firstly, many issues arise in inverting the response matrix. The response matrix is a function of both neutron kinetic energy and light output and is not necessarily a square matrix. Additionally, any small uncertainties in

the response function can impact the inversion significantly. Thus, additional methods must be employed to solve this problem and will be discussed more in detail in Section 6.5.

All of this assumes the availability of an accurate detector response function covering the desired neutron energy range. For the neutron energies of interest in this work, acquiring this response function is a task requiring careful consideration. Two main methods exist for calculating this response function matrix: using actual measurements taken in a laboratory or using a code to simulate the detector response. Either way, the response matrix is generated by combining the resulting pulse height spectra (measured or simulated) for numerous monoenergetic neutron sources or sources with a distinct range of neutron energies. The advantage of using actual lab measurements is that the physics seen in the response function exactly represent what is seen in the lab. However, monoenergetic high energy (>100 MeV) neutron sources do not exist, so a quasi-monoenergetic source with a very prominent single neutron energy peak (but still with a spectrum of lower energy neutrons) must be used instead [29]. Additionally, conducting a trial at a single energy or energy range is much more labor and time-intensive than just running an equivalent simulation. This means that response functions generated from laboratory data are usually less finely resolved (with responses at fewer different neutron energies) than simulated response functions. Simulated response functions can use perfectly monoenergetic or perfectly distributed neutron sources, and different runs at many different neutron energies are easy to code and can provide a higher resolution response function. However, the physics within the code must accurately reflect reality for the response functions to be accurate.

While one could conduct the lab work on their own, these response functions have been measured by a number of different research efforts in the past. Finding the perfectly suitable response function is difficult due to the detectors of different sizes and materials used by each research group. Additionally, researchers only produce response functions in the energy range of interest to them. Extensive work has been conducted in measuring the neutron response up to 15 MeV of liquid scintillators, but this research endeavor wishes to evaluate neutron spectra with elements beyond 100 MeV. One research group in Japan measured the response function of a 5" x 5" NE213 scintillator in the neutron energy range of 50 MeV

to 800 MeV [29]. This appears to be the highest-energy neutron liquid scintillator response research using similar detectors that has been performed in a laboratory setting.

Since this research desires a response function with components as low as 1 MeV and up to, ideally, several hundred MeV, the response functions used in this work were generated with simulations. Generating a response function/matrix is discussed in Section 6.4, and using a response matrix to deconvolute a pulse height spectrum is covered in Section 6.5. The extraction of QDC data from ROOT and conversion to pulse height spectra is covered next in Section 6.2, and this is followed by a short discussion on the rebinning of the pulse height spectra and the acceptance criteria applied to them in Section 6.3. The uncertainty quantification of the deconvoluted results is discussed in Section 6.6, and the performance of these methods is demonstrated in Section 6.7.

6.2 Exporting QDC spectra from ROOT

The QDC spectra, which contain the charge deposition distributions, are converted into pulse height spectra (PHSs). Before this, the QDC spectra must first be extracted from ROOT. In Section 4.2.4, selecting a QDC channel below which neutrons and photons could not be distinguished (Q_{total} cut) was discussed. This Q_{total} cut will still be applied here since it is still desirable not to contaminate the neutron data with photons. Overall, exporting the QDC data from ROOT is very similar to what was done for exporting the TDC spectra. Four text files are written for each detector/projectile/target combination:

- Unshadowed, unattenuated QDC spectrum
- Unshadowed, attenuated QDC spectrum
- Shadowed, unattenuated QDC spectrum
- Shadowed, attenuated QDC spectrum

In this analysis, only the "shadowed" files are relevant for the downstream target-produced and room scattered neutron characterization. However, pulse height spectra can also be composed for the upstream target-produced neutrons using the same background subtraction

methodology employed for the time-of-flight analysis. The normalization process is still the same as discussed in Section 4.4 (normalizing to live time and number of good beam events). While deconvoluted results from the upstream target are not used in the final results of this work, they serve as an important benchmark of this methodology used for the other neutrons. In Section 6.7, the upstream target neutron yields calculated with this new deconvolution methodology are compared to those obtained from the more traditional time-of-flight techniques employed earlier in Section 4.6.

The primary difference in the initial composition of the QDC spectra is that each final spectrum will be composed of a combination of the unattenuated and attenuated spectra. Using the QDC calibration curves (discussed in Section 4.3.2), the channels for the un/attenuated spectra can be converted to units of MeVee. Unlike the neutron spectra where the TDC axis translated to an energy axis differently for each detector/projectile/target combination, the QDC channel to MeVee translation is the exact same for all runs in each detector. The QDC calibration curve fitting parameters for the November 2016 experiment data, earlier shown in Table 4.3, are copied here to Table 6.1 for convenience.

$$y(\text{keVee}) = m \cdot x(\text{channel } \#) + b \tag{6.3}$$

Note that if only the unattenuated QDC spectra were used, the resulting pulse height spectra would be limited. Substituting the final QDC channel number of 2048 into Equation 6.3 with the N1 unattenuated fitting parameters produces a maximum light yield of 29.6 MeVee. In actuality, this number is even lower since unattenuated data is ignored below

Table 6.1: QDC channel to light yield fitting parameters for Equation 6.3

	Unattenuated `NX.t_qdc`		Attenuated `NX.ta_qdc`	
Detector	m (keVee/ch)	b (keVee)	m (keVee/ch)	b (keVee)
N1	14.6194	-354.0848	61.1630	-2878.8183
N2	12.3348	-382.1599	54.7282	-1209.2806
N3	12.9661	-302.2524	57.7672	-1506.6862
N4	3.9458	-87.3884	17.1850	-432.7622
N5	2.6451	-56.9052	11.2565	-279.4153
N6	1.8279	-24.8576	7.9312	-188.4455

N1.t_qdc channel 1995, the arbitrary cutoff channel selected just left of the pileup peak in each of the unattenuated NX.t_qdc spectra.

However, after shifting the upper bound to channel 2048 of the attenuated N1.ta_qdc spectrum, the maximum light production increases to 122.4 MeVee. In the final pulse height spectra, the lower MeVee bound was set by the original, lowest, Q_{total} cut values. The range of pulse heights seen by each detector is shown in Table 6.2.

After converting QDC channels to MeVee, the two pulse height spectra from the unattenuated and attenuated datasets must be stitched together into a single pulse height spectrum. Choosing where to truncate each unattenuated spectrum is simple. The lower bound is set by the Q_{total} cut values and the upper bound is set by NX.t_qdc channel 1995. These channel numbers can be converted to MeVee using the QDC calibration curves. Where to cut off the bottom of each attenuated spectrum to stitch to the end of each unattenuated spectrum can be determined by finding the first MeVee bin minimum of the attenuated spectrum that exceeds the MeVee bin maximum of NX.t_qdc channel 1995 and using that point. The maximum of the final stitched spectrum is simply the final channel of the NX.ta_qdc spectrum.

Ultimately, the range of available pulse heights is limited due to the fairly high voltages the detectors were operated at, especially for the higher angle detectors, but the covered range should be sufficient for the detectors most affected by the downstream target (N1, N2, and N3).

Table 6.2: Actual QDC spectra MeVee bounds

Detector	MeVee_{min}	MeVee_{max}
N1	1.9119	122.4442
N2	1.3324	110.9288
N3	1.3315	116.8583
N4	0.9267	34.7793
N5	0.5118	22.7852
N6	0.5107	16.0626

6.3 Experimental PHS rebinning

After collecting all of the QDC data and converting the bin edge values from channel number to MeVee, the pulse height spectra can be combined into an upstream target (unshadowed - shadowed) set and downstream target plus room scattered (shadowed only) set using the same normalization techniques employed for the TDC spectra analysis (Section 4.4). Afterward, the spectra need to be rebinned to be of any use in deconvolution.

Since the deconvolution technique is quite sensitive, having as few statistical fluctuations in the pulse height spectra as possible is desirable. Thus, rebinning criteria more strict than those covered in Section 4.11.3 are employed here. These spectra have fewer criteria to meet (no minimum bin width due to timing resolution, no constraint of energy resolution being less than bin width, etc.), making the statistical criterion the main rebinning requirement. With the time-of-flight spectra, a minimum of ten bins each with at most 10% fractional uncertainty per bin was set as an initial goal, but, in cases with insufficient statistics, any number of bins with fractional uncertainty no greater than 20% would ultimately be accepted. Here, the goal is at least 10 bins of 5% or lower fractional uncertainty, but that requirement will be loosened to at worst 5 bins of 10% fractional uncertainty each if necessary. If this latter criteria cannot even be met, the spectrum is rejected and regarded as unusable due to poor statistics. Figure 6.1 shows which of the back target spectra across all three experiments were deemed viable (blue) and not viable (red) for deconvolution with these criteria. After this rebinning, the pulse height spectra are ready for deconvolution.

6.4 Generating response matrices

There are a number of different ways to create response matrices. Generally, one would create one experimentally using a known mono-energetic neutron source at a number of different energies. Unfortunately, there are no reliably mono-energetic neutron sources at the relatively high energies seen in this work. Thus, one must use software to generate a response matrix.

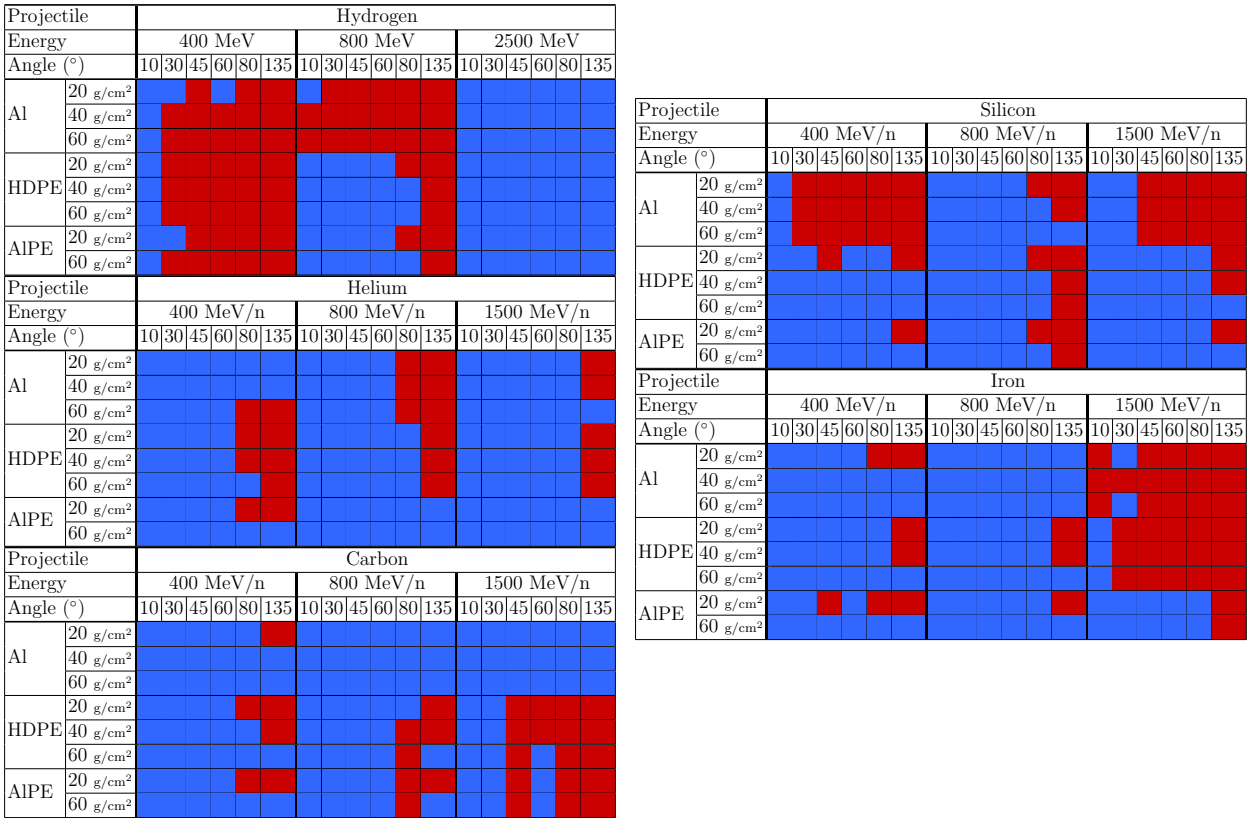


Figure 6.1: Viable combinations for deconvolution (blue=viable, red = not viable)

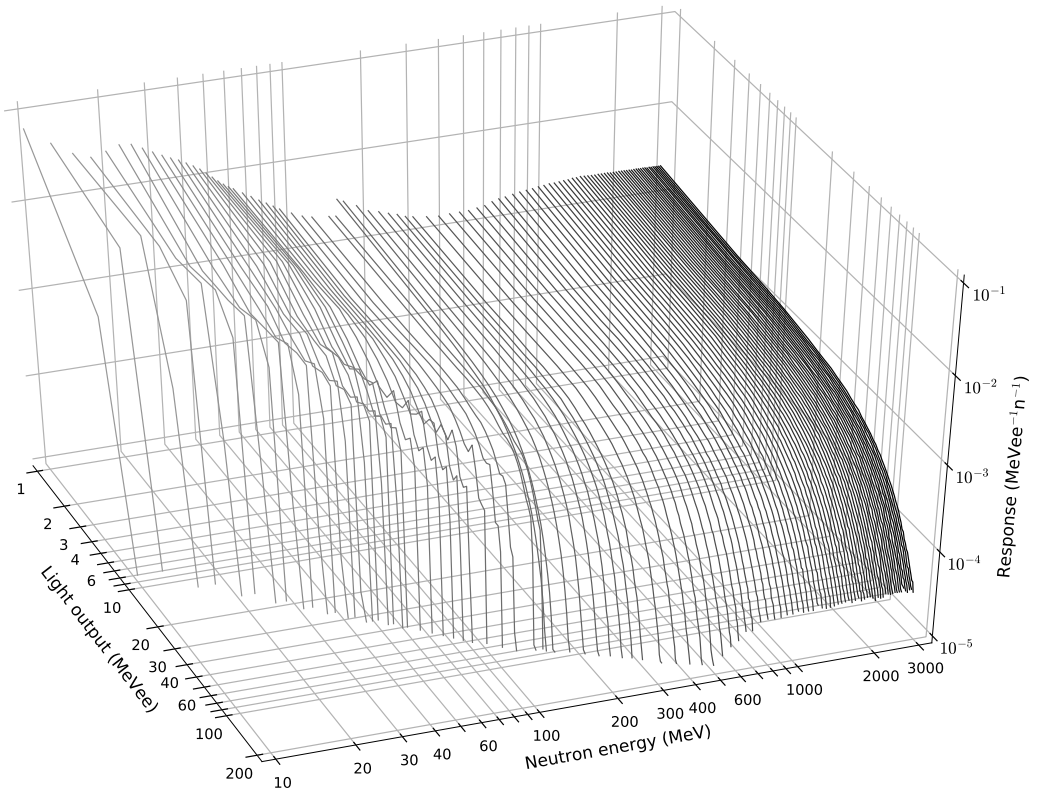


Figure 6.2: Pictured is an example response matrix from SCINFUL-QMD.

SCINFUL-QMD is a JAEA-developed code designed explicitly for modeling liquid scintillator response to high-energy neutrons, which is convenient for this work [26]. After running SCINFUL-QMD, the output can be parsed to generate a response matrix. The default fine binning by SCINFUL-QMD is preserved for now since it will be rebinned later many times to match the binning of each experimentally measured PHS for deconvolution. Figure 6.2 shows an example response matrix generated by SCINFUL-QMD with a basic level of rebinning applied to each constituent pulse height spectrum.

The first feature to note is the discontinuity at 150 MeV. Below 150 MeV, SCINFUL-QMD relies on nuclear reaction cross section data from the SCINFUL library, and above 150 MeV, the code uses the quantum molecular dynamics plus statistical decay model (QMD+SDM) for cross section modeling [26]. This switching is partially the cause of the change in behavior beyond 150 MeV.

In EJ-301, 12.7 cm of material will range out a 123.473 MeV proton (calculated with SRIM [36]). The longest possible chord in these detectors is 17.96 cm, which would just

barely stop a 150.405 MeV proton [36]. It is unlikely that a neutron would interact right at this edge and generate a 150 MeV proton with the precise angle to reach the opposite "corner" of the detector, but it serves as a good bounding case.

So, 150 MeV is at (or slightly above) the maximum neutron energy that can be reliably characterized with this method. As can be seen in Figure 6.2, around 120 MeV the peak characteristic of the maximum-recoil energy proton disappears, which makes sense given only neutrons which enter from different angles or undergo numerous scattering reactions within the detector can possibly deposit more energy. At higher energies, the pulse height spectra of the response matrix become increasingly more difficult to distinguish from each other. Thus, proton range in the scintillator is one of the limiting factors of this methodology. For larger scintillator volumes, the maximum detectable neutron energy with this methodology increases since the response matrix could be reliably extended to higher neutron energies with distinct constituent pulse height spectra. Therefore, a response matrix which only includes neutron energies up to 150 MeV is employed in this research and is shown in Figure 6.3.

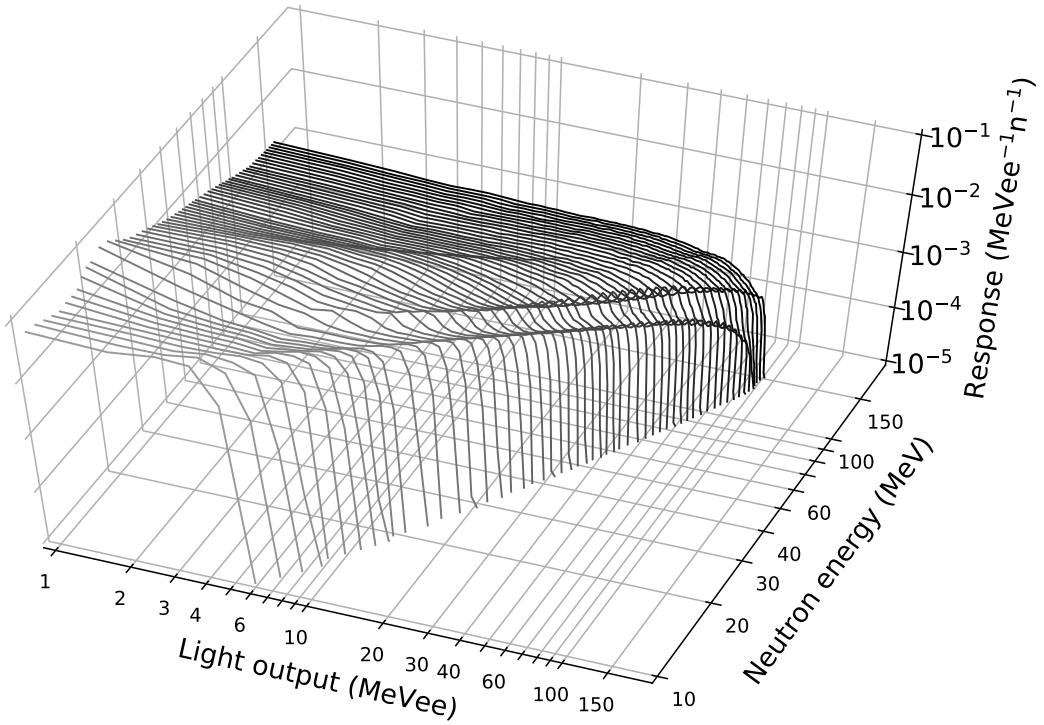


Figure 6.3: The finer response matrix from SCINFUL-QMD used before rebinning

Note that at this point the response matrix is much more finely resolved than will be necessary. This is done to make the later condensation of the response matrix (rebinning both neutron energy and light output axes) for each PHS to be deconvoluted more accurate, minimizing the amount of interpolation that will be required. For the deconvolution to be valid, the output quantity (neutron energy) needs to have a number of bins less than or equal to the number on input bins (pulse heights) [37]. In other words, the number of energy bins needs to equal or be less than the number of pulse height bins for each input spectrum.

6.4.1 Preparing the response matrix for deconvolution

At this point, all of the experimentally gathered pulse height spectra are ready to be deconvoluted, and a response matrix has been prepared. However, there is one more step that needs to be taken before the deconvolution can occur: The response matrix must be rebinned to match the light bins of the experimentally gathered pulse height spectra. Since each spectrum collected is uniquely binned to a set of criteria, the response matrix must be copied and rebinned for each spectrum to be deconvoluted. Ultimately, a massive array is generated containing many copies of the original response matrix each rebinned specifically to match the light bins of each input PHS.

After the response matrix is rebinned on the MeVee light yield axis to match each individual input PHS, the MeV neutron energy axis also needs to be rebinned to make the number of energy bins less than or equal to the number of light bins. This is an opportunity to make the matrix square; however, a few considerations must be made first. In the case that the input PHS had very good statistics and many bins still after rebinning, trying to match that same number of energy bins could result in oversampling the response function during the deconvolution process, producing an overregularized solution. In this instance, using a preset maximum number of energy bins is more appropriate. In this work, 10 evenly log-spaced neutron energy bins were used unless there were even fewer light yield bins in the input PHS, in which case the number of neutron energy bins was set equal to the number of pulse height bins.

The response matrix used was generated from many mono-energetic SCINFUL-QMD runs; these individual response spectra from mono-energetic neutron sources need to be

combined/rebinned into only 10 (or fewer) energy bins. The minimum neutron energy for a given detector is determined by its Q_{total} cut as discussed earlier, and the maximum neutron energy is set to 150 MeV by the response matrix. Additionally, the energy bin spacing, for the sake of robustness, should be done in an evenly log-spaced regime. In practice, the earlier mentioned massive array containing each response matrix rebinned to each PHS on the MeVee axis also undergoes a rebinning of the MeV axis for every individual response matrix it contains. Since the pulse height and neutron energy bins of the response matrix are known exactly (due to being generated in SCINFUL-QMD), the rebinning methodology discussed in Section 4.11.1 where original bin edges are not preserved (values from edge bins are split and redistributed instead) is employed in rebinning the light output and neutron energy axes of the response matrices. After this array of custom response matrices has been assembled for the upstream and downstream target spectra, all of the collected data are ready for deconvolution.

6.5 Deconvolution

Once the response matrices have been generated, they can be used to deconvolute the rebinned pulse height spectra. This section will cover the deconvolution process and its rationale in a step-by-step fashion. Figure 6.4, presented toward the end of this section, showcases each individual step within the deconvolution process, starting with the post-rebinning input PHS in Figure 6.4a, for an example system of downstream target-produced neutrons in the 10° detector from 800 MeV/n Fe projectiles incident on the 60 g/cm^2 HDPE upstream target followed by the 60 g/cm^2 HDPE downstream target.

The matrix problem posed in Equation 6.1 can be solved using a non-negative least squares method (NNLS). The `scipy.optimize.nnls` function located in the SciPy optimization library was explicitly designed for this purpose and was utilized here. From the web page documenting the function (on docs.scipy.org): "The algorithm is an active set method. It solves the KKT (Karush-Kuhn-Tucker) conditions for the non-negative least squares problem." The function simply requires the response matrix $\overline{\overline{R}}$ and a pulse height

spectrum $\vec{L}$ and will output the incident neutron energy spectrum solution $\vec{\phi}$. It solves Equation 6.4.

$$min_{\vec{\phi}} \left\| \overline{\overline{R}}\vec{\phi} - \vec{L} \right\|_2 \tag{6.4}$$

The NNLS deconvoluted result using a tailor rebinned response matrix is shown in Figure 6.4b. Despite being the most mathematically optimal solution, its jaggedness is clearly nonphysical; another approach is necessary.

Tikhonov regularization followed by L-curve analysis is employed in this research as a solution to this issue. Usage of deconvolution techniques for neutrons of the energies relevant to this experiment appear to be relatively uncommon; though, this type of scenario where deconvolution is a desirable approach is fairly widespread in nuclear security applications for the lower energy fission neutrons of interest in that field. One such effort which employed a similar combination of Tikhonov regularization and L-curve analysis (among other tested methods) was performed by Dr. Chris Lawrence for arms-control verification applications [35]. Tikhonov regularization relies on a regularization parameter μ. The "optimum" value of μ is one that characterizes the elbow of the L-curve where a balance is struck between sacrificing the least amount of mathematical precision to gain the most solution smoothness. This method is effectively solving Equation 6.5.

$$min_{\vec{\phi}} \left\| \overline{\overline{S}}_\mu \vec{\phi}_\mu - \vec{M} \right\|_2 \text{ where } \overline{\overline{S}}_\mu = \begin{bmatrix} \overline{\overline{R}} \\ \mu\overline{\overline{\mathrm{I}}} \end{bmatrix} \text{ and } \vec{M} = \begin{bmatrix} \vec{L} \\ 0 \end{bmatrix} \tag{6.5}$$

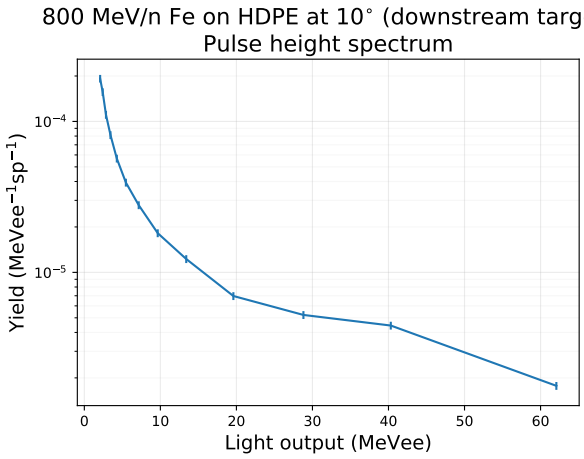
Thus, to generate the L-curve (Figure 6.4c), one must calculate the residual norm $||\overline{\overline{S}}_\mu \vec{\phi}_\mu - \vec{M}||_2$ and the solution norm $||\vec{\phi}_\mu||_2$ for a variety of values of μ. This research used approximately 30 different values of μ to generate the L-curve for each spectrum. The curvature of the L-curve κ (Equation 6.6) was calculated over the L-curve (Figure 6.4d); the maximum value of the curvature identifies the value of μ associated with the elbow. The curvature calculation is performed by fitting a circle to three points, $(x_1, y_1), (x_2, y_2), (x_3, y_3)$, and taking the inverse of the radius of this circle. A "curvier" portion of a curve, such as an elbow-like bend, would be fit with a circle of smaller radius and thus higher curvature

κ. By default, twenty values of μ ranging from 10^{-3} to 10^{1} are used, but these ranges are expanded if the calculated L-curve elbow point is too close to either of the bounds. Once a rough guess of μ has been made, finer values of μ around the initial value are sampled to determine a more precise value of μ. A thorough explanation of Tikhonov regularization and the L-curve can be found in Reference 38 with a more in-depth look at the L-curve specifically in Reference 39.

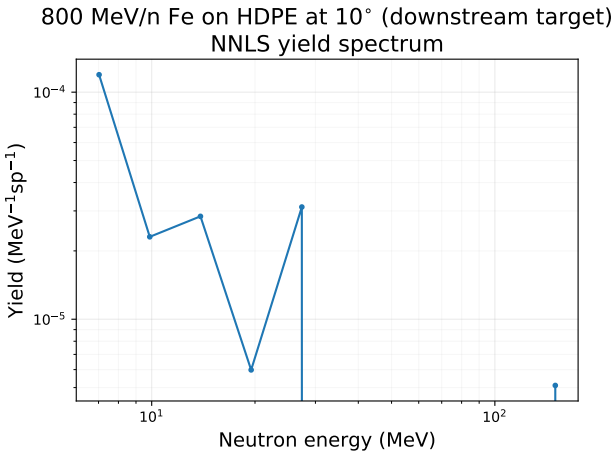
$$\kappa = \frac{2 \cdot [((x_2 - x_1) \cdot (y_3 - y_2)) - ((y_2 - y_1) \cdot (x_3 - x_2))]}{\sqrt{[(x_2 - x_1)^2 + (y_2 - y_1)^2] \cdot [(x_3 - x_2)^2 + (y_3 - y_2)^2] \cdot [(x_1 - x_3)^2 + (y_1 - y_3)^2]}} \tag{6.6}$$

In this example, the spectrum shown in Figure 6.4e is the final output from the deconvolution with Tikhonov regularization. While still possessing some sharp features, it is considerably smoother than the NNLS result (and is continuous). As will be discussed in greater detail in Section 6.6, this deconvolution process is repeated many times in a Monte Carlo fashion for the sake of statistical uncertainty propagation. This not only allows for a statistical uncertainty to be assigned to each final bin but also allows for some degree of additional smoothing by evaluating the mean value of each energy bin over a large number of trials. Figure 6.4f shows the Monte Carlo average NNLS (yellow) and Tikhonov regularized (teal) results with corresponding statistical error bars alongside the original "exact" results from a single pass of deconvolution (NNLS as blue points and Tikhonov regularized as the red line).

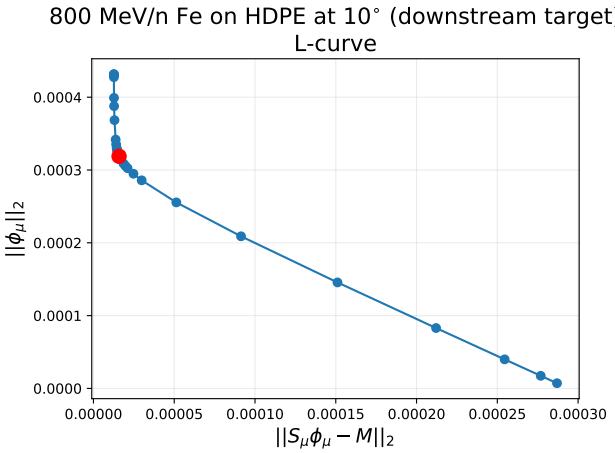
The L-curve is one of several ways this problem could be solved, and the curvature κ is just one convenient way to select a value for the regularization parameter μ. Traditionally, one would manually pick a value for μ that just provided the subjectively best-looking solution. The curvature calculation is a more concrete method of achieving a best guess for μ. Additionally, the methods utilized here were selected for being automatable without need for input of human judgment which would come at the expense of time and an additional incurred systematic uncertainty associated with this human judgment. This deconvolution process is conducted for every PHS deemed statistically viable from both the upstream and downstream target datasets.



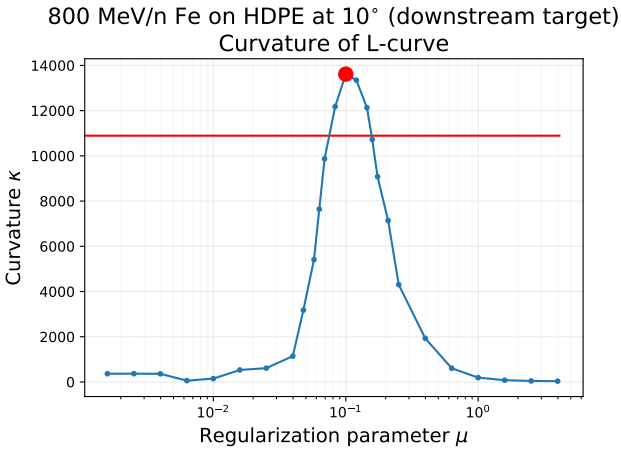
(a) Input PHS



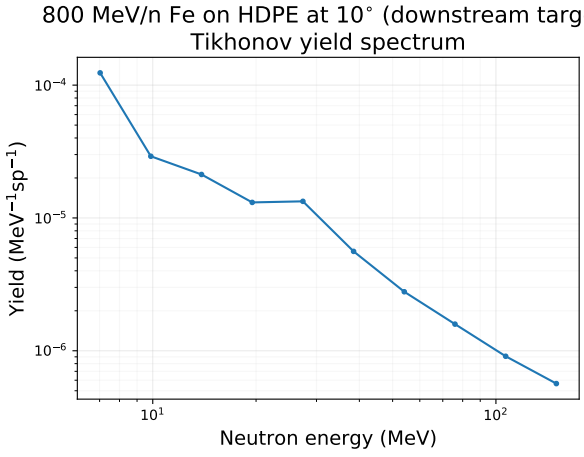
(b) NNLS output spectrum



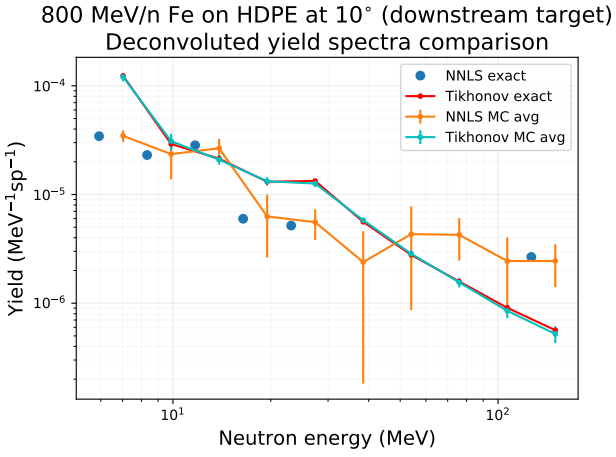
(c) L-curve



(d) L-curve curvature κ



(e) Tikhonov output spectrum



(f) Spectra after Monte Carlo

Figure 6.4: This figure highlights the individual steps of the deconvolution process.

6.5.1 Normalization of deconvoluted results

The resulting neutron energy spectra will not have undergone any normalization when outputted from the deconvolution process. While all spectra can be normalized to neutron energy bin width, only the upstream target spectra can be normalized to solid angle adequately. The solid angle correction employed on the deconvoluted upstream target results uses the same production point and effective target thickness as a function of neutron energy and beam system configuration calculations as was covered in Section 4.9.1 except the deconvoluted neutron energy is taken to be true; no iteration is performed.

The individual pulse height spectra comprising the response matrices outputted by SCINFUL-QMD when in response matrix mode (rather than only efficiency mode) are normalized to neutrons which underwent interactions, not just the number of incident neutrons. This means that, after deconvolution, it is necessary to perform the same efficiency correction as was done with the time-of-flight dataset using the energy-dependent efficiency curves (also generated alongside the response matrices with SCINFUL-QMD). This step could be performed on the response matrices immediately prior to deconvolution or afterward as was done here.

The energy bin width normalization is straightforward for the Tikhonov-regularized deconvoluted spectra since they are continuous, but tackling this issue for the non-negative least squares (NNLS) solutions is a more complicated task. The NNLS spectra are very prone to being jagged, often resulting in a few populated bins with all other surrounding and nearby bins having a value of zero (as illustrated in Figure 6.5). Interpreting and normalizing these bins can be a challenge. In reality, each of these positive points represents its own bin and some amount of the surrounding bins set to zero, meaning the populated bin should be normalized to an energy bin width wider than what it has initially. Addressing this concern can be done in a few different ways.

First, one can manually "smooth" the NNLS spectra by redistributing counts from each populated bin to its neighboring bins. This method can produce cleaner results but is susceptible to large systematic uncertainties since one must assume some distribution of how the counts should be spread to surrounding bins.

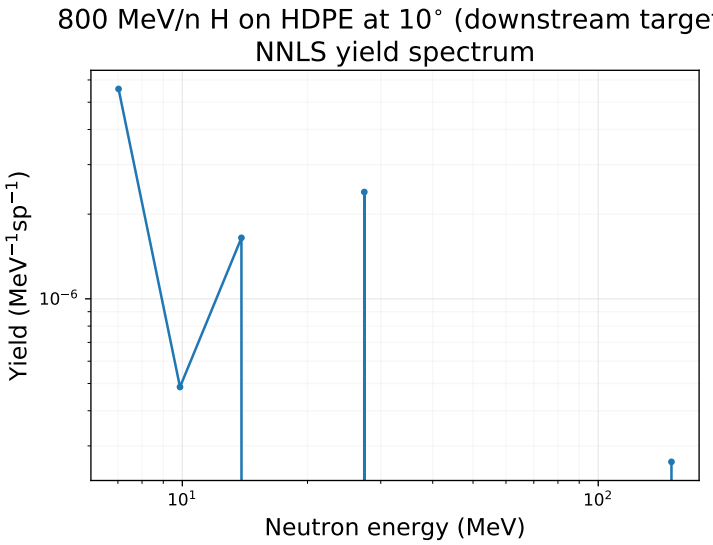


Figure 6.5: Shadowed neutrons detected at 10° from the NNLS deconvolution for 800 MeV H incident on the 60° HDPE upstream target followed by the 60 g/cm^2 HDPE downstream target

Another approach involves reducing the spectra to only the bins containing the positive values by reassigning the minimum and maximum x values (energies) associated with each bin. This method involves making an assumption about what portion of the unpopulated region surrounding a nonzero bin can be attributed to that nonzero bin. The simplest way to do this is to evenly split the unpopulated region between two nonzero points to each of the two nonzero points. Where this line is drawn can be decided in a number of ways though. One may assign ownership of an unpopulated set of bins to the following populated bin rather than splitting it, or one may choose to split the region but by using the logarithmically spaced center rather than the linear center. If enough slope information is present, which it usually is not with the NNLS results, one could also assume a distribution between two nonzero bins and attempt to split the ownership of the encompassed unpopulated bins using that.

Ultimately, the unreliability of the NNLS method alone and how forced some of these smoothing methods are make its use unjustifiable. Fortunately, Tikhonov regularization followed by L-curve analysis serves this exact purpose (providing smoother results) and is mathematically justifiable. As seen in Figure 6.6 (which is for the same system shown in Figure 6.5), this method produces much more realistic-looking spectra than the NNLS

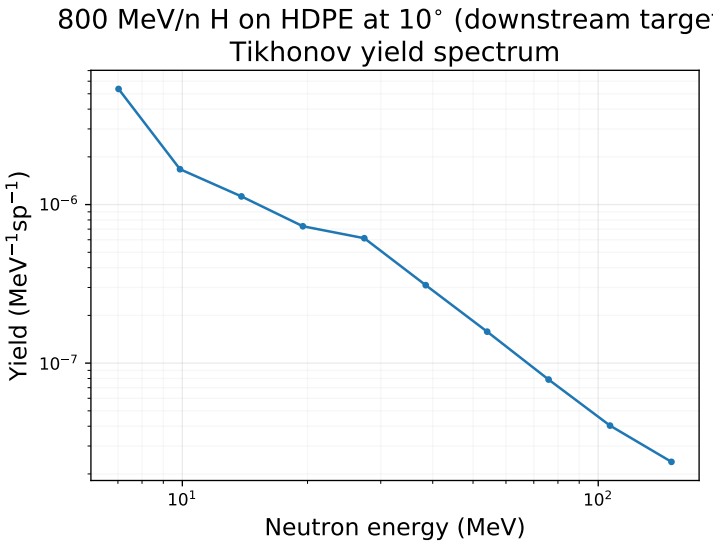


Figure 6.6: Shadowed neutrons detected at 10° from Tikhonov regularization followed by L-curve analysis for 800 MeV H incident on the 60° HDPE upstream target followed by the 60 g/cm^2 HDPE downstream target

method alone. So, all final deconvoluted results utilize Tikhonov regularization followed by L-curve analysis; however, the NNLS results are not completely ignored. As is discussed in the following section, they play a role in the quantification of one component of the systematic uncertainty.

6.6 Uncertainty quantification of deconvolution

There is no direct way to propagate the statistical uncertainties present in the pulse height spectra through the deconvolution process. In order to observe the effect of the statistical uncertainties of the measured pulse height spectra on the final deconvoluted energy spectra, a Monte Carlo approach must be employed. Every data point in each PHS has some associated standard deviation from the statistical uncertainty. The deconvolution process for each input PHS can be repeated for a large number of trials N_T ($N_T = 10,000$ in this work) where, rather than using the mean y-value of each PHS data point, each y-data point in the PHS is re-sampled using a normally distributed random number from the Gaussian distribution formed by that data point's mean value and standard deviation. This will result in N_T different energy spectra with identical energy binning for the single input PHS. Then, a

new mean value and standard deviation can be calculated for each energy bin using the N_T values. For many trials, the statistical uncertainty error bars will converge to a minimum amount. Figure 6.7 showcases these results for an example case of 800 MeV H incident on the 60 g/cm^2 HDPE upstream target followed by the 60 g/cm^2 HDPE downstream target. After ten thousand trials, the Tikhonov Monte Carlo result has converged and practically overlaps with the initial solution. However, the NNLS results, while at least populating more energy bins over the ten thousand trials, still show sizable fluctuations.

This only factors in the effect of statistical uncertainty though (with some quantity of systematic uncertainty coupled to it as well). As was the case with the time-of-flight results, these results also posses several components of systematic uncertainty.

Earlier in Section 5.3, a systematic uncertainty was introduced to the time-of-flight results which stemmed from the efficiency correction which was calculated with SCINFUL-QMD. In this deconvolution methodology, the final deconvoluted spectra are also divided by an efficiency correction; additionally though, the deconvoluted results have folded in them the systematic uncertainties associated with the accuracy of the response matrices. As was done for the time-of-flight uncertainty quantification, this systematic uncertainty associated with

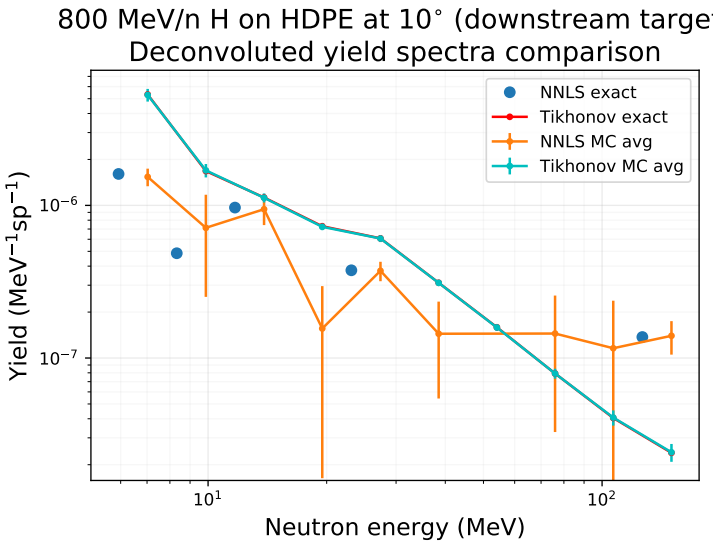


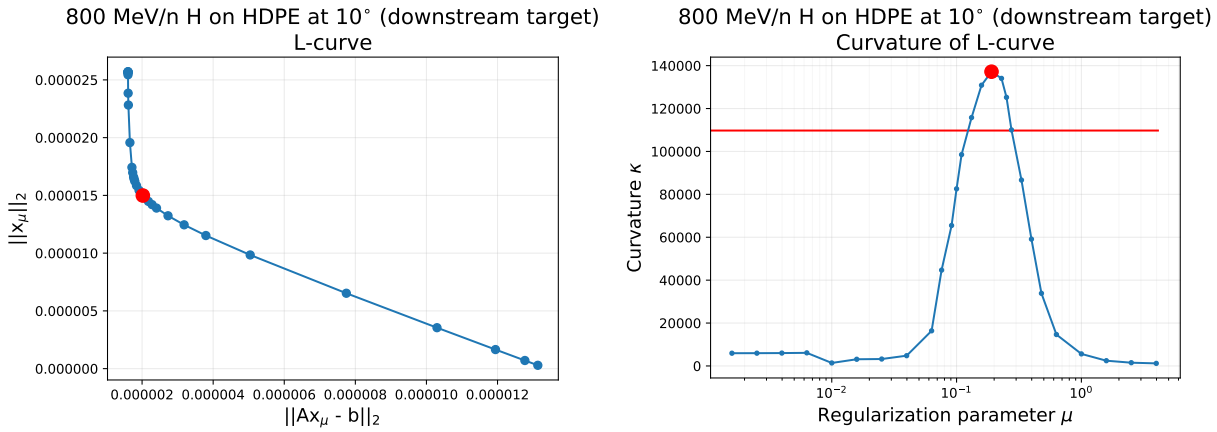
Figure 6.7: Shadowed neutrons detected at 10° for 800 MeV H incident on the 60° HDPE upstream target followed by the 60 g/cm^2 HDPE downstream target (Tikhonov exact and MC average results overlap.)

SCINFUL-QMD is assumed to be the same value of about 10%. This serves as a measure of general confidence in SCINFUL-QMD's ability to model detector response; thus, it is only counted for once and simultaneously serves as the assumed systematic uncertainty of the response matrices and of the efficiency correction. As a result, this systematic uncertainty can be factored in at the end of the analysis. This folds in more than just probability of interaction though; it includes confidence in reaction channel cross sections and light yield of the products of those reaction channels.

The choice of the regularization parameter μ and deviation from the "truest" solution from the NNLS calculation is not reflected in the statistical uncertainty calculation; thus, a method to quantify the uncertainty involved in this deconvolution method needs to be developed. For determining the uncertainty from use of regularization at all, the NNLS and Tikhonov Monte Carlo mean results can be compared. This is done simply by taking the fractional error between the Monte Carlo averaged (over 10,000 trials) NNLS and Tikhonov spectra bin by bin, taking the Tikhonov values as the "reference" values in the calculation. This is the most dominant component driving the total systematic uncertainty of this methodology.

For the specific choice of regularization parameter, one can look at the influence of choosing the specific optimal μ rather than a neighboring one with a similar κ value. This is done by taking the average of all spectra whose $\kappa(\mu)$ exceed some threshold equal to at least 80% of the maximum κ value and comparing that to the final spectrum produced with the optimal μ using a similar fractional error calculation. This is illustrated in Figure 6.8b where the red line indicates this 80% threshold and Figure 6.8a shows the L-curve from which this curvature plot was derived. The red dot on each of the plots denotes the value of μ associated with the maximum value of κ for all μ.

This analysis method is also subject to the same graphical cut systematic uncertainty as discussed in Section 5.3.2, and it is calculated in the exact same fashion here. For the deconvoluted upstream target neutron spectra, the same energy-dependent solid angle systematic uncertainty as discussed in Section 5.3.1 should be included if normalizing the data to solid angle.



(a) L-curve

(b) L-curve curvature

Figure 6.8: The L-curve and its curvature for shadowed neutrons detected at 10° for 800 MeV H incident on the 60° HDPE upstream target followed by the 60 g/cm^2 HDPE downstream target

6.7 Validation of the deconvoluted results

Now that deconvolution has been performed, one may wonder: Are these results trustworthy at all? The first and most obvious available form of validation is to compare deconvoluted upstream target neutron energy spectra with time-of-flight-calculated upstream target neutron energy spectra. If the two are in agreement, this deconvolution methodology would be proven as credible. Additionally, agreement between the two methods would serve to strengthen the time-of-flight-derived results as well since it would show that two completely different methodologies could be used to arrive at the same result.

As has been mentioned several times throughout this chapter, the pulse height spectra from the forward neutrons underwent the same deconvolution process in tandem with the downstream target and room scattered neutrons. The only additional steps required for the upstream target neutrons were the background subtraction and solid angle normalization.

An additional note to be made here is that the response matrix used in this work only had energy bins up to 150 MeV, meaning deconvoluted results even for the upstream target will only extend to 150 MeV. While this is not typically an issue for the downstream target-produced and room scattered neutrons which typically have lower energies due to

being predominantly from target fragment evaporation, this is not the case for the forward neutrons, particularly those at lower detector angles relative to the beamline.

Taking one of the example systems from Chapter 4, the spectra from the two methods will be first compared for the 400 MeV/n C beam incident on the 20 g/cm^2 Al upstream target system. Figure 6.9 showcases this for the 10° detector. The yield values are fairly close, but the deconvolution over predicts the time-of-flight results at lower energies. This ends up being a common trend in this comparison exercise for the 10° detector where a considerable amount of the neutron yield spectrum is typically beyond the 150 MeV limit of the deconvolution methodology. The additional yield which cannot be attributed to higher energy neutrons appears to be redistributed to lower energy neutrons.

This same trend, though to a slightly lesser extent, is seen in the 30° (Figure 6.10) and 45° detectors where a moderate amount of neutron yield is still present above 150 MeV.

However, the major differences between the two methods subside fairly quickly with increasing detector angle. Figure 6.11 shows this comparison for the 60° and 80° detectors where the agreement between the two methods is very strong since the majority of neutrons striking these detectors are below 150 MeV.

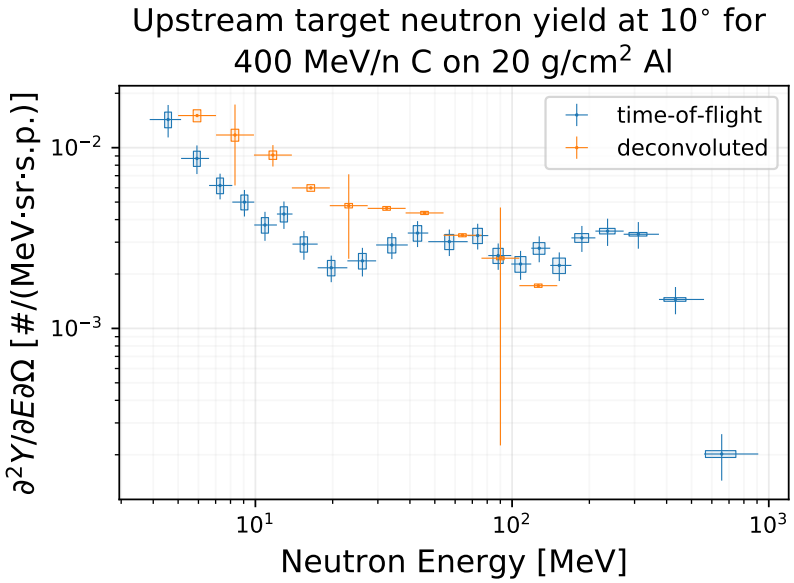


Figure 6.9: Comparison of time-of-flight and deconvolution methods for neutrons detected at 10° for 400 MeV/n C incident on the 20 g/cm^2 Al upstream target

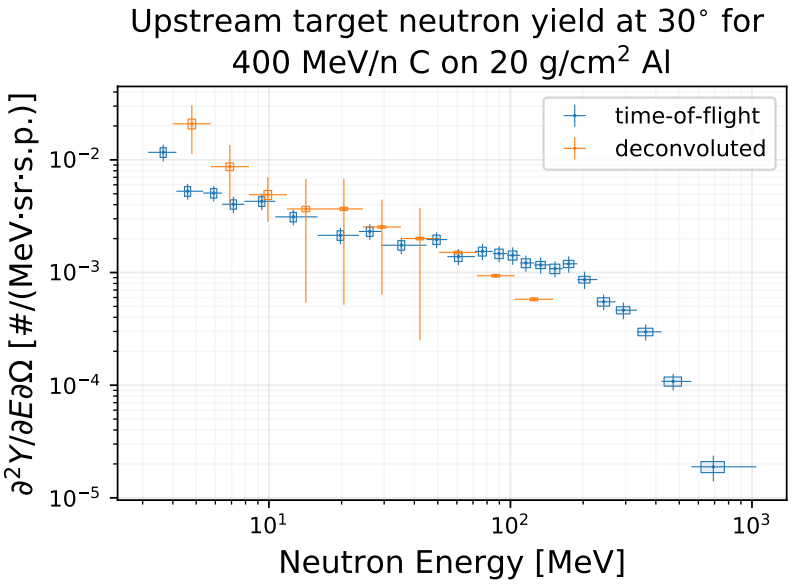
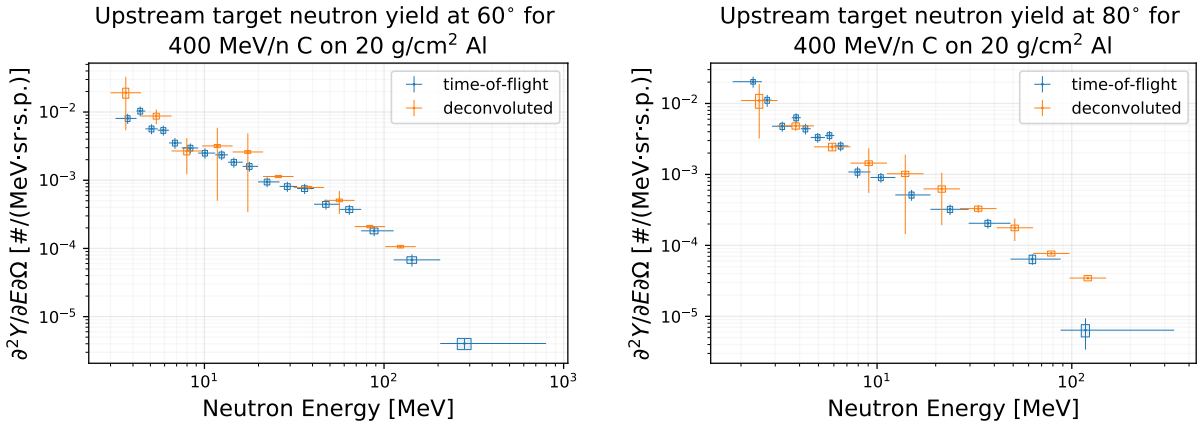


Figure 6.10: Comparison of time-of-flight and deconvolution methods for neutrons detected at 30° for 400 MeV/n C incident on the 20 g/cm^2 Al upstream target



(a) 60° (b) 80°

Figure 6.11: Comparison of time-of-flight and deconvolution methods for neutrons detected at 60° and 80° for 400 MeV/n C incident on the 20 g/cm^2 Al upstream target

Since these upstream target deconvoluted results are not presented alongside the final results of this work (discussed later in Chapter 8), this serves as the best opportunity to provide several more examples across various projectile and target combinations to solidify the conclusion that the deconvolution method, under the right conditions of the majority of the neutron flux being in the energy range of the response matrix, produces trustworthy results which agree with those derived using the time-of-flight techniques. By proving this agreement and the trustworthiness of this methodology here, the discrepancies shown later in Chapter 8 between the deconvoluted downstream target neutron results and the Monte Carlo simulated equivalent results can be more strongly attributed to inaccuracies in the codes or tally methodology rather than issues with the deconvolution methodology. There are several reasons why these deconvoluted upstream target results are not presented alongside their time-of-flight counterparts in the final results:

1. The information is redundant.
2. The time-of-flight technique provides results with finer energy resolution which also extend out to higher energies.
3. The systematic uncertainties associated with the time-of-flight methodology are generally lower.
4. The time-of-flight techniques are more historically established.

Each of the four pages following this discussion contains a figure showcasing a comparison of these two methodologies at all six detector angles for a given projectile and target combination.

First, the upstream target neutron yields for 1500 MeV/n He incident on the 60 g/cm^2 Al upstream target are shown in Figure 6.12. In this case, the extra high-energy neutrons in the 10° detector result in the deconvoluted yields to be inflated in the region beyond 10 MeV. At all five other detector angles, the deconvoluted results are in strong agreement with each other.

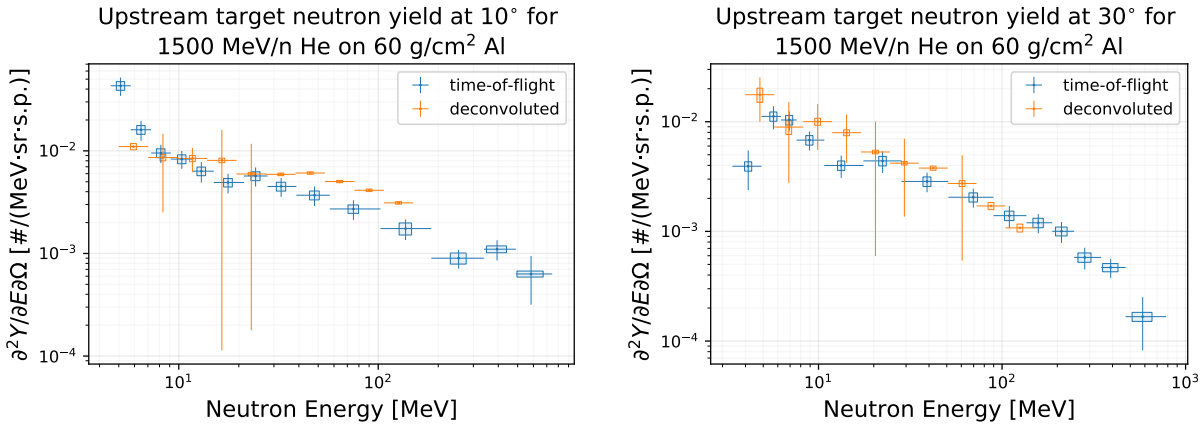
Next, Figure 6.13 shows the spectra for 400 MeV H incident on the 20 g/cm^2 Al upstream target. These plots show the measurement taken at the very end of the November 2017

experiment; this particular system was also measured in the March 2016 experiment. Of particular note in this case is the strong agreement at all angles since the neutron yield component beyond 150 MeV at all angles is relatively minor in comparison to the yield at lower neutron energies.

Figure 6.14 shows the results for the 400 MeV/n Si beam incident on the 20 g/cm^2 HDPE upstream target. In this case, a substantial portion of the neutron yield at 10° (and a still notable amount at 30° and even 45°) is above 150 MeV, causing the deconvoluted results to disagree with the time-of-flight results. However, the agreement between the two methodologies at the highest three angles is still quite strong.

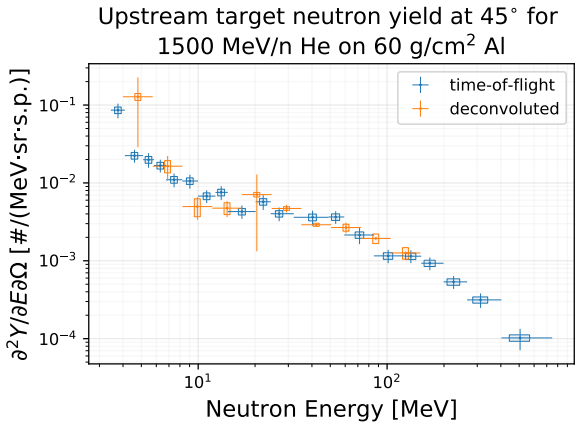
Finally, Figure 6.15 displays spectra for 800 MeV/n Si projectiles incident on the 60 g/cm^2 AlPE hybrid target. This same trend of agreement when a vast majority of the neutron yield is below 150 MeV still holds. Figure 6.15d showing the 60° results for this system illustrates that the deconvoluted results can suffer statistically when the rebinning algorithm has to compromise on the ideal 5% statistical uncertainty per PHS bin criterion.

Thus, this comparison of the two methodologies for determining neutron yield directly from the upstream target confirms the trustworthiness of the deconvolution methodology and further validates the results found with the time-of-flight technique. The deconvolution methodology's accuracy is reliant on the detected neutron yields being within the energy range of the response matrix used for deconvolution. Fortunately, this is more or less always the case for the downstream target-produced and room scattered neutrons in this experiment for which this deconvolution methodology was primarily developed.

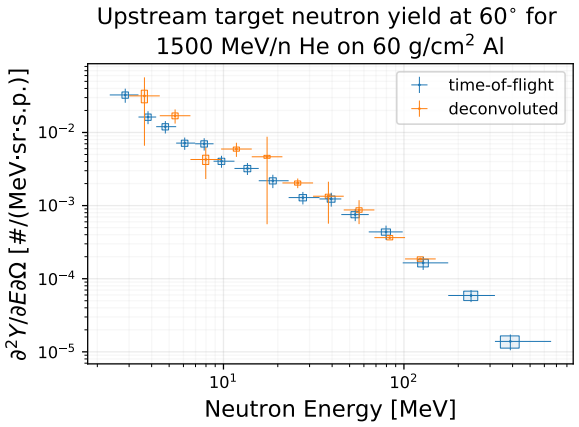


(a) 10°

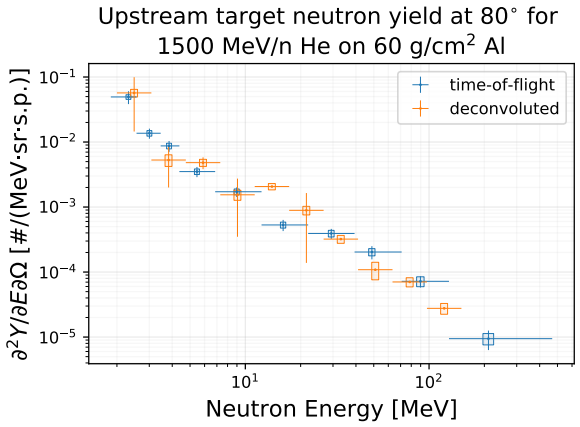
(b) 30°



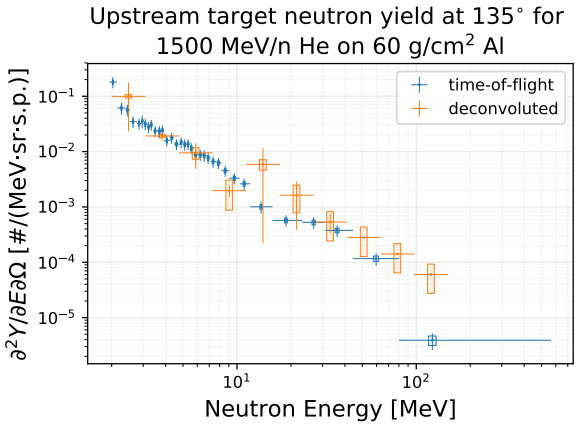
(c) 45°



(d) 60°

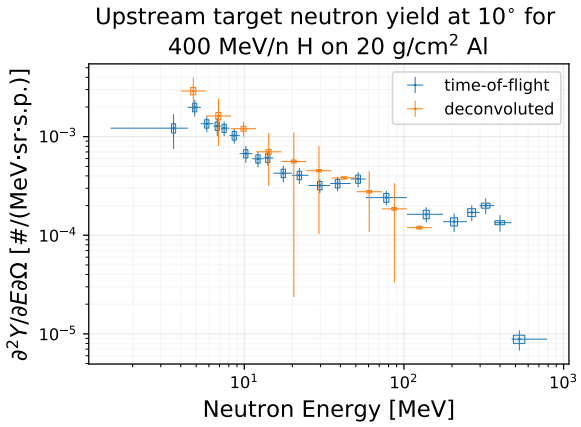


(e) 80°

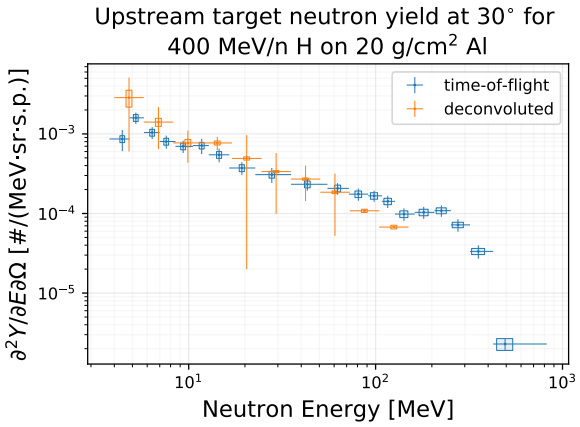


(f) 135°

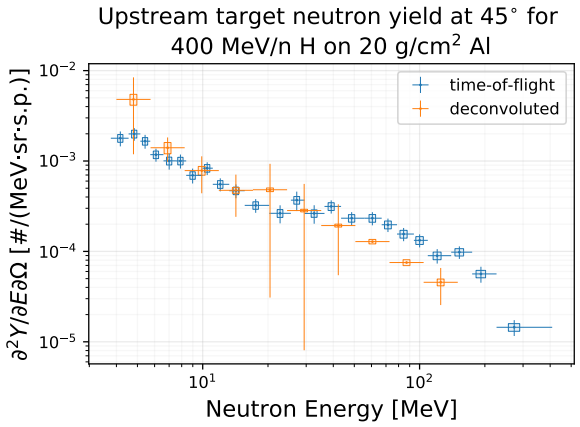
Figure 6.12: Comparison of time-of-flight and deconvolution methods for neutrons detected at all angles for 1500 MeV/n He incident on the 60 g/cm^2 Al upstream target



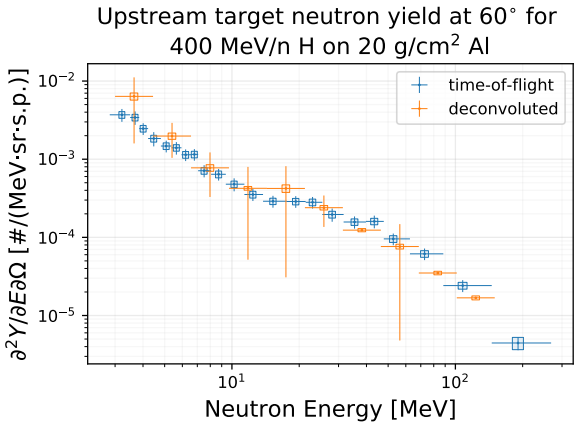
(a) 10°



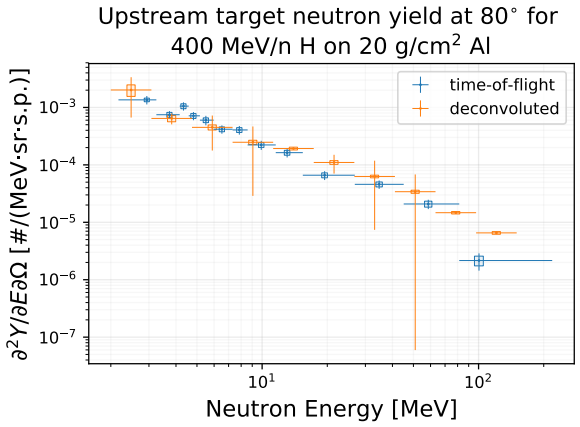
(b) 30°



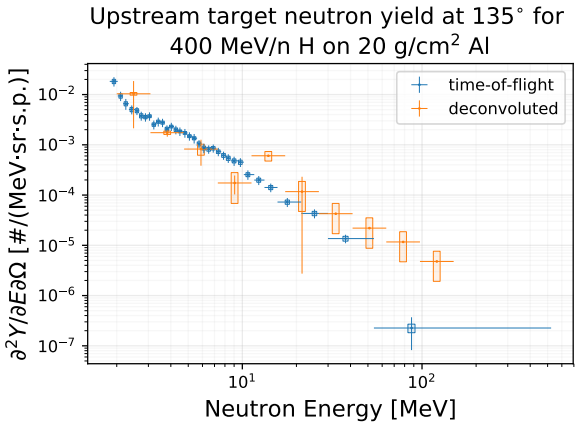
(c) 45°



(d) 60°

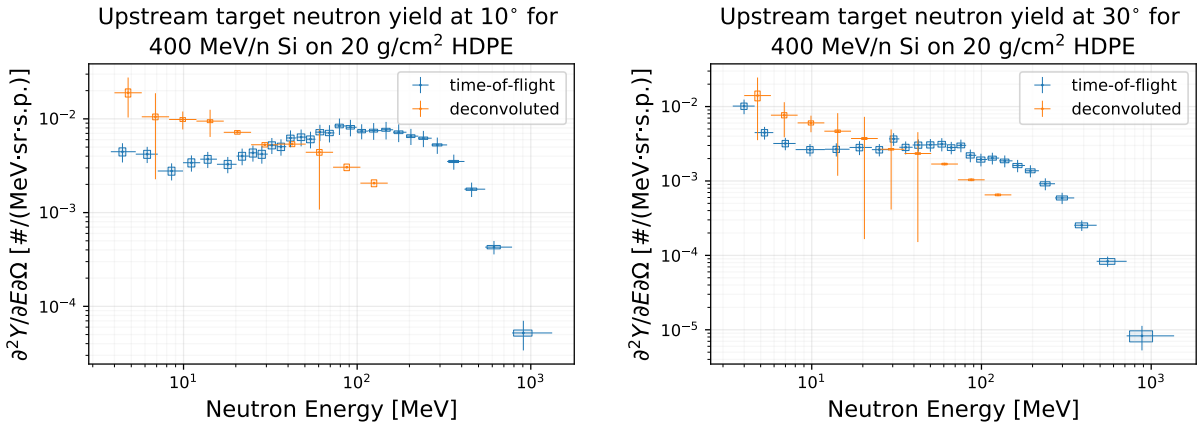


(e) 80°



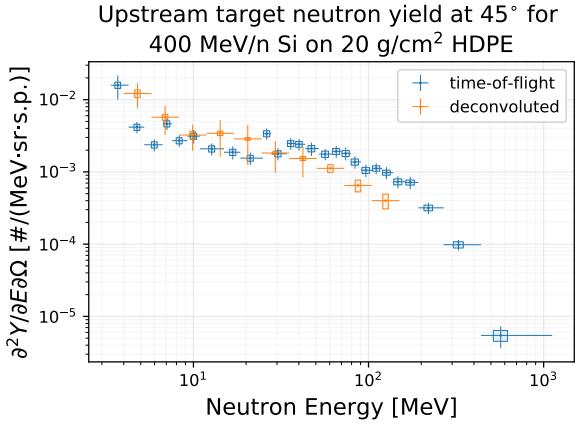
(f) 135°

Figure 6.13: Comparison of time-of-flight and deconvolution methods for neutrons detected at all angles for 400 MeV H incident on the 20 g/cm^2 Al upstream target

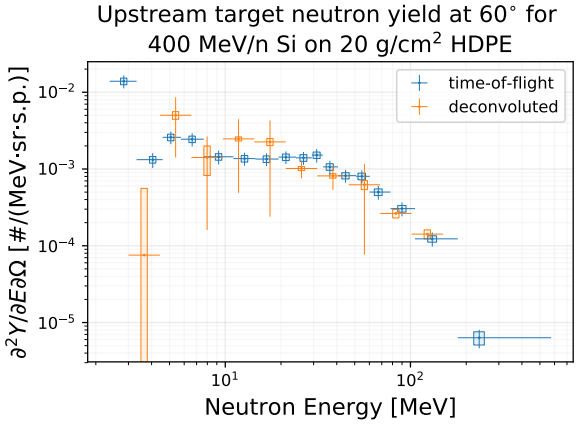


(a) 10°

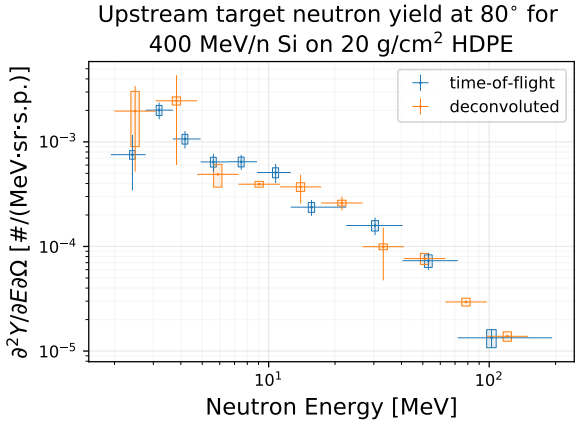
(b) 30°



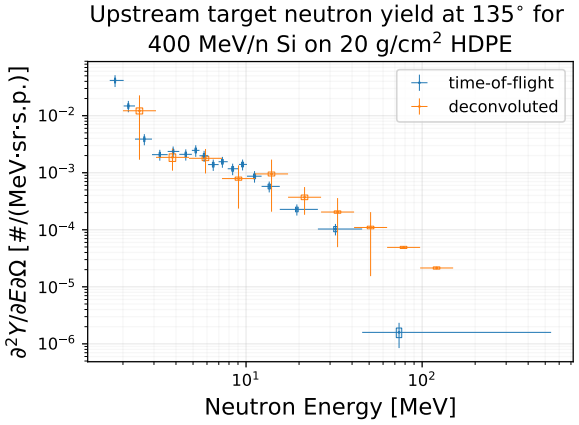
(c) 45°



(d) 60°

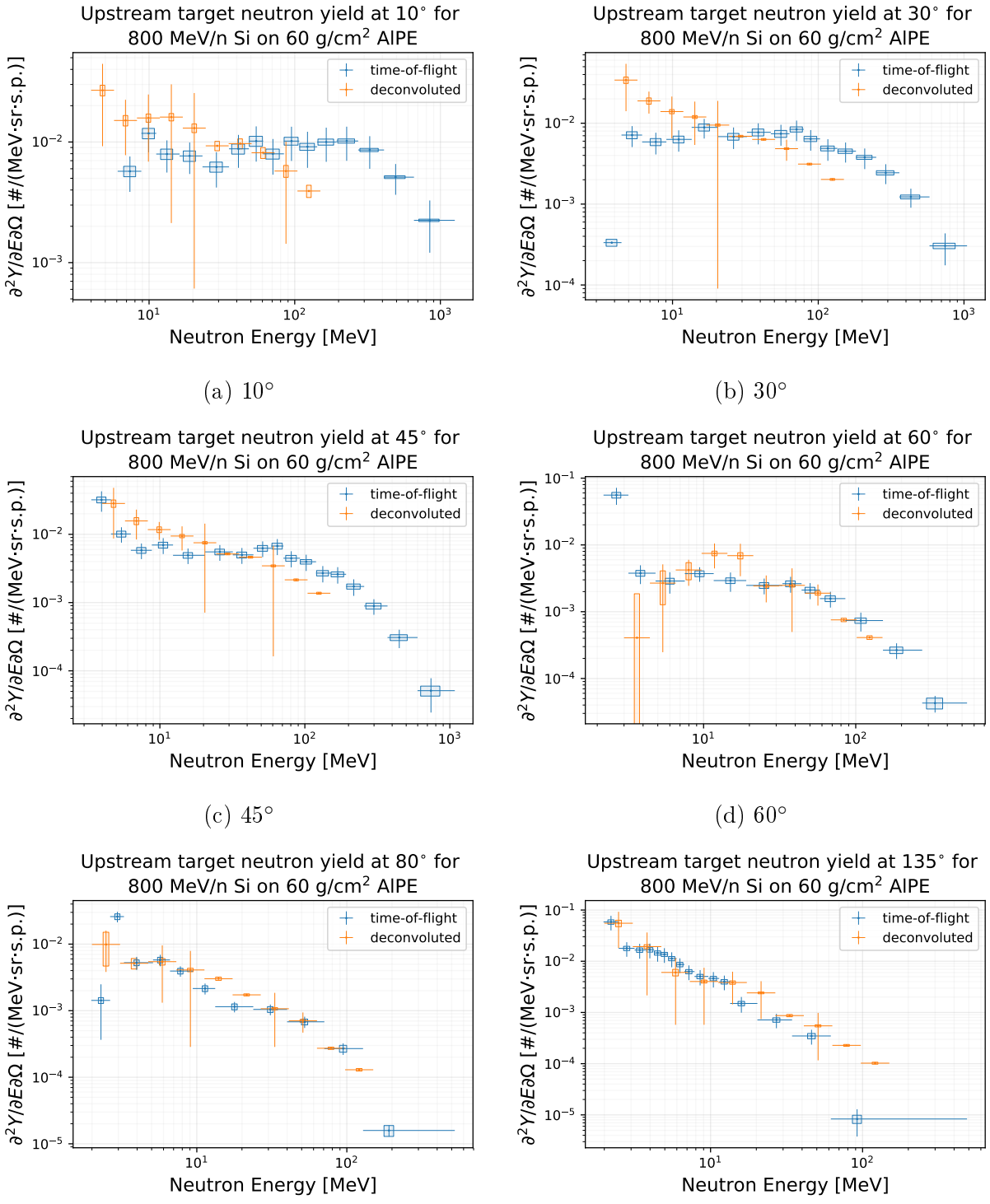


(e) 80°



(f) 135°

Figure 6.14: Comparison of time-of-flight and deconvolution methods for neutrons detected at all angles for 400 MeV/n Si incident on the 20 g/cm^2 HDPE upstream target



(a) 10°

(b) 30°

(c) 45°

(d) 60°

(e) 80°

(f) 135°

Figure 6.15: Comparison of time-of-flight and deconvolution methods for neutrons detected at all angles for 800 MeV/n Si incident on the 60 g/cm^2 AlPE upstream target

Chapter 7

Monte Carlo full-room simulations

One of the primary focuses of this work was to determine how well modern Monte Carlo transport codes predict secondary particle production from the experimental GCR-like beams interacting with the spacecraft-material-like targets. In this analysis, two transport codes are employed: MCNP6 (developed by LANL [5]) and PHITS 2.88 (developed by JAEA [6]).

The full-room MCNP geometry used was developed by Dr. Luis Castellanos for the simulations of the March 2016 experiment where his research pertained to the charged particles incident on the OLS detectors [3]. Though, due to the computational expense of modeling the full experimental setup, his simulations were set up to tally neutrons in the OLS detectors (for Dr. Natalie McGirl's work [2]) and charged particles in the NaI detectors (for Dr. Ashwin Srikrishna's work [4]) as well.

The PHITS simulations used in the works analyzing results from the March 2016 experiment were developed by another student, Hui-Chen Wang, and employed a very simplified ring geometry devoid of any room features aside from the upstream thick target. However, since the ring geometry both did not provide the finer angular resolution within each NaI array and could not produce any results for the downstream target-produced and room scattered neutrons, an equivalent full-room PHITS simulation was necessary. Hui-Chen Wang developed a full-room simulation largely based off of the MCNP model developed by Dr. Castellanos since the input geometry syntax between the two codes is quite similar, though distinct differences are present in the finer details. This dissertation work developed the neutron tallies used for the PHITS full-room simulations since the exact methodology

used for compiling the flux from everywhere except for the upstream target in MCNP did not have a direct analog in PHITS. The room geometry, which is common between the two codes, is discussed in Section 7.1, and the specific challenges associated with each transport code are presented in Sections 7.2 (MCNP) and 7.3 (PHITS). Results from these transport codes are featured alongside the experimental results discussed in Chapter 8 and are studied in greater detail specifically in Section 8.2.

7.1 Modeled room geometry

Since the input geometry used in the two codes was (intentionally) almost identical, it will be discussed here independent of the specifics of each code. For particles with flight paths directly from the upstream target, the upstream target and detectors are the only necessary components of the room geometry. However, to correctly emulate the neutrons produced in the downstream target and scattered throughout the room, which cannot be distinguished from each other experimentally, the whole room containing the experiment must be modeled.

Inclusion of additional room features comes at the cost of increased computational resources necessary to complete each simulation, so it is important to only include the most impactful room features. In this work, all detectors, their casings, their front veto detectors, and the top platform portion of their stands were modeled. In addition to the upstream and downstream targets, the steel rails along the beamline, the beam dump, and the concrete walls were also modeled. Figure 7.1 shows a 3D rendering of this geometry made using the `[T-3Dshow]` tally in PHITS in an example system using the 20 g/cm^2 aluminum upstream target.

As an additional perspective, Figure 7.2 shows a top-down-like view of the room—a horizontal slice at the height of the detectors—for the 60 g/cm^2 AlPE configuration generated with MCNP's included interactive plotter (and recolored in post). This image nicely illustrates the thickness of the concrete walls in dark gray (and the beam dump in brown) that were simulated, making these full room simulations much more computationally taxing than ring geometry simulations devoid of any room features.

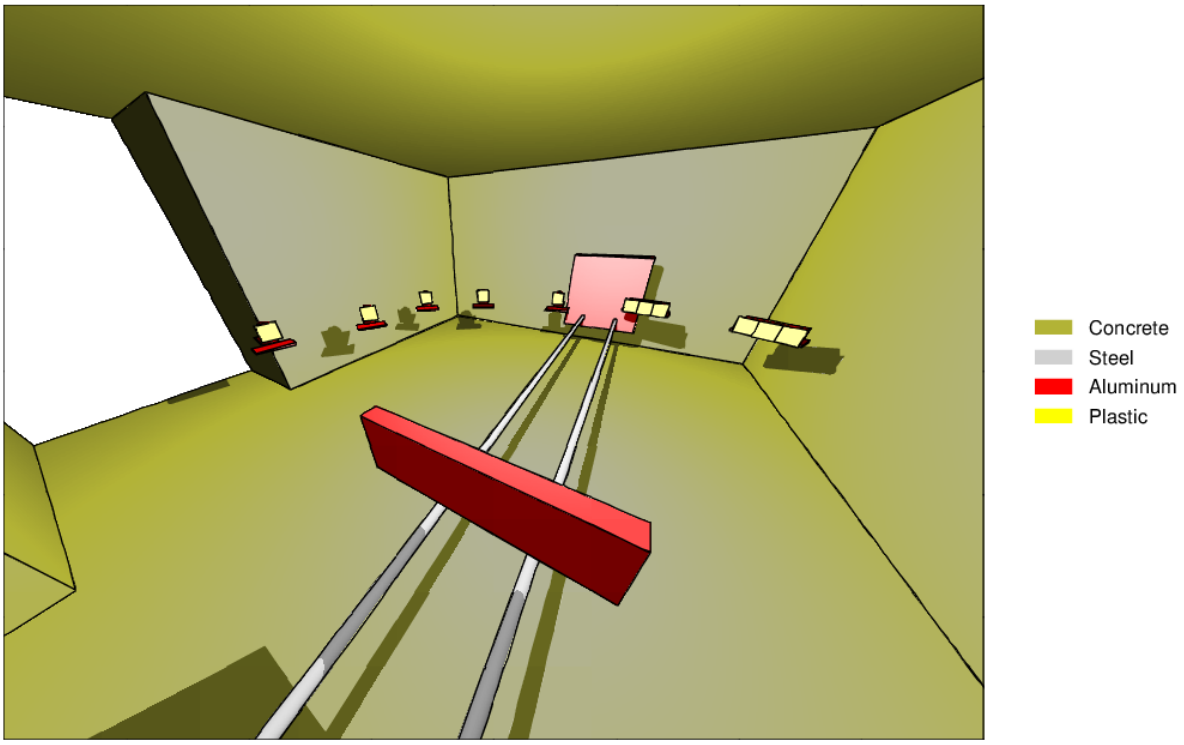


Figure 7.1: 3D render of the modeled geometry using the `[T-3Dshow]` tally in PHITS

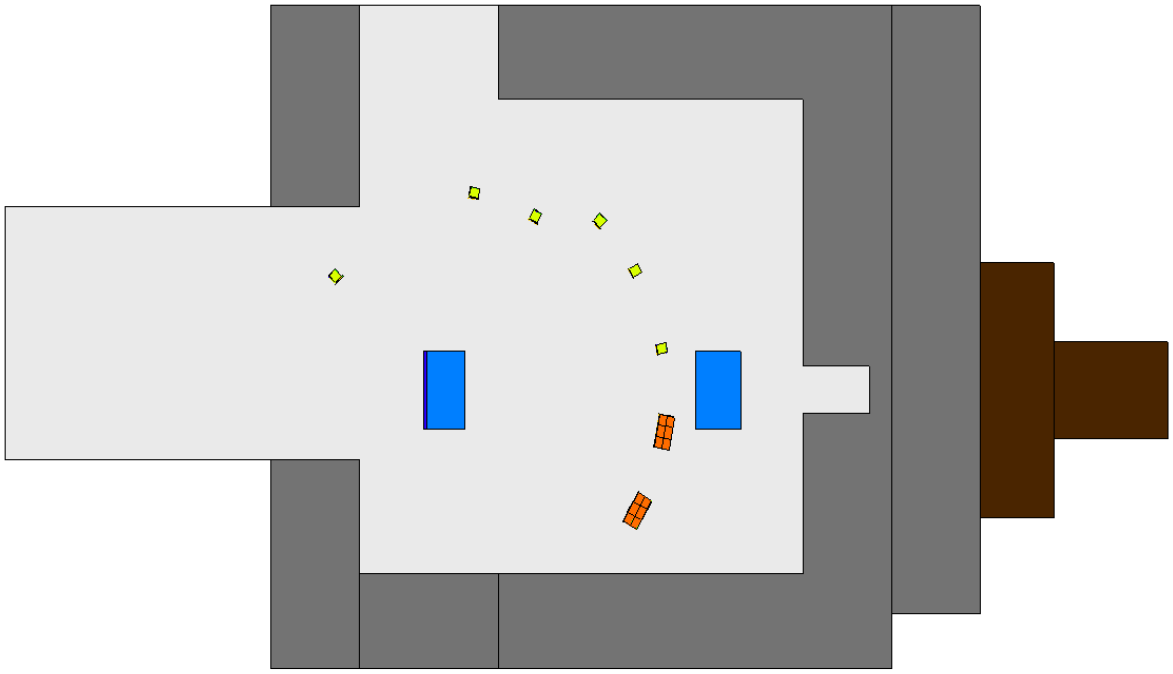


Figure 7.2: Horizontal slice of room geometry at detector height in 60 g/cm^2 AlPE configuration

One may note that this geometry excludes a critical feature of the experiment's design: shadow bars. While in an ideal world with infinite computational resources and/or time one could perfectly model every aspect of the experiment, this is not the case here. Each simulation already requires on the order of CPU days to CPU weeks (or even CPU months for the most expensive simulations), and quadrupling the number of simulations required was an unacceptable cost. Fortunately, since these are computer transport codes, data can be collected and binned in ways not possible in an experimental setting. Using different methodologies within each transport code, every particle striking each detector was collected along with information on its energy, time, position, direction, and species. In a way, this is similar to how the data is collected experimentally (on an event by event basis), though an experimentalist could only dream of an acquisition output so convenient.

Since positional and directional information is known for each neutron striking each detector, an approximate shadow bar correction can be applied in post-processing. For each particle striking a detector's front face, the angle between the particle's trajectory and the normal vector of the detector face, $\theta_{\perp}$, can be calculated since the position and orientation of each detector is known. Then, a value k can be calculated by taking the cosine of this angle as shown in Equation 7.1. This k is the same value used in a Monte Carlo code's surface flux tally which tallies the number of particle crossings over the surface divided by its surface area and k.

$$k = \cos\theta_{\perp} \tag{7.1}$$

This k can be used to discriminate particles which would had been obscured by the shadow bar or not. In this work, particles with $k > 0.97$ were taken to be those which the shadow bars would had blocked, and thus are what constituted the upstream target flux. The downstream target and room scattered flux is composed of all other particles striking the detectors. How these values are specifically calculated varies in each code and will be discussed in their respective following sections; though, the fundamental approach taken between the two is the same.

7.2 MCNP simulations

Aside from the experimental systems of the March 2016 experiment which were modeled by Dr. Luis Castellanos, I generated, ran, and processed all other MCNP simulations. It should be noted that the simulations conducted by Dr. Luis Castellanos used MCNPX while those performed in this work used MCNP6. However, since both codes were configured to use the same physics models for these simulations, the results between the two versions of MCNP are comparable.

The generation of the MCNP input decks was automated using a Python script since the primary differences between each system were the target material and thickness, the source ion of the beam, and the approximate number of simulated histories required to produce sufficient statistics in each detector. Since an iron beam generates many more secondary particles than a hydrogen beam, it requires fewer histories simulated to result in the same number of neutrons tallied in a given detector. This is a fortunate outcome since the heavier beams are more computationally taxing to simulate.

The MCNP6 input files were ran primarily on the "NE cluster" owned by the Department of Nuclear Engineering at The University of Tennessee Knoxville (https://necluster.ne.utk.edu/) as well as on my local work desktop computer. In total, over 20 CPU years were required to complete the MCNP6 simulations of the November 2016 and 2017 experiments. Though, if done again, this could likely be reduced to slightly under 10 CPU years (if using the same hardware) by raising minimum particle transport energies to higher cutoff values. Additionally, it should be noted that the reason that these simulations were performed in MCNP6 rather than MCNPX is due to MCNPX functionality and support disappearing with an operating system update to the NE cluster which occurred after the simulations of Dr. Castellanos were completed but prior to those of this work being conducted.

7.2.1 MCNP tally methodology

Unlike PHITS, MCNP does not have a very convenient methodology for tallying particles on an event by event basis when using physics models. (The PTRAC functionality within MCNP6 is only compatible with calculations reliant on cross section data lookup tables, not

those utilizing physics models.) However, there is a somewhat roundabout way in which this can be accomplished. The "Surface Source Write" or SSW card was designed to collect data on particles crossing a surface on an event by event basis when running MCNP calculations in its dedicated fission mode. The binary output of this card was intended to then be reread in by a following normal MCNP calculation as a source term. However, the SSW card can work in any calculation, including those utilizing physics models, and the event by event information is present in the binary file and can be extracted as if it were a tally.

MCNP tally results extraction

Extracting this binary data can be challenging. While third-party scripts for direct parsing of the SSW binary files and reprinting to ASCII text files are available for MCNPX, the same is not true for those of MCNP6 which use different formating. Fortunately, the Monte Carlo Particle Lists (MCPL) code package provides a solution to this issue [40]. First, the MCPL code is used to convert a binary SSW file to the binary `.mcpl` format developed in Reference 40. Since the MCPL format is very well documented, a Python script was then written to perform the calculation of k for each particle using its momentum/direction vector (u, v, w) and normal vector of the detector's face (identified using the surface number recorded by the SSW tally). This script also then generated text files formated in the same way as those generated by the "mc-tools" library (`https://github.com/kbat/mc-tools`) which was used for processing SSW files from MCNPX into text files in the work of Dr. Castellanos. This allowed the remainder of the output extraction and analyzation to utilize the same tools used and developed by Dr. Castellanos.

These text files are first converted to ROOT files using a C script. Then, a ROOT macro was used to filter out each secondary particle in each detector meeting the previously discussed $k > 0.97$ criterion. This process effectively functioned as a manual surface flux tally (though without the area normalization) since the code summed all desired events, multiplying by particle weight and dividing by k, and binned them into 360 predefined energy bins. These results were then written to text files which could be imported and processed by another code. The normalization to number of simulated source particles was performed later once imported into Python.

While additional ROOT macros could had been written to extract neutrons not meeting this $k > 0.97$ criterion (and is very similar to what is done with the PHITS results), this ignores one flaw of the SSW methodology: Only particles which crossed the front face of the detector were tallied. This ignores all particles which enter through the back or side of the detector but never cross the front face. Due to how the SSW card tallies particles, adjusting the present SSW card to tally all particles crossing the detector cylinder is not an elegant solution either; doing so would require using the position coordinates and direction vector of each particle crossing the surface to determine if it were leaving or entering the detector such that only those entering could be counted. While this could be done, another objective here was to find a solution which did not require rerunning of the March 2016 MCNPX simulations to extract back target and room scattered neutron data.

Fortunately, the volumetric cell flux, which included neutrons incident from every direction, had been tallied in each detector cell as well. Thus, given a neutron flux from only the upstream target derived from the SSW methodology and a neutron flux for neutrons from all directions, a background subtraction similar to that performed experimentally could be conducted. However, while the SSW results were not normalized to area, the cell flux tally results were normalized to area, resulting in a units conflict which must be resolved prior to any background subtraction. In Monte Carlo transport codes, a volumetric flux is calculated as the track length within a cell divided by the volume of the cell, resulting in units of $\#/cm^2$. However, the quantity being measured in this experiment is neutron yield, not neutron flux. The units for yield exclude this areal dependence; thus, the units of the flux tallied in MCNP must be converted to units of yield for comparison with experimentally collected data.

MCNP tally background subtraction and area normalization

The two known quantities are a yield-like quantity for neutrons from the upstream target (from the SSW methodology) and a volumetric flux of neutrons from all directions. These two must be made equivalent prior to a background subtraction. While one could choose to convert the yield to a flux or the flux to a yield, the strongest argument can be made for converting the simulated upstream target yield to a flux, performing the background

subtraction, and then converting the resulting flux to a yield. This is due to how the area normalization is determined.

For the upstream target neutrons, this is quite simple. Since the average track of front target neutrons is close to perpendicular to the faces of each detector, which is a cylinder, the track length (l) divided by the volume of the cylinder ($\pi r^2 l$) is just the inverse of the area of the detector face ($(\pi r^2)^{-1}$). So, the simulated upstream target flux values are found by dividing the tallied yield-like value by the area of the detector face. This does assume that the average track length can be represented as just the average chord length (the length of the detector here). This assumption could be further refined to include neutron scattering within the detector, but the improvement in the accuracy of this value gained by factoring this in is not worth the amount of effort it would take implement it into the calculation. One could also make the argument that, if including scattering in the track length calculation, the increased track length by neutrons being further scattered inside the detector is counterbalanced by the decreased track length of neutrons being prematurely scattered outside of the detector.

Once the upstream target flux is obtained, it can be subtracted from the tallied flux for all neutrons, leaving just the downstream target and room scattered neutron flux. Now, this value must be converted back to units of yield. This problem of undoing the area normalization is considerably more complicated for the back target and room scattered neutrons. The core simplifying assumption that all neutrons are incident perpendicular to the detector face is no longer valid; these neutrons can come from any and all directions. Note that, however, assuming that neutrons are equally incident from every direction is still more simple than assuming some degree of isotropy with an additional large component from a single direction. Making this more simple assumption more valid is the reasoning behind the choice made in first converting the upstream target yields to fluxes, performing the background subtraction using the particle fluxes, and then undoing the area normalization rather than the alternative of converting the tallied flux for all neutrons to a yield prior to performing the background subtraction.

Fortunately though, this is a problem which has already been considered by the reactor physics community. The average chord length through any three-dimensional convex body

for an isotropically distributed source is described by Equation 7.2 where R_{avg} is the average chord length, V is the cell volume, and $A_{\text{projected,avg}}$ is the average projected area [41].

$$R_{\text{avg}} = \frac{V}{A_{\text{projected,avg}}} \tag{7.2}$$

In some past works, the average chord length of a convex body would be calculated with $R_{avg} = 4V/S$ where S is the surface area of the three-dimensional body, but Kruijf demonstrates in his paper that this is not a universally applicable approach and only works for shapes with specific symmetries [41].

The projected area is defined as the area of a three-dimensional object when projected onto a two-dimensional plane. The projected area of a cylinder with radius r and length l as viewed along its axis is πr^2 while if viewed from an angle parallel to the faces is $2rl$. The liquid scintillators in this experiment have dimensions of $r = 2.5$ in (6.35 cm) and $l = 5$ in (12.7 cm); thus, the apparent area as viewed from the side is $4r^2$. This is further complicated if viewing angles in between these two extremes are considered. Fortunately, this problem can be collapsed in the azimuthal direction θ due to the cylinder's rotational symmetry in that direction. Rotating the cylinder in the zenith direction between the two extremes of $\phi = 0°$ and $\phi = 90°$ while holding θ constant will fairly sample all possible projected areas of the cylinder; this is equivalent to just moving the observation angle of the cylinder from $\phi = 0°$ to $\phi = 90°$ while keeping the fixed θ. This coordinate system is displayed on Figure 7.3.

At any zenith angle, the projected area is composed of two portions: (1) a contribution from the curved side and (2) a contribution from the single exposed circular face of the cylinder. In reality, this takes the form of (1) a rectangle with an elliptical pit on the end of the exposed circular face and an equal elliptical protrusion on the other end and (2) an ellipse at the end of the exposed circular face. The total area is the sum of these two shapes which is equivalent to the sum of the areas of the full rectangle and the ellipse. The width of the rectangle is a constant $w = 2r$ and the major radius of the ellipse is constantly $r_1 = r$. The height h of the rectangle and the minor radius r_2 of the ellipse will change with rotating zenith angle.

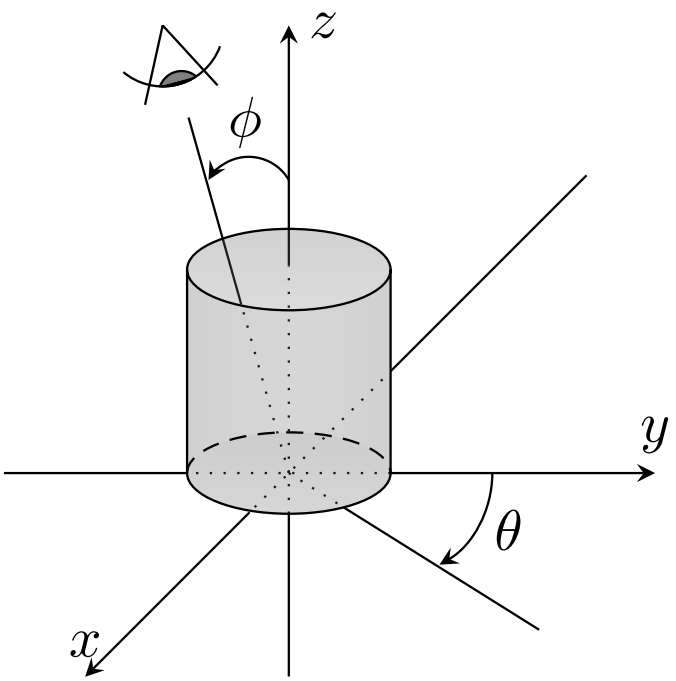


Figure 7.3: Pictured is the described coordinate system for the cylinder with an eye symbol denoting the viewing perspective used for two-dimensional areal projections.

For the sake of this analysis, the $\phi = 0° = 0$ orientation is taken to be the one looking at the cylinder's circular face directly, and the $\phi = 90° = \pi/2$ orientation is taken to be the one looking at the cylinder from the side, seeing only the rectangle. The eye symbol in Figure 7.3 illustrates this. The variable rectangle height is $h = l\sin(\phi)$, and the variable ellipse minor radius is $r_2 = r\cos(\phi)$. The total projected area at any given zenith angle ϕ can be calculated as shown in Equation 7.3.

$$\begin{aligned} A_{\text{projected}} &= wh + \pi r_1 r_2 \\ &= (2r)\,(l\sin(\phi)) + \pi(r)\,(r\cos(\phi)) \\ &= 2rl\sin(\phi) + \pi r^2\cos(\phi) \end{aligned} \tag{7.3}$$

The average value of the projected area can be found by using the calculus approach of evaluating a function's average value over discrete bounds and is calculated in Equation 7.4 for the OLS detectors of this work.

$$
\begin{aligned}
A_{\text{projected,avg}} &= \frac{1}{\pi/2 - 0} \int_0^{\pi/2} 2rl\sin(\phi) + \pi r^2 \cos(\phi) d\phi \\
&= \frac{2}{\pi}\Big[-2rl\cos(\phi) + \pi r^2 \sin(\phi) \Big]_{\phi=0}^{\phi=\frac{\pi}{2}} \\
&= \frac{2}{\pi}\left(\pi r^2 + 2rl\right) \\
&= 2r^2 + \frac{4rl}{\pi} \\
&= 2(6.35\text{ cm})^2 + \frac{4(6.35\text{ cm})(12.7\text{ cm})}{\pi} \\
&= 183.325\text{ cm}^2
\end{aligned}
\tag{7.4}
$$

Now that the value of the projected area has been calculated, it can be used to convert the MCNP units of flux to units of yield. The flux values need to be multiplied by the volume of the cell divided by the average track length; this simplifies to multiplying by just the projected area as shown in Equation 7.5.

$$
\frac{V}{l_{\text{track,avg}}} = \frac{V}{R_{\text{avg}}} = V \Big/ \left(\frac{V}{A_{\text{projected,avg}}} \right) = A_{\text{projected,avg}} \tag{7.5}
$$

Unsurprisingly, this area is greater than that of just the full rectangular view (161.29 cm^2) and the full circular view (126.68 cm^2). It is worthwhile to note that this exercise validates Kruijf's argument against use of $R_{avg} = 4V/S$ for chord length which would evaluate to $V/l_{\text{track,avg}} = 190.015$ cm^2, though it does reasonably approximate the actual result [41]. It is interesting to note the different possible values for $l_{\text{track,avg}}$ and $V/l_{\text{track,avg}}$ depending on what assumptions could be made here; these are highlighted below in Table 7.1.

Table 7.1: Possible track lengths and flux-to-yield conversion values

Projection method	Average track length $l_{\text{track,avg}}$ (cm)	Volume / average track length $V/l_{\text{track,avg}}$ (cm^2)
Circular face view	12.7	126.68
Rectangular side view	9.97	161.29
$4V/S$ approximation	8.47	190.02
Actual projected area	8.78	183.33

In reality, the integral shown in Equation 7.4 could be modified for each detector with some weighting function to favor viewing angles (neutron trajectories) coming directly from the back target, but this function would realistically be too difficult to characterize. Additionally, the same logic used earlier with the front target neutrons concerning factoring in neutron scattering within the detector in the track length calculations can be applied here, meaning it is not worth implementing for back target and room scattered neutrons either.

7.2.2 MCNP results rebinning and remaining normalizations

After performing the background subtraction, two quantities have been obtained: upstream target neutron yield and downstream target plus room-scattered neutron yield, both in units of $\#/s.p.$. Prior to the remaining normalizations, these values must be rebinned since they are still in the 360 fine energy bins described earlier. Each MCNP neutron spectrum was rebinned to match the energy bins of the experimentally obtained results using the rebinning methodology discussed in Section 4.11.1 where bin edges were not necessarily preserved. Since one can reasonably assume that the results would not appear much different with finer binning and longer simulation times, use of this methodology is fair.

Once rebinned to match the experimental data, the upstream target results are normalized to the same projectile, target, and neutron energy dependent solid angles. Both sets of data are also normalized to energy bin width. This results in equivalent simulated values for comparison with the time-of-flight-derived neutrons from the upstream target and the deconvolution-derived neutrons from elsewhere.

7.3 PHITS simulations

As was mentioned earlier, the PHITS input decks used in this work were largely assembled by Hui-Chen Wang, though I developed the neutron tallies and corresponding post-processing methodologies. The full-room PHITS simulations were carried out by Dr. Tony Slaba on a computing cluster at the NASA Langley Research Center.

One of the core complications of the MCNP analysis was undoing the area normalization of the tallied flux; this issue stemmed from limitations of the SSW card and the desire to not repeat already completed calculations. However, neither of these issues were present with the PHITS simulations. Since no full-room PHITS simulations had been conducted prior to this work, tallies could be set up in a way which circumvented this need to convert to and/or from fluxes and instead avoids any area normalization altogether. This is also enabled by the fact that PHITS, unlike MCNP, has an easy to use "dump" flag that can be enabled for any tally which causes all of the information about any particle (species, energy, time, position, momentum, etc.) which is tallied to also be written to a dump file. This allowed for the construction of a simulation tally much more directly analogous to the experiment where particles were simply counted with no area normalizations involved. Two tallies were constructed: one which counted all neutrons entering the detector and another which counted only neutrons entering from the front face of the detector.

The lengthy dump files created by these tallies could then be parsed by a Python script and reprinted into text files of the same format used in the MCNP analysis. These could then be converted to ROOT files in the same fashion as was done for the MCNP results. The difference in the ROOT macros utilized for the PHITS analysis is that no division by k was ever performed; neutrons were simply counted in the same fashion as was done in the experiment. The final output files from these ROOT macros parsing PHITS data were files for (1) neutrons which entered the detector through the front face and had $k > 0.97$ and (2) neutrons which entered the detector from any direction. Once imported to Python, the background subtraction to obtain the downstream target and room-scattered neutrons was as simple as subtracting the upstream target neutron counts from the total neutron counts.

After isolating the upstream target neutrons and downstream target neutrons, the remaining analysis of the PHITS data is identical to what was done to the MCNP data. Each spectrum underwent rebinning using the methods discussed in Section 4.11.1 to match the experimentally determined energy bins, and the solid angle and energy bin width normalizations were handled in the same way as well, resulting in PHITS neutron spectra ready for comparison to the experimental results.

Chapter 8

Results and trends

After the analysis and rebinning, what remains are finalized neutron yield spectra as a function of energy. This chapter seeks to first take a look at the yield spectra from both neutron sources considered in this work and note some general trends by studying some sample spectra in Section 8.1. After noting general spectral trends, a more comprehensive analysis on the performance of the Monte Carlo codes against the experimental results is explored in Section 8.2. Following that, Section 8.3 attempts to condense various experimental axes through effective dose calculations and make observations on the effects of shielding (upstream target) choice on astronaut neutron effective dose.

8.1 Yield spectra

Each energy bin contains several pieces of information. Figure 8.1 shows a visual explanation of what is plotted for each energy bin in the final plots containing yield spectra. The point itself is plotted at an x-coordinate of E_{avg}, a weighted average (by y-value) of the energy midpoints of each final bin's constituent original bins, and a y-coordinate of each bin's normalized yield. A shaded box is drawn around the point showing the energy resolution uncertainty in x and the statistical uncertainty in y. While the "true" value could be located anywhere within this box, the probability is normally distributed with the most probable location being the spot marked with the point. Additionally, the systematic uncertainty in yield is shown as a vertical bar, and the total bin's width is denoted by a horizontal

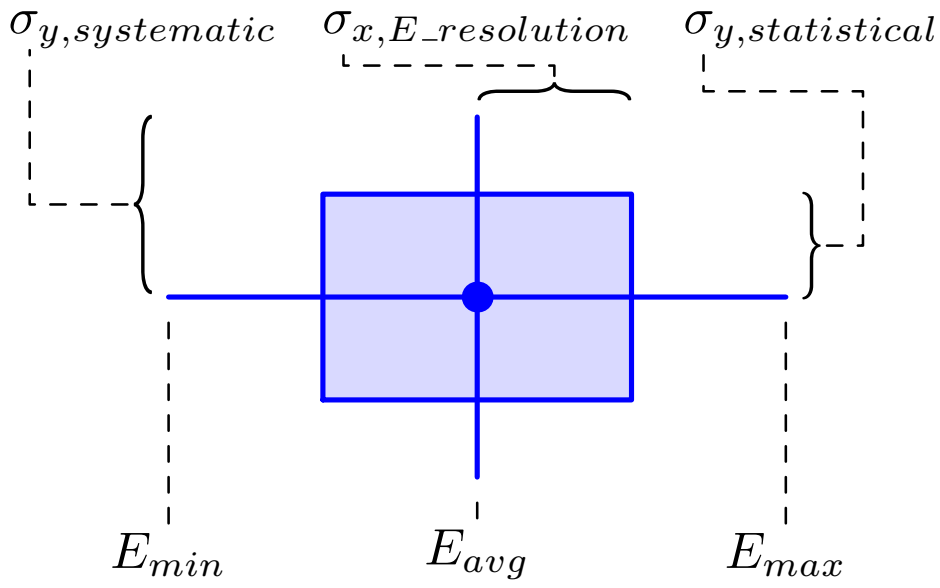


Figure 8.1: Explanation of each plotted energy bin

bar. It should be noted that for the deconvoluted results the shaded boxes are drawn with an arbitrary width (since there is no energy uncertainty in that dataset) to allow for the statistical and systematic uncertainties to be differentiated, and the energy midpoints are simply the bin midpoints in $\log E$ space.

While the context and units of yield should make it evident whether the data shown in each plot are from the upstream or downstream target results, the plots also contain the "ToF ^{1}n" label for the upstream target neutrons characterized with time-of-flight methodologies or the "DC ^{1}n" label for the downstream target and room scattered neutrons characterized with the deconvolution methodology. Additionally, where included, MCNP results are represented with dashed lines while PHITS results are represented with dotted lines [5, 6, 42].

8.1.1 Double-differential upstream target neutron yields

A discussion on the general trends in the data while highlighting some known physical phenomena will be presented in this section. Note that due to the high number of possible plots which could be used to illustrate a given idea, the plots presented here are typically those which illustrate a trend with the most clarity; this is usually determined by those with the best statistics. Additionally, in places where experimental datasets are being compared to one another, Monte Carlo results are sometimes omitted if they cause visual clutter due

to disagreement with the data. All double-differential upstream target neutron yield spectra from this work are plotted individually alongside their MCNP and PHITS simulated versions in Appendix C.1. Note that spectra produced in the work of Reference 2 from the March 2016 experiment are excluded here when comparing individual spectra to one another. However, these results are incorporated into the comparisons of Monte Carlo codes in Section 8.2 and the effective dose analyses of Section 8.3.

The most logical place to begin comparison is by observing the trends in the magnitude of the neutron yields from the various projectile species, holding all else equal. Figure 8.2 shows this for 400 MeV/n projectiles incident on the 20 g/cm^2 hybrid AlPE upstream target in the 10° neutron detector.

As one would expect, when normalized to incident source particle, the source ions with the most nucleons result in the highest neutron yields. This is, at most, a two-order of magnitude difference between iron and hydrogen projectiles. The difference in magnitude due to source ion is most severe with the thinnest targets and becomes less extreme with the thicker targets as the heavier projectiles and their secondaries begin to have more difficulty penetrating the upstream target, as shown in Figure 8.3. This is true for the pure aluminum and polyethylene targets too.

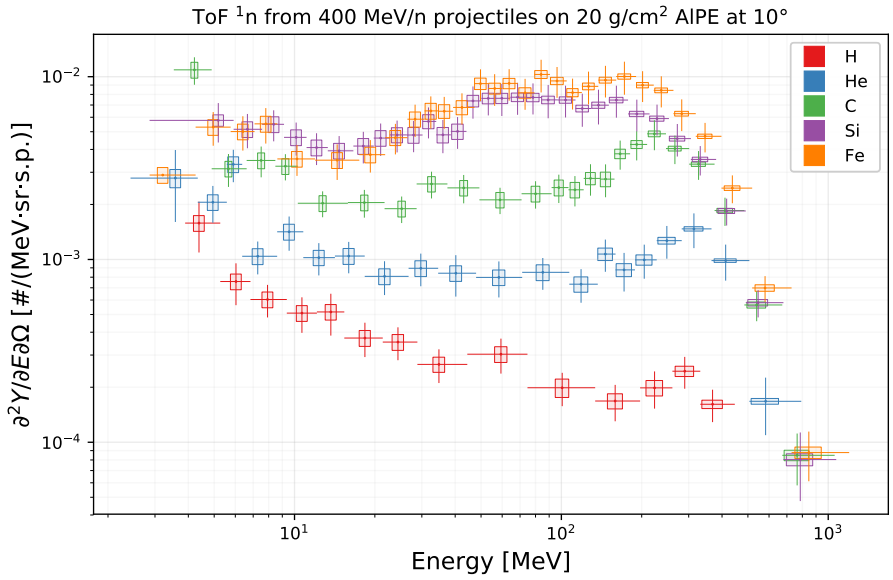


Figure 8.2: Neutrons detected at 10° from all 400 MeV/n projectile species incident on the 20 g/cm^2 AlPE upstream target

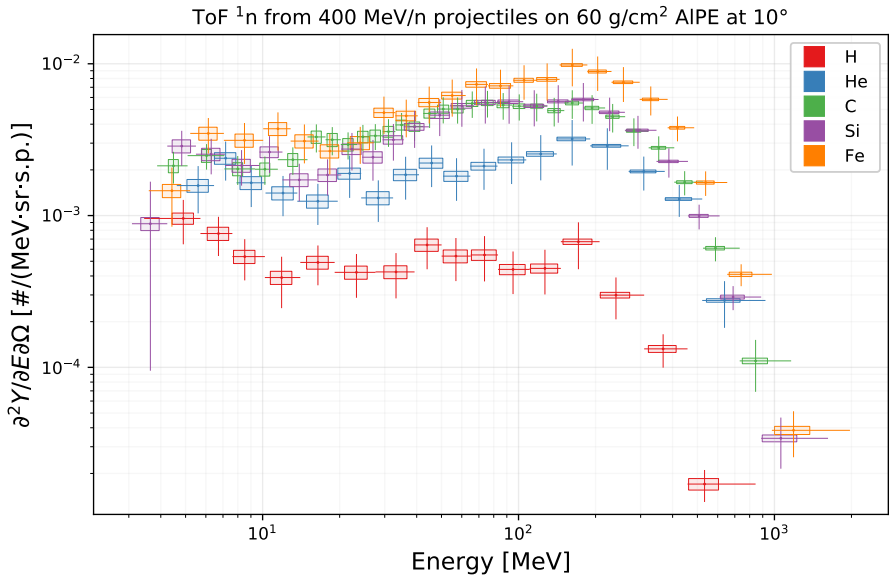


Figure 8.3: Neutrons detected at 10° from all 400 MeV/n projectile species incident on the 60 g/cm^2 AlPE upstream target

The Fermi momentum of the projectile ion nucleons can be seen in these figures. The highest energy neutrons are those which fragmented off of the projectile and retained most of their momentum. Due to the motion of the individual nucleons within the projectile nucleus, at any instant individual nucleons can possess velocity in the lab frame in excess of that of the whole projectile nucleus. When a nuclear reaction occurs and neutrons are sheared or evaporated from the projectile fragment, they retain their prior momentum, resulting in some neutrons striking the detectors at kinetic energies greater than the beam energy (per nucleon). This effect is amplified for heavier nuclei and is illustrated in these figures.

Figure 8.4 is the same as Figure 8.2 but with the Monte Carlo code results also included. This first glance at the simulated results illustrates that while in some areas the codes agree well with the data, notable discrepancies are present. Particularly, the high energy peak characteristic of projectile fragments appears to be overestimated by the Monte Carlo codes.

As was discussed earlier in Section 2.2, a nuclear collision results in multiple source terms being produced. Using the abrasion-ablation model, this is broken into three excited sources: the target fragment (relatively at rest in the lab frame), the projectile fragment (retaining a majority of its initial velocity in the lab frame), and the "fireball" or intermediate rapidity (the blob of nucleons in the overlap region of the collision with velocities about one third

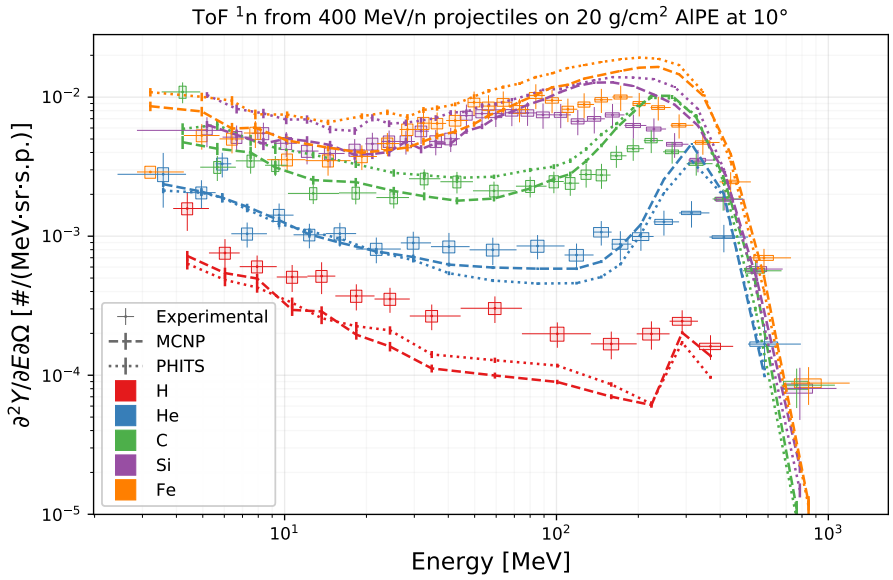


Figure 8.4: Neutrons detected at 10° from all 400 MeV/n projectile species incident on the 20 g/cm^2 AlPE upstream target alongside Monte Carlo simulated results

to one half that of the projectile fragment). The lowest energy neutrons are predominantly attributable to the evaporation of the target fragment while the highest energy neutrons are attributable to projectile fragment ablation. These projectile fragment neutrons are forward peaked in the lab frame, meaning their influence diminishes with increasing detector angle. The target fragment evaporation neutrons are emitted more isotropically in the lab frame. Neutrons from the intermediate rapidity fall in between these two extremes.

Figure 8.5 shows the yield spectra in the six detectors for 400 MeV/n Si projectiles incident on the 20 g/cm^2 HDPE upstream target. As seen in the figure, the maximum neutron energy detected falls off with increasing detector angle. However, at lower energies where target fragment evaporation is the primary source of neutrons, the relative isotropy of that process can be seen by the convergence of the yield values with decreasing neutron energy.

The 80° spectrum seems to be depressed more than one would anticipate given the pattern present among the other angles. This is a common trend, and the 80° detector was usually the most difficult to obtain reasonable statistics for. It and the 135° detector are dominated by target evaporation neutrons; however, the 80° detector has a few experimental disadvantages in comparison to the 135° detector. The 135° detector is 50 cm closer to the target center

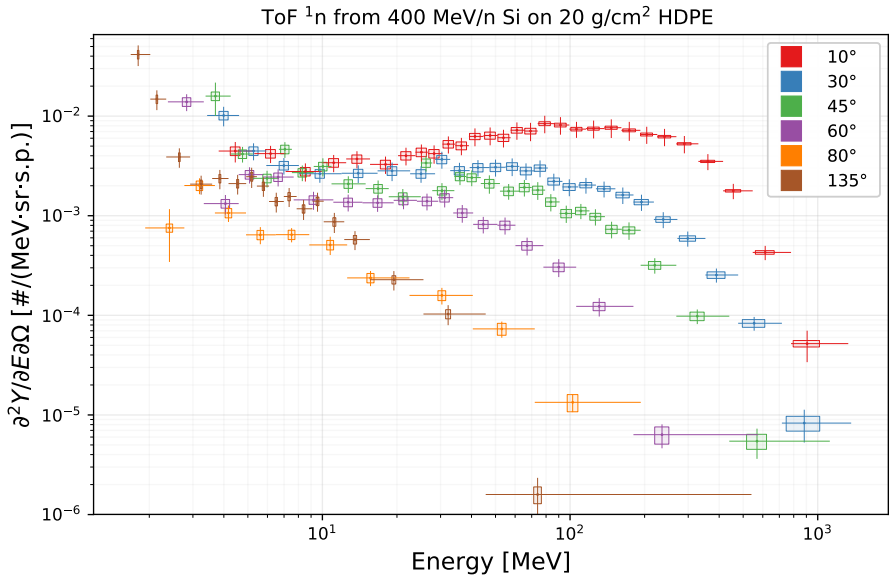


Figure 8.5: Neutrons detected at all angles from all 400 MeV/n Si incident on the 20 g/cm^2 HDPE upstream target

point than the 80° detector, providing it with more neutrons to detect. Though, since the results are normalized to solid angle, this should not be the cause for this relative depression. Instead, the 80° detector's decrease in neutron count is caused by the width of the upstream target. Recalling the to-scale overhead schematic of the experiment layout (Figure 3.5), neutrons produced with angles close to 90° relative to the beamline need to pass through significantly more target material than neutrons bound for the lower angled detectors; the distance between the beam axis and edge of the target was always 50 cm. Ultimately, this is the cause of the extra attenuation of the neutron spectra seen in the 80° detector.

This depression of the 80° curve is also quite apparent on Figure 8.6 where the same plot is presented but each detector angle is spaced apart by a factor of 10 and the Monte Carlo code results are included too. The simulated results generally agree with the experimentally observed behavior. For the lowest angled detectors, the Monte Carlo codes generally are in best agreement at energies below 100 MeV and tend to deviate at higher energies, over predicting the high-energy peak seen at lower detector angles. This would imply that the modeled target evaporation within the codes performs quite well, but the portions of the codes handling the fireball and projectile fragmentation could be refined, perhaps in their neutron angular distributions within the deexciting fragments.

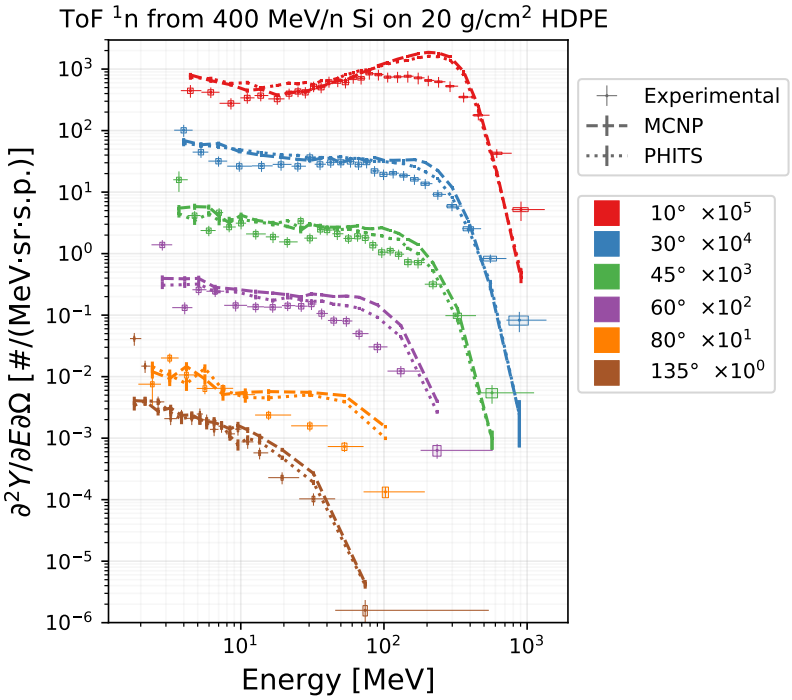


Figure 8.6: Neutrons detected at all angles (spaced apart by powers of 10) from all 400 MeV/n Si incident on the 20 g/cm^2 HDPE upstream target with Monte Carlo code results included

The severity of the overestimation is made even more evident when looking at the 10° plot on its own as shown in Figure 8.7. The Monte Carlo codes predict the peak to be over a factor of 2 (almost a factor of 3) above the experimentally collected data.

Up to this point, only results from 400 MeV/n projectiles have been presented. This is for a number of reasons. One is that the 400 MeV/n beams provided the best statistics because they were ran at the highest beam currents (as mentioned in the discussions in Section 3.3 on beam constraints and optimizations). Additionally, due to the limited flight paths possible in the experiment room at NSRL, the maximum neutron energies which can be characterized with this methodology are limited to around 1 GeV or slightly lower. As was discussed in Section 4.11.3, neutron events with flight times too close to those of the prompt photons produced in the upstream target are removed, and this is ultimately what caps the discernible neutron energies. While longer flight paths would help alleviate this, they would also reduce the solid angle of each detector and result in requiring more beam time to achieve sufficient statistics.

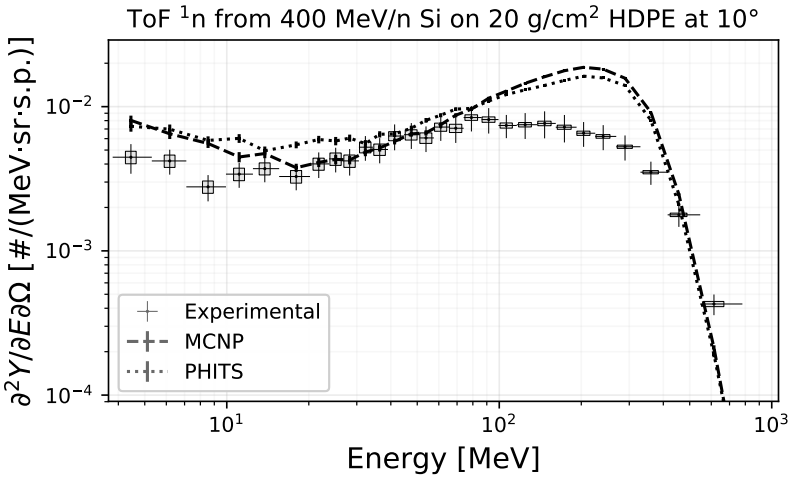
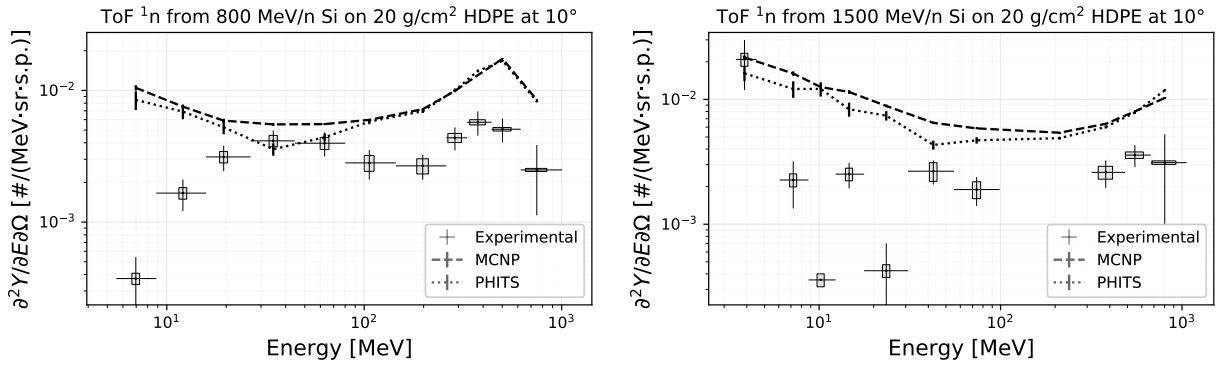


Figure 8.7: Neutrons detected at 10° from 400 MeV/n Si projectiles incident on the 20 g/cm^2 HDPE upstream target alongside Monte Carlo simulated results

Figure 8.8 shows the 10° yield spectra for silicon projectiles incident on the same 20 g/cm^2 HDPE upstream target but for the 800 MeV/n and 1500 MeV/n beam energies. In Figure 8.8a, it is evident that 800 MeV/n is at the cusp of where the forward peak can still be identified with the current experimental setup. Figure 8.8b illustrates two important limitations to this analysis. First is the absence of the forward-focused projectile fragment neutron peak. Second is a fundamental limitation of the experiment resulting in lower quality data for higher energy beams; in this case, two points appear more depressed than they should be while no points populate the region from about 100 MeV to 300 MeV. Part of this is a statistical limitation due to the operational beam currents, but the primary issue here is the neutron background subtraction.

The 10° detector is in close proximity to the downstream target and is easily overwhelmed by neutrons from it in this heavy and high energy beam case. Ultimately, this results in cases where after normalization the shadowed background counts in some bins exceed the counts collected when the detector was unshadowed, producing bins of depressed, or in the worst cases negative, yield. While this is clearly not physical, not much can be done further to resolve this issue aside from the pulse height threshold stitching methods discussed earlier in Section 4.10, an analysis procedure explicitly designed to mitigate this effect as much as possible. Fortunately, bins of negative yield only occur in a handful of cases across the whole



(a) 800 MeV/n Si

(b) 1500 MeV/n Si

Figure 8.8: Neutrons detected at 10° from 800 and 1500 MeV/n Si projectiles incident on the 20 g/cm^2 HDPE upstream target alongside Monte Carlo simulated results

experimental dataset and are primarily isolated to the 1500 MeV/n Si and 1500 MeV/n Fe projectile cases.

While this limitation seems quite severe, note that it primarily impacts data collected in the 10° detector; the 1500 MeV/n results in the detectors at higher angles usually do not suffer from these same issues as illustrated in Figure 8.9 for the same 1500 MeV/n Si beam incident on 20 g/cm^2 HDPE case but for neutrons detected at 45°.

To see the impact of projectile energy, the carbon projectiles can be studied since they generally yielded the best statistics. The yields from the thinnest and thickest aluminum upstream targets for all three carbon energies are shown in Figure 8.10.

In theory, the highest energy projectiles should produce the highest total neutron yields since secondary particles/fragments produced in a system with more energy are more likely themselves to go on to generate more secondaries/fragments. This is not necessarily evident here since the range of neutron energies this methodology can detect given the experimental flight paths is lower than the maximum energy of neutrons actually being produced, meaning these spectra (primarily those from the highest energy projectiles) are cut off prematurely. However, at the very least in Figure 8.10b, the thicker target allows for a more notable buildup of the production of lower energy neutrons as beam energy increases.

This serves as a convenient point to switch to exploring the trends present when modifying target material/thickness now that the impact of the projectile species/energy and detection angle have been discussed. As was shown for aluminum in Figure 8.10, thicker targets

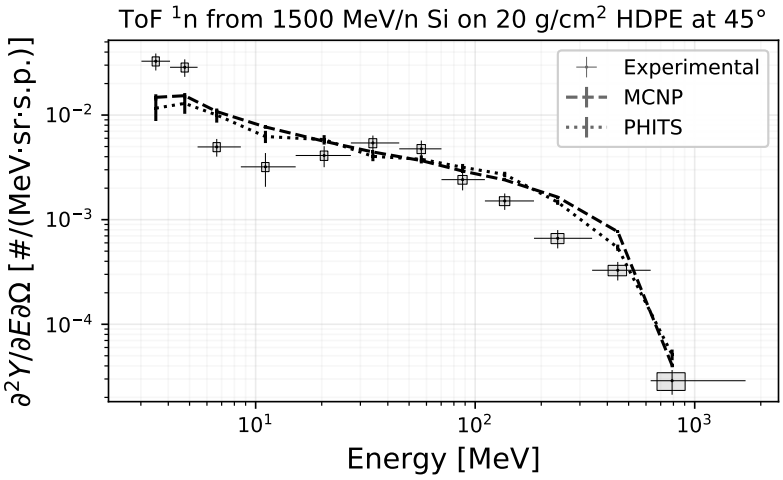
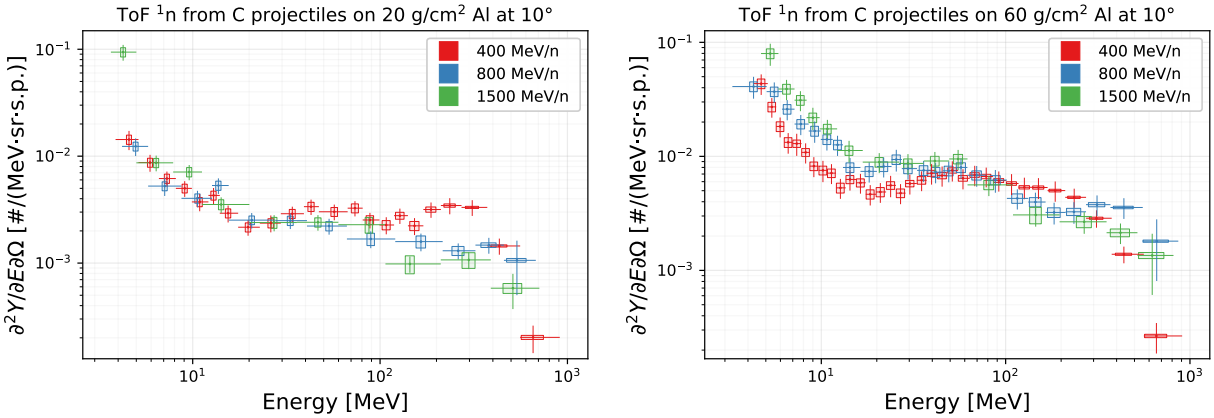


Figure 8.9: Neutrons detected at 45° from 1500 MeV/n Si projectiles incident on the 20 g/cm^2 HDPE upstream target alongside Monte Carlo simulated results



(a) 20 g/cm^2 (b) 60 g/cm^2

Figure 8.10: Neutrons detected at 10° from C projectiles incident on the 20 g/cm^2 and 60 g/cm^2 Al upstream targets

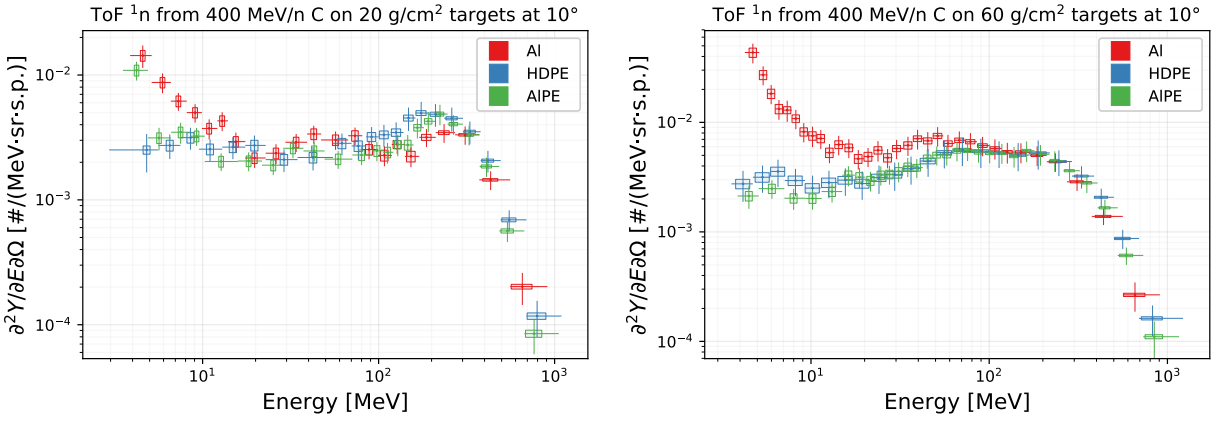
allow for more interactions and thus higher neutron yields. This effect for all three target material compositions is shown in Figure 8.11 for an example system of 400 MeV/n C projectiles. Noting the slightly different y-axis boundaries, it is clear that this trend of increased neutron yield from thicker targets holds for all three target material compositions, though the magnitude of this difference is more significant for aluminum than it is for polyethylene, particularly at lower neutron energies.

One interesting observation here is the behavior of the hybrid AlPE target. The AlPE target typically behaves more like the HDPE target than the aluminum target. This is not surprising for the 60 g/cm^2 AlPE target since the 10 g/cm^2 of Al are followed by 50 g/cm^2 of HDPE, but it is interesting for the 20 g/cm^2 target. One would intuitively expect the hybrid target to behave more like a combination of the two materials. This behavior, however, is actually a general trend across the various beams as illustrated further in Figure 8.12; though, there are also cases where the AlPE target neutron yields look more like a combination of the yields from the two pure targets as well.

For the same example system of 400 MeV/n C projectiles used earlier, Figure 8.13 shows the impact of target thickness for each material. In these figures for both target materials, the 20 g/cm^2 neutron yields are less than those for the thicker targets, but the 40 g/cm^2 and 60 g/cm^2 yields are much closer to each other. Referring to Table 3.3 which showcased where each beam ranged out (in the upstream target, downstream target, or beam dump), one will note that the 400 MeV/n C beam penetrates the 20 g/cm^2 upstream targets for both materials but is stopped in the thicker two upstream targets of each material, explaining this observed trend.

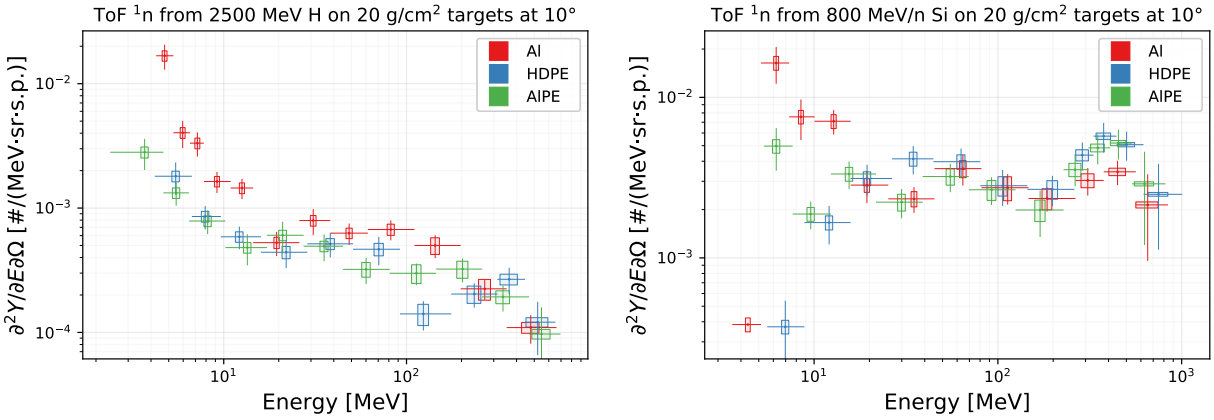
Since neutron yield is dependent on the number of nuclear reactions occurring in the upstream target, this trend is not universal. For heavier and faster 800 MeV/n Si projectiles, the 60 g/cm^2 targets indeed result in higher yields than the 40 g/cm^2 targets as shown in Figure 8.14.

Additionally, sometimes the yields are very similar or the thinnest targets actually result in higher yields due to the thicker target attenuating more secondary particles/fragments than are being produced by the additional material as shown in Figure 8.15.



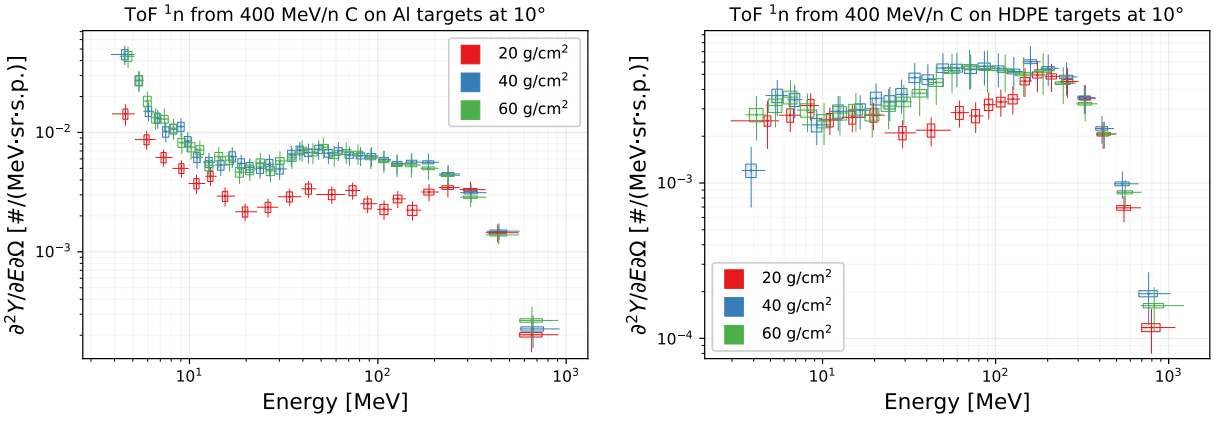
(a) 20 g/cm^2 (b) 60 g/cm^2

Figure 8.11: Neutrons detected at 10° from 400 MeV/n C projectiles incident on the three materials of each upstream target for the 20 g/cm^2 and 60 g/cm^2 thicknesses



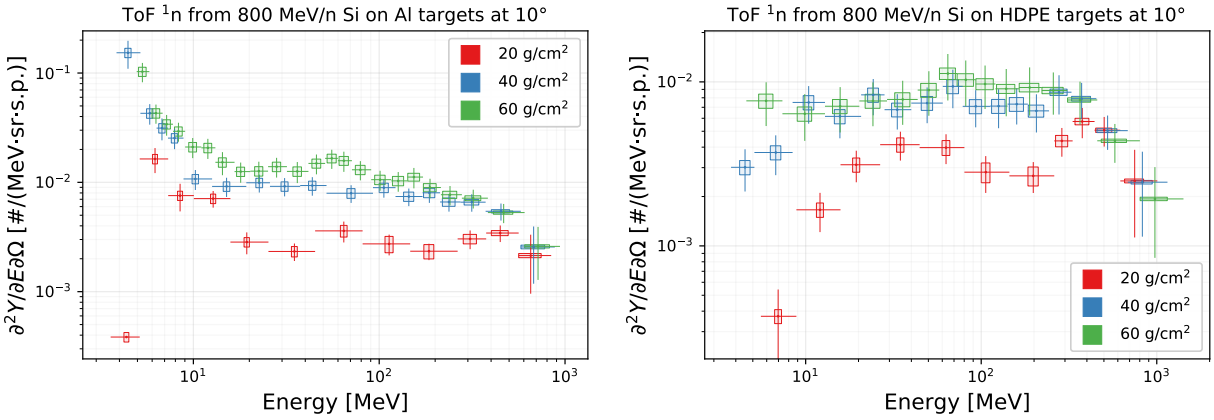
(a) 2500 MeV H (b) 800 MeV/n Si

Figure 8.12: Neutrons detected at 10° from projectiles incident on the 20 g/cm^2 upstream targets



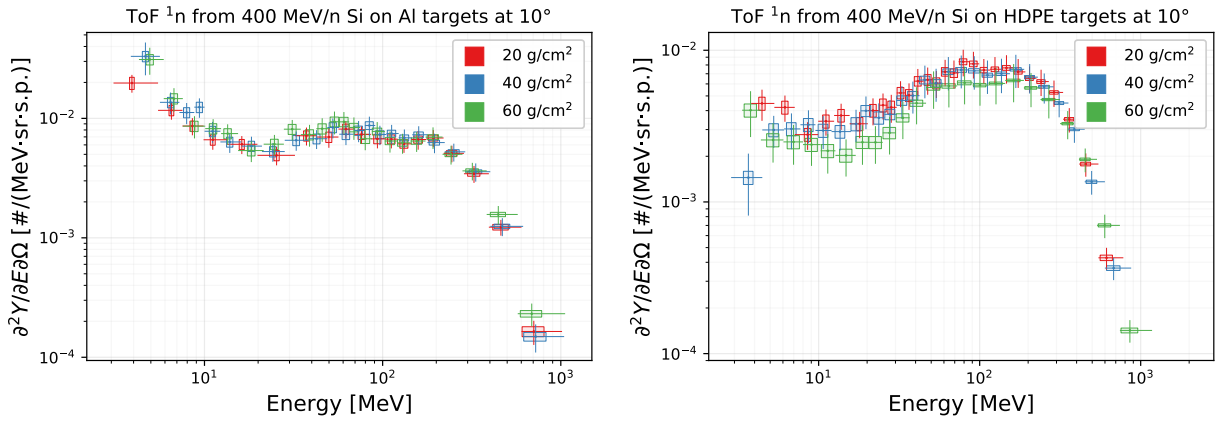
(a) Al (b) HDPE

Figure 8.13: Neutrons detected at 10° from 400 MeV/n C projectiles incident on the three thicknesses of each pure upstream target



(a) Al (b) HDPE

Figure 8.14: Neutrons detected at 10° from 800 MeV/n Si projectiles incident on the three thicknesses of each pure upstream target



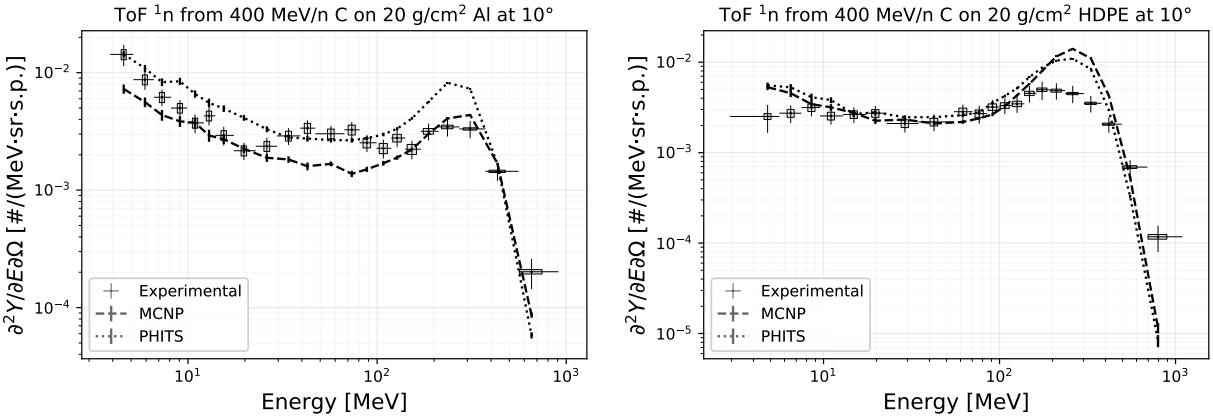
(a) Al (b) HDPE

Figure 8.15: Neutrons detected at 10° from 400 MeV/n Si projectiles incident on the three thicknesses of each pure upstream target

The primary observation from this is that the net neutron yield trends from a given combination of beam species, beam energy, target material, and target thickness is complex due to the various production and removal channels that are present, making the trends not something that necessarily can be predicted easily. However, yield generally increases with target thickness through most experimentally sampled beams since the effect of increased secondary production (from heavier and/or more penetrating beams) generally outweighs the additional attenuation of secondary particles by the thicker targets.

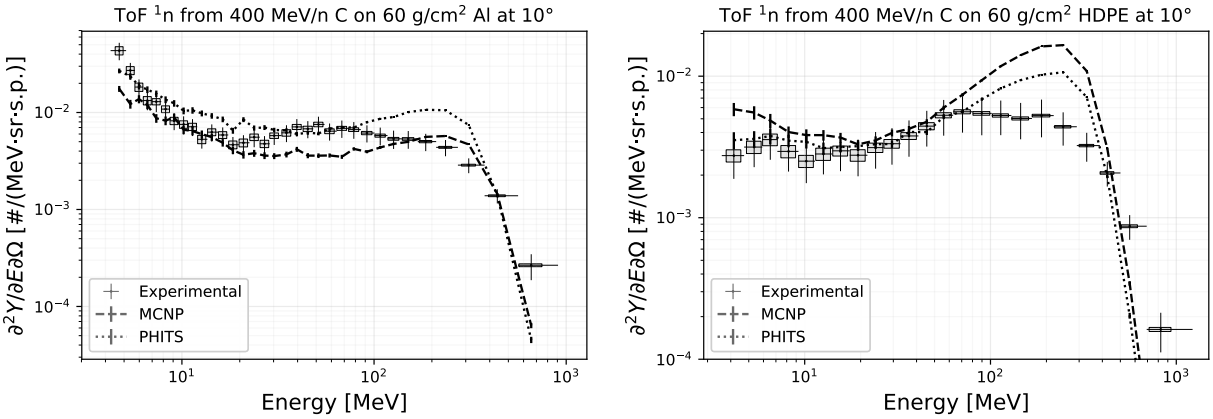
To expand the discussion beyond experimental results, it is interesting to compare how the Monte Carlo codes deviate from the collected data. This is comprehensively covered later in Section 8.2, but a few example plots highlighting some trends are presented here. One interesting trend which arises is a discrepancy on how the aluminum and polyethylene target yields vary between PHITS and MCNP. Figure 8.16 shows this behavior for 400 MeV/n C beams incident on the targets. PHITS notably over estimates MCNP for aluminum targets, and the reverse is true, though to a lesser extent, for HDPE targets. As featured earlier, the Monte Carlo codes tend to over predict the magnitude of the high energy neutron peak characteristic of projectile fragment neutrons at the lower detector angles.

One additional trend worth noting is that both Monte Carlo codes consistently over predict the experimental data at higher detector angles at higher neutron energies as seen in Figure 8.17.



(a) 20 g/cm^2 Al

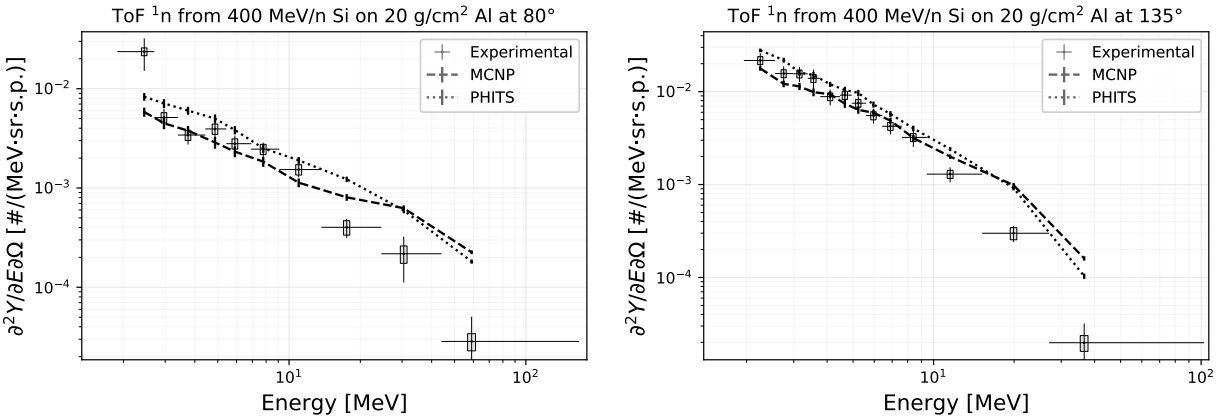
(b) 20 g/cm^2 HDPE



(c) 60 g/cm^2 Al

(d) 60 g/cm^2 HDPE

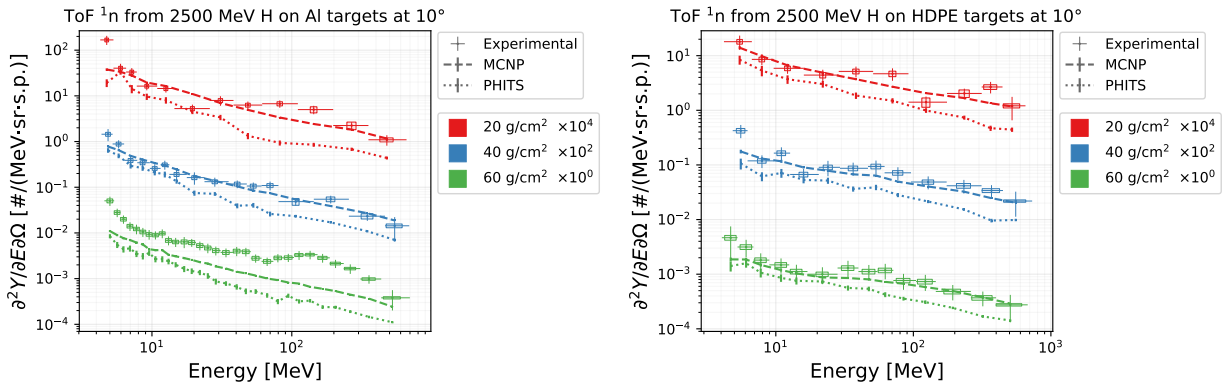
Figure 8.16: Neutrons detected at 10° from 400 MeV/n C projectiles incident on the 20 g/cm^2 and 60 g/cm^2 Al and HDPE upstream targets alongside Monte Carlo simulated results



(a) 80°

(b) 135°

Figure 8.17: Neutrons detected at 80° and 135° from 400 MeV/n Si projectiles incident on the 20 g/cm^2 Al upstream target alongside Monte Carlo simulated results



(a) Al (b) HDPE

Figure 8.18: Neutrons detected at 10° from 2500 MeV H projectiles incident on the three thicknesses of each pure upstream target (spaced apart by powers of 100) alongside Monte Carlo simulated results

To provide a more general observation on the performance of the Monte Carlo codes, some additional example plots are presented here. To avoid clutter, different spectra are spaced apart by powers of 10 or 100 as was done earlier in Figure 8.6 when showcasing the various detector angles. First, Figure 8.18 shows the PHITS and MCNP results plotted alongside experimental results from 2500 MeV H ions incident on the various thicknesses (separated by powers of 100) of the pure targets. Interestingly, this case contradicts the earlier found trend of PHITS predicting higher yields from aluminum targets than MCNP; however, as will be covered in more detail later in Section 8.2.3, this is one of the few exceptions to this trend. It also illustrates another trend which will be better demonstrated later where PHITS generally under predicts MCNP for the lightest projectiles. A particularly interesting observation here in Figure 8.18a is the 60 g/cm^2 Al line at the bottom where both codes share a moderate level of disagreement with each other while simultaneously neither predicting the experimental data very well.

Putting the differences between MCNP and PHITS aside momentarily, both codes generally under predict yield from hydrogen projectiles, and with increasing projectile mass the codes eventually both over predict the observed neutron yields for the heavier projectiles as illustrated in Figure 8.19. The figure also illustrates how the codes predict increasingly large buildups of the forward neutron peak for heavier projectiles, a trend not seen to the same extent in the experimentally collected data.

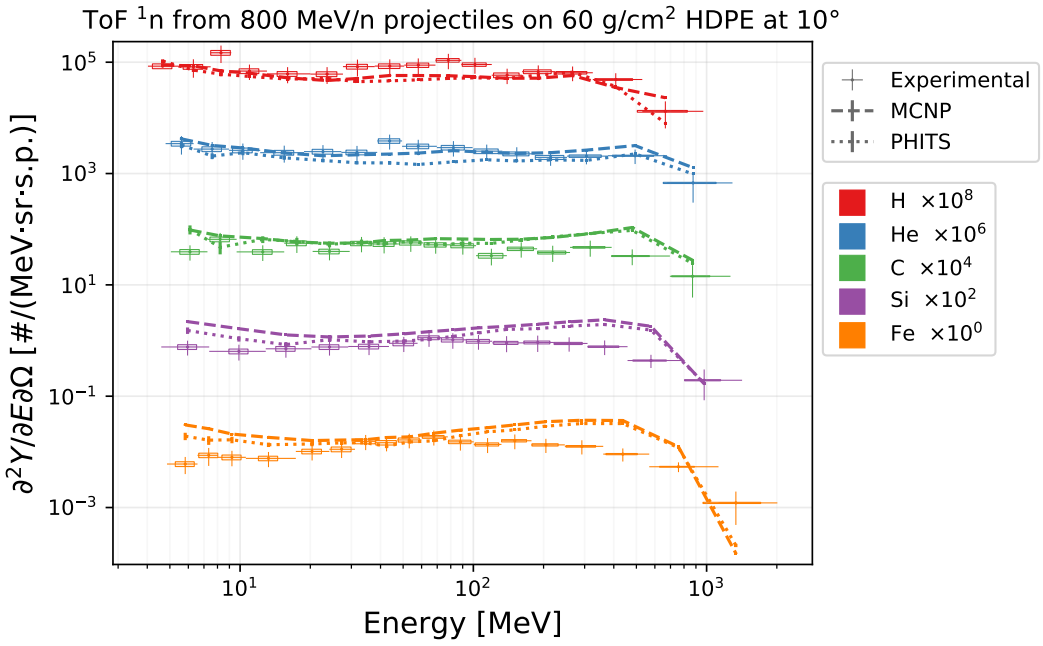
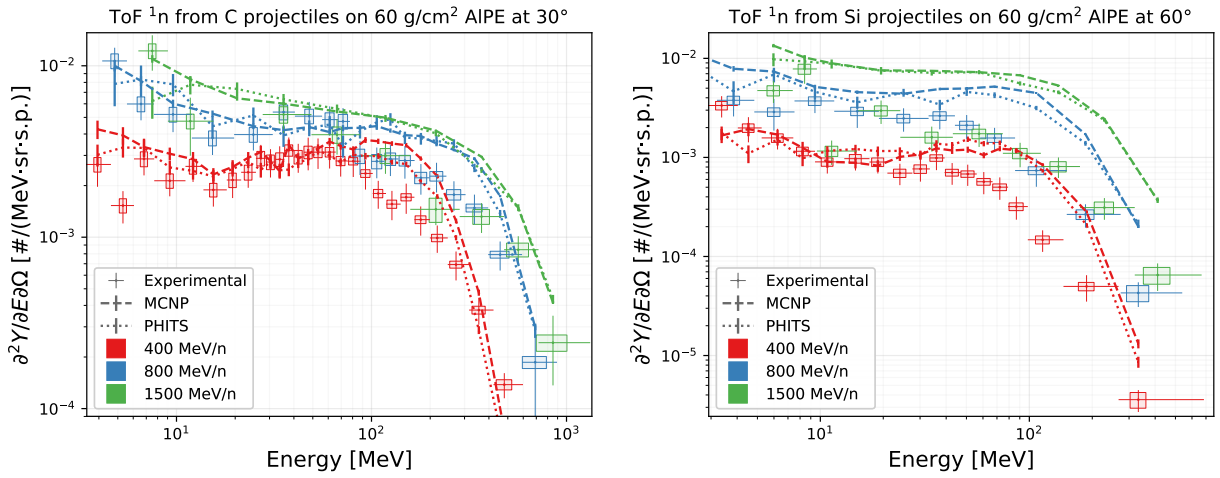


Figure 8.19: Neutrons detected at 10° from 800 MeV/n projectiles (spaced apart by powers of 100) incident on the 60 g/cm^2 HDPE upstream targets alongside Monte Carlo simulated results

The Monte Carlo codes predict the intuitive increase in neutron yield with increasing projectile energy as displayed in Figure 8.20. This trend is sometimes difficult to observe in the experimental data due to issues with obtaining clean and statistically sufficient spectra for the highest beam energies at the lower detector angles, so Figure 8.20 shows spectra at 30° and 60°. Despite the disagreements in the magnitude of the neutron yields, particularly notable in Figure 8.20b, the trends seen in the simulated results for increasing beam energies are generally similar to the experimentally observed trends.

To avoid portraying an overly negative outlook on the performance of the Monte Carlo codes, it is worth stating now that the codes do generally predict the data well; this is illustrated for several example systems in Figure 8.21. The cases where the agreement is worse are just more interesting to study since those scenarios illustrate potential areas where the codes can be improved.



(a) 30°, C projectiles

(b) 60°, Si projectiles

Figure 8.20: Neutrons detected at 30° from C projectiles and at 60° for Si projectiles incident on the 60 g/cm^2 AlPE upstream targets alongside Monte Carlo simulated results

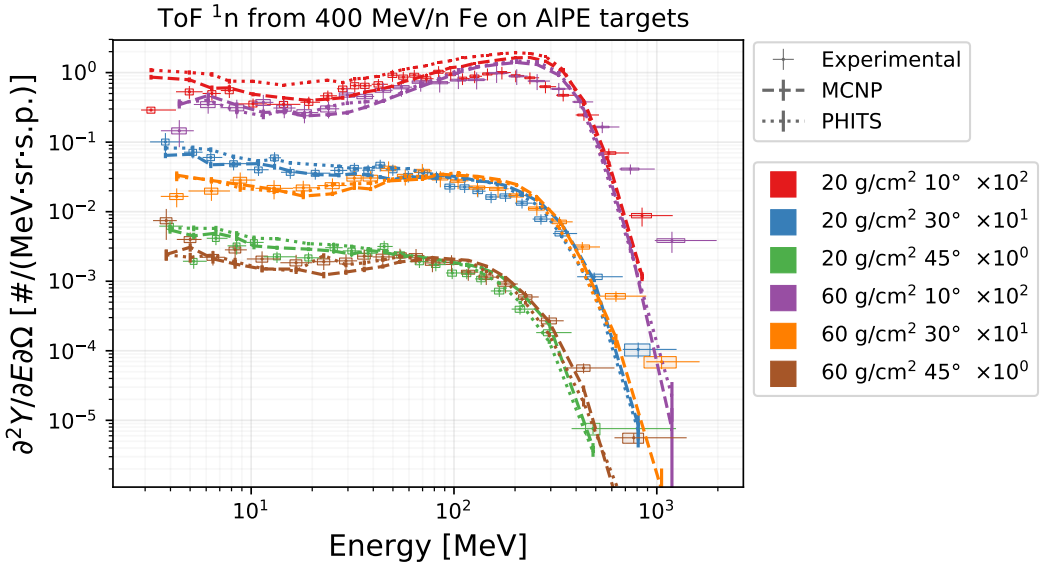


Figure 8.21: Neutrons detected at 10°, 30°, and 45° (spaced apart by powers of 10) from 400 MeV/n Fe projectiles incident on the 20 g/cm^2 and 60 g/cm^2 AlPE upstream targets alongside Monte Carlo simulated results

8.1.2 Energy-dependent differential downstream target neutron yields

This section is structured in a similar fashion to the previous one but for the energy-dependent differential neutron yields for all neutrons which were not produced in the upstream target and flew directly to a detector. For the detectors closest to the downstream target, neutrons produced in the downstream target become the largest contributor of neutron yield. However, neutrons produced elsewhere and those scattered throughout the room and eventually interacting in a detector become increasingly more significant when moving away from the downstream target. For the sake of clarity, all of these neutrons are simply referred to as downstream target neutrons, shadowed neutrons, and/or deconvoluted neutrons.

One important note to be made here is the increase in complexity of the factors influencing the final downstream neutron spectra. For the neutrons produced in the upstream target, most trends were fairly predictable. The most complicating factor present was that yields for the beams with the shortest ranges in the upstream target material would sometimes be lower than one would intuitively expect due to the neutron loss terms within the front target (such as scattering) becoming more significant relative to the neutron production terms (fragmentation of projectile, target, and secondary particles) due to the increased flight path through the target material before reaching the air and then the detectors. This influence is still present in these downstream spectra too, but even more complications are present.

First, as alluded to previously, there are multiple neutron sources in this experiment. Since the time-of-flight neutrons are only concerned with those produced in the upstream target, this discussion was not particularly valuable earlier. However, now it is warranted, and it makes the most sense to discuss neutron production along the beam line, moving upstream to downstream. First, neutrons can be created in the air or start scintillators before reaching the upstream target, but those are relatively insignificant contributions.

Next, neutrons are produced within the upstream target and, depending on the beam/target combination, can be the largest source of neutrons in the room. More precisely, neutrons and secondary projectile/target fragments are produced. While the target

fragments usually have lower energies and typically will only produce more neutrons within the upstream target through evaporation or more nuclear reactions, the projectile fragments can often posses enough energy to penetrate the remainder of the upstream target material in their path and are generally forward peaked enough in the lab frame such that they are traveling in a direction bound for the downstream target.

Within the downstream target, uninteracted beam particles, secondary fragments created in the upstream target, and protons/neutrons can undergo reactions to produce more neutrons as well. However, the contribution of each of these to neutron production in the back target is highly variable on the beam/upstream target combination. Beam particles which stop in the upstream target and whose secondary fragments are likely to do so as well will not result in many neutrons produced in the back target since only neutrons and perhaps very fast and light charged secondaries will reach the downstream target.

Any neutron produced not bound immediately for a detector has the opportunity to scatter throughout the room before striking a detector. Additionally, all of the charged secondary fragments, predominately light ions, which miss the detectors can also strike the walls of the experiment room to produce more neutrons. All of these production terms result in a fairly complex system where making any general observations about the downstream target neutrons can be challenging.

A manifestation of this complication is observed when trying to recreate the same plot from the previous section illustrating the functionality of neutron yield on projectile mass from 400 MeV/n projectiles. As seen in Figure 8.22, the same trend is no longer present.

While it is apparent that the fewest neutrons were produced from hydrogen projectiles and that helium neutron yields certainly fall beneath that of the heavier three projectiles, it is not obvious how the neutron yields of the three heavier projectiles should be ranked. This is a clear illustration of the influence of the upstream target. The heavier projectiles have shorter ranges in the upstream target, and this ultimately results in fewer neutrons being produced in the downstream target, especially where the beam does not penetrate the upstream target (Si and Fe beams here). Figure 8.23 shows what this plot becomes when all beams are capable of penetrating the upstream target. This results in the same expected trend seen with the upstream target where neutron yield scaled with projectile mass.

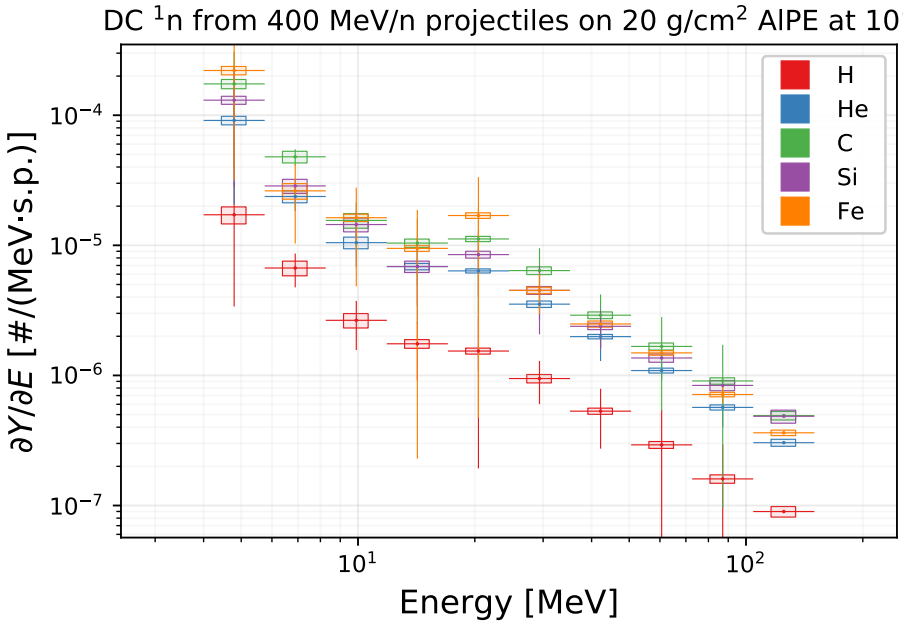


Figure 8.22: Shadowed neutrons detected at 10° from all 400 MeV/n projectile species incident on the 20 g/cm^2 AlPE upstream target

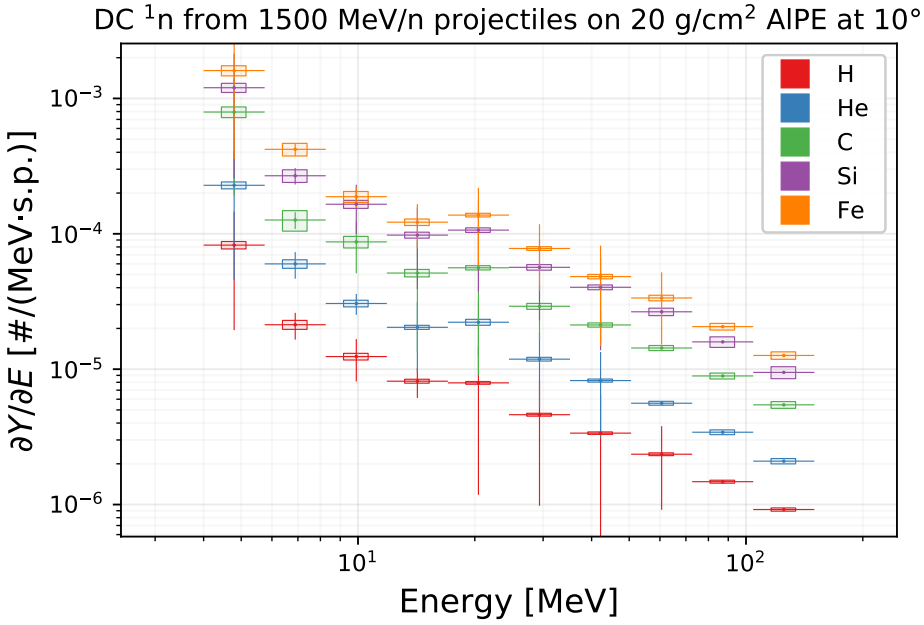


Figure 8.23: Shadowed neutrons detected at 10° from all 1500 MeV/n projectile species (2500 MeV H) incident on the 20 g/cm^2 AlPE upstream target followed by the 60 g/cm^2 HDPE downstream target

Discerning specific trends with detector angle in this case is difficult and not practical due to the lack of any solid angle normalization for these shadowed neutrons. Additionally, due to insufficient statistics, many beam/target combinations did not yield viable shadowed neutron spectra at all six detector angles. Still, the general trend present is that yield scales with proximity to the neutron sources of the room barring neutrons produced in the upstream target and traversing directly to a detector. Typically, this results in yield scaling with proximity to the downstream target, and thus the 10° detector almost always sees the highest shadowed neutron yield due to being very close to the downstream target. This is illustrated in Figure 8.24. Most plots presented for the shadowed neutrons showcase results from the 10° detector due to it having the most statistically viable spectra as well as it just being the most interesting detector to study of this dataset due to its proximity to the downstream target, the unique design component of this experiment.

The shadowed neutron yield increases with increasing beam energy as shown in Figure 8.25. This is because higher beam energies always result in more particles (beam ions and fragments) striking the downstream target, resulting in more secondary neutrons.

How the downstream neutron yield scales with upstream target thickness varies for different source ions. However, as illustrated in Figures 8.26 and 8.27, the trends present for each target material are fairly universal across the dataset. The aluminum upstream and downstream targets result in higher neutron yields than the polyethylene targets or the hybrid upstream target followed by the HDPE downstream target. Additionally, the AlPE systems, which are identical to the HDPE systems except the first 10 g/cm^2 of the HDPE upstream target are replaced with Al, tend to have lower yields than the HDPE equivalents. This would seem to (preliminarily) imply that the hybrid target would make for the best shielding material over choosing pure aluminum or polyethylene.

An important note to be made about Figure 8.27 is that, for the 800 MeV/n Fe beams incident on the 60 g/cm^2 upstream targets, the AlPE and HDPE yields become very similar. It makes sense that as the hybrid target converges to being the same as the HDPE target that their yields would also converge. However, this is not necessarily a universal trend; as was discussed earlier, these relations are complex and dependent on many variables such as beam stopping location and where secondary particles are being produced and lost.

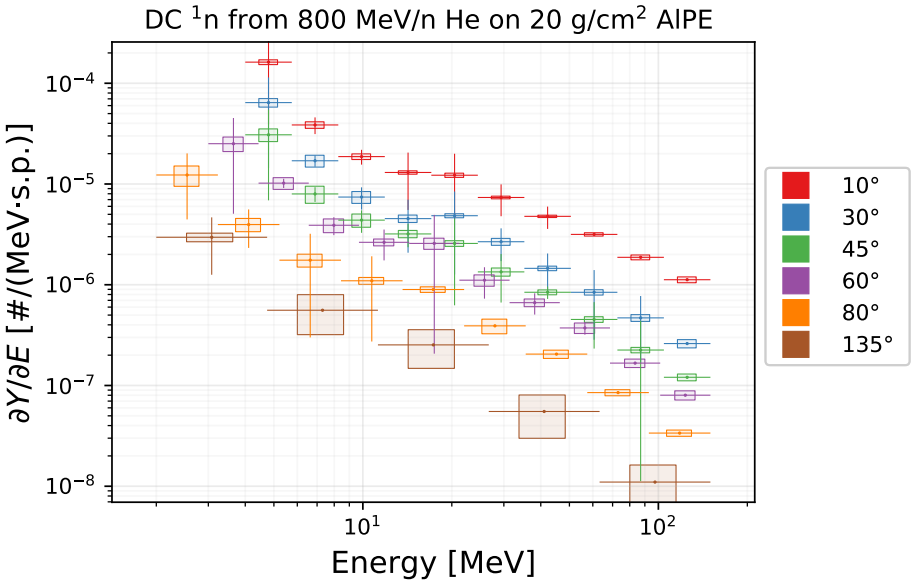
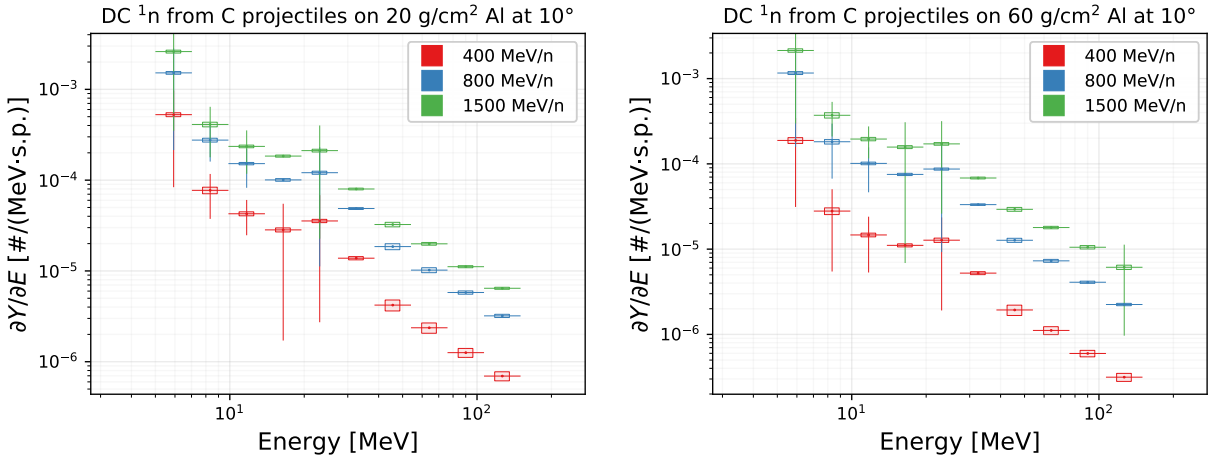


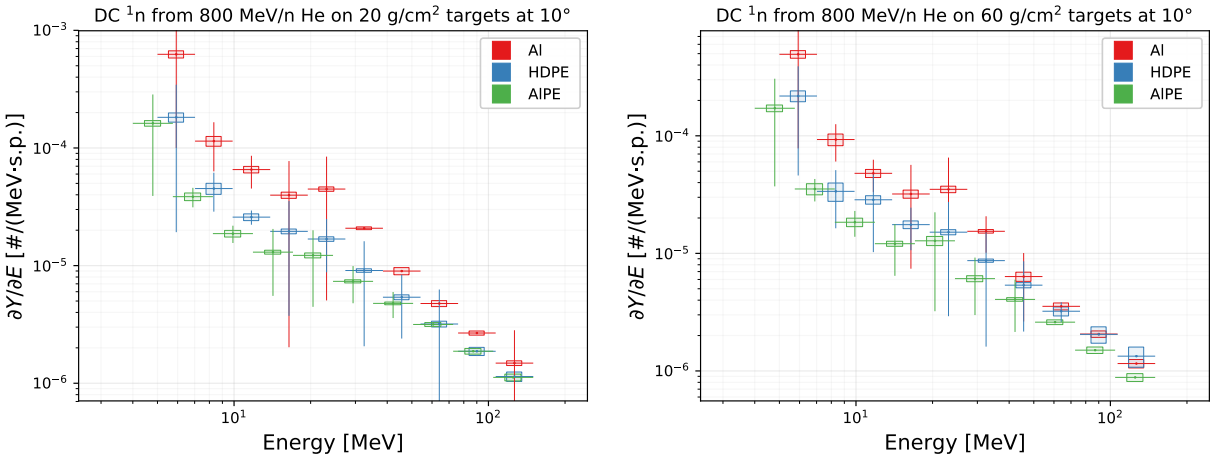
Figure 8.24: Shadowed neutrons detected at each detector angle from all 800 MeV/n He projectiles incident on the 20 g/cm^2 AlPE upstream target followed by the 60 g/cm^2 HDPE downstream target



(a) 20 g/cm^2 Al upstream target

(b) 60 g/cm^2 Al upstream target

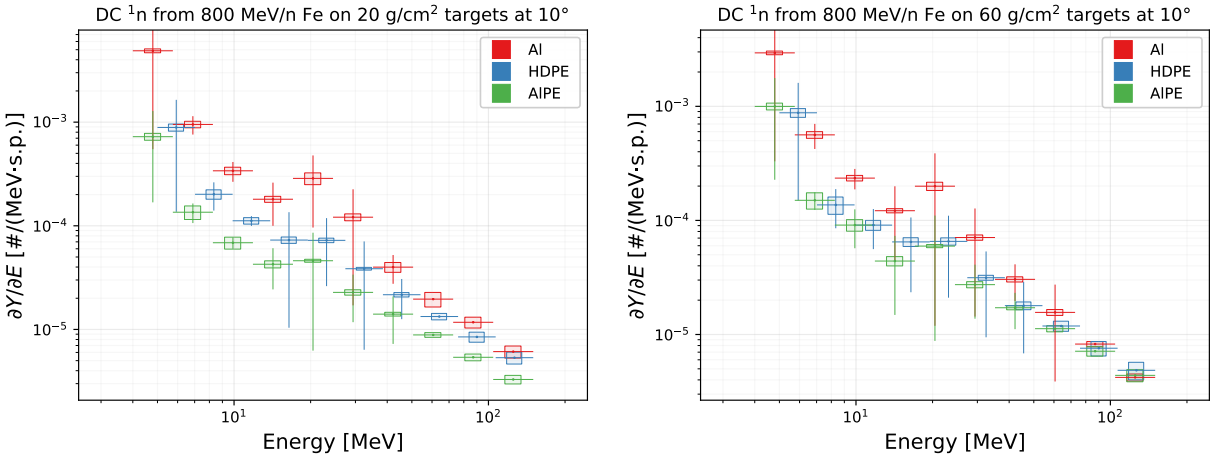
Figure 8.25: Shadowed neutrons detected at 10° from C projectiles incident on the 20 g/cm^2 and 60 g/cm^2 Al upstream targets followed by the 60 g/cm^2 Al downstream target



(a) 20 g/cm^2 upstream targets

(b) 60 g/cm^2 upstream targets

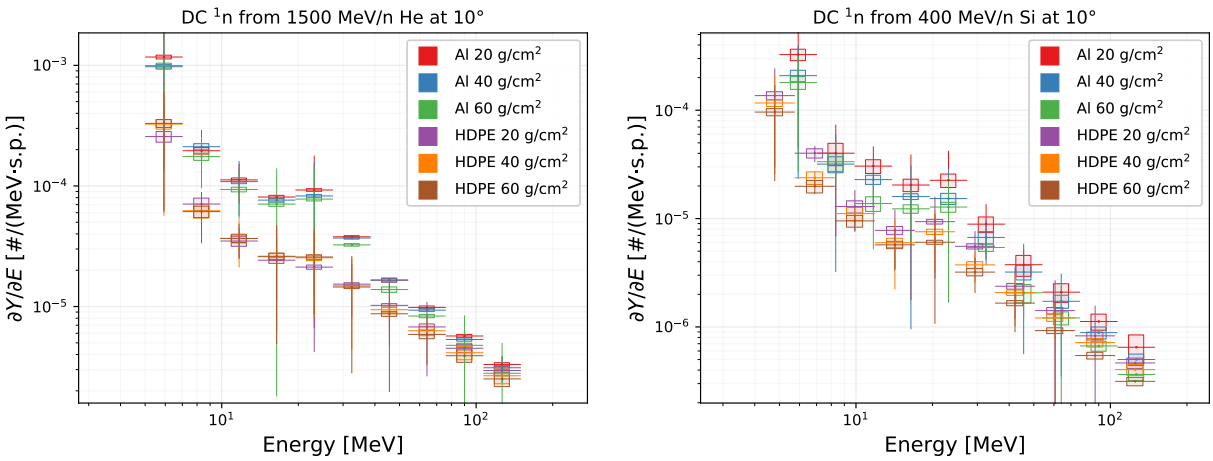
Figure 8.26: Shadowed neutrons detected at 10° from 800 MeV/n He projectiles incident on the 20 g/cm^2 and 60 g/cm^2 thicknesses of each upstream material composition targets followed by the 60 g/cm^2 downstream target of the same material



(a) 20 g/cm^2 upstream targets

(b) 60 g/cm^2 upstream targets

Figure 8.27: Shadowed neutrons detected at 10° from 800 MeV/n Fe projectiles incident on the 20 g/cm^2 and 60 g/cm^2 thicknesses of each upstream material composition targets followed by the 60 g/cm^2 downstream target of the same material



(a) 1500 MeV/n He

(b) 400 MeV/n Si

Figure 8.28: Shadowed neutrons detected at 10° from 1500 MeV/n He and 400 MeV/n Si projectiles incident on the three thicknesses of each pure upstream target material followed by the 60 g/cm^2 downstream target of the same material

Additionally, for the more penetrating beams, the upstream target material plays a more significant role than the upstream target thickness on the final neutron yield. Though, for beams which can struggle to penetrate the upstream target, its thickness does begin to play a more prominent role. This is shown in Figure 8.28 where the yields from the completely penetrating 1500 MeV/n He beam are primarily dependent on material while the yields from the 400 MeV/n Si beam (which is stopped by all upstream targets) are fairly dependent on both target material and thickness.

Now that the general trends with the data has been covered, a brief illustration of trends present with the Monte Carlo codes can be shown. First, as shown in Figure 8.29, while the codes and data agree fairly well for H and He projectiles, the codes notably over estimate yields for the heavier projectiles, particularly Si and Fe. Though, at the very least, the trends of each yield spectrum as a function of energy are in agreement between the data and codes except at higher energies where MCNP and PHITS appear to deviate from each other. This over prediction of shadowed neutron yields for heavier ions is a fairly prominent trend in this dataset. Isolating the cause of this is difficult given the complexity of all possible interactions that produce neutrons.

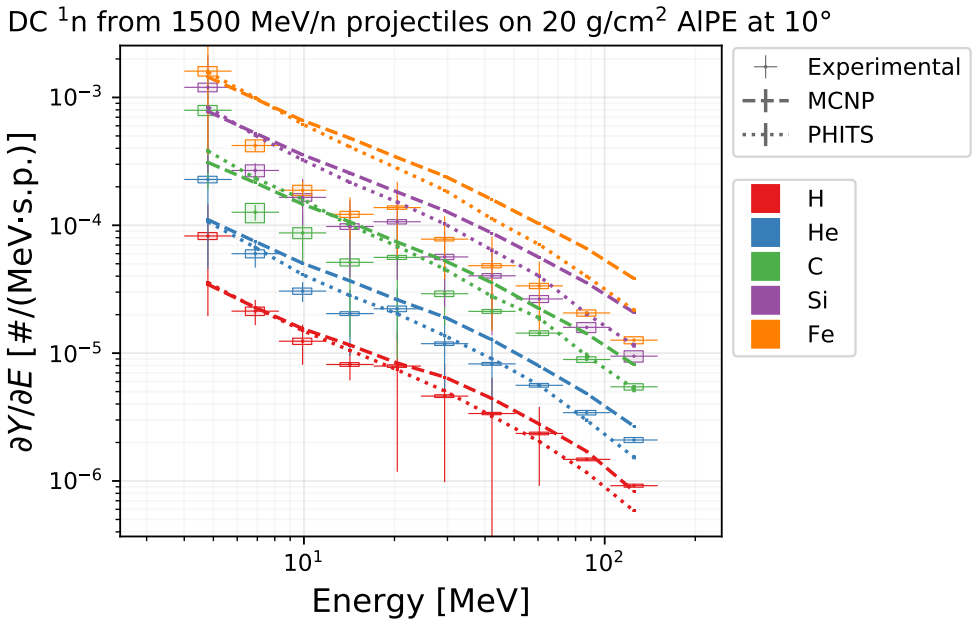


Figure 8.29: Shadowed neutrons detected at 10° from all 1500 MeV/n projectile species (2500 MeV H) incident on the 20 g/cm^2 AlPE upstream target followed by the 60 g/cm^2 HDPE downstream target alongside Monte Carlo simulated results

Since the deconvolution methodology appears to produce results in agreement with the Monte Carlo codes for the lighter projectiles and was demonstrated to produce upstream target neutron yield spectra in agreement with those characterized with the time-of-flight methodology in Section 6.7, it appears that the deconvolution methodology is sound and not responsible for the discrepancies.

It is interesting to note that the experimental deconvoluted results are generally in agreement with the modeled results for each detector angle as seen in Figure 8.30. Additionally, the scaling of neutron yield with increasing projectile energy also is in agreement between the simulated and experimentally obtained results as shown in Figure 8.31, though some disagreement is present in the magnitude of the curves for the higher energy beams. The behavior of PHITS over predicting MCNP for aluminum target yields and the opposite for HDPE yields is also seen in the downstream target results as illustrated in Figure 8.32.

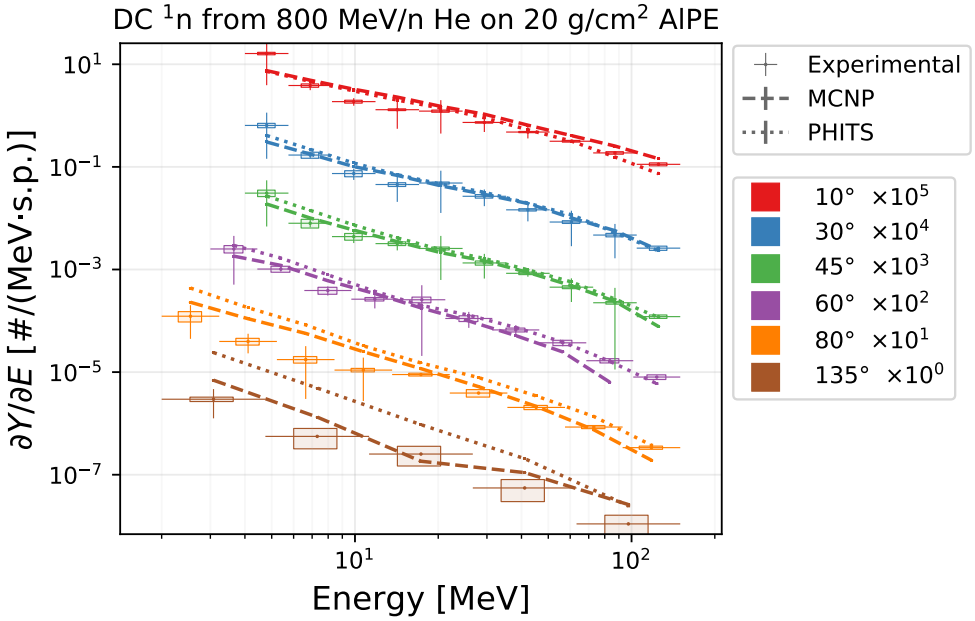


Figure 8.30: Shadowed neutrons detected at each detector angle (spaced apart by powers of 10) from 800 MeV/n He projectiles incident on the 20 g/cm^2 AlPE upstream target followed by the 60 g/cm^2 HDPE downstream target alongside Monte Carlo simulated results

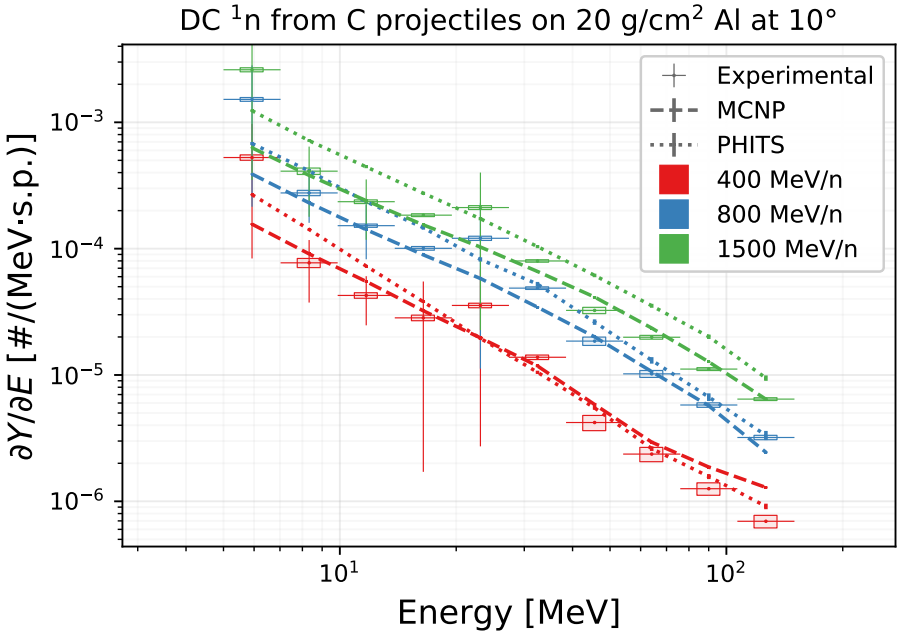
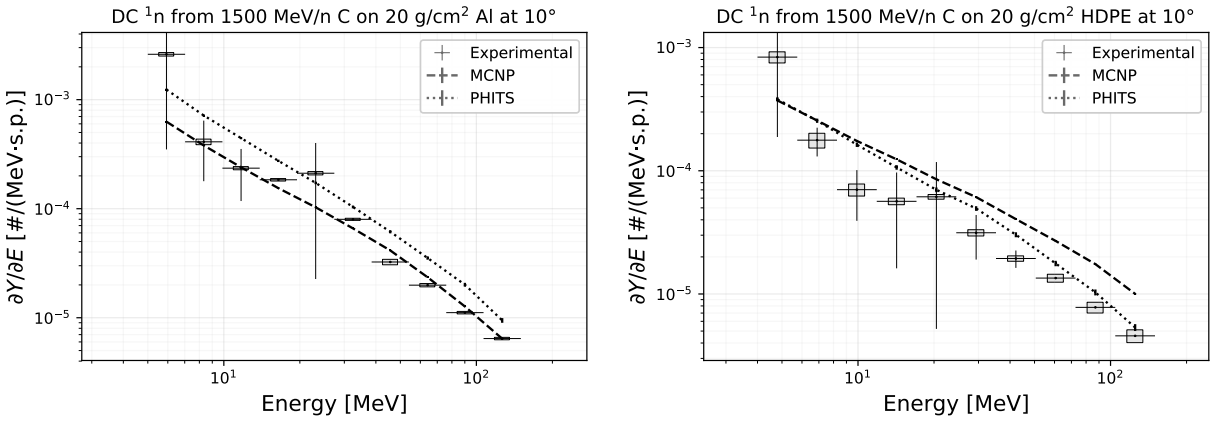


Figure 8.31: Shadowed neutrons detected at 10° from C projectiles incident on the 20 g/cm^2 Al upstream target followed by the 60 g/cm^2 Al downstream target alongside Monte Carlo simulated results



(a) 20 g/cm^2 Al

(b) 20 g/cm^2 HDPE

Figure 8.32: Downstream target-produced and room scattered neutrons detected at 10° from 400 MeV/n C projectiles incident on the 20 g/cm^2 Al and HDPE upstream targets followed by the 60 g/cm^2 downstream target of the same material alongside Monte Carlo simulated results

8.1.3 Energy-dependent differential combined neutron yields

Due to the solid angle normalization, the upstream target double-differential yields cannot be directly compared to the downstream target and room scattered neutron results. However, if the solid angle normalization is undone, the two can be fairly compared. This subsection seeks to provide a brief glance at the total neutron yield spectra broken down by upstream target contribution and the contributions from everywhere else using this methodology. Figure 8.33 shows this plot at the 10° detector for 400 MeV/n C projectiles incident on the 20 g/cm^2 AlPE upstream target followed by the 60 g/cm^2 HDPE downstream target. These plots illustrate the prevalence of where the most neutrons within a spacecraft would be coming from as a function of neutron energy. At lower energies, the neutron yield is dominated by neutrons produced in the back target primarily through target fragment evaporation, though a moderate contribution from target evaporation from the upstream target is also present. Beyond 40 MeV, the upstream target contribution overtakes the downstream target contribution and dominates the neutron yield entirely beyond 100 MeV.

Figure 8.34 highlights these trends for the most penetrating beam tested, 2500 MeV protons, when varying target material and thickness. For the 20 g/cm^2 upstream targets, the neutron yield is dominated by the downstream target. However, for the thicker 60 g/cm^2

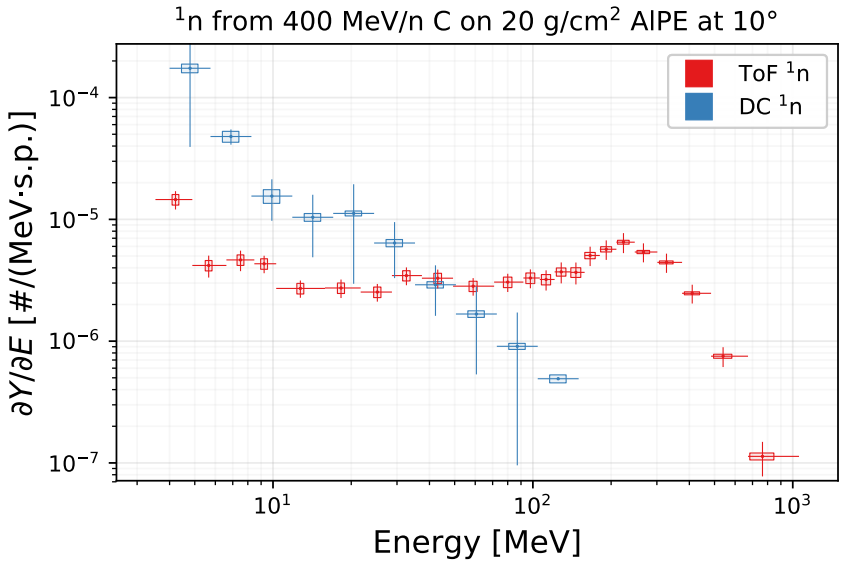
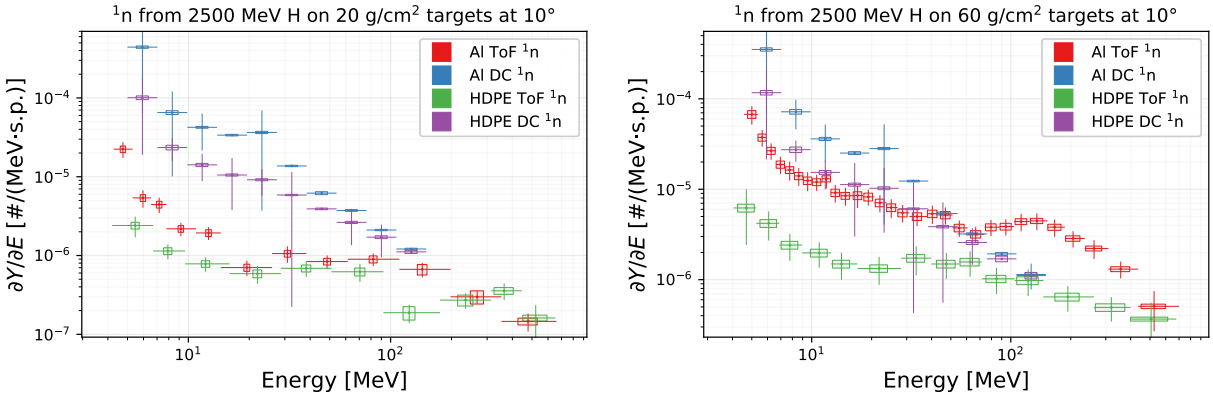


Figure 8.33: All neutrons detected at 10° from 400 MeV/n C projectiles incident on the 20 g/cm^2 AlPE upstream target followed by the 60 g/cm^2 HDPE downstream target



(a) 20 g/cm^2 upstream targets

(b) 60 g/cm^2 upstream targets

Figure 8.34: All neutrons detected at 10° from 2500 MeV H projectiles incident on the 20 g/cm^2 and 60 g/cm^2 Al and HDPE upstream targets followed by the 60 g/cm^2 downstream target of the same material

upstream targets, the contribution from the aluminum upstream target rises significantly while the HDPE upstream target contribution remains relatively low. This is perhaps a good illustration of a contributing factor to the dose plateau for HDPE and rise for Al beyond the 20 g/cm^2 thickness as discussed in Dr. Slaba's work in Reference 1 which motivated these experiments.

Figure 8.35 shows a copy of Figure 8.34b but with the 60 g/cm^2 AlPE target results added as well. As one can see, both neutron contributions are lower for the AlPE target than for the HDPE target which are, in turn, lower than that of the aluminum targets.

On the opposite end of the spectrum of penetrating power, the 400 MeV/n Fe beam incident on all 20 g/cm^2 and 60 g/cm^2 upstream targets is shown in Figure 8.36. Here, since so many fewer beam particles/fragments make it to the downstream target, the prominence of the upstream target contribution is much stronger. Below 40 MeV though, the downstream target contribution still exceeds the upstream target contribution. The difference is fairly subtle, but the neutron yields for both contributions are generally lower for the 60 g/cm^2 targets than for the 20 g/cm^2 targets.

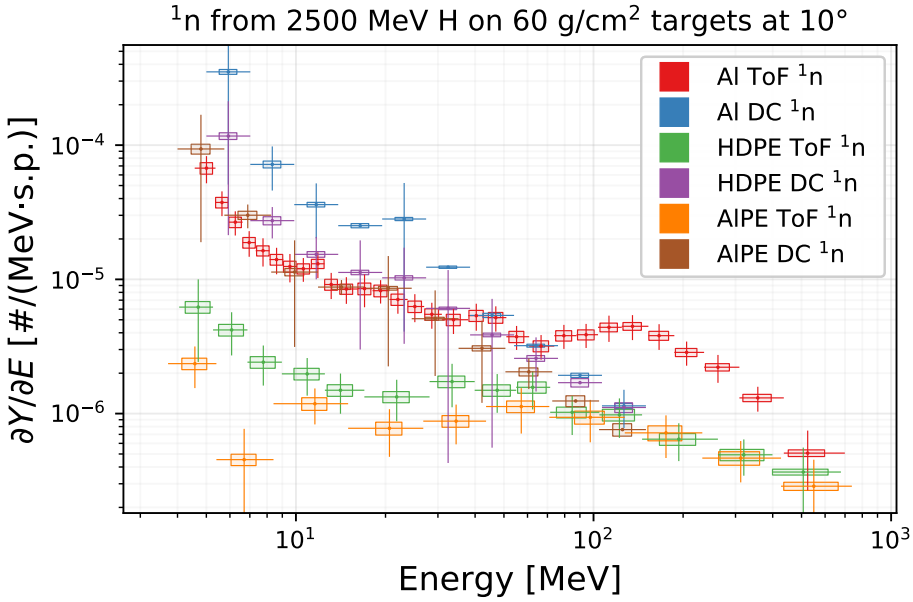
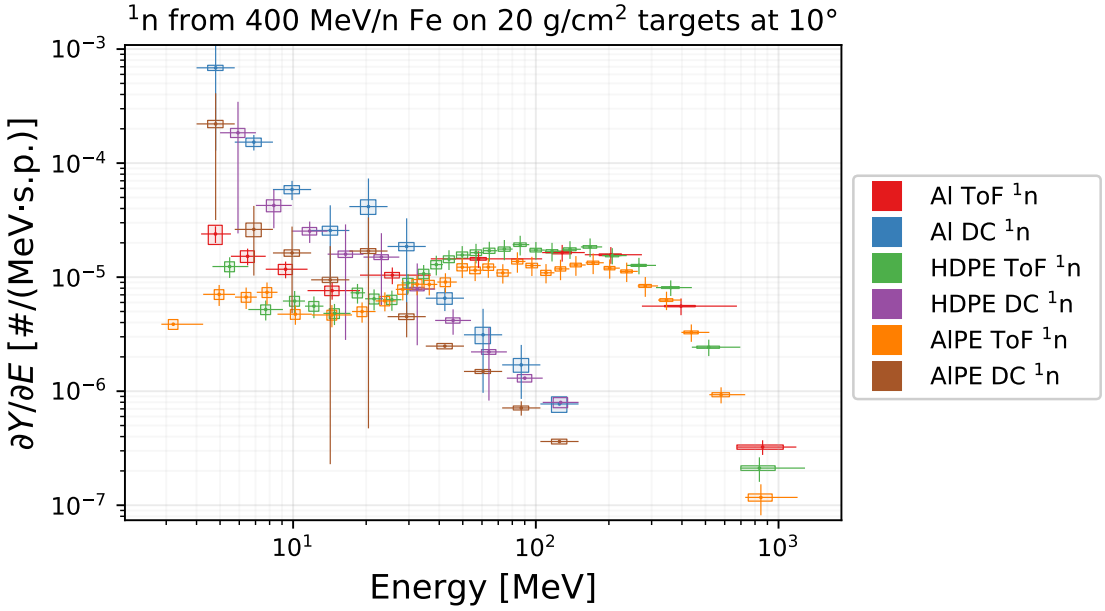
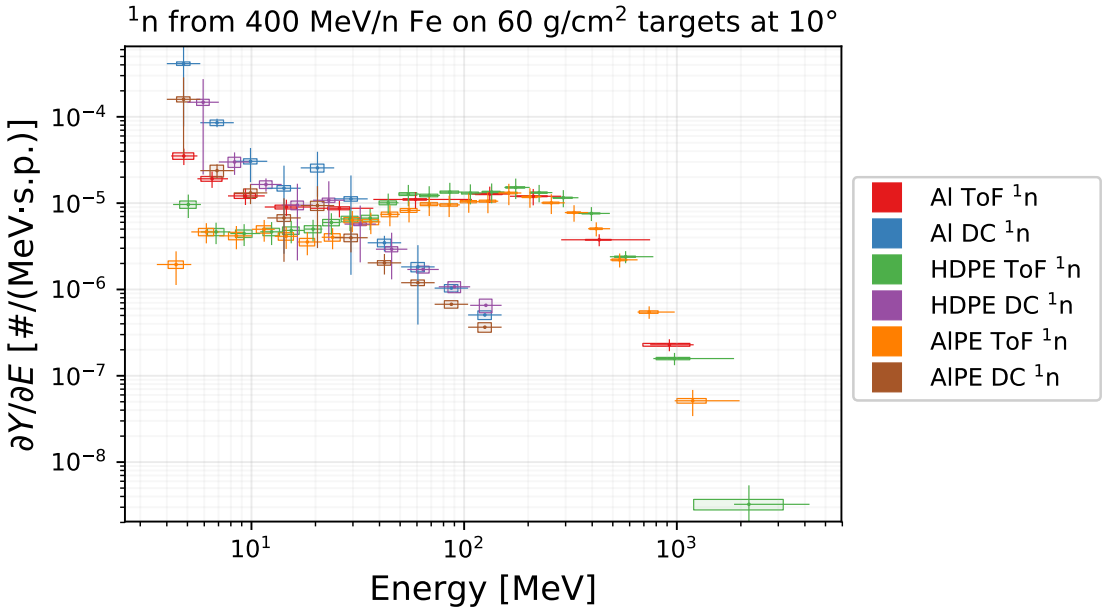


Figure 8.35: All neutrons detected at 10° from 2500 MeV H projectiles incident on all 60 g/cm^2 upstream target combinations



(a) 20 g/cm^2 upstream targets



(b) 60 g/cm^2 upstream targets

Figure 8.36: All neutrons detected at 10° from 400 MeV/n Fe projectiles incident on all 20 g/cm^2 and 60 g/cm^2 upstream targets followed by the 60 g/cm^2 downstream target of the same material

8.2 Performance of Monte Carlo results against the data

One of the primary goals of this work was identification of areas where the Monte Carlo codes and the physics models within them can be improved. Here, a more comprehensive analysis of how MCNP and PHITS compare to the collected data is presented to provide more concrete evidence of the trends observed and discussed earlier. It should be noted here that statisticians at NASA Langley Research Center are performing a far more detailed and complex statistical analysis of the experimental data and simulated results produced in the work surrounding these experiments. This section only seeks to use a basic analysis to assist in discerning general trends in the neutron datasets.

Due to the order of magnitude or greater differences possible in this study, ratios of values tend to offer more information than percent error and difference calculations. In this analysis, the three ratios listed below were calculated for every single neutron data point.

- MCNP / Experiment
- PHITS / Experiment
- PHITS / MCNP

After performing these calculations for every single collected neutron spectrum, a detailed analysis is conducted. One must be careful in combining comparisons from different systems; for example, the performance of the transport codes in the region around 400 MeV has different implications for 1500 MeV/n projectiles than it does for 400 MeV/n projectiles. However, for this analysis, the most sensible approach is to combine everything first and then afterward expand each collapsed axis to observe trends.

8.2.1 Monte Carlo vs. data: Upstream target results

Figure 8.37 shows a scatter plot of every ratio of the MCNP and PHITS data to the experimental data for upstream target neutrons. A dark line has been drawn at $y = 1$ to indicate where the Monte Carlo results would be in exact agreement with the experimental findings, and two slightly less dark lines have also been drawn at $y = 0.5$ and $y = 2$ to

illustrate the band containing all points within a factor of two of the experimental results. Additionally, each point is only drawn at 40% opacity to provide more clarity on the density of points as well.

Table 8.1 contains a summary of some of the key findings from this plot. The first interesting conclusion to draw is that both Monte Carlo codes over predict the data more often than not, 58.3% of points for MCNP and 64.5% of points for PHITS. The mean versus median values illustrate that the influence of outliers can be significant; thus, the median likely does a better job of representing the magnitude of each code's overall over prediction of yield. While it is notable that over 97% of points from both codes lie within an order of magnitude of the experimental values, that number falls below 70% when considering points within a factor of two of the experimental values. Additionally, from the figure one can see that the codes are more likely to overestimate the experimental results at higher neutron energies; however, there is also a tail on the far right of the plot where the codes under predict the experimental results at the highest energies. This trend of under prediction appears to also be the case at the lowest neutron energies. Lastly, a distinct feature is present starting

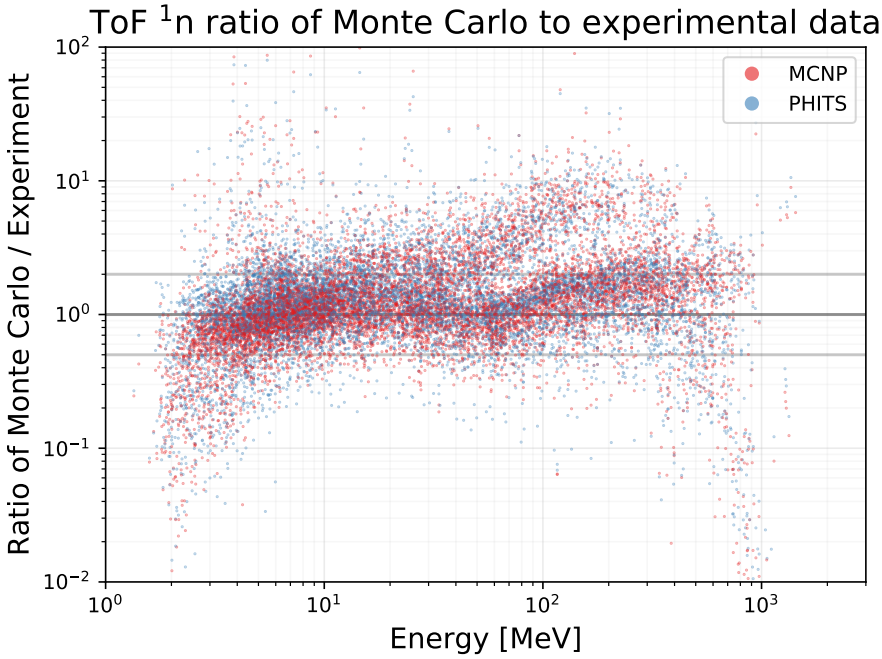


Figure 8.37: Ratio of Monte Carlo results to experimental results for every data point from the upstream target neutron dataset

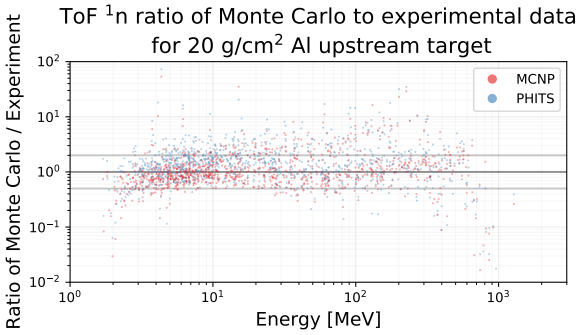
Table 8.1: Upstream target neutron overall results comparison to Monte Carlo

Quantity	MCNP	PHITS
Median ratio	1.125	1.238
Mean ratio	1.761	1.787
Percentage of ratios over 1	58.30%	64.53%
Percentage of points within a factor of 10	97.34%	97.08%
Percentage of points within a factor of 2	69.47%	67.95%

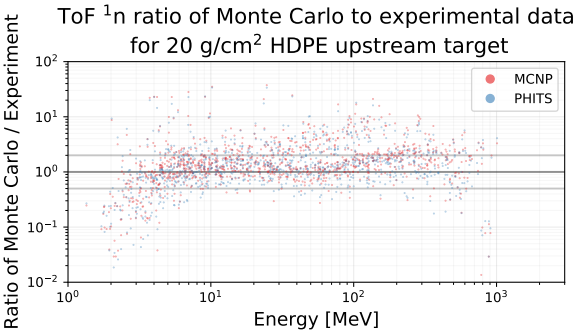
at around 40 MeV that resembles a second arm extending above the rest of the ratios with a notable amount of separation.

To better study these trends, the next step is to see how this plot changes when observing each experimental axis on its own, a task accomplished by the plots on the next four pages. First, Figure 8.38 shows the isolated results from each front target (material and thickness). Next, Figure 8.39 reproduces these plots except featuring each detector angle. Figure 8.40 isolates each projectile species, and Figure 8.41 following it isolates each projectile energy (though the 2500 MeV H results are plotted together with the other 1500 MeV/n results). Each of these figures contains trends warranting further discussion.

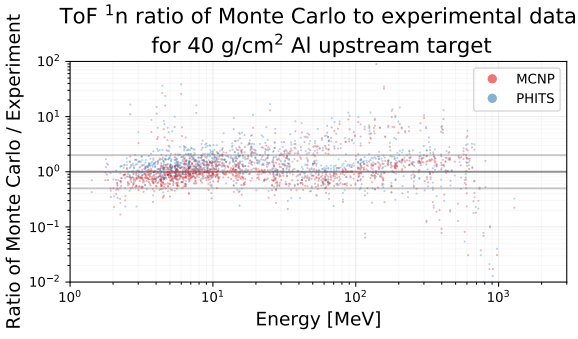
First, the results as a function of the various upstream targets are shown in Figure 8.38. At first, they all seem quite similar to one another, each possessing most of the traits discussed earlier; however, one of the trends of the overall comparison plot does appear to be isolated by this exercise. The low energy tail where the codes underestimate the experimental data appears to only be present in the upstream targets containing HDPE; the pure aluminum targets do not produce this same feature. The plots for the hybrid AlPE targets also possess this trend, but its magnitude appears to fall between that of the Al and HDPE targets, indicating that the HDPE material's presence is the cause of under predicting neutron yields below 10 MeV. Since neutron scattering and transport are generally considered to be the most established features of these codes, the inaccuracy likely stems from the production of neutrons rather than their scattering and transport. Since the issue is present for HDPE and not aluminum, one possibility is that the transport codes are not modeling the nuclear reactions with target carbon nuclei as accurately.



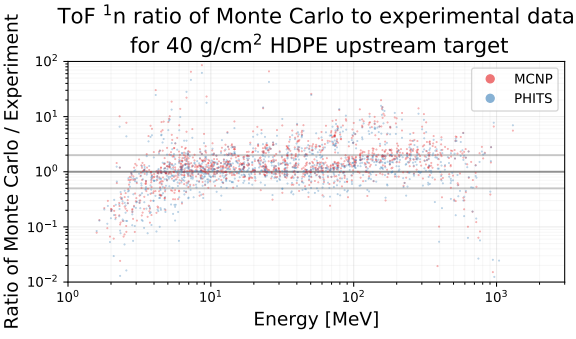
(a) 20 g/cm^2 Al



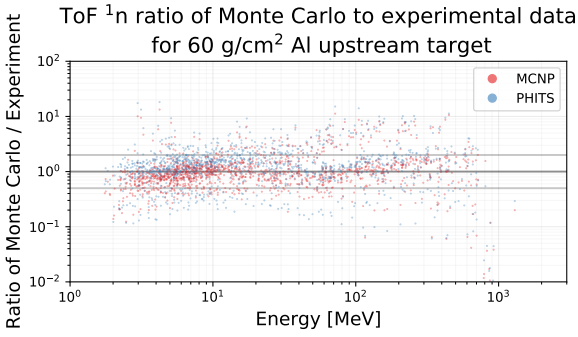
(b) 20 g/cm^2 HDPE



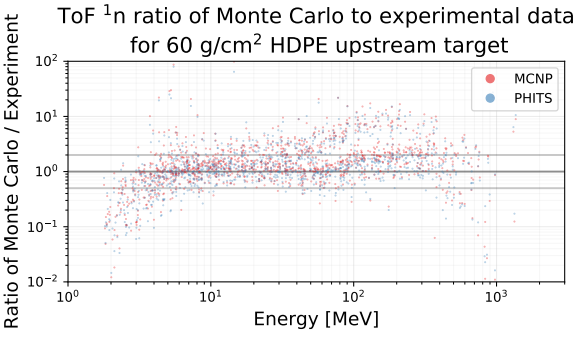
(c) 40 g/cm^2 Al



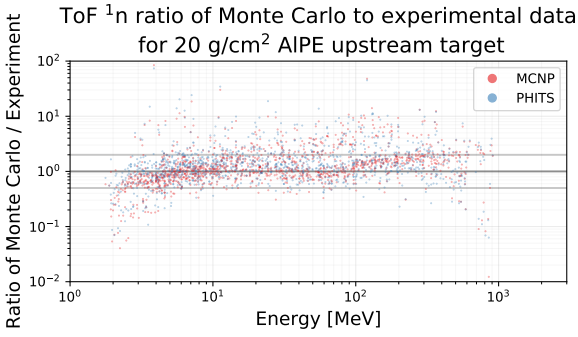
(d) 40 g/cm^2 HDPE



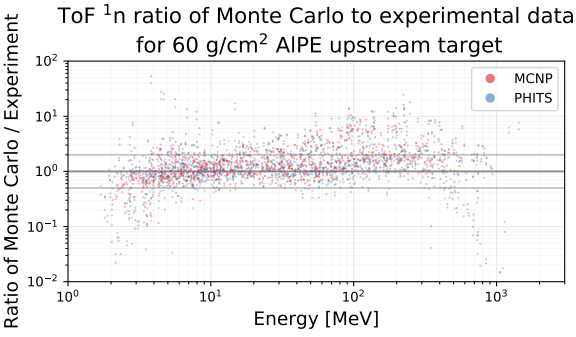
(e) 60 g/cm^2 Al



(f) 60 g/cm^2 HDPE

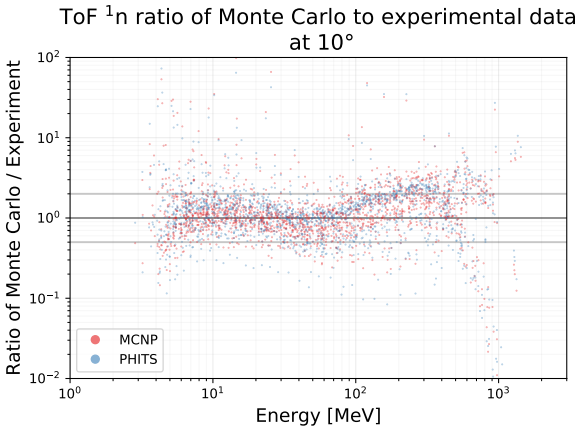


(g) 20 g/cm^2 AlPE

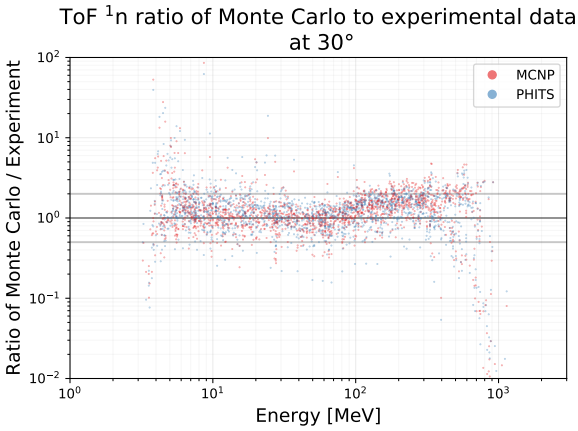


(h) 60 g/cm^2 AlPE

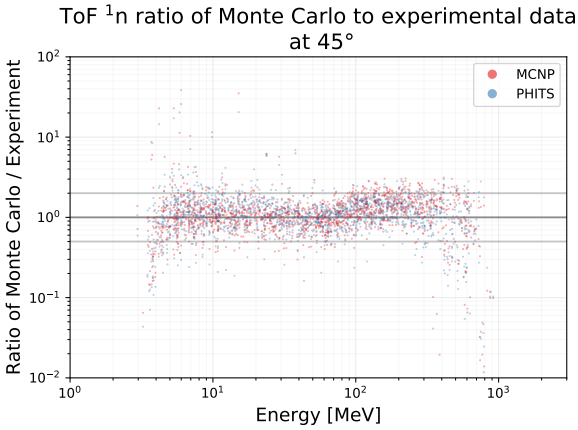
Figure 8.38: Components of Figure 8.37 for each front target



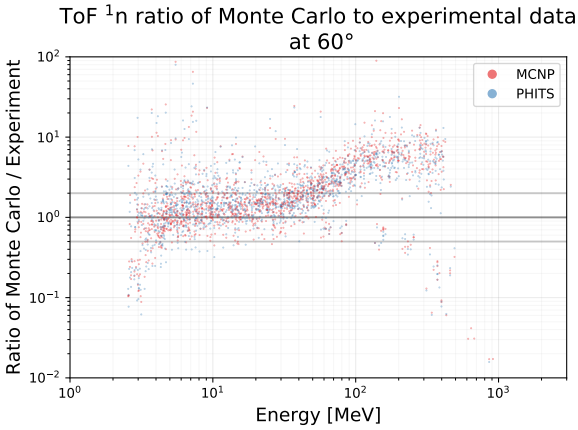
(a) 10°



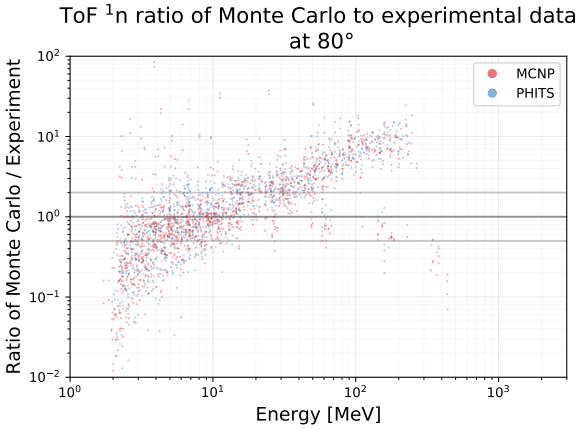
(b) 30°



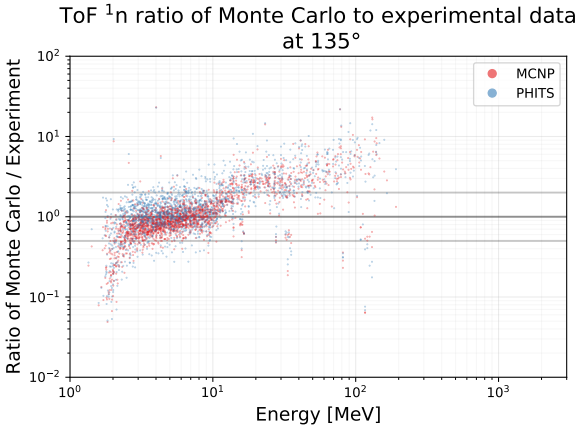
(c) 45°



(d) 60°

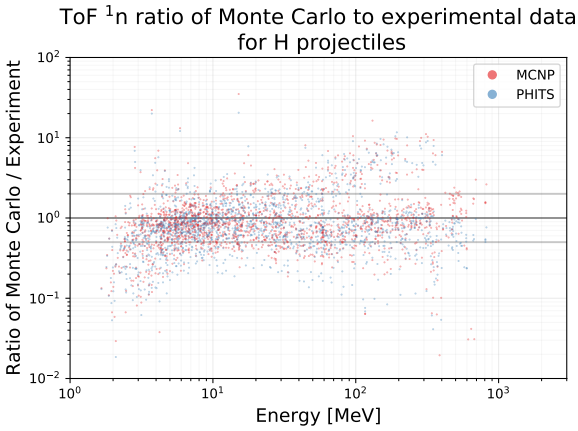


(e) 80°

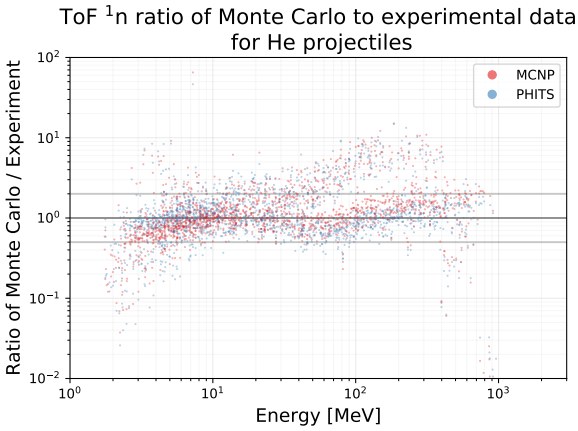


(f) 135°

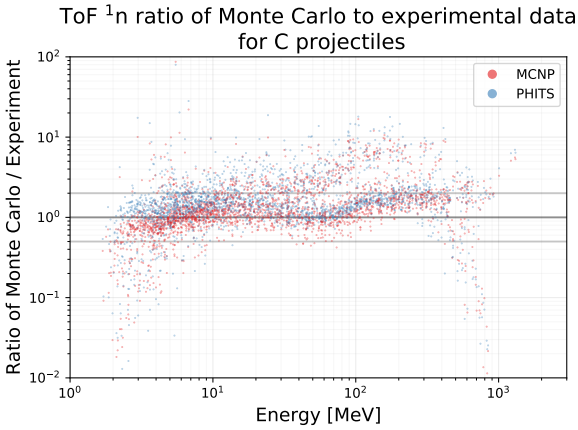
Figure 8.39: Components of Figure 8.37 for each detector angle



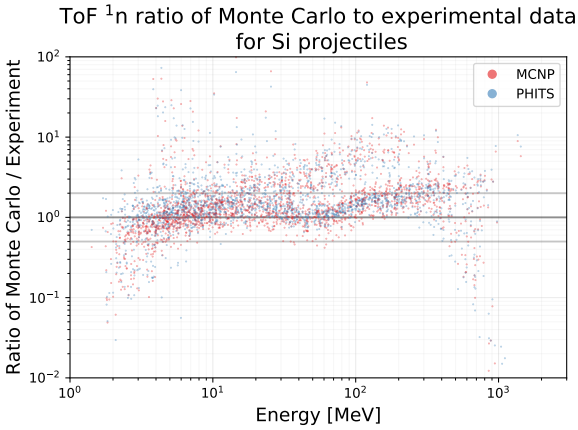
(a) H



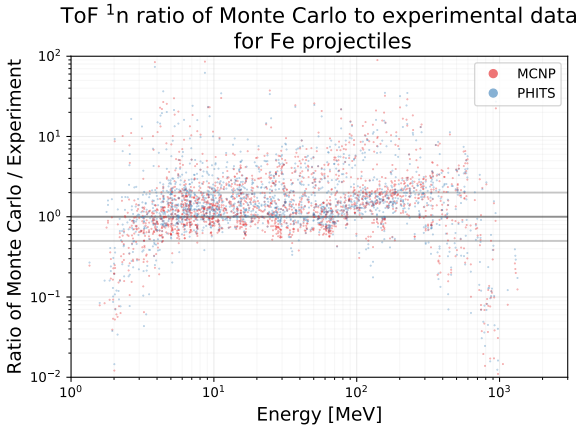
(b) He



(c) C

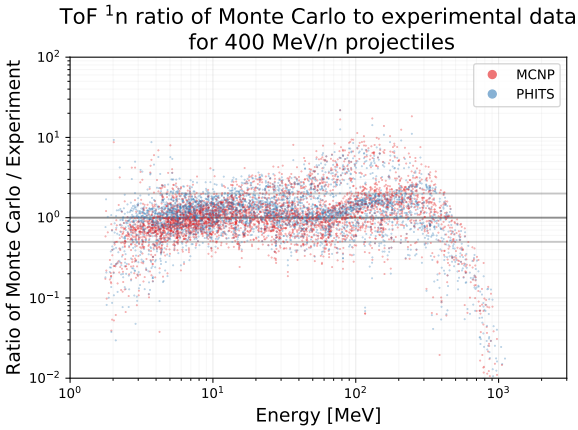


(d) Si

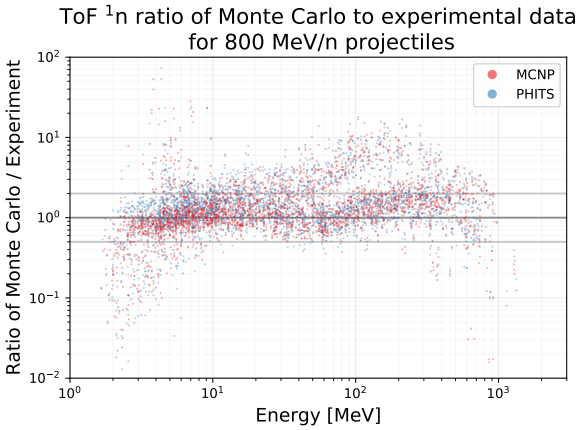


(e) Fe

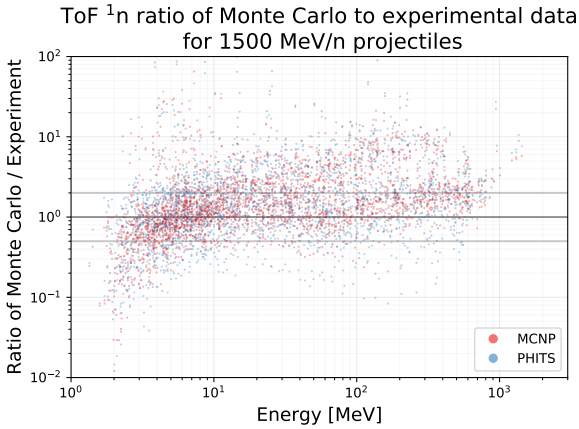
Figure 8.40: Components of Figure 8.37 for each projectile species



(a) 400 MeV/n



(b) 800 MeV/n



(c) 1500 MeV/n (2500 MeV for H)

Figure 8.41: Components of Figure 8.37 for each projectile energy

Next, Figure 8.39 isolates each of the six detector angles. Several features are immediately noticeable. First, the under prediction of the low energy neutron yield appears to be most prominent in the 80° detector, though it is also the case at the very lowest energies for all of the other detectors, particularly those at higher angles. Additionally, each plot has features resembling the high energy under estimation tail, meaning detector angle is likely not the cause of that trend. One of the most obvious features is the presence of the "arm" reaching up around 40 MeV; it is very clearly attributable to detector angle. It is most severe in the 80° detector but is also prominent in the 60° and 135° plots as well. While it is easier to call experimental results of the 80° detector into question for the reasons discussed earlier in the chapter, the trend's presence in the other two detectors at the highest angles makes it clear that this trend is not an experimental outlier. It appears that at above 10 MeV to 40 MeV the Monte Carlo codes over predict neutrons produced at high angles. Interestingly though, since the simulated neutron production appears to be roughly in line with the experimental results at lower angles, it would imply that either the models are over predicting total neutron production which manifests itself primarily at higher angles or there is indeed some unseen systematic issue with the experiment at the higher angles. Additionally, one can notice in the 10° plot (and to a lesser extent in the 30° and 45° plots) a hump where the codes consistently over predict the yields in the high energy forward peak from projectile fragment neutrons.

Figure 8.40 then compares each projectile ion species. All of these plots contain the low energy neutron depression and "arm" features discussed previously. However, the prominence of the high energy tail increases with increasing projectile mass, possibly implying that the codes are under predicting the production of the highest energy neutrons in heavier systems. Interestingly, it also seems that neutron production across all energies is under predicted for hydrogen projectiles and somewhat for helium projectiles (particularly at lower and intermediate energies), and neutron production is generally over predicted for projectiles of higher mass. This could imply that the Monte Carlo codes are over predicting the production of individual nucleons from these fragmentation reactions (rather than complex light ions), and this would scale with increasing projectile mass as observed here.

Lastly, Figure 8.41 shows these plots for each of the three projectile energies. Each plot possess the low energy neutron depression and "arm" features, but only the 400 MeV/n plot

features the prominent high neutron energy under prediction tail. As was shown in Figure 8.40, this tail also is increasingly prominent in the heavier projectiles. The cause of this could come from multiple sources. First, it is possible that this under prediction of the neutrons above the beam energy is from the models within the codes under estimating the impact of Fermi momentum. However, this could also partially be an artifact of the neutron production point correction discussed in Section 4.9 whose net effect was shifting the highest energy neutrons to even higher energies; it is possible that the production point correction could had slightly over compensated for the heavier projectiles. Though, this is likely not the case either since similar trends are seen with comparisons to cross section data. An additional note to be made of these plots is on the apparent quality of the experimental data. The results from the 1500 MeV/n beams generally suffered statistical issues, and this is apparent in Figure 8.41c where the spread in ratios is much greater than it is for the lower energy beams.

While the Monte Carlo codes are indeed in general agreement with the experimental data in most cases, there are strong discrepancies with the results above 10 MeV in the 60°, 80°, and 135° detectors where the codes consistently over predict the experimental results. While less severe, the Monte Carlo codes also appear to under predict neutron production at the energy extremes. At the lower energies, this under prediction is primarily seen in systems with upstream targets containing HDPE, though it also appears to be somewhat linked to the anomalies in the 60°, 80°, and 135° detectors too. The under prediction of the high energy neutron yield is predominantly from the 400 MeV/n beams, particularly those of heavier species. While this trend could be attributable to physics models within the code, this could also be partially an artifact of the neutron production point correction.

8.2.2 Monte Carlo vs. data: Downstream target results

This section is structured in the same fashion as the previous one except pertaining to the downstream target and room scattered neutron results obtained with the deconvolution methodology developed in this work. Figure 8.42 is the same as Figure 8.37 but for these downstream target and room scattered neutrons, showcasing the ratios of simulated to experimental results. Rather than appearing as a hazy cloud of points, discrete vertical

lines are present here from the discrete energy bins which were selected for each spectrum prior to deconvolution.

Similar to the previous section, the overall trends are quantified in Table 8.2. The quality of the simulated results here appear to be comparable to that of the upstream target neutrons with an even higher percentage of points within an order of magnitude of the experimental results (over 98.5% for both codes) and roughly the same percentage within a factor of two (around 70%). However, The Monte Carlo results seem to more often over predict the downstream target-produced neutrons than those from the upstream target with 62.31% of MCNP points and 71.9% of PHITS points being greater than the experimental values. Additionally, a larger discrepancy between MCNP and PHITS is present in these comparisons; the differences between the two transport codes are explored in greater detail in Sections 8.2.3 and 8.2.4.

The codes tend to consistently under predict the experimental results around 5 MeV but then consistently over predict them around 10 MeV; the model predictions then become, on average, centered at roughly the experimental value at 20 MeV and slowly trend toward

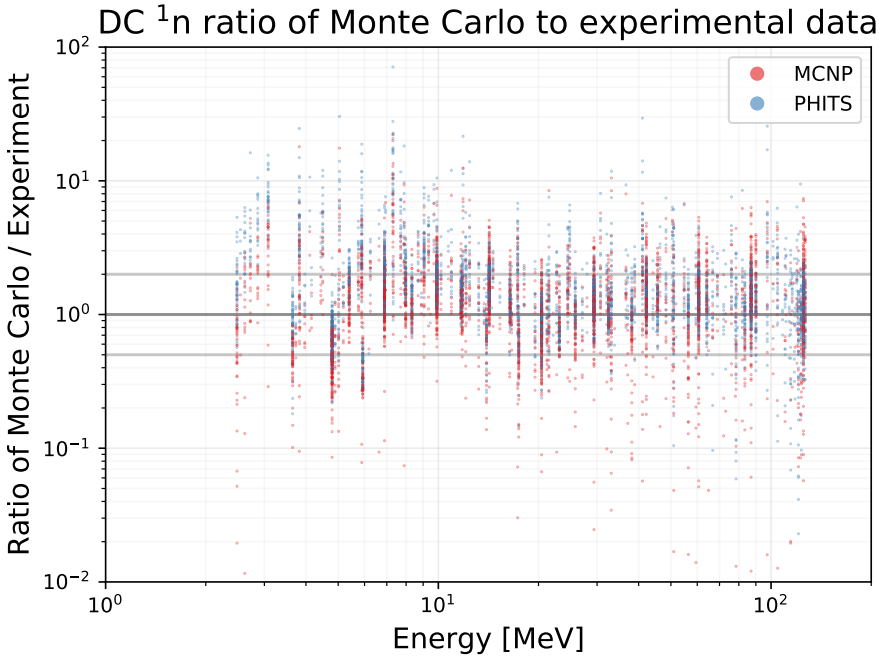


Figure 8.42: Ratio of Monte Carlo results to experimental results for every data point from the downstream target neutron dataset

Table 8.2: Downstream target neutron overall results comparison to Monte Carlo

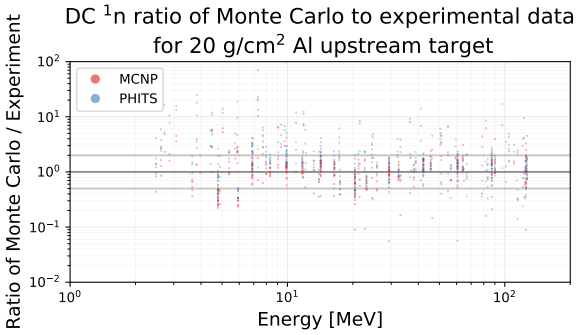
Quantity	MCNP	PHITS
Median ratio	1.202	1.351
Mean ratio	1.470	1.900
Percentage of ratios over 1	62.31%	71.90%
Percentage of points within a factor of 10	98.53%	98.60%
Percentage of points within a factor of 2	67.55%	70.82%

over prediction at higher energies. This could be an artifact of the deconvolution and regularization processes. Additionally, the spread in how well the Monte Carlo codes predict the data appears to increase at higher neutron energies.

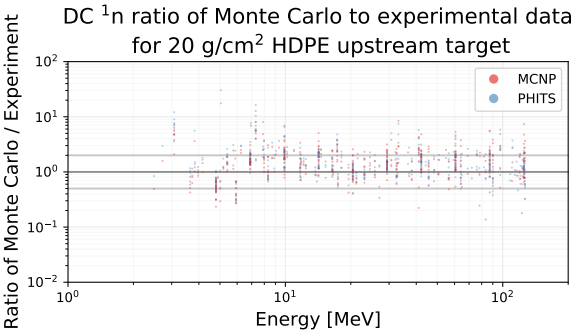
Similar to the previous section, the following four pages contain plots showcasing versions of Figure 8.42 where individual experimental axes are isolated. Figure 8.43 isolates the various upstream target combinations; Figure 8.44 isolates each detector angle. Figure 8.45 isolates each projectile ion species, and Figure 8.46 isolates each projectile ion energy.

Spotting trends in these plots is somewhat more challenging than it was for the upstream target neutrons due to the discrete vertical lines. First, in Figure 8.43 an initial glance does not yield anything obvious. After closer inspection though, one may note that the degree of over prediction of the Monte Carlo codes changes as a function of target thickness. For the HDPE and AlPE targets, the over prediction is least severe for the 60 g/cm^2 thickness. While not as apparent, a similar trend is subtly present in the plots for the aluminum targets as well. Overall, this effect is minimal.

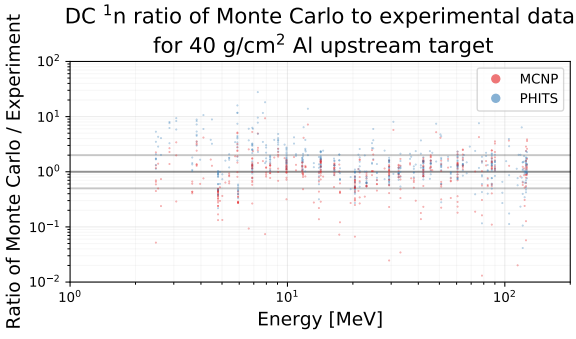
Figure 8.44 shows a few trends across the various detector angles. As a reminder, it should be noted that there are fewer spectra for the higher angled detectors due to the lack of sufficient statistics for deconvolution. Of these results, it appears that the 10° and 30° simulated results best agree with the experimental data, and the results for the 45° and 60° detectors also compare reasonably well. This is fortunate since these detectors are closest to the downstream target. Of note is the divergence in the predictions of MCNP and PHITS at higher neutron energies at 10°; this is covered in greater detail later in Section 8.2.4. The depression in neutron production around 5 MeV is present in the 10°, 30°, and 45° detectors. The 80° results show significant over prediction by the codes below 10 MeV, and the spread



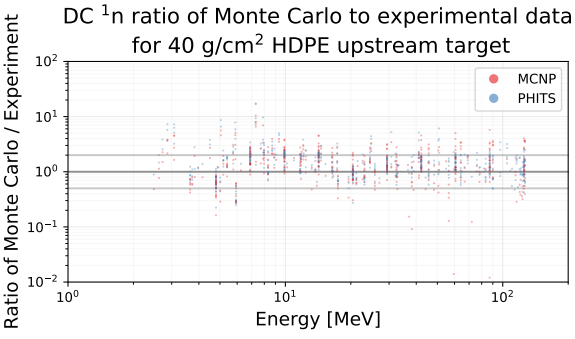
(a) 20 g/cm^2 Al



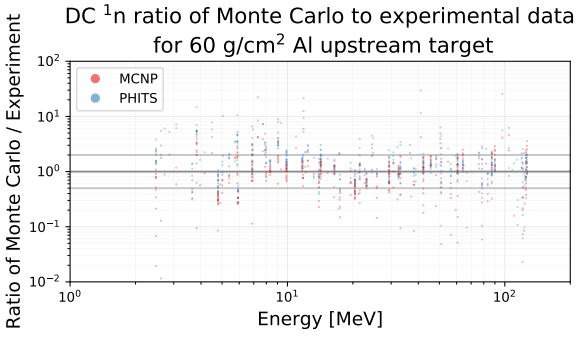
(b) 20 g/cm^2 HDPE



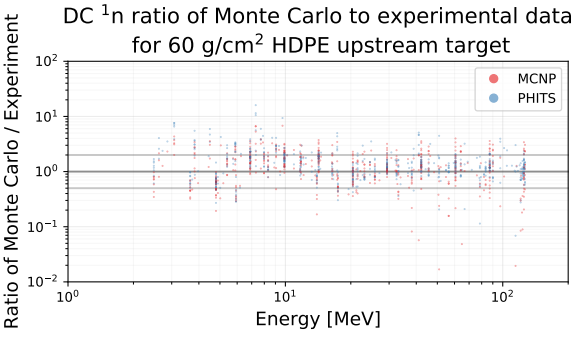
(c) 40 g/cm^2 Al



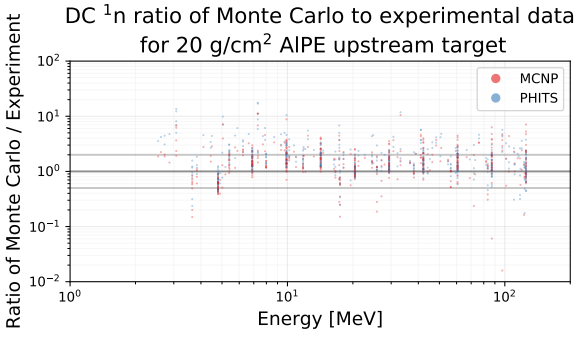
(d) 40 g/cm^2 HDPE



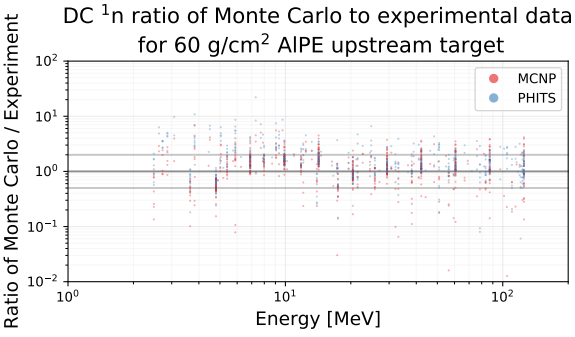
(e) 60 g/cm^2 Al



(f) 60 g/cm^2 HDPE

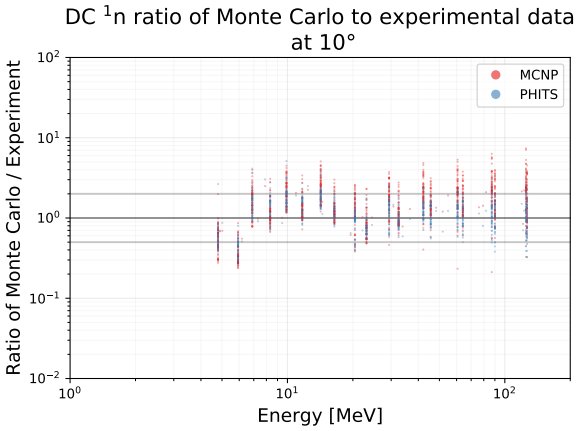


(g) 20 g/cm^2 AlPE

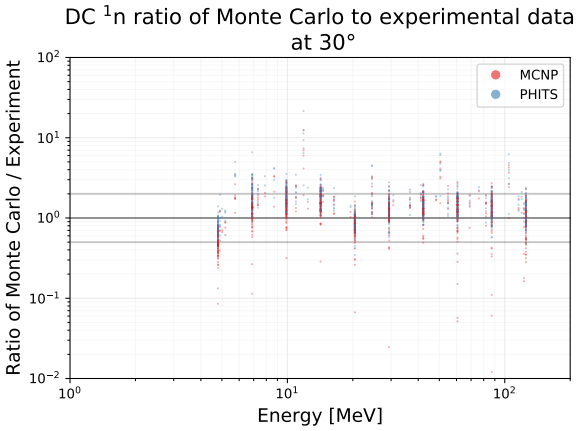


(h) 60 g/cm^2 AlPE

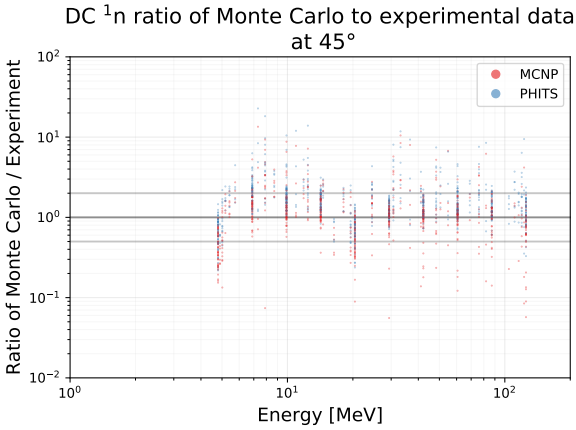
Figure 8.43: Components of Figure 8.42 for each front target



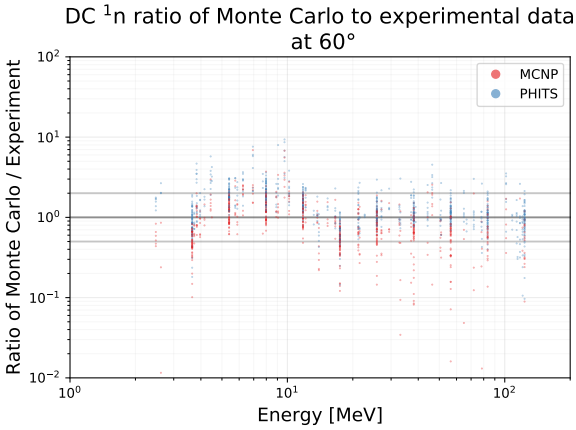
(a) 10°



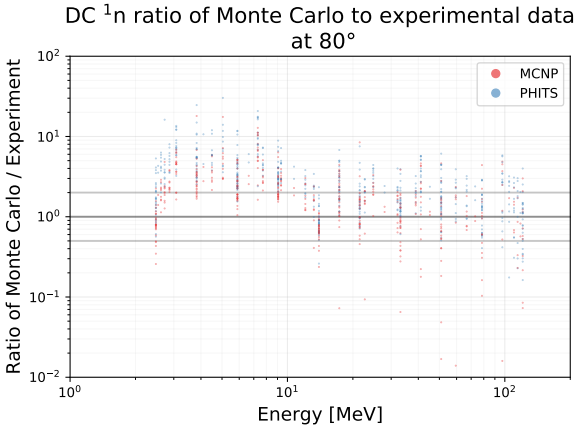
(b) 30°



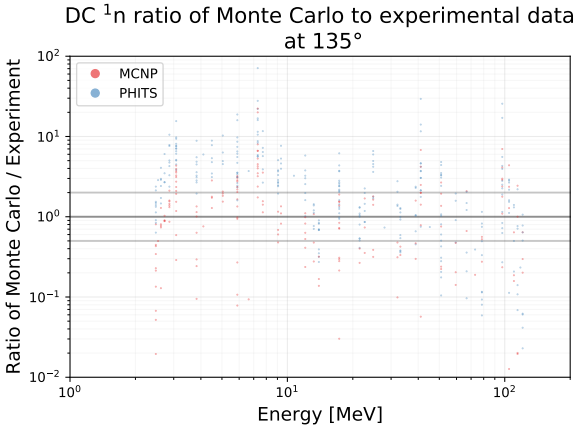
(c) 45°



(d) 60°

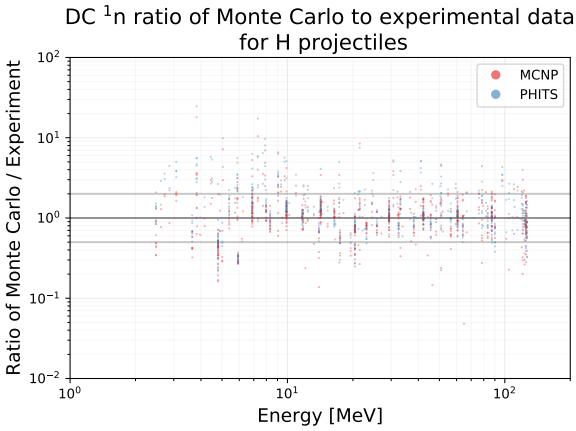


(e) 80°

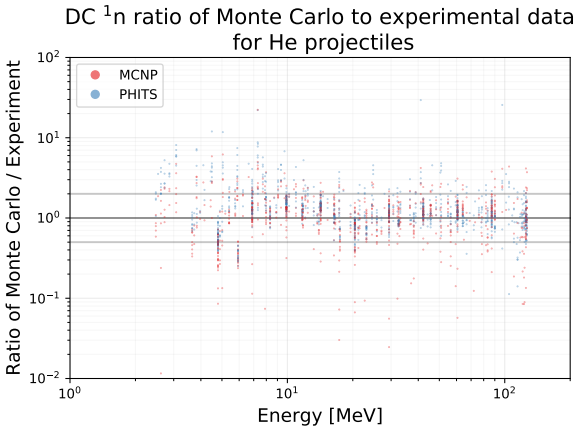


(f) 135°

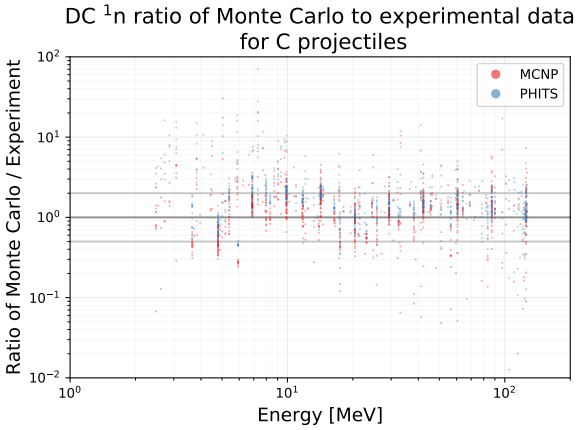
Figure 8.44: Components of Figure 8.42 for each detector angle



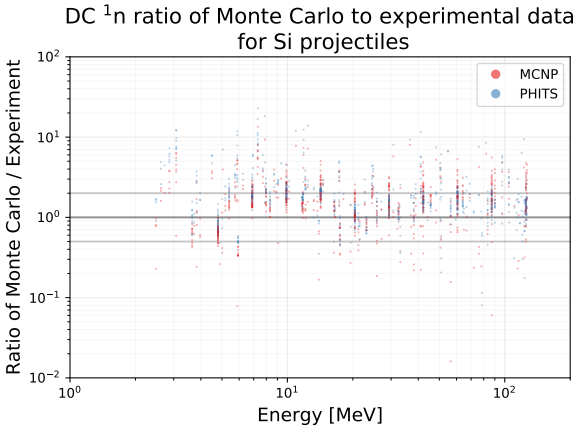
(a) H



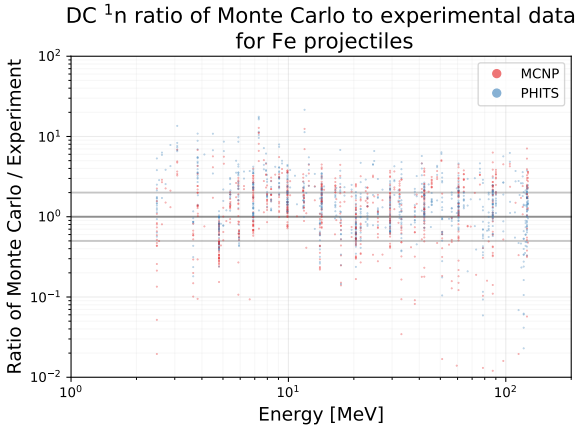
(b) He



(c) C

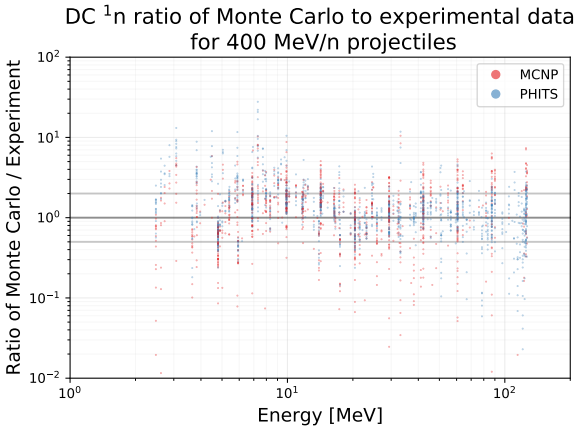


(d) Si

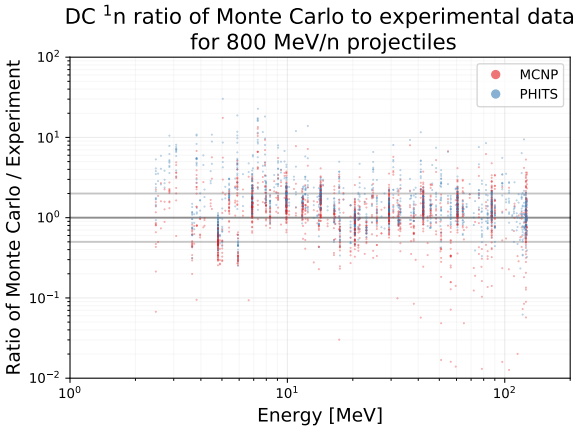


(e) Fe

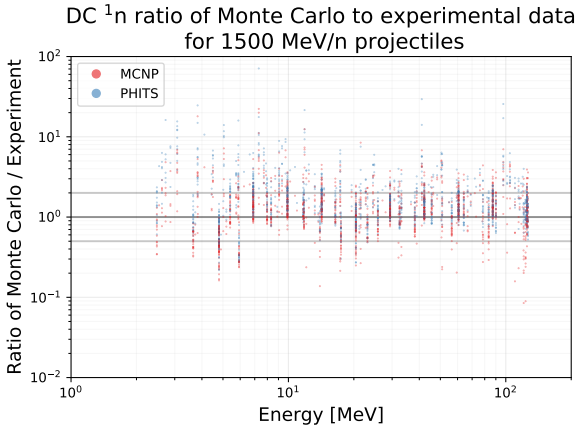
Figure 8.45: Components of Figure 8.42 for each projectile species



(a) 400 MeV/n



(b) 800 MeV/n



(c) 1500 MeV/n (2500 MeV for H)

Figure 8.46: Components of Figure 8.42 for each projectile energy

in how well the codes predict the experimental results is higher across all energies for the 80° and 135° detectors. While these large angle detectors are less important for this analysis since they are more influenced by neutrons scattering throughout the room rather than those produced in the downstream target, it is still interesting to note. As noted earlier, some of these systematic trends in the spectra, such as the dip around 20 MeV, could partially be an artifact of the deconvolution and regularization processes rather than a model discrepancy, though that too is possible.

Next, Figure 8.45 shows the impact of each source ion species on the overall trends. While subtle, the degree of over prediction of the codes appears to increase with increasing projectile mass. This trend is in line with what was observed with the upstream target neutron modeled results as a function of projectile mass. One may also note that the under prediction at 5 MeV is most severe for hydrogen (and helium) and less for the heavier projectiles. The over prediction at 10 MeV also appears to be more severe for the heavier projectiles. The increase in deviation of the models from the experimental data at higher energies appears to also increase with projectile mass.

Lastly, the trends for each beam energy are shown in Figure 8.46. Interestingly, the 1500 MeV/n results tend to be in the most agreement with the experimental results; the variance in the performance of the codes against the data, particularly at high neutron energies, increases at lower beam energies. Notably, and as will be explored more later in Section 8.2.4, the MCNP and PHITS predictions for high energy neutrons for the lower beam energies diverge. For PHITS, the over prediction of neutron yield increases with increasing beam energy; the opposite appears to be true for MCNP.

Discerning trends in the comparison of the Monte Carlo codes to the deconvoluted results is more challenging than it was for the upstream target-produced neutrons, but some trends exist that are worth discussion. Most notably, the over prediction of neutron yield scaling with projectile mass agrees with what was found with the upstream target results, hinting at a possible area for improvement within the transport code models. Additionally, the codes appear to better predict results for the detectors closest to the downstream target.

The discrepancies between the downstream target neutron simulated and experimental results could originate from a number of factors. First, these neutron datasets are far

more sensitive to the modeled room geometry than the upstream results; simplifications in the room model could have had some bearing on these trends. Next, a portion of these discrepancies could be attributable to the deconvolution and regularization processes. Lastly, some of these discrepancies are likely attributable to the physics models within the transport codes themselves. Distinguishing these sources is somewhat challenging, though the trends observed in both this dataset and the upstream target dataset make a reasonably strong case for some issues being within the Monte Carlo codes.

8.2.3 PHITS vs. MCNP: Upstream target results

In this and the following section, the ratio of the PHITS to the MCNP results is analyzed in a similar fashion to the previous two sections. This section pertains to the upstream target-produced neutrons while the following section explores the downstream target-produced and room scattered neutrons. Figure 8.47 shows a similar plot as earlier but focused in on a factor of plus or minus one order of magnitude rather than two. Generally, the PHITS and MCNP codes agree with each other more than they do with the experimental data, though

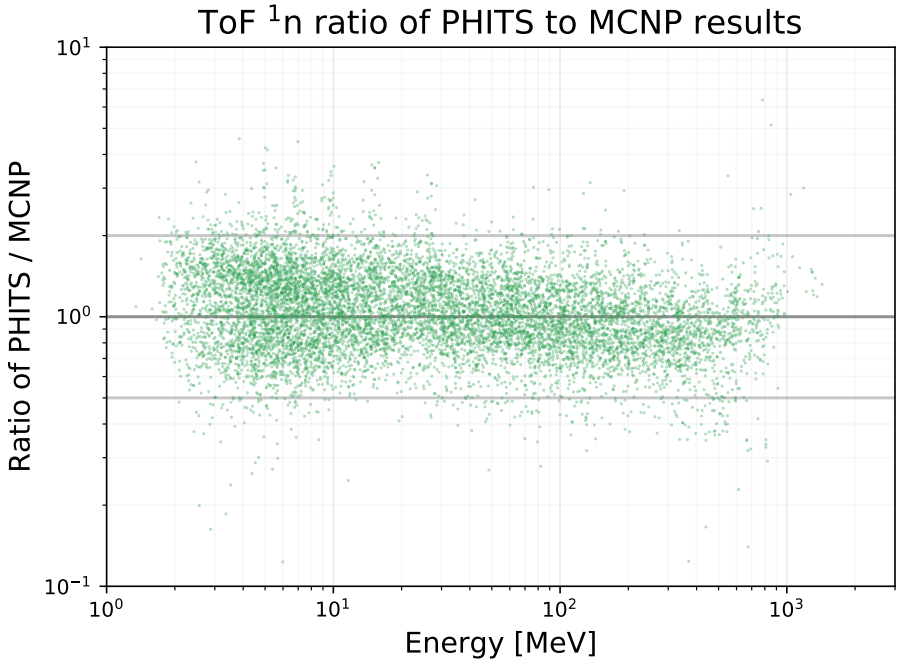


Figure 8.47: Ratio of PHITS results to MCNP results for every data point from the upstream target neutron dataset

Table 8.3: Upstream target neutron overall comparison of PHITS vs. MCNP

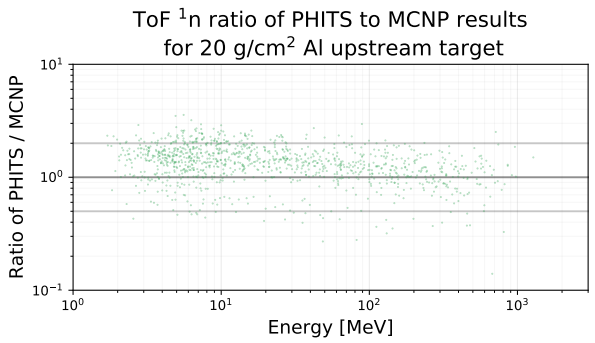
Quantity	Value
Median ratio	1.033
Mean ratio	1.1056
Percentage of ratios over 1	53.57%
Percentage of points within a factor of 10	99.96%
Percentage of points within a factor of 2	94.98%

some variance is present. Of particular note, PHITS appears to over predict MCNP at lower energies and under predict MCNP at higher energies. Since the geometry and tally methodologies between MCNP and PHITS were fundamentally the same for the upstream target analysis, this provides a fair comparison of how the two codes perform against each other for these experimental systems.

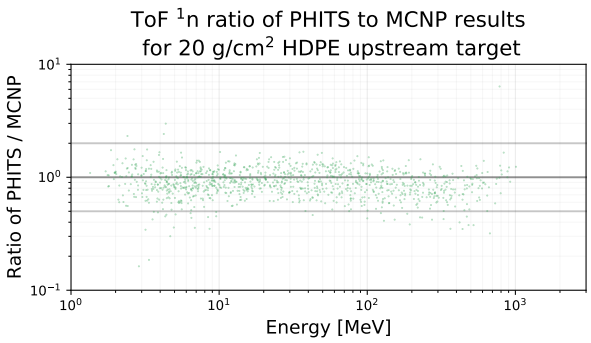
Table 8.3 contains some of the statistical values highlighting the general agreement of the two codes. The PHITS results exceed the MCNP predictions 53.6% of the time, and the PHITS results are within an order of magnitude of the MCNP results 99.96% of the time and within a factor of two almost 95% of the time. This illustrates strong general agreement between the two codes. However, just because this is true over all results does not necessarily mean it will remain so when studying individual experimental axes.

In a similar fashion to the previous sections, the following four pages show Figure 8.47 but isolating the various experimental axes—upstream target (Figure 8.48), detector angle (Figure 8.49), projectile species (Figure 8.50), and projectile energy (Figure 8.51).

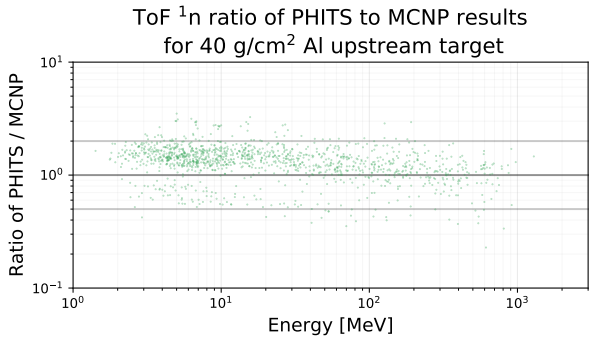
Before discussing the trends and differences, a note should be made about the phrasing and intent here to avoid confusion. In this and the following section, PHITS is being compared relative to MCNP. This choice was arbitrary, and the opposite could had been done instead. So, when speaking of PHITS relative to MCNP, one should not interpret the discrepancies as being flaws in PHITS not present within MCNP; the very opposite could be the case. It is simply convenient to select one code as a baseline to compare the other to. Any phrase in this section could be reversed to say the opposite about MCNP relative to PHITS. A more concrete picture of the absolute performance of each code can be made by



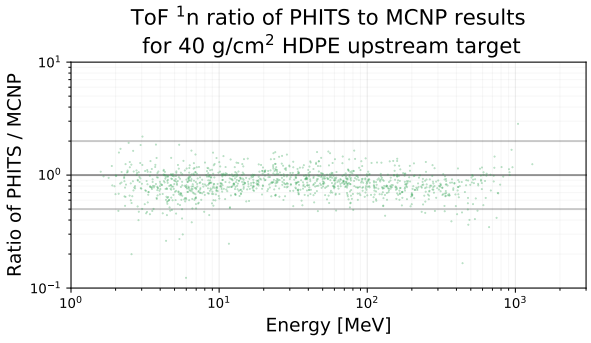
(a) 20 g/cm^2 Al



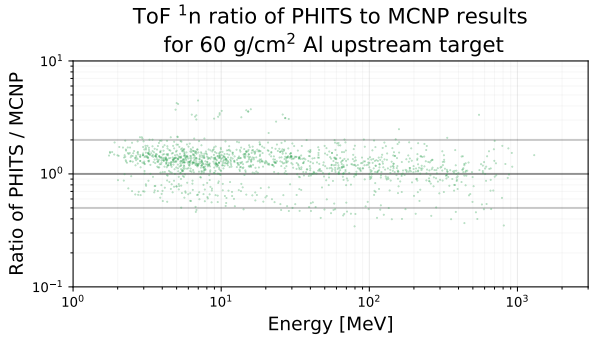
(b) 20 g/cm^2 HDPE



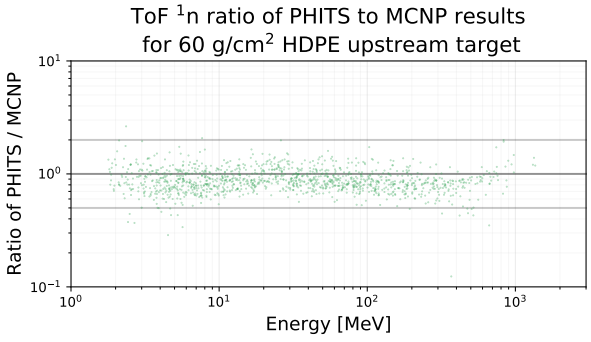
(c) 40 g/cm^2 Al



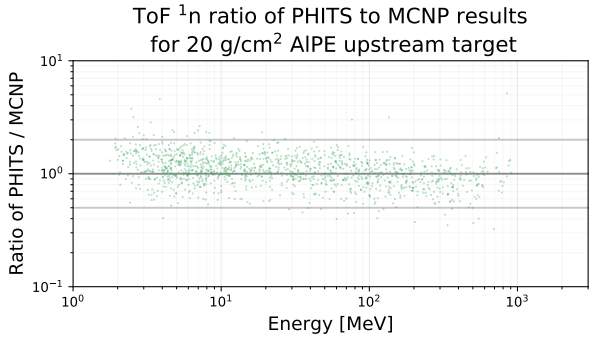
(d) 40 g/cm^2 HDPE



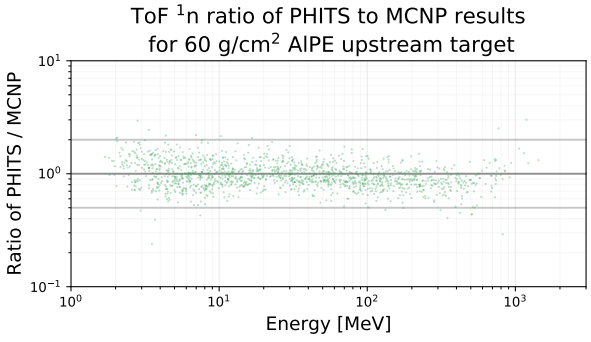
(e) 60 g/cm^2 Al



(f) 60 g/cm^2 HDPE

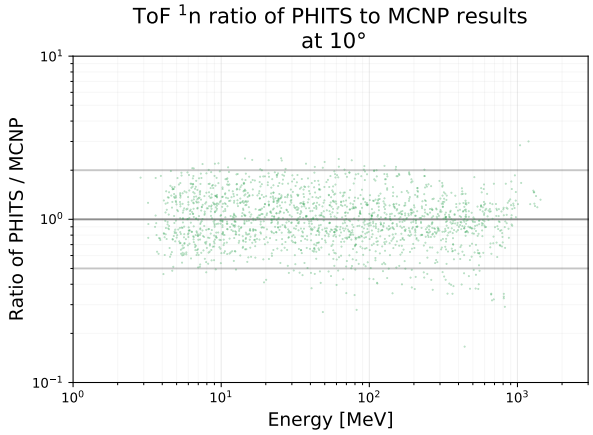


(g) 20 g/cm^2 AlPE

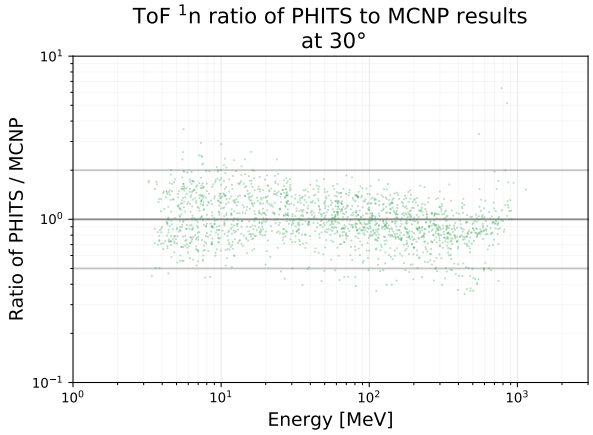


(h) 60 g/cm^2 AlPE

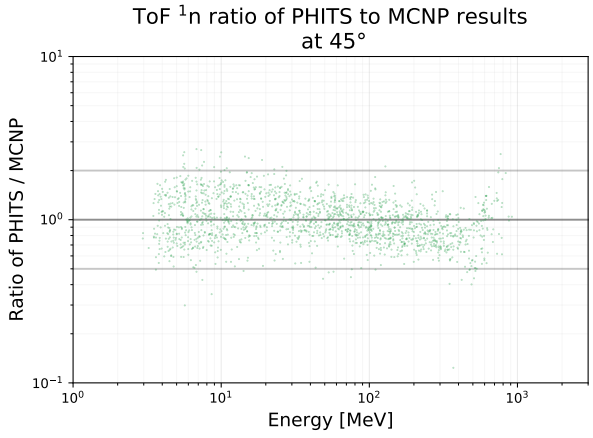
Figure 8.48: Components of Figure 8.47 for each front target



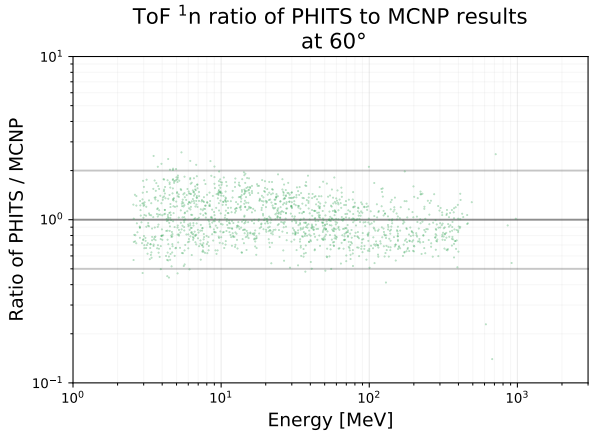
(a) 10°



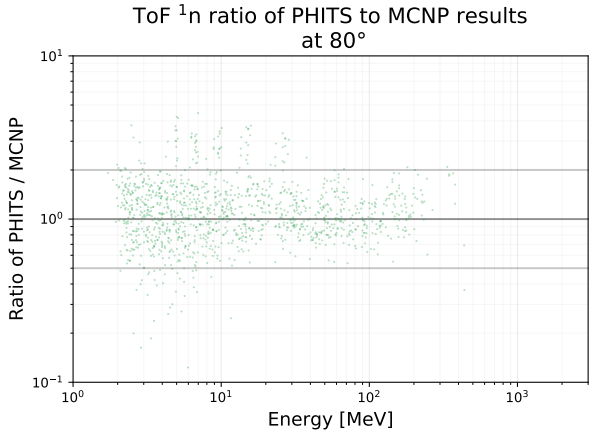
(b) 30°



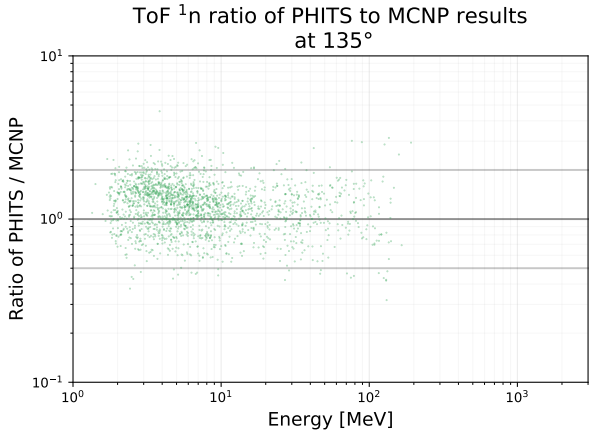
(c) 45°



(d) 60°

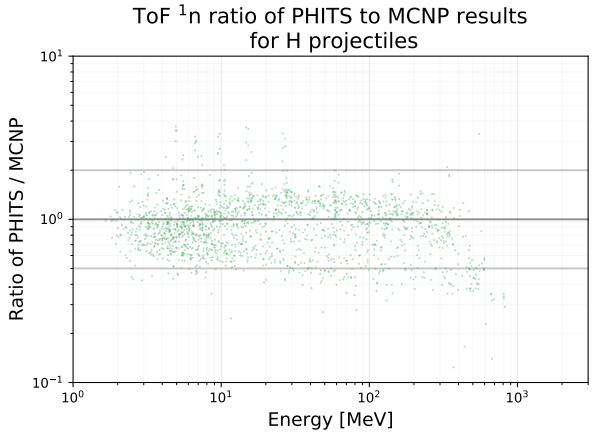


(e) 80°

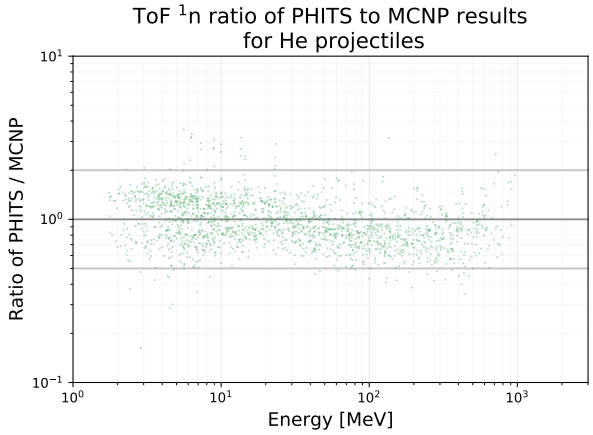


(f) 135°

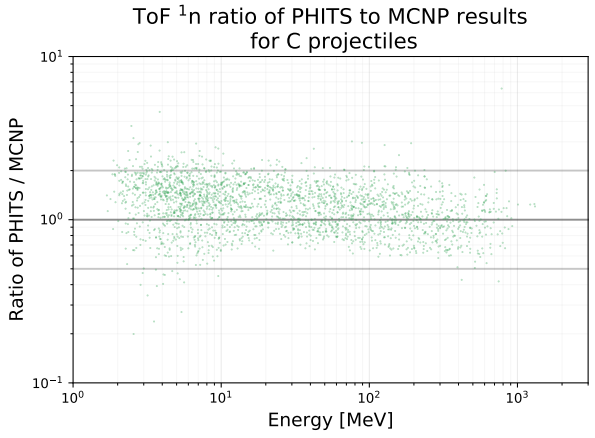
Figure 8.49: Components of Figure 8.47 for each detector angle



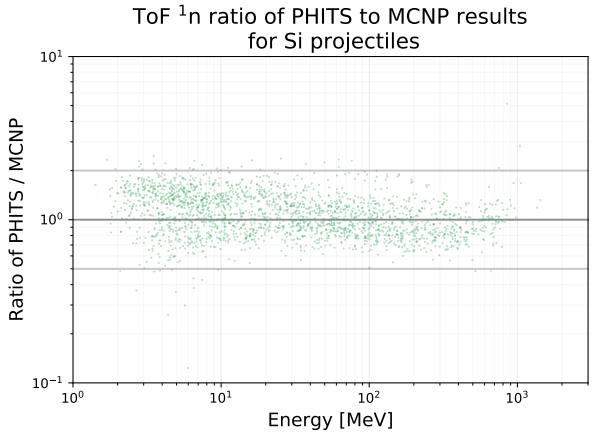
(a) H



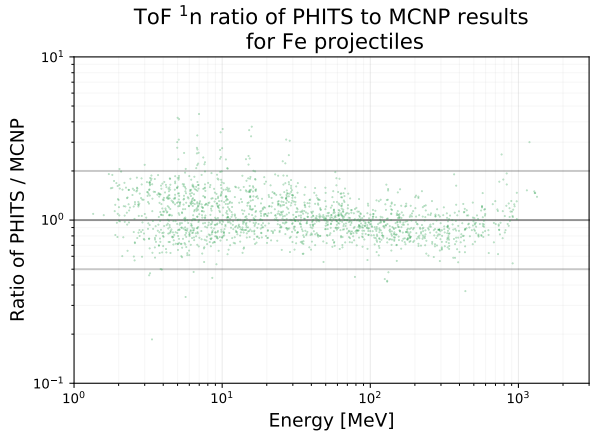
(b) He



(c) C

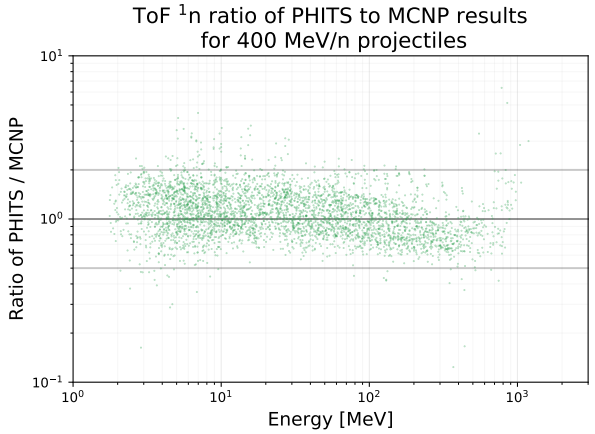


(d) Si

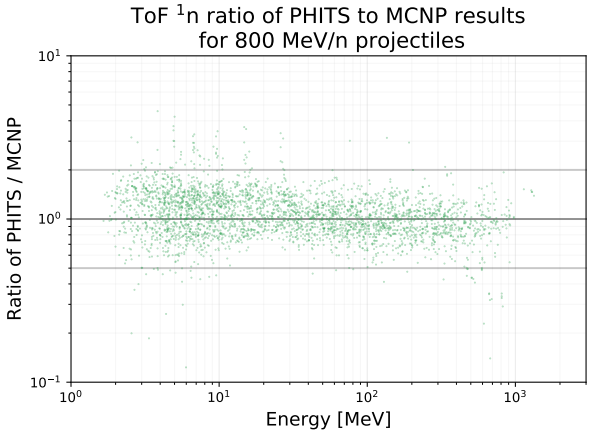


(e) Fe

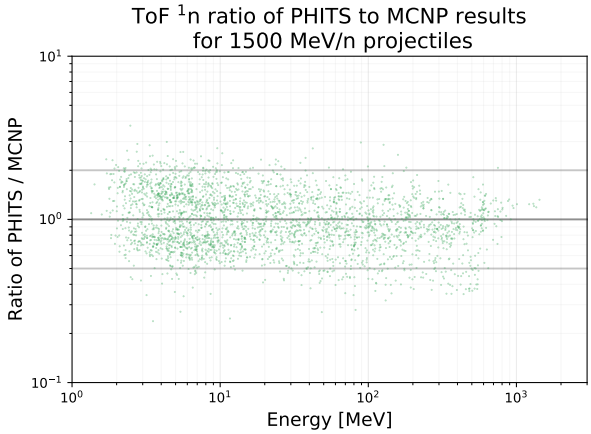
Figure 8.50: Components of Figure 8.47 for each projectile species



(a) 400 MeV/n



(b) 800 MeV/n



(c) 1500 MeV/n (2500 MeV for H)

Figure 8.51: Components of Figure 8.47 for each projectile energy

combining the comments of this section with those made earlier in Section 8.2.1, an exercise performed later in Section 8.2.5.

Upon investigating Figure 8.48, a clear trend emerges: PHITS predicts higher neutron yields from aluminum upstream targets than MCNP but lower yields from HDPE targets. This trend is more severe for the aluminum targets than it is for the HDPE targets. In the 20 g/cm^2 AlPE target, which is composed of 10 g/cm^2 of each material, PHITS still consistently over predicts MCNP. However, with the 60 g/cm^2 target, the increased neutron yields from the 10 g/cm^2 aluminum appears to just about cancel out the relative under prediction from the 50 g/cm^2 of HDPE. These trends are apparent at all energies but slightly more prevalent at lower neutron energies.

Next, Figure 8.49 shows the relative performance of the codes as a function of detector angle. The trends here are less informative of any differences between the codes because MCNP and PHITS are generally in close agreement, but one can note that PHITS generally under predicts MCNP at 10° through 60° above 100 MeV. Additionally, PHITS over predicts MCNP at 80° and 135°, particularly at lower energies (less than around 30 MeV).

The PHITS predictions relative to MCNP's are shown for the various projectile ion species in Figure 8.50. For hydrogen and helium projectiles, PHITS generally under predicts MCNP, though some outliers appear below 30 MeV where the reverse is true. For the three heavier projectiles, PHITS generally over predicts MCNP at lower energies and under predicts MCNP at higher energies.

Figure 8.51 shows this comparison for the three categories of projectile energy. While the two codes are in general agreement, the case of PHITS over predicting neutron yield at low neutron energies and under predicting yield at high neutron energies relative to MCNP is most severe for 400 MeV/n projectiles. Interestingly, this trend appears more prevalent for 1500 MeV/n than 800 MeV/n, meaning that this discrepancy does not just scale monotonically with beam energy.

So, the most interesting trend observed in this analysis between the two codes is that PHITS predicts greater neutron yields for aluminum targets but lower yields for HDPE targets. Additionally, the over prediction of low-energy neutrons and under prediction of high-energy neutrons relative to MCNP appears to be a consistent trend.

8.2.4 PHITS vs. MCNP: Downstream target results

Like the previous section, this section seeks to compare the two Monte Carlo codes to each other except for the downstream target-produced and room scattered neutrons. One should note that unlike the upstream target-produced neutrons, the methodologies employed to tally the downstream target and room scattered neutrons in PHITS were slightly different to those used in MCNP as was discussed in Chapter 7. As a result, it is possible that differences in these methodologies are at least partially the cause of discrepancies present between the two codes here. Figure 8.52 shows the ratio of the PHITS to MCNP results for every final data point. Generally, PHITS predicts greater yields than MCNP, particularly at lower energies.

Table 8.4 summarizes the overall differences observed between the two codes. Here, agreement between the two codes is much less strong. While 98.63% of MCNP and PHITS points are within an order of magnitude of each other, only 82.91% are within a factor of two, much worse agreement than what was seen for the upstream target-produced neutrons. Additionally, just over 70% of PHITS points were greater than their MCNP equivalents.

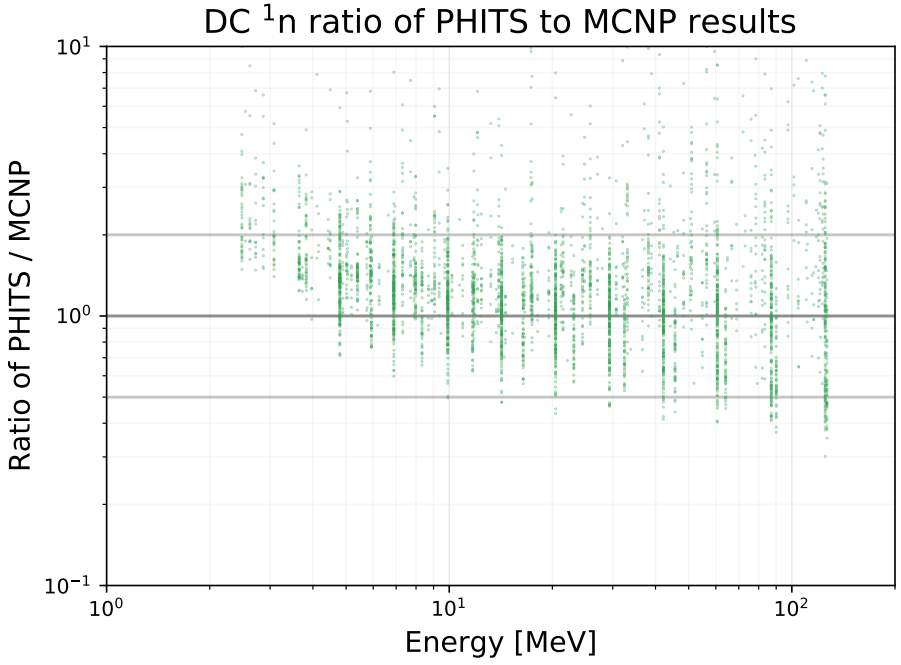


Figure 8.52: Ratio of PHITS results to MCNP results for every data point from the downstream target neutron dataset

Table 8.4: Downstream target neutron overall comparison of PHITS vs. MCNP

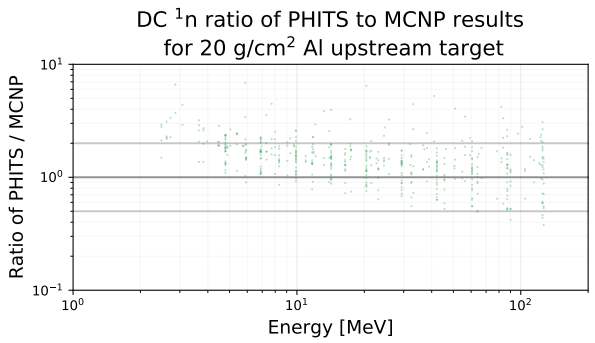
Quantity	Value
Median ratio	1.2307
Mean ratio	2.9296
Percentage of ratios over 1	70.31%
Percentage of points within a factor of 10	98.63%
Percentage of points within a factor of 2	82.91%

As with the previous sections, Figure 8.52 is shown on the following four pages gated along the various experimental axes—upstream target (Figure 8.53), detector angle (Figure 8.54), projectile species (Figure 8.55), and projectile energy (Figure 8.56).

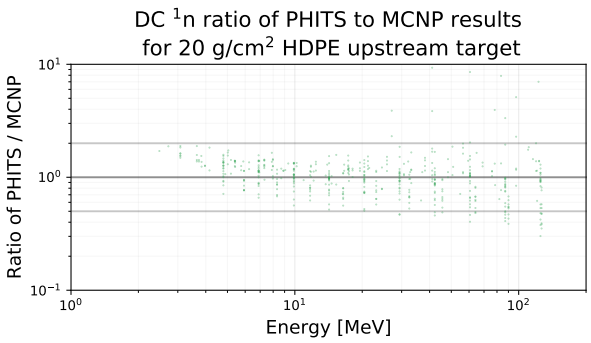
The same trends with the target materials seen in the previous section are also present here as shown in Figure 8.53: PHITS over predicts MCNP for neutron yields from aluminum targets and under predicts MCNP for yields from HDPE targets. Since a large number of the neutrons present in these spectra are produced in the downstream target, one would expect the hybrid target trends to follow those of the HDPE upstream target rather than straddle the aluminum and HDPE trends since the 60 g/cm^2 HDPE downstream target was used with the AlPE upstream targets. Looking at Figures 8.53g and 8.53h in comparison to Figures 8.53b and 8.53f, this is indeed the case. This serves as a reasonably strong confirmation of the trend of differing neutron production in aluminum and HDPE between PHITS and MCNP.

Studying Figure 8.54 where each detector angle is compared, some more interesting trends arise. At 10°, PHITS tends to under predict MCNP; the opposite is true at all other detector angles. In fact, the degree by which the PHITS results exceed MCNP's increases with increasing detector angle. While this could be an interesting difference between the physics models within the two codes, it is quite likely that this discrepancy stems from how the background/downstream target neutron tallies were isolated in MCNP. Still, the two codes remain in reasonable agreement for the detectors closest to the downstream target.

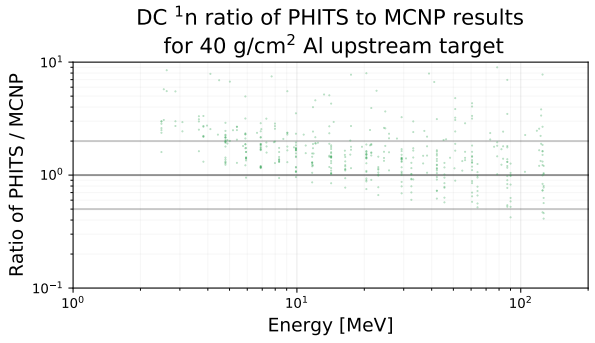
Next, Figure 8.55 compares the projectile species. The general trends tend to be the same for every projectile species. The primary difference is that the variance in how well the codes agree/disagree increases for the heavier projectiles.



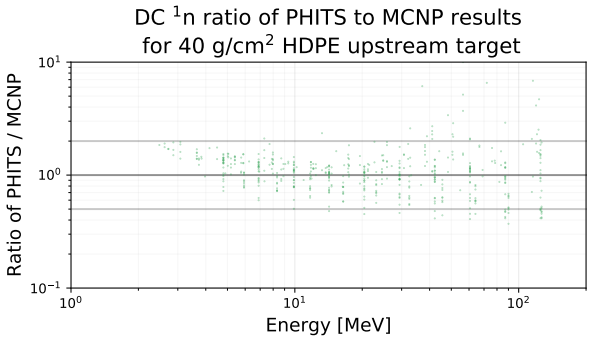
(a) 20 g/cm^2 Al



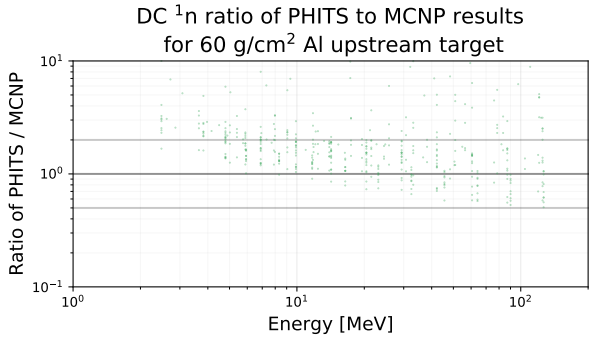
(b) 20 g/cm^2 HDPE



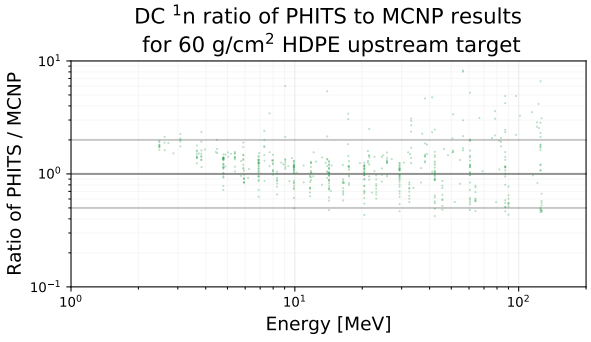
(c) 40 g/cm^2 Al



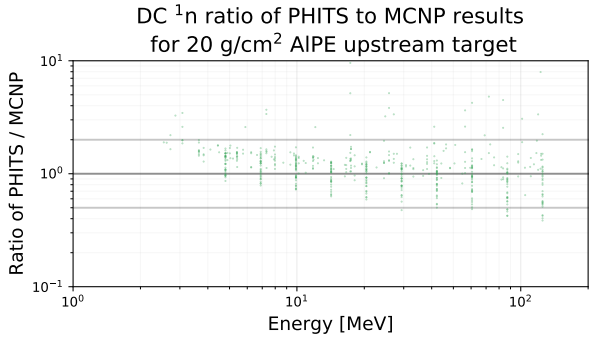
(d) 40 g/cm^2 HDPE



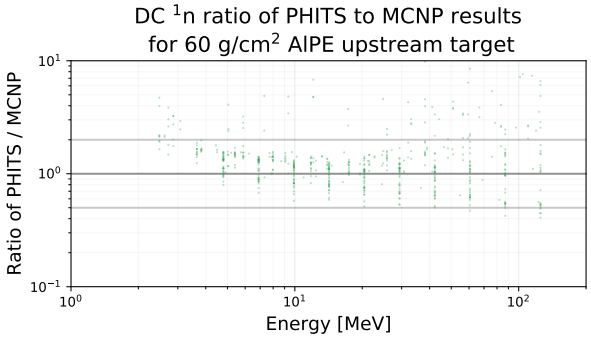
(e) 60 g/cm^2 Al



(f) 60 g/cm^2 HDPE

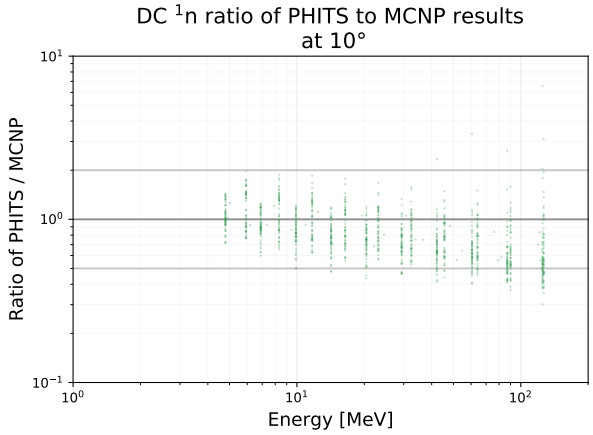


(g) 20 g/cm^2 AlPE

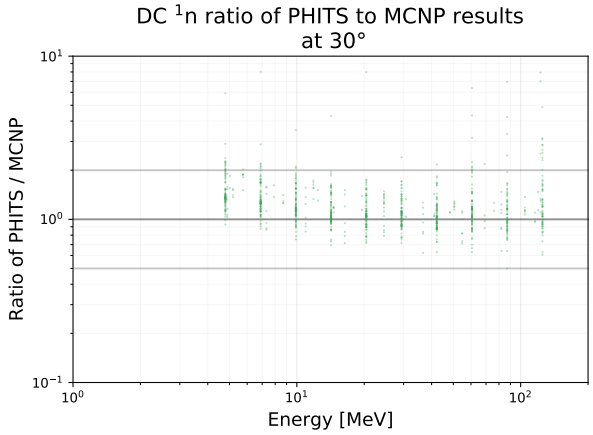


(h) 60 g/cm^2 AlPE

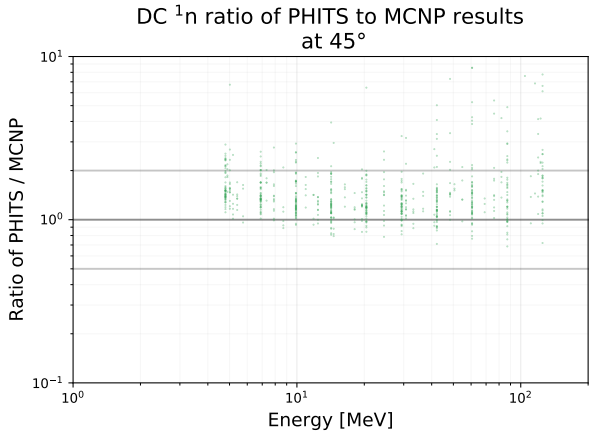
Figure 8.53: Components of Figure 8.52 for each front target



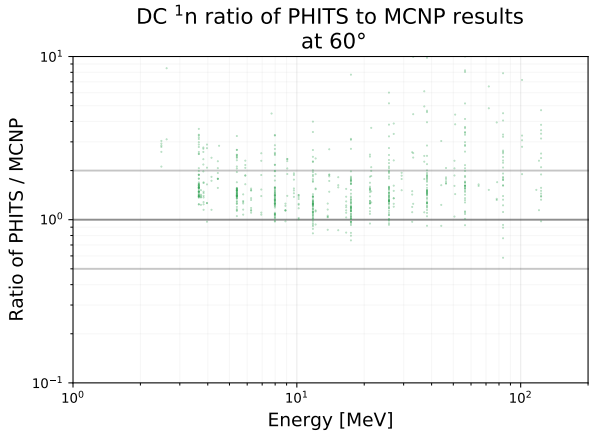
(a) 10°



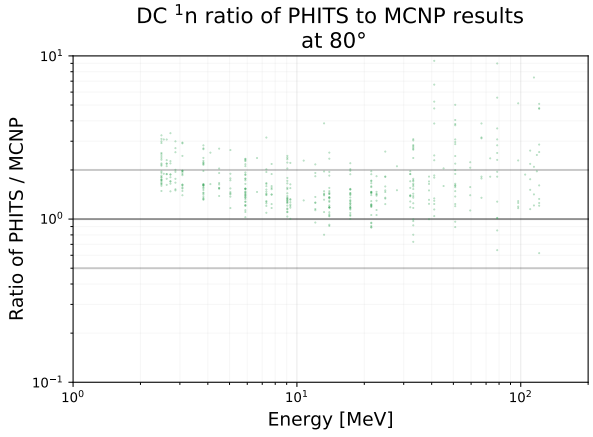
(b) 30°



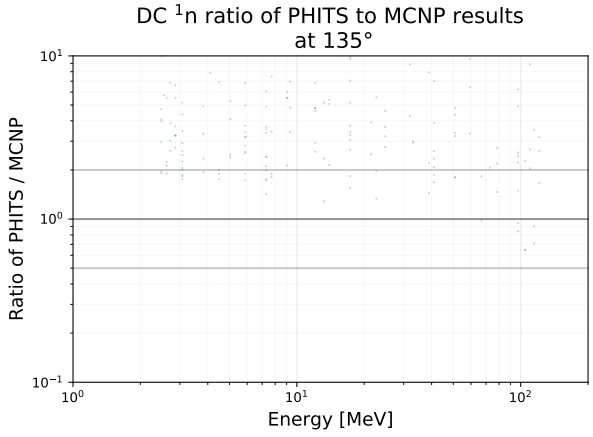
(c) 45°



(d) 60°

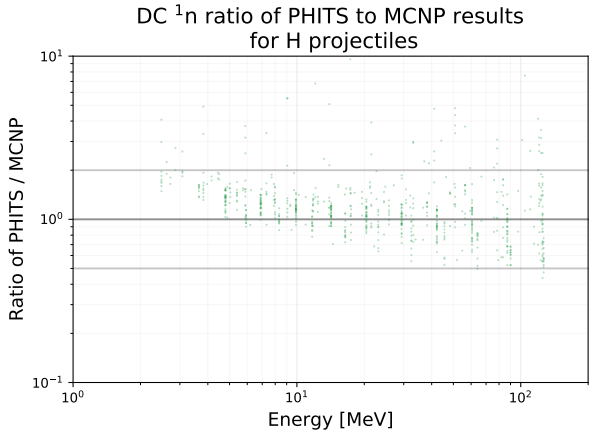


(e) 80°

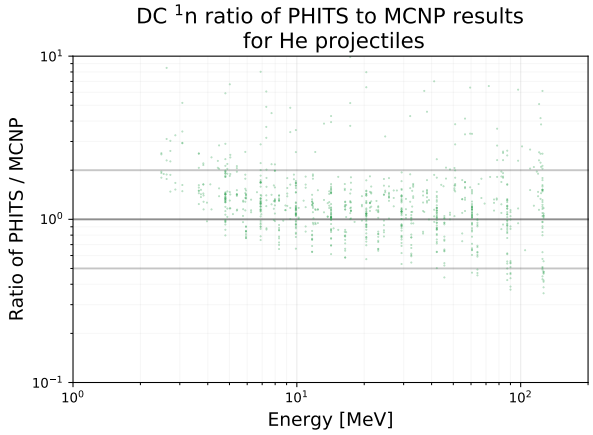


(f) 135°

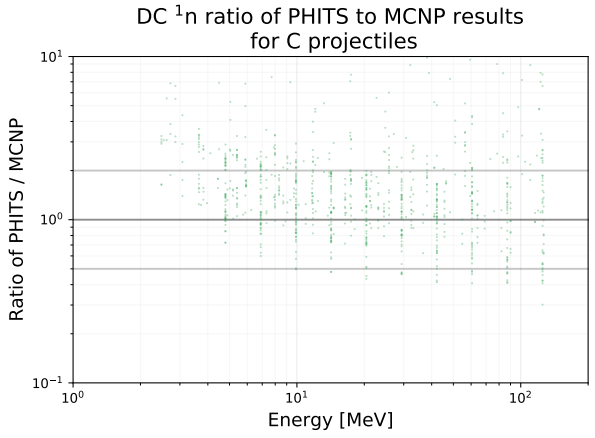
Figure 8.54: Components of Figure 8.52 for each detector angle



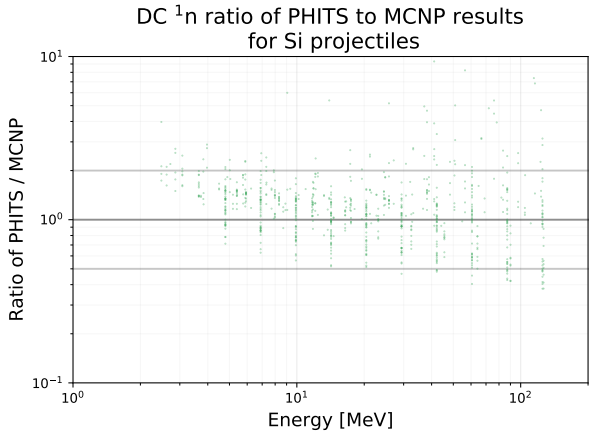
(a) H



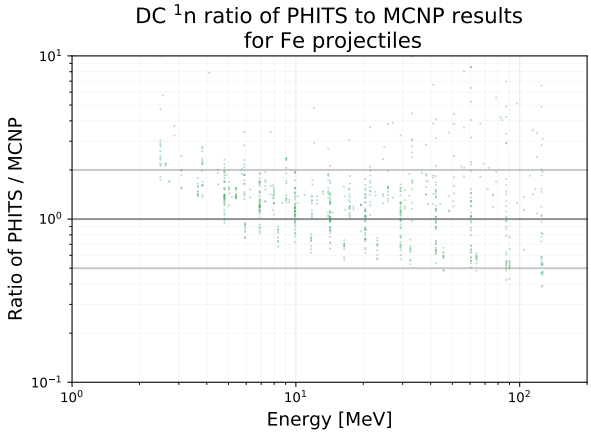
(b) He



(c) C

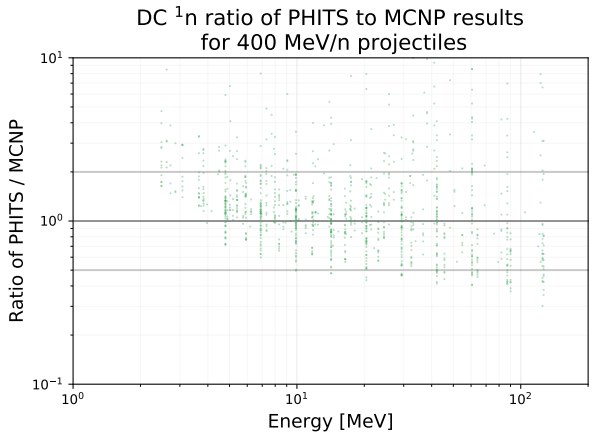


(d) Si

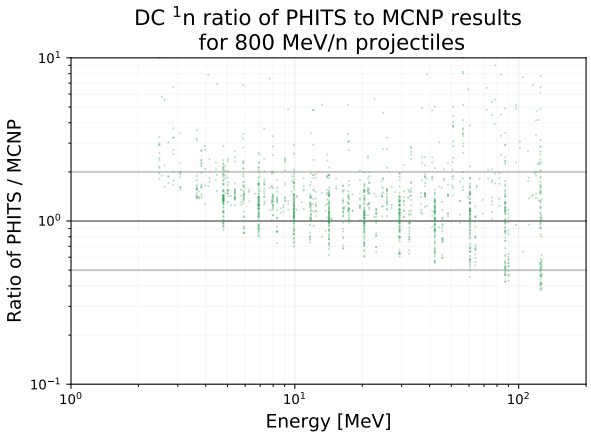


(e) Fe

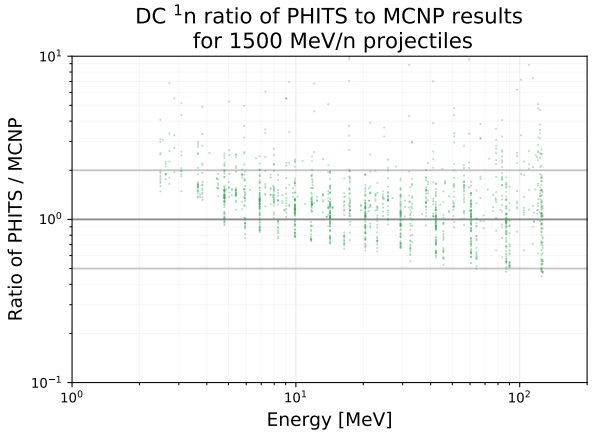
Figure 8.55: Components of Figure 8.52 for each projectile species



(a) 400 MeV/n



(b) 800 MeV/n



(c) 1500 MeV/n (2500 MeV for H)

Figure 8.56: Components of Figure 8.52 for each projectile energy

Lastly, the projectile energies are compared in Figure 8.56. Interestingly, the codes actually best agree with each other for the 1500 MeV/n projectiles with the disagreement increasing at lower beam energies. This is quite likely due to more beam particles penetrating the upstream targets at 1500 MeV/n, resulting in increased relative contribution from the downstream target. This would imply that the increased disagreement for 400 MeV/n projectiles stems from the room scattered neutron contribution.

So, the most interesting conclusion from this analysis seems to be the additional confirmation of the target material discrepancy. The over prediction of PHITS relative to MCNP at lower energies is largely driven by the 30° and higher angled detectors, and the under prediction at higher energies is largely driven by the 10° detector. While some of these discrepancies could likely be attributed to the differences in tally methodology, intrinsic differences in the codes and their physics models certainly play a role.

8.2.5 Summary of the performance of PHITS and MCNP

This section seeks to briefly summarize the individual performances of PHITS and MCNP in this work relative to the experimental data and where the two codes differ. This is done by combining observations made in the previous four sections. For the sake of convenience, the key trends observed when comparing the Monte Carlo codes against the experimental results are listed below.

- Both Monte Carlo codes under predict low energy neutron yields in systems with upstream targets containing HDPE.
- The 80° detector is attributable for most of this low energy under prediction, though at the very lowest energies the trend is present in all detectors.
- Both Monte Carlo codes severely over predict neutron yield above 10 to 40 MeV at the highest detector angles, primarily in the 80° detector but also significantly in the 60° and 135° detectors (at least by a factor of 2 and often approaching a factor of 10).
- Both codes over predict the high energy peak from projectile fragment neutrons (typically by a factor of about 2 but sometimes as high as 5).

- In general, across all energies neutron production is under predicted for hydrogen projectiles and for increasing projectile mass beyond helium eventually becomes over predicted. This is seen in both the upstream and downstream target neutron datasets.
- High energy neutron production is under predicted for heavier projectiles at 400 MeV/n.

Additionally, the main trends observed when comparing the PHITS and MCNP results to each other are summarized in the list below.

- As a general trend, PHITS predicts higher neutron yields at lower neutron energies than MCNP and lower yields at higher energies. This is generally true for both upstream and downstream target datasets.
- PHITS predicts notably greater neutron yields from aluminum targets than MCNP. MCNP, on the other hand, predicts greater neutron yields than PHITS for HPDE targets, though the extent of this effect is slightly less severe than that for aluminum. This trend is clearly present in both upstream and downstream target datasets.
- PHITS generally over predicts MCNP, and this is more severe for the downstream target results than for the upstream target results. This is likely primarily an artifact of the previous point.
- Above 100 MeV at angles from 10° through 60°, MCNP predicts greater upstream target-produced neutron yields than PHITS.
- Below 30 MeV and at 80° and 135°, PHITS over predicts MCNP in production of neutrons from the upstream target.
- PHITS generally predicts lower yields than MCNP for hydrogen and helium projectiles. For heavier projectiles, the earlier stated trend of PHITS over predicting MCNP at low energies and the opposite at higher energies holds true.
- For the downstream target neutrons, PHITS slightly under predicts MCNP at 10° and over predicts MCNP at the remaining detector angles.

Generally, MCNP and PHITS perform quite similarly; MCNP better predicts the experimental data than PHITS for 53.6% of all calculated values (51.5% of all upstream target points and 58.1% of all downstream target points). Broadly speaking, PHITS performs better relative to MCNP for the upstream target results than the downstream target results. However, there are a number of situations where one code better predicts the experimental data than the other.

One of the most notable discrepancies between the two codes was with neutron yield from interactions in aluminum versus polyethylene targets. In most cases involving aluminum targets (64.7% of points), the MCNP simulated results were in better agreement with the experimental data; for the HDPE target scenarios, the PHITS simulated results were more often closer to the data than MCNP (55.2% of points). These two material effects are nearly canceled out in the hybrid target case where MCNP better predicts the experimental data than PHITS for 50.2% of the data points. Overall, the code which under predicted the other was usually favored. This is in line with the earlier observed trend that the Monte Carlo codes generally over predicted the experimental results; thus, it seems natural that in the cases where this over prediction is dampened that the codes would be in better agreement with the data. However, if this general over production issue was corrected, perhaps the opposite could be said about which code would fare better for each target material.

The other primary location where the two codes tend to notably deviate is in neutron yields in the 135° detector from the upstream target. As noted earlier, PHITS tends to predict more lower energy neutrons and fewer higher energy neutrons than MCNP in these cases. Here, MCNP tends to fit the data better marginally more often (for 55.6% of points). The predictors of which code performs better here are most strongly target material and projectile species. Interestingly, a similar trend is seen in the downstream target experimental results comparison to simulated results. Since target fragment evaporation is a core component of the neutrons seen in both of these scenarios, that appears to be a likely candidate for explaining this discrepancy between the two codes.

Otherwise, the two codes generally agree reasonably well with each other, and making more specific statements about where one code outperforms the other is impossible as their relative performance becomes extremely situational, varying on a case by case basis.

8.3 Effective dose calculations

While not a part of the original scope of the project, it is useful to extract effective dose information after the yield spectra have already been generated. Presently, there are 7 different variables to compare across this whole experiment:

- Projectile species (mass and atomic number)
- Projectile energy per nucleon
- Target material (aluminum and/or HDPE)
- Target thickness (20, 40, or 60 g/cm^2)
- Secondary particle species
- Secondary particle energy
- Secondary particle's flightpath angle from beam axis

Since this analysis is specifically looking at neutrons only, this number is reduced to 6 variables. This is still too many dimensions to be able to cleanly and concisely visualize (in a table or plot). The number of variables can be reduced by integrating the yield over the whole energy range. But, the neutron energy information is important and should be retained, if possible. Fortunately though, effective dose serves as an additional piece of information that can be used to integrate over the energy axis while folding in and weighting (in the form of KERMA/biological damage) the energy-dependent characteristics of the data. Effective dose is quite convenient for comparing different beam/target systems since it allows each yield spectrum to be collapsed down into a single number. Since there are only three different upstream target material compositions, it does not make sense to represent them on their own axis; instead, the Al, HDPE, and AlPE target datasets can be studied separately. Additionally, separate plots can be made for each of the three thicknesses of each material, reducing the number of axes to represent to three:

- Projectile species (mass and atomic number)

- Projectile energy per nucleon
- Secondary particle's flightpath angle from beam axis

This still results in too much information to be included on a single effective dose plot. However, this can be somewhat circumvented by multiplying the dose values of another axis by different powers of 10 or 100 to space them out like what was done with some of the earlier yield plots. This results in plots with dose on the y-axis and projectile mass A on the x-axis containing six sets (for each angle) of three lines (for each projectile energy).

ICRP 116 contains neutron flux to effective dose conversion factors (in units of pSv·cm^2) for neutrons from 1 meV to 10 GeV, fully containing the range of neutron energies present in this study [43]. Flux has not been calculated in this work though; yield (in units of #/(sp·sr·MeV)) was calculated. This, however, is fine. If someone in the future attempts to extract dose information from this data, they will only need to multiply this source particle normalized data by the actual source particle flux (in #/cm^2) to obtain a dose value.

The steps to be performed in this calculation are as follows:

1. For each energy bin, interpolate the ICRP 116 dose curve to find a conversion factor.
2. Multiply every yield bin by this conversion factor. (Units: (pSv·cm^2)/(sp·sr·MeV))
3. Multiply every yield bin by its energy bin width. (Units: (pSv·cm^2)/(sp·sr))
4. Sum all of the effective dose bins into a single value with units of (pSv·cm^2)/(sp·sr)

Since the energy dependence of the ICRP 116 neutron effective dose factors appears to be several linear segments when plotted on a log-log scale, a log-log linear interpolation is used to find the dose conversion factor for each bin. Also, while ICRP has conversion factors for six different directions, only the isotropic conversion factors are used here since the GCR field in space is isotropic rather than behaving like a unidirectional broad beam. All calculated upstream target-produced neutron dose values can be found tabulated in Appendix D.1.

Plots of all of these effective dose values calculated from the upstream target neutron yields are shown in Figure 8.57 as a function of projectile mass for each detector angle from each of the eight upstream targets. As one would expect, effective dose increases with

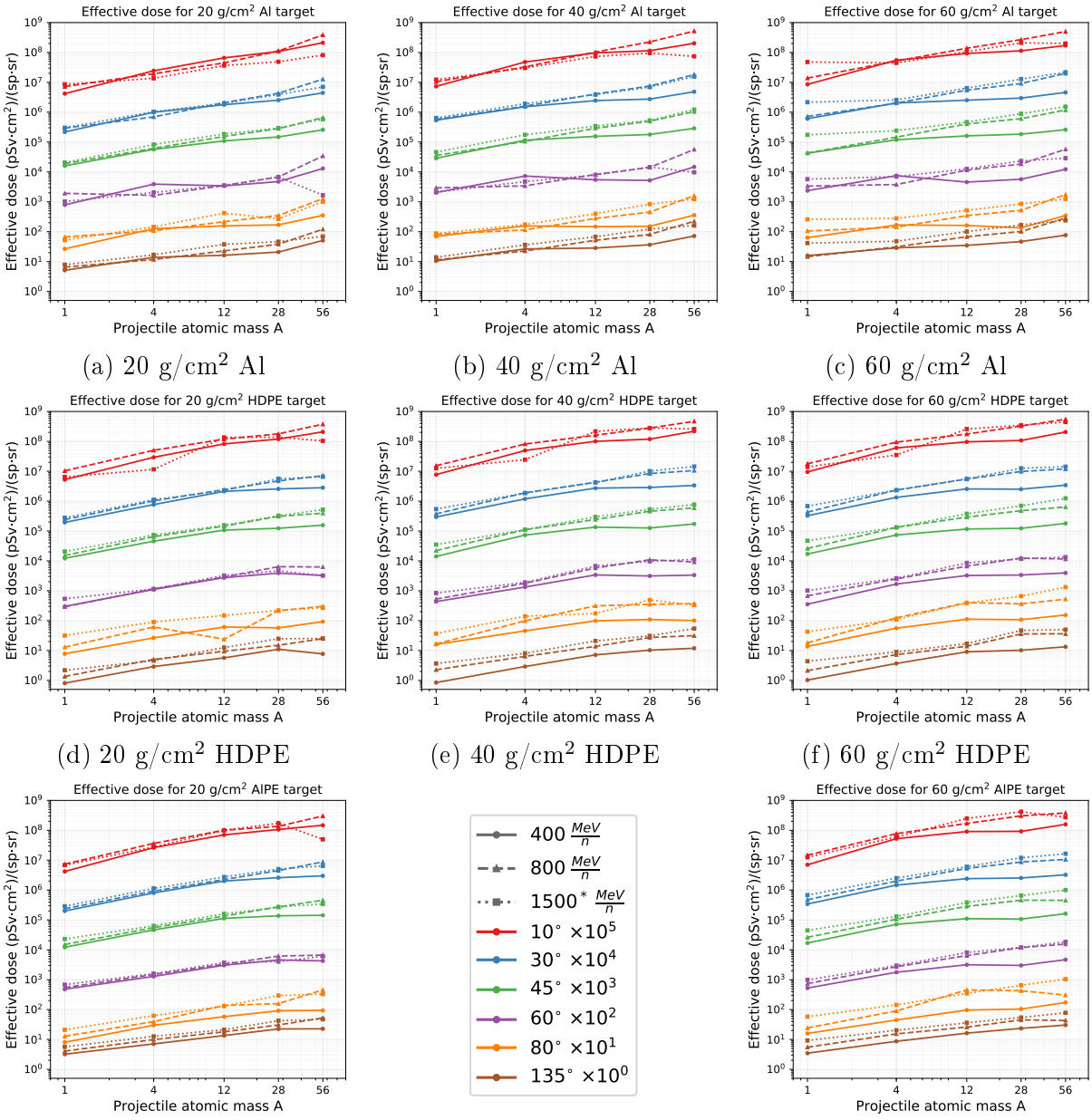
projectile mass. As was discussed earlier, this is because total neutron yield increases with projectile mass due to there being more projectile nucleons and more interactions occurring. There are some exceptions to this trend though. Some of these exceptions are with the heavier 1500 MeV/n beams where statistics suffered, and some depressed or negative yield bins were still present.

Figure 8.58 shows the same information as Figure 8.57 but plotted as a function of detector angle for each species and upstream target. As one would expect, effective dose decreases with increasing detector angle. The exception to this is that in some cases effective dose in the 135° detector actually exceeds that in the 80° detector. As was discussed earlier, this is due to the width of the upstream target where any secondaries bound for the 80° detector must pass through more target material before escaping than for any other detector angle. Once again, some of the points which appear to break from the common trends were those heavy 1500 MeV/n beam cases.

In general, dose increases with increasing beam projectile mass and energy because those are also the factors which total yield scaled with. By looking across each row of the grid of plots, one can also see that effective dose also generally increases with increasing target thickness as was observed with the yield values as well. The following section further condenses this information by also collapsing the projectile species and projectile energy axes in this effective dose analysis.

8.3.1 Compilation of a hybrid GCR-like effective dose

While the effective dose calculation itself collapses the energy axis, the remaining axes still make comparison a somewhat daunting task. Since one of the primary interests of this experiment was experimental confirmation of the optimal spacecraft shielding thickness hypothesis which is believed to be predominately caused by neutron production in the back wall of a spacecraft (made in Reference 1), it makes sense to combine these effective dose results for different source ions into a single "GCR-like" source. In this scenario, the only remaining uncollapsed axes are target material, target thickness, and detector angle; these are the base values one would likely wish to compare anyways. There are two primary challenges in this exercise:



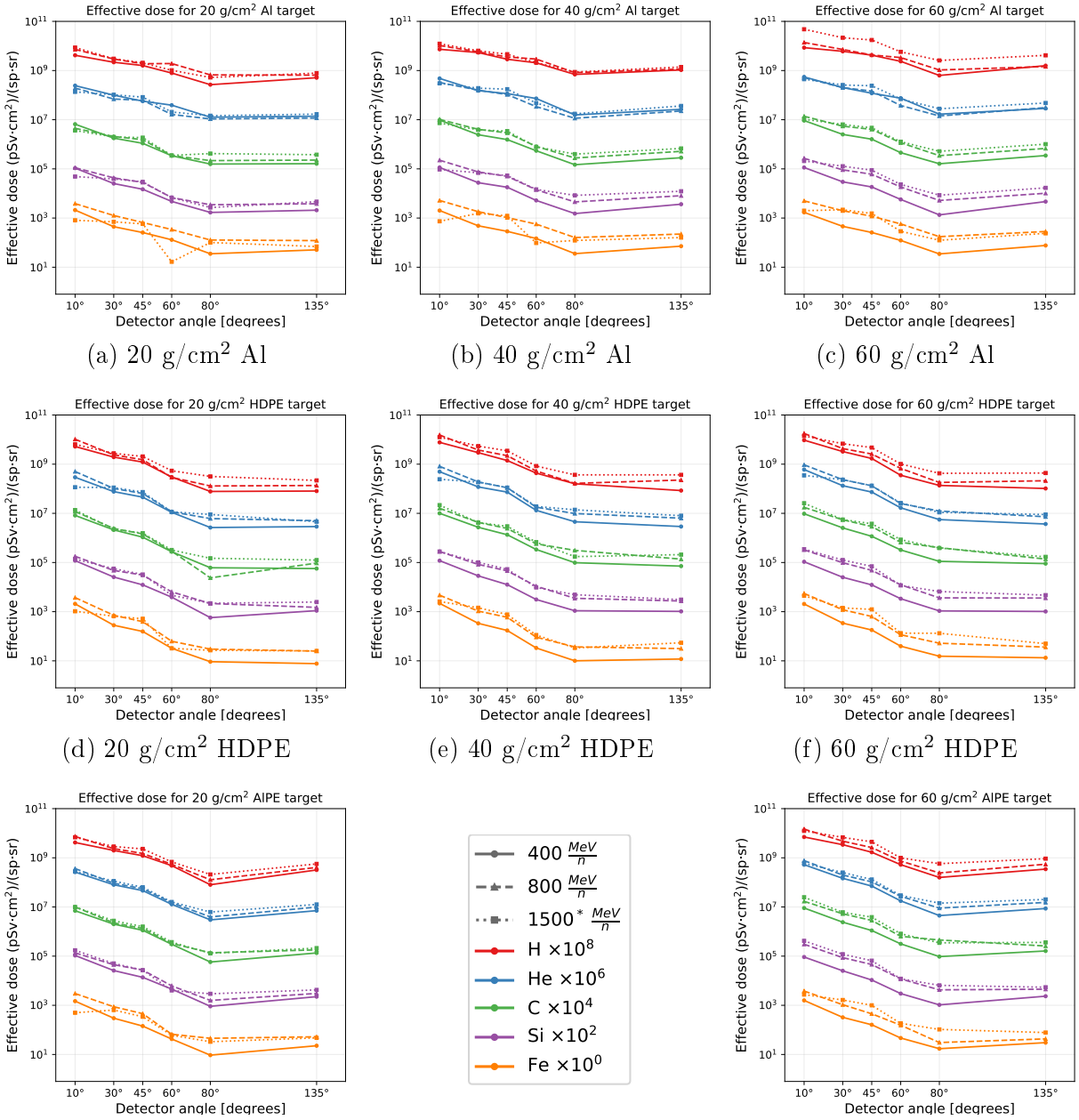
(a) 20 g/cm^2 Al (b) 40 g/cm^2 Al (c) 60 g/cm^2 Al

(d) 20 g/cm^2 HDPE (e) 40 g/cm^2 HDPE (f) 60 g/cm^2 HDPE

(g) 20 g/cm^2 AlPE (h) 60 g/cm^2 AlPE

*2500 MeV instead of 1500 MeV/n for H beams; sometimes slightly below 1500 for C/Si/Fe

Figure 8.57: Effective dose versus projectile mass for all systems



(a) 20 g/cm^2 Al (b) 40 g/cm^2 Al (c) 60 g/cm^2 Al

(d) 20 g/cm^2 HDPE (e) 40 g/cm^2 HDPE (f) 60 g/cm^2 HDPE

(g) 20 g/cm^2 AlPE (h) 60 g/cm^2 AlPE

*2500 MeV instead of 1500 MeV/n for H beams; sometimes slightly below 1500 for C/Si/Fe

Figure 8.58: Effective dose versus detector angle for all systems

1. How can the upstream target and downstream target results be fairly combined?

2. How should doses for each source ion be weighted when combined into a single dose?

This first challenge is straightforward to overcome. The only normalization which really differentiates the upstream and downstream results is the one done for solid angle. It can be easily undone for the upstream results, leaving both as energy-dependent differential neutron yields. While this directly couples these results to the specific experiment/room geometry, there is no justifiable solid angle correction to be made on the back target results due to the flight paths being unknown and highly variable.

As an example of this exercise, Table 8.5 shows the effective doses for C projectiles at 10° for both neutron sources (and their sums). While the trends seen in this table differ from those for different projectile species and detector angles, a few common notes can be made already. At lower energies where the beam and its secondaries have more difficulty penetrating the upstream target, especially for greater thicknesses, the downstream target dose is depressed. However, at higher beam energies the downstream target contribution increases as particle flux on the downstream target increases. Interestingly, one can see that in the 10° detector for 1500 MeV/n C projectiles that the aluminum dose being greater than the HDPE effective dose is largely attributable to the increased neutron production in the downstream target. This also makes sense since the driving production mechanism for the downstream target neutrons is target fragment evaporation which will be more prominent for the heavier Al target nuclei.

Another interesting trend seen in this table that is generally true across the experimental dataset is that the total effective doses from the hybrid AlPE target are lower than the those from either of the pure targets of the same thickness. Since the hybrid AlPE target used the HDPE downstream target, it makes sense that the downstream target effective dose would be lower than that for aluminum due to the decreased target fragment evaporation neutrons. One can see that the downstream target effective doses for the HDPE and AlPE targets are typically quite comparable. What pushes the AlPE effective dose below that for HDPE is the upstream target contribution. A comprehensive listing of these effective dose tables for every projectile species and detector angle can be found in Appendix D.2.

Table 8.5: Experimentally calculated effective dose for C projectiles at 10°

E_{proj} (MeV/n)	Target material	z_{target} (g/cm^2)	Effective dose in $\left(\frac{nSv \cdot cm^2}{s.p.}\right)$		
			Upstream target	Downstream target	Total
400	Al	20	875.46 ± 11.32	732.02 ± 18.66	1607.48 ± 21.83
		40	1281.37 ± 11.69	371.51 ± 12.78	1652.88 ± 17.32
		60	1204.95 ± 9.58	272.14 ± 9.86	1477.09 ± 13.75
	HDPE	20	1088.93 ± 12.71	260.64 ± 9.95	1349.57 ± 16.14
		40	1283.45 ± 11.46	179.73 ± 7.48	1463.18 ± 13.69
		60	1172.23 ± 8.40	144.66 ± 5.13	1316.89 ± 9.85
	AlPE	20	941.60 ± 11.33	266.36 ± 8.97	1207.96 ± 14.46
		60	1117.83 ± 8.05	130.56 ± 4.69	1248.39 ± 9.32
800	Al	20	596.25 ± 17.98	2435.97 ± 39.55	3032.21 ± 43.44
		40	1372.90 ± 23.67	2044.13 ± 33.93	3417.04 ± 41.37
		60	1840.34 ± 25.66	1761.22 ± 31.74	3601.56 ± 40.82
	HDPE	20	1578.45 ± 22.68	765.95 ± 19.16	2344.40 ± 29.69
		40	2105.23 ± 27.61	757.64 ± 19.53	2862.87 ± 33.82
		60	2241.06 ± 27.26	717.96 ± 18.59	2959.02 ± 32.99
	AlPE	20	1355.03 ± 20.02	724.91 ± 17.73	2079.95 ± 26.74
		60	2210.75 ± 27.75	706.80 ± 20.14	2917.55 ± 34.29
1500	Al	20	486.93 ± 28.52	4161.85 ± 69.42	4648.79 ± 75.05
		40	979.67 ± 40.89	3808.89 ± 65.32	4788.56 ± 77.06
		60	1397.02 ± 48.29	3526.31 ± 71.46	4923.34 ± 86.25
	HDPE	20	1809.45 ± 56.36	1427.17 ± 52.52	3236.61 ± 77.04
		40	2835.48 ± 75.87	1611.85 ± 69.26	4447.33 ± 102.73
		60	3346.60 ± 89.50	1389.64 ± 58.18	4736.24 ± 106.75
	AlPE	20	1347.58 ± 44.00	1401.90 ± 43.56	2749.48 ± 61.91
		60	3245.17 ± 88.50	1326.33 ± 53.78	4571.50 ± 103.57

Abstractly, the answer to the second challenge is also straightforward; each source ion should be weighted using its abundance in the GCR spectrum. The complication arises in accounting for the fact that five ions sampled at three energies is a dramatic simplification of the true GCR spectrum. Fortunately, calculating GCR flux as a function of ion species and energy is straightforward.

In this work, the GCR model developed by Dr. Daniel Matthiä was utilized [44]. The model requires input of the source ion atomic number Z, source ion energy E (in MeV/n), and a model parameter W and will output the flux for that ion at that energy in units of $(\text{s}\cdot\text{sr}\cdot\text{cm}^2\cdot\text{MeV/n})^{-1}$. The W parameter accounts for the modulation of the GCR flux by the solar wind which is a function of time with the solar cycle. W is fairly close to the 12 month averaged International Sun Spot Number which ranges from 0 to slightly below 200; both of these values trend inversely with Oulu neutron monitor count rates. In this work, a value of $W = 80$ was arbitrarily selected. A W of 80 corresponds roughly to an average GCR flux between that at solar minimum and solar maximum. Assuming that the GCR spectrum was only composed of the experimentally sampled ions and energies here, the relative abundances of each source ion are shown in Table 8.6 below.

These are the values which will be used as weighting factors in combining the calculated effective dose values. For the sake of illustration, Table 8.7 shows these same values except when calculated with $W = 10$ which corresponds to a somewhat extreme solar minimum, and Table 8.8 shows these same values except when calculated with $W = 140$ which corresponds to a somewhat extreme solar maximum.

To present a more comprehensive picture of this effect, Figure 8.59 shows the full flux spectra from 10 MeV/n to 1 TeV/n for these five source ions and three values of W. Near solar maximum, the increased solar wind deflects a significant fraction of the ions with

Table 8.6: GCR relative abundances of experimentally sampled ions ($W = 80$)

Energy	H	He	C	Si	Fe
400 MeV/n	36.082%	6.7888%	0.18689%	0.027541%	0.019111%
800 MeV/n	35.534%	4.8931%	0.13664%	0.020366%	0.013959%
1500 MeV/n	13.634%	2.5732%	0.072564%	0.011094%	0.007557%

*2500 MeV instead of 1500 MeV/n for H beams; sometimes slightly below 1500 for C/Si/Fe

Table 8.7: Sampled GCR relative abundances with $W = 10$ (solar minimum)

Energy	H	He	C	Si	Fe
400 MeV/n	47.812%	5.4048%	0.14879%	0.021881%	0.014616%
800 MeV/n	33.536%	3.1447%	0.087814%	0.013069%	0.0087144%
1500 MeV/n	8.3403%	1.4177%	0.03998%	0.0061057%	0.0040796%

*2500 MeV instead of 1500 MeV/n for H beams; sometimes slightly below 1500 for C/Si/Fe

Table 8.8: Sampled GCR relative abundances with $W = 140$ (solar maximum)

Energy	H	He	C	Si	Fe
400 MeV/n	22.785%	7.9492%	0.21884%	0.032334%	0.023547%
800 MeV/n	33.659%	7.5525%	0.2109%	0.031498%	0.02239%
1500 MeV/n	22.462%	4.8792%	0.13759%	0.021066%	0.014731%

*2500 MeV instead of 1500 MeV/n for H beams; sometimes slightly below 1500 for C/Si/Fe

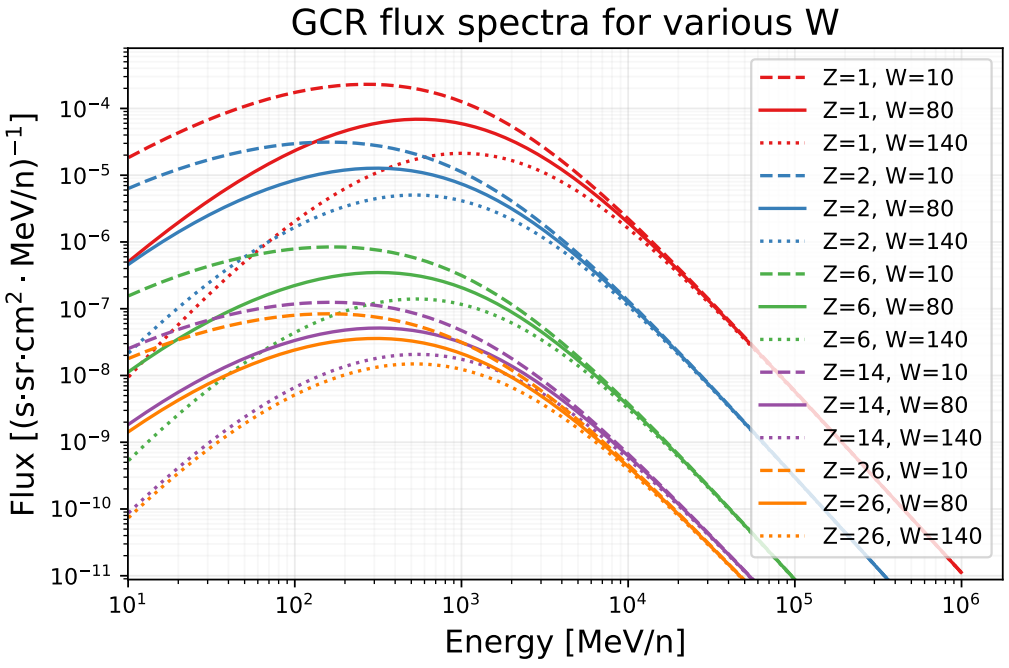


Figure 8.59: Pictured is the impact of solar cycle on GCR flux.

lower energies, and, as one would expect, fewer lower energy particles are deflected at solar minimum. The net result for the relative abundances is that the peak of each spectrum is shifted to higher energies for increased solar activity.

Beyond 10 GeV/n, the effect of solar modulation is insignificant. However, since all of the beam energies sampled are in the region strongly affected by solar modulation, this is an important consideration to make for this analysis.

To provide a more explicitly mathematical explanation of how this weighting is performed, for S source species each represented with $\mathcal{E}$ energies each with relative fractional abundance of w, effective dose values E from each source can combined into a single GCR effective dose E_{GCR} as shown in Equation 8.1.

$$E_{GCR} = \sum_{i}^{S} \sum_{j}^{\mathcal{E}_i} w_{i,j} \cdot E_{i,j} \tag{8.1}$$

While this equation works for combining all of the upstream target effective doses, a few issues arise for the downstream target effective doses. As was shown earlier in Figure 6.1, there were a number of combinations where statistics were too insufficient for the deconvolution methodology to be employed reliably. There are spectra at 10° for almost every system, but for the other angles the availability of data is much less consistent. Thus, a method must be developed to still combine all projectiles for a given target and detector and still allow for fair comparison with other targets.

The fairest way to accomplish this is to re-weight each component of the sampled GCR spectrum such that the individual weights for the components whose corresponding effective doses could be calculated (due to being deconvolution viable) still add up to 100%. Mathematically expressed, a correction factor $\mathcal{Z}$, which is a function of which effective dose values are zero / could not be calculated that is represented by ζ (Equation 8.2), is introduced in Equation 8.3. This correction factor $\mathcal{Z}$ is then used to calculate a new GCR effective dose E'_{GCR} as shown in Equation 8.4.

$$\zeta_{i,j}(x) = \begin{cases} 0 & x \neq 0 \\ 1 & x = 0 \end{cases} \tag{8.2}$$

$$\mathcal{Z} = \sum_{i}^{S} \sum_{j}^{\mathcal{E}_i} w_{i,j} \cdot \zeta_{i,j}(E_{i,j}) \tag{8.3}$$

$$E'_{GCR} = E_{GCR} \cdot \frac{1}{1 - \mathcal{Z}} \tag{8.4}$$

This process can then be repeated for the MCNP and PHITS results to mirror the calculation performed on the experimental results. After all of this has been completed, the plot shown in Figure 8.60 can be generated, showing all results for the 10° detector in a single, concise image.

This plot illustrates a number of interesting features. First, one can see that without the downstream target that effective dose would only continue to rise with increasing target thickness (until reaching some point where the upstream target attenuates/scatters more neutrons than it produces). It is clear that even with the downstream target in place that effective dose from the aluminum shielding continues to rise for the thicker targets. However, the expected plateau in effective dose for the HDPE targets is not seen, though the rise from

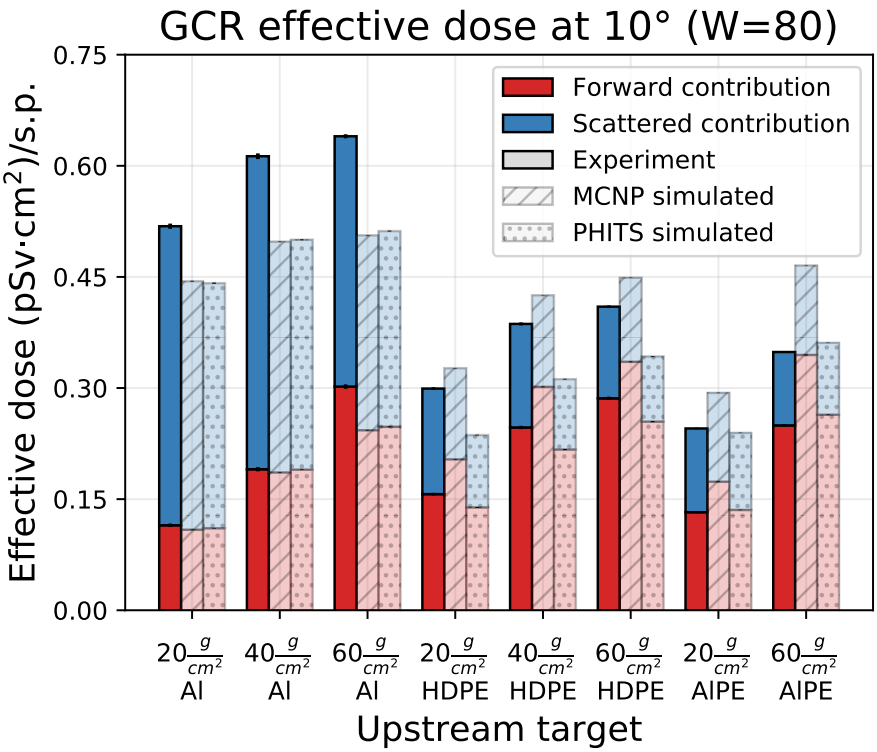
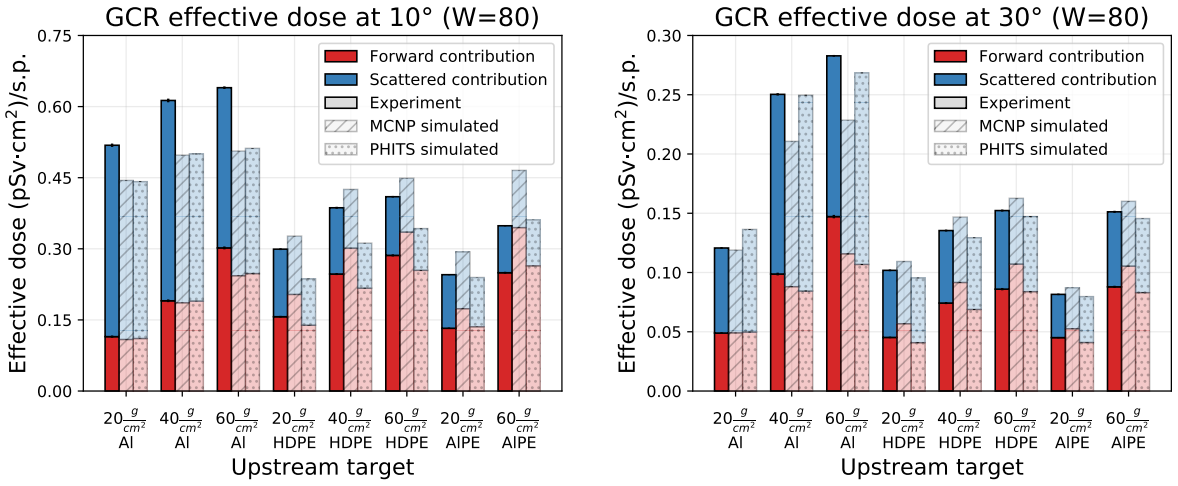


Figure 8.60: Total GCR effective dose E_{GCR} at 10°

40 g/cm^2 to 60 g/cm^2 is fairly small. Another note is that both AlPE shield thicknesses result in a lower effective dose than either of the pure Al or HDPE targets of the same thicknesses. While this trend is seen in the experimental data, it is not true in the Monte Carlo simulated results which show that while the 20 g/cm^2 AlPE shield is better than either of the pure ones the 60 g/cm^2 HDPE target should result in lower effective dose than the 60 g/cm^2 AlPE target.

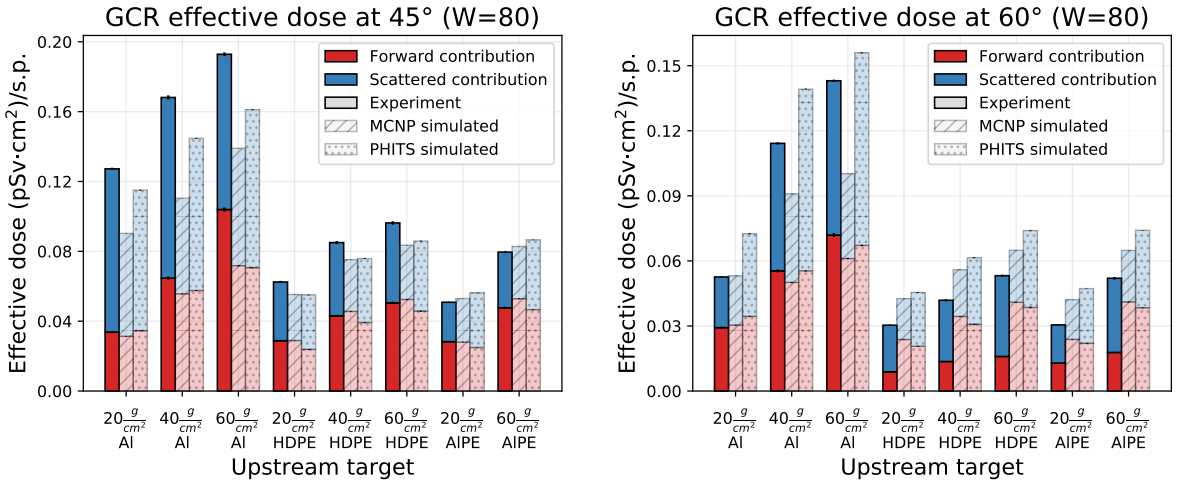
The Monte Carlo results seem to under predict the effective dose consistently for the aluminum targets. For the 20 g/cm^2 and 40 g/cm^2 targets, this is mostly from the downstream target contribution, but the 60 g/cm^2 Al target experimental results notably exceeded both Monte Carlo codes. Additionally, MCNP and PHITS tend to be in moderately strong agreement with each other for the Al targets. As was discussed earlier, PHITS tends to predict greater neutron yields from aluminum targets than MCNP; however, this seems to be counterbalanced by MCNP predicting greater neutron yields than PHITS for 10° to 60° above 100 MeV and for hydrogen and helium projectiles. For the pure HDPE targets, one can clearly see the effect of MCNP's production of more neutrons than PHITS. One may recall that, overall, PHITS over predicted MCNP (which both, overall, over predict the data), but due to the weighting factors of GCR abundance, MCNP's higher neutron yield from H and He projectiles relative to PHITS result in MCNP over estimating PHITS even more. The end result is that MCNP predicts a higher GCR effective dose than the experimental results while PHITS predicts a lower GCR effective dose, and the MCNP values appear to be slightly closer to the experimental values than the PHITS ones. These trends can also be seen in the AlPE targets, but in this case the increased neutron production from the aluminum bumps the PHITS GCR effective dose to being closest to the experimental data while MCNP continues to over predict it.

Figure 8.61 showcases this same plot but for all six detectors. An interesting note to make here is that while the 10° detector is very close to the downstream target, the 45° detector is about equidistant from both targets. The 45° detector sees fewer projectile fragment neutrons than the 10° detector, but the target evaporation neutrons from both targets should be roughly equal influences on the 45° detector. This is visible on Figure 8.61c where the upstream and downstream target contributions appear to be closer to each other than in any



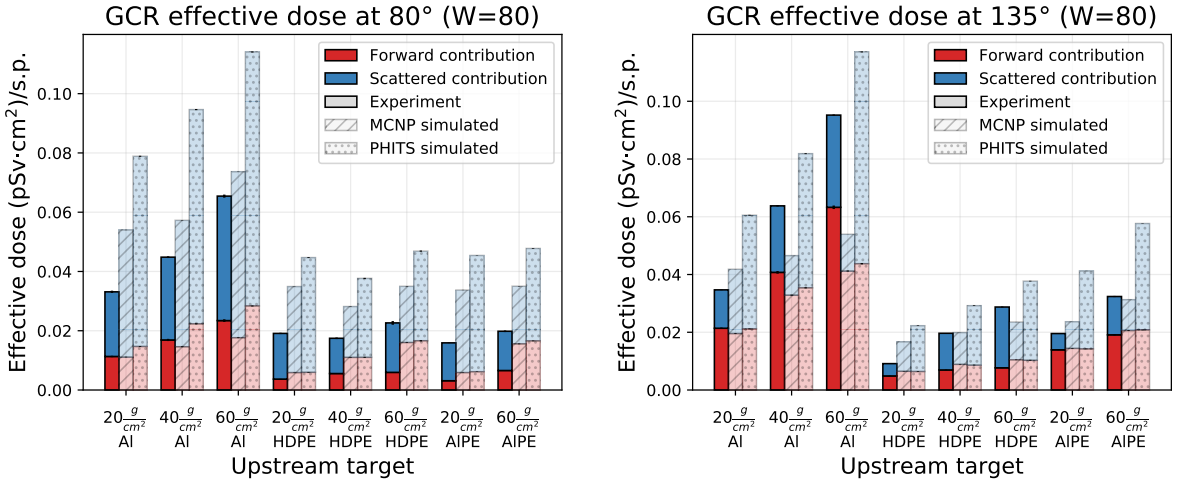
(a) 10°

(b) 30°



(c) 45°

(d) 60°



(e) 80°

(f) 135°

Figure 8.61: GCR effective dose for W=80 in each detector

other detector. One particularly interesting trend to note is the growing discrepancy between the PHITS and MCNP effective doses for the aluminum targets with increasing detector angle. It is primarily from differences in the downstream target contribution, meaning this discrepancy could stem from the differing tally methods used; however, it is not clear whether this is exactly the case and, if so, which method is superior. Most likely, this discrepancy is a convolution of factors pertaining to both the tally methodologies as well as the neutron production in the codes.

To gain a better understanding of these trends, viewing the prominence of each source ion's contribution in each target provides useful information. Figure 8.62 shows the breakdown of the GCR effective dose from each source ion for the upstream target-produced neutrons seen in the 10° detector. Figure 8.63 recreates this plot with only the downstream target contribution, and Figure 8.64 shows the total contribution from both targets. Versions of Figures 8.62, 8.63, and 8.64 with values for all six detectors are displayed in Figures 8.65, 8.66, and 8.67, respectively.

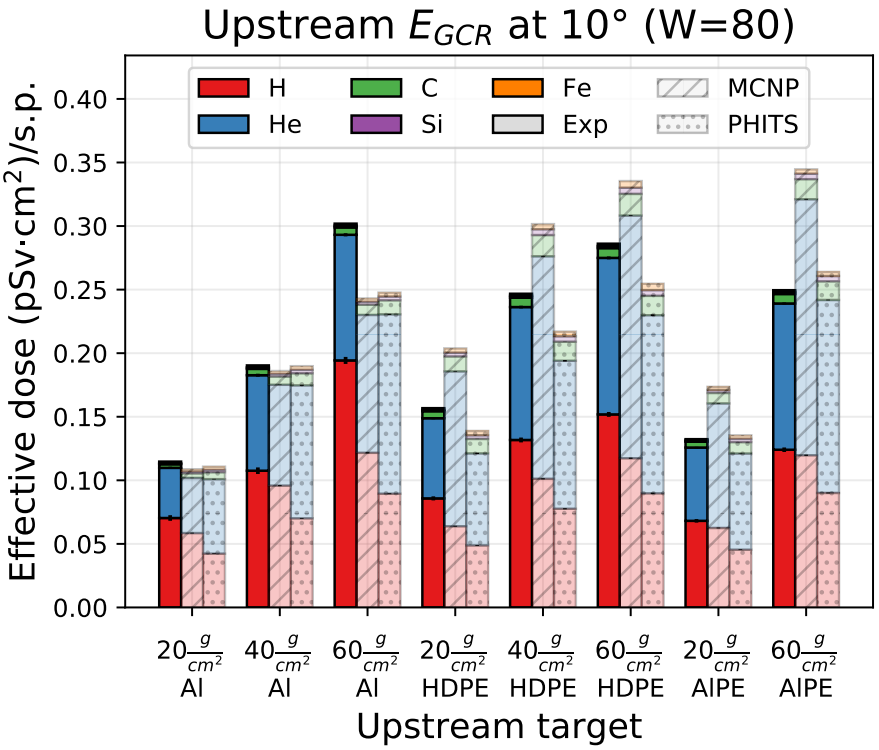


Figure 8.62: Upstream contribution to total GCR effective dose E_{GCR} at 10°

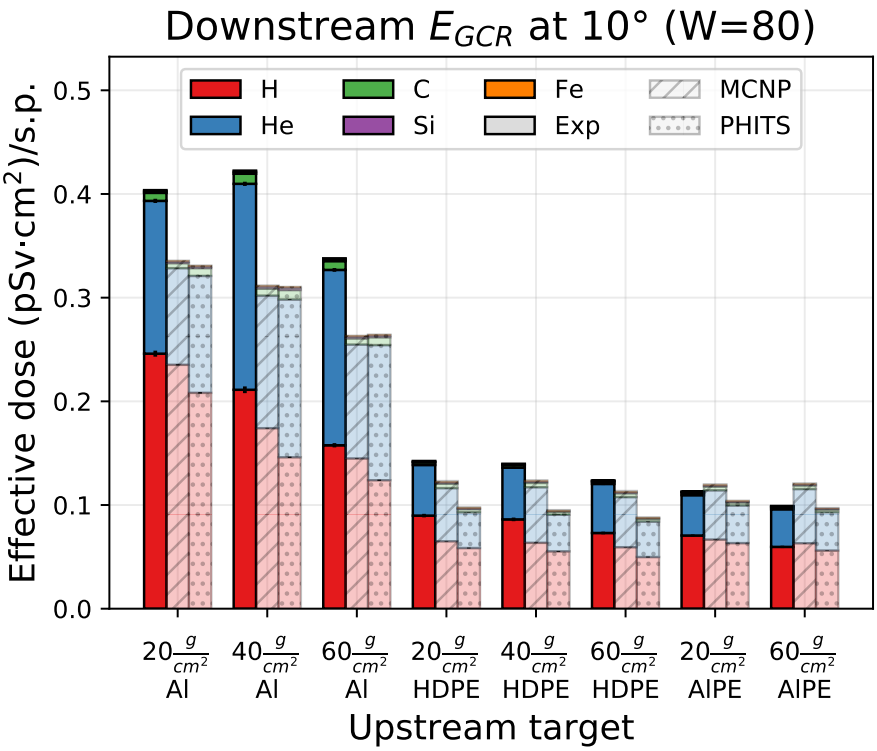


Figure 8.63: Downstream contribution to total GCR effective dose E_{GCR} at 10°

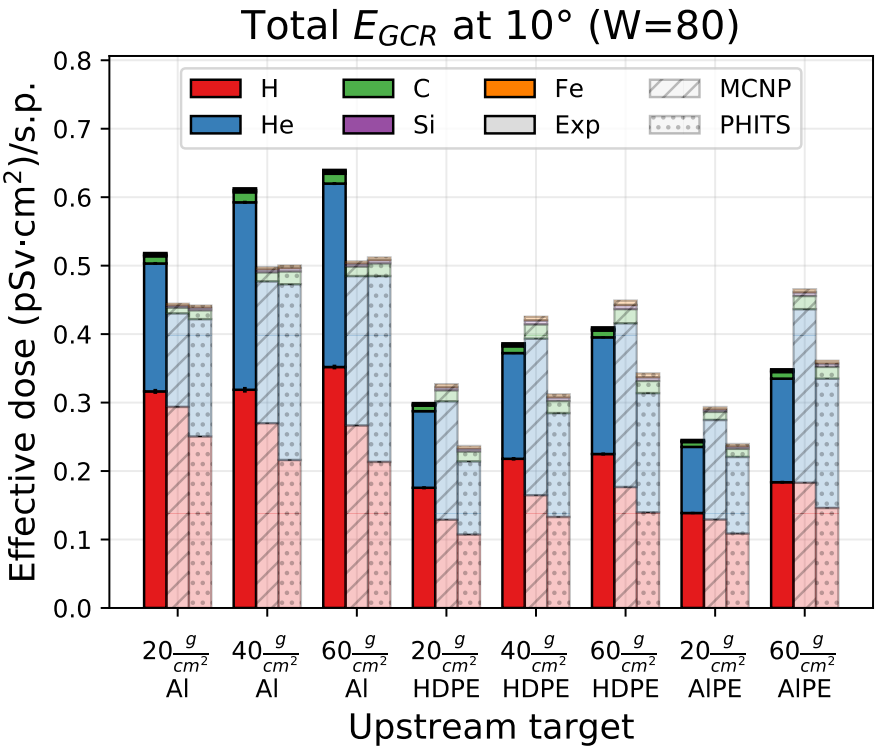
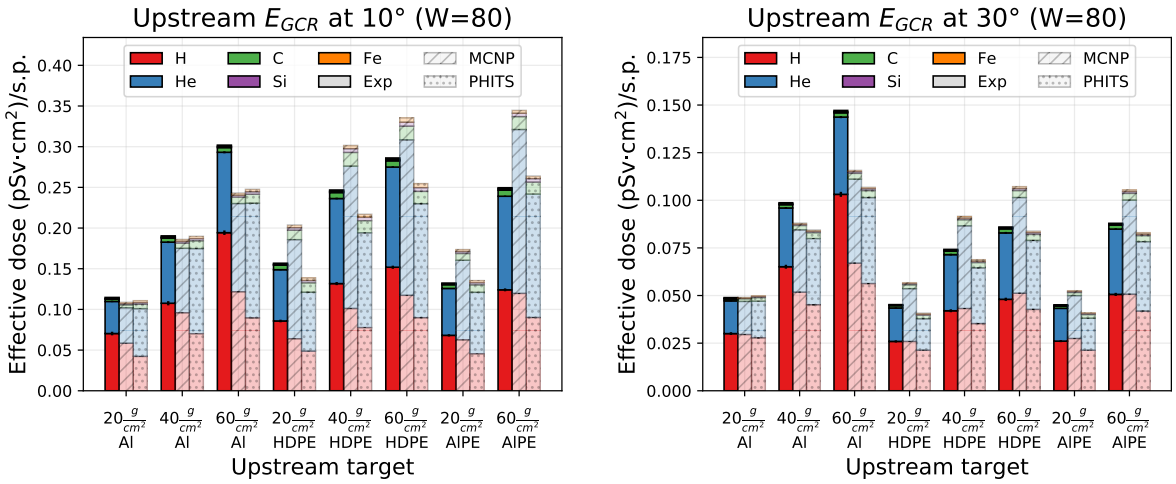
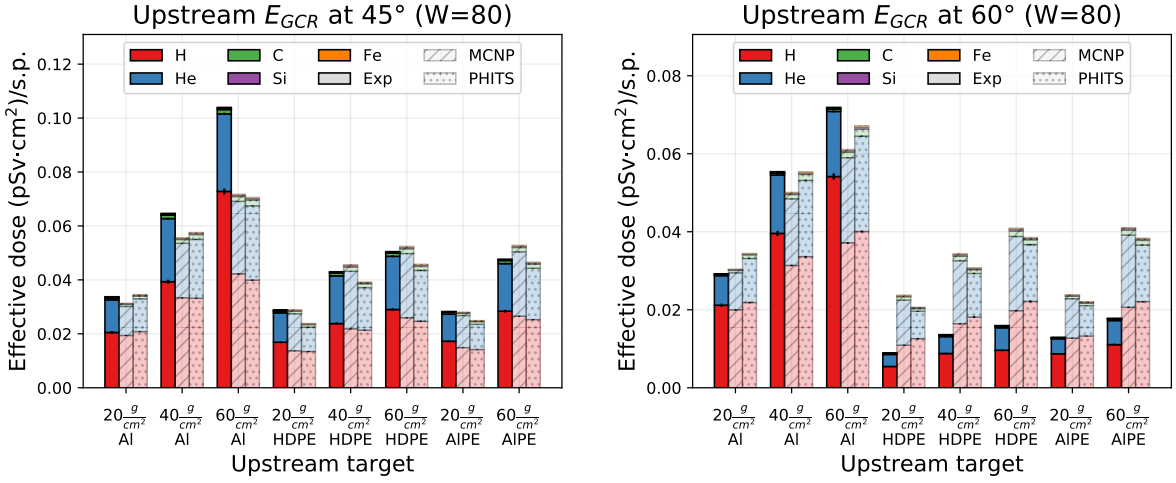


Figure 8.64: Total GCR effective dose E_{GCR} at 10° by source ion



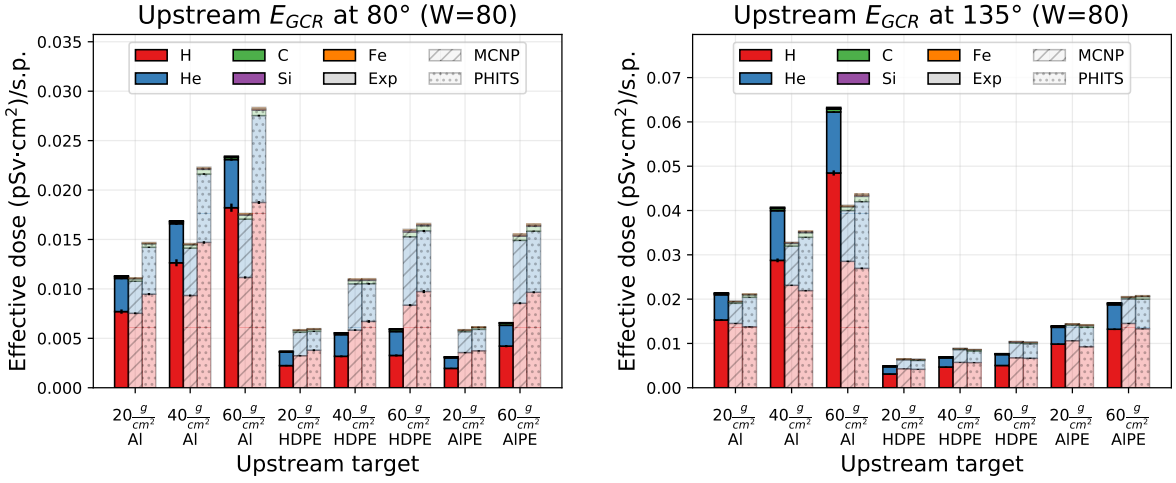
(a) 10°

(b) 30°



(c) 45°

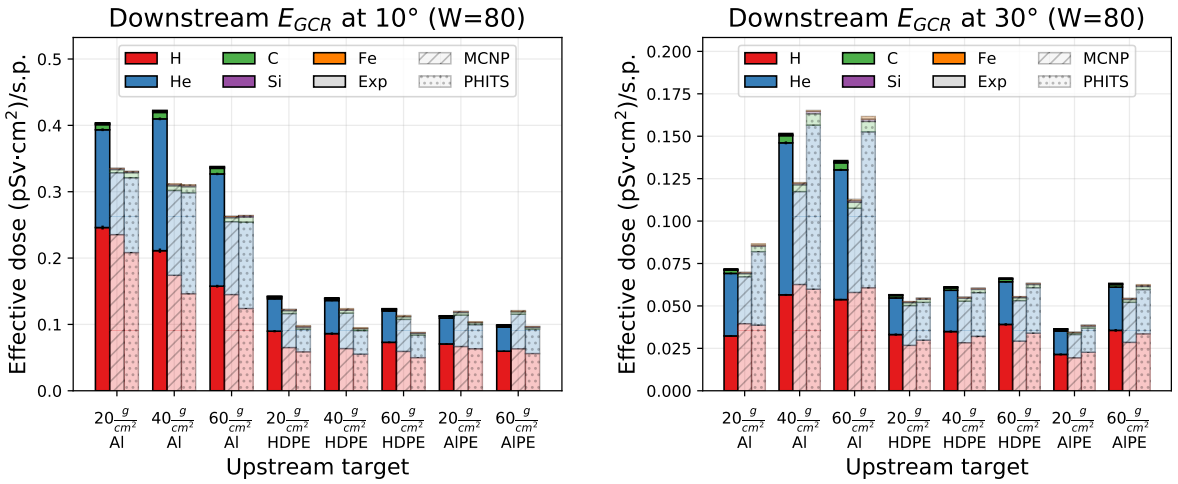
(d) 60°



(e) 80°

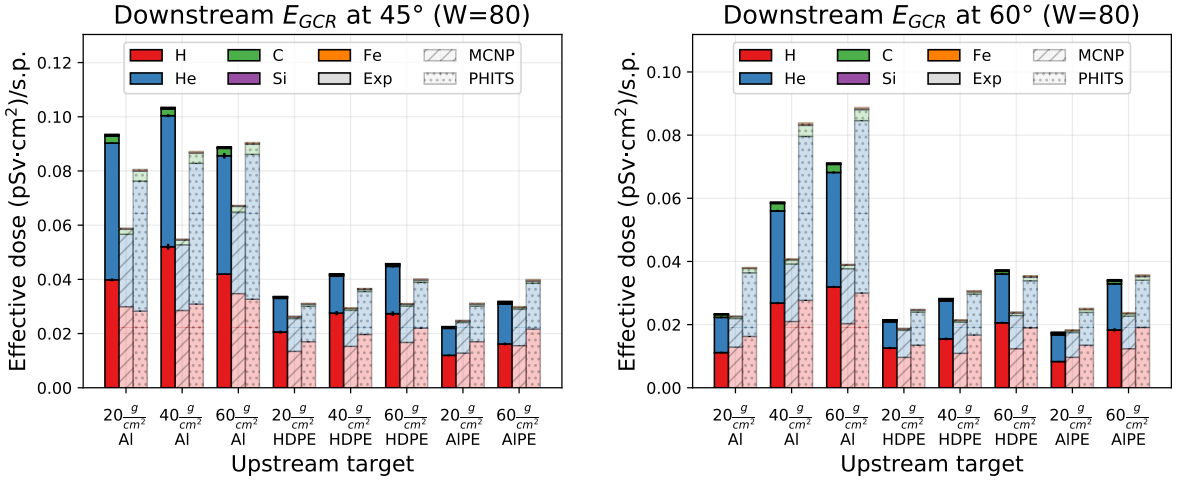
(f) 135°

Figure 8.65: GCR effective dose originating from the upstream target for W=80 in each detector broken down by source ion species contribution



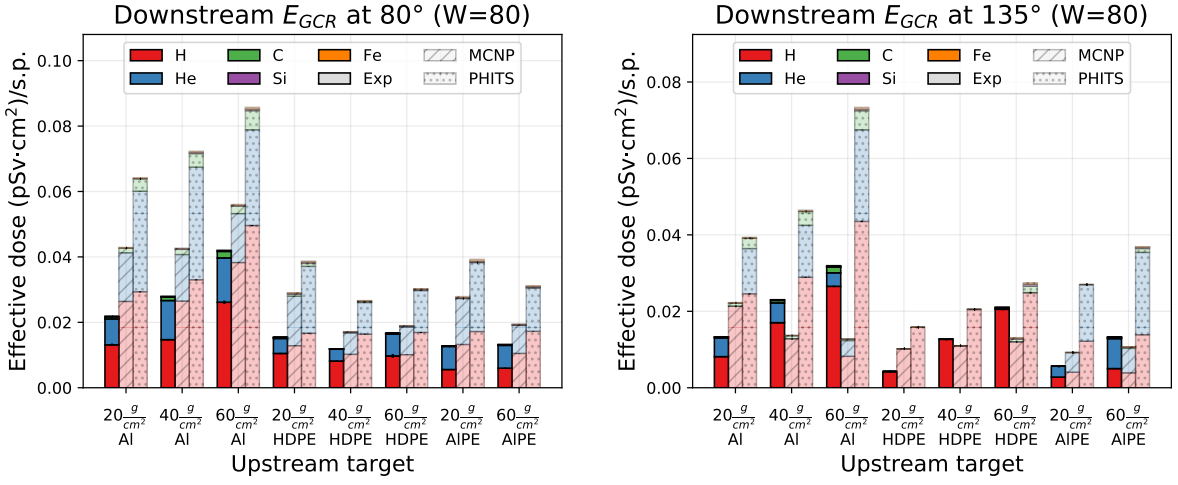
(a) 10°

(b) 30°



(c) 45°

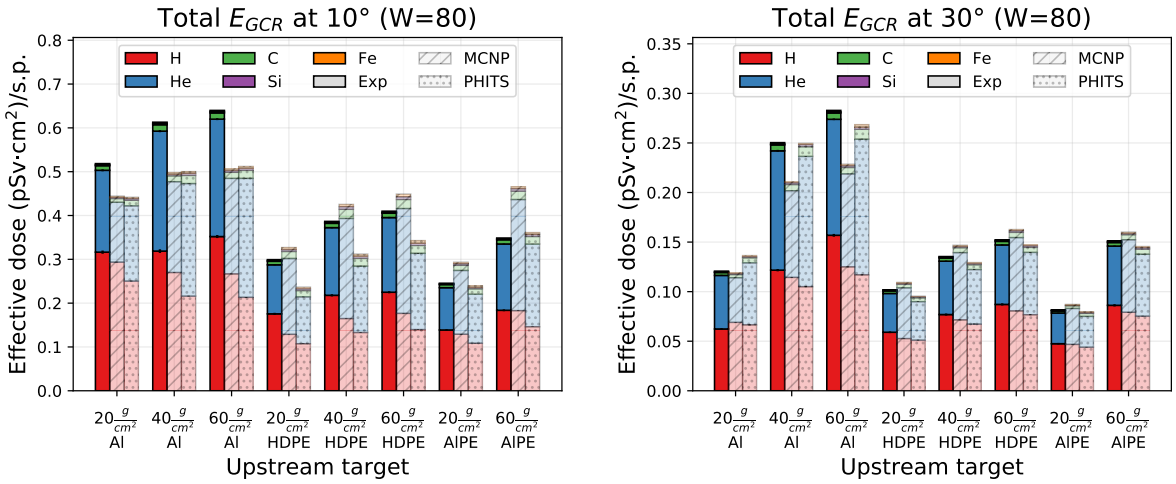
(d) 60°



(e) 80°

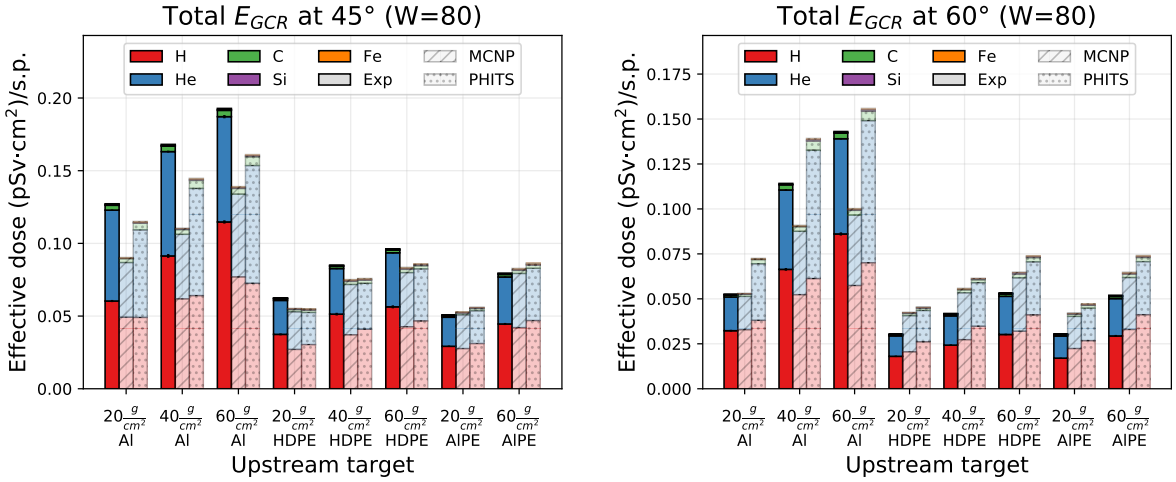
(f) 135°

Figure 8.66: GCR effective dose originating from the downstream target and room scattering for W=80 in each detector broken down by source ion species contribution



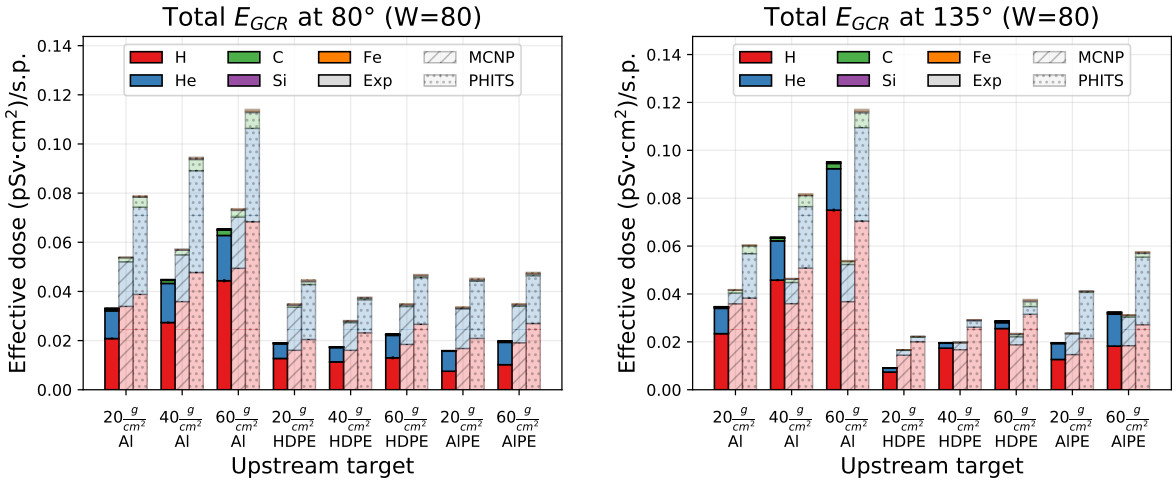
(a) 10°

(b) 30°



(c) 45°

(d) 60°



(e) 80°

(f) 135°

Figure 8.67: Total GCR effective dose for W=80 in each detector broken down by source ion species contribution

As they dominate the GCR spectrum, hydrogen and helium are the primary contributors to this neutron effective dose. This figure also clearly outlines MCNP's over prediction of neutron yield from hydrogen projectiles relative to PHITS. Additionally, this showcases the more general trend of both Monte Carlo codes under predicting neutron production from hydrogen and slowly trending toward over predicting yield for heavier projectiles.

As seen in Figure 8.65 for all six detectors, the general trends of the Monte Carlo codes against the data remain, but a few more interesting trends on the behavior of the codes can be illustrated. At 10° MCNP over predicts neutron yield from hydrogen projectiles relative to PHITS. However, with increasing detector angle to 80°, this trend appears to reverse. This is likely due to MCNP over predicting the forward-peaked neutrons in the lab frame to a greater extent.

Analyzing the plots for the downstream target and room scattering contributions is somewhat more challenging than for the upstream target due to missing datasets. Fortunately, at 10° (Figure 8.63) only neutrons from 800 MeV H on 40 g/cm^2 Al and 60 g/cm^2 Al and 1500 MeV/n Fe on all three Al targets are missing. As seen with the red bars for H on Al at 10° , the correction for missing data appears to work at least reasonably well. The general trends at 10° are consistent with the earlier observed trends of aluminum targets resulting in higher neutron yields while all HDPE-containing upstream targets (which all used the same 60 g/cm^2 HDPE downstream target) had similar effective doses to each other.

As seen in Figure 8.66 for the downstream contribution in all six detectors, the issue of missing information grows. Immediately, one can see that the two Monte Carlo codes are in agreement for the 10° detector but diverge at higher angles, most severely at 135°. Which simulated results, MCNP or PHITS, are closest to the experimental data varies quite substantially between targets and detectors, though PHITS is generally closer overall. One positive coincidence to note here is that the earlier noted discrepancy between the deconvoluted experimental results and the equivalent simulated results for heavier projectiles (where the codes significantly over predict the data) is suppressed in this exercise since the lightest projectiles, where there is the most agreement, are weighted the strongest in the GCR weighting of the effective dose calculation.

After combining the upstream and downstream target contributions to obtain the total (Figures 8.64 and 8.67), the same general trends as previously discussed can be observed here too. An interesting note to make is that the helium component of E_{GCR} is almost as much as the hydrogen component despite the hydrogen fluence being about six times that of helium.

This process can be repeated for any value of W with its own weighting factors (like those shown earlier in Tables 8.6, 8.7, and 8.8). Doing this over the whole valid range of W from 0 to 200 yields the plot shown in Figure 8.68.

Like with the previous set of plots, these values should be interpreted as being per unit incident GCR ion. For increasing W (greater solar activity), the higher relative abundance of the heavier and more energetic ions causes the effective dose per source particle to rise. At solar minimum, the two thickest aluminum targets actually result in comparable effective doses, though the 60 g/cm^2 upstream target gains increasingly more effective dose over the 40 g/cm^2 target as solar maximum is approached. The aluminum targets remain consistently above the HDPE-containing targets in GCR effective dose though. The 20 g/cm^2 AlPE target does the best at minimizing effective dose while the 60 g/cm^2 AlPE target results straddle the effective doses of the 20 g/cm^2 and 40 g/cm^2 HDPE targets.

Figure 8.69 showcases these plots for all six detectors where more interesting trends arise. While the ranking of neutron effective doses in the eight targets remained uncharged for various W for the 10° detector, which targets minimize neutron effective dose for the other detector angles do vary with solar modulation. 60 g/cm^2 Al remains the target for maximum effective dose for all W and angles, and, except at 135°, the 20 g/cm^2 AlPE target remains the best at minimizing effective dose. At 135°, the 20 g/cm^2 HDPE upstream target minimizes effective dose while the 20 g/cm^2 AlPE and 40 g/cm^2 HDPE targets narrowly compete for second place in minimization of E_{GCR}. At 60°, the performance of the 20 g/cm^2 AlPE and HDPE targets is quite close across all W. At 30°, all of the 20 g/cm^2 upstream targets do a better job of minimizing effective dose than the thicker ones except when nearing solar maximum where the 20 g/cm^2 Al effective dose approaches the 40 g/cm^2 HDPE effective dose.

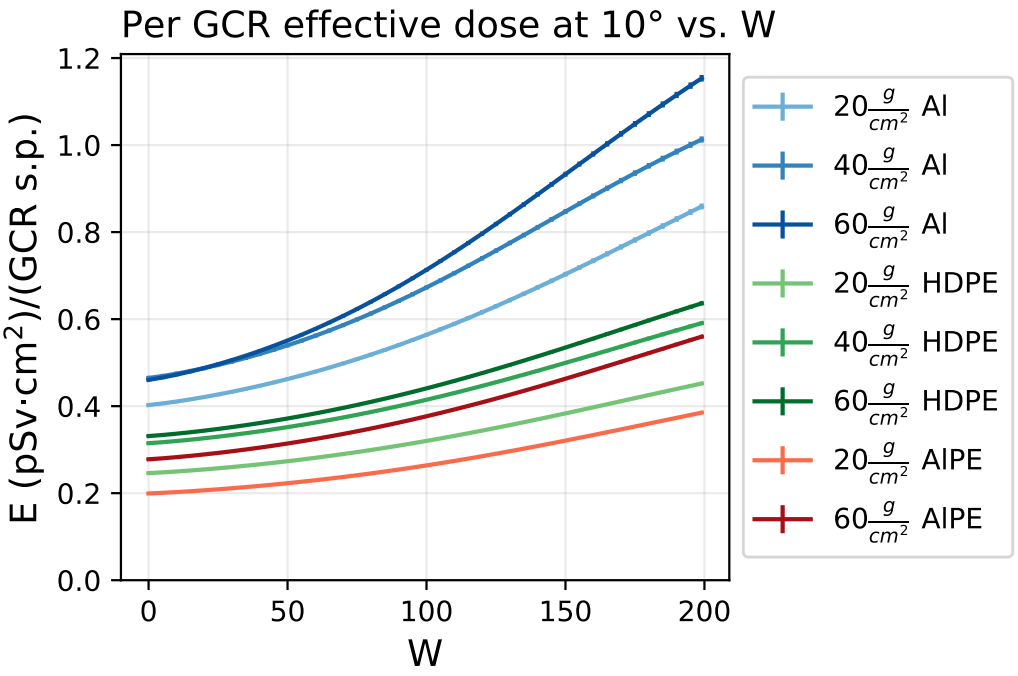
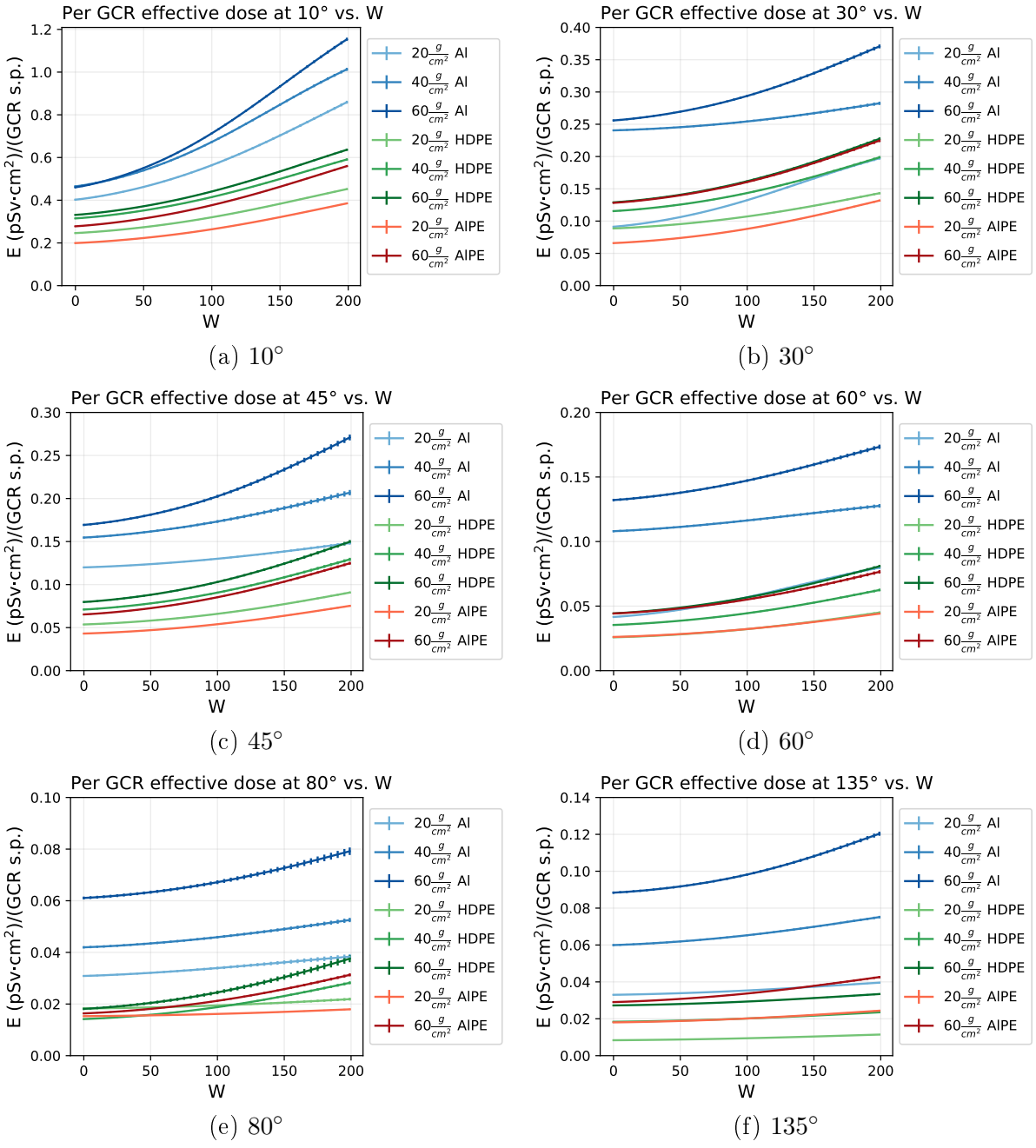


Figure 8.68: Total GCR effective dose E_{GCR} at 10° for various W



(a) 10°

(b) 30°

(c) 45°

(d) 60°

(e) 80°

(f) 135°

Figure 8.69: Effective dose per GCR source particle for whole range of W values in each detector

At first glance, the previous set of plots seem counterintuitive since effective dose is shown to rise with increasing W which corresponds to increasing solar activity which trends with decreasing GCR flux. This is because those plots were normalized to each incident GCR ion. Since the heavier ions, which produce more secondary neutrons and thus higher neutron effective dose, become more abundant relative to the lighter ions during increased solar activity, the plots displayed increasing dose with increasing W. To make this comparison more realistic and highlight the impact of solar modulation, it would be beneficial to regenerate these plots except to perform the normalization to the maximum total GCR fluence, when W=0. This is done in Figure 8.70.

This exercise does not change the relative trends previously discussed (which are easiest to see when plotted as before). However, it does illustrate that while performance of these materials relative to each other changes with solar activity, the total GCR neutron effective dose is more strongly influenced by solar activity (controlled by when a mission is planned to occur relative to the solar cycle) than by shielding choice. That being said, shielding choice can still make a significant difference in total GCR neutron effective dose when putting solar activity aside. This plot for all six detectors is shown in Figure 8.71.

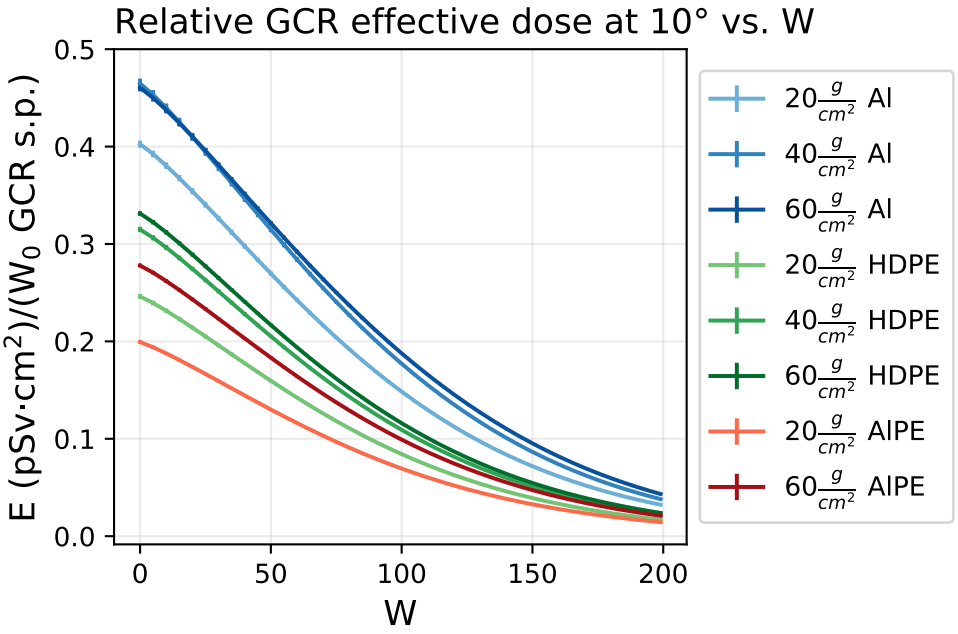
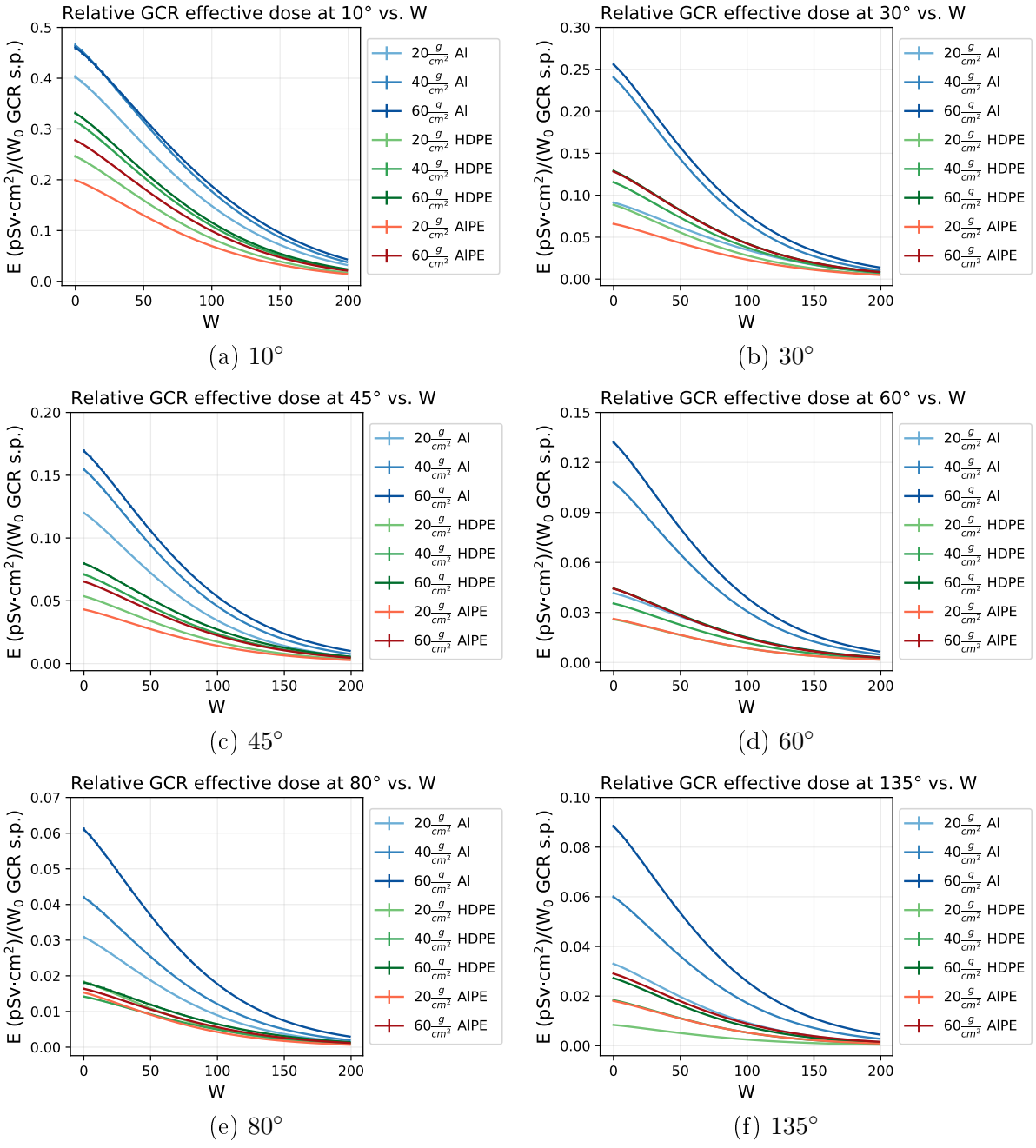


Figure 8.70: Total GCR effective dose E_{GCR} at 10° for various W but normalized to abundances associated with W=0



(a) 10°

(b) 30°

(c) 45°

(d) 60°

(e) 80°

(f) 135°

Figure 8.71: Relative effective dose per W=0 GCR source particle for whole range of W values in each detector

Chapter 9

Data availability

While the study of the final results featured in this work provides a basic overview of the trends and features of the data, there is likely still more information that could be drawn from it. However, that is a task best accomplished by numerous experts in the field rather than a lone individual. This presents an interesting challenge: How can this goal of getting as many experts as possible studying the data collected at NSRL be accomplished? Abstractly, the solution is quite simply to lower the barrier to entry for study of the data. How is that to be accomplished though?

While all data from this experimental campaign will be publicly available through NASA and UT in the form of a repository of text files (discussed in more detail in Section 9.1), this is quite a high barrier to entry, placing the onus of extracting information from the text files and performing comparative studies solely on those wishing to further study these datasets. Another approach would be to make visualizations of each spectrum available for viewing (as is done in Appendix C of this document for all neutron results of this work), but this makes comparison of spectra somewhat inconvenient and would still require delving into the text file repositories if wishing to perform any precise comparisons.

The solution to this challenge developed in this work is an online-accessible tool which can arbitrarily plot any combination of spectra from this experimental campaign (not limited to just neutron results). It is discussed in greater detail in Section 9.2. Aside from making the navigation to the tool slightly more streamlined, this is perhaps the lowest possible barrier to entry for further study of this data by individuals not involved with the experiment and

already in possession of the data. It simply requires access to the internet, a web browser, and the following of a few simple instructions.

9.1 NASA and UT data repositories

In accordance to legal requirements for projects funded by federal grants, this data must be made publicly available. Presently, the completed dataset should be available on three platforms: a NASA hosted repository, a UT hosted repository (intended to fulfill this legal requirement), and from within the tool developed in this work and discussed in Section 9.2. The repositories hosted by UT and NASA will likely share the same structure detailed in Appendix E. The NASA version of the repository will be available through request to the NASA Langley Research Center, and the University of Tennessee version of the repository will be available through TRACE, the Tennessee Research and Creative Exchange, online at `trace.utk.edu`.

Dr. Luis Castellanos had initially been responsible for curation of all data from the student research group at UT, but I assumed those data curation responsibilities at the start of 2018 after Dr. Castellanos completed his dissertation. This provided me with ultimate final control of the data repository structure, though the core organization of the repository was left unchanged barring a few reorganization requests made by the scientists at NASA who used the results within the repository for their own analyses. Within the top-level directory of the repository is an up-to-date README document explaining the repository folder hierarchy and formating of its ASCII data files; this explanation is also provided in Appendix E.

Due to having this more intimate interfacing with all data from this experimental campaign, development of an online tool for easy viewing of all results seemed like a natural challenge for me to undertake and is detailed in the following section.

9.2 SHAEDIT online tool

I developed the Space Hadron Accelerator Experiment Data Investigation Tool (SHAEDIT) for quick, easy, and intuitive viewing of all data collected in the experiments at NSRL [45]. The tool is an interactive Jupyter Notebook (formerly known as IPython) statically hosted on GitHub and fully available when built with Binder. Links to all of these are contained in Table 9.1.

While, ideally, one could provide a single URL for the tool, a few more steps are involved in accessing SHAEDIT due to the level of interactivity desired in the tool. The steps intended for users to access and use SHAEDIT are listed below.

1. Visit https://github.com/Lindt8/SHAEDIT
2. Scroll down to the description which provides additional instructions:
   (a) Open the link to the Binder build of the repository (https://mybinder.org/v2/gh/Lindt8/SHAEDIT/master).
   (b) Wait for the repository to be built / load
   (c) Once loaded, click on the "SHAEDIT.ipynb" file/link.
   (d) Follow the instructions stated within the notebook.
      i. Mark the Jupter Notebook as "Trusted" in the top-right area of the UI.

Table 9.1: SHAEDIT links

Name	URL	Description
GitHub repository	https://github.com/Lindt8/SHAEDIT	Contains all files, version history, and initial instructions
Binder build	https://mybinder.org/v2/gh/Lindt8/SHAEDIT/master	Link to interactive version of SHAEDIT
SHAEDIT DOI	https://doi.org/10.5281/zenodo.1287860	DOI which automatically links to most up-to-date release of SHAEDIT
Jupyter homepage	https://jupyter.org/	Platform on which SHAEDIT was written
GitHub homepage	https://github.com/	Host of all files for SHAEDIT
Binder homepage	https://mybinder.org/	Website used for making SHAEDIT work online for anyone

ii. Rerun all cells of the notebook using the "▷▷" button at the top of the page.

iii. SHAEDIT is ready to make plots and compare data!

While it is likely possible that a single HTML page containing a comparable version of this code could possibly be written in JavaScript or be made available through some other more advanced means, use of a Jupyter Notebook hosted on Binder was the most optimal choice for me due to my existing coding experience in Python. Additionally, an interactive Jupyter Notebook also allows any user to edit any of the code present or add more code if desired, providing an extra level of flexibility and customization; though, the code is hidden by default when first initialized to keep the interface simple but can be shown by a simple click of a button in the Jupyter Notebook. The usage and functionalities of SHAEDIT are showcased in Section 9.2.1.

9.2.1 SHAEDIT usage walk-through

This section provides a visual walk-through of SHAEDIT and serves as an opportunity to highlight the current features of the tool. First, after following the Binder link of the SHAEDIT repository (https://mybinder.org/v2/gh/Lindt8/SHAEDIT/master), the user will be greeted with a page like that shown in Figure 9.1.

After loading, the user will land on a page that looks like that pictured in Figure 9.2. Three links have been highlighted with red boxes; these are the only items on this page the user may wish to interact with. The first two are folders where any saved plots or text files will be temporarily stored for download from the website, and the third boxed item is the link the user should follow to use the SHAEDIT Jupyter Notebook.

After following the link, the user will be on the interactive SHAEDIT page. However, before SHAEDIT can be used, the user must mark the notebook as "Trusted" and then rerun all of the cells using the buttons highlighted in Figure 9.3 and answering the prompts for each as shown in Figure 9.4.

After that, SHAEDIT is ready to be used. These initial instructions must be repeated only when the Binder repository is reloaded, meaning that it usually only must be done once at the beginning of each session of using SHAEDIT. Figure 9.5 shows all of the plot options

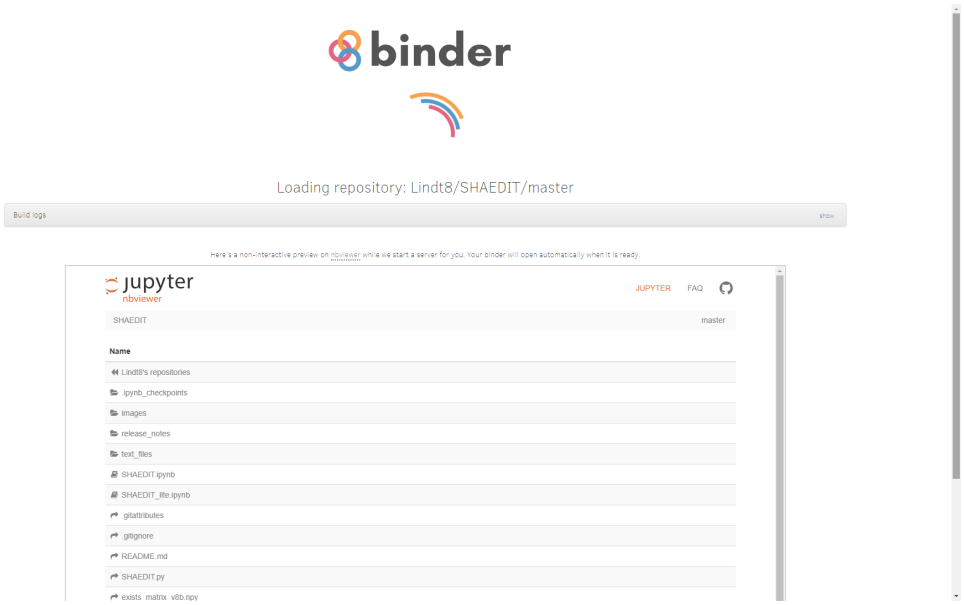


Figure 9.1: Binder loading screen



Figure 9.2: Binder repository directory

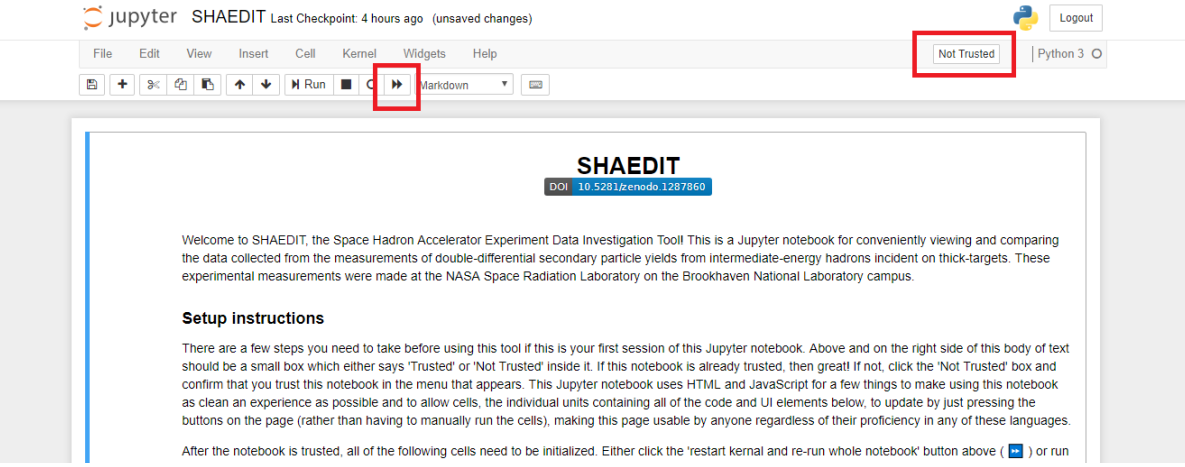


Figure 9.3: Initial SHAEDIT page

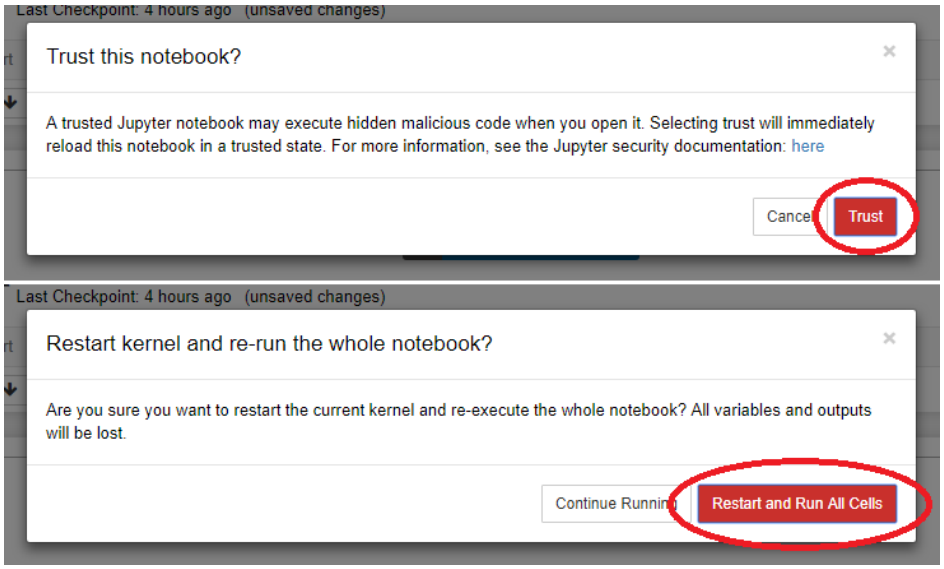


Figure 9.4: Mandatory initial prompts for running SHAEDIT

available in SHAEDIT. All of the buttons and checkboxes work intuitively as one would expect and truly allow for any and every possible combination of data collected at NSRL to be plotted. SHAEDIT also includes the functionality of spacing apart data by powers of 10 or 100 along any of the experimental axes to better study trends that would otherwise be difficult to observe due to overlap of plots.

One other goal of SHAEDIT is to be able to produce high-quality (and publication-ready) plots quickly and easily. Thus, alongside with the legend placement option specified before plotting, the plot can be freely resized and zoomed in/out as well as shown with the example case in Figure 9.6.

Lastly, to more closely investigate the data, one can view the corresponding text files from the NASA/UT repositories from within SHAEDIT for each spectrum plotted as shown in Figure 9.7. This allows the user to see things not apparent from the plots such as which components of the systematic uncertainty are most significant or various pieces of metadata about the experimental run for a particular spectrum.

All of the plots featured in Section 8.1 showing yield spectra were generated using SHAEDIT with no modifications to the stock code. While only time will tell how well SHAEDIT will accomplish this goal of bringing in more experts to view the experimental data, the code successfully accomplishes the goal of notably reducing the barrier to entry of studying these results.

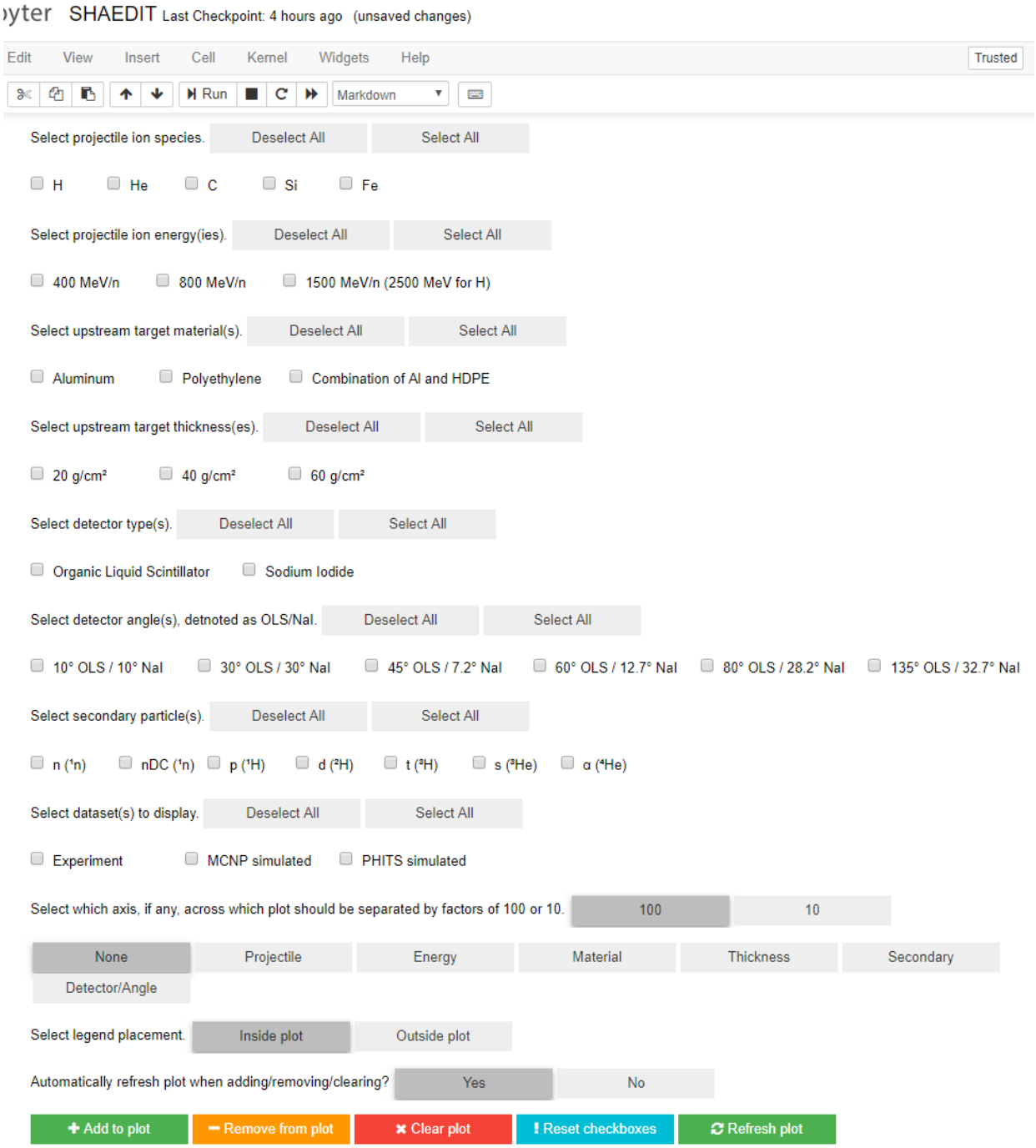


Figure 9.5: SHAEDIT plot construction options

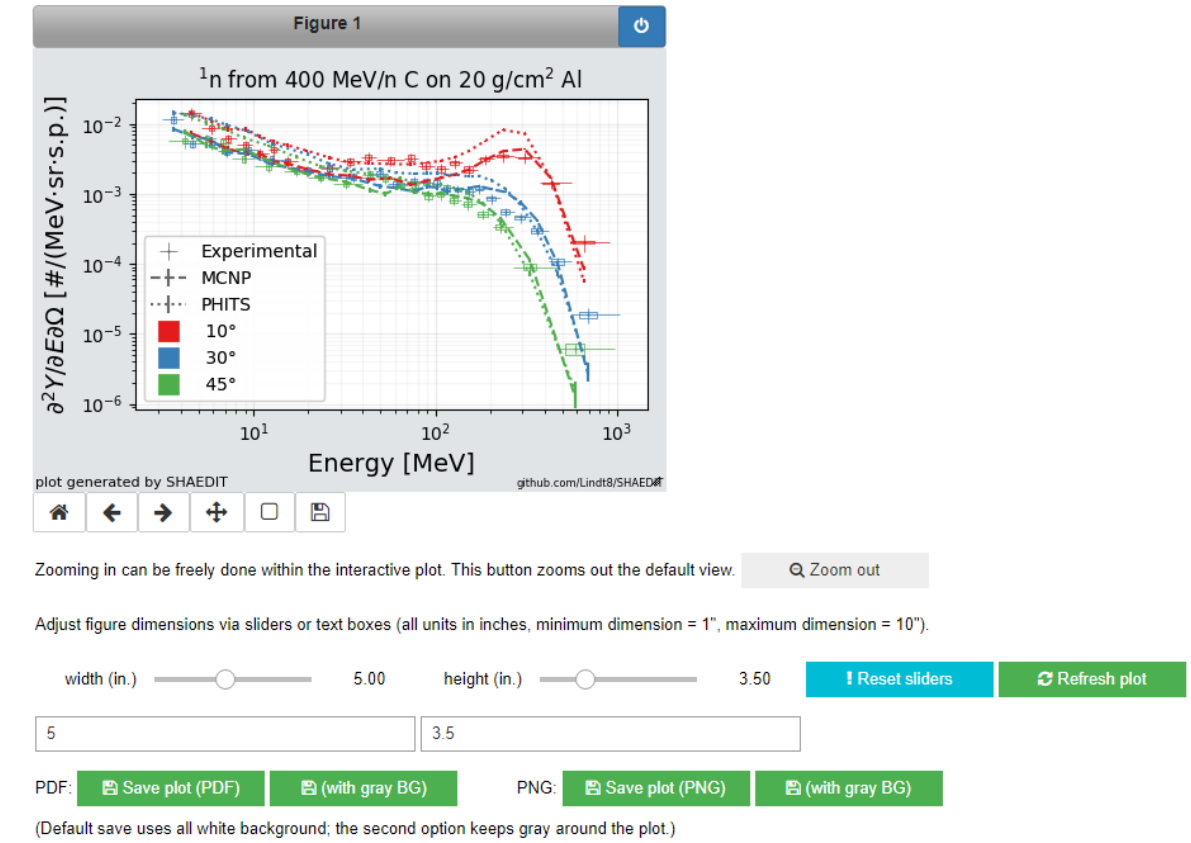


Figure 9.6: SHAEDIT example plot and other options

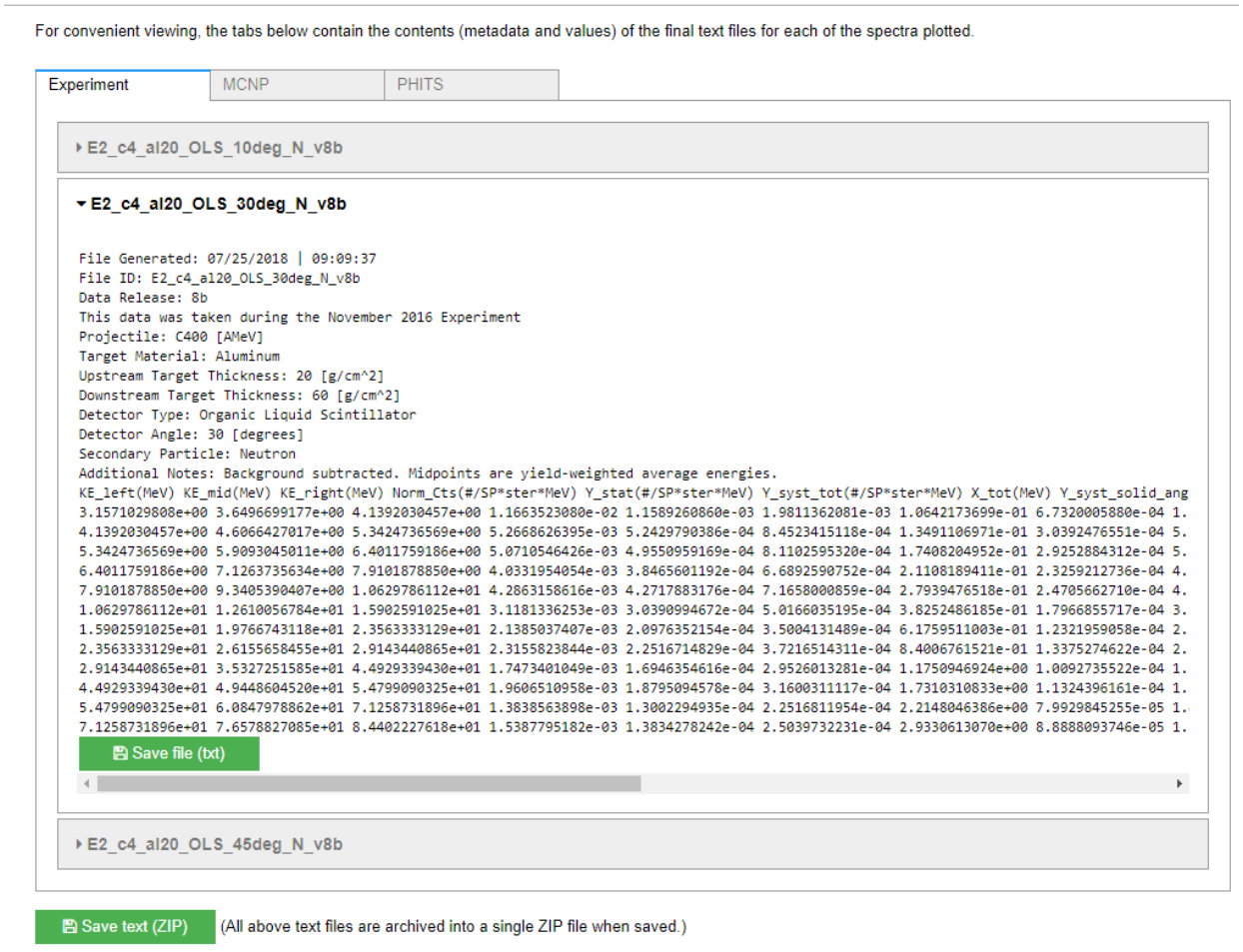


Figure 9.7: SHAEDIT interface for viewing text files of plotted spectra

Chapter 10

Conclusions

This dissertation includes a large volume of secondary neutron measurements taken across 500 hours of beam time spread across three experiments in March 2016, November/December 2016, and November 2017 where H, He, C, Si, and Fe beams at 400, 800 and 1500 MeV/n (2500 MeV instead for H beams) were accelerated into thick targets consisting of 20, 40, and 60 g/cm^2 of pure aluminum or HDPE or a combination of the two with a second 60 g/cm^2 pure aluminum or HDPE target located further downstream. Neutrons were detected in six organic liquid scintillation detectors located at 10°, 30°, 45°, 60°, 80°, and 135° with respect to the beamline axis and origin point of the experiment room.

Double-differential thick-target (DDTT) neutron yields were calculated for neutrons produced in the upstream target and flying directly to an OLS detector using time-of-flight techniques for all experimental systems tested except for those performed in the March 2016 experiment (400 MeV H, 800 MeV H, 400 MeV/n He, 400 MeV/n Fe, and 800 MeV/n Fe incident on the three thicknesses of pure aluminum targets). A number of improvements to the methodology used to characterize these neutrons were developed throughout this work.

This work also encompasses the development and implementation of a pulse height spectrum deconvolution methodology used to characterize the energy-dependent differential yield spectra of neutrons produced in the downstream target and scattered throughout the room prior to striking an OLS detector for all tested systems across the 500 hours of beam

time. The validity and performance of this methodology was confirmed by comparing time-of-flight-derived yield spectra to deconvolution-derived yield spectra for neutrons produced in the upstream target.

The trends in the yield spectra illustrate the general physical features one would expect with total neutron yield increasing as a function of target thickness. It is interesting to note that the hybrid Al+HDPE targets produced the lowest neutron yields when compared to equal thicknesses of either pure aluminum or HDPE, signifying the combination of the two materials would make for the best neutron shield.

The systematic comparison of the MCNP6 and PHITS results against the measured results and the two codes against each other revealed a number of noteworthy discrepancies. At the lowest angles, the magnitude of the high energy peak attributable to the projectile fragment in the neutron yield spectra is significantly overestimated in a similar fashion by both transport codes. However, for the absolute highest energies, above the beam energy, attributable to the Fermi momentum of the projectile nucleons, the Monte Carlo codes underestimate neutron yield. For the highest neutron energies at higher angles, the Monte Carlo codes consistently overestimate neutron yield by a notable margin. Both codes also underestimate neutron yield from the upstream target at the lowest neutron energies for polyethylene-containing upstream targets. As a general trend, neutron production is underestimated for lighter projectiles and overestimated for heavier projectiles. Between PHITS and MCNP, an interesting discrepancy between the two codes was seen in their treatment of neutron production in aluminum versus polyethylene. PHITS predicts greater neutron production in aluminum-containing targets than MCNP6, and the reverse is true, though to a lesser extent, for HDPE. Generally, whichever code predicts the lower yields in either of these cases is typically closer to the experimental results.

Effective dose calculations were performed to help make this large volume of data easier to digest and draw conclusions from. These effective dose values were then further condensed into "GCR effective doses" by weighting the effective dose calculated for each beam by its relative abundance in the GCR spectrum. This exercise confirmed that neutron effective dose does indeed increase for increasing shield thicknesses. However, one should be careful not to interpret this to mean confirmation of the optimal shielding thickness discussed earlier.

The buildup of neutron effective dose is expected for increasing shield thickness; the effective dose behavior of proton and other charged particle contributions are necessary to determine whether the total effective dose for increasing shield thicknesses will decrease, increase, or level-off. Regardless, when comparing the upstream target and downstream target (plus room scattered) contributions, the significance of the secondary target on neutron effective dose is greatly emphasized. This exercise also illustrated an interesting point regarding modeling spacecraft in deep space environments: If neutrons are the only secondary particle of concern, one could likely obtain reasonably accurate flux and dose results if only modeling the hydrogen and helium components of the GCR spectrum; the contribution of the higher mass ions is comparatively insignificant. Additionally, it was shown that, if designing a spacecraft with the goal of minimizing neutron effective dose to astronauts while constrained to selecting one of the experimentally-tested target configurations as the spacecraft shielding design, the one utilizing the hybrid upstream target consisting of 10 g/cm^2 of Al followed by 10 g/cm^2 of HDPE best minimizes neutron effective dose.

Lastly, an online tool, called SHAEDIT, was developed as a way to make this vast quantity of data publicly available and easily accessible. The tool successfully accomplishes the mission of allowing users to arbitrarily plot any (and all) datasets from this experiment and accompanying MCNP6 and PHITS simulations, allowing for comparison of any combination of spectra imaginable. It serves as an excellent way to quickly assess and visualize trends in the data. Due to the sheer volume of the experimental dataset though, one must be careful not to draw overarching conclusions from looking at only a handful of individual spectra.

While this specific project has come to a close, the larger NASA Thick GCR Shielding Project, of which this work was a part, still has much left to be accomplished. All of the data from this work and the other students at the University of Tennessee working on the data analyses from this experimental campaign will be utilized as a benchmark dataset for NASA to use to run additional simulations, quantify uncertainty related to astronaut dose and risk in heavily shielded spacecraft, quantify transport uncertainties in thick shields, ultimately determine the validity and (if true) value of the optimal shielding thickness, and assemble a shielding efficiency database for a variety of materials and thicknesses for use in future spacecraft design efforts.

Additionally, this work's comparisons of the experimental and modeled results highlight other areas which warrant additional experimental measurements and model improvements. In a number of places, it is obvious that the models would require notable improvement before agreeing with the experimental results. Since these measurements involved neutron yields in thick targets and represent total neutron production from all reactions between primary and secondary particles and the target materials, discerning precisely what within the models is the source of the disagreements showcased in this work can be difficult. I recommend the experimental measurement of these reaction cross sections to provide the data necessary to further improve the physics models within the modern transport codes.

Bibliography

[1] T. C. Slaba, A. A. Bahadori, B. D. Reddell, R. C. Singleterry, M. S. Clowdsley, and S. R. Blattnig, "Optimal shielding thickness for galactic cosmic ray environments," *Life Sciences in Space Research*, vol. 12, pp. 1 – 15, 2017. doi: https://doi.org/10.1016/j.lssr.2016.12.003. [Online]. Available: http://www.sciencedirect.com/science/article/pii/S2214552416300992 iv, xi, 14, 15, 185, 221

[2] N. A. McGirl, "Double differential neutron yields produced by proton, helium, and iron interactions in thick aluminum targets," Ph.D. dissertation, The University of Tennessee, Knoxville, 2017. xii, 2, 3, 4, 5, 21, 28, 31, 51, 67, 101, 143, 158

[3] L. A. Castellanos, "Thick-target measurements of light ion yields relevant to radiation transport calculations," Ph.D. dissertation, The University of Tennessee, Knoxville, 2018. 4, 5, 6, 21, 143

[4] A. P. Srikrishna, "Double differential thick target yields of secondary light-ion transport from intermediate-energy hadron experiments," Ph.D. dissertation, The University of Tennessee, Knoxville, 2018. 4, 22, 143

[5] T. Goorley, M. James, T. Booth, F. Brown, J. Bull, L. J. Cox, J. Durkee, J. Elson, M. Fensin, R. A. Forster, J. Hendricks, H. G. Hughes, R. Johns, B. Kiedrowski, R. Martz, S. Mashnik, G. McKinney, D. Pelowitz, R. Prael, J. Sweezy, L. Waters, T. Wilcox, and T. Zukaitis, "Initial MCNP6 release overview," *Nuclear Technology*, vol. 180, no. 3, pp. 298–315, 2012. doi: 10.13182/NT11-135. [Online]. Available: https://doi.org/10.13182/NT11-135 7, 143, 157

[6] T. Sato, Y. Iwamoto, S. Hashimoto, T. Ogawa, T. Furuta, S. ichiro Abe, T. Kai, P.-E. Tsai, N. Matsuda, H. Iwase, N. Shigyo, L. Sihver, and K. Niita, "Features of Particle and Heavy Ion Transport code System (PHITS) version 3.02," *Journal of Nuclear Science and Technology*, vol. 55, no. 6, pp. 684–690, 2018. doi: 10.1080/00223131.2017.1419890. [Online]. Available: https://doi.org/10.1080/00223131.2017.1419890 7, 143, 157

[7] J. M. Ryan, J. A. Lockwood, and H. Debrunner, "Solar energetic particles," *Space Science Reviews*, vol. 93, no. 1, pp. 35–53, Jul 2000. doi: 10.1023/A:1026580008909. [Online]. Available: https://doi.org/10.1023/A:1026580008909 9

[8] J. A. Simpson, "Elemental and isotopic composition of the galactic cosmic rays," *Annual Review of Nuclear and Particle Science*, vol. 33, no. 1, pp. 323–382, 1983. 9, 10

[9] K. Hayatsu, M. Hareyama, S. Kobayashi, N. Yamashita, M. Miyajim, K. Sakurai, and N. Hasebe, "Radiation doses for human exposed to galactic cosmic rays and their secondary products on the lunar surface," *Biological Sciences in Space*, vol. 22, no. 2, pp. 59–66, 2008. doi: 10.2187/bss.22.59 xi, 10

[10] C. Zeitlin, T. Cleghorn, F. Cucinotta, P. Saganti, V. Andersen, K. Lee, L. Pinsky, W. Atwell, R. Turner, and G. Badhwar, "Overview of the Martian radiation environment experiment," *Advances in Space Research*, vol. 33, no. 12, pp. 2204 – 2210, 2004. doi: https://doi.org/10.1016/S0273-1177(03)00514-3 Mercury, Mars and Saturn. [Online]. Available: http://www.sciencedirect.com/science/article/pii/S0273117703005143 10

[11] M.-h. Y. Kim, S. A. Thibeault, L. C. Simonsen, and J. Wilson, "Comparison of Martian Meteorites and Martian Regolith as Shield Materials for Galactic Cosmic Rays," 11 1998. xi, 10, 11

[12] L. W. Townsend, J. W. Wilson, J. W. Norbury, and H. B. Bidasaria, *An abrasion-ablation model description of galactic heavy-ion fragmentation*, ser. NASA technical paper. National Aeronautics and Space Administration, Scientific and Technical Information Branch, 1984. [Online]. Available: https://books.google.com/books?id=xrjEs2Ks_40C 12, 13

[13] F. A. Cucinotta, J. W. Wilson, and L. W. Townsend, "Abrasion-ablation model for neutron production in heavy ion collisions," *Nuclear Physics A*, vol. 619, no. 1, pp. 202 – 212, 1997. doi: https://doi.org/10.1016/S0375-9474(97)00130-9. [Online]. Available: http://www.sciencedirect.com/science/article/pii/S0375947497001309 12, 13

[14] M. Durante and F. A. Cucinotta, "Physical basis of radiation protection in space travel," *Rev. Mod. Phys.*, vol. 83, pp. 1245–1281, Nov 2011. doi: 10.1103/RevModPhys.83.1245. [Online]. Available: https://link.aps.org/doi/10.1103/RevModPhys.83.1245 xi, 12, 13

[15] Y. Iwata, T. Murakami, H. Sato, H. Iwase, T. Nakamura, T. Kurosawa, L. Heilbronn, R. M. Ronningen, K. Ieki, Y. Tozawa, and K. Niita, "Double-differential cross sections for the neutron production from heavy-ion reactions at energies $e/a = 290--600$MeV," *Phys. Rev. C*, vol. 64, p. 054609, Oct 2001. doi: 10.1103/PhysRevC.64.054609. [Online]. Available: https://link.aps.org/doi/10.1103/PhysRevC.64.054609 13

[16] J. Gosset, H. H. Gutbrod, W. G. Meyer, A. M. Poskanzer, A. Sandoval, R. Stock, and G. D. Westfall, "Central collisions of relativistic heavy ions," *Phys. Rev. C*, vol. 16, pp. 629–657, Aug 1977. doi: 10.1103/PhysRevC.16.629. [Online]. Available: https://link.aps.org/doi/10.1103/PhysRevC.16.629 xi, 13, 14

[17] L. Sihver, D. Mancusi, K. Niita, T. Sato, L. Townsend, C. Farmer, L. Pinsky, A. Ferrari, F. Cerutti, and I. Gomes, "Benchmarking of calculated projectile fragmentation cross-sections using the 3-D, MC codes PHITS, FLUKA, HETC-HEDS, MCNPX$_{HI}$, and NUCFRG2," *Acta Astronautica*, vol. 63, no. 7, pp. 865 – 877, 2008. doi: https://doi.org/10.1016/j.actaastro.2008.02.012. [Online]. Available: http://www.sciencedirect.com/science/article/pii/S009457650800060X 14

[18] J. H. Heinbockel, T. C. Slaba, R. K. Tripathi, S. R. Blattnig, J. W. Norbury, F. F. Badavi, L. W. Townsend, T. Handler, T. A. Gabriel, L. S. Pinsky, B. Reddell, and A. R. Aumann, "Comparison of the transport codes HZETRN, HETC and FLUKA for galactic cosmic rays," *Advances in Space Research*, vol. 47, no. 6, pp. 1089 – 1105, 2011. doi: https://doi.org/10.1016/j.asr.2010.11.013. [Online]. Available: http://www.sciencedirect.com/science/article/pii/S0273117710007428 14

[19] J. W. Wilson, T. C. Slaba, F. F. Badavi, B. D. Reddell, and A. A. Bahadori, "Advances in NASA radiation transport research: 3DHZETRN," *Life Sciences in Space Research*, vol. 2, pp. 6 – 22, 2014. doi: https://doi.org/10.1016/j.lssr.2014.05.003. [Online]. Available: http://www.sciencedirect.com/science/article/pii/S2214552414000297 14

[20] G. F. Knoll, *Radiation Detection and Measurement*. Wiley, 2000. ISBN 9780471073383. [Online]. Available: https://books.google.com/books?id=HKBVAAAAMAAJ 18

[21] R. A. Cecil, B. D. Anderson, and R. Madey, "Improved predections of neutron detection efficiency for hydrocarbon scintillators from 1 MeV to about 300 MeV," *Nuclear Instruments and Methods*, vol. 161, no. 3, pp. 439 – 447, 1979. doi: https://doi.org/10.1016/0029-554X(79)90417-8. [Online]. Available: http://www.sciencedirect.com/science/article/pii/0029554X79904178 18, 19

[22] M. Tajik, N. Ghal-Eh, G. R. Etaati, and H. Afarideh, "Modeling NE213 scintillator response to neutrons using an mcnpx-photrack hybrid code," *Nuclear Instruments and Methods in Physics Research Section A: Accelerators, Spectrometers, Detectors and Associated Equipment*, vol. 704, pp. 104 – 110, 2013. doi: http://dx.doi.org/10.1016/j.nima.2012.12.001. [Online]. Available: http://www.sciencedirect.com/science/article/pii/S0168900212015343 18, 19

[23] R. L. Craun and D. L. Smith, "Analysis of response data for several organic scintillators," *Nuclear Instruments and Methods*, vol. 80, no. 2, pp. 239 – 244, 1970. doi: https://doi.org/10.1016/0029-554X(70)90768-8. [Online]. Available: http://www.sciencedirect.com/science/article/pii/0029554X70907688 18

[24] S. Nyibule, J. Tõke, E. Henry, W. U. Schröder, L. Acosta, L. Auditore, G. Cardella, E. D. Filippo, L. Francalanza, S. Gianì, T. Minniti, E. Morgana, E. V. Pagano, S. Pirrone, G. Politi, L. Quattrocchi, P. Russotto, A. Trifirò, and M. Trimarchi, "Birks' scaling of the particle light output functions for the EJ 299-33 plastic scintillator," *Nuclear Instruments and Methods in Physics Research Section A: Accelerators, Spectrometers, Detectors and Associated Equipment*, vol. 768, pp. 141 – 145, 2014. doi: https://doi.org/10.1016/j.nima.2014.09.056. [Online]. Available: http://www.sciencedirect.com/science/article/pii/S0168900214010845 18

[25] V. V. Verbinski, W. R. Burrus, T. A. Love, W. Zobel, N. W. Hill, and R. Textor, "Calibration of an organic scintillator for neutron spectrometry," *Nuclear Instruments*

and Methods, vol. 65, no. 1, pp. 8 – 25, 1968. doi: https://doi.org/10.1016/0029-554X(68)90003-7. [Online]. Available: http://www.sciencedirect.com/science/article/pii/0029554X68900037 18, 47, 51

[26] D. Satoh, S. Kunieda, Y. Iwamoto, N. Shigyo, and K. Ishibashi, "Development of SCINFUL-QMD code to calculate the neutron detection efficiencies for liquid organic scintillator up to 3 GeV," *Journal of Nuclear Science and Technology*, vol. 39, no. sup2, pp. 657–660, 2002. doi: 10.1080/00223131.2002.10875185. [Online]. Available: https://doi.org/10.1080/00223131.2002.10875185 19, 101, 122

[27] J. K. Dickens, "SCINFUL: A Monte Carlo based computer program to determine a scintillator full energy response to neutron detection for E/sub n/ between 0. 1 and 80 MeV: Program development and comparisons of program predictions with experimental data," Tech. Rep., apr 1988. [Online]. Available: https://doi.org/10.2172/7166672 19

[28] N. Nakao, T. Kurosawa, T. Nakamura, and Y. Uwamino, "Absolute measurements of the response function of an NE213 organic liquid scintillator for the neutron energy range up to 206 mev," *Nuclear Instruments and Methods in Physics Research Section A: Accelerators, Spectrometers, Detectors and Associated Equipment*, vol. 463, no. 1–2, pp. 275 – 287, 2001. doi: http://dx.doi.org/10.1016/S0168-9002(01)00260-1. [Online]. Available: http://www.sciencedirect.com/science/article/pii/S0168900201002601 19

[29] M. Sasaki, N. Nakao, T. Nakamura, T. Shibata, and A. Fukumura, "Measurements of the response functions of an NE213 organic liquid scintillator to neutrons up to 800 MeV," *Nuclear Instruments and Methods in Physics Research Section A: Accelerators, Spectrometers, Detectors and Associated Equipment*, vol. 480, no. 2–3, pp. 440 – 447, 2002. doi: http://dx.doi.org/10.1016/S0168-9002(01)00948-2. [Online]. Available: http://www.sciencedirect.com/science/article/pii/S0168900201009482 19, 116, 117

[30] D. Satoh, T. Sato, A. Endo, Y. Yamaguchi, M. Takada, and K. Ishibashi, "Measurement of Response Functions of a Liquid Organic Scintillator for Neutrons up to 800 MeV," vol. 43, pp. 714–719, 07 2006. 19

[31] J. Turner, *Atoms, Radiation, and Radiation Protection*, ser. No Longer used. Wiley, 2008. ISBN 9783527616985. [Online]. Available: https://books.google.com/books?id=-NjMPZEt2yUC 26

[32] R. Brun and F. Rademakers, "Root - an object oriented data analysis framework," in *AIHENP'96 Workshop, Lausane*, vol. 389, 1996, pp. 81–86. 35

[33] P.-E. Tsai, "Study of secondary particles produced from heavy-ion interactions," Ph.D. dissertation, The University of Tennessee, Knoxville, 2015. 51, 101

[34] T. Nakamura and L. Heilbronn, *Handbook on Secondary Particle Production and Transport by High-energy Heavy Ions:(with CD-ROM)*. World Scientific, 2006. 101, 112

[35] C. C. Lawrence, "Neutron spectrum unfolding with organic scintillators for arms-control verification," Ph.D. dissertation, The University of Michigan, 2014. 115, 126

[36] J. F. Ziegler, M. D. Ziegler, and J. P. Biersack, "Srim – the stopping and range of ions in matter (2010)," *Nuclear Instruments and Methods in Physics Research Section B: Beam Interactions with Materials and Atoms*, vol. 268, no. 11, pp. 1818 – 1823, 2010. doi: https://doi.org/10.1016/j.nimb.2010.02.091 19th International Conference on Ion Beam Analysis. [Online]. Available: http://www.sciencedirect.com/science/article/pii/S0168583X10001862 122, 123

[37] P. Žugec, N. Colonna, M. Sabate-Gilarte, V. Vlachoudis, C. Massimi, J. Lerendegui-Marco, A. Stamatopoulos, M. Bacak, and S. G. Warren, "A direct method for unfolding the resolution function from measurements of neutron induced reactions," *Nuclear Instruments and Methods in Physics Research Section A: Accelerators, Spectrometers, Detectors and Associated Equipment*, vol. 875, pp. 41 – 50, 2017. doi: https://doi.org/10.1016/j.nima.2017.09.004. [Online]. Available: http://www.sciencedirect.com/science/article/pii/S0168900217309610 124

[38] D. Calvetti, S. Morigi, L. Reichel, and F. Sgallari, "Tikhonov regularization and the L-curve for large discrete ill-posed problems," *Journal of Computational*

and Applied Mathematics, vol. 123, no. 1–2, pp. 423 – 446, 2000. doi: http://dx.doi.org/10.1016/S0377-0427(00)00414-3 Numerical Analysis 2000. Vol. III: Linear Algebra. [Online]. Available: http://www.sciencedirect.com/science/article/pii/S0377042700004143 127

[39] P. C. Hansen, "The L-Curve and its use in the numerical treatment of inverse problems," in *in Computational Inverse Problems in Electrocardiology, ed. P. Johnston, Advances in Computational Bioengineering.* WIT Press, 2000, pp. 119–142. 127

[40] T. Kittelmann, E. Klinkby, E. B. Knudsen, P. Willendrup, X. X. Cai, and K. Kanaki, "Monte Carlo Particle Lists: MCPL," *Computer Physics Communications*, vol. 218, pp. 17 – 42, 2017. doi: https://doi.org/10.1016/j.cpc.2017.04.012. [Online]. Available: http://www.sciencedirect.com/science/article/pii/S0010465517301261 148

[41] W. J. M. de Kruijf and J. L. Kloosterman, "On the average chord length in reactor physics," *Annals of Nuclear Energy*, vol. 30, no. 5, pp. 549 – 553, 2003. doi: https://doi.org/10.1016/S0306-4549(02)00107-X. [Online]. Available: http://www.sciencedirect.com/science/article/pii/S030645490200107X 151, 153

[42] Y. Iwamoto, T. Sato, S. Hashimoto, T. Ogawa, T. Furuta, S. ichiro Abe, T. Kai, N. Matsuda, R. Hosoyamada, and K. Niita, "Benchmark study of the recent version of the PHITS code," *Journal of Nuclear Science and Technology*, vol. 54, no. 5, pp. 617–635, 2017. doi: 10.1080/00223131.2017.1297742. [Online]. Available: https://doi.org/10.1080/00223131.2017.1297742 157

[43] ICRP, "Conversion coefficients for radiological protection quantities for external radiation exposures. ICRP publication 116," *Annals of the ICRP*, vol. 40, no. 2-5, pp. 1–257, 2010. doi: 10.1016/j.icrp.2011.10.001. [Online]. Available: https://doi.org/10.1016/j.icrp.2011.10.001 220

[44] D. Matthiä, T. Berger, A. I. Mrigakshi, and G. Reitz, "A ready-to-use galactic cosmic ray model," *Advances in Space Research*, vol. 51, no. 3, pp. 329 – 338, 2013. doi: http://dx.doi.org/10.1016/j.asr.2012.09.022. [Online]. Available: http://www.sciencedirect.com/science/article/pii/S0273117712005947 226

[45] H. N. Ratliff, "SHAEDIT: Space Hadron Accelerator Experiment Data Investigation Tool," Jun. 2018. [Online]. Available: https://doi.org/10.5281/zenodo.1287860 245

Appendices

Appendix A

Equipment

Below in Table A.1 is a list of all of the logic units used in the experiments.

Table A.1: List of logic units and their manufacturers

Manufacturer	Logic unit
Wiener	CC-USB CAMAC Controller with USB interface
CAEN	HVPS SY5527 (Geco 2020 software)
Bertan	HVPS Model 323
CAEN	16 Channel CFD Model N843
LeCroy	Multiplicity Logic Unit Model 380A
-	Majority Coincidence Model C314/NL
LeCroy	Dual Gate Generator Model 222
P/S	Quad Gate/Delay Generator Model 794
LeCroy	Logic Fan In/Fan Out Model 429
LeCroy	Octal Discriminator Model 623
LeCroy	Octal Discriminator Model 623B
Joerger	Scaler Model S12
-	Japanese Module 6 Ch. PSD
LeCroy	8 Channel TDC Model 2228A
LeCroy	12 Channel ADC Model 2249A
LeCroy	12 Channel ADC Model 2249W
BNL	Splitters
BNL	Delays

Appendix B

Production point correction plots

This appendix contains plots for all production point corrections used for the November 2016 and 2017 experiments as was detailed in Section 4.9.

B.1 Condensed plots

In Figures B.1 and B.2 are very condensed plots illustrating the final production point and effective target thicknesses used in the analysis for every system measured in the November 2016 and 2017 experiments.

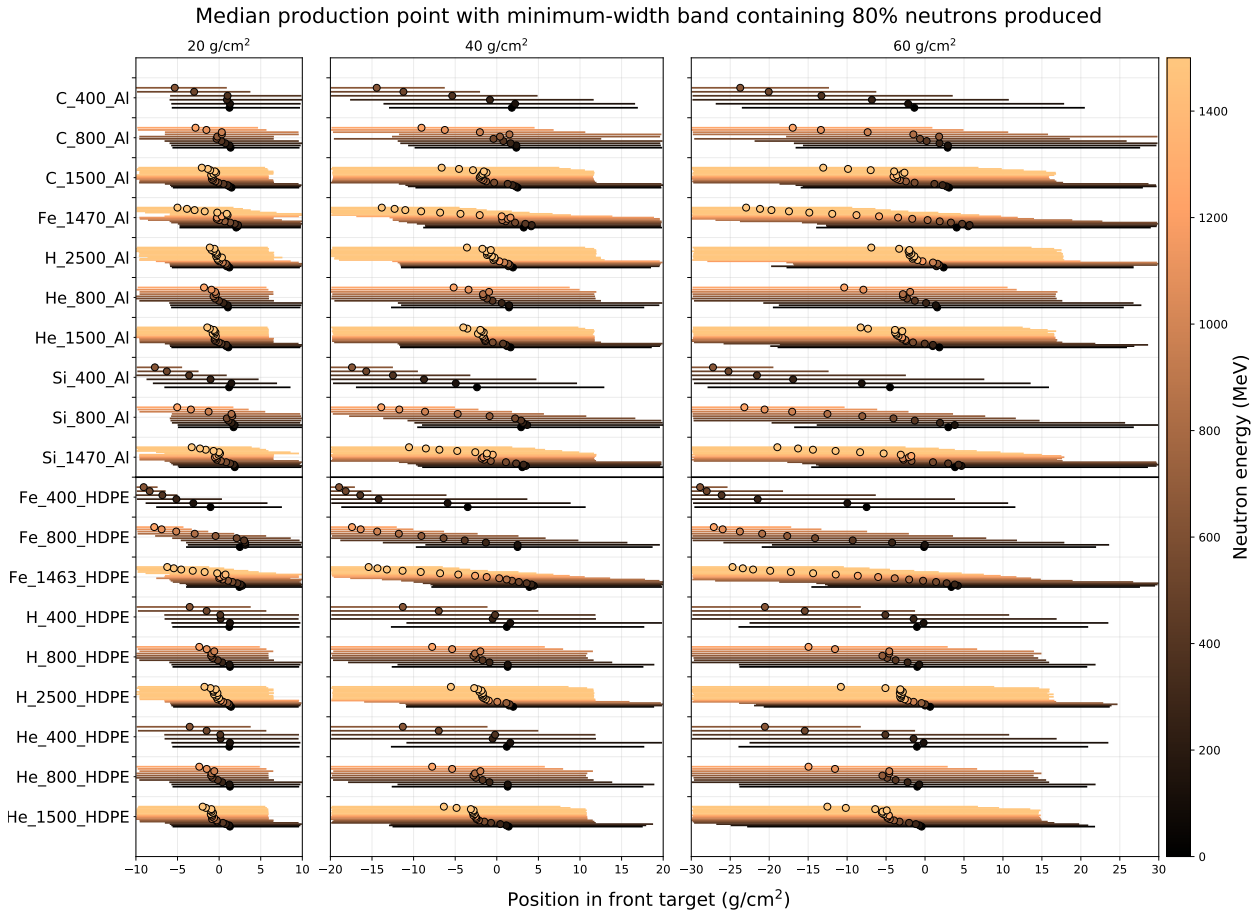


Figure B.1: Production point (median) and effective target thickness (minimum thickness containing 80% of neutrons produced in a given energy bin) for all systems measured in the November 2016 experiment.

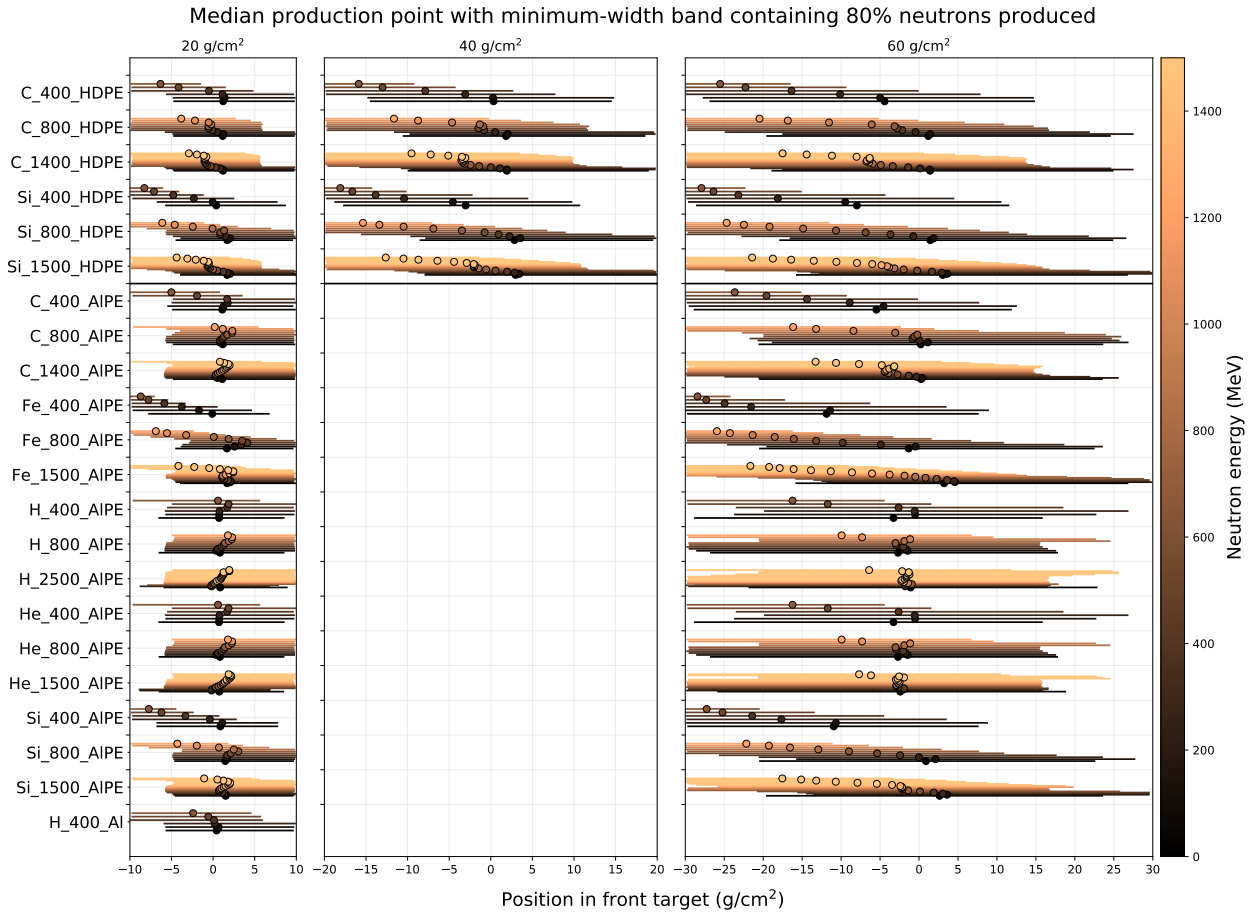
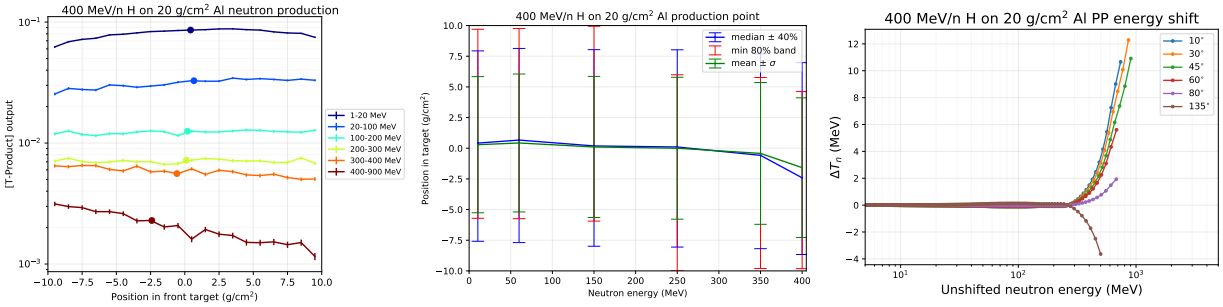


Figure B.2: Production point (median) and effective target thickness (minimum thickness containing 80% of neutrons produced in a given energy bin) for all systems measured in the November 2017 experiment.

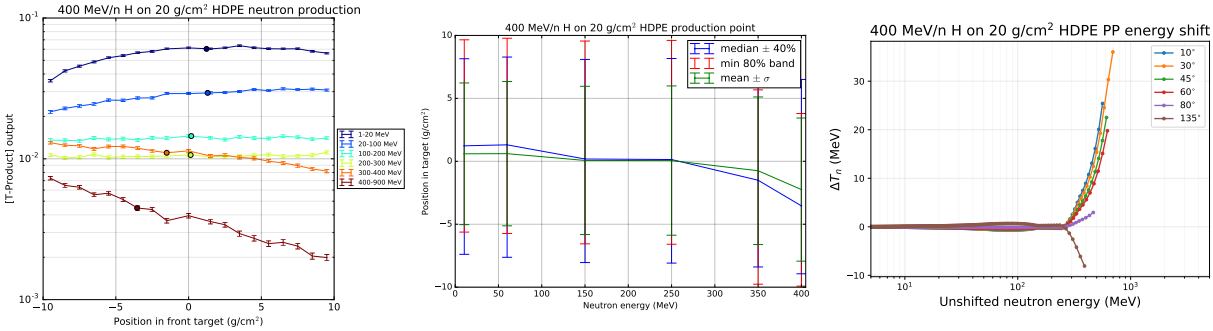
B.2 All individual plots

This section contains the three plots highlighting the main steps of the production point and effective target thickness corrections for every measured system in the November 2016 and 2017 experiments. The first of each set of three plots shows the neutron production as a function of neutron energy and location within the target. The second plot shows the mean and median production points along with the three effective target thicknesses discussed in Section 4.9.1. Finally, the third plot shows the shift in neutron energy caused by this production point correction for each detector.



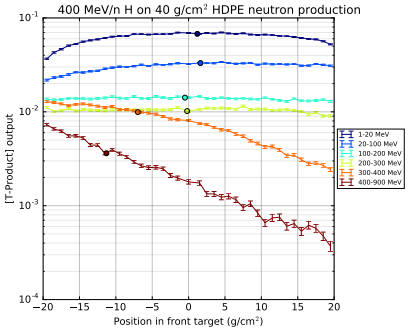
(a) n production distribution (b) effective target thickness (c) n energy shift

Figure B.3: Neutron production corrections for 400 MeV H on 20 g/cm^2 Al

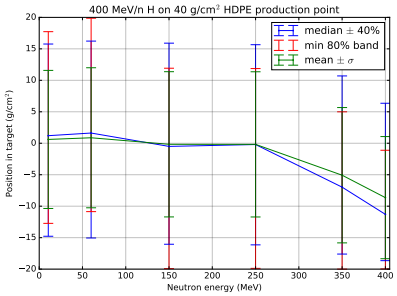


(a) n production distribution (b) effective target thickness (c) n energy shift

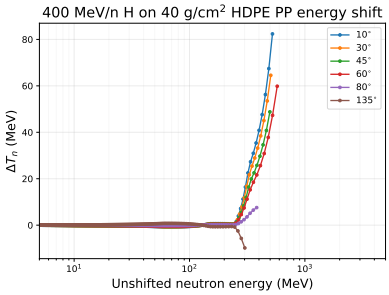
Figure B.4: Neutron production corrections for 400 MeV H on 20 g/cm^2 HDPE



(a) n production distribution

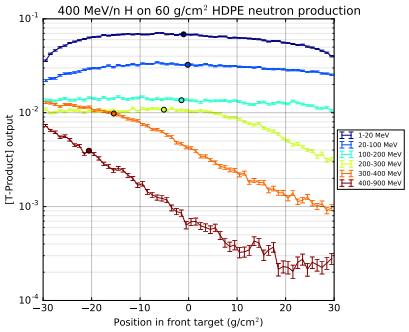


(b) effective target thickness

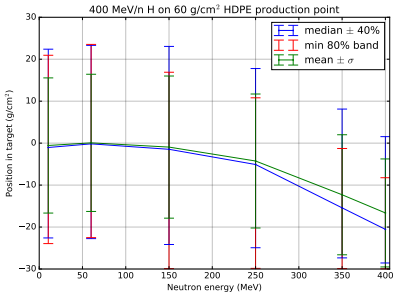


(c) n energy shift

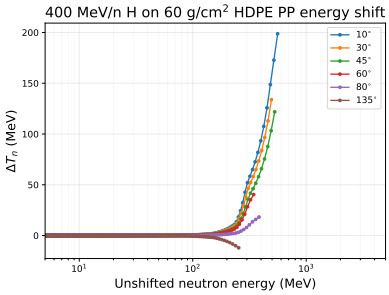
Figure B.5: Neutron production corrections for 400 MeV H on 40 g/cm^2 HDPE



(a) n production distribution

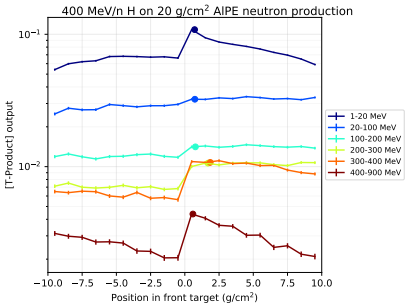


(b) effective target thickness

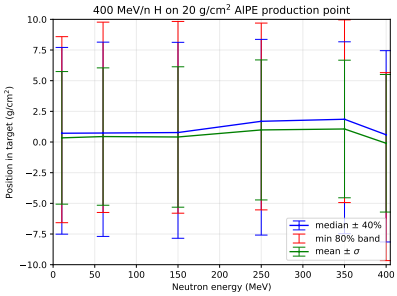


(c) n energy shift

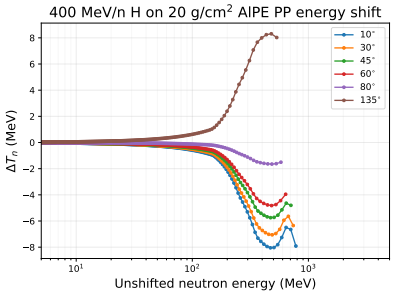
Figure B.6: Neutron production corrections for 400 MeV H on 60 g/cm^2 HDPE



(a) n production distribution

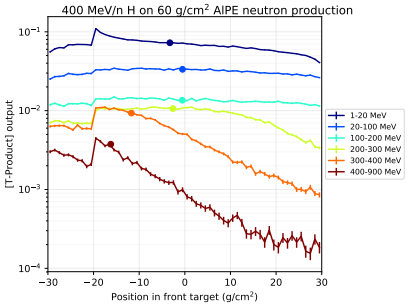


(b) effective target thickness

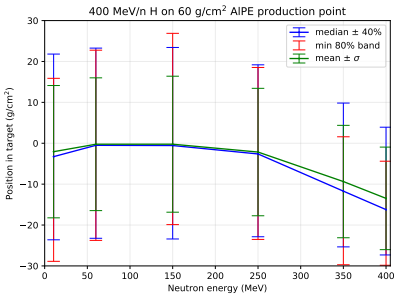


(c) n energy shift

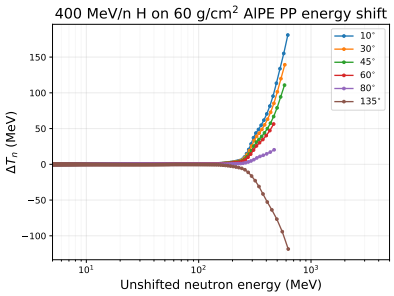
Figure B.7: Neutron production corrections for 400 MeV H on 20 g/cm^2 AlPE



(a) n production distribution

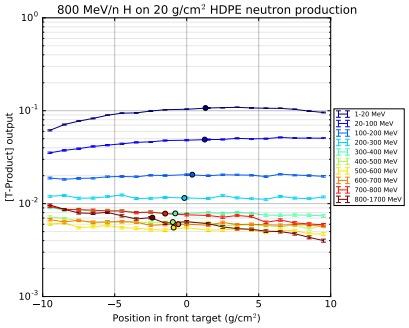


(b) effective target thickness

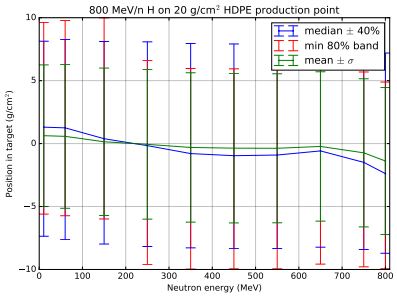


(c) n energy shift

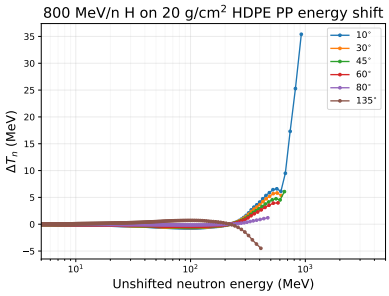
Figure B.8: Neutron production corrections for 400 MeV H on 60 g/cm^2 AlPE



(a) n production distribution

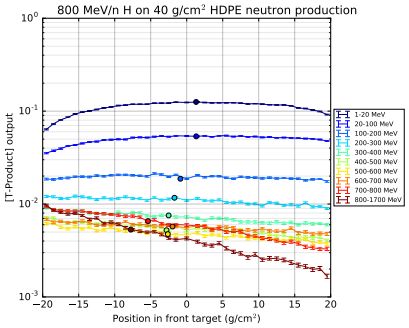


(b) effective target thickness

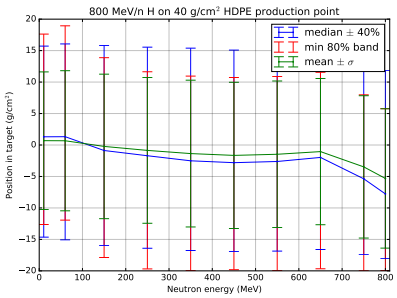


(c) n energy shift

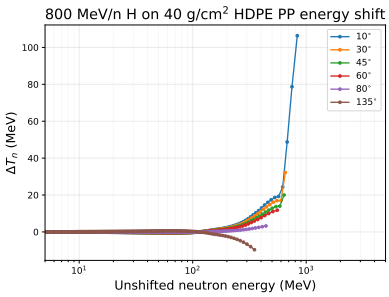
Figure B.9: Neutron production corrections for 800 MeV H on 20 g/cm^2 HDPE



(a) n production distribution

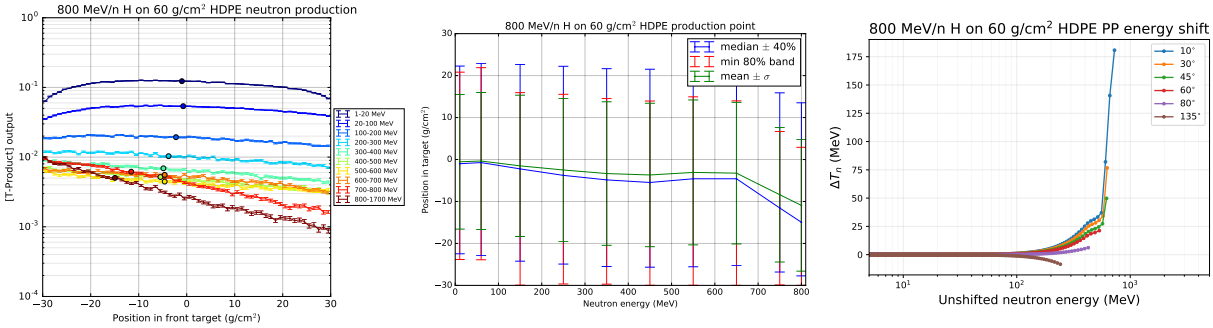


(b) effective target thickness



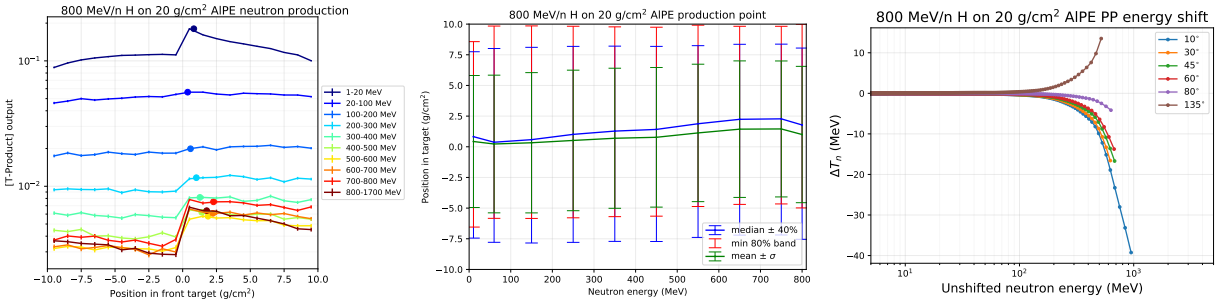
(c) n energy shift

Figure B.10: Neutron production corrections for 800 MeV H on 40 g/cm^2 HDPE



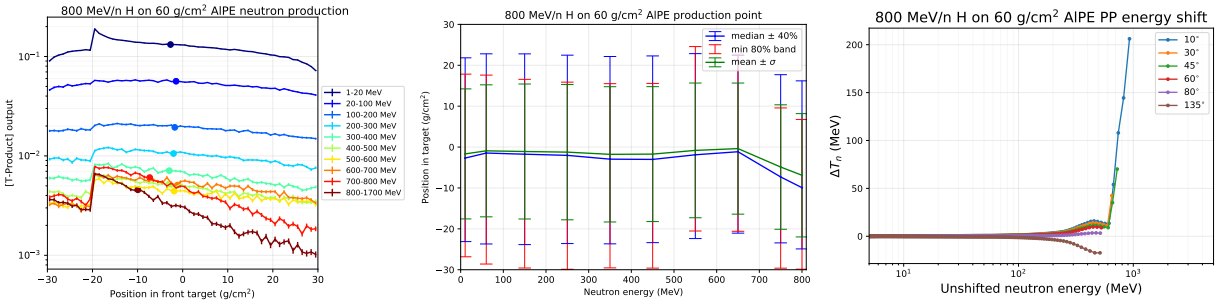
(a) n production distribution (b) effective target thickness (c) n energy shift

Figure B.11: Neutron production corrections for 800 MeV H on 60 g/cm^2 HDPE



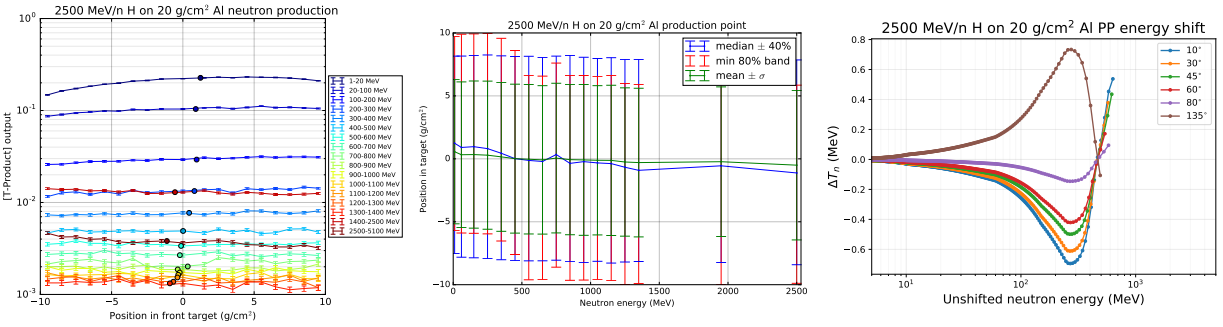
(a) n production distribution (b) effective target thickness (c) n energy shift

Figure B.12: Neutron production corrections for 800 MeV H on 20 g/cm^2 AlPE



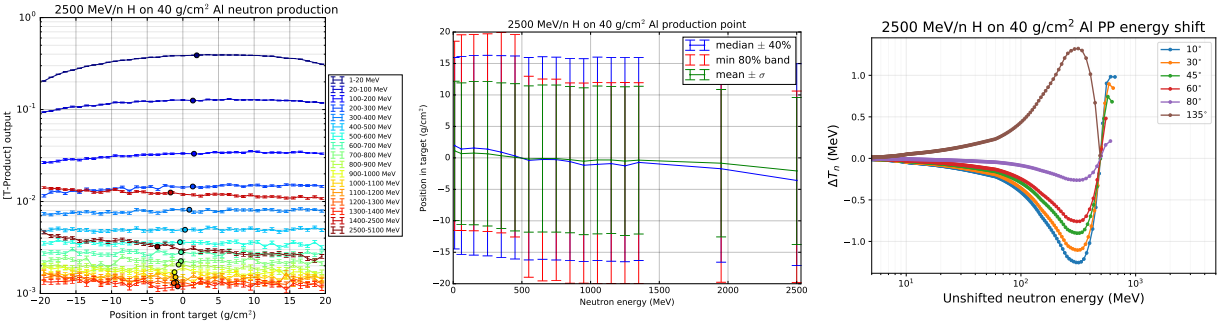
(a) n production distribution (b) effective target thickness (c) n energy shift

Figure B.13: Neutron production corrections for 800 MeV H on 60 g/cm^2 AlPE



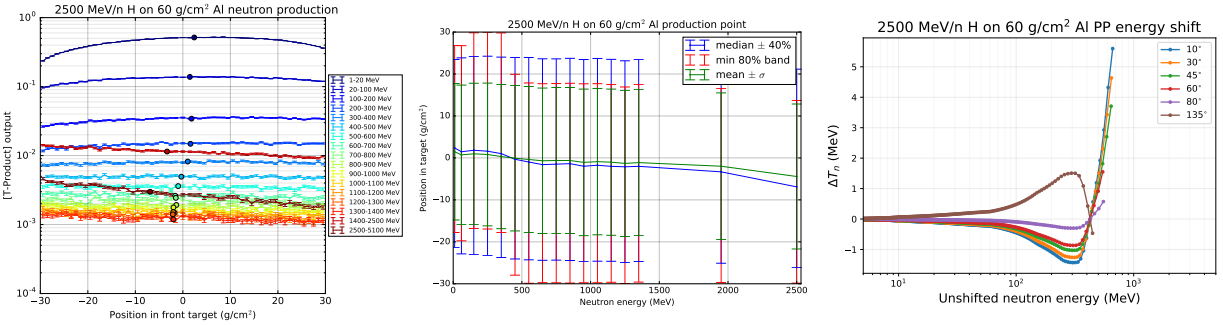
(a) n production distribution (b) effective target thickness (c) n energy shift

Figure B.14: Neutron production corrections for 2500 MeV H on 20 g/cm^2 Al



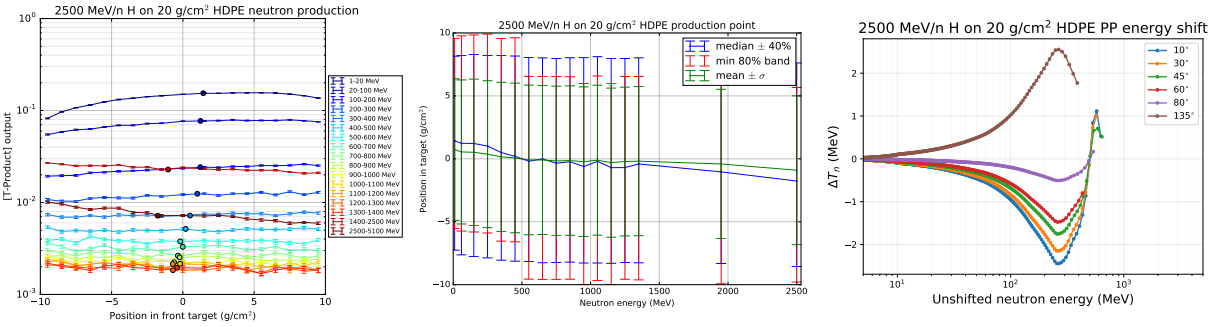
(a) n production distribution (b) effective target thickness (c) n energy shift

Figure B.15: Neutron production corrections for 2500 MeV H on 40 g/cm^2 Al



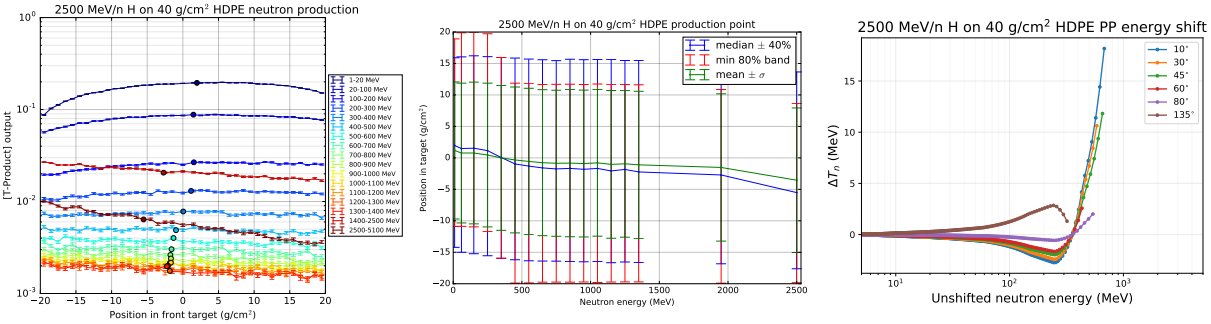
(a) n production distribution (b) effective target thickness (c) n energy shift

Figure B.16: Neutron production corrections for 2500 MeV H on 60 g/cm^2 Al



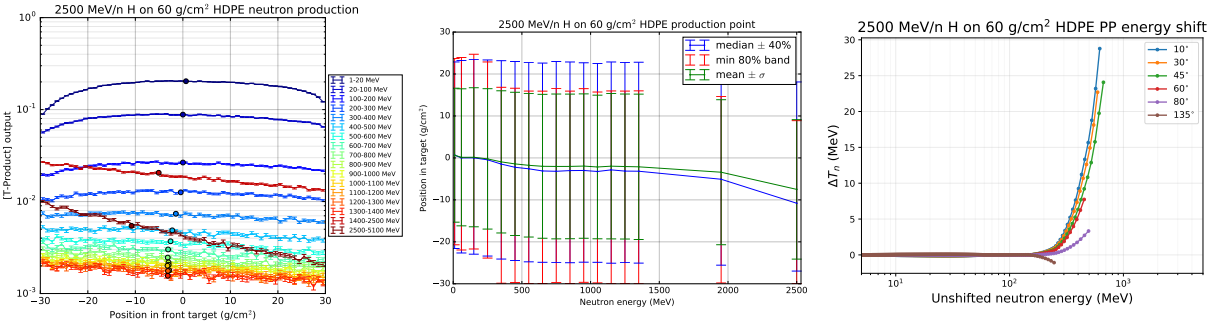
(a) n production distribution (b) effective target thickness (c) n energy shift

Figure B.17: Neutron production corrections for 2500 MeV H on 20 g/cm^2 HDPE



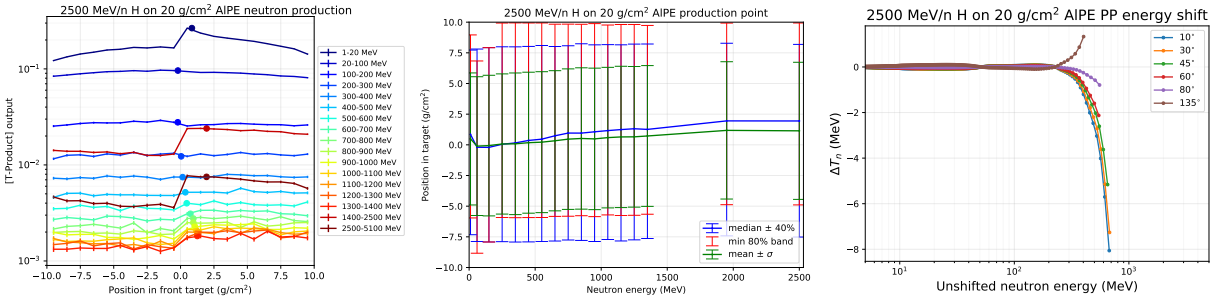
(a) n production distribution (b) effective target thickness (c) n energy shift

Figure B.18: Neutron production corrections for 2500 MeV H on 40 g/cm^2 HDPE



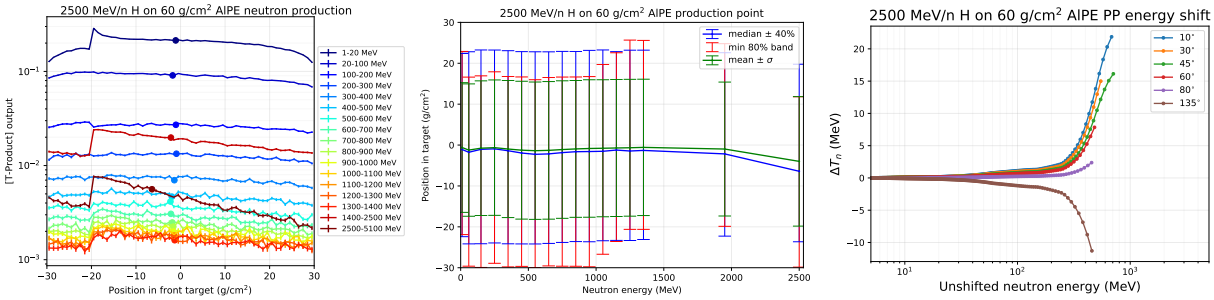
(a) n production distribution (b) effective target thickness (c) n energy shift

Figure B.19: Neutron production corrections for 2500 MeV H on 60 g/cm^2 HDPE



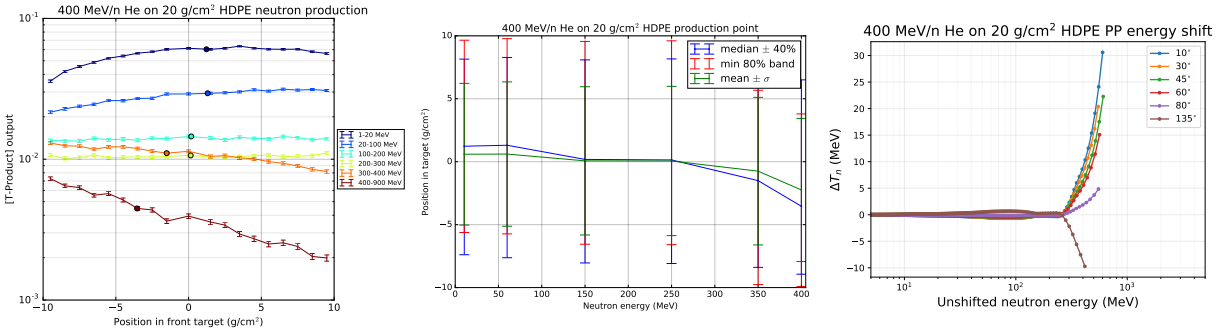
(a) n production distribution (b) effective target thickness (c) n energy shift

Figure B.20: Neutron production corrections for 2500 MeV H on 20 g/cm^2 AlPE



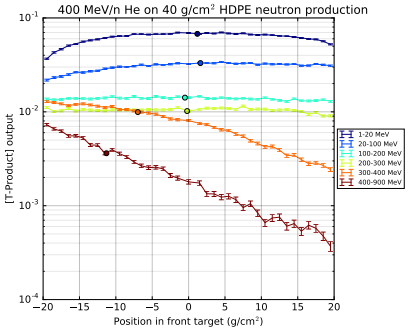
(a) n production distribution (b) effective target thickness (c) n energy shift

Figure B.21: Neutron production corrections for 2500 MeV H on 60 g/cm^2 AlPE

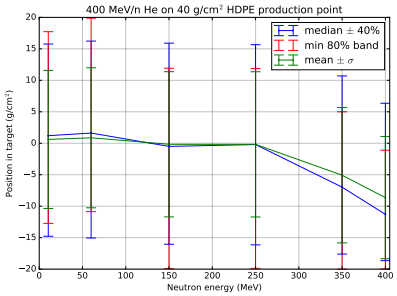


(a) n production distribution (b) effective target thickness (c) n energy shift

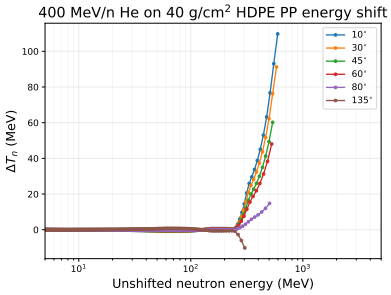
Figure B.22: Neutron production corrections for 400 MeV/n He on 20 g/cm^2 HDPE



(a) n production distribution

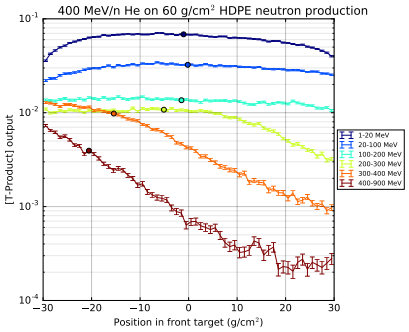


(b) effective target thickness

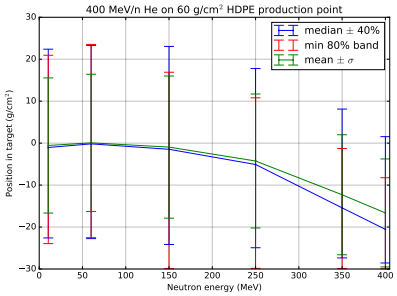


(c) n energy shift

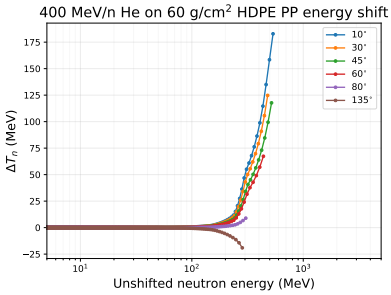
Figure B.23: Neutron production corrections for 400 MeV/n He on 40 g/cm^2 HDPE



(a) n production distribution

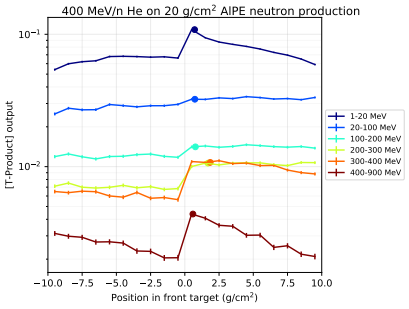


(b) effective target thickness

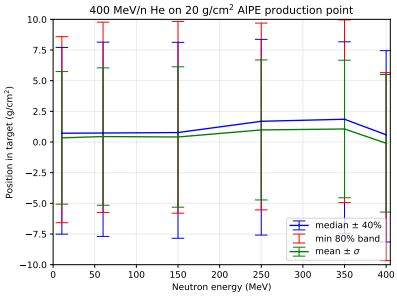


(c) n energy shift

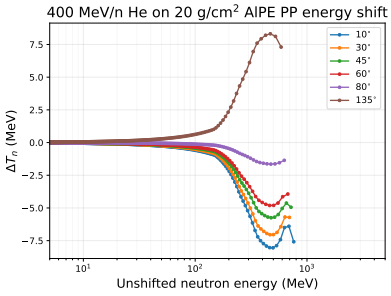
Figure B.24: Neutron production corrections for 400 MeV/n He on 60 g/cm^2 HDPE



(a) n production distribution

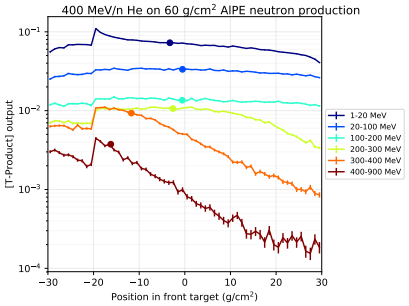


(b) effective target thickness

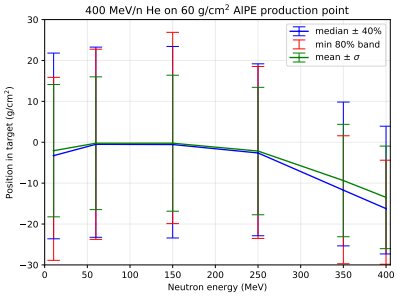


(c) n energy shift

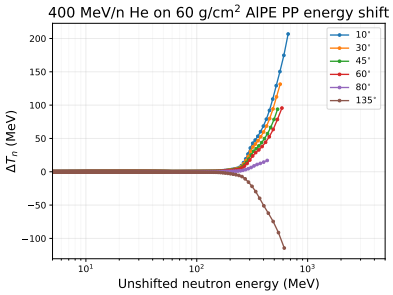
Figure B.25: Neutron production corrections for 400 MeV/n He on 20 g/cm^2 AlPE



(a) n production distribution

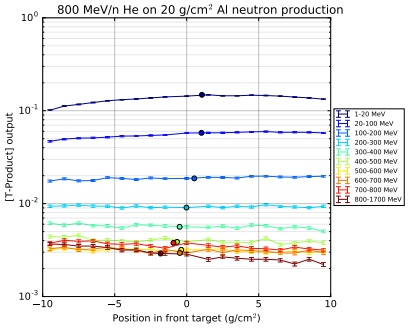


(b) effective target thickness

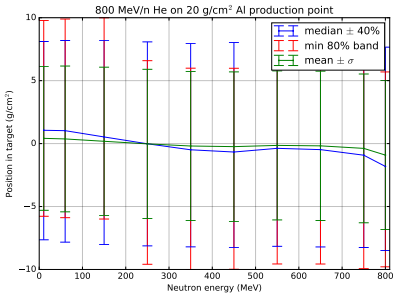


(c) n energy shift

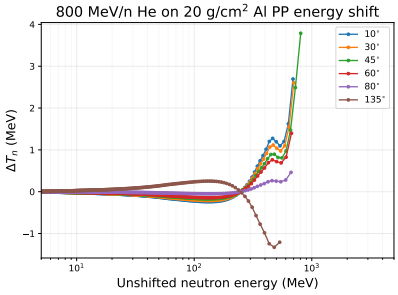
Figure B.26: Neutron production corrections for 400 MeV/n He on 60 g/cm^2 AlPE



(a) n production distribution

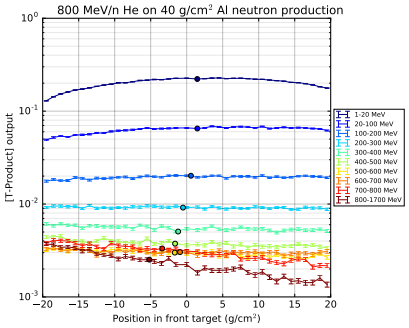


(b) effective target thickness

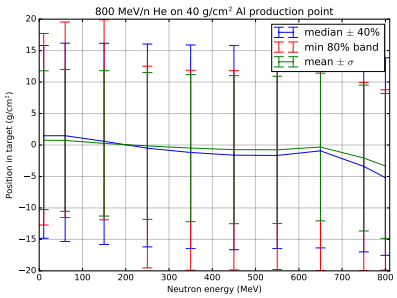


(c) n energy shift

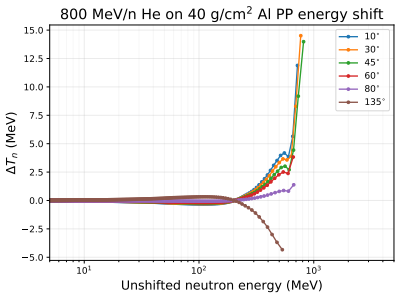
Figure B.27: Neutron production corrections for 800 MeV/n He on 20 g/cm^2 Al



(a) n production distribution

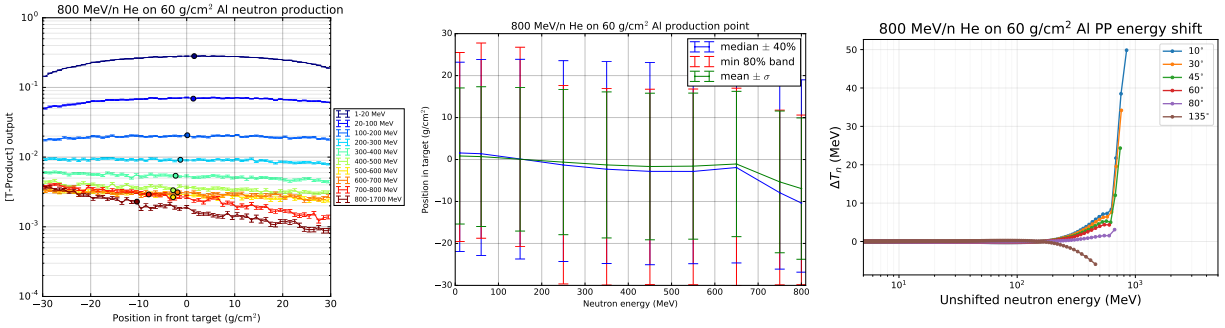


(b) effective target thickness



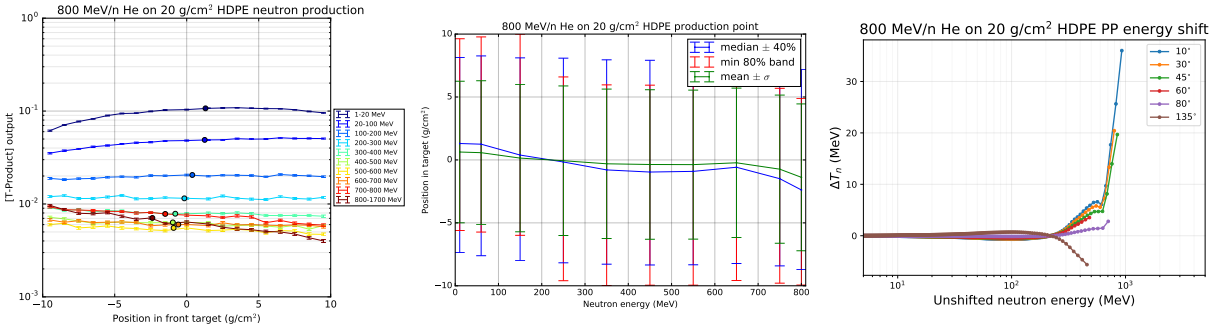
(c) n energy shift

Figure B.28: Neutron production corrections for 800 MeV/n He on 40 g/cm^2 Al



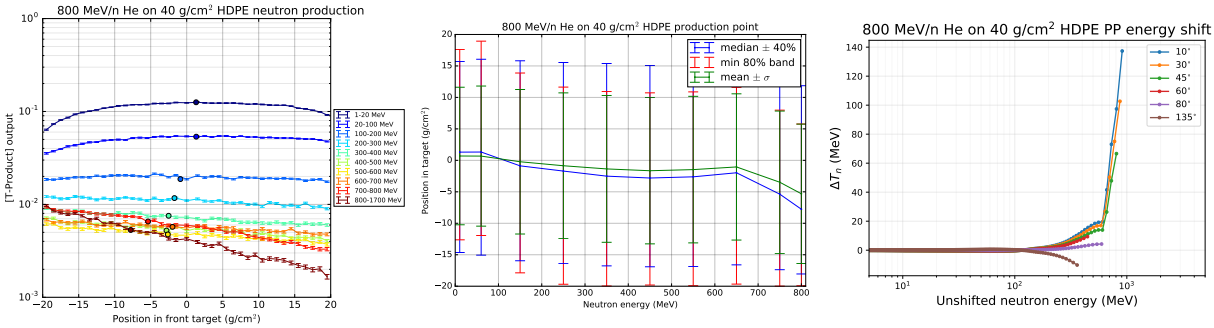
(a) n production distribution (b) effective target thickness (c) n energy shift

Figure B.29: Neutron production corrections for 800 MeV/n He on 60 g/cm^2 Al



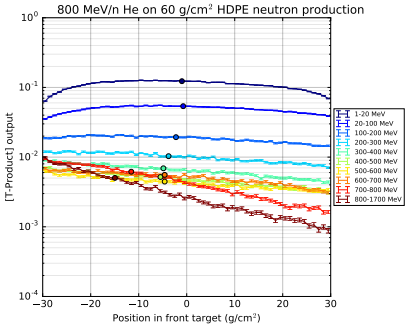
(a) n production distribution (b) effective target thickness (c) n energy shift

Figure B.30: Neutron production corrections for 800 MeV/n He on 20 g/cm^2 HDPE

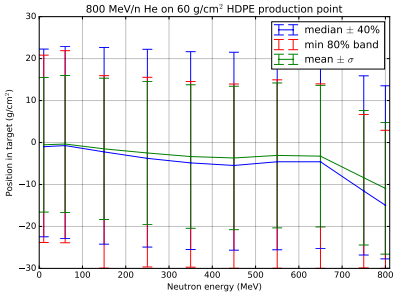


(a) n production distribution (b) effective target thickness (c) n energy shift

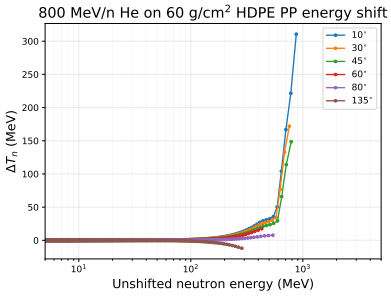
Figure B.31: Neutron production corrections for 800 MeV/n He on 40 g/cm^2 HDPE



(a) n production distribution

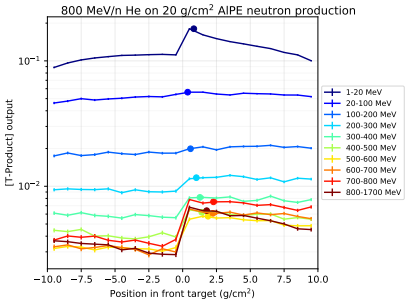


(b) effective target thickness

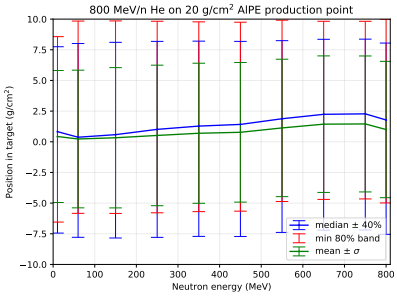


(c) n energy shift

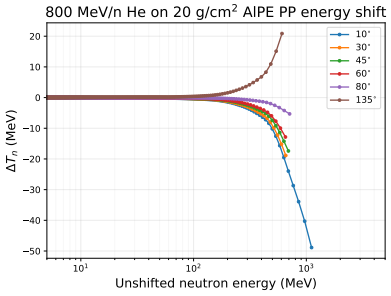
Figure B.32: Neutron production corrections for 800 MeV/n He on 60 g/cm^2 HDPE



(a) n production distribution

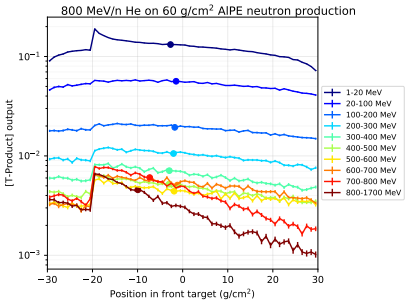


(b) effective target thickness

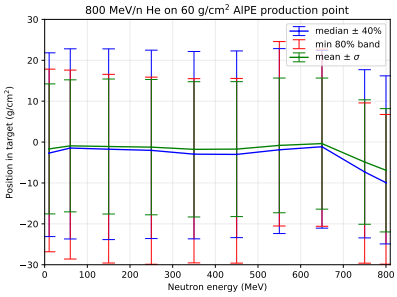


(c) n energy shift

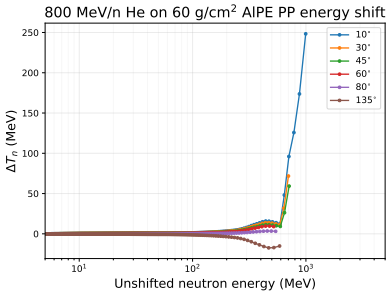
Figure B.33: Neutron production corrections for 800 MeV/n He on 20 g/cm^2 AlPE



(a) n production distribution

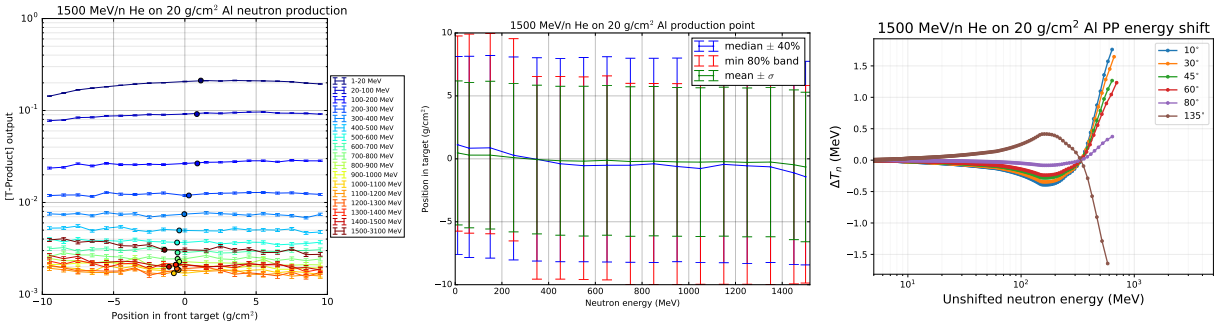


(b) effective target thickness



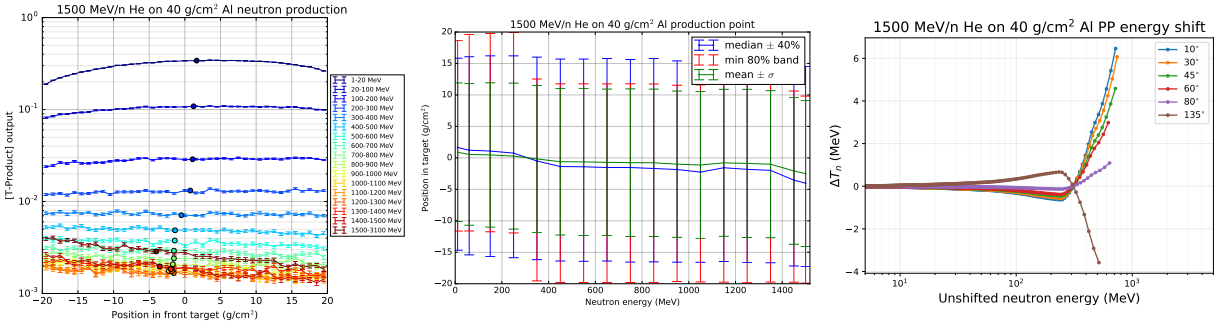
(c) n energy shift

Figure B.34: Neutron production corrections for 800 MeV/n He on 60 g/cm^2 AlPE



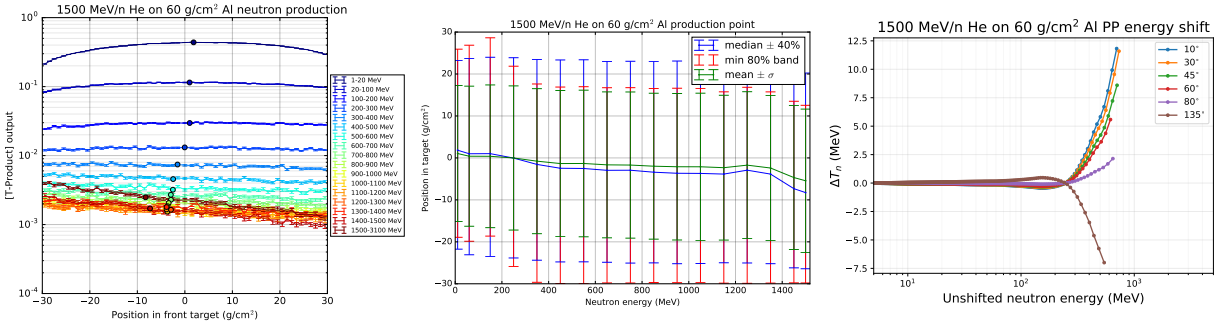
(a) n production distribution (b) effective target thickness (c) n energy shift

Figure B.35: Neutron production corrections for 1500 MeV/n He on 20 g/cm^2 Al



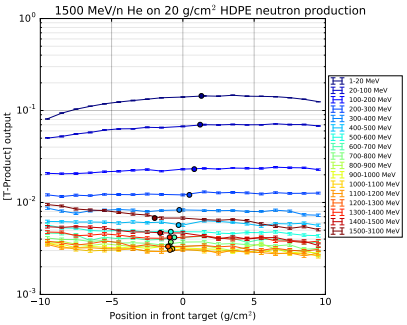
(a) n production distribution (b) effective target thickness (c) n energy shift

Figure B.36: Neutron production corrections for 1500 MeV/n He on 40 g/cm^2 Al

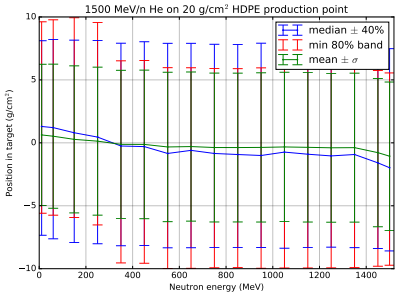


(a) n production distribution (b) effective target thickness (c) n energy shift

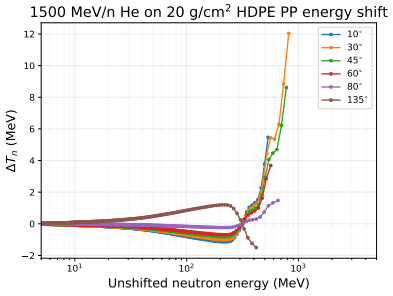
Figure B.37: Neutron production corrections for 1500 MeV/n He on 60 g/cm^2 Al



(a) n production distribution

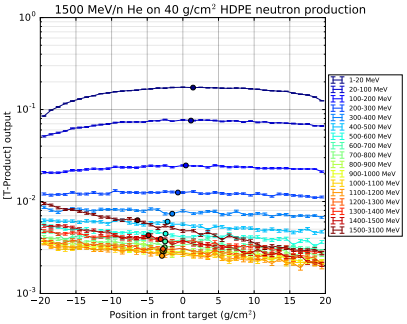


(b) effective target thickness

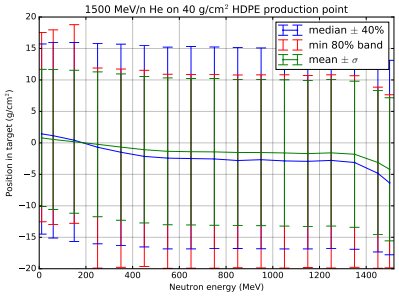


(c) n energy shift

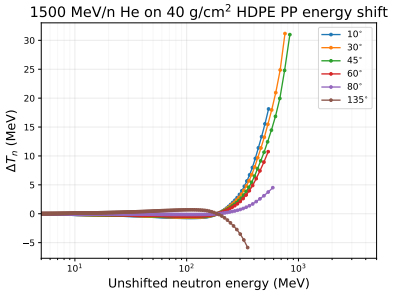
Figure B.38: Neutron production corrections for 1500 MeV/n He on 20 g/cm^2 HDPE



(a) n production distribution

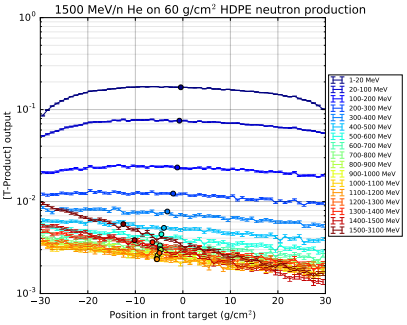


(b) effective target thickness

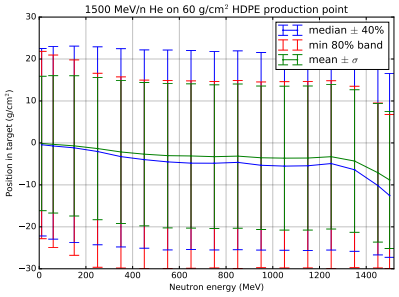


(c) n energy shift

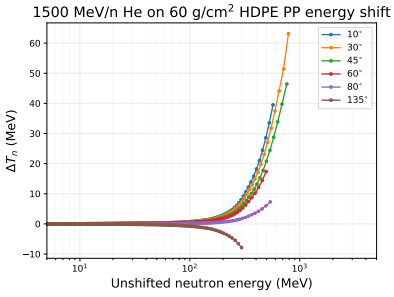
Figure B.39: Neutron production corrections for 1500 MeV/n He on 40 g/cm^2 HDPE



(a) n production distribution

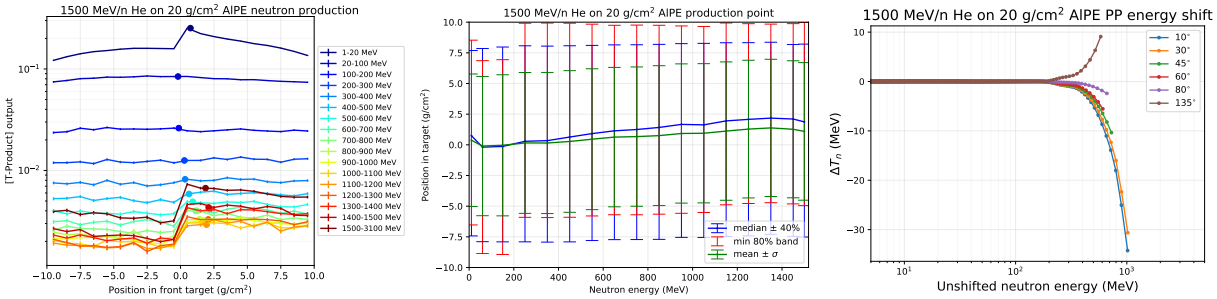


(b) effective target thickness



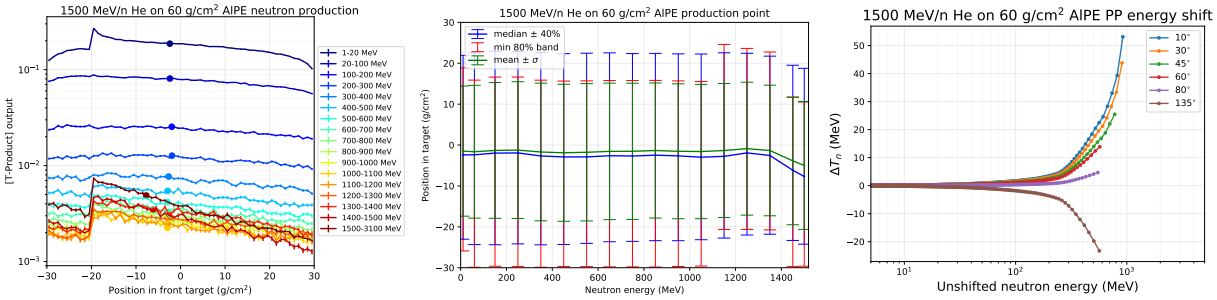
(c) n energy shift

Figure B.40: Neutron production corrections for 1500 MeV/n He on 60 g/cm^2 HDPE



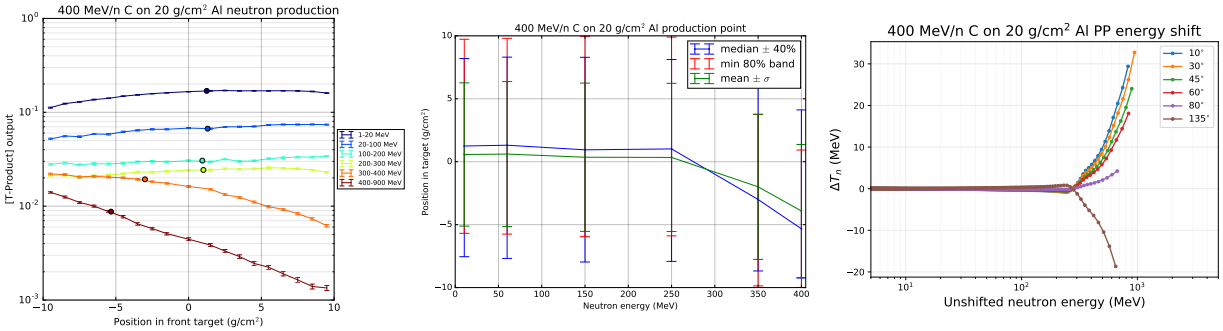
(a) n production distribution (b) effective target thickness (c) n energy shift

Figure B.41: Neutron production corrections for 1500 MeV/n He on 20 g/cm^2 AlPE



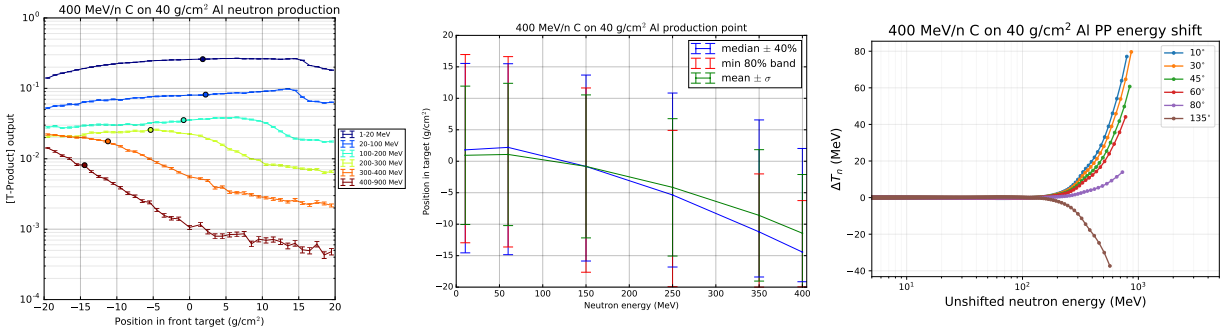
(a) n production distribution (b) effective target thickness (c) n energy shift

Figure B.42: Neutron production corrections for 1500 MeV/n He on 60 g/cm^2 AlPE



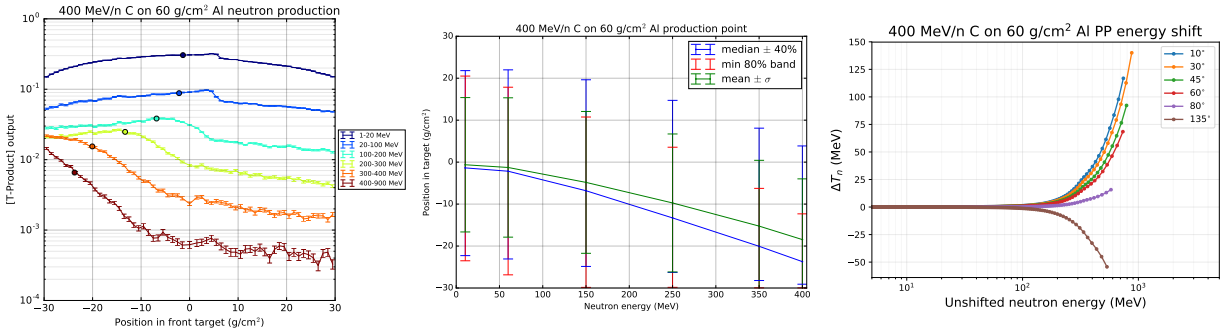
(a) n production distribution (b) effective target thickness (c) n energy shift

Figure B.43: Neutron production corrections for 400 MeV/n C on 20 g/cm^2 Al



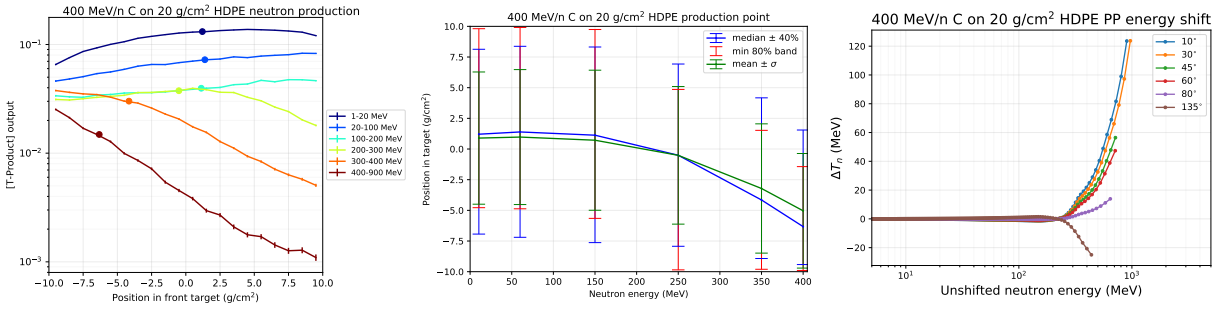
(a) n production distribution (b) effective target thickness (c) n energy shift

Figure B.44: Neutron production corrections for 400 MeV/n C on 40 g/cm^2 Al



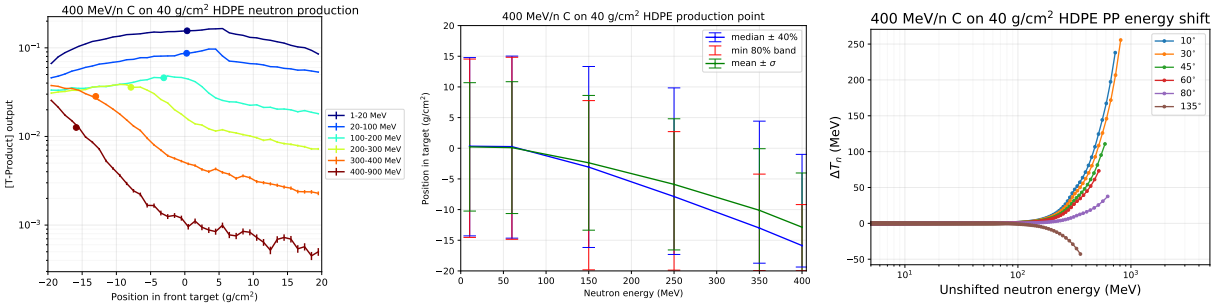
(a) n production distribution (b) effective target thickness (c) n energy shift

Figure B.45: Neutron production corrections for 400 MeV/n C on 60 g/cm^2 Al



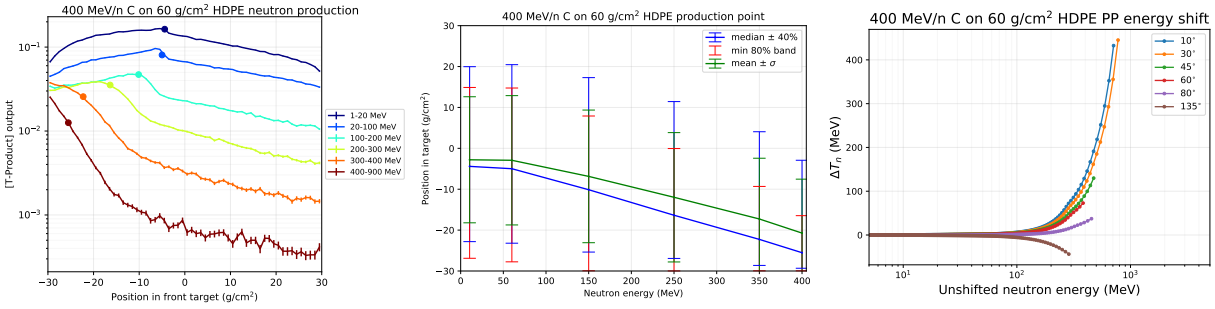
(a) n production distribution (b) effective target thickness (c) n energy shift

Figure B.46: Neutron production corrections for 400 MeV/n C on 20 g/cm^2 HDPE



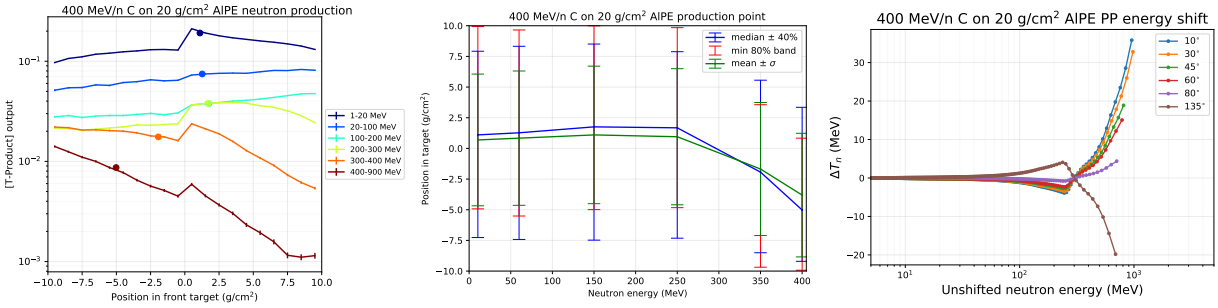
(a) n production distribution (b) effective target thickness (c) n energy shift

Figure B.47: Neutron production corrections for 400 MeV/n C on 40 g/cm^2 HDPE



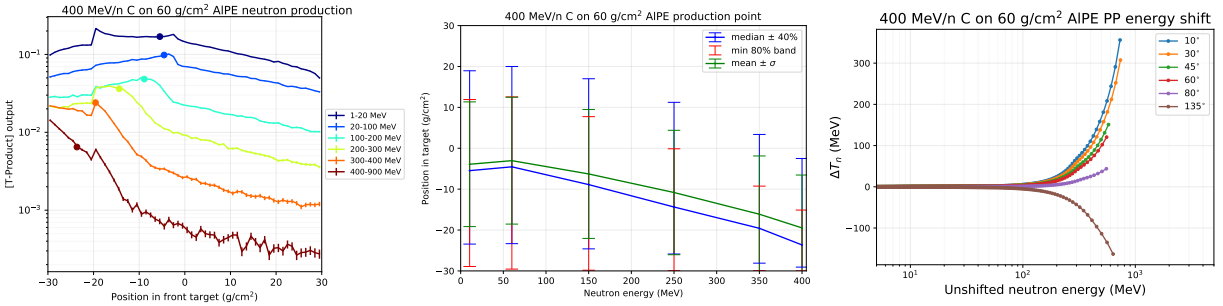
(a) n production distribution (b) effective target thickness (c) n energy shift

Figure B.48: Neutron production corrections for 400 MeV/n C on 60 g/cm^2 HDPE



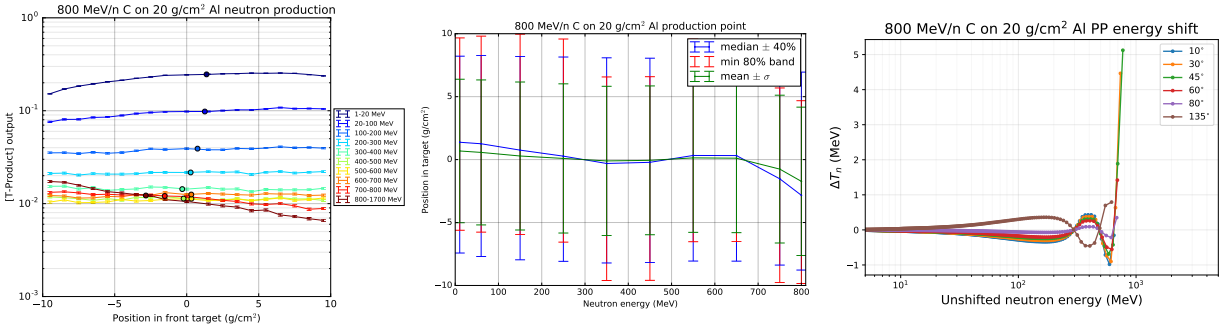
(a) n production distribution (b) effective target thickness (c) n energy shift

Figure B.49: Neutron production corrections for 400 MeV/n C on 20 g/cm^2 AlPE



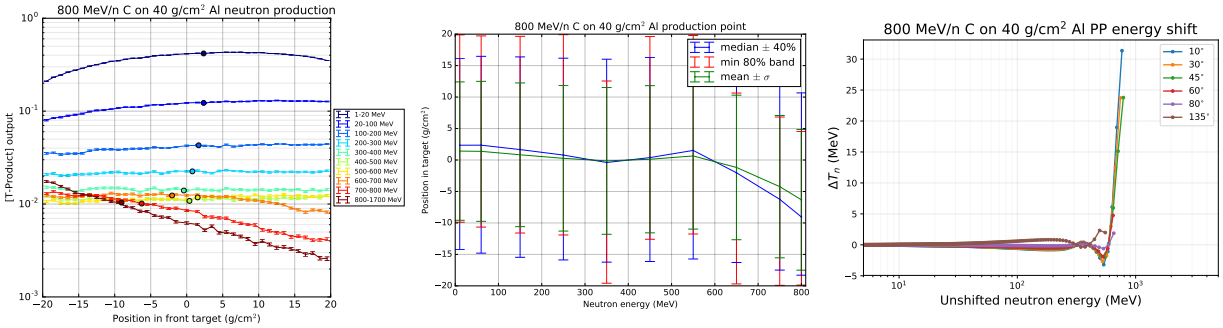
(a) n production distribution (b) effective target thickness (c) n energy shift

Figure B.50: Neutron production corrections for 400 MeV/n C on 60 g/cm^2 AlPE



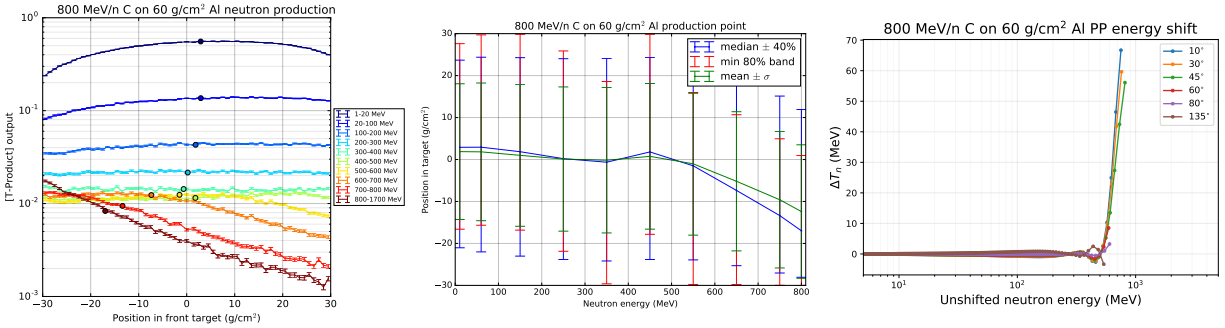
(a) n production distribution (b) effective target thickness (c) n energy shift

Figure B.51: Neutron production corrections for 800 MeV/n C on 20 g/cm^2 Al



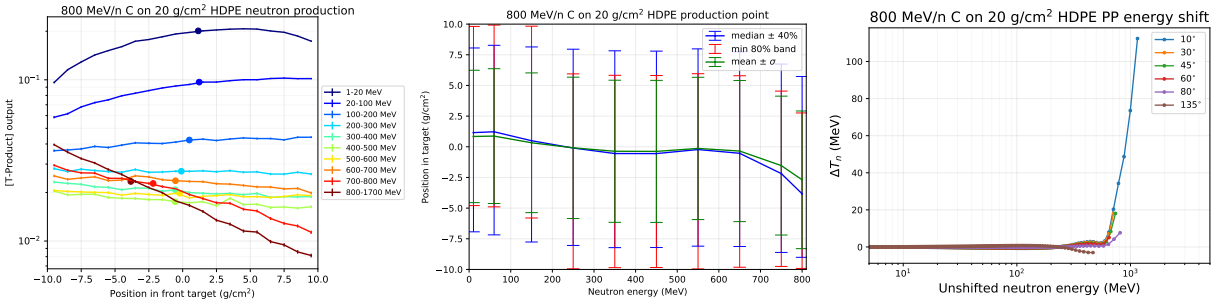
(a) n production distribution (b) effective target thickness (c) n energy shift

Figure B.52: Neutron production corrections for 800 MeV/n C on 40 g/cm^2 Al



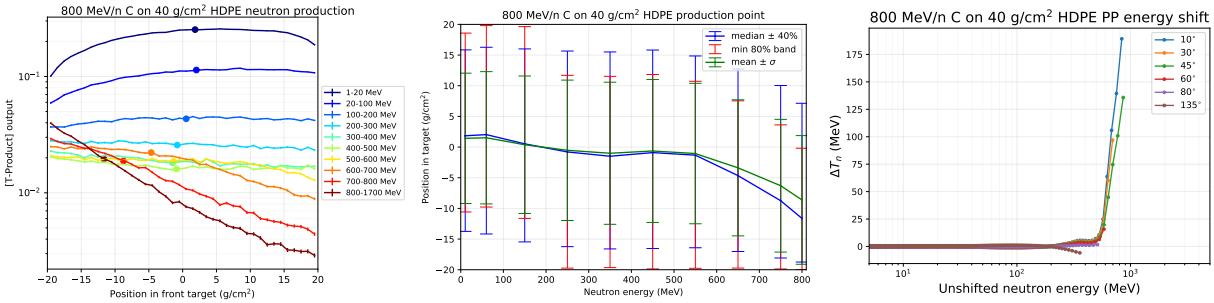
(a) n production distribution (b) effective target thickness (c) n energy shift

Figure B.53: Neutron production corrections for 800 MeV/n C on 60 g/cm^2 Al



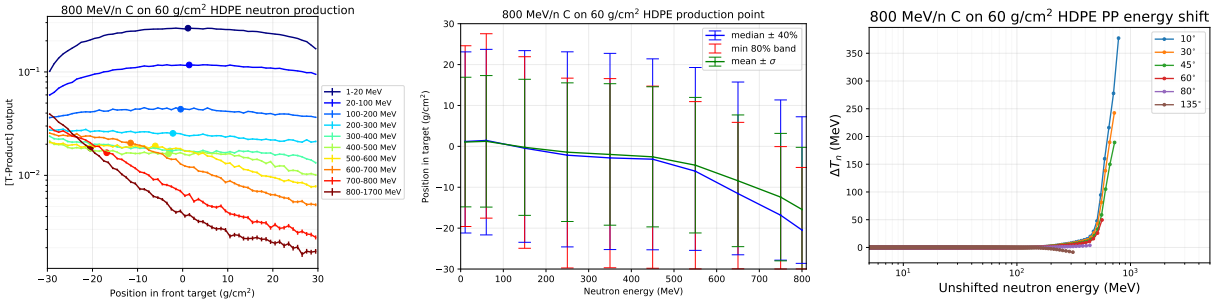
(a) n production distribution (b) effective target thickness (c) n energy shift

Figure B.54: Neutron production corrections for 800 MeV/n C on 20 g/cm^2 HDPE



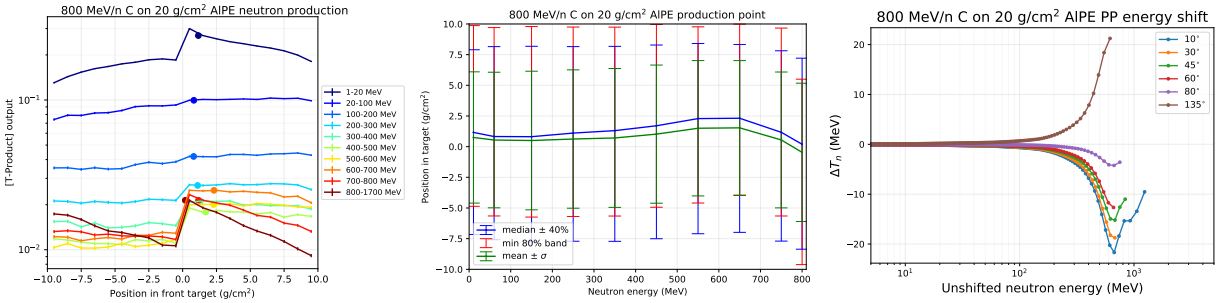
(a) n production distribution (b) effective target thickness (c) n energy shift

Figure B.55: Neutron production corrections for 800 MeV/n C on 40 g/cm^2 HDPE



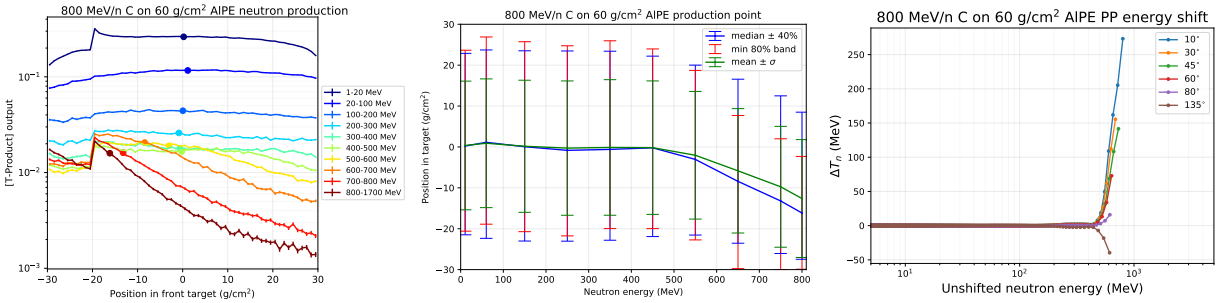
(a) n production distribution (b) effective target thickness (c) n energy shift

Figure B.56: Neutron production corrections for 800 MeV/n C on 60 g/cm^2 HDPE



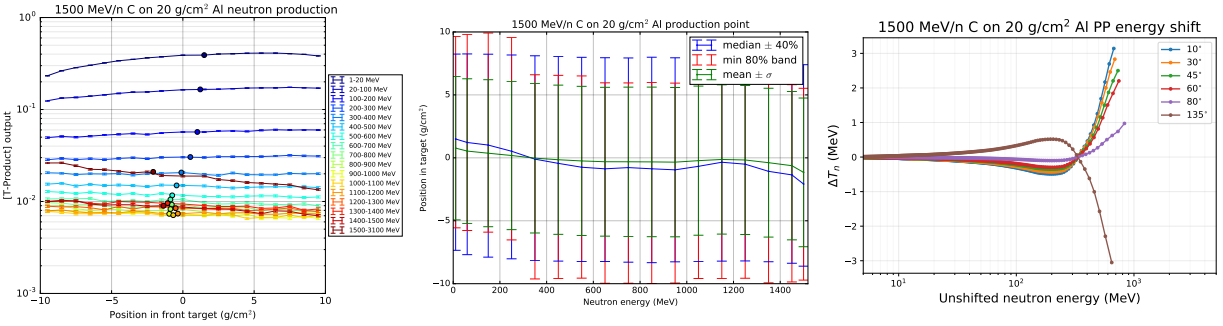
(a) n production distribution (b) effective target thickness (c) n energy shift

Figure B.57: Neutron production corrections for 800 MeV/n C on 20 g/cm^2 AlPE



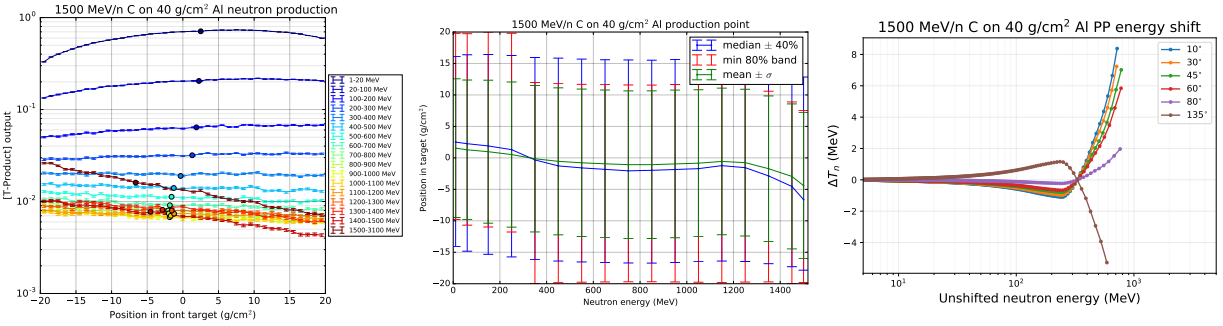
(a) n production distribution (b) effective target thickness (c) n energy shift

Figure B.58: Neutron production corrections for 800 MeV/n C on 60 g/cm^2 AlPE



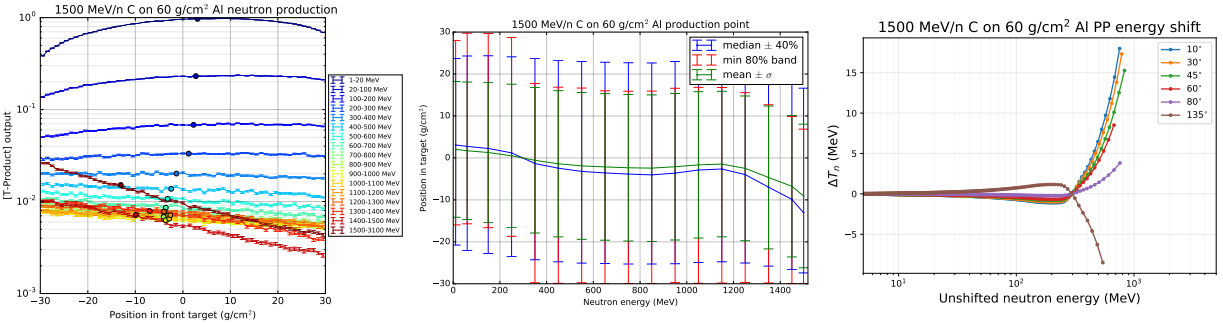
(a) n production distribution (b) effective target thickness (c) n energy shift

Figure B.59: Neutron production corrections for 1500 MeV/n C on 20 g/cm^2 Al



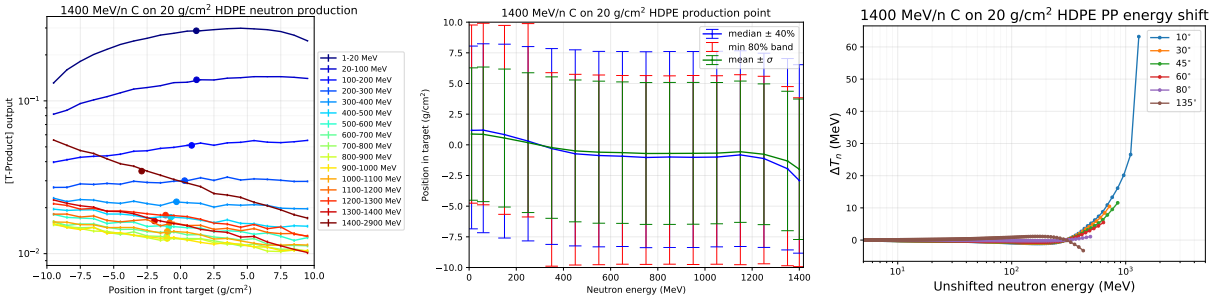
(a) n production distribution (b) effective target thickness (c) n energy shift

Figure B.60: Neutron production corrections for 1500 MeV/n C on 40 g/cm^2 Al



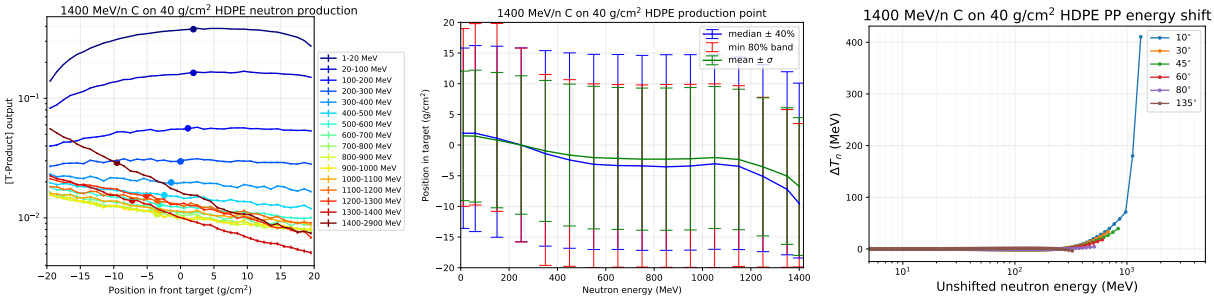
(a) n production distribution (b) effective target thickness (c) n energy shift

Figure B.61: Neutron production corrections for 1500 MeV/n C on 60 g/cm^2 Al



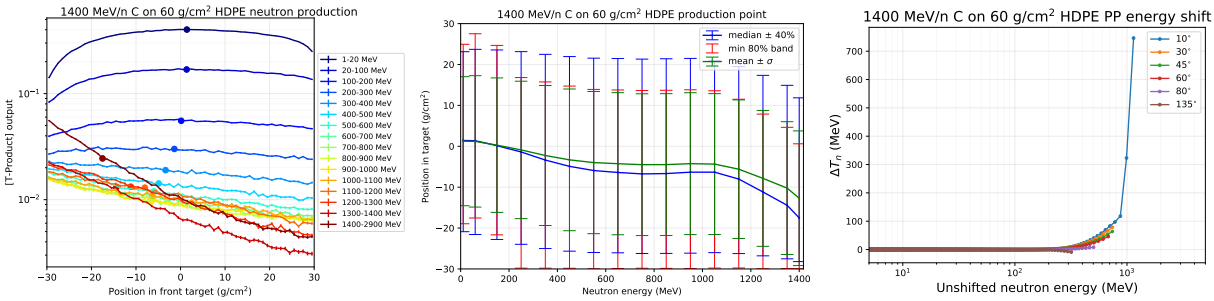
(a) n production distribution (b) effective target thickness (c) n energy shift

Figure B.62: Neutron production corrections for 1500 MeV/n C on 20 g/cm^2 HDPE



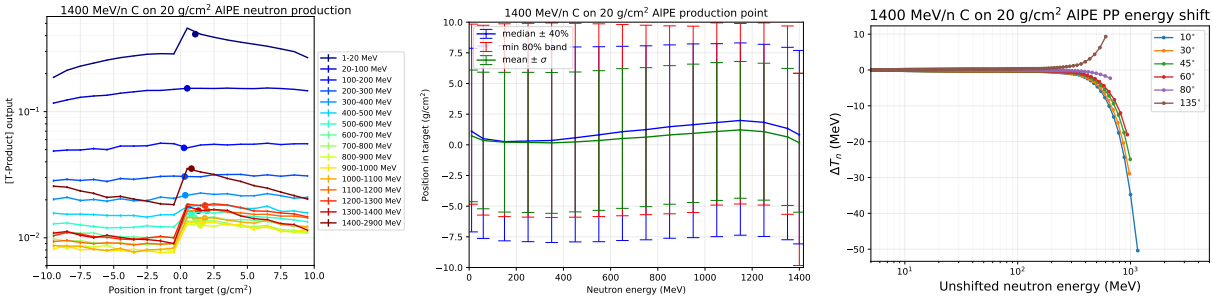
(a) n production distribution (b) effective target thickness (c) n energy shift

Figure B.63: Neutron production corrections for 1500 MeV/n C on 40 g/cm^2 HDPE



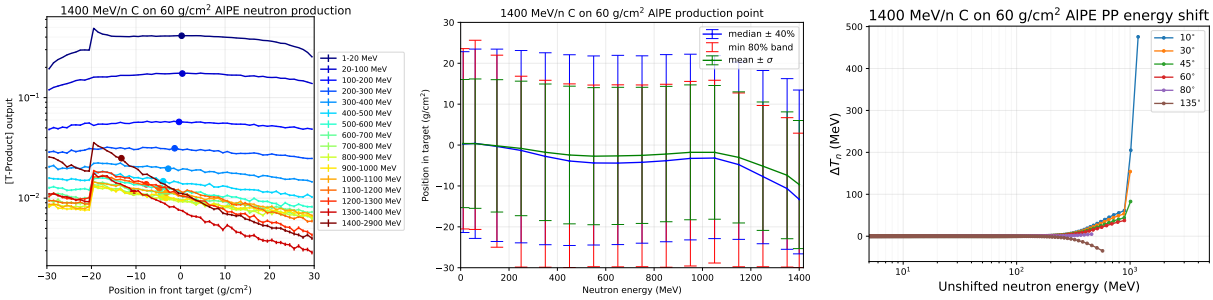
(a) n production distribution (b) effective target thickness (c) n energy shift

Figure B.64: Neutron production corrections for 1500 MeV/n C on 60 g/cm^2 HDPE



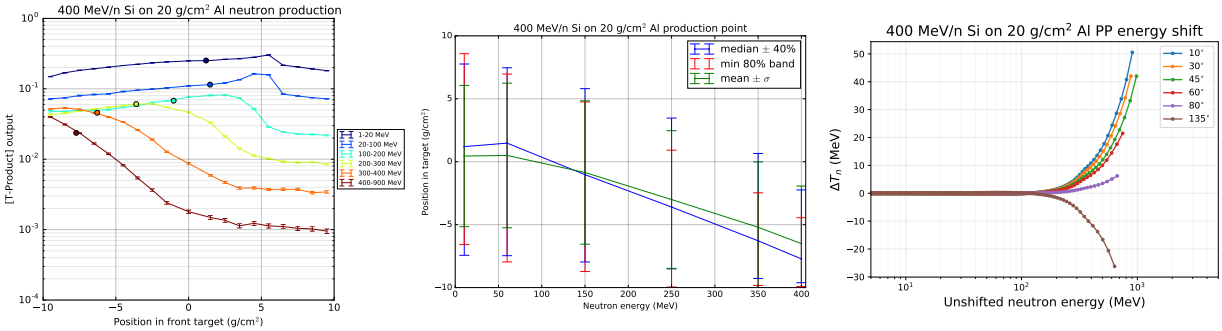
(a) n production distribution (b) effective target thickness (c) n energy shift

Figure B.65: Neutron production corrections for 1500 MeV/n C on 20 g/cm^2 AlPE



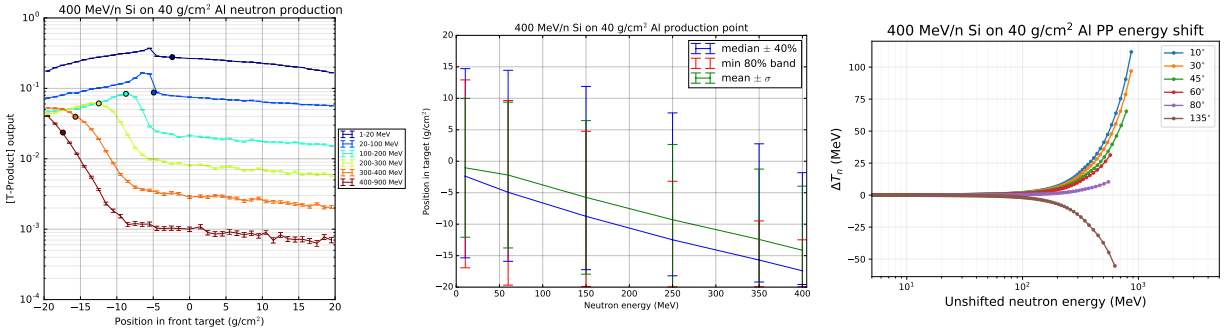
(a) n production distribution (b) effective target thickness (c) n energy shift

Figure B.66: Neutron production corrections for 1500 MeV/n C on 60 g/cm^2 AlPE



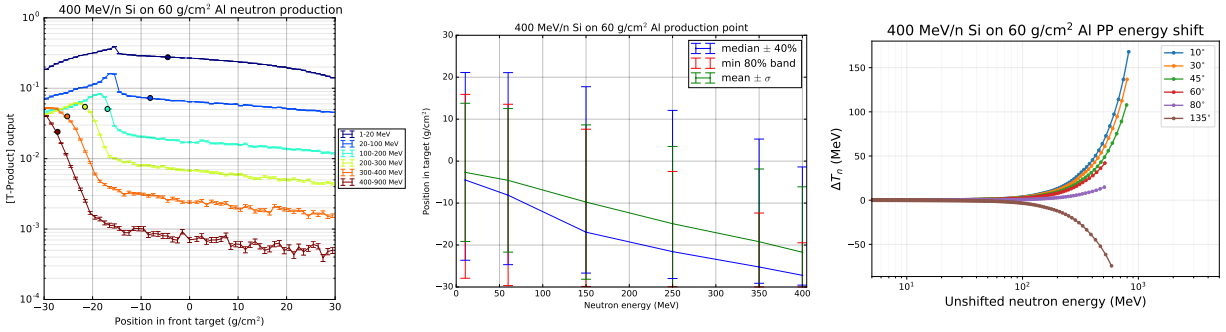
(a) n production distribution (b) effective target thickness (c) n energy shift

Figure B.67: Neutron production corrections for 400 MeV/n Si on 20 g/cm^2 Al



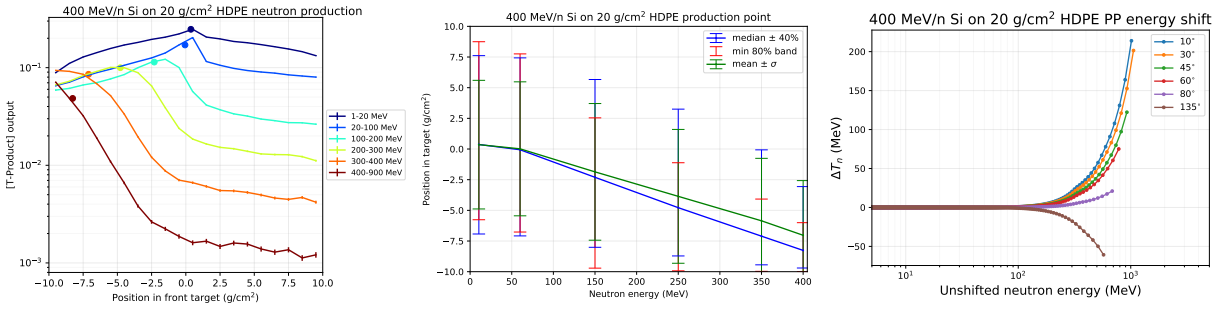
(a) n production distribution (b) effective target thickness (c) n energy shift

Figure B.68: Neutron production corrections for 400 MeV/n Si on 40 g/cm^2 Al



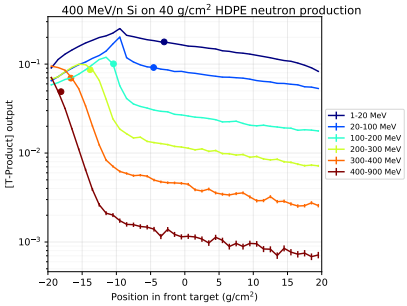
(a) n production distribution (b) effective target thickness (c) n energy shift

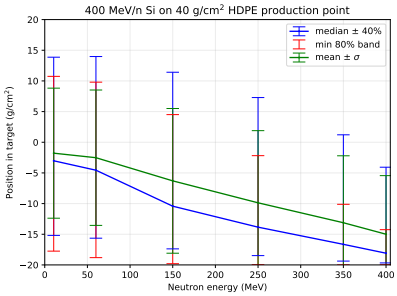
Figure B.69: Neutron production corrections for 400 MeV/n Si on 60 g/cm^2 Al

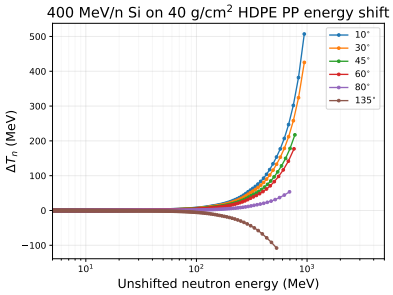


(a) n production distribution (b) effective target thickness (c) n energy shift

Figure B.70: Neutron production corrections for 400 MeV/n Si on 20 g/cm^2 HDPE

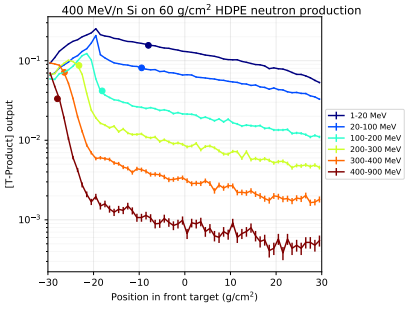


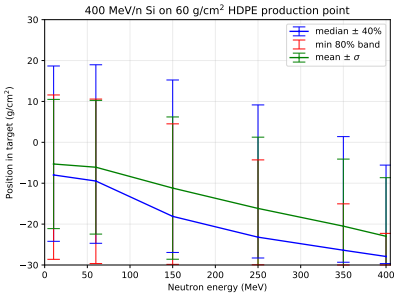


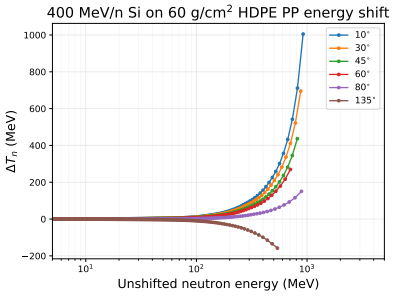


(a) n production distribution (b) effective target thickness (c) n energy shift

Figure B.71: Neutron production corrections for 400 MeV/n Si on 40 g/cm^2 HDPE

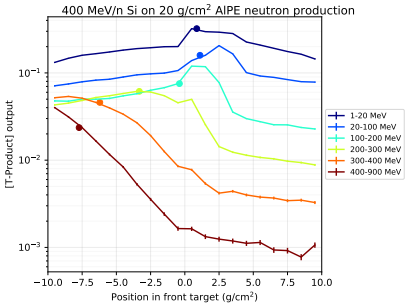


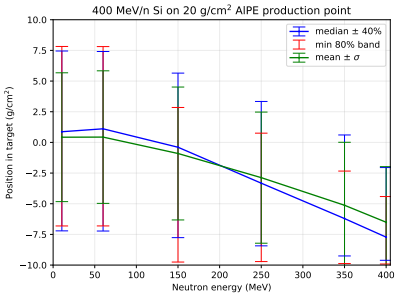


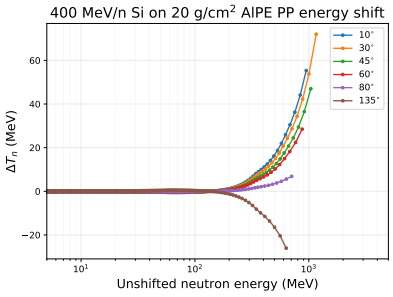


(a) n production distribution (b) effective target thickness (c) n energy shift

Figure B.72: Neutron production corrections for 400 MeV/n Si on 60 g/cm^2 HDPE

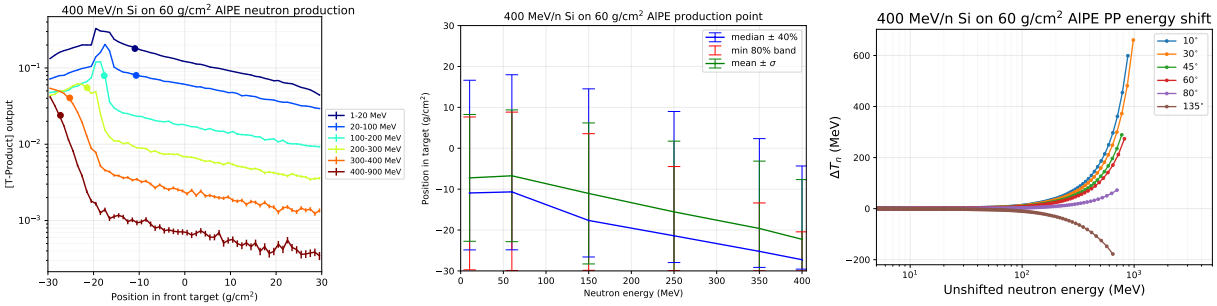






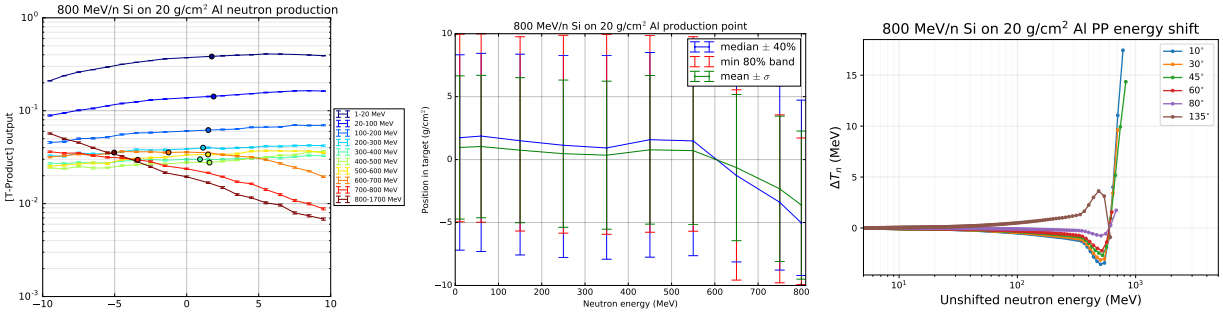
(a) n production distribution (b) effective target thickness (c) n energy shift

Figure B.73: Neutron production corrections for 400 MeV/n Si on 20 g/cm^2 AlPE



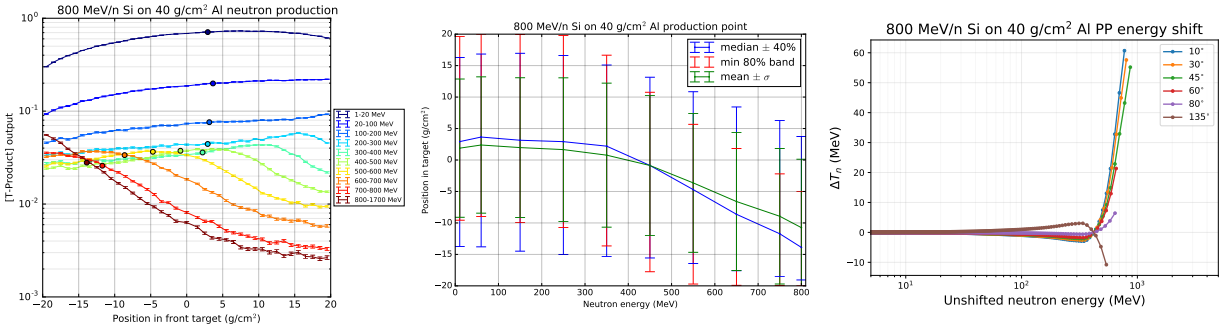
(a) n production distribution (b) effective target thickness (c) n energy shift

Figure B.74: Neutron production corrections for 400 MeV/n Si on 60 g/cm^2 AlPE



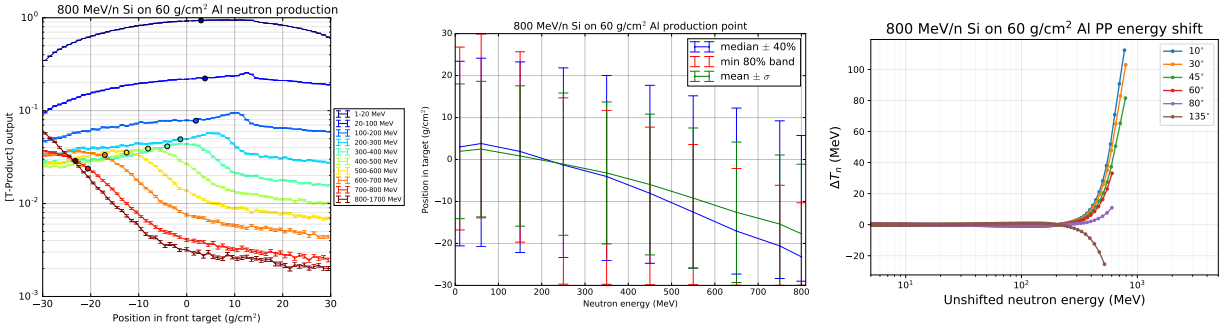
(a) n production distribution (b) effective target thickness (c) n energy shift

Figure B.75: Neutron production corrections for 800 MeV/n Si on 20 g/cm^2 Al



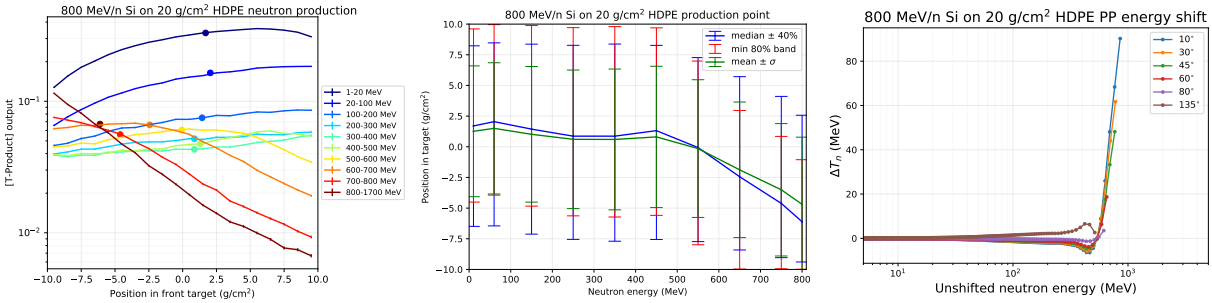
(a) n production distribution (b) effective target thickness (c) n energy shift

Figure B.76: Neutron production corrections for 800 MeV/n Si on 40 g/cm^2 Al



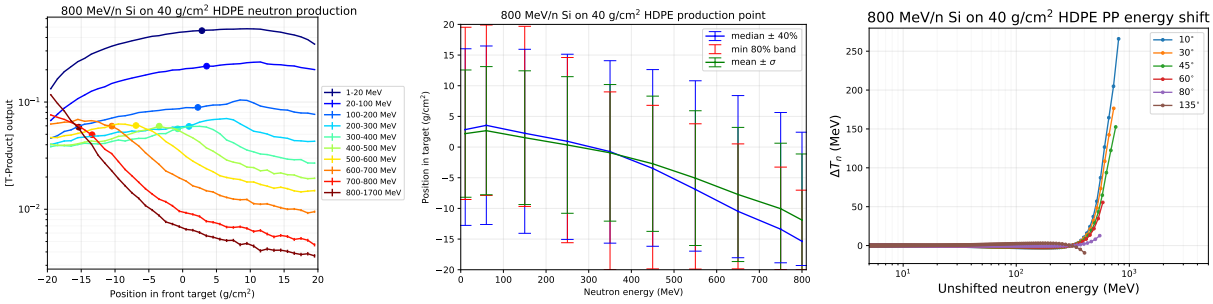
(a) n production distribution (b) effective target thickness (c) n energy shift

Figure B.77: Neutron production corrections for 800 MeV/n Si on 60 g/cm^2 Al



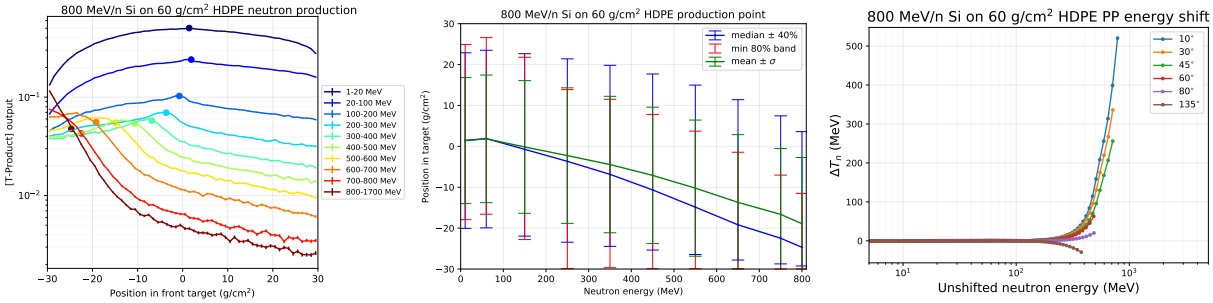
(a) n production distribution (b) effective target thickness (c) n energy shift

Figure B.78: Neutron production corrections for 800 MeV/n Si on 20 g/cm^2 HDPE



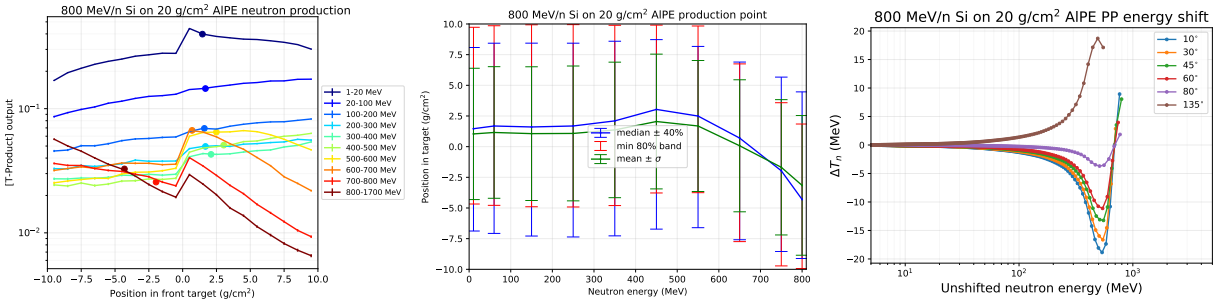
(a) n production distribution (b) effective target thickness (c) n energy shift

Figure B.79: Neutron production corrections for 800 MeV/n Si on 40 g/cm^2 HDPE



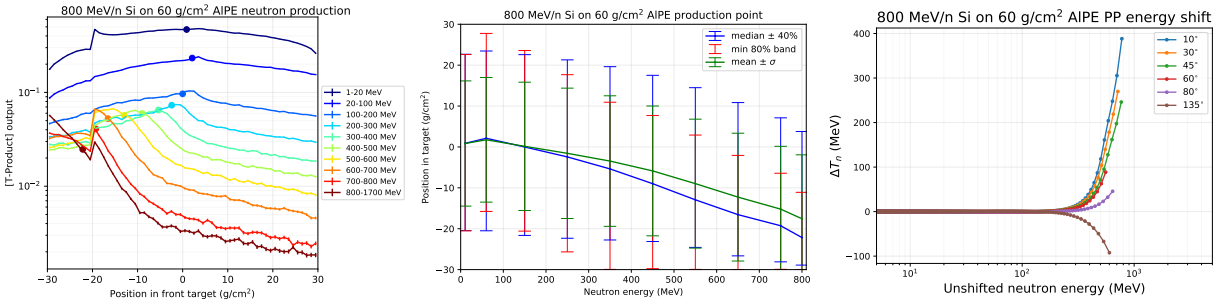
(a) n production distribution (b) effective target thickness (c) n energy shift

Figure B.80: Neutron production corrections for 800 MeV/n Si on 60 g/cm^2 HDPE



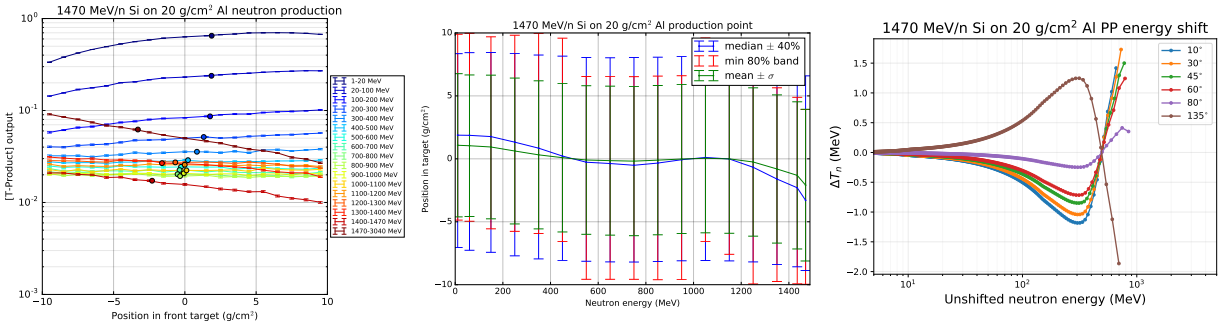
(a) n production distribution (b) effective target thickness (c) n energy shift

Figure B.81: Neutron production corrections for 800 MeV/n Si on 20 g/cm^2 AlPE



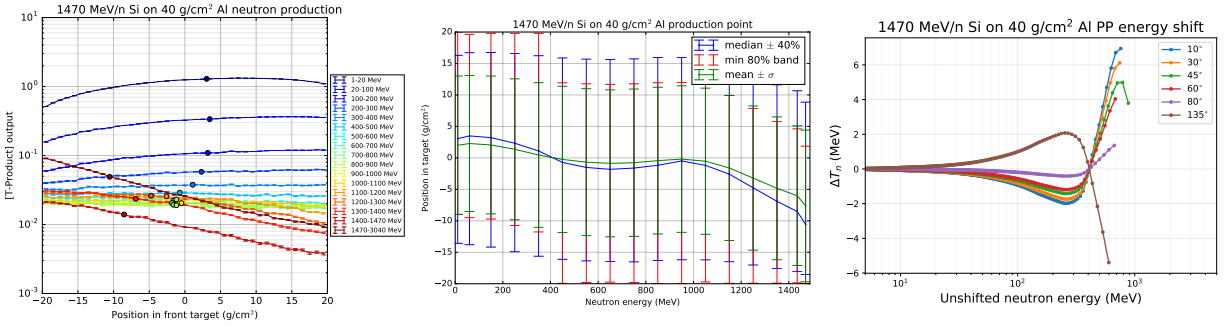
(a) n production distribution (b) effective target thickness (c) n energy shift

Figure B.82: Neutron production corrections for 800 MeV/n Si on 60 g/cm^2 AlPE



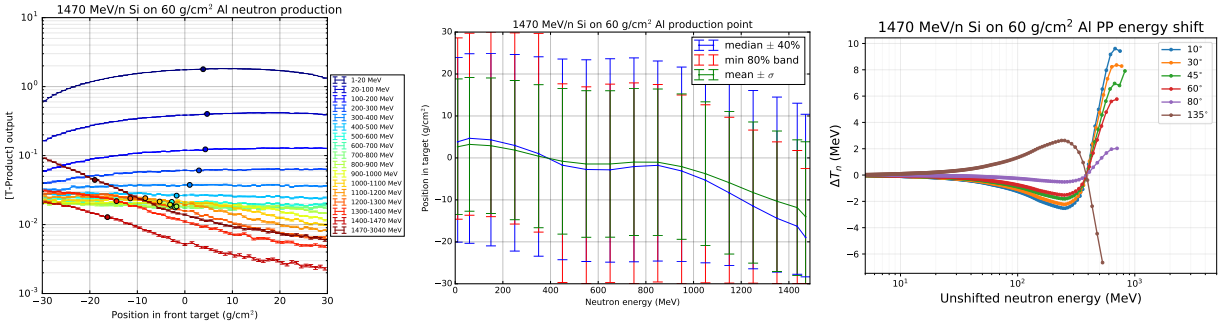
(a) n production distribution (b) effective target thickness (c) n energy shift

Figure B.83: Neutron production corrections for 1500 MeV/n Si on 20 g/cm^2 Al



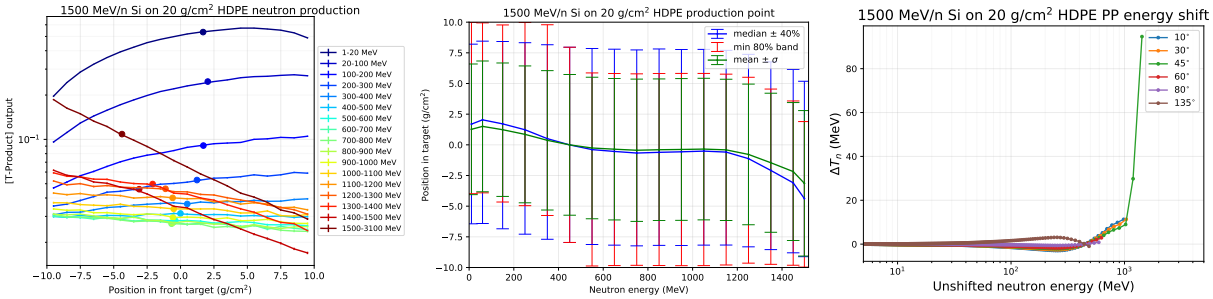
(a) n production distribution (b) effective target thickness (c) n energy shift

Figure B.84: Neutron production corrections for 1500 MeV/n Si on 40 g/cm^2 Al



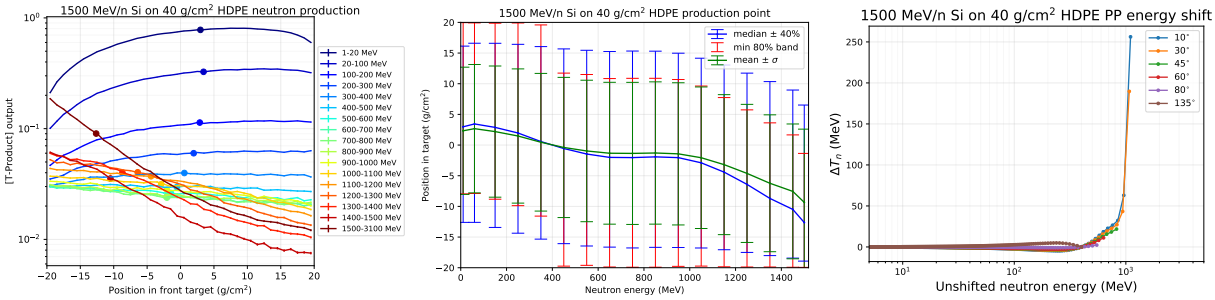
(a) n production distribution (b) effective target thickness (c) n energy shift

Figure B.85: Neutron production corrections for 1500 MeV/n Si on 60 g/cm^2 Al



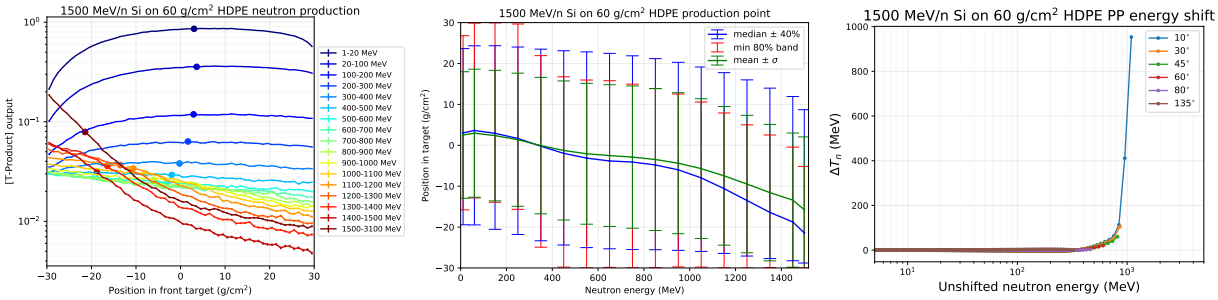
(a) n production distribution (b) effective target thickness (c) n energy shift

Figure B.86: Neutron production corrections for 1500 MeV/n Si on 20 g/cm^2 HDPE



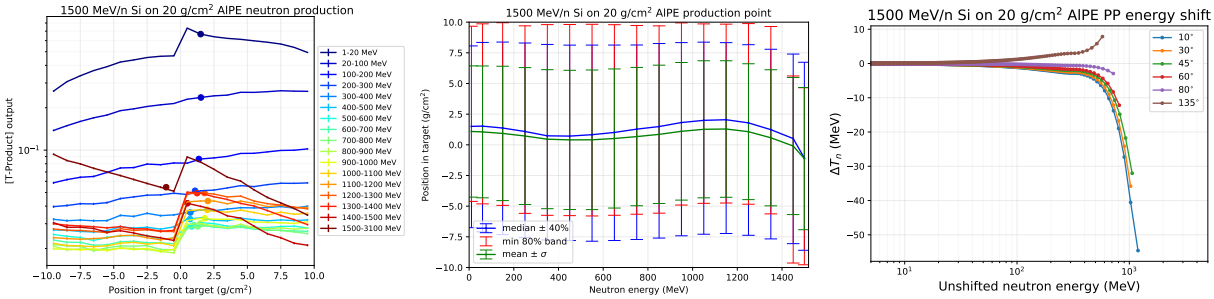
(a) n production distribution (b) effective target thickness (c) n energy shift

Figure B.87: Neutron production corrections for 1500 MeV/n Si on 40 g/cm^2 HDPE



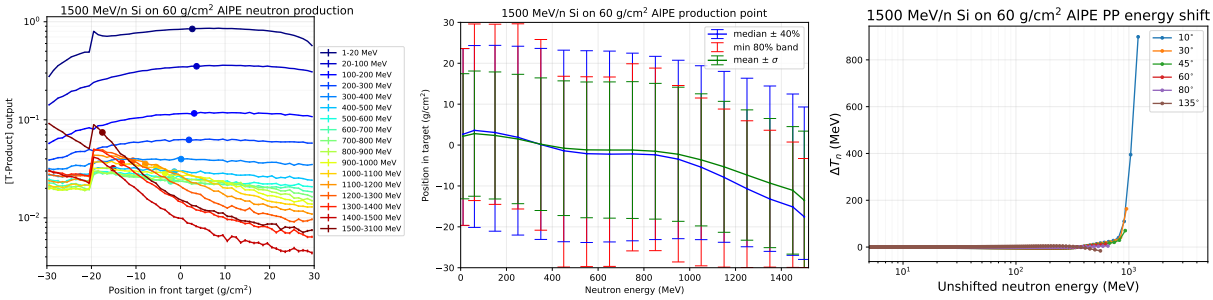
(a) n production distribution (b) effective target thickness (c) n energy shift

Figure B.88: Neutron production corrections for 1500 MeV/n Si on 60 g/cm^2 HDPE



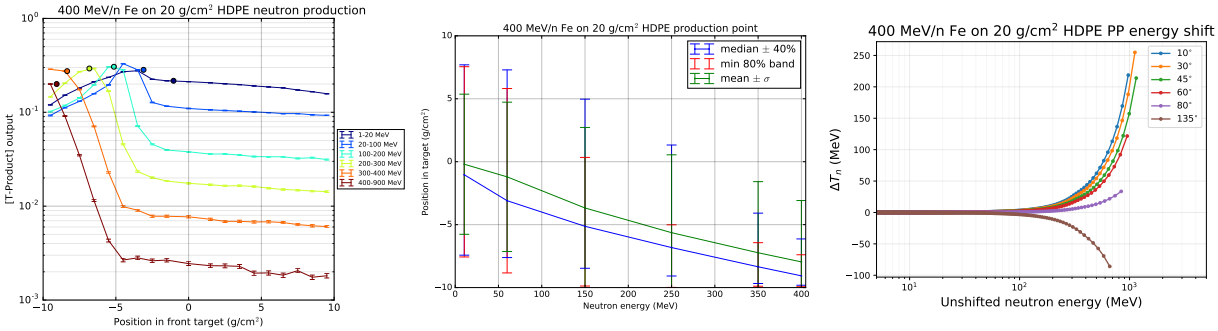
(a) n production distribution (b) effective target thickness (c) n energy shift

Figure B.89: Neutron production corrections for 1500 MeV/n Si on 20 g/cm^2 AlPE



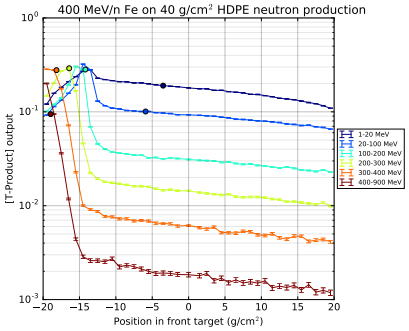
(a) n production distribution (b) effective target thickness (c) n energy shift

Figure B.90: Neutron production corrections for 1500 MeV/n Si on 60 g/cm^2 AlPE

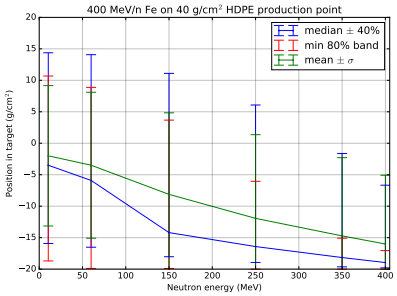


(a) n production distribution (b) effective target thickness (c) n energy shift

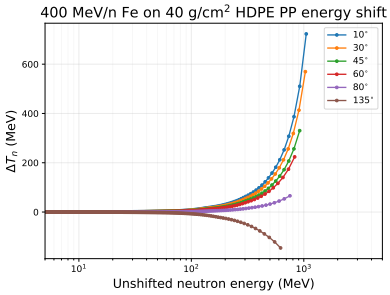
Figure B.91: Neutron production corrections for 400 MeV/n Fe on 20 g/cm^2 HDPE



(a) n production distribution

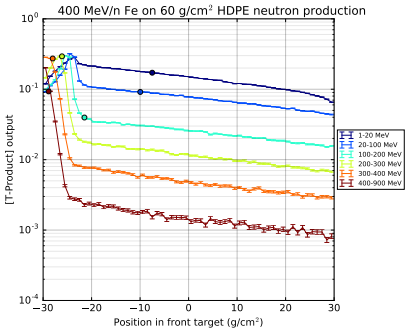


(b) effective target thickness

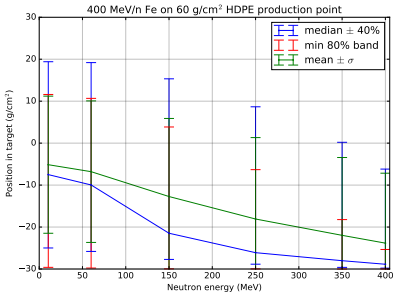


(c) n energy shift

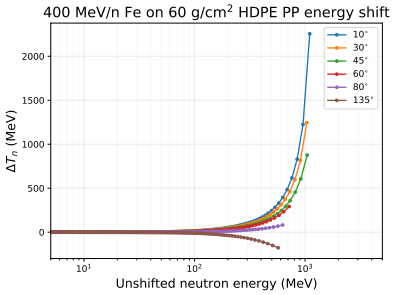
Figure B.92: Neutron production corrections for 400 MeV/n Fe on 40 g/cm^2 HDPE



(a) n production distribution

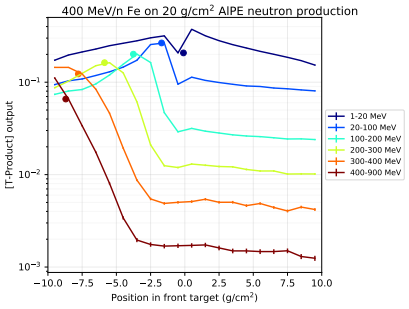


(b) effective target thickness

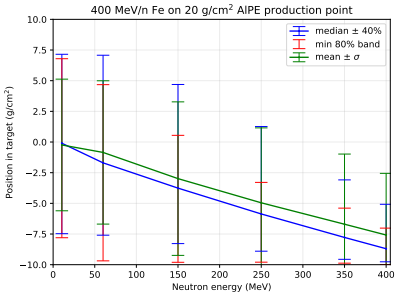


(c) n energy shift

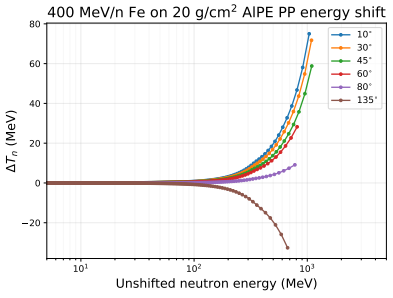
Figure B.93: Neutron production corrections for 400 MeV/n Fe on 60 g/cm^2 HDPE



(a) n production distribution

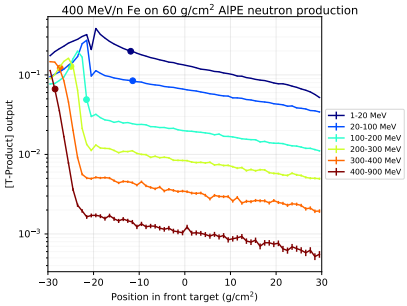


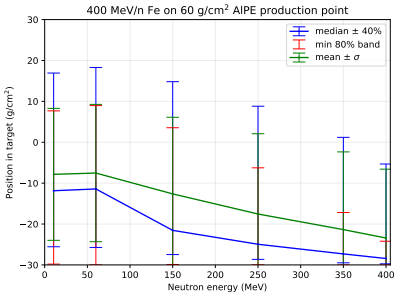
(b) effective target thickness

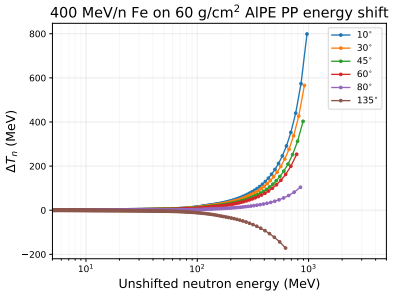


(c) n energy shift

Figure B.94: Neutron production corrections for 400 MeV/n Fe on 20 g/cm^2 AlPE

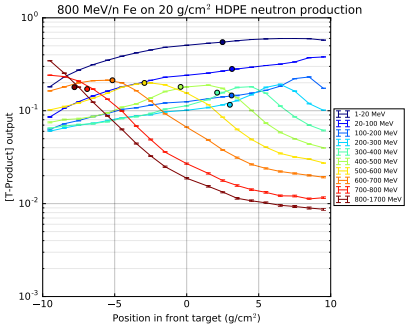


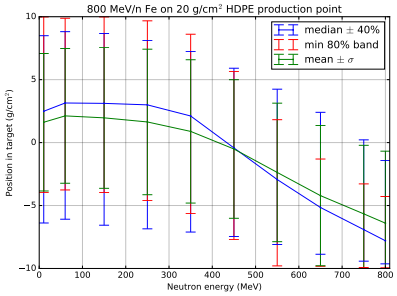


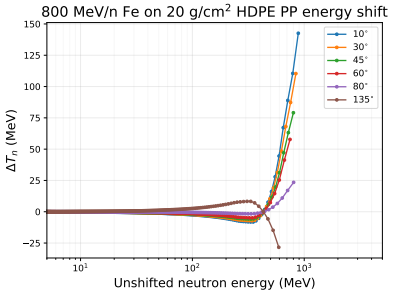


(a) n production distribution (b) effective target thickness (c) n energy shift

Figure B.95: Neutron production corrections for 400 MeV/n Fe on 60 g/cm^2 AlPE

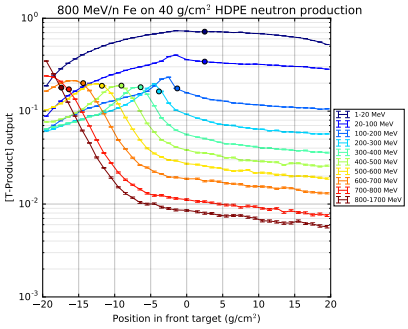


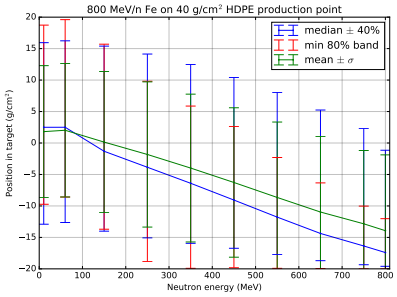


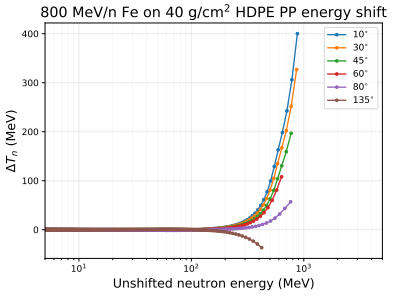


(a) n production distribution (b) effective target thickness (c) n energy shift

Figure B.96: Neutron production corrections for 800 MeV/n Fe on 20 g/cm^2 HDPE

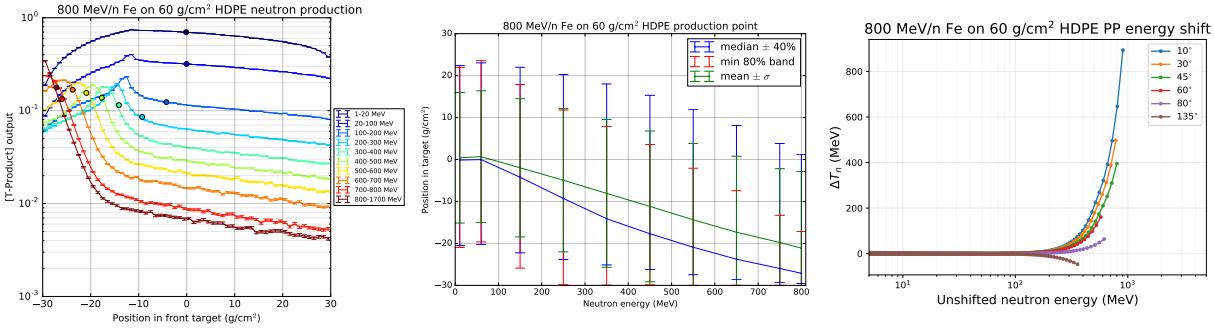






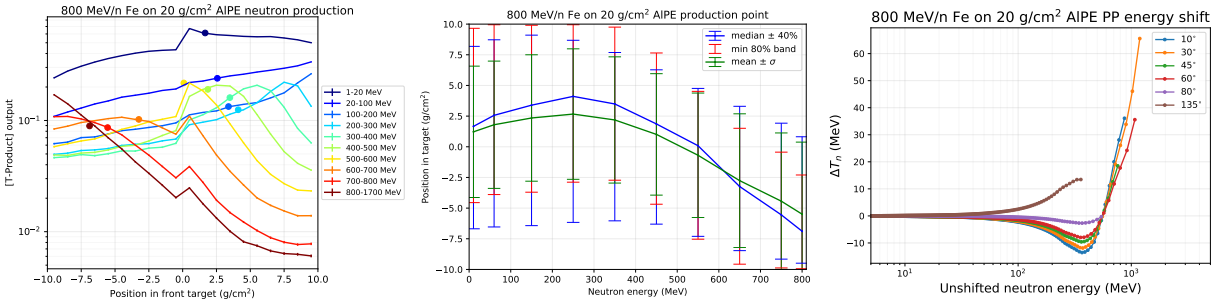
(a) n production distribution (b) effective target thickness (c) n energy shift

Figure B.97: Neutron production corrections for 800 MeV/n Fe on 40 g/cm^2 HDPE



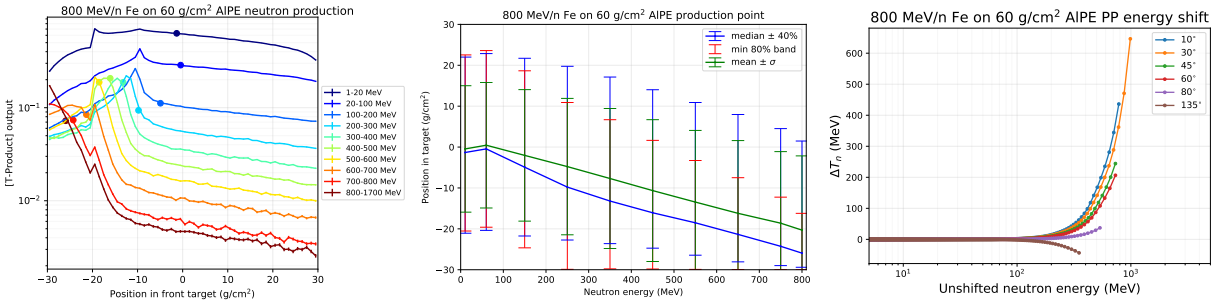
(a) n production distribution (b) effective target thickness (c) n energy shift

Figure B.98: Neutron production corrections for 800 MeV/n Fe on 60 g/cm^2 HDPE



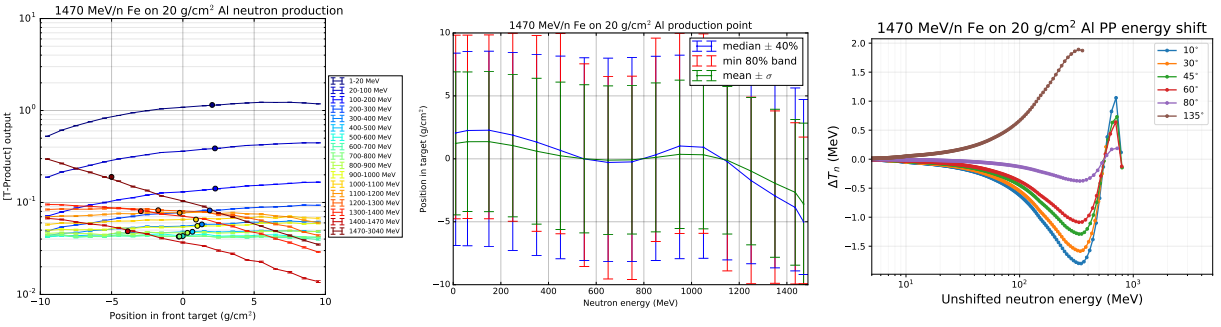
(a) n production distribution (b) effective target thickness (c) n energy shift

Figure B.99: Neutron production corrections for 800 MeV/n Fe on 20 g/cm^2 AlPE



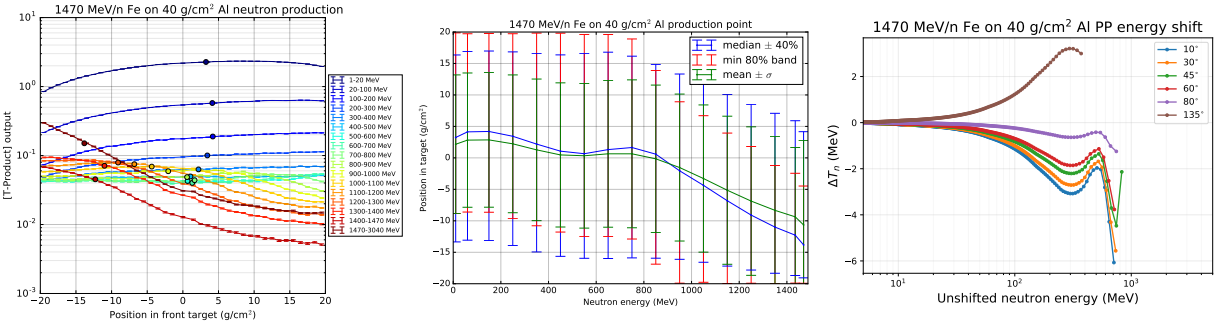
(a) n production distribution (b) effective target thickness (c) n energy shift

Figure B.100: Neutron production corrections for 800 MeV/n Fe on 60 g/cm^2 AlPE



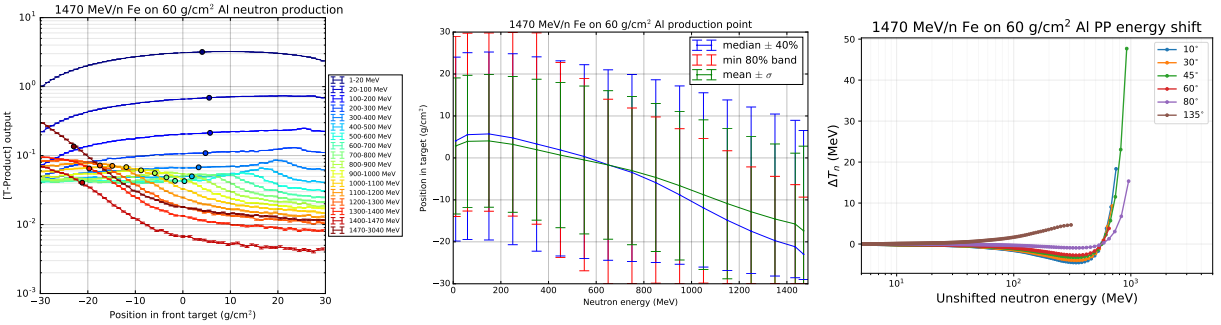
(a) n production distribution (b) effective target thickness (c) n energy shift

Figure B.101: Neutron production corrections for 1500 MeV/n Fe on 20 g/cm^2 Al



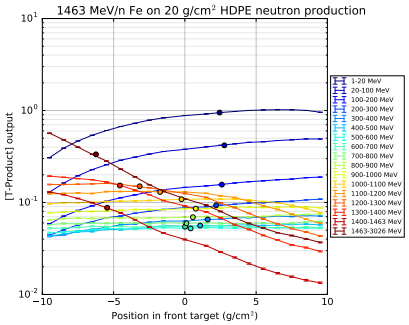
(a) n production distribution (b) effective target thickness (c) n energy shift

Figure B.102: Neutron production corrections for 1500 MeV/n Fe on 40 g/cm^2 Al

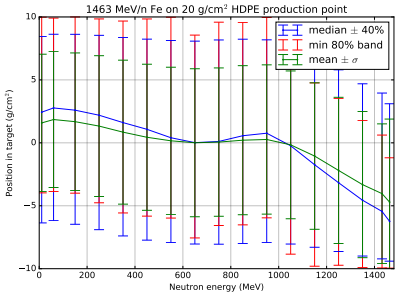


(a) n production distribution (b) effective target thickness (c) n energy shift

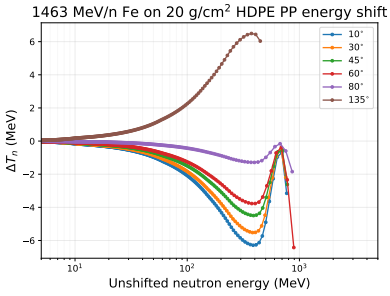
Figure B.103: Neutron production corrections for 1500 MeV/n Fe on 60 g/cm^2 Al



(a) n production distribution

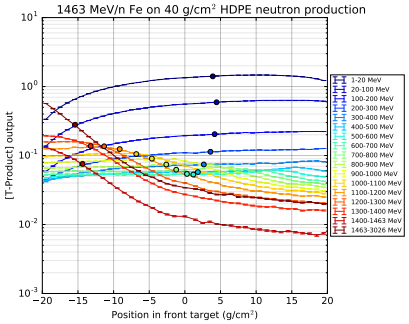


(b) effective target thickness

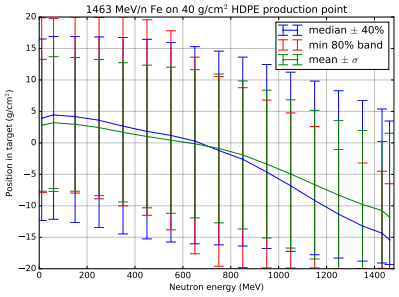


(c) n energy shift

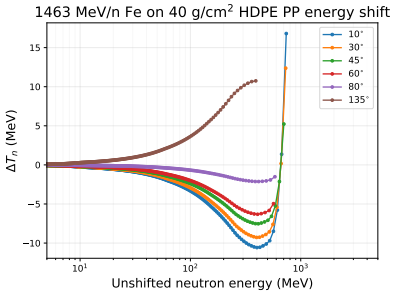
Figure B.104: Neutron production corrections for 1500 MeV/n Fe on 20 g/cm^2 HDPE



(a) n production distribution

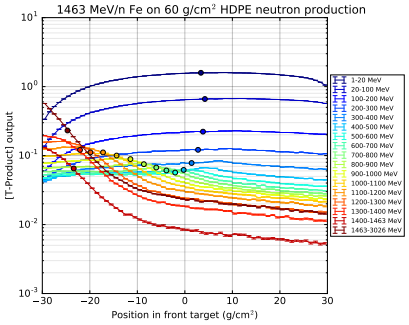


(b) effective target thickness

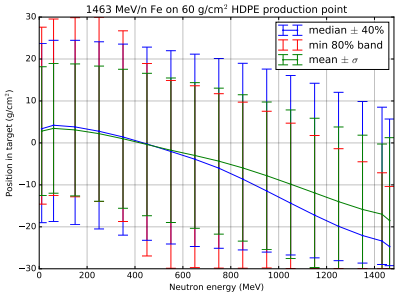


(c) n energy shift

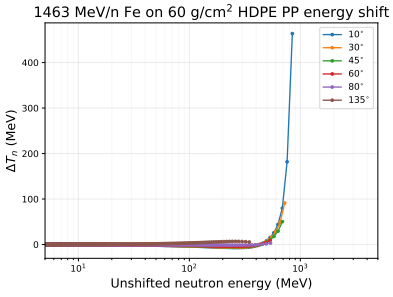
Figure B.105: Neutron production corrections for 1500 MeV/n Fe on 40 g/cm^2 HDPE



(a) n production distribution

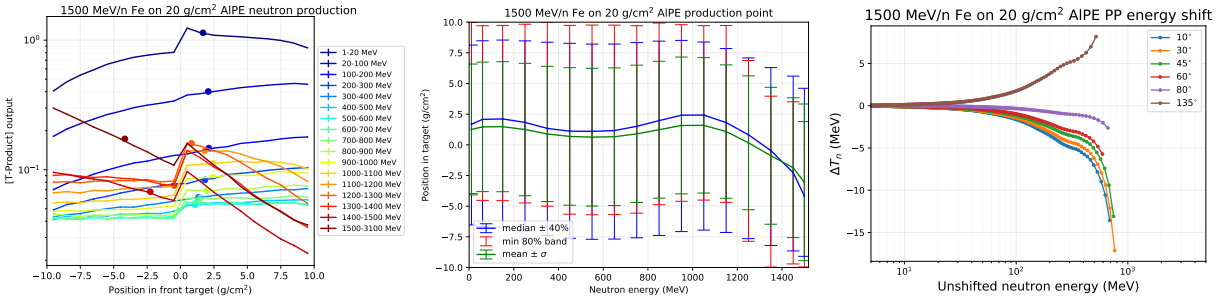


(b) effective target thickness



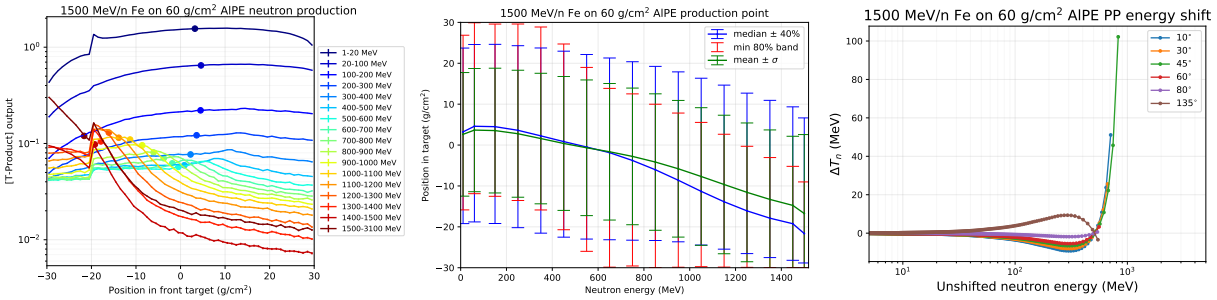
(c) n energy shift

Figure B.106: Neutron production corrections for 1500 MeV/n Fe on 60 g/cm^2 HDPE



(a) n production distribution (b) effective target thickness (c) n energy shift

Figure B.107: Neutron production corrections for 1500 MeV/n Fe on 20 g/cm^2 AlPE



(a) n production distribution (b) effective target thickness (c) n energy shift

Figure B.108: Neutron production corrections for 1500 MeV/n Fe on 60 g/cm^2 AlPE

Appendix C

Yield spectra plots

This appendix section contains plots for every single spectrum produced in this research.

C.1 Upstream target plots

All time-of-flight upstream target spectra generated in this work are showcased in this section.

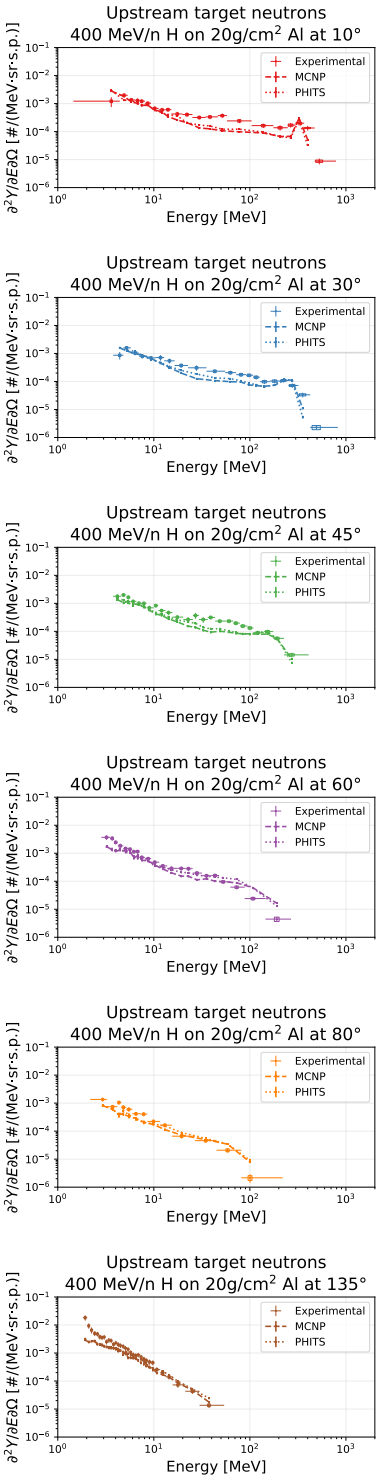


Figure C.1: Upstream target neutrons from 400 MeV/n H incident on Al targets

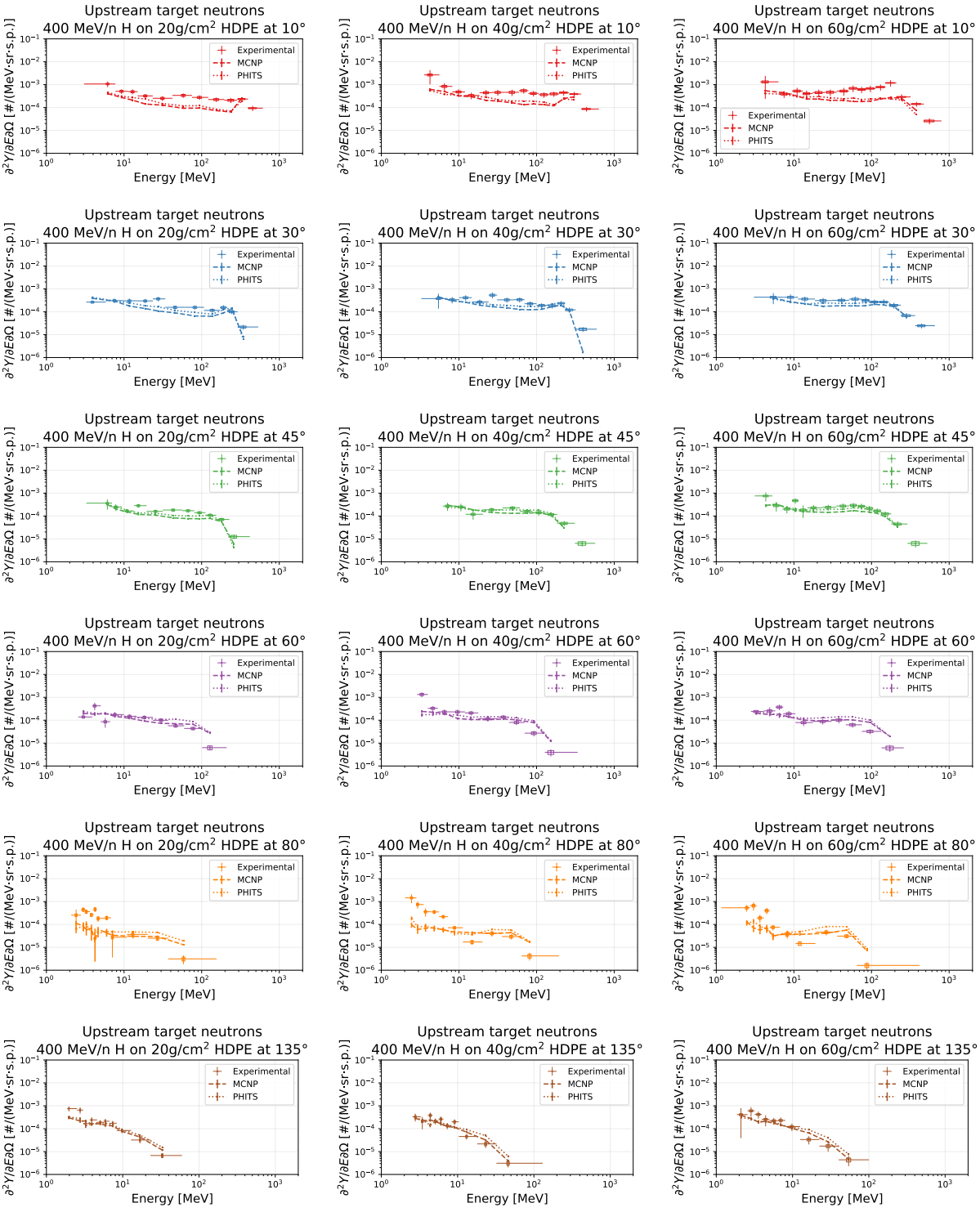


Figure C.2: Upstream target neutrons from 400 MeV/n H incident on HDPE targets

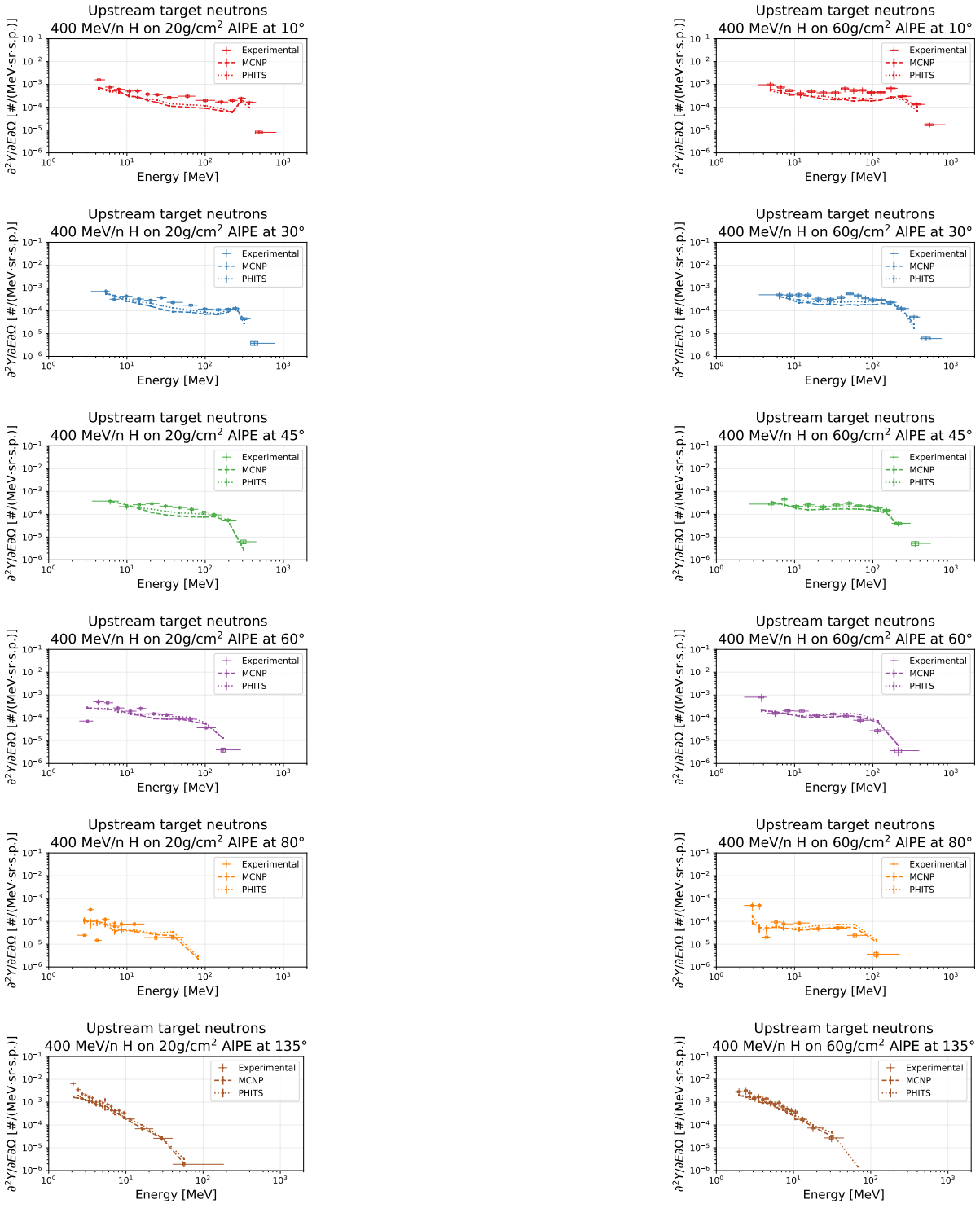


Figure C.3: Upstream target neutrons from 400 MeV/n H incident on AlPE targets

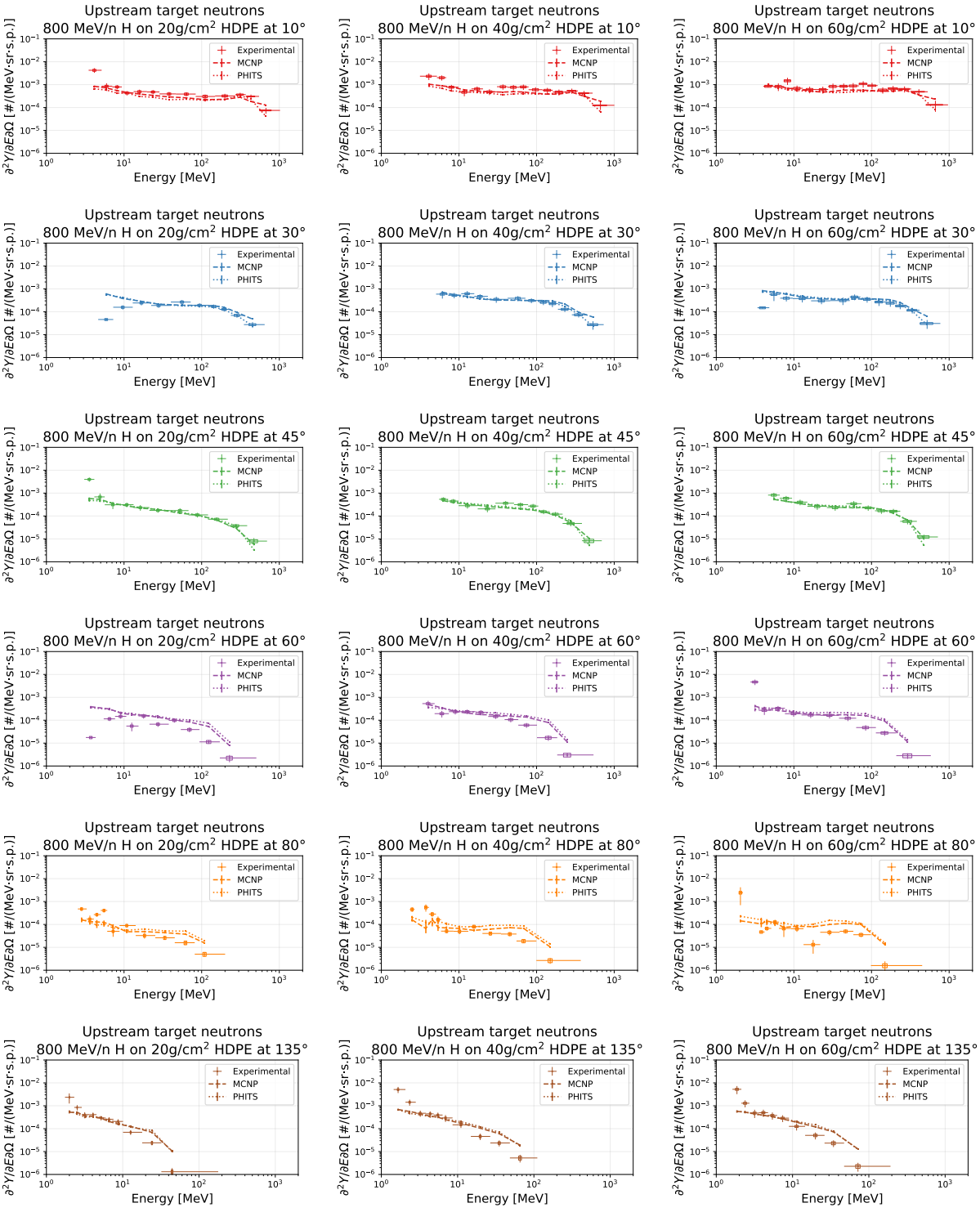


Figure C.4: Upstream target neutrons from 800 MeV/n H incident on HDPE targets

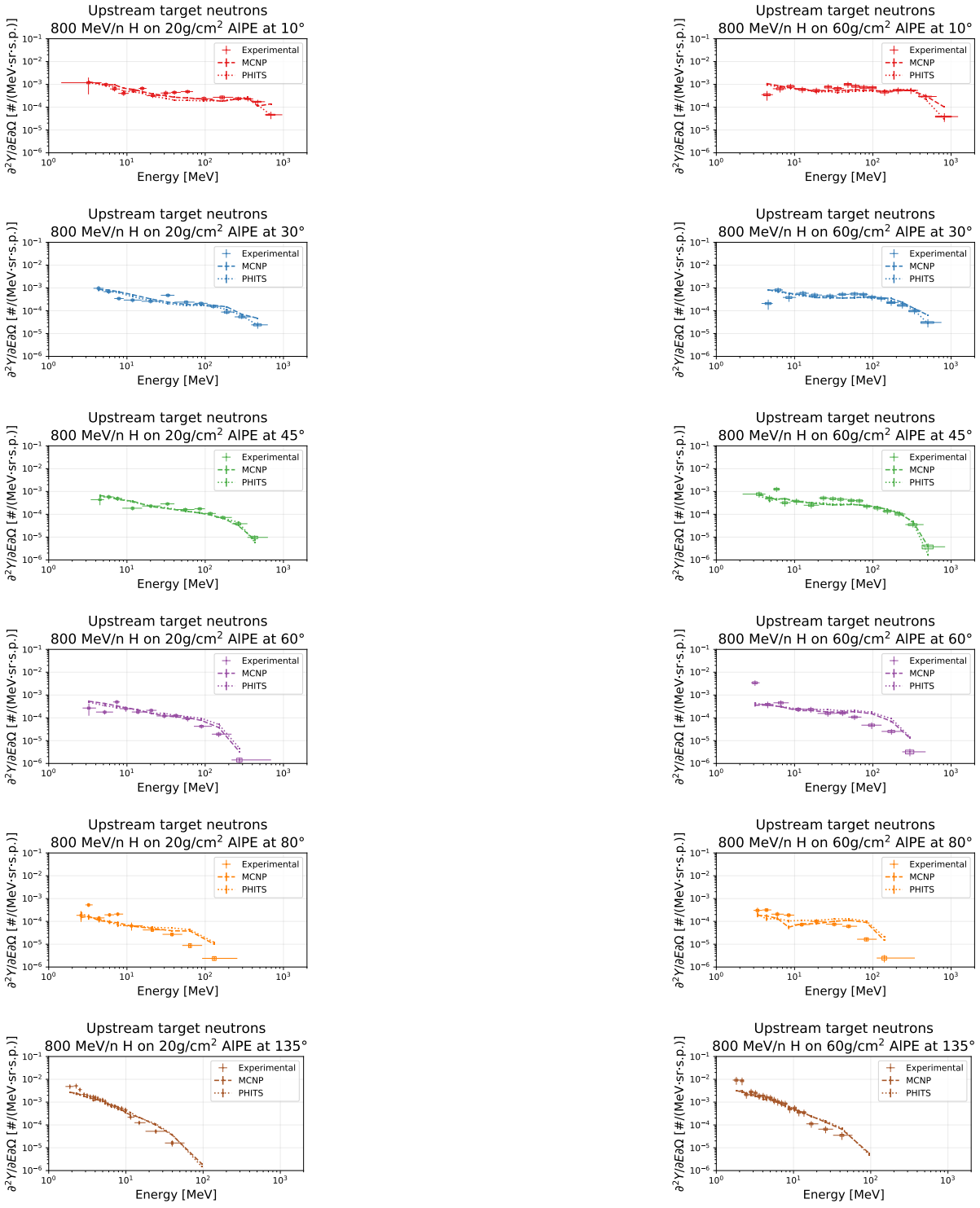


Figure C.5: Upstream target neutrons from 800 MeV/n H incident on AlPE targets

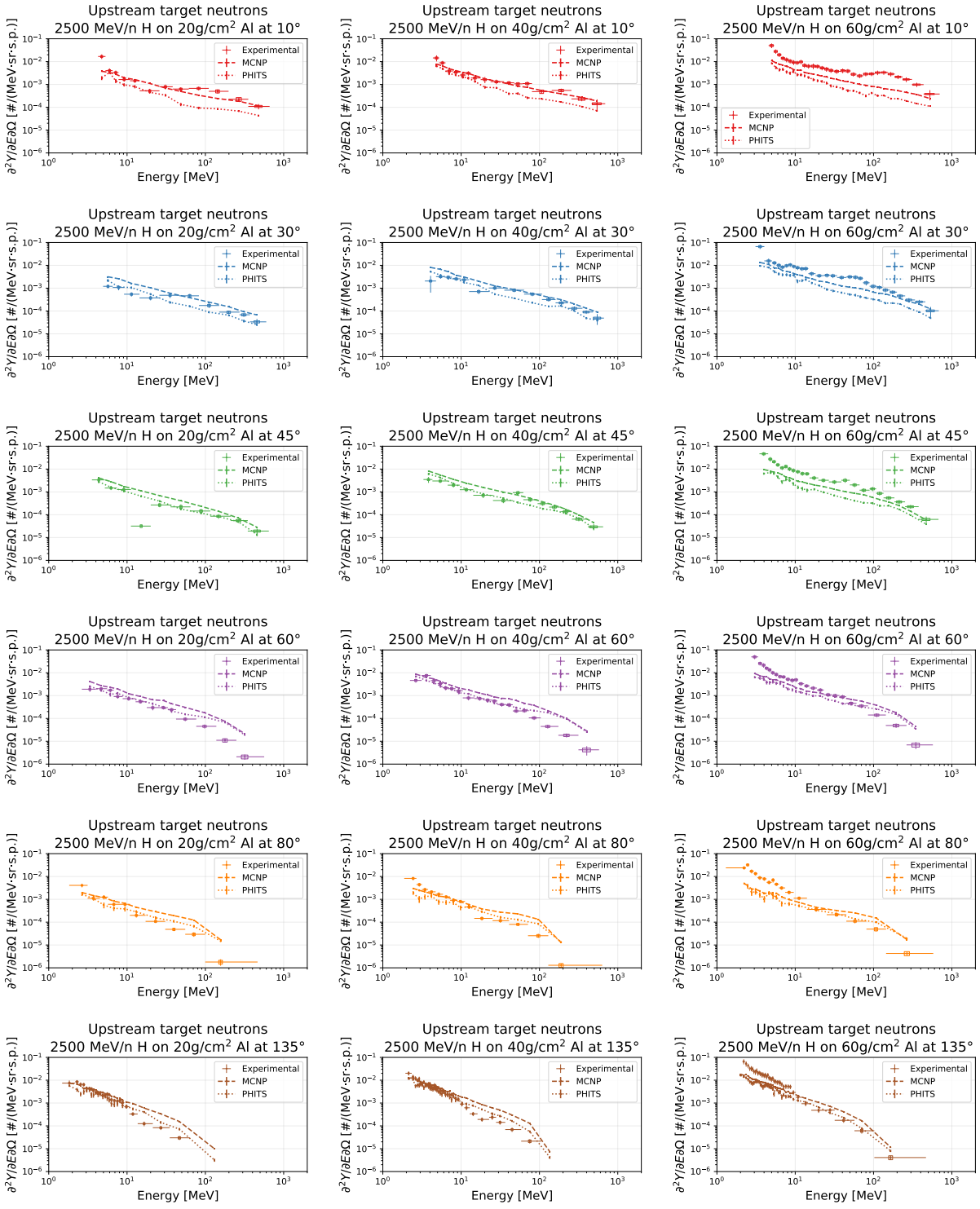


Figure C.6: Upstream target neutrons from 2500 MeV/n H incident on Al targets

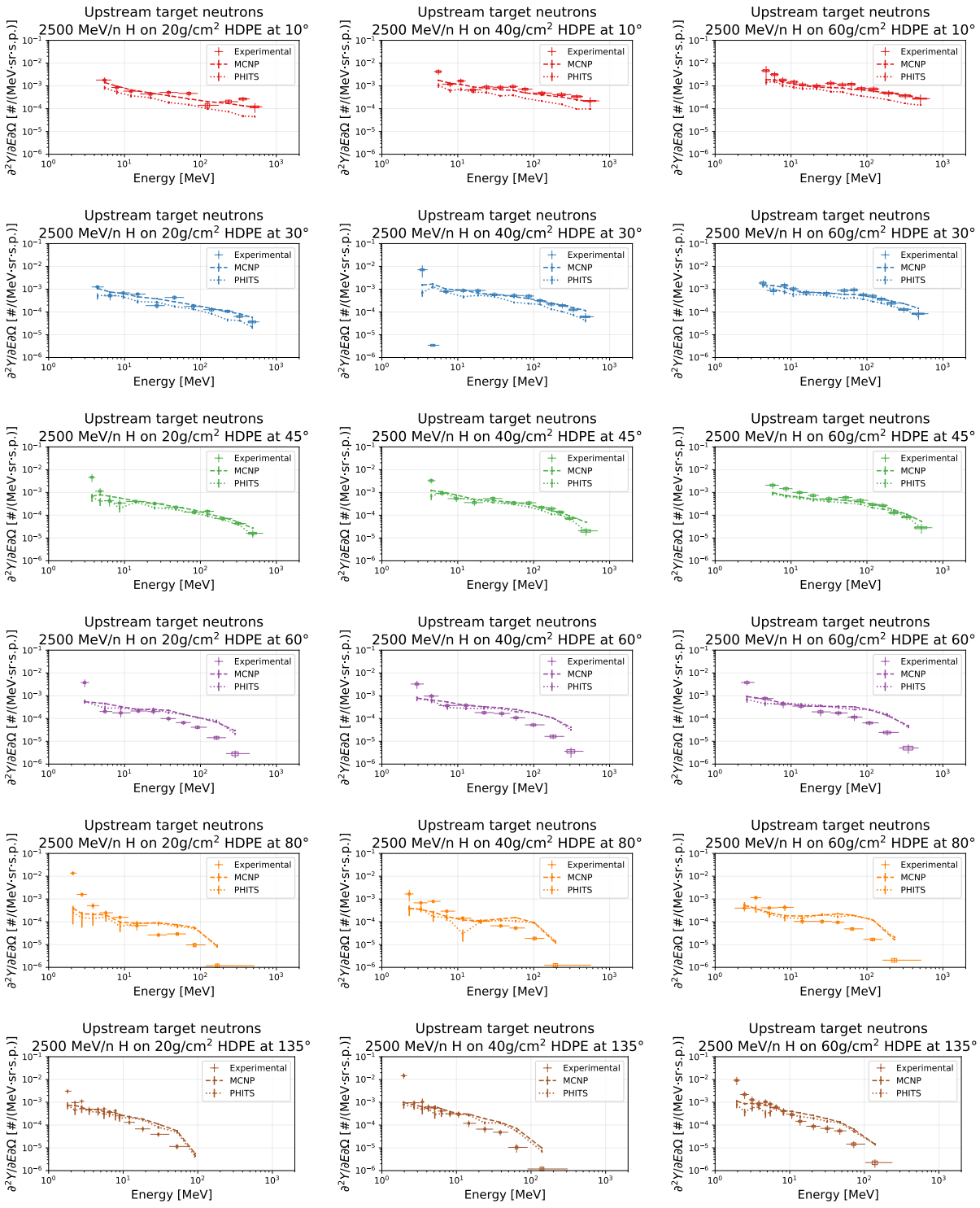


Figure C.7: Upstream target neutrons from 2500 MeV/n H incident on HDPE targets

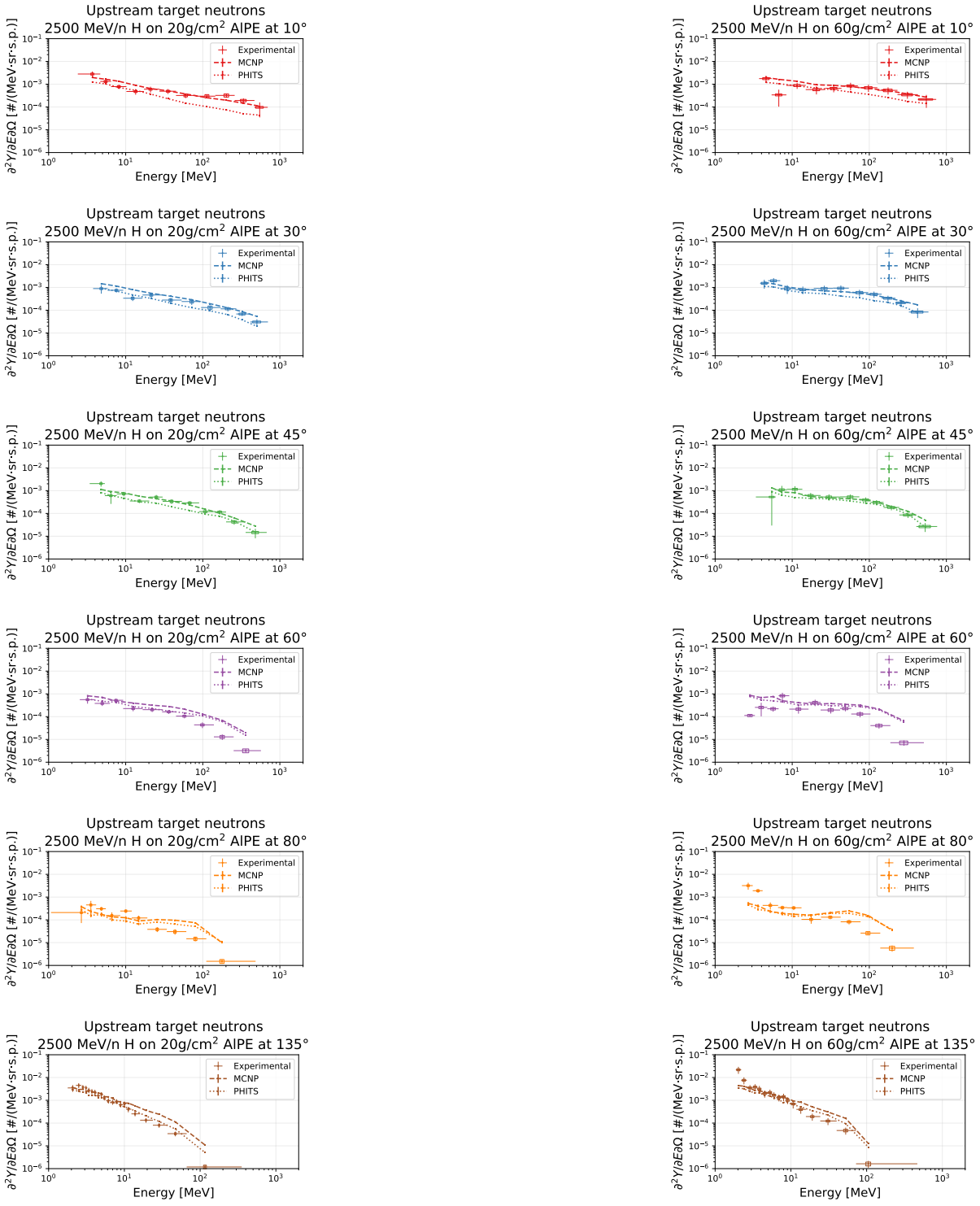


Figure C.8: Upstream target neutrons from 2500 MeV/n H incident on AlPE targets

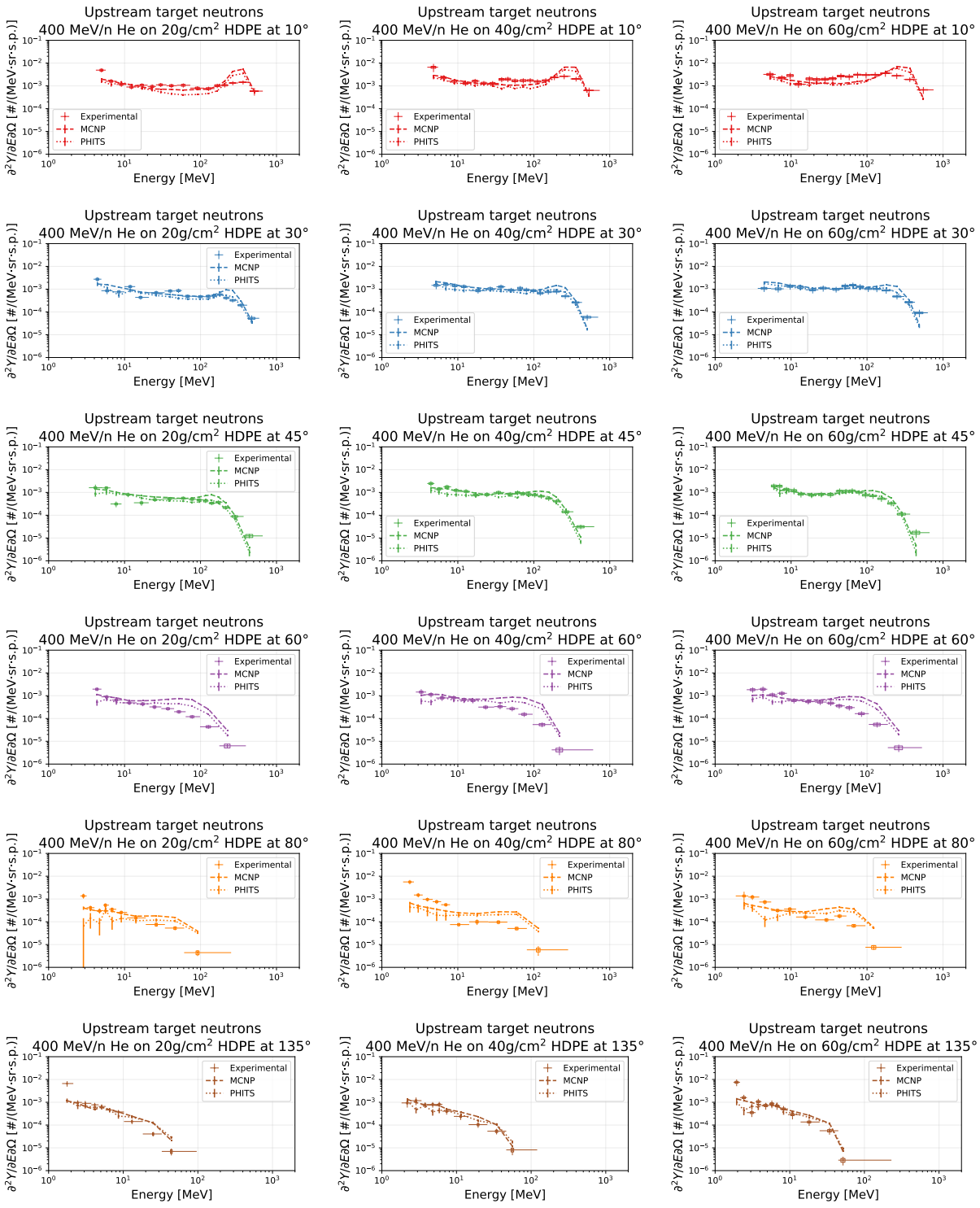


Figure C.9: Upstream target neutrons from 400 MeV/n He incident on HDPE targets

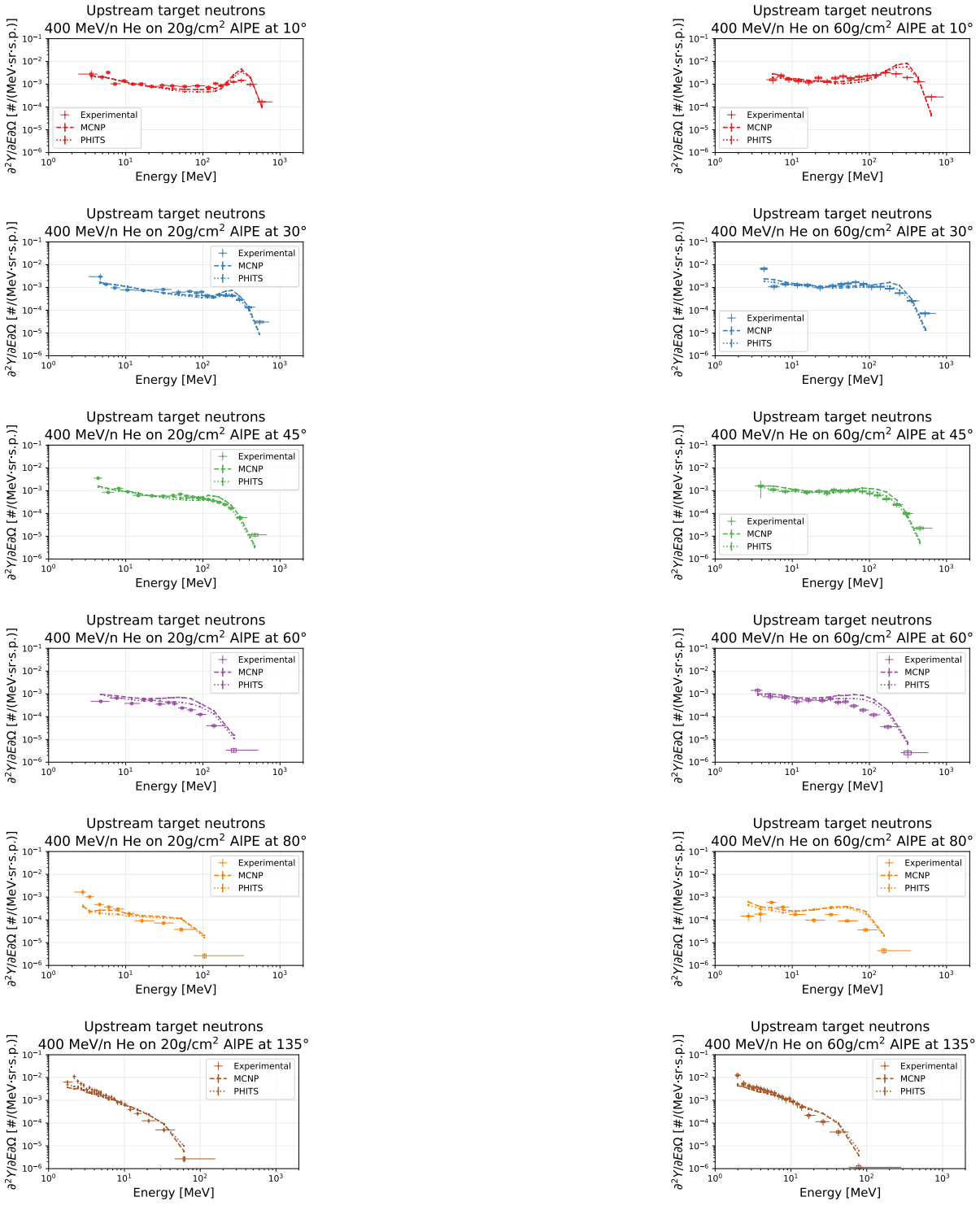


Figure C.10: Upstream target neutrons from 400 MeV/n He incident on AlPE targets

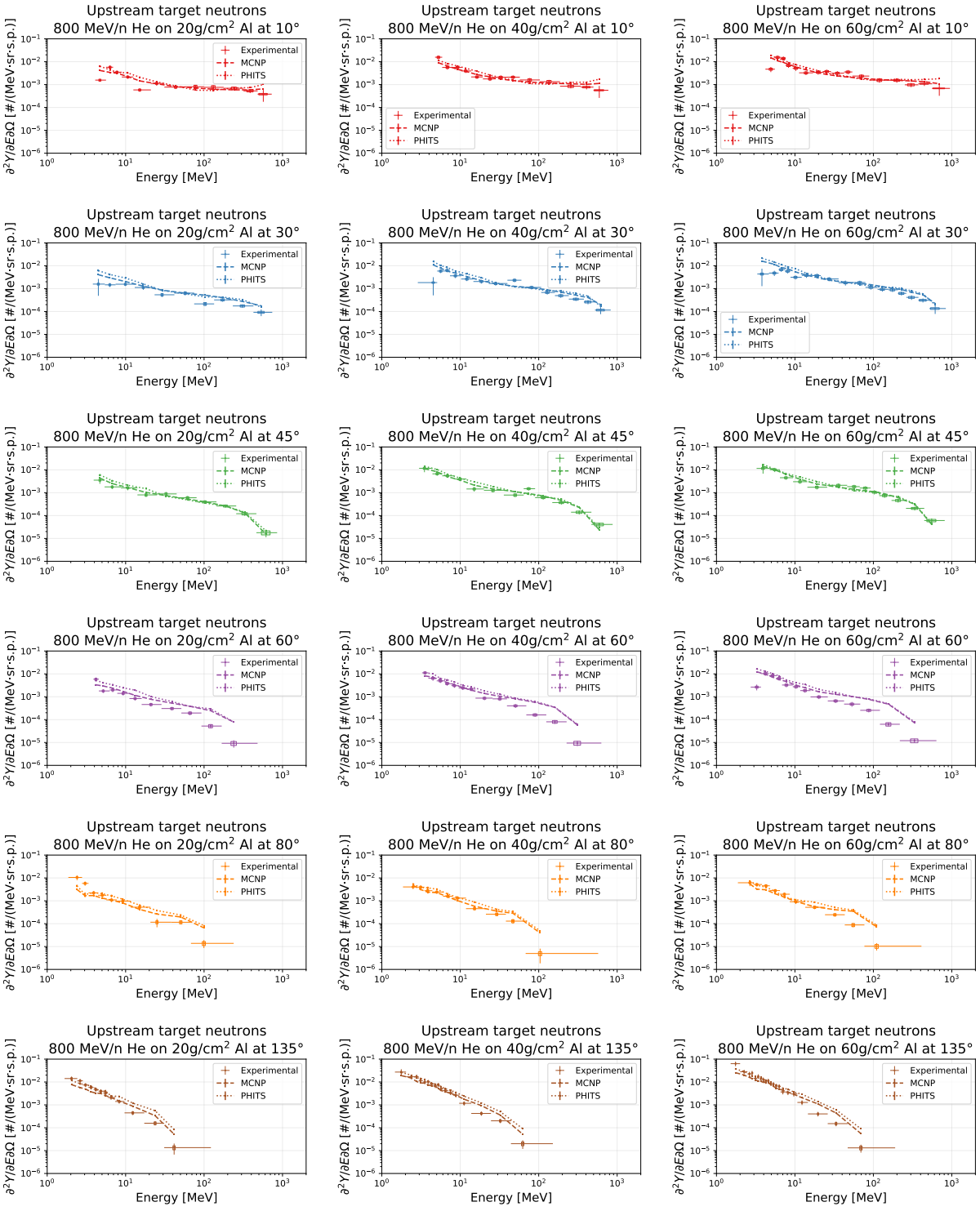


Figure C.11: Upstream target neutrons from 800 MeV/n He incident on Al targets

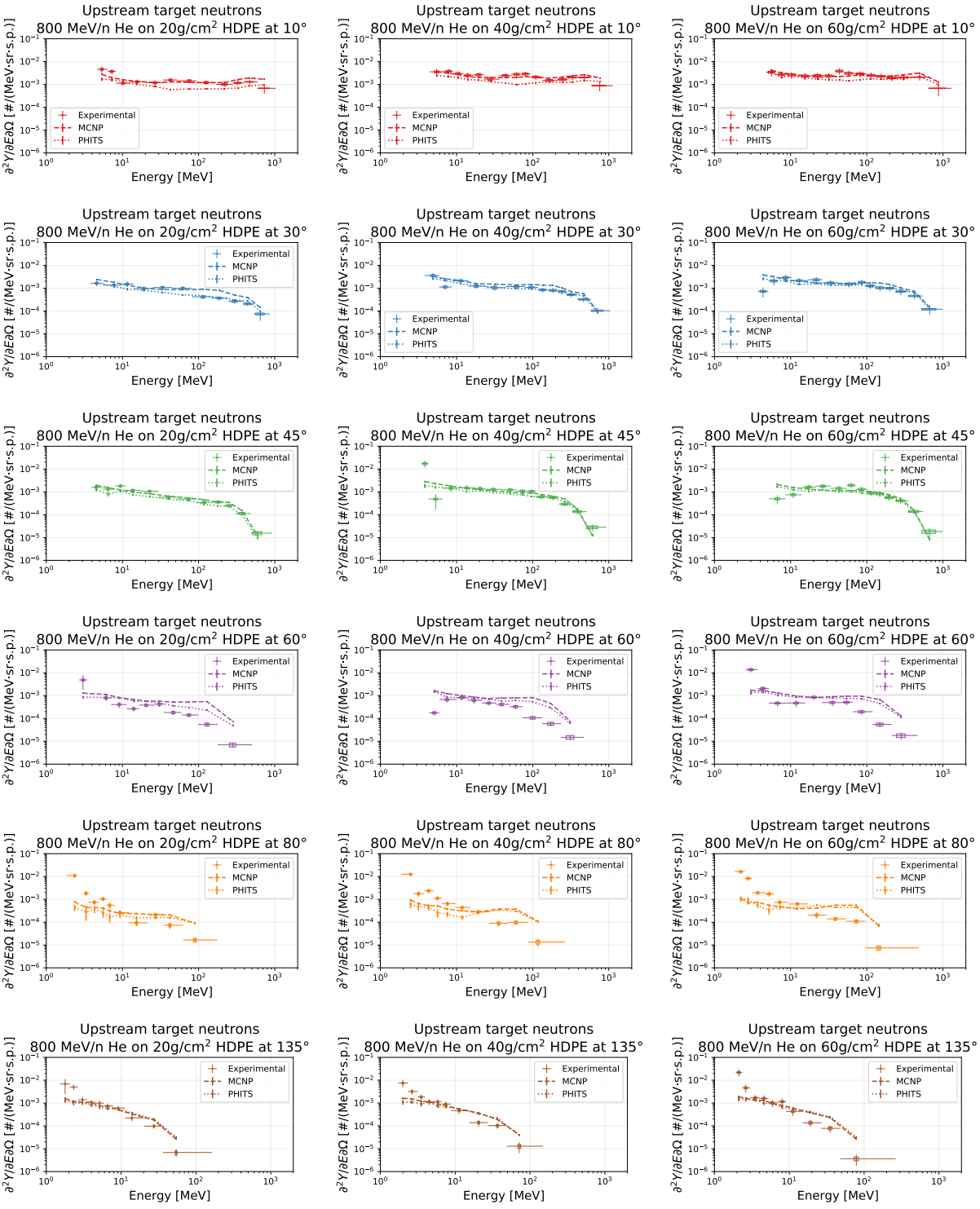


Figure C.12: Upstream target neutrons from 800 MeV/n He incident on HDPE targets

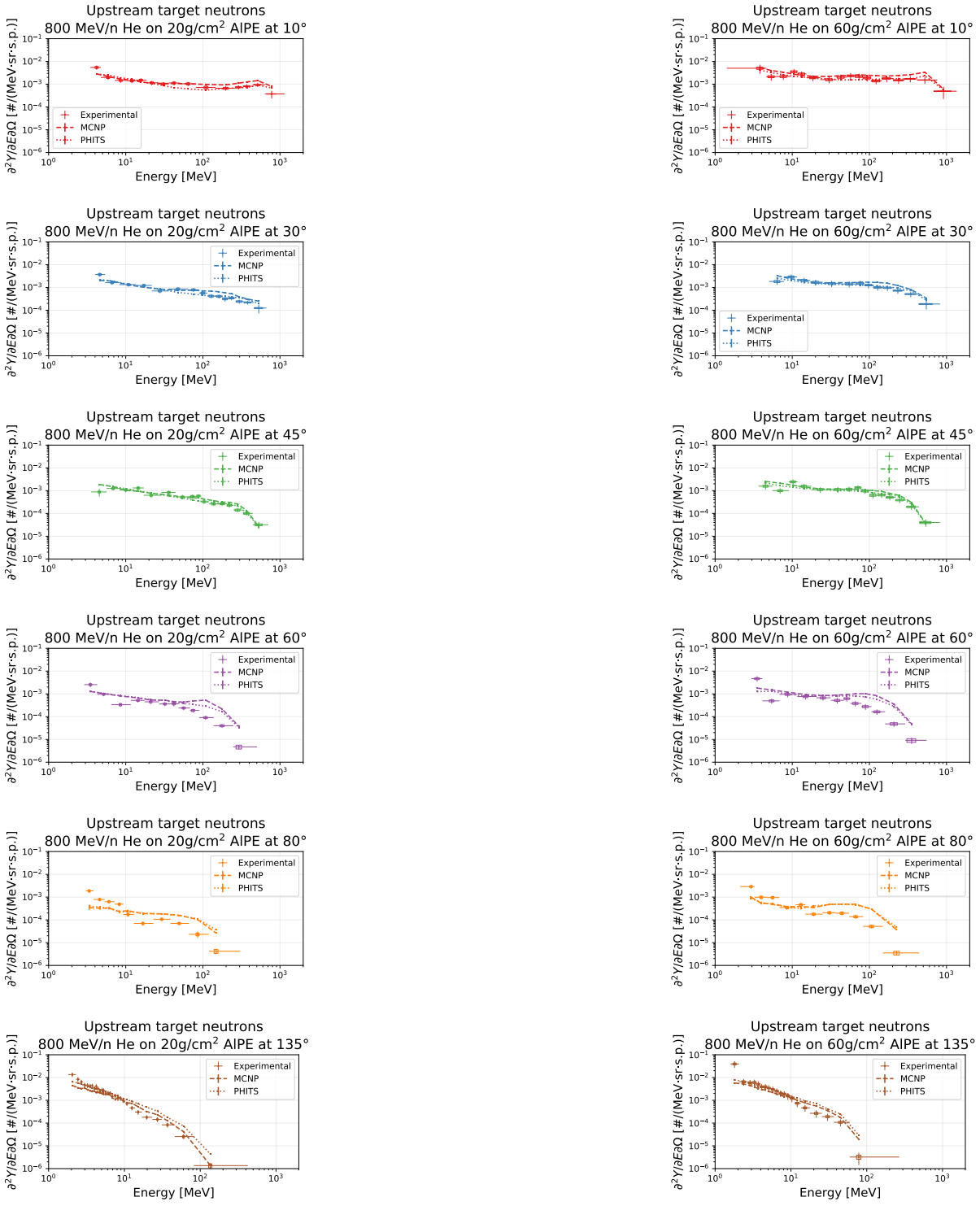


Figure C.13: Upstream target neutrons from 800 MeV/n He incident on AlPE targets

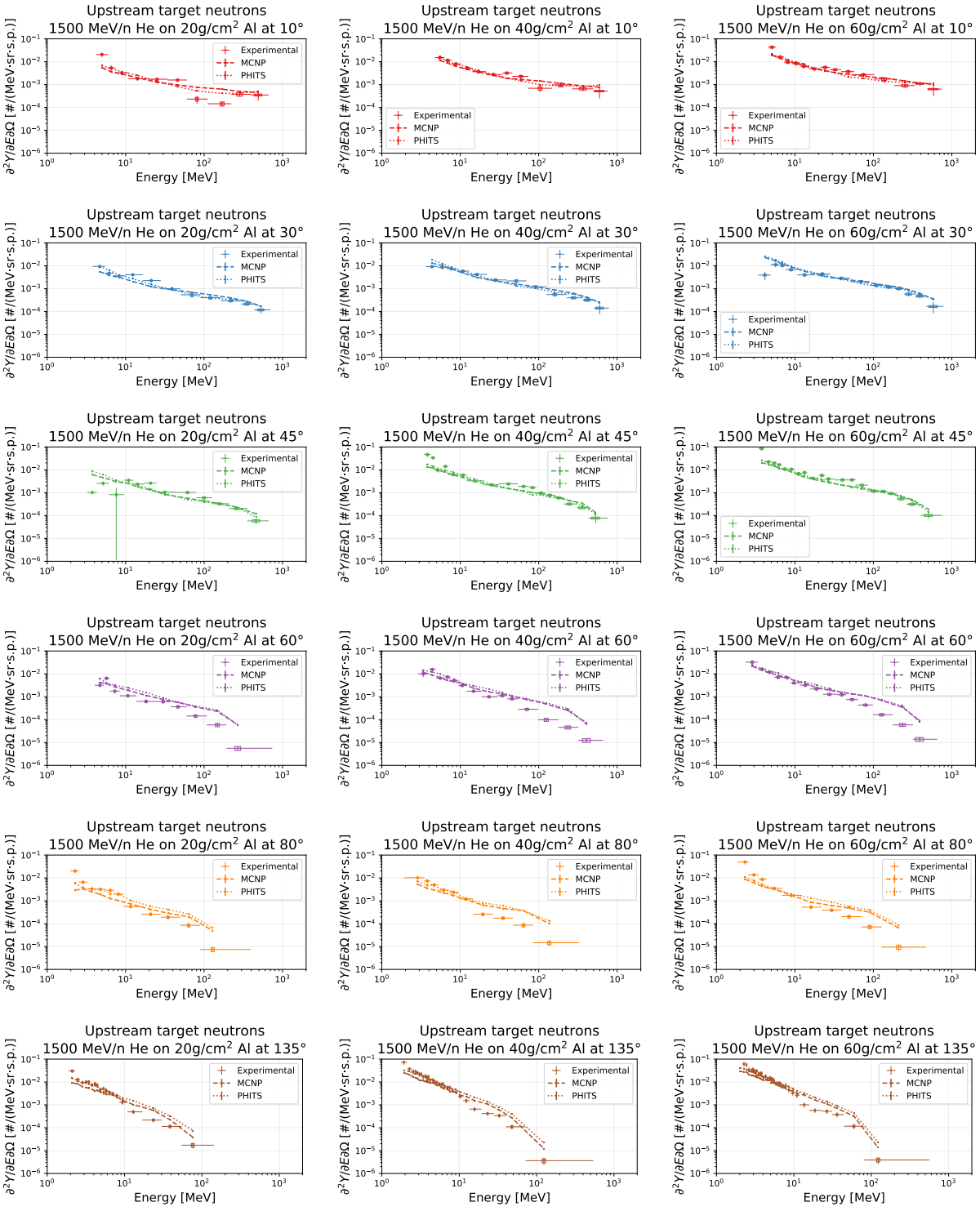


Figure C.14: Upstream target neutrons from 1500 MeV/n He incident on Al targets

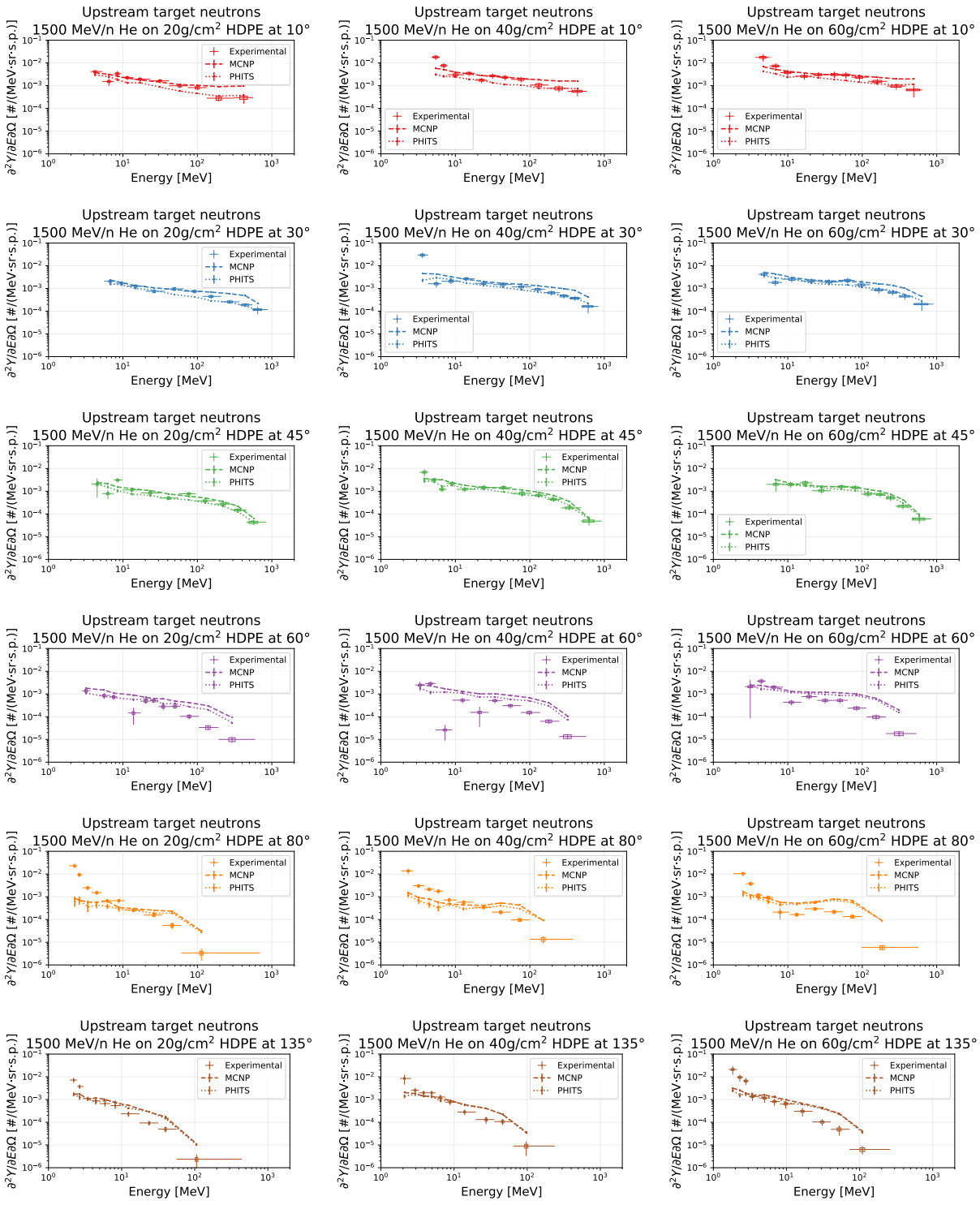


Figure C.15: Upstream target neutrons from 1500 MeV/n He incident on HDPE targets

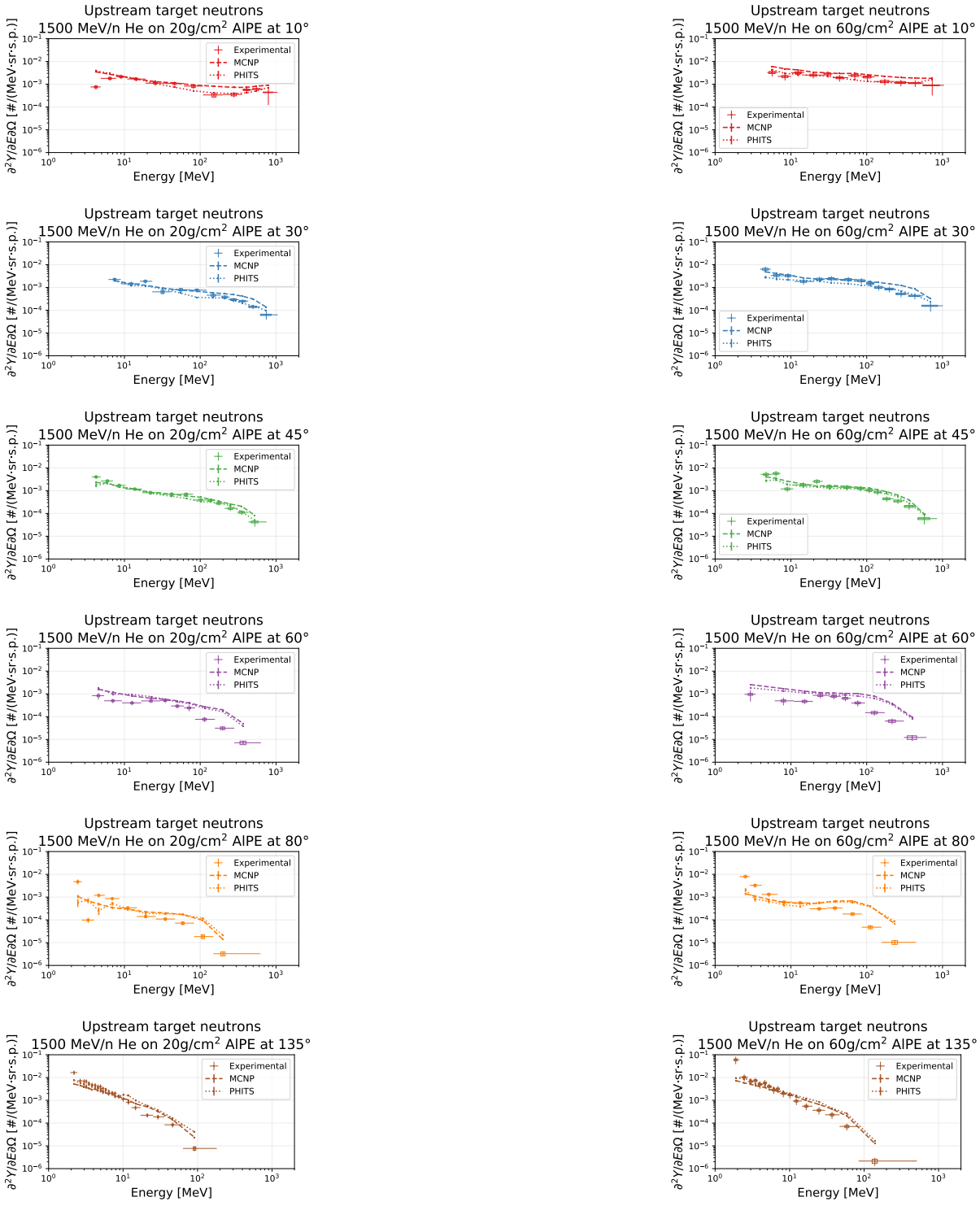


Figure C.16: Upstream target neutrons from 1500 MeV/n He incident on AlPE targets

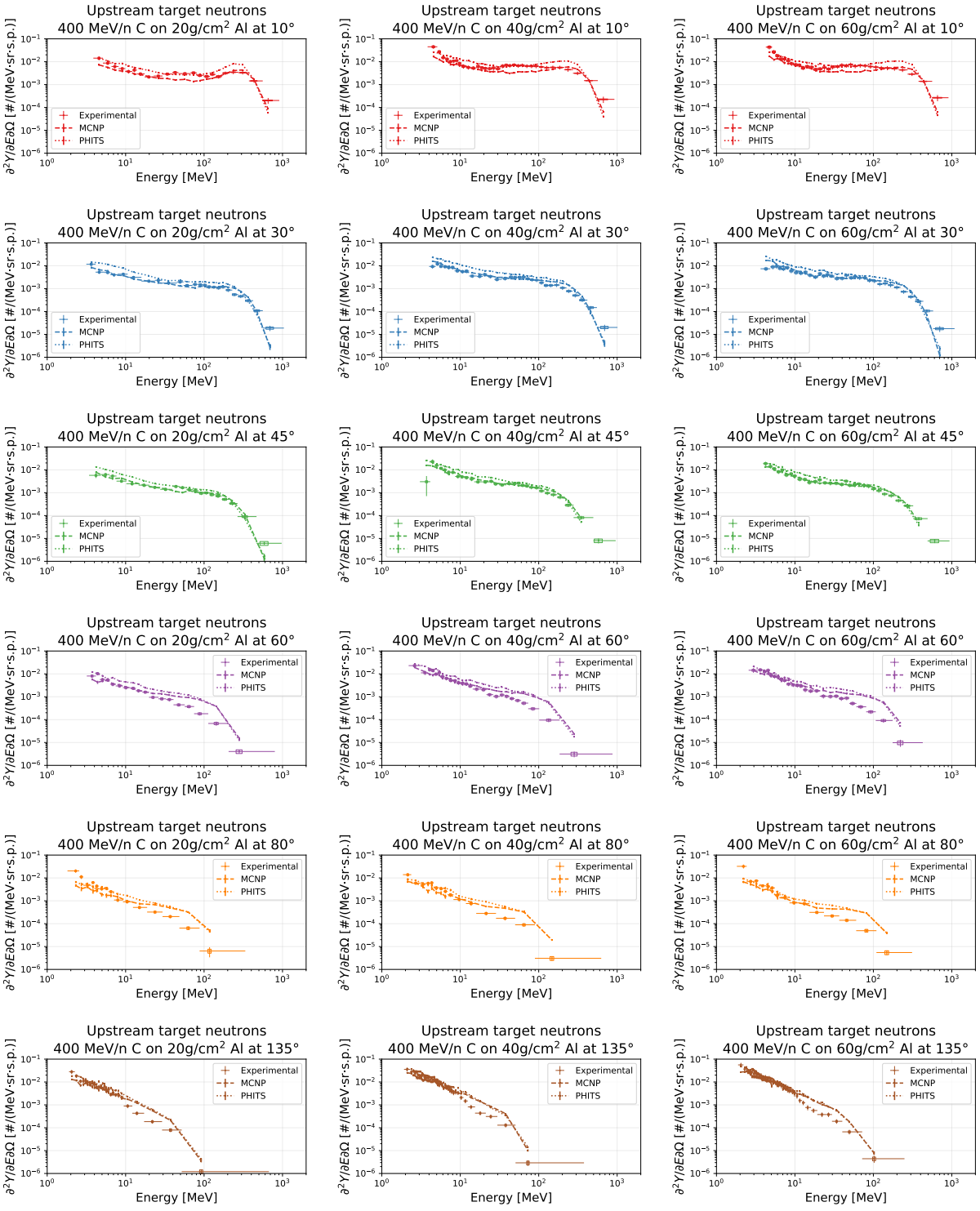


Figure C.17: Upstream target neutrons from 400 MeV/n C incident on Al targets

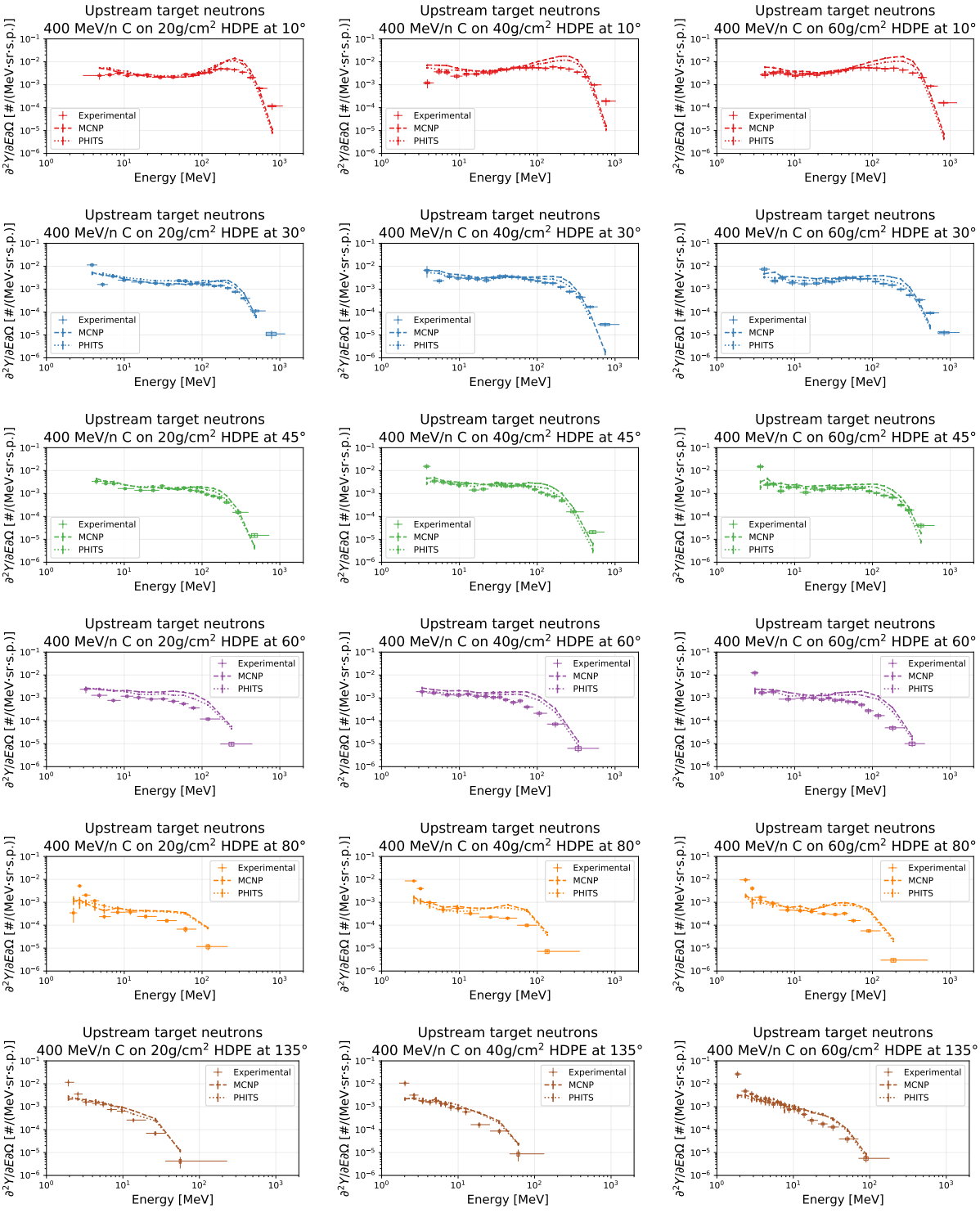


Figure C.18: Upstream target neutrons from 400 MeV/n C incident on HDPE targets

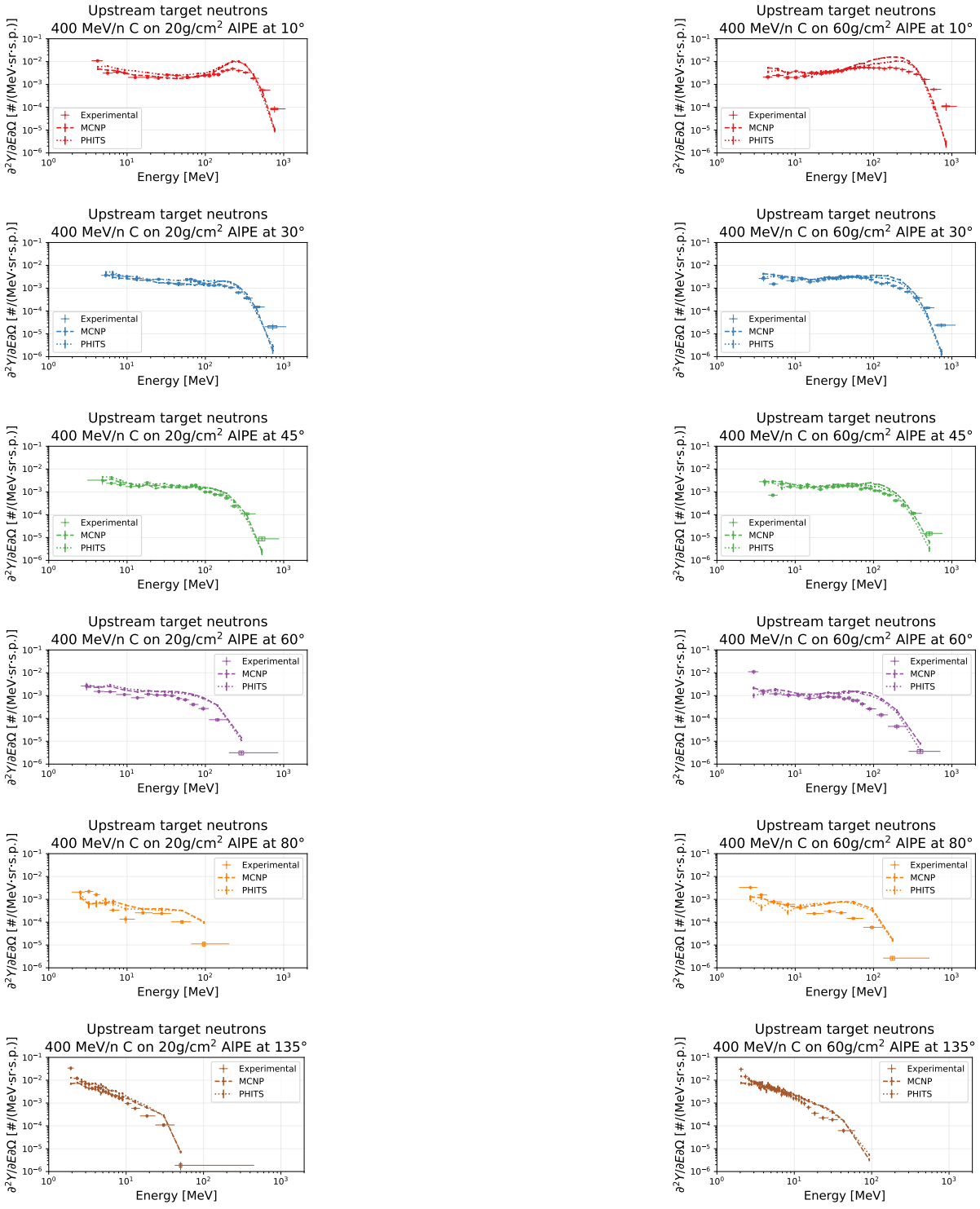


Figure C.19: Upstream target neutrons from 400 MeV/n C incident on AlPE targets

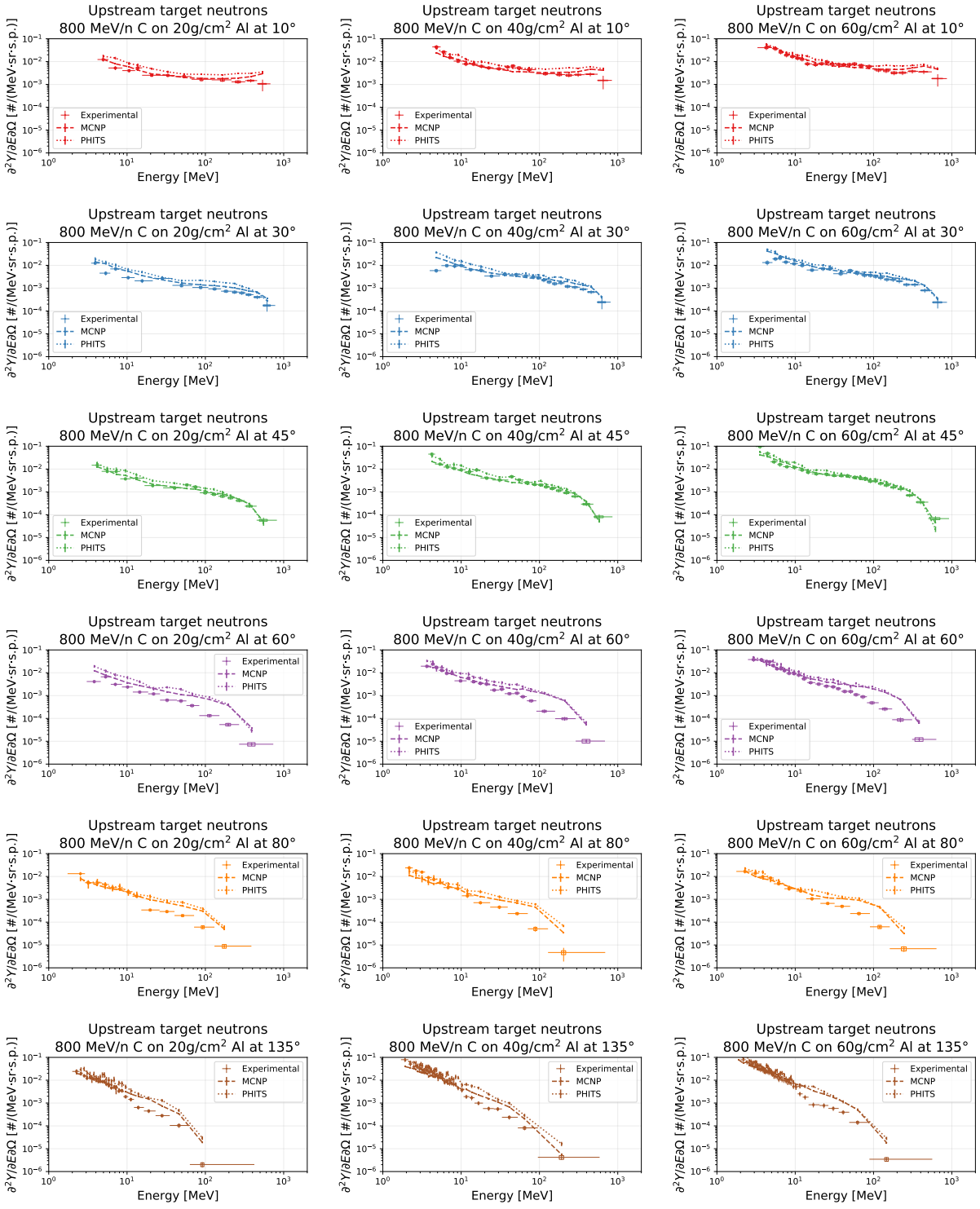


Figure C.20: Upstream target neutrons from 800 MeV/n C incident on Al targets

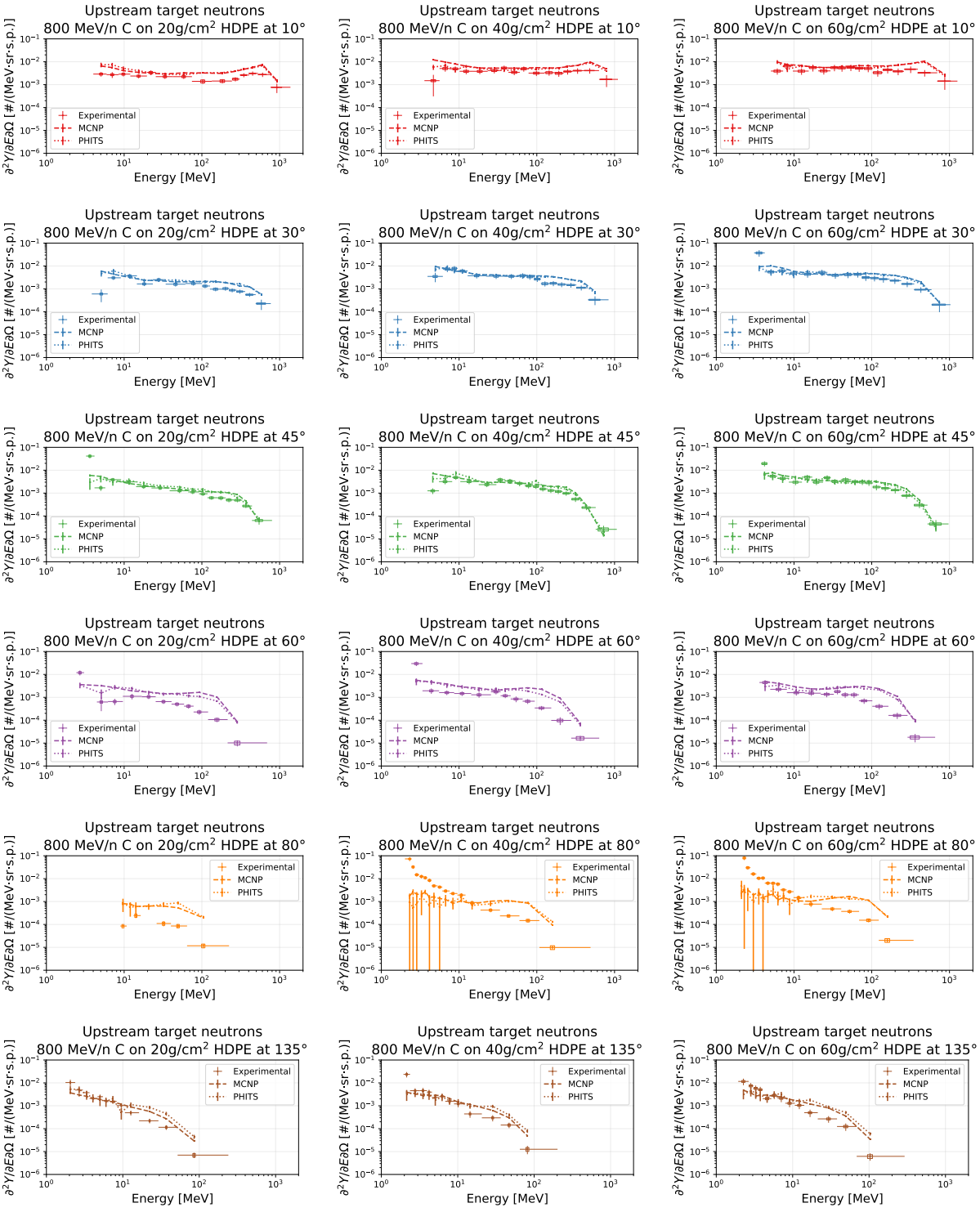


Figure C.21: Upstream target neutrons from 800 MeV/n C incident on HDPE targets

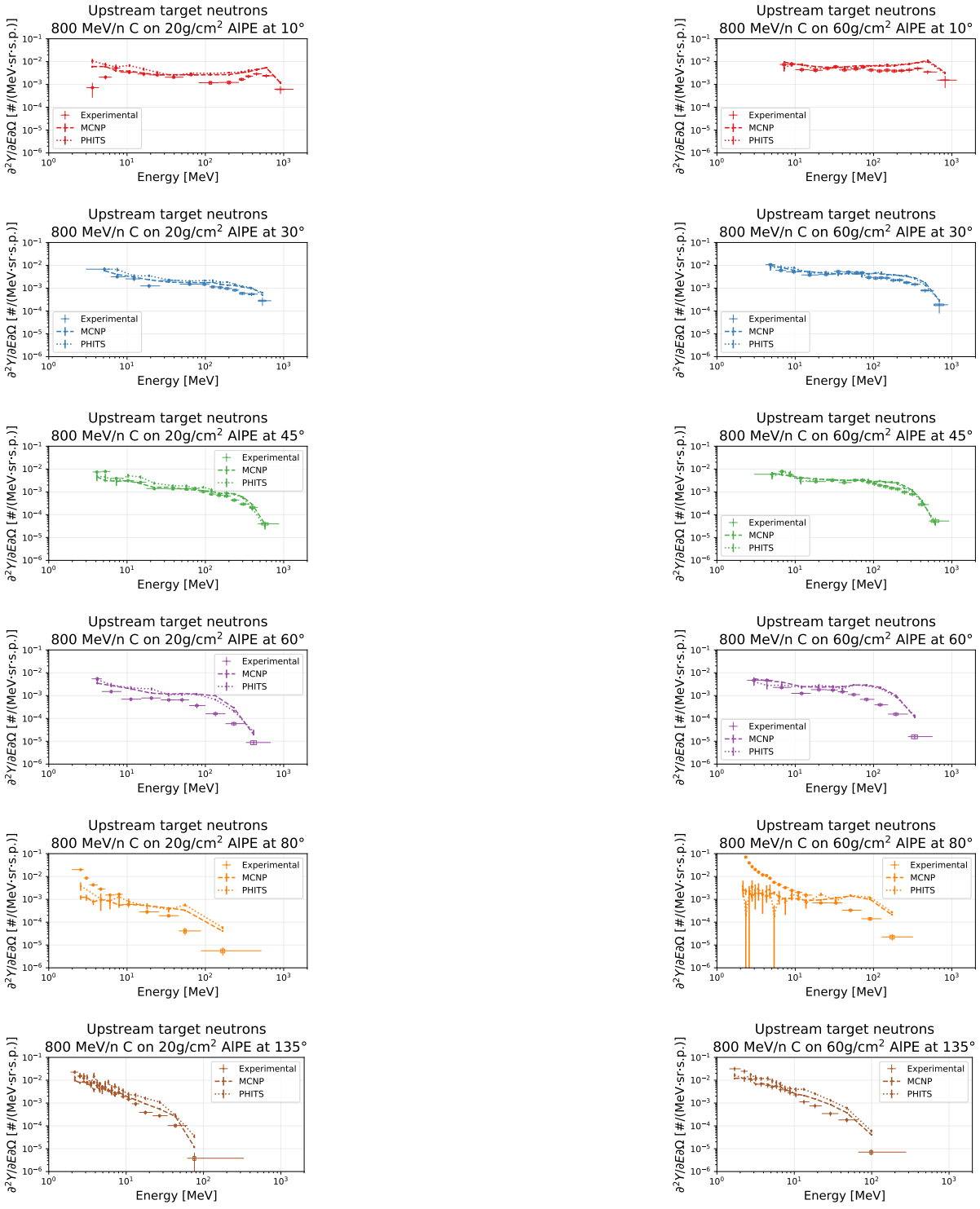


Figure C.22: Upstream target neutrons from 800 MeV/n C incident on AlPE targets

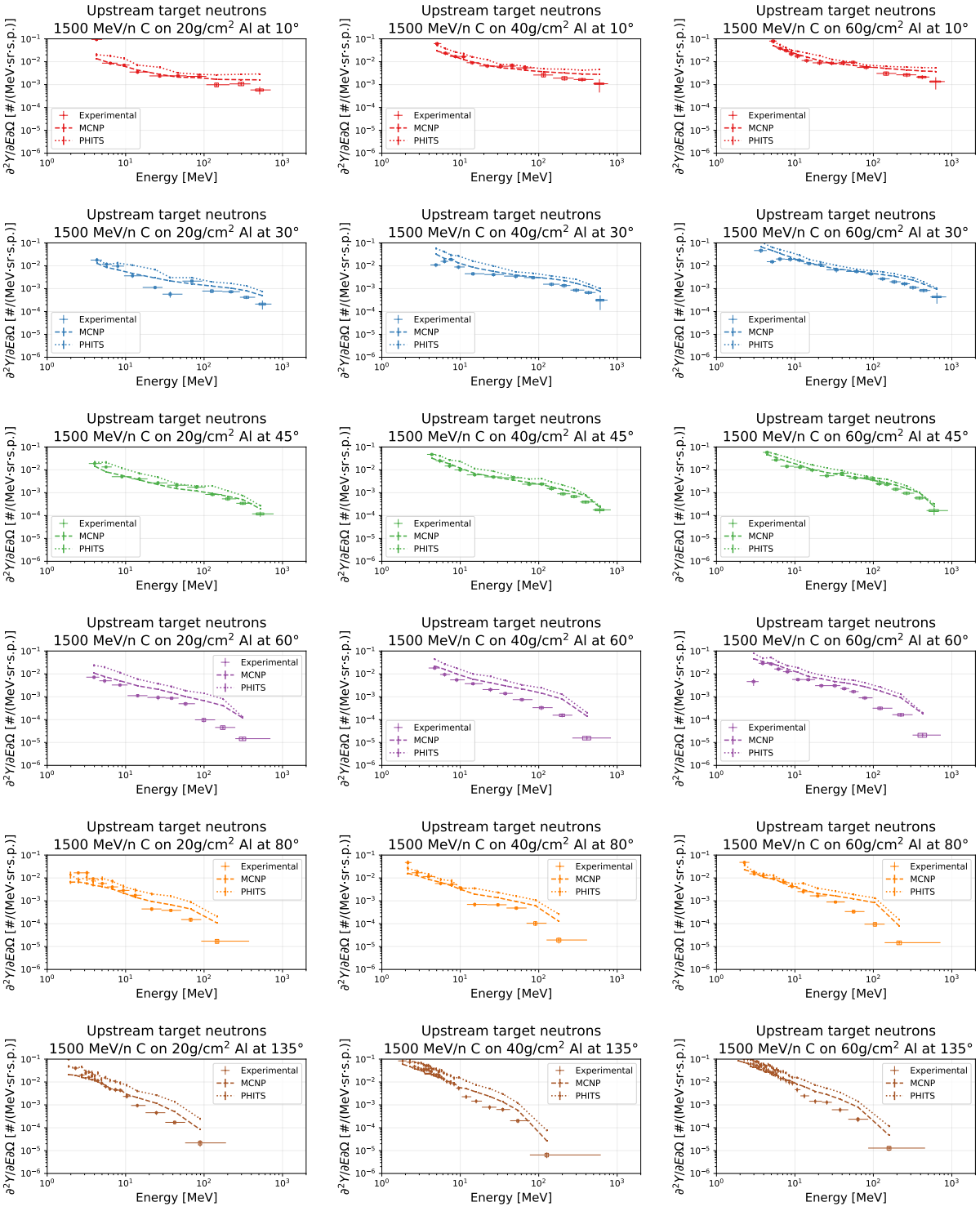


Figure C.23: Upstream target neutrons from 1500 MeV/n C incident on Al targets

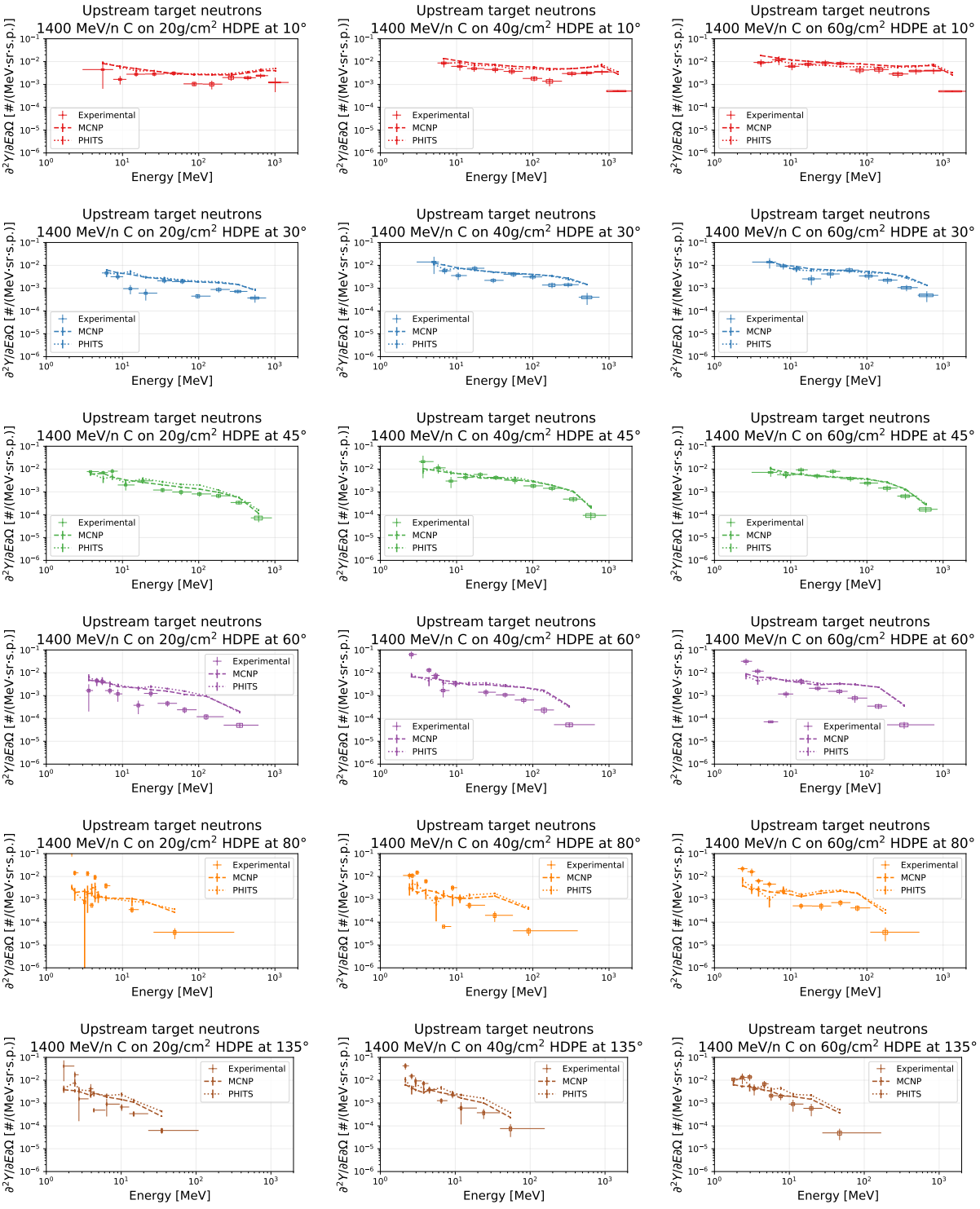


Figure C.24: Upstream target neutrons from 1400 MeV/n C incident on HDPE targets

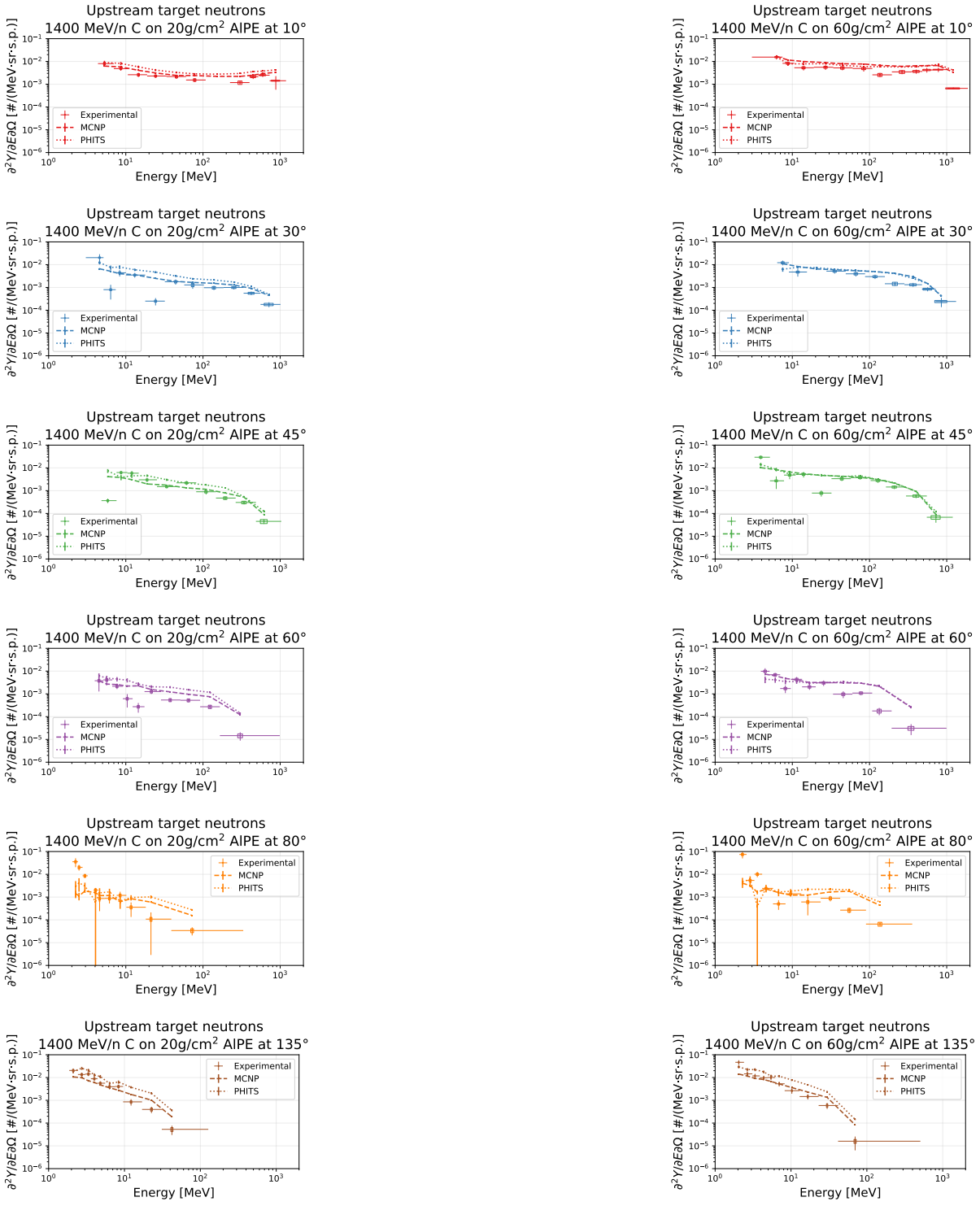


Figure C.25: Upstream target neutrons from 1400 MeV/n C incident on AlPE targets

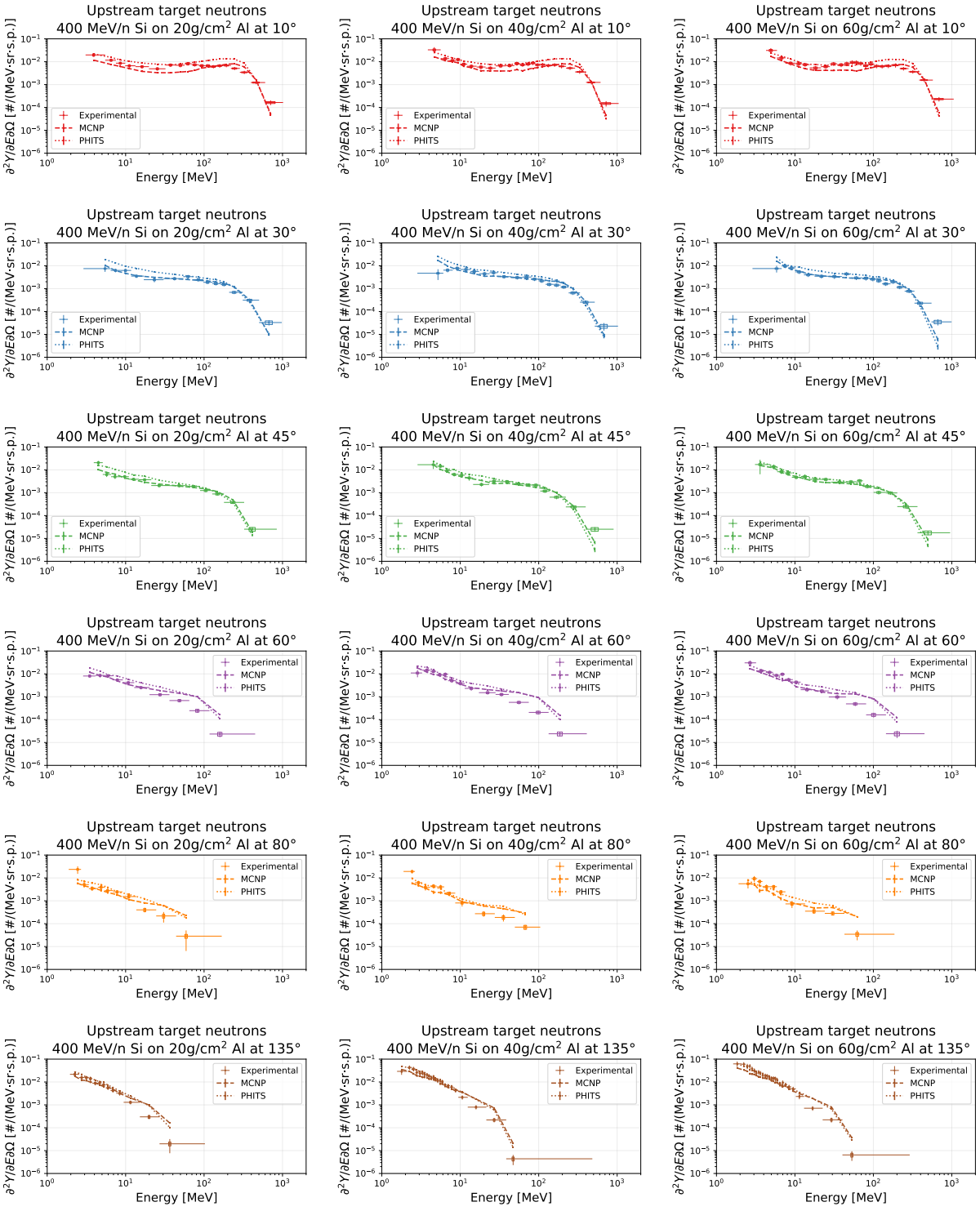


Figure C.26: Upstream target neutrons from 400 MeV/n Si incident on Al targets

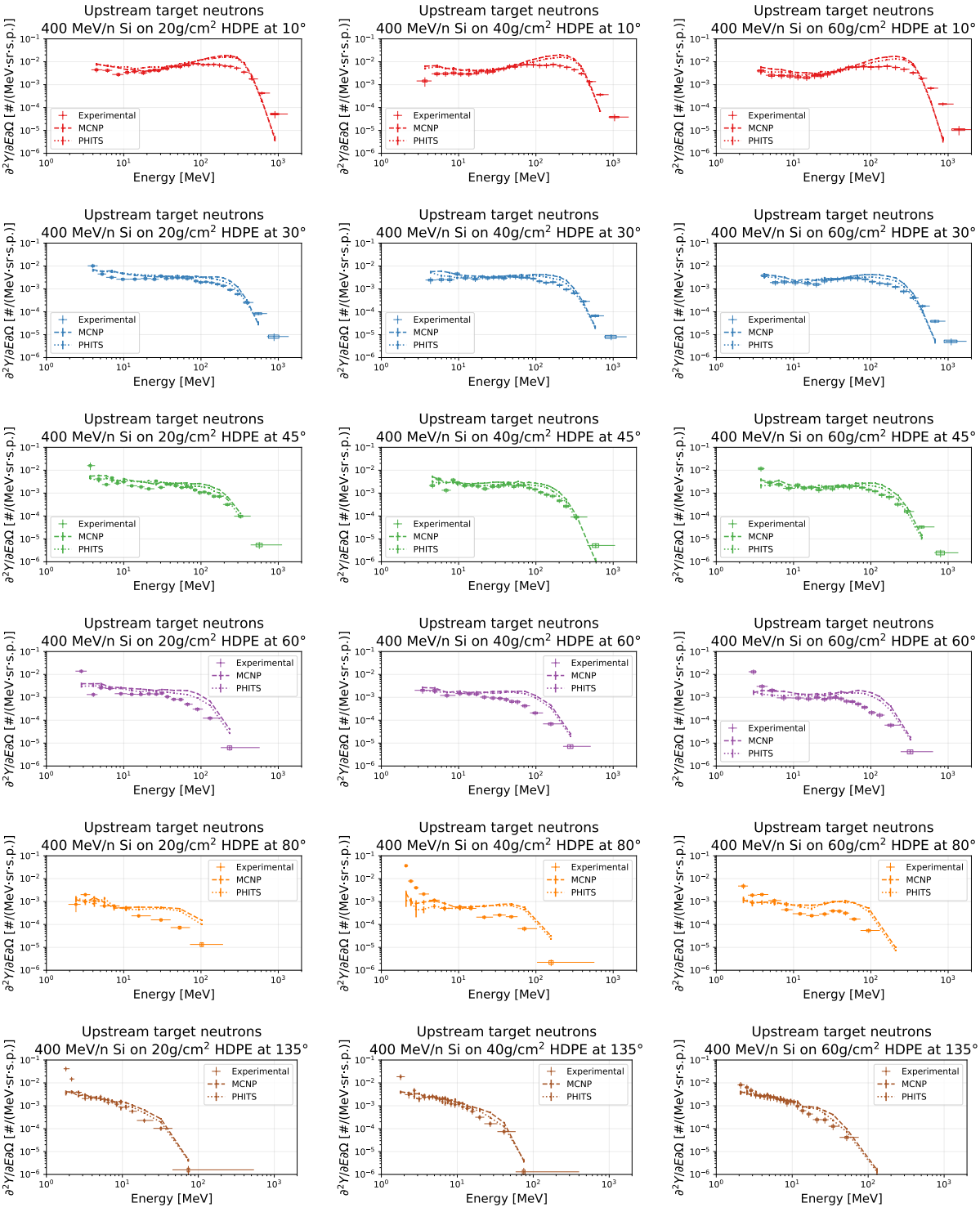


Figure C.27: Upstream target neutrons from 400 MeV/n Si incident on HDPE targets

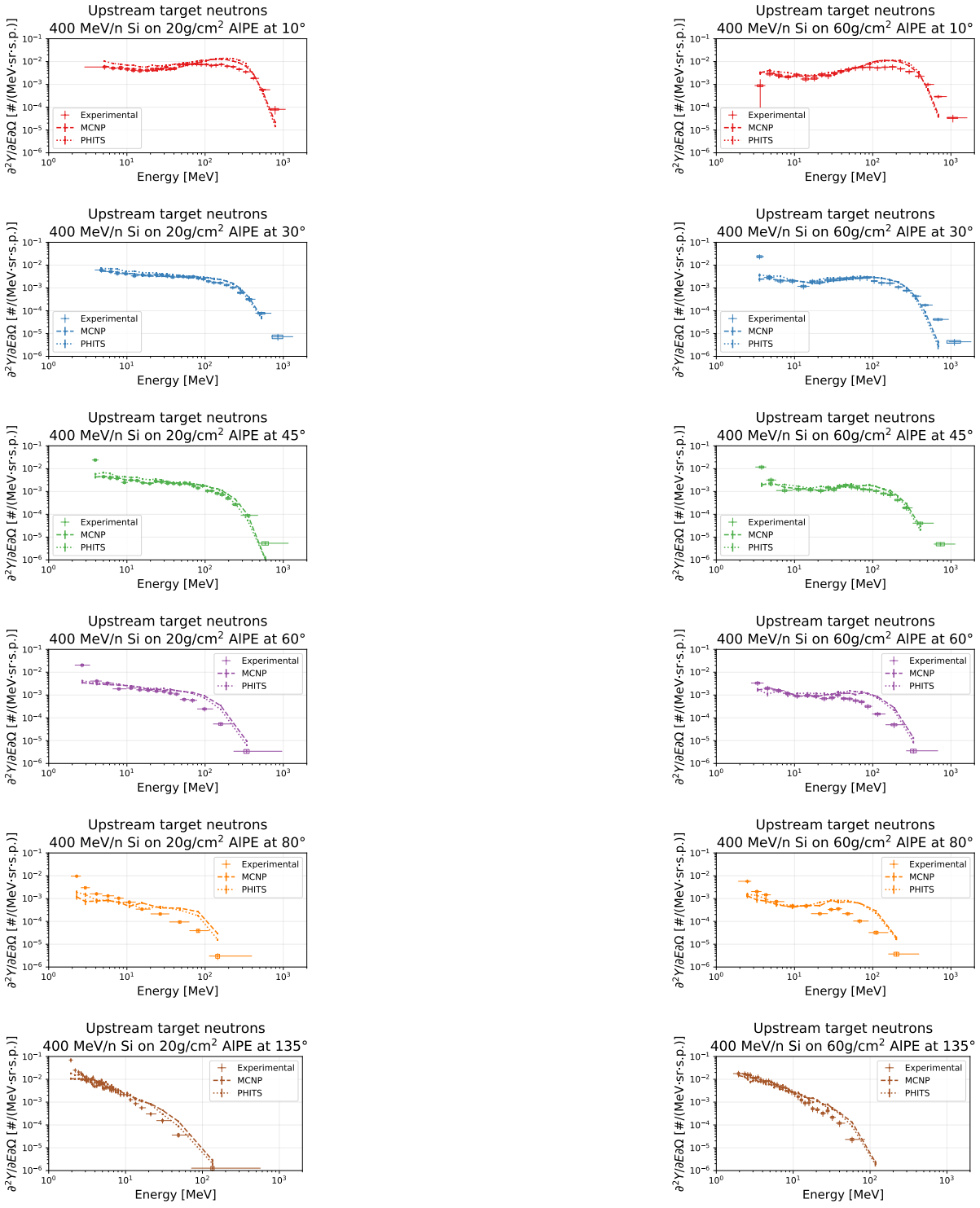


Figure C.28: Upstream target neutrons from 400 MeV/n Si incident on AlPE targets

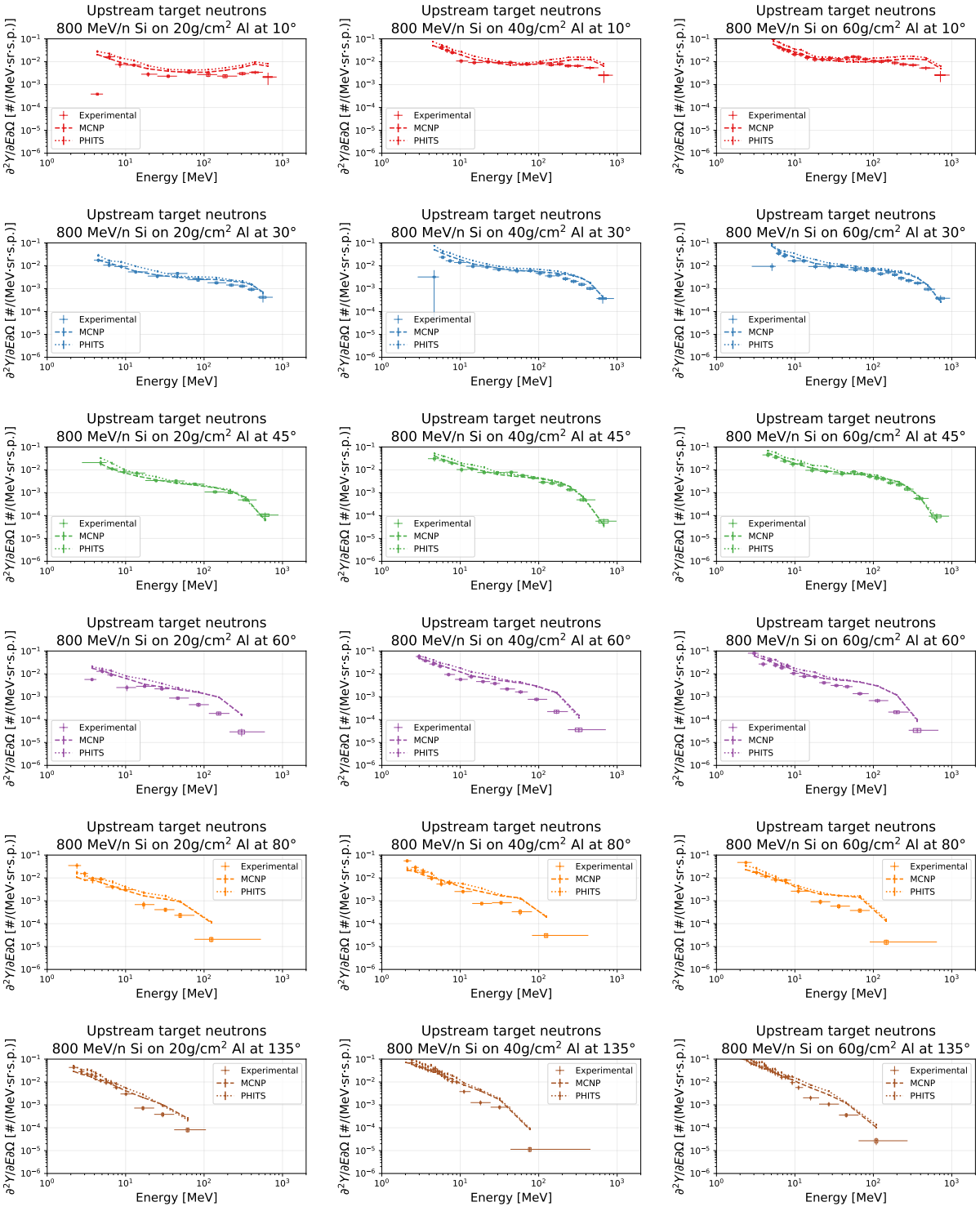


Figure C.29: Upstream target neutrons from 800 MeV/n Si incident on Al targets

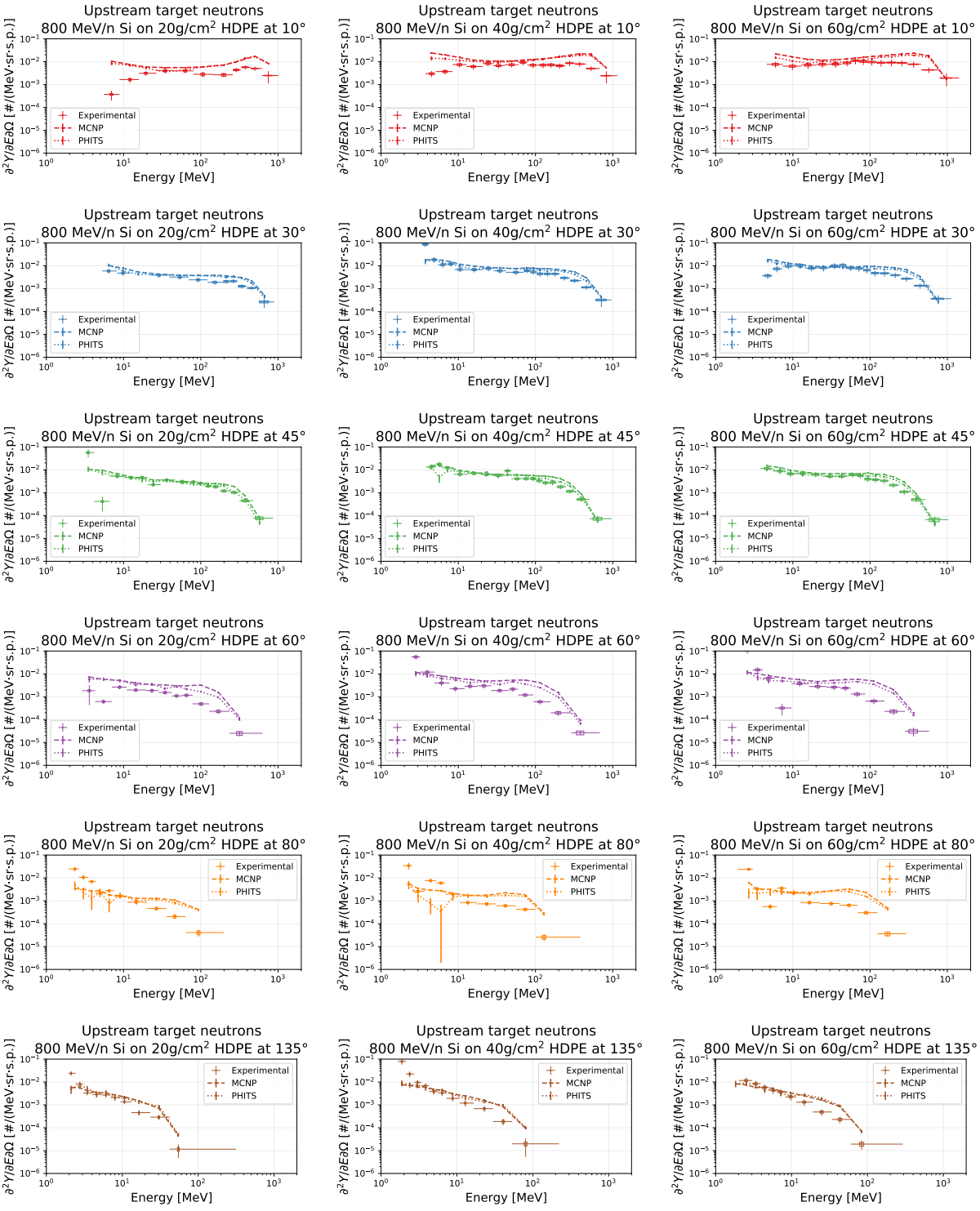


Figure C.30: Upstream target neutrons from 800 MeV/n Si incident on HDPE targets

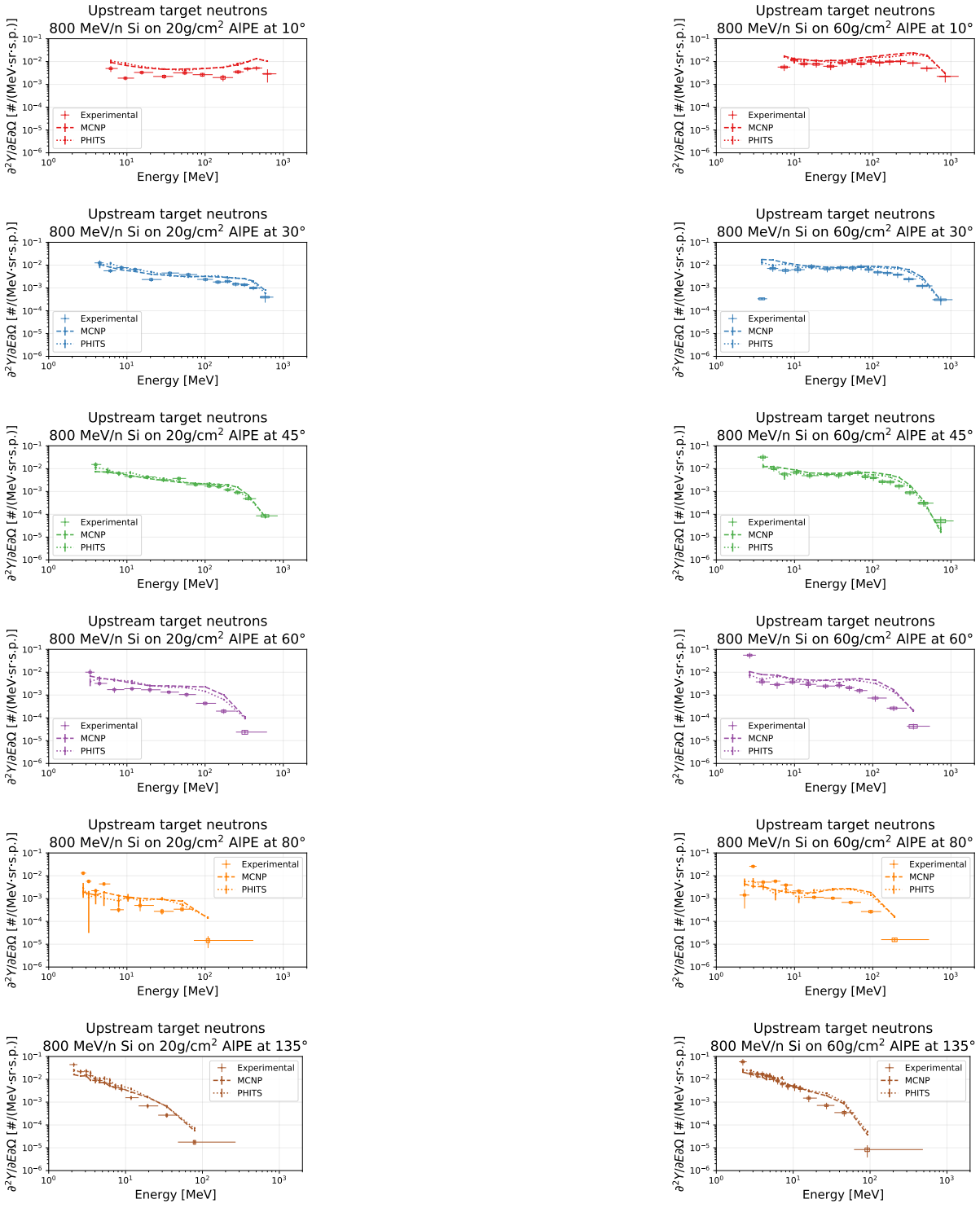


Figure C.31: Upstream target neutrons from 800 MeV/n Si incident on AlPE targets

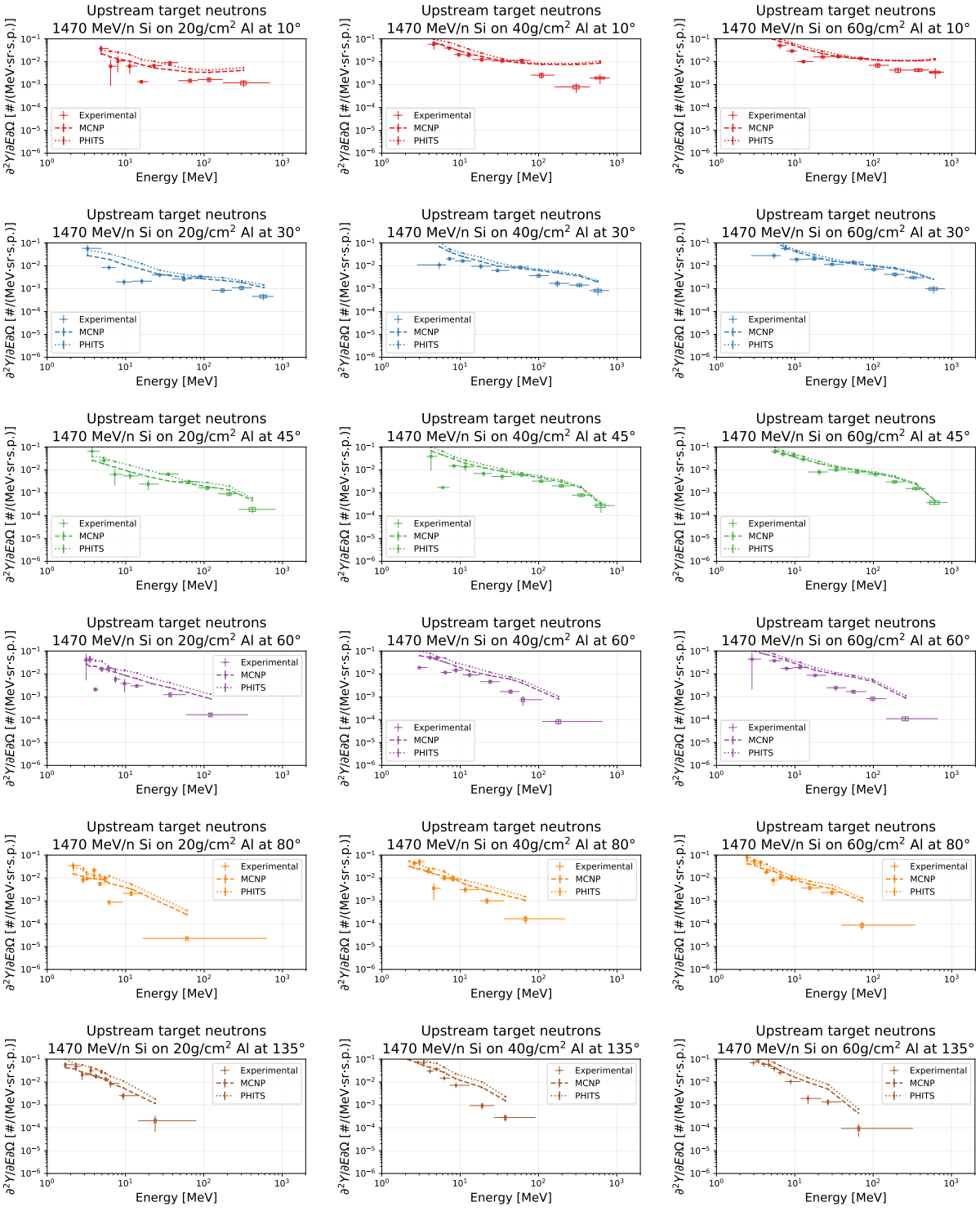


Figure C.32: Upstream target neutrons from 1470 MeV/n Si incident on Al targets

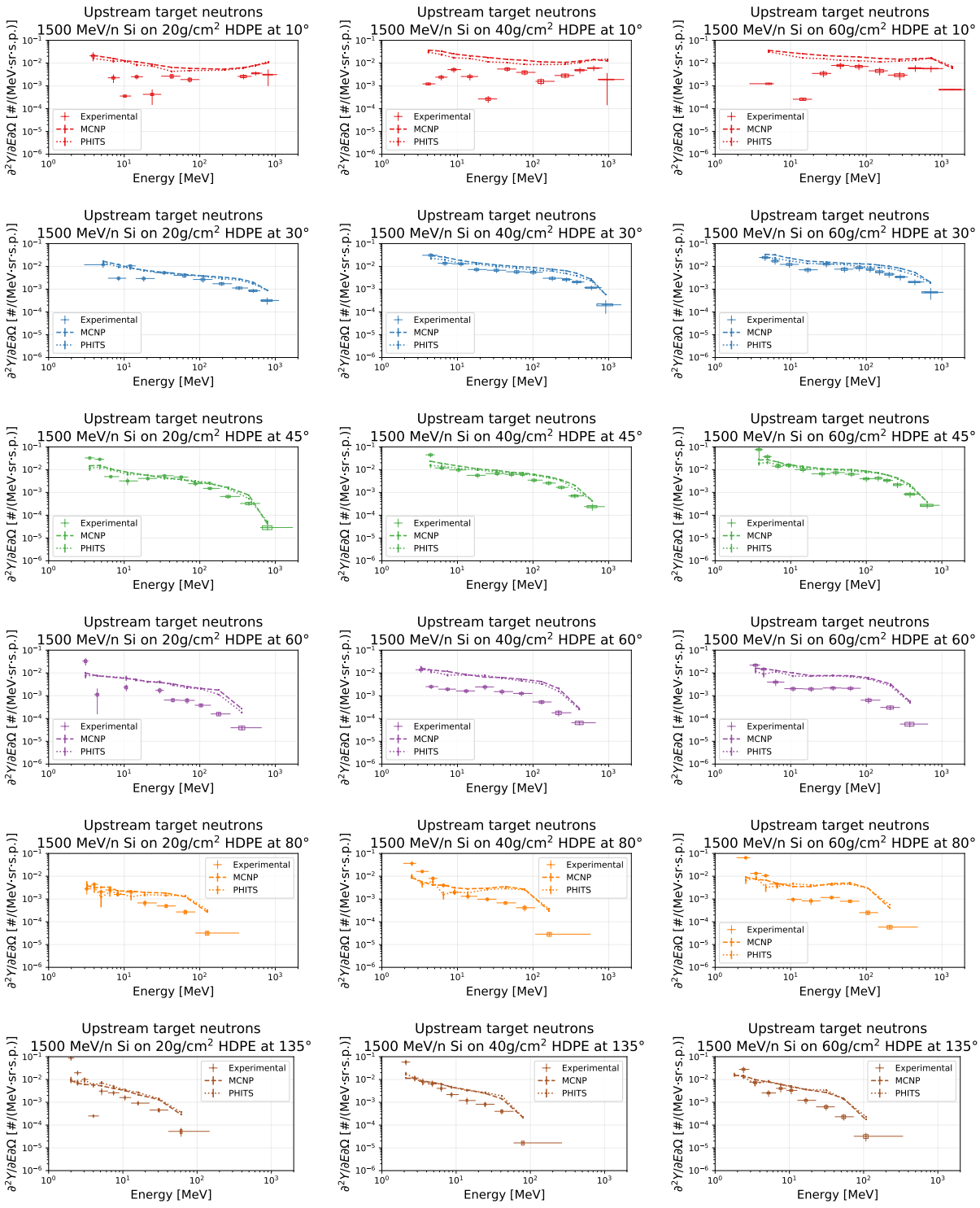


Figure C.33: Upstream target neutrons from 1500 MeV/n Si incident on HDPE targets

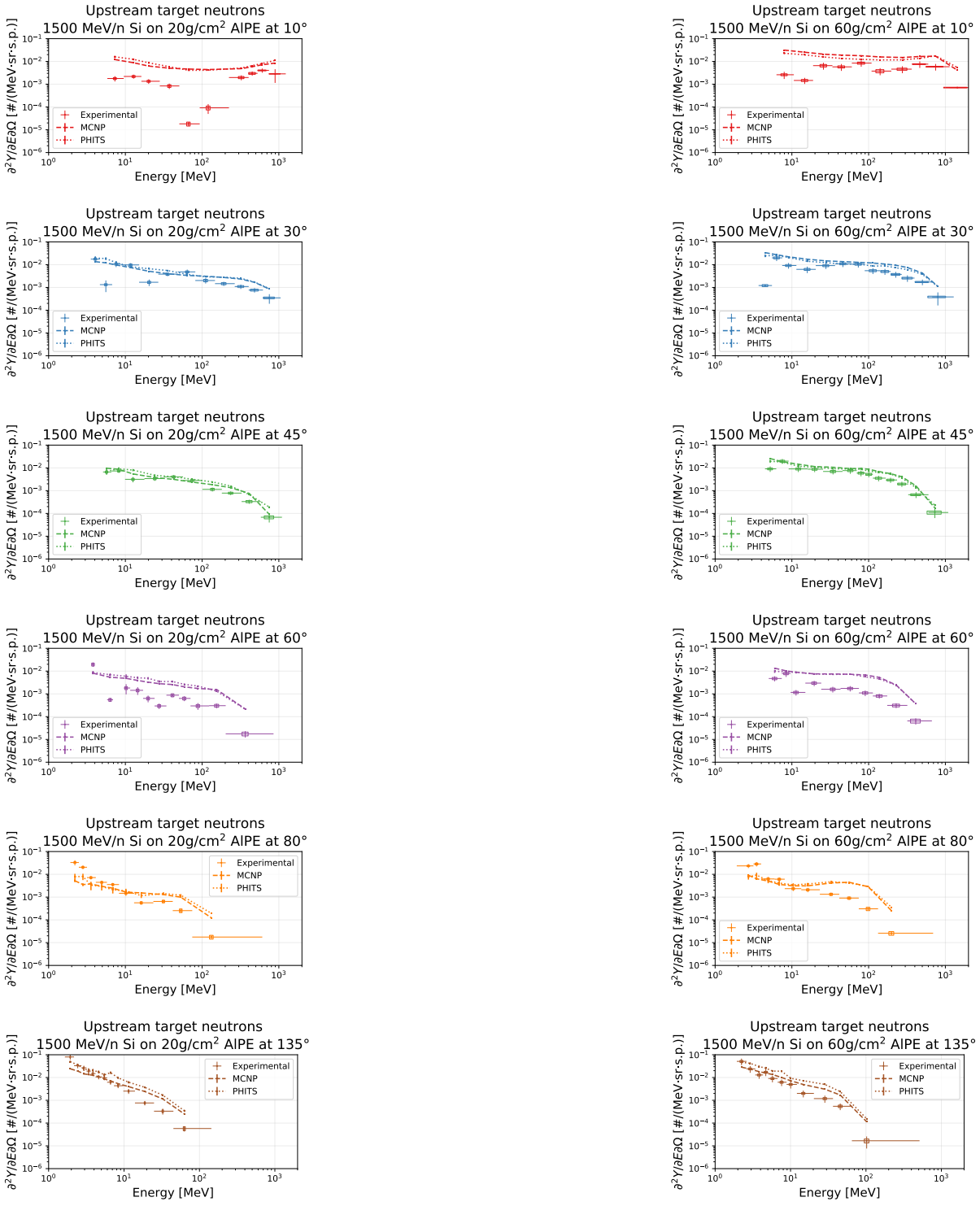


Figure C.34: Upstream target neutrons from 1500 MeV/n Si incident on AlPE targets

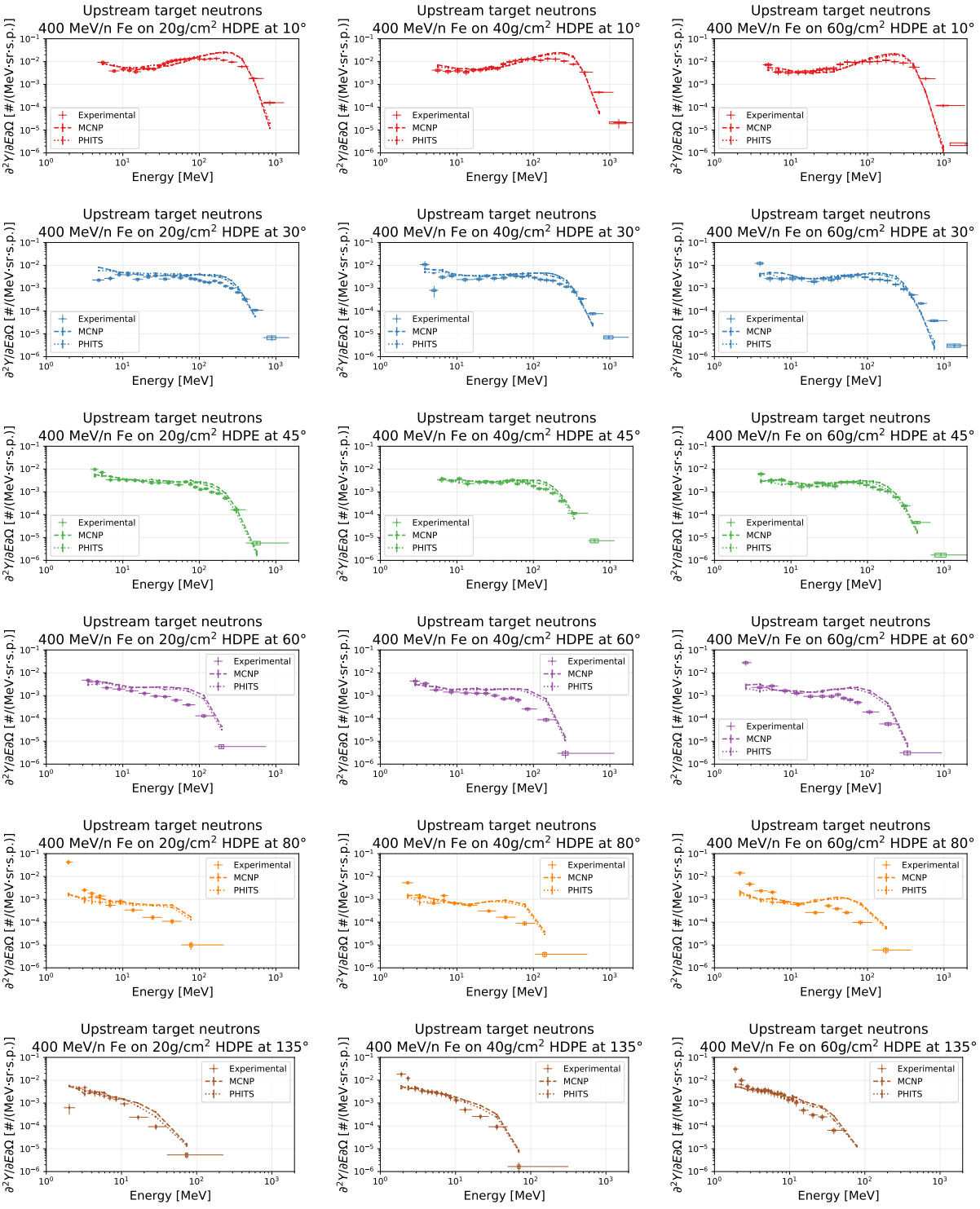


Figure C.35: Upstream target neutrons from 400 MeV/n Fe incident on HDPE targets

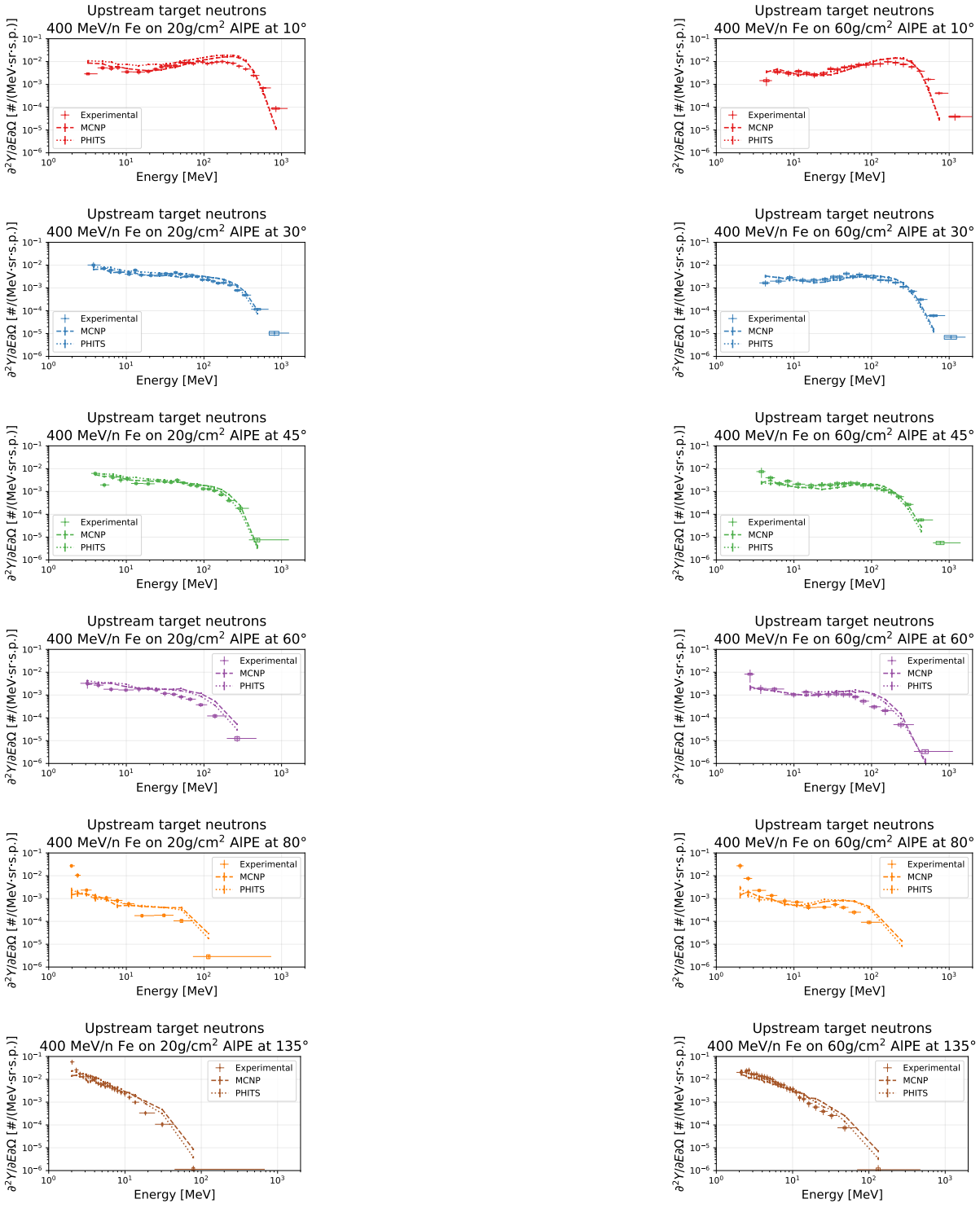


Figure C.36: Upstream target neutrons from 400 MeV/n Fe incident on AlPE targets

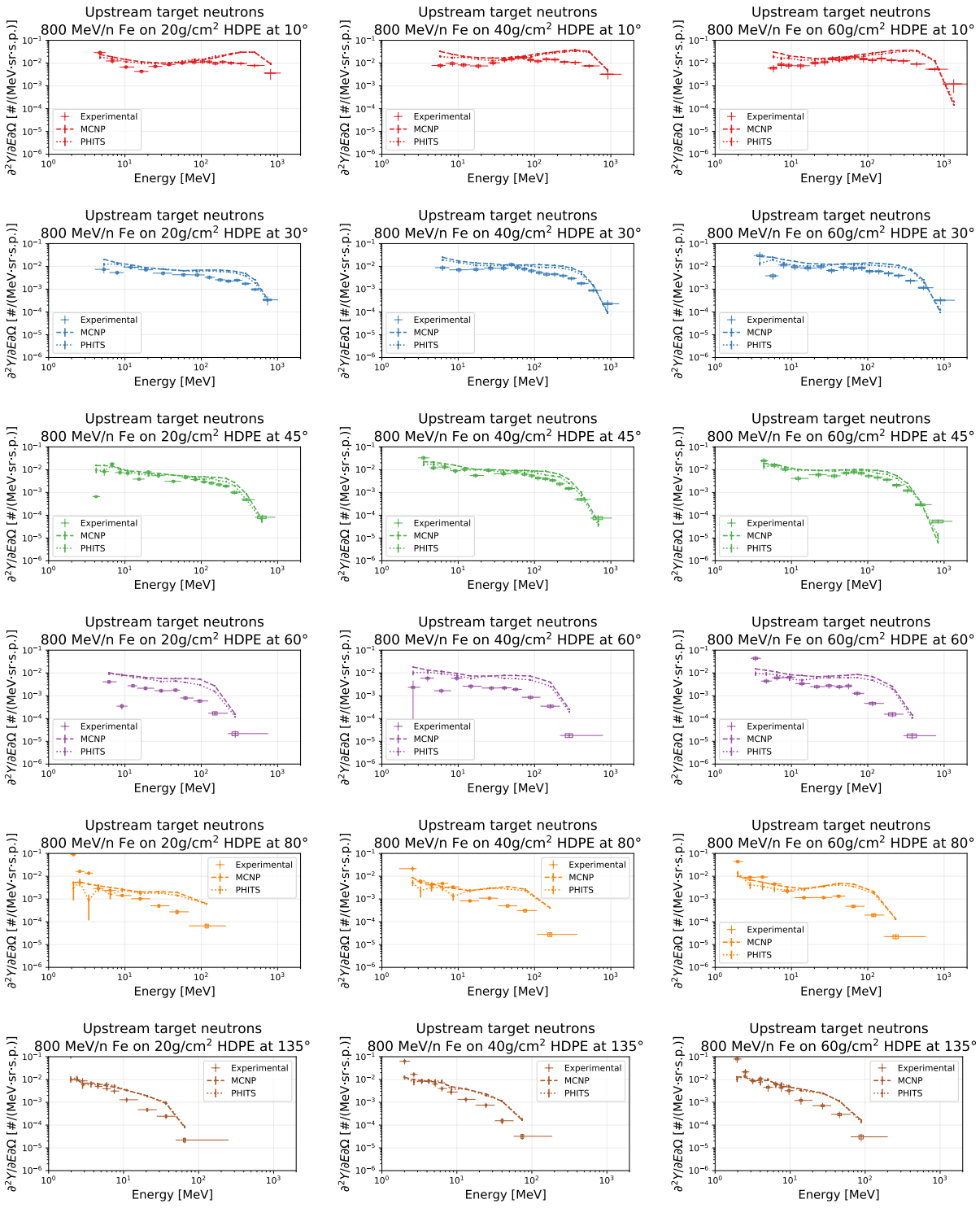


Figure C.37: Upstream target neutrons from 800 MeV/n Fe incident on HDPE targets

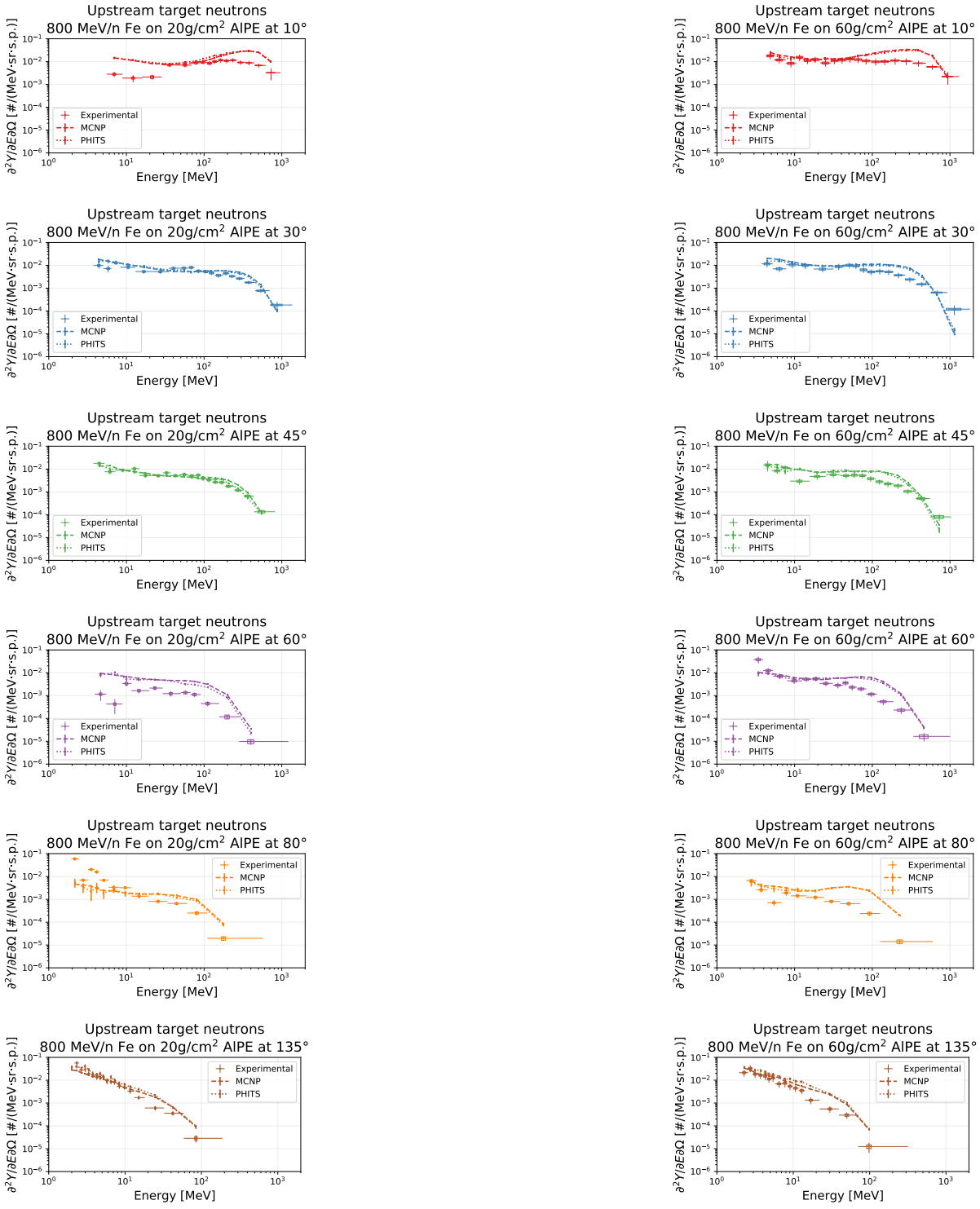


Figure C.38: Upstream target neutrons from 800 MeV/n Fe incident on AlPE targets

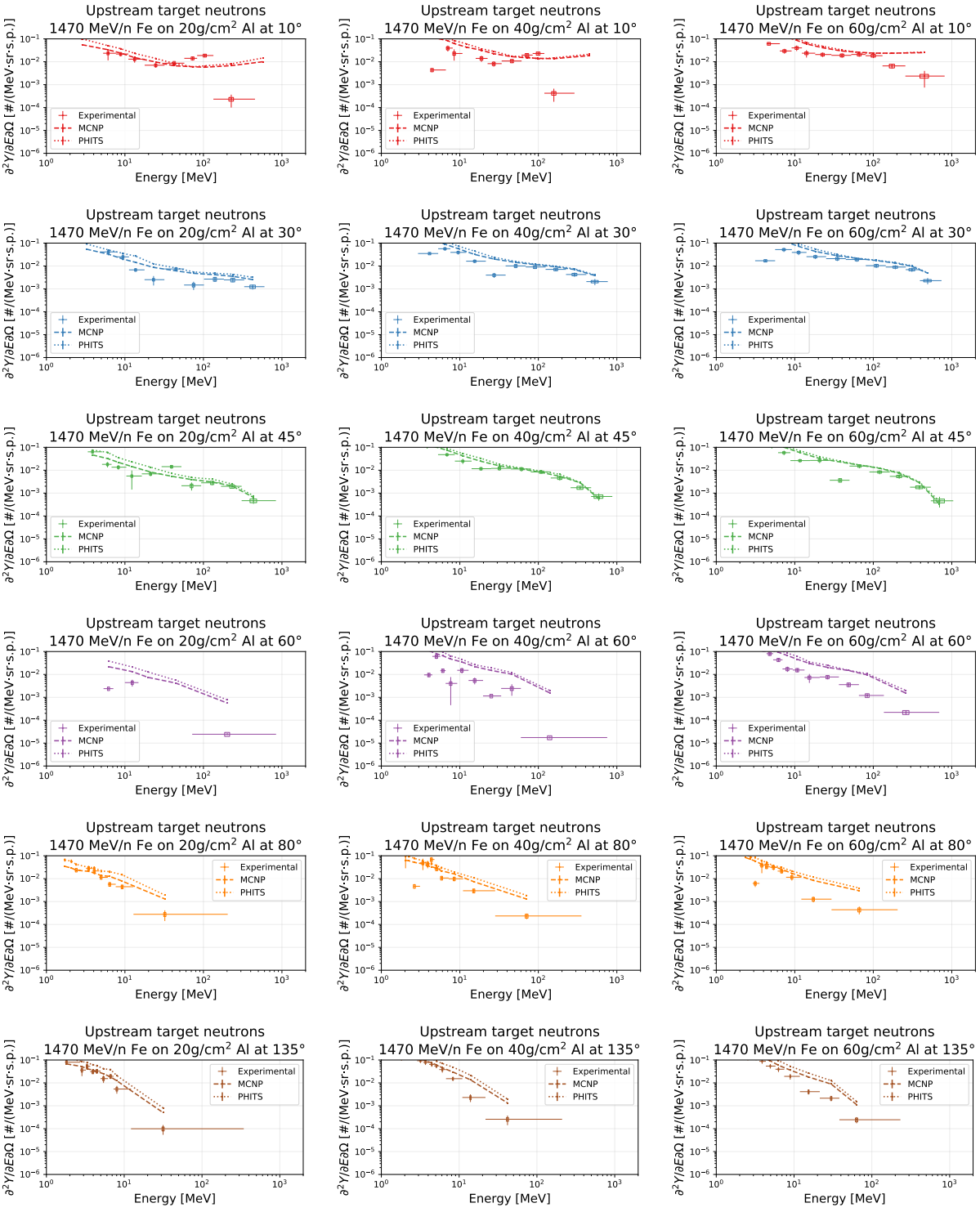


Figure C.39: Upstream target neutrons from 1470 MeV/n Fe incident on Al targets

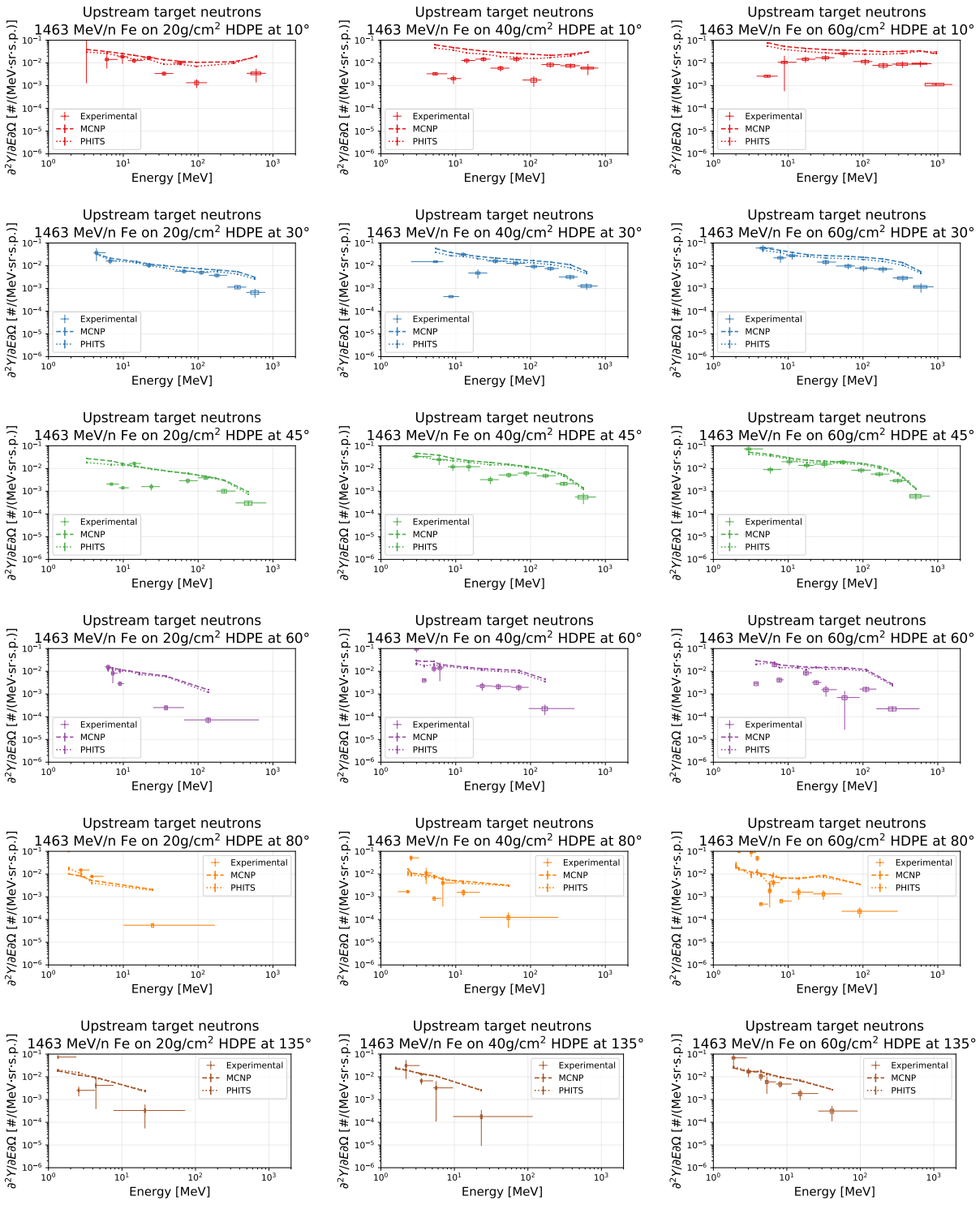


Figure C.40: Upstream target neutrons from 1463 MeV/n Fe incident on HDPE targets

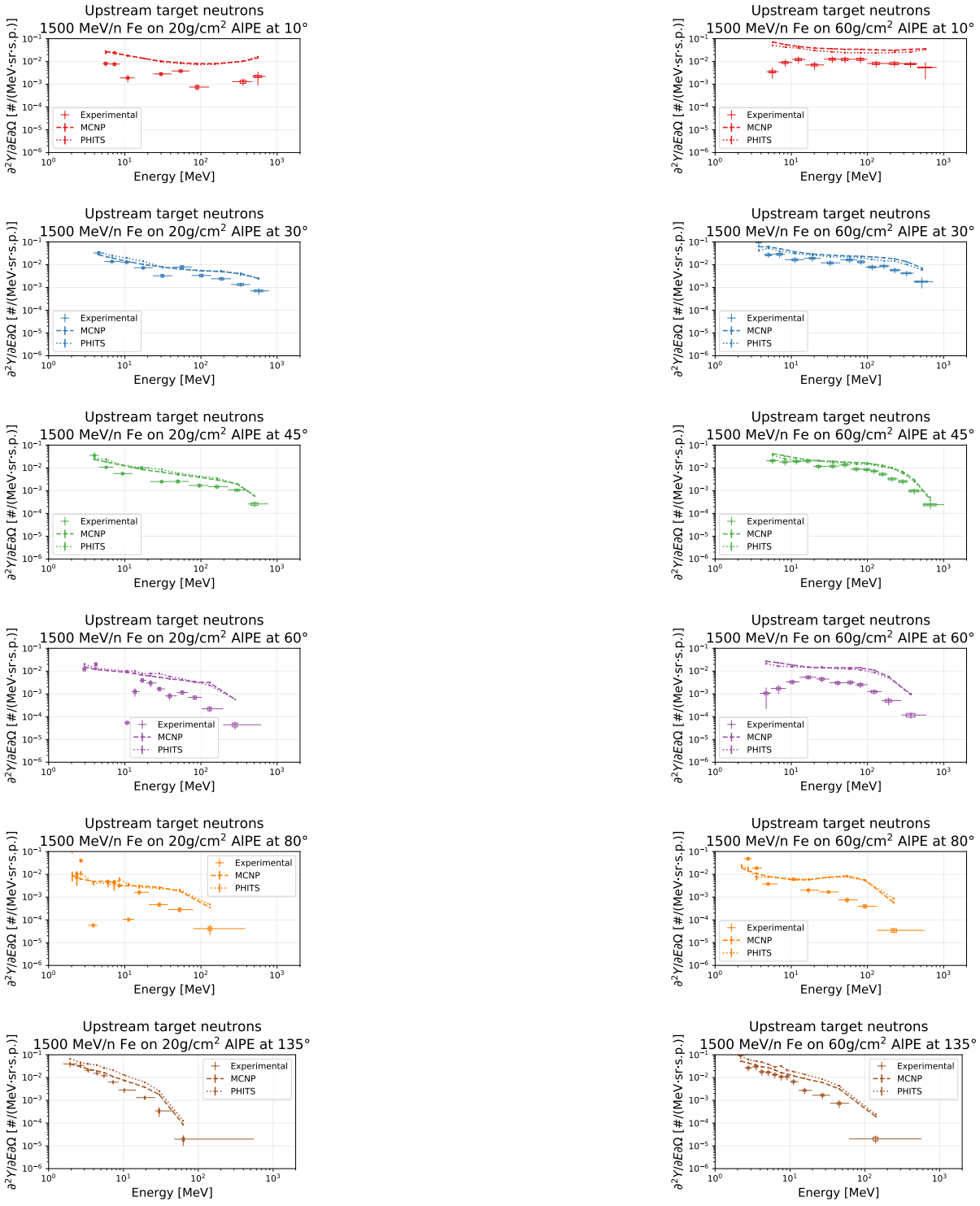


Figure C.41: Upstream target neutrons from 1500 MeV/n Fe incident on AlPE targets

C.2 Downstream target plots

All deconvoluted downstream target spectra generated in this work are showcased in this section.

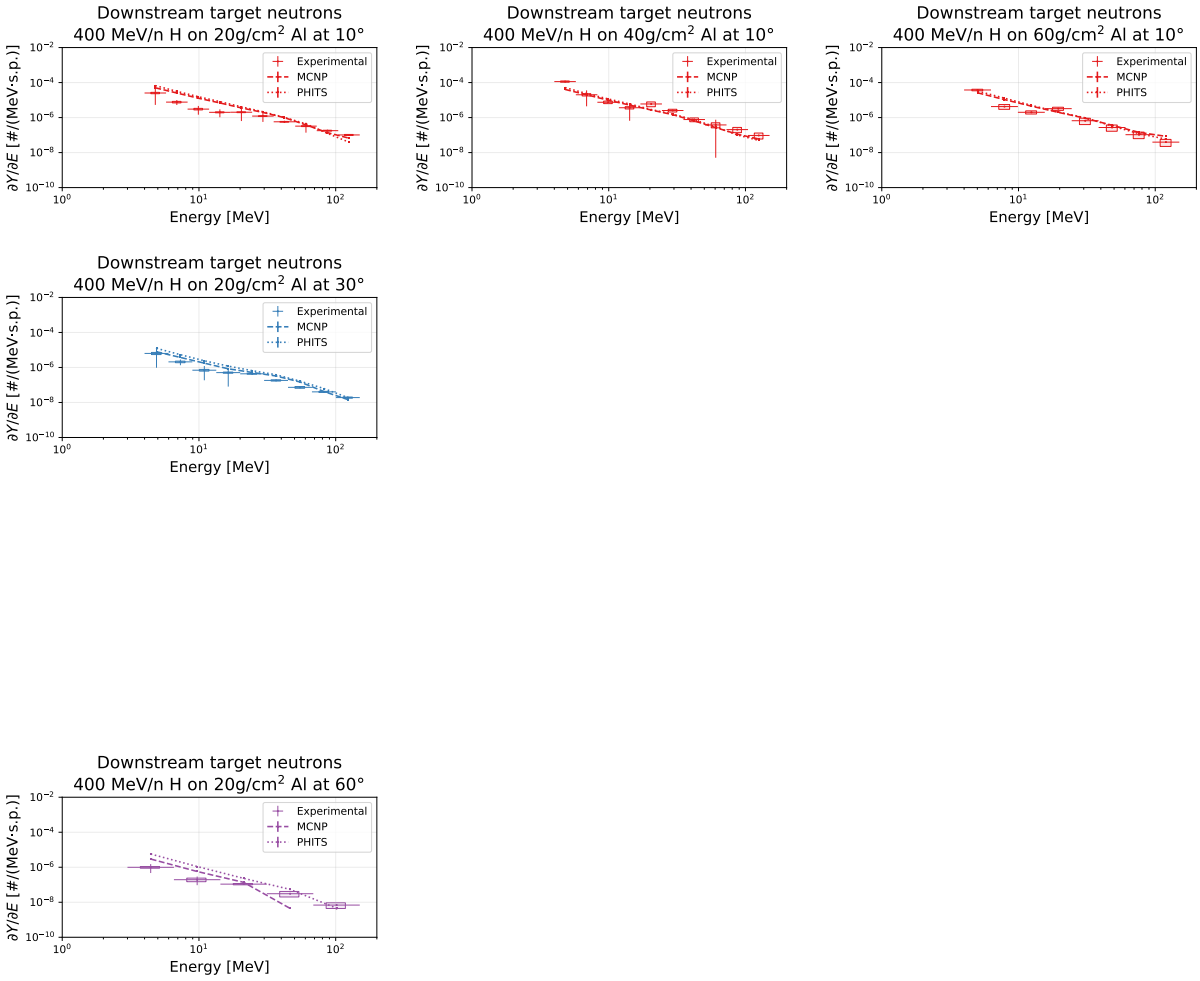


Figure C.42: Downstream target neutrons from 400 MeV/n H incident on Al targets

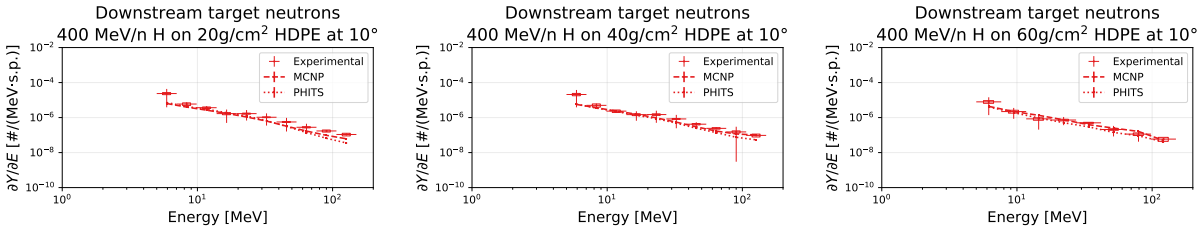
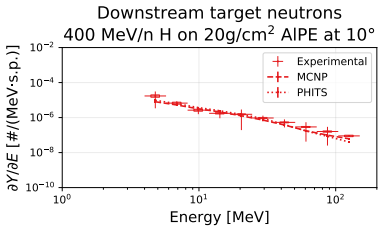
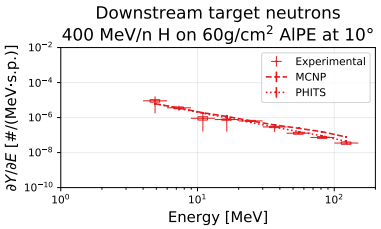


Figure C.43: Downstream target neutrons from 400 MeV/n H incident on HDPE targets





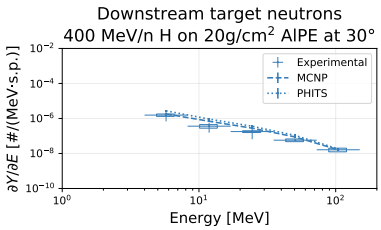


Figure C.44: Downstream target neutrons from 400 MeV/n H incident on AlPE targets

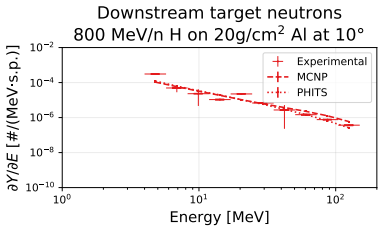


Figure C.45: Downstream target neutrons from 800 MeV/n H incident on Al targets

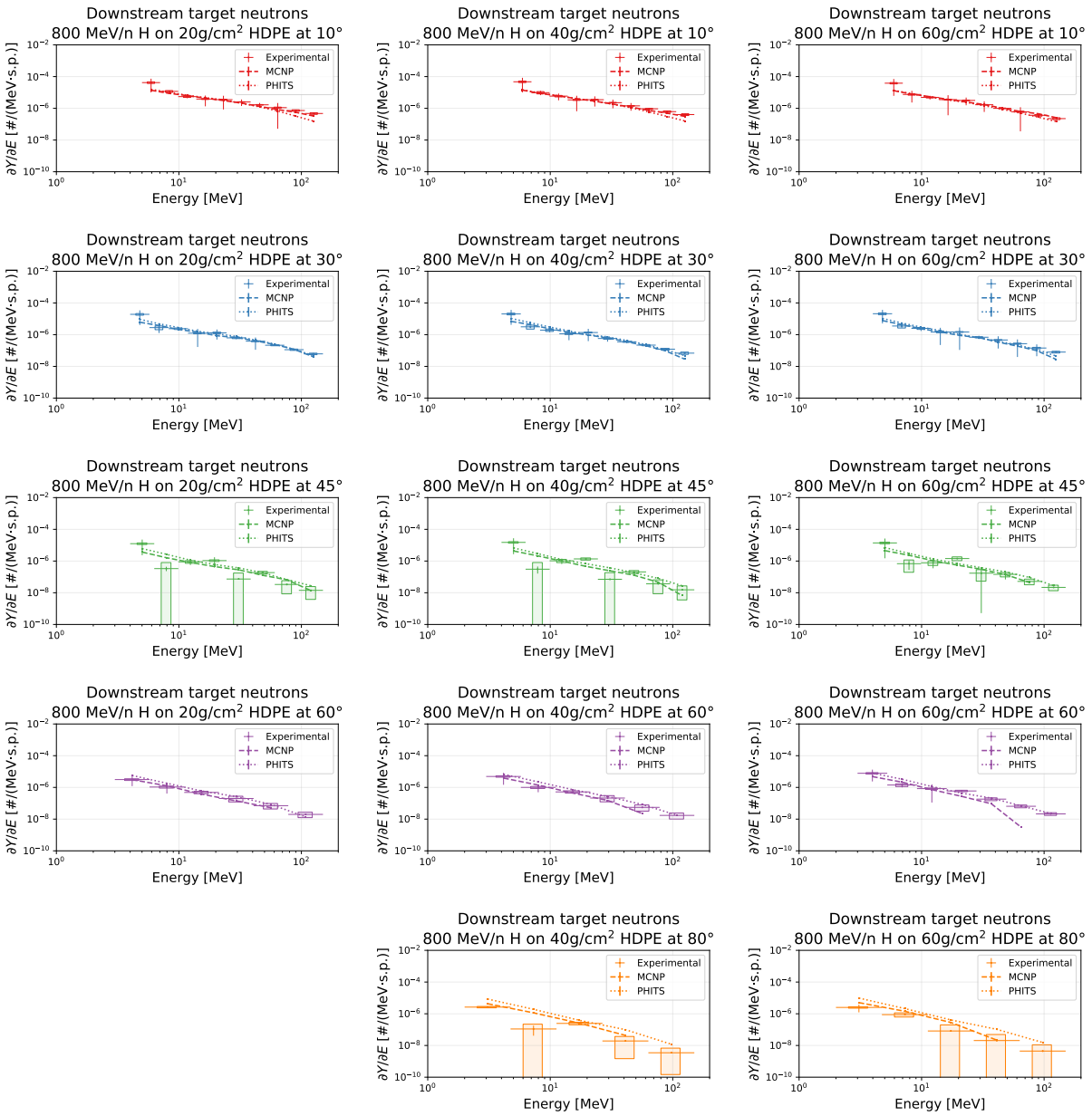


Figure C.46: Downstream target neutrons from 800 MeV/n H incident on HDPE targets

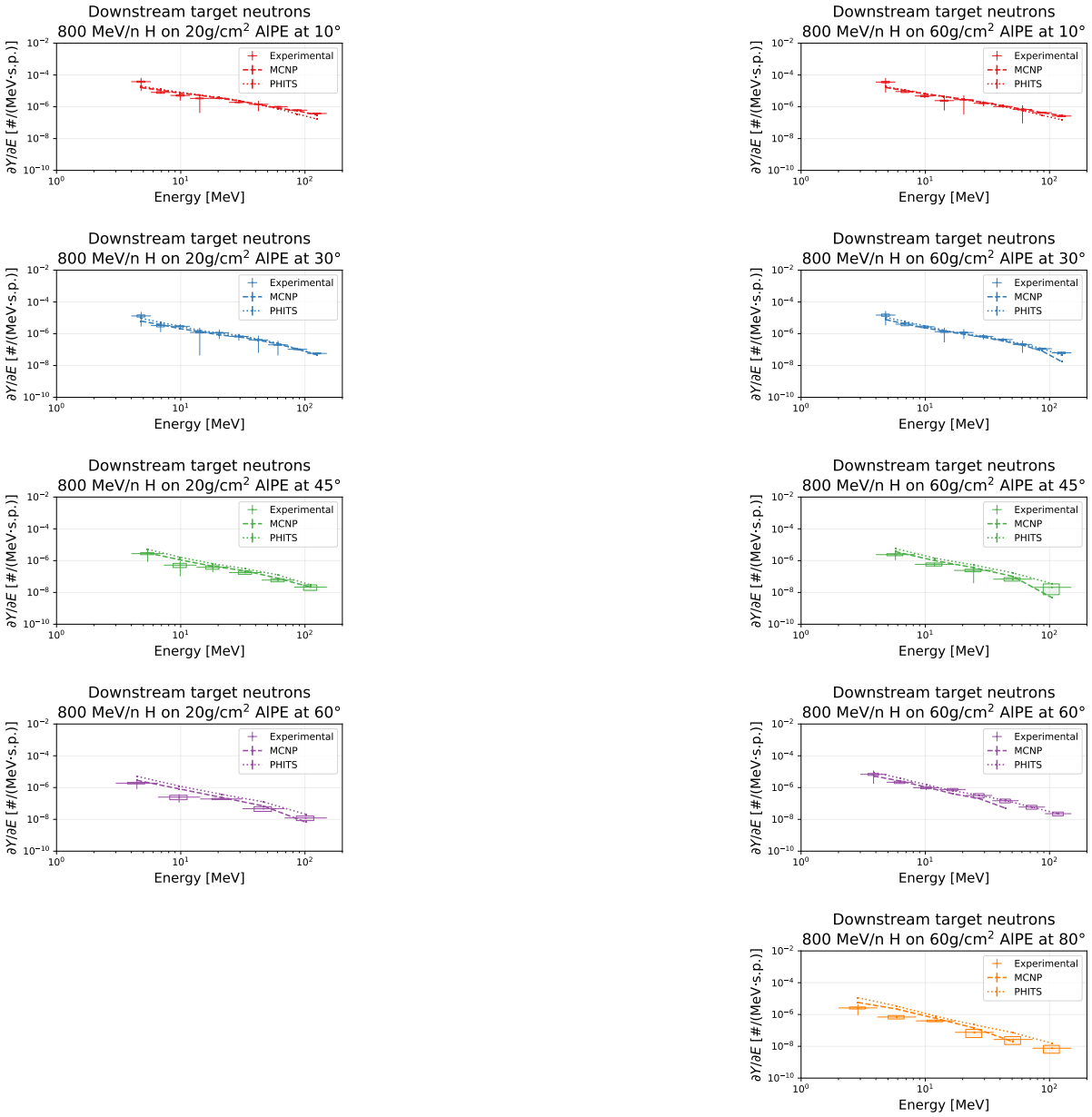


Figure C.47: Downstream target neutrons from 800 MeV/n H incident on AlPE targets

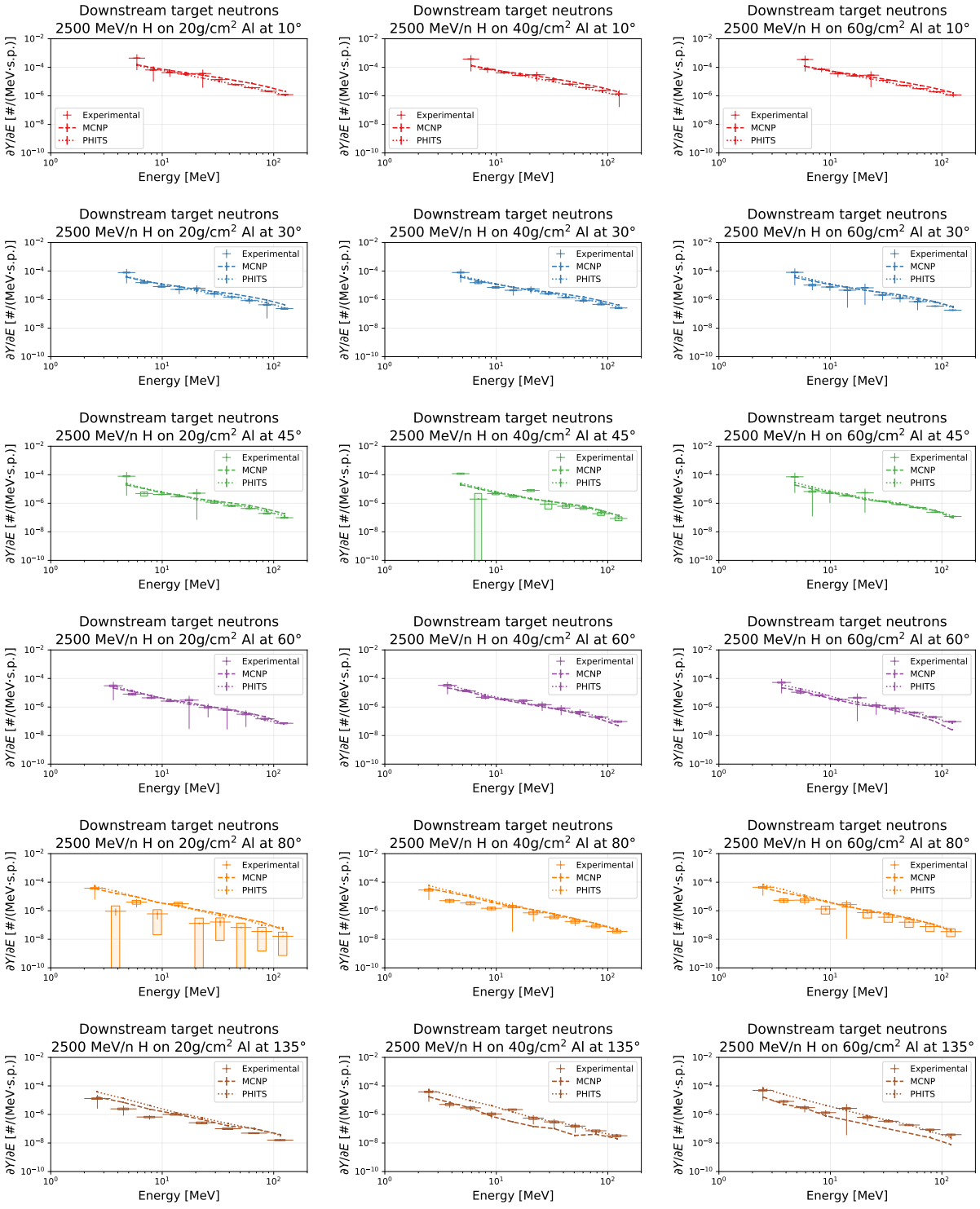


Figure C.48: Downstream target neutrons from 2500 MeV/n H incident on Al targets

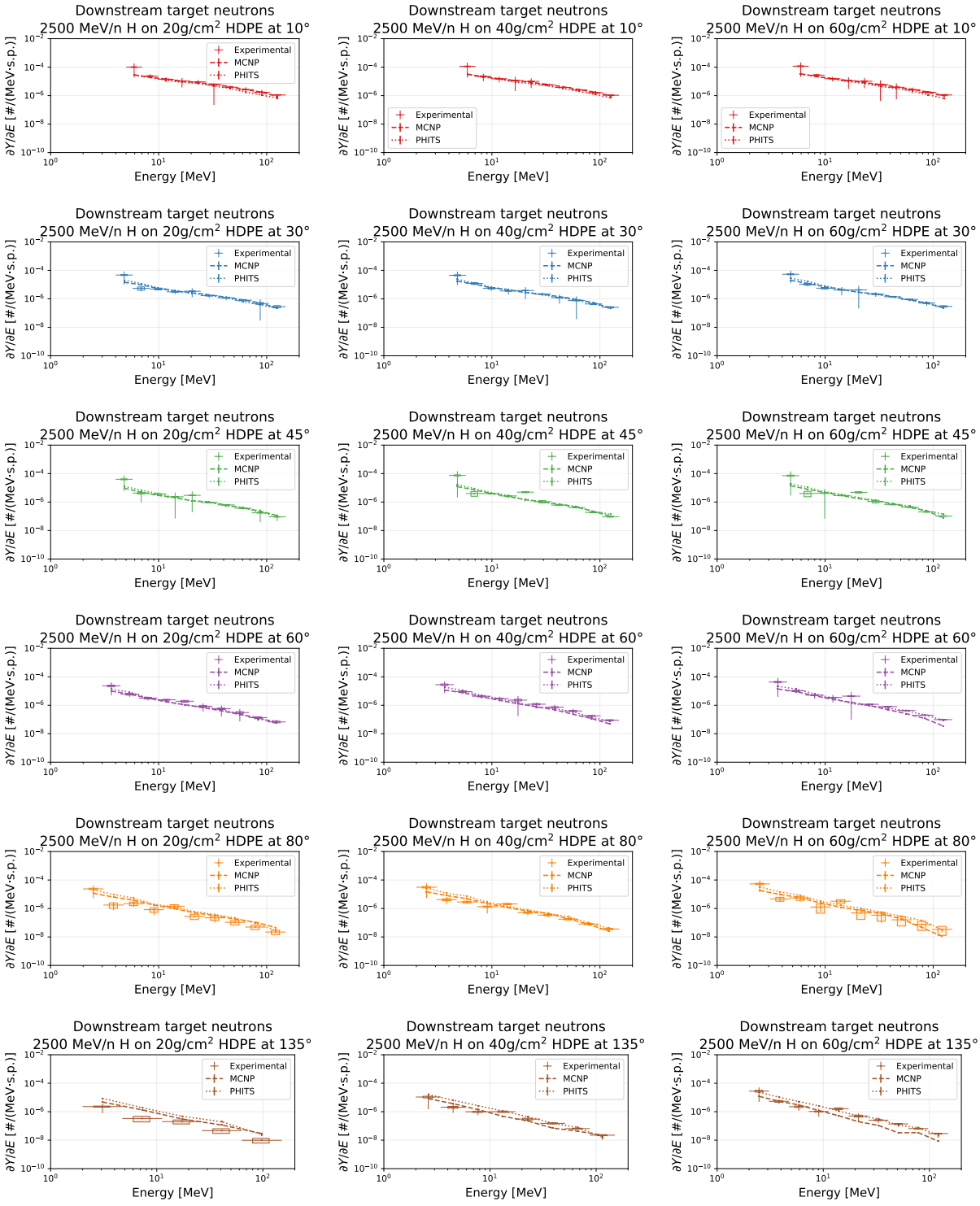


Figure C.49: Downstream target neutrons from 2500 MeV/n H incident on HDPE targets

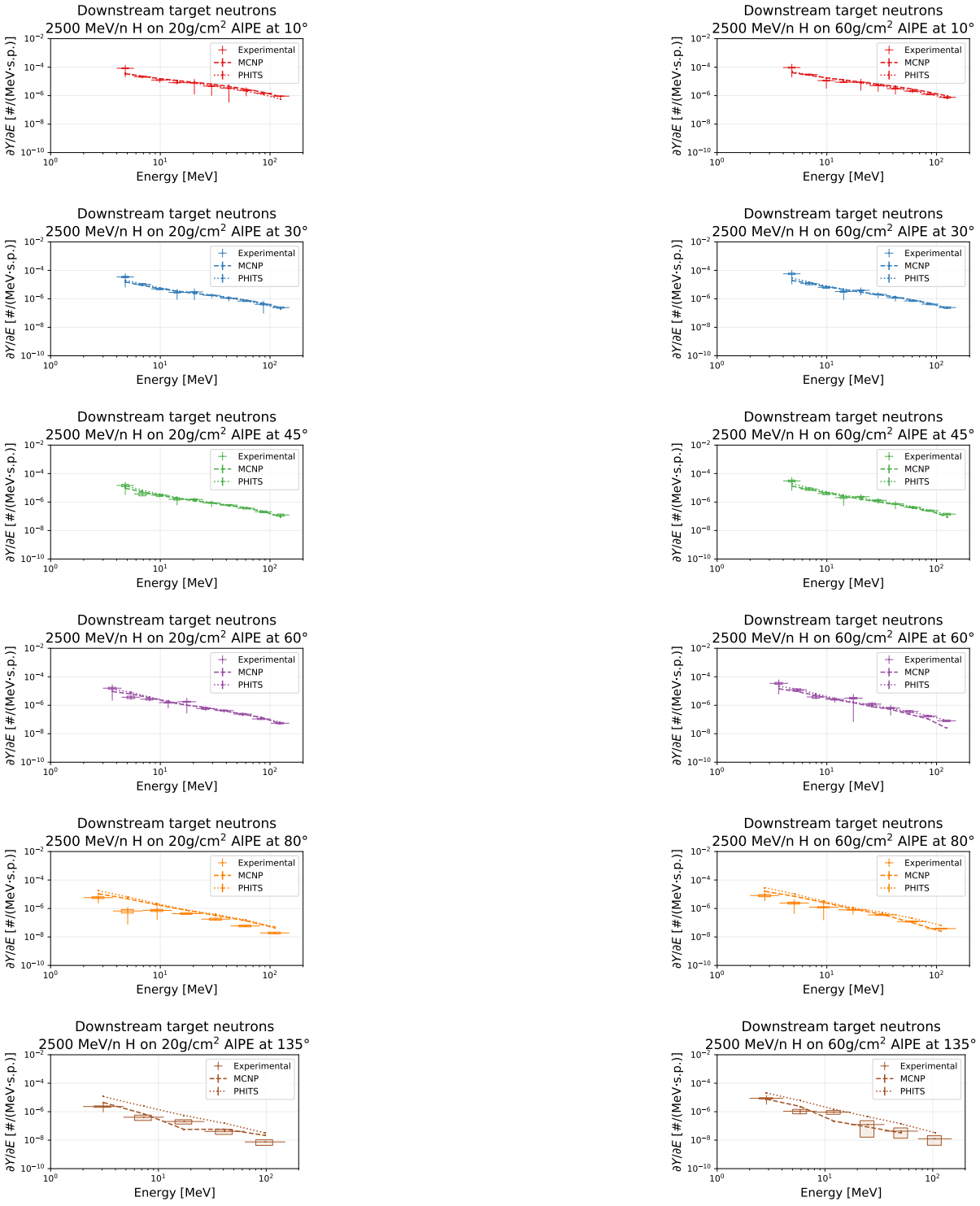


Figure C.50: Downstream target neutrons from 2500 MeV/n H incident on AlPE targets

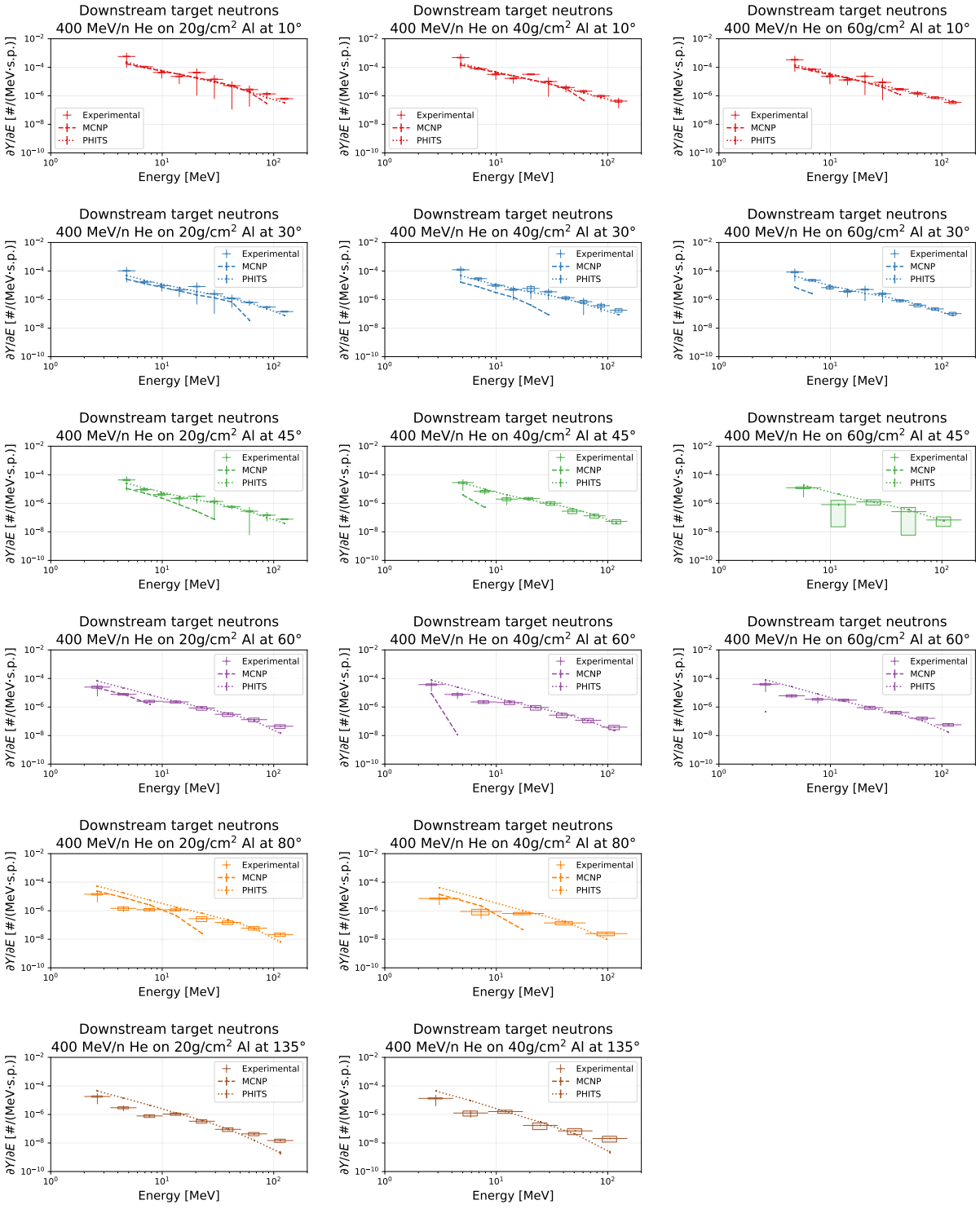


Figure C.51: Downstream target neutrons from 400 MeV/n He incident on Al targets

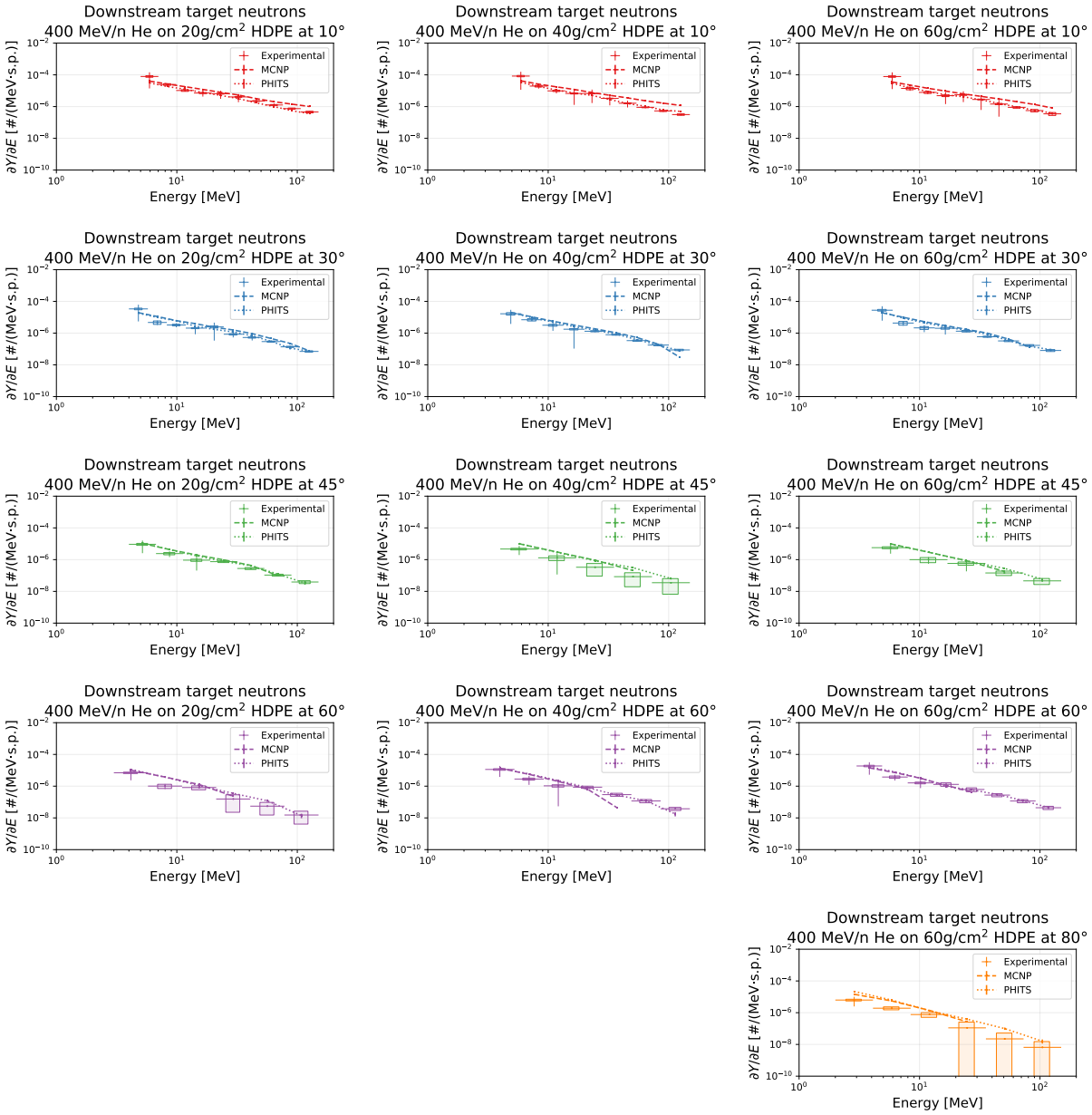


Figure C.52: Downstream target neutrons from 400 MeV/n He incident on HDPE targets

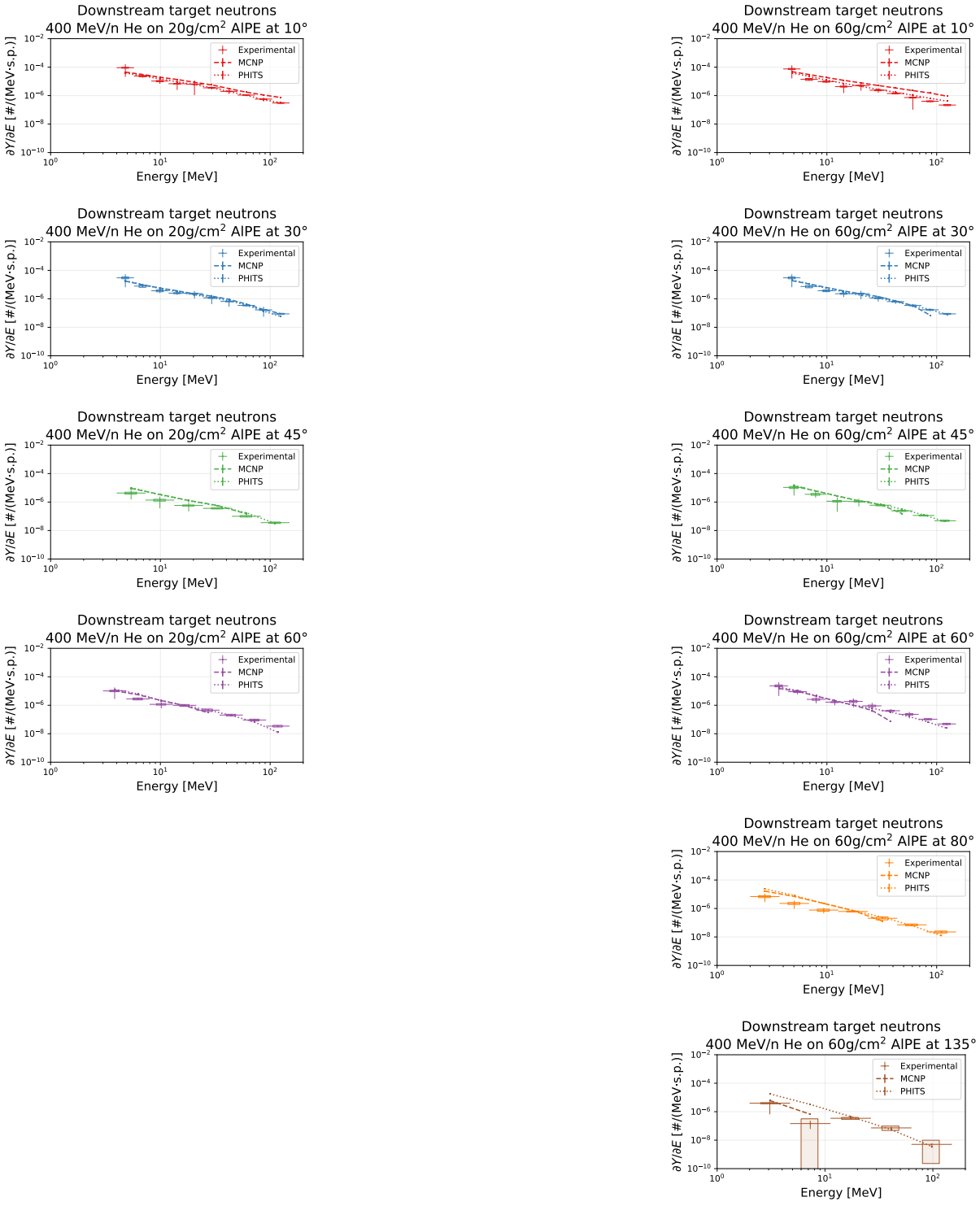


Figure C.53: Downstream target neutrons from 400 MeV/n He incident on AlPE targets

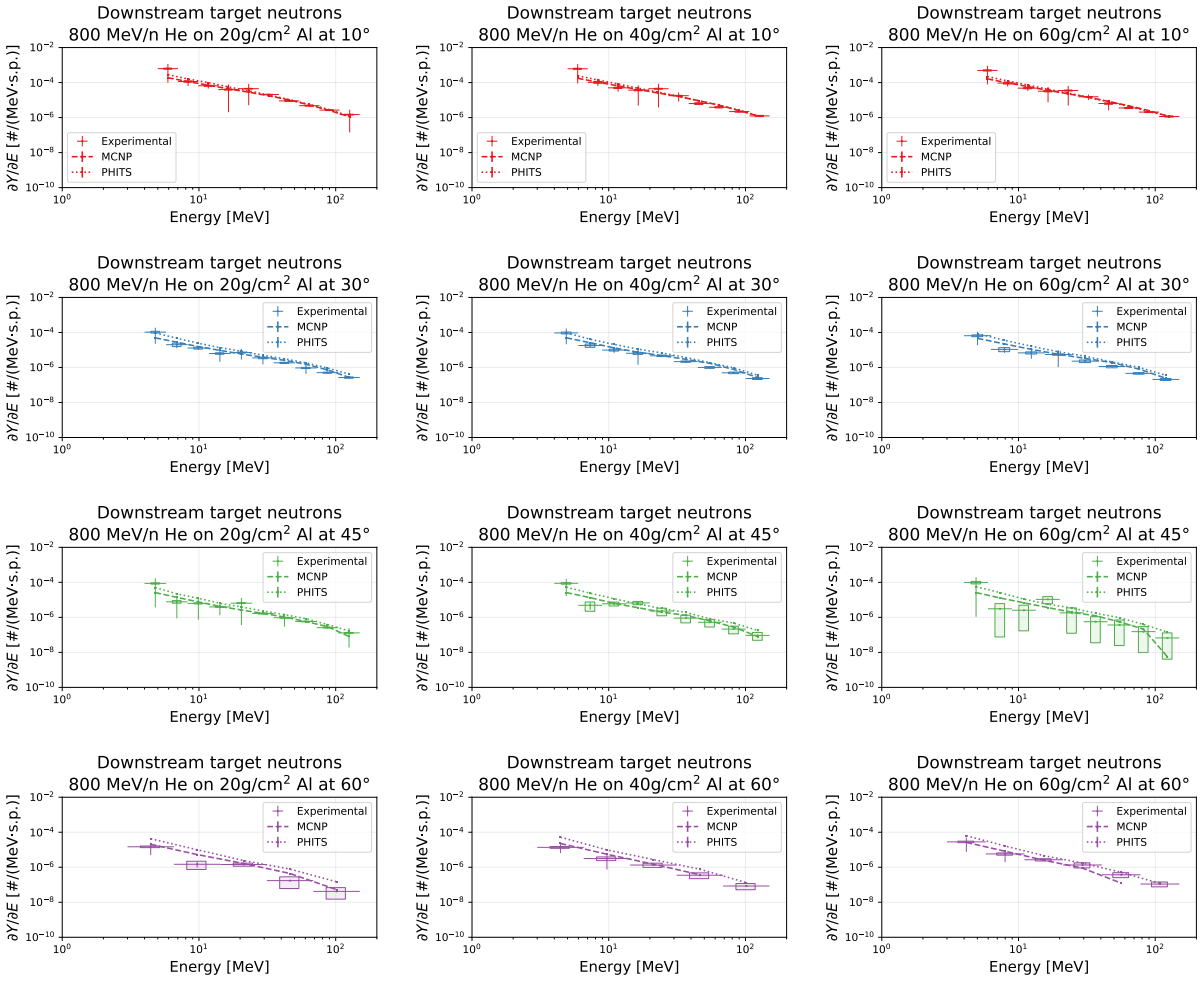


Figure C.54: Downstream target neutrons from 800 MeV/n He incident on Al targets

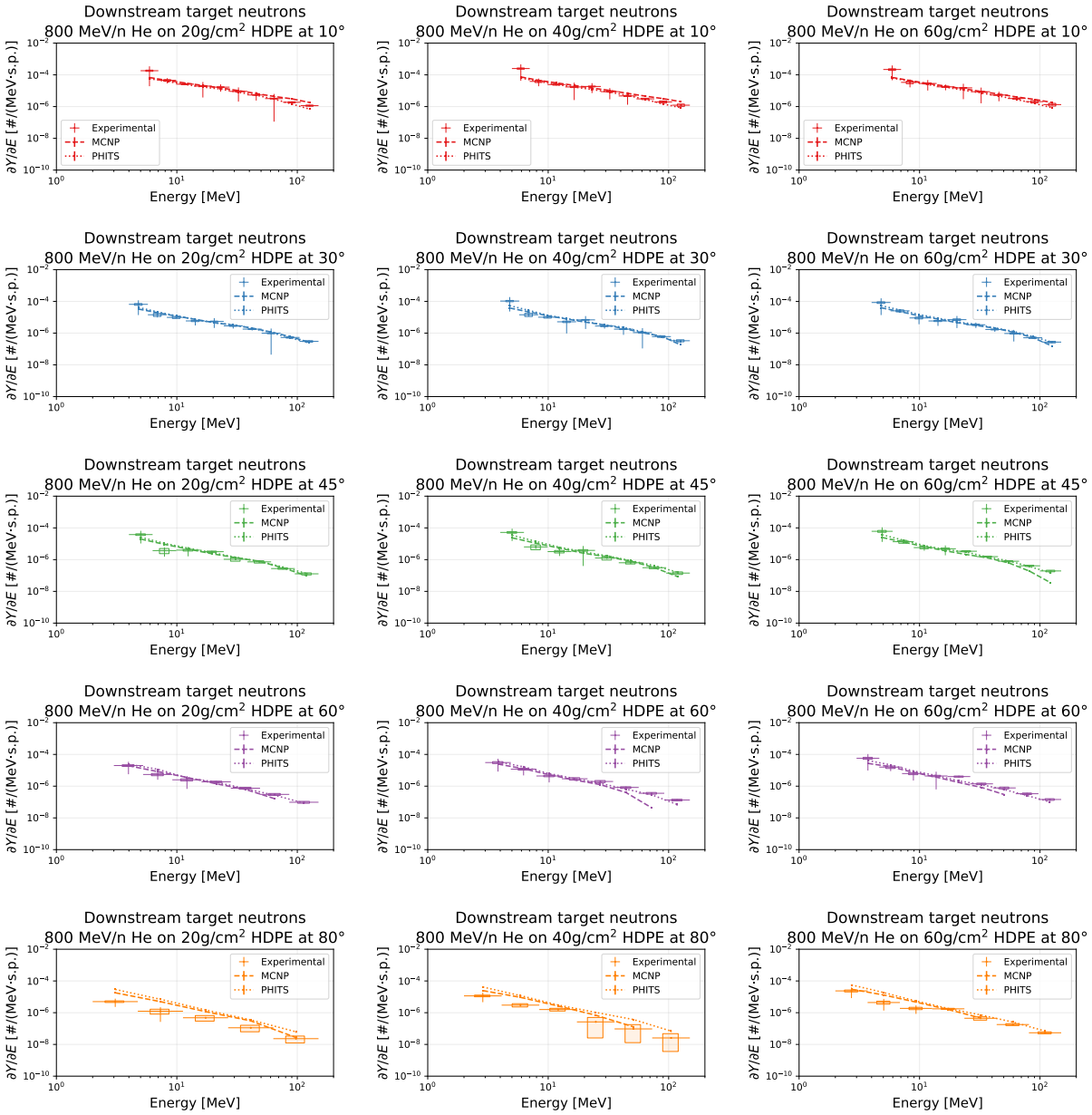


Figure C.55: Downstream target neutrons from 800 MeV/n He incident on HDPE targets

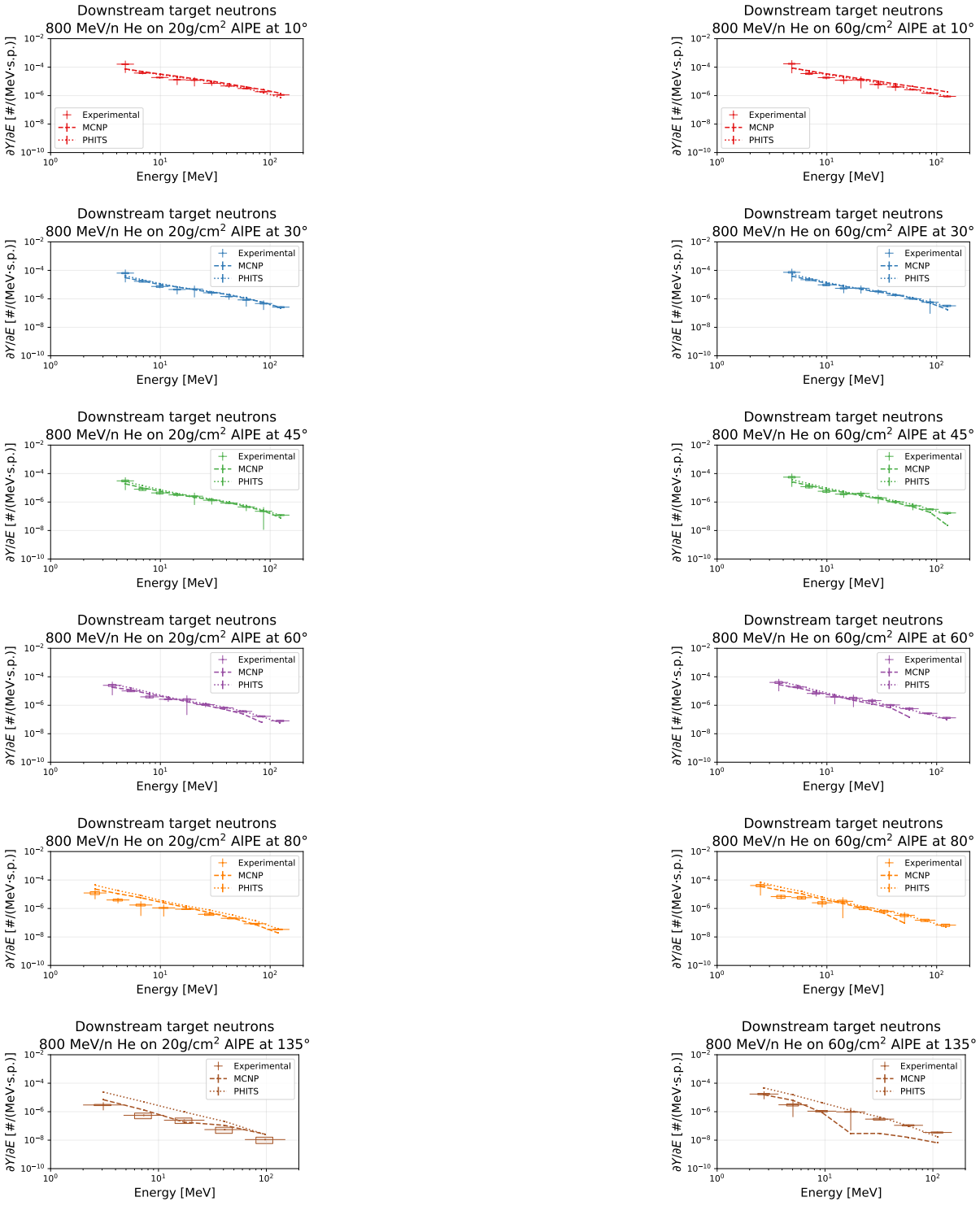


Figure C.56: Downstream target neutrons from 800 MeV/n He incident on AlPE targets

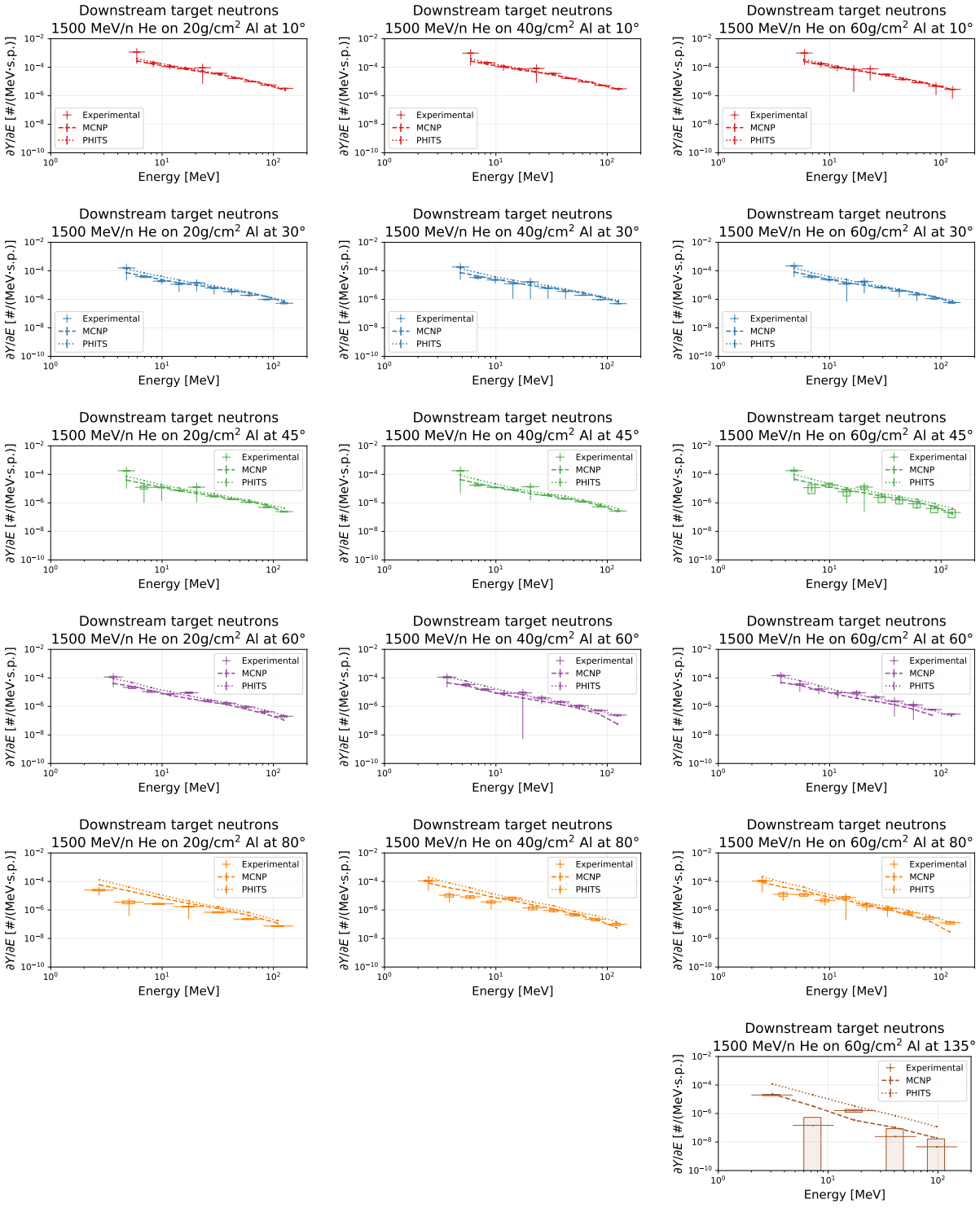


Figure C.57: Downstream target neutrons from 1500 MeV/n He incident on Al targets

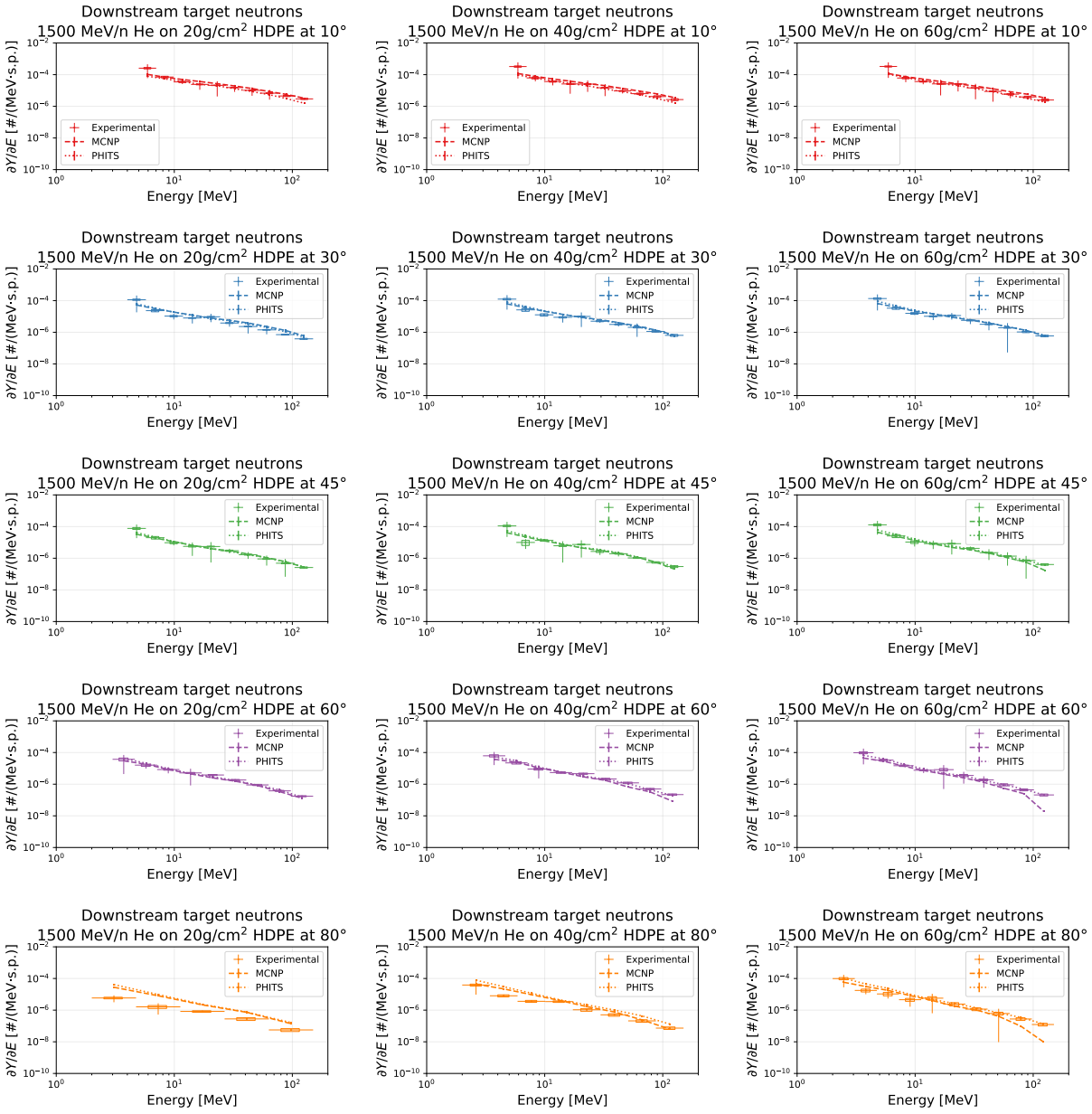


Figure C.58: Downstream target neutrons from 1500 MeV/n He incident on HDPE targets

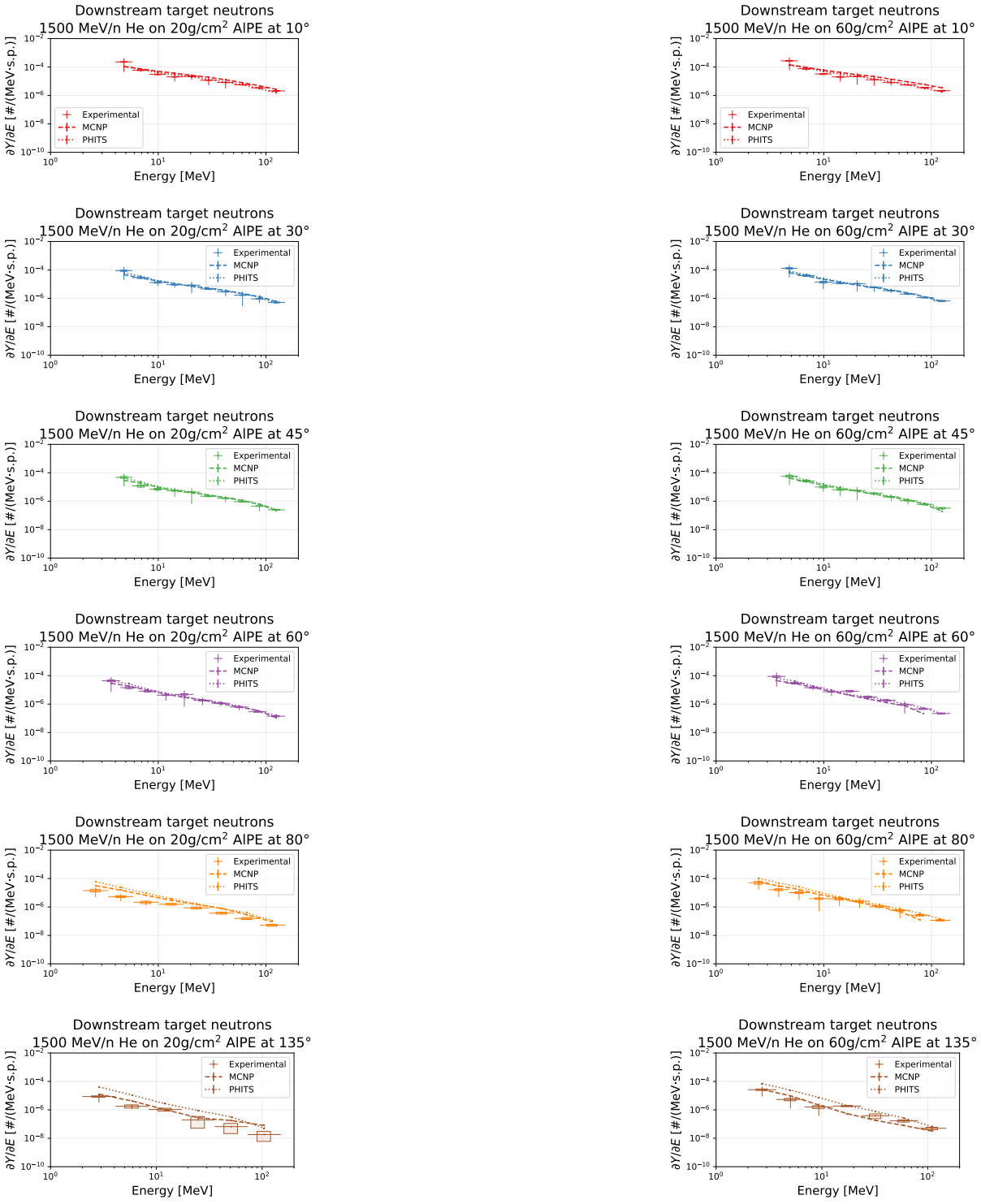


Figure C.59: Downstream target neutrons from 1500 MeV/n He incident on AlPE targets

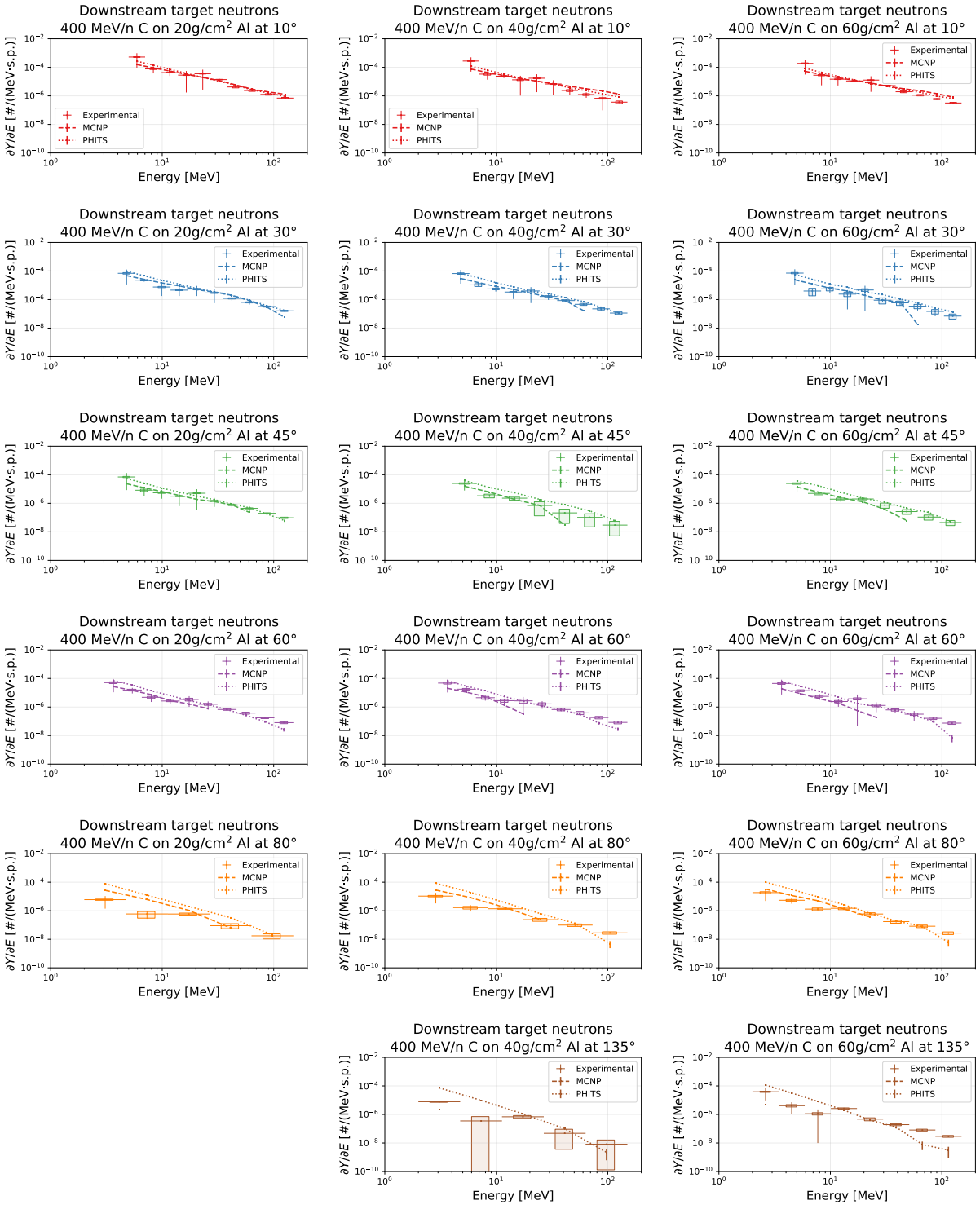


Figure C.60: Downstream target neutrons from 400 MeV/n C incident on Al targets

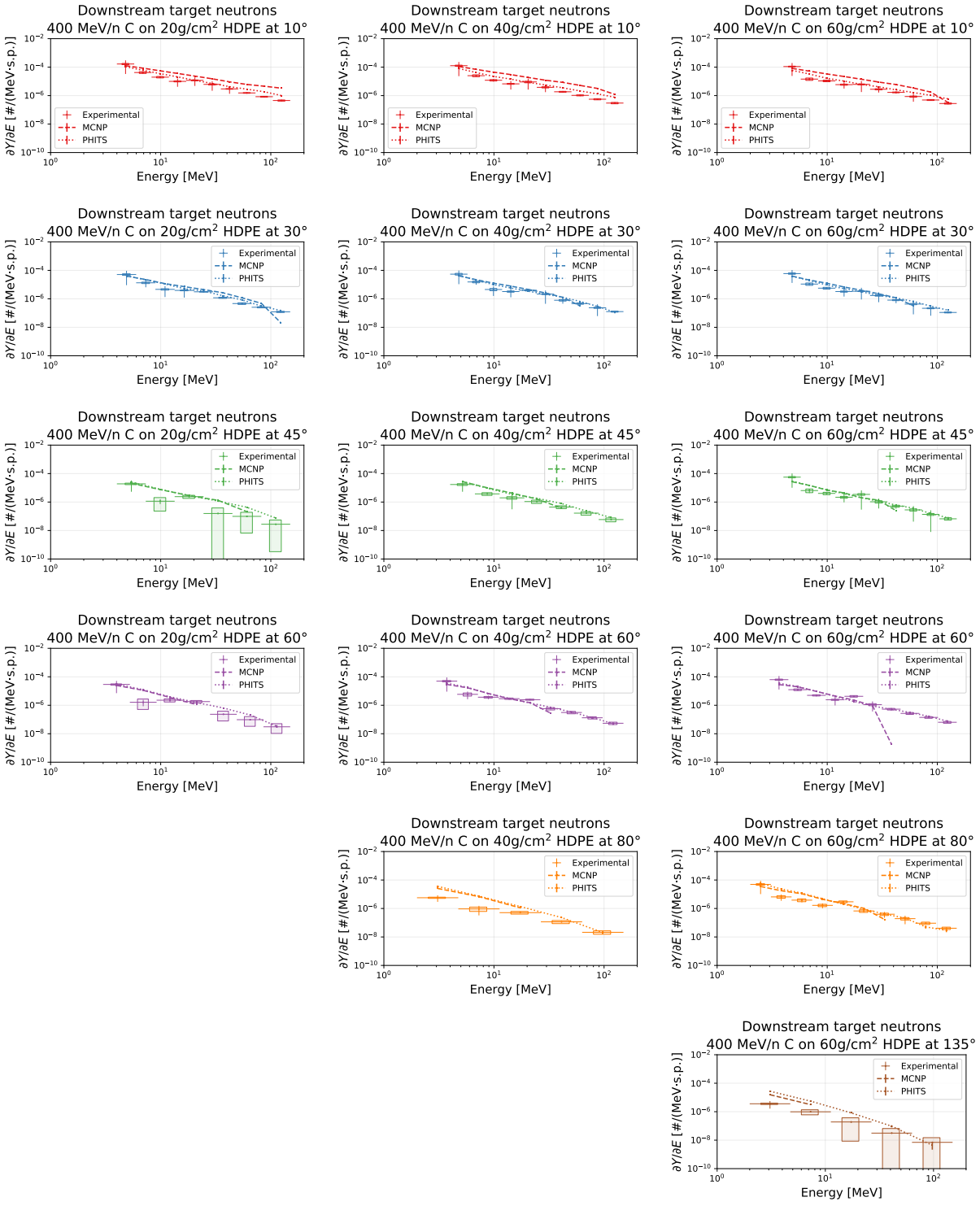


Figure C.61: Downstream target neutrons from 400 MeV/n C incident on HDPE targets

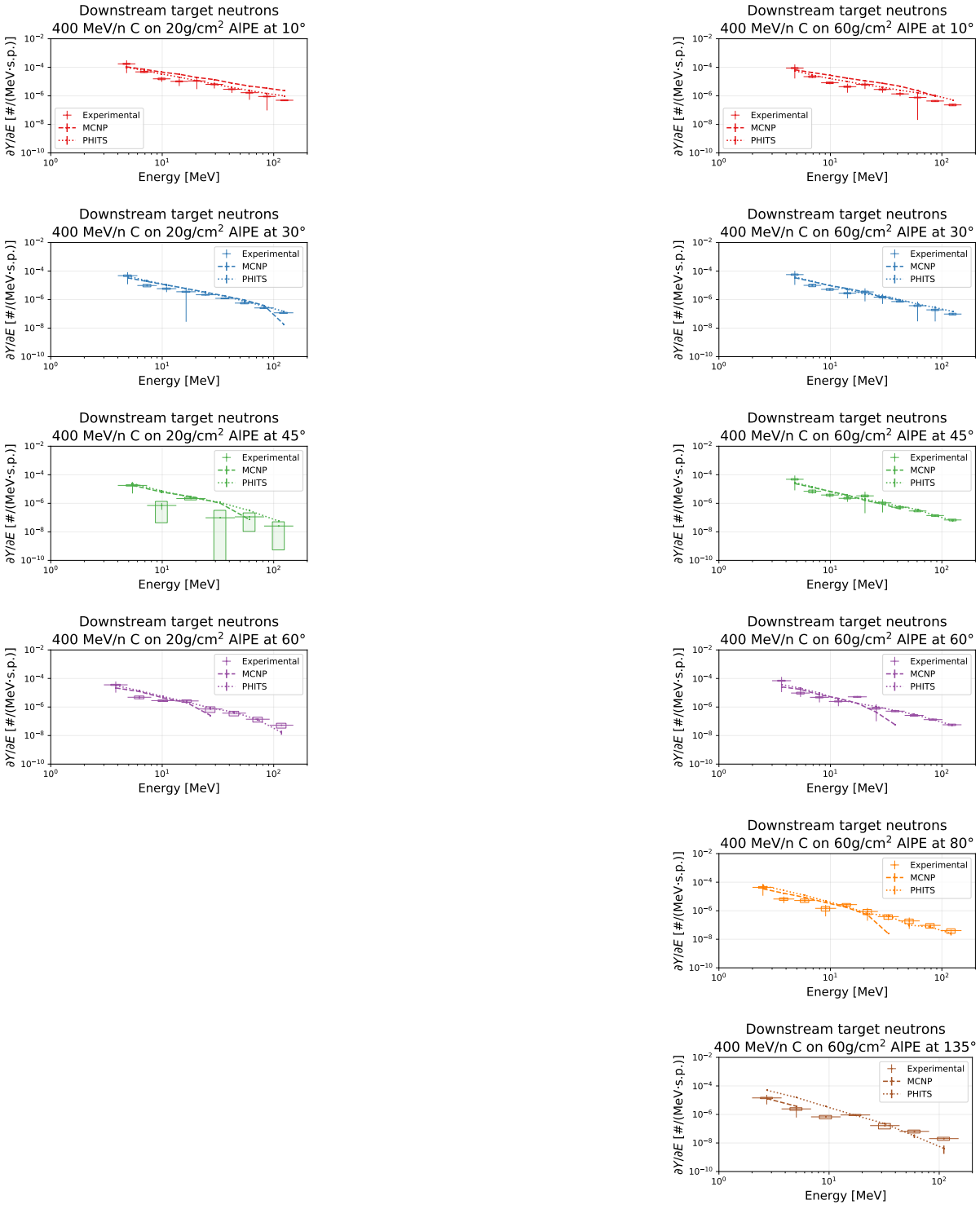


Figure C.62: Downstream target neutrons from 400 MeV/n C incident on AlPE targets

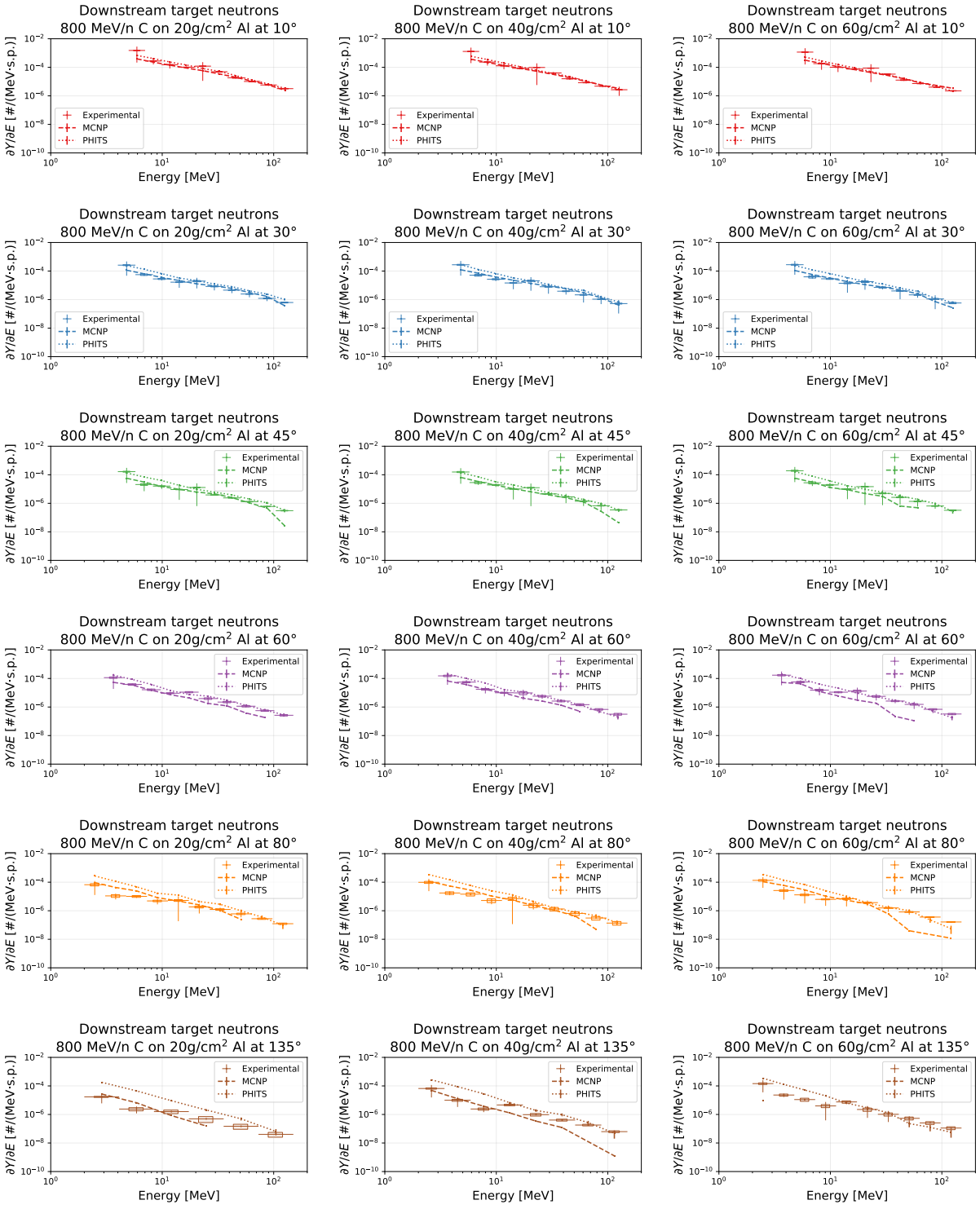


Figure C.63: Downstream target neutrons from 800 MeV/n C incident on Al targets

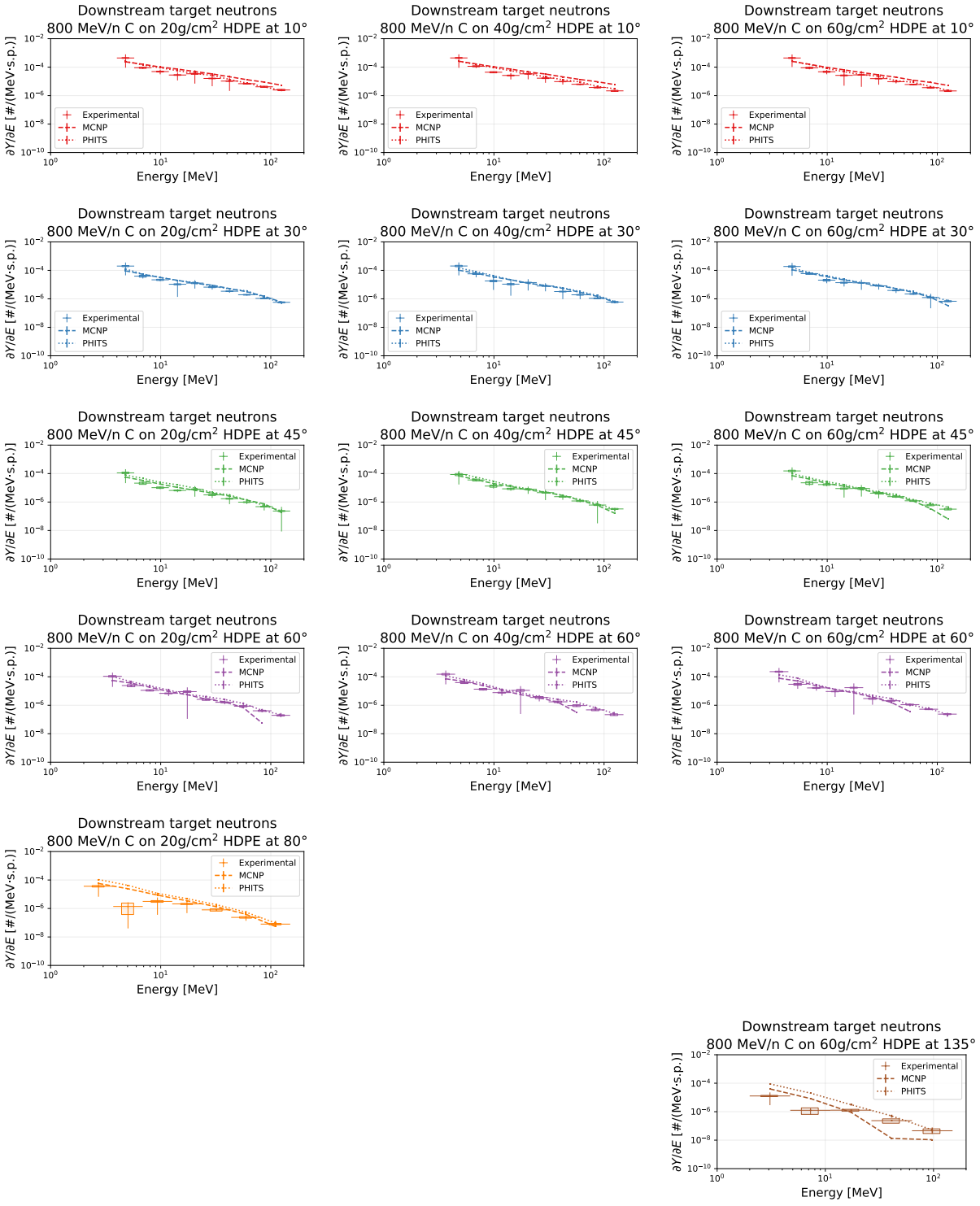


Figure C.64: Downstream target neutrons from 800 MeV/n C incident on HDPE targets

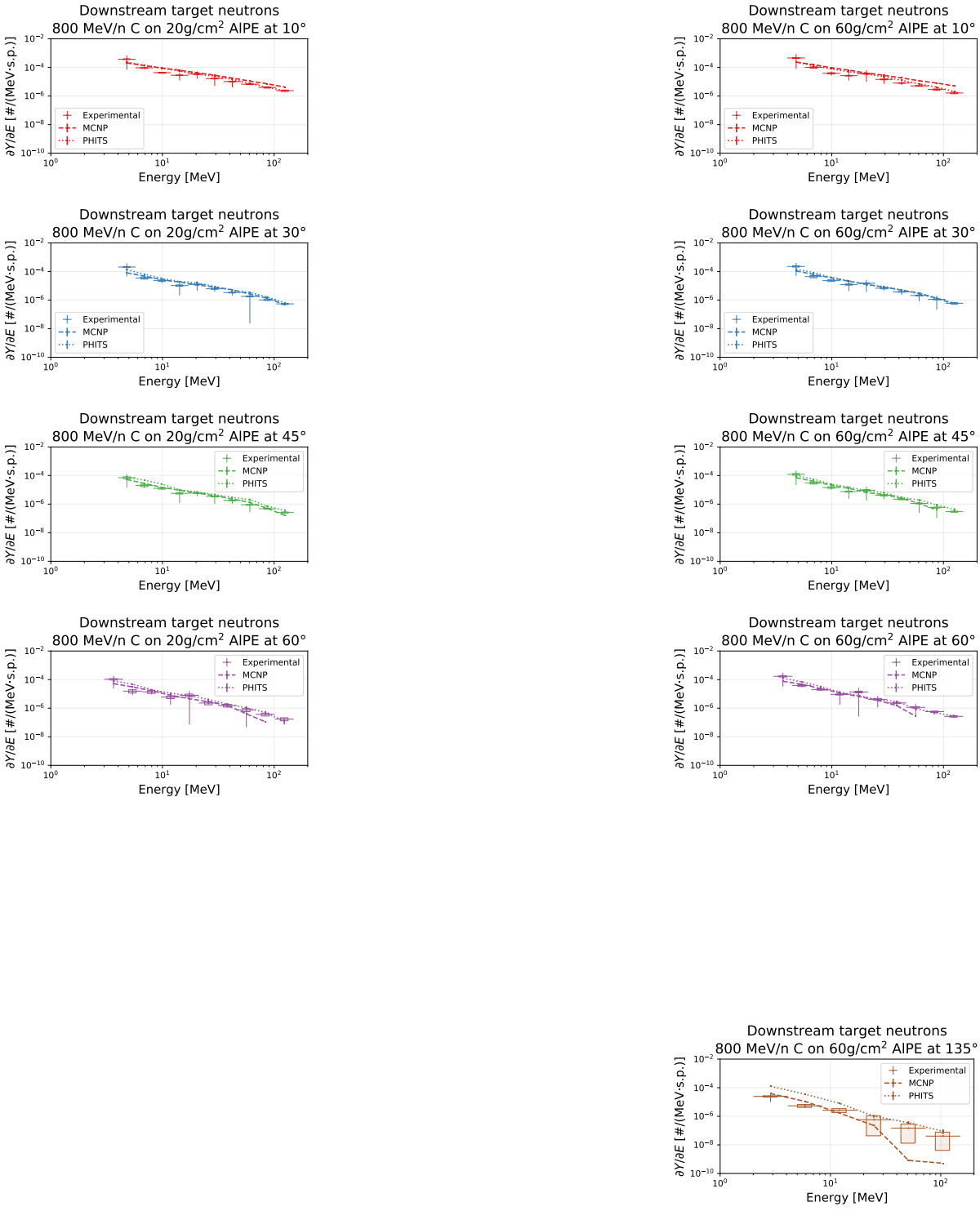


Figure C.65: Downstream target neutrons from 800 MeV/n C incident on AlPE targets

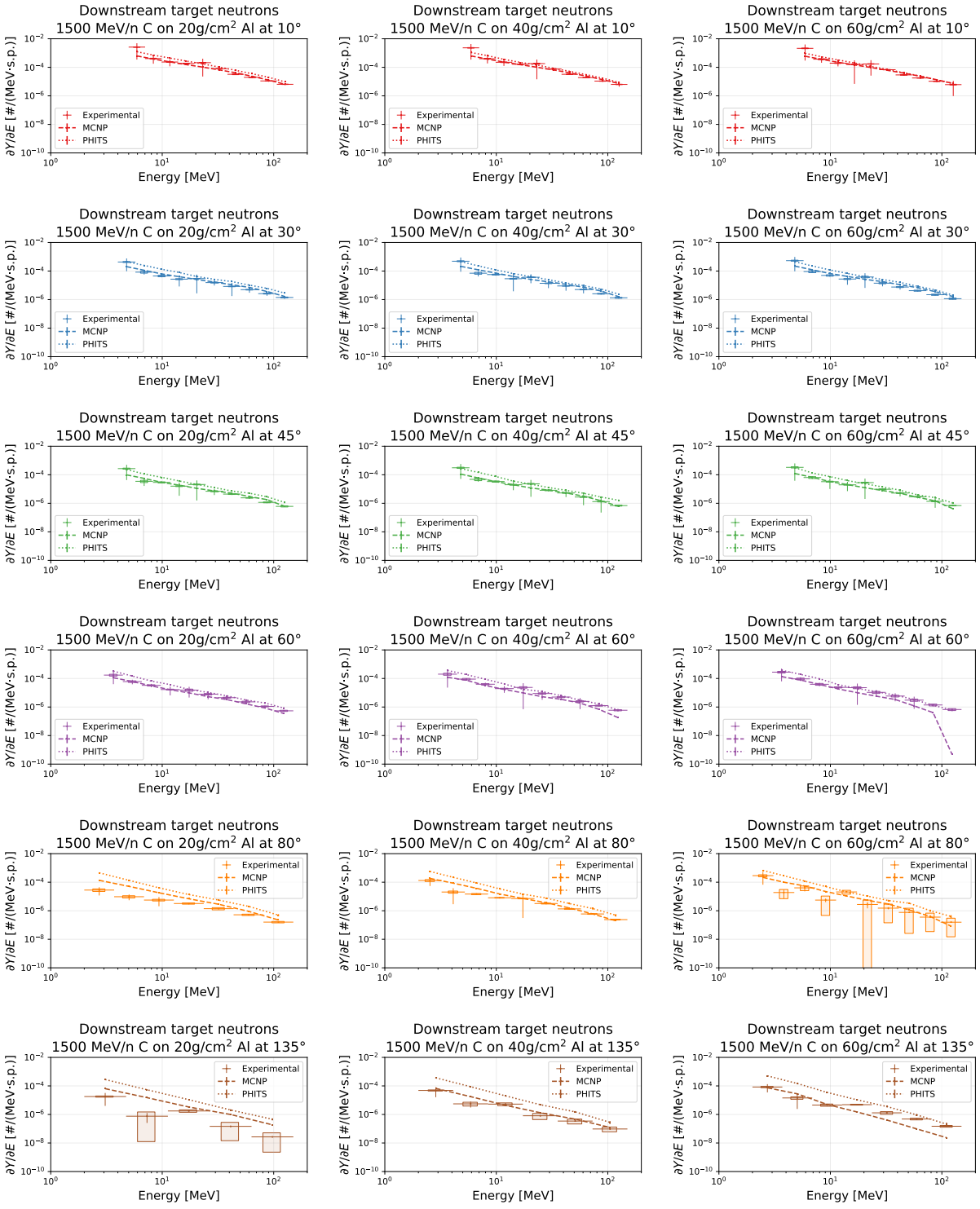


Figure C.66: Downstream target neutrons from 1500 MeV/n C incident on Al targets

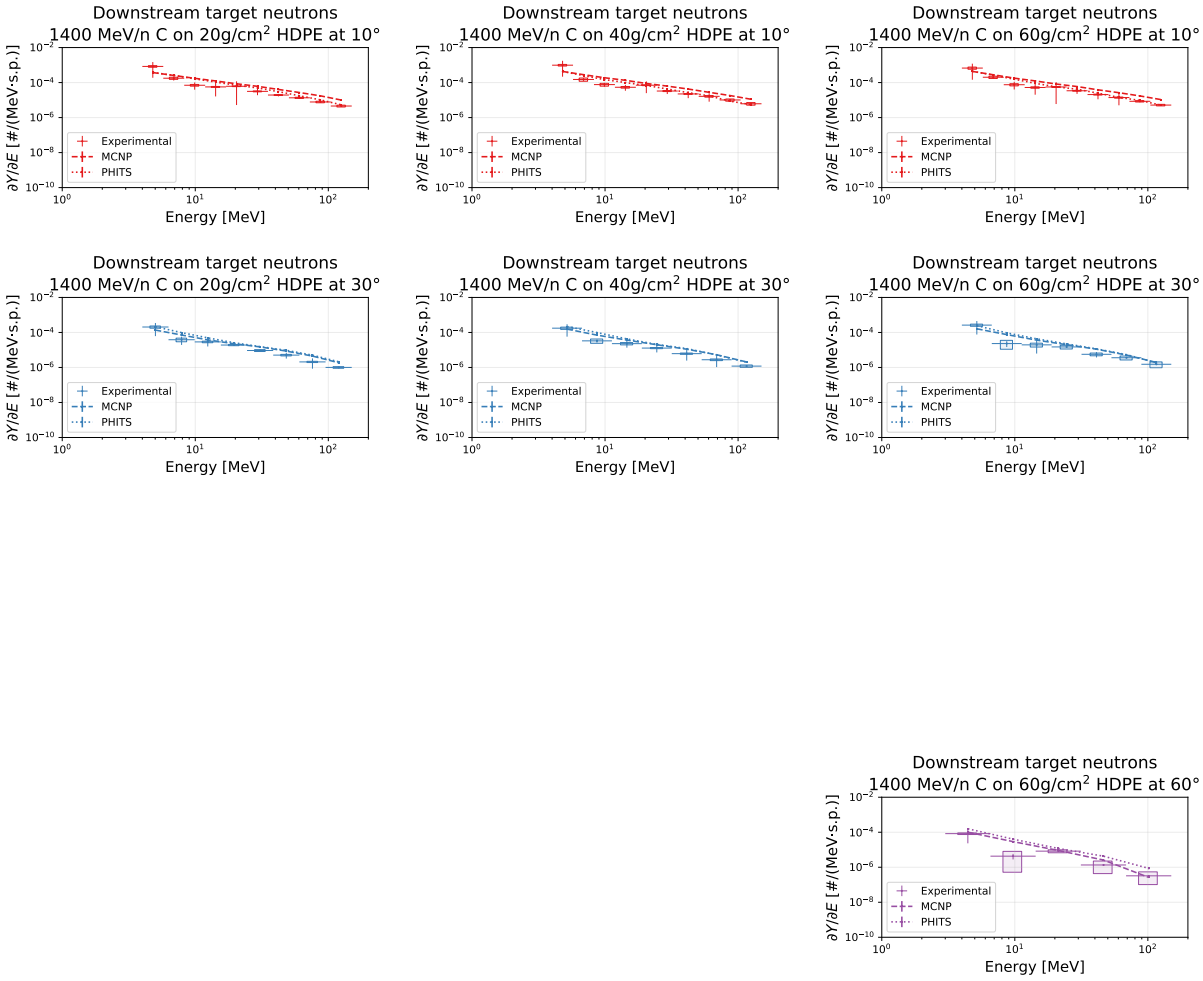


Figure C.67: Downstream target neutrons from 1400 MeV/n C incident on HDPE targets

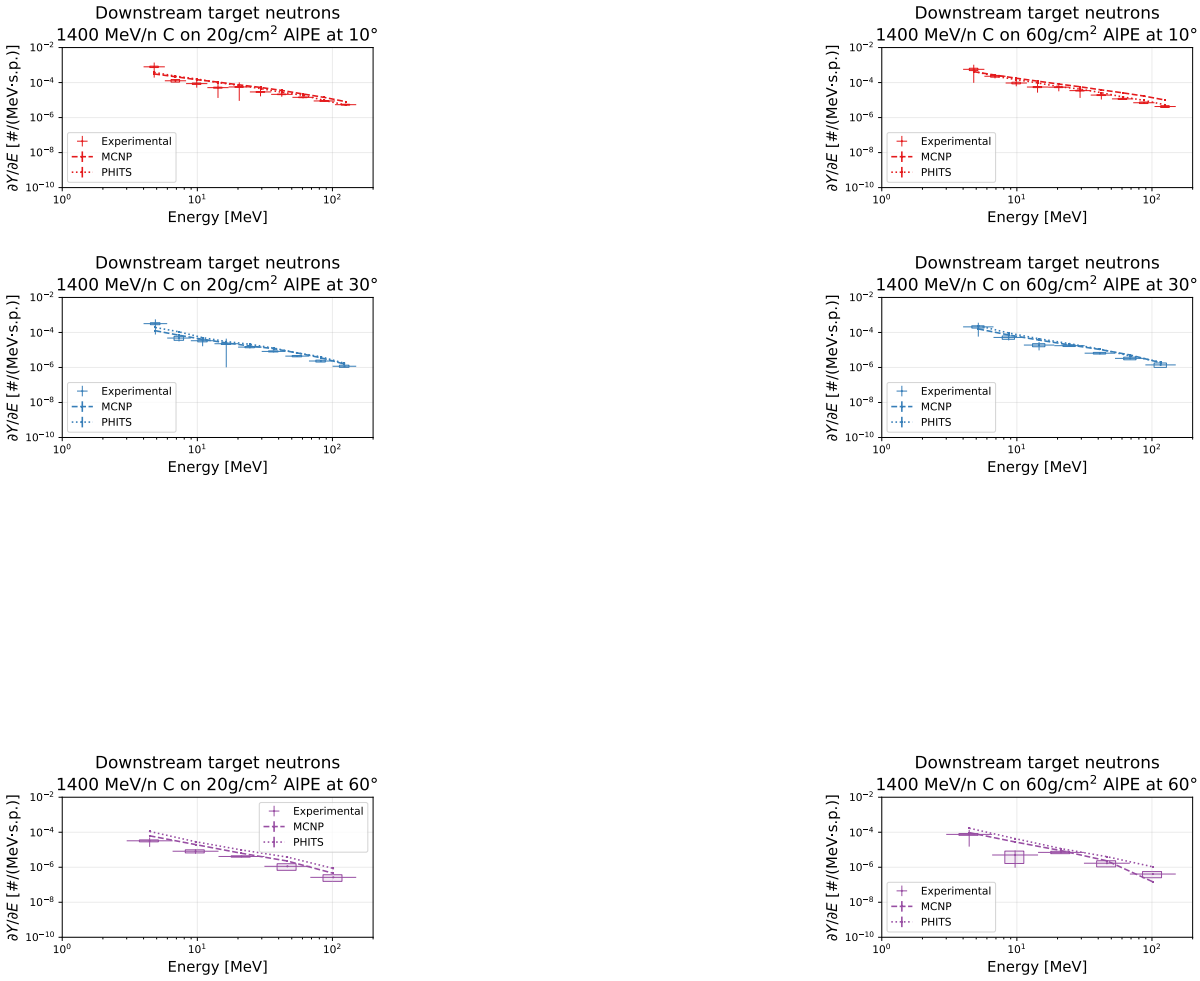


Figure C.68: Downstream target neutrons from 1400 MeV/n C incident on AlPE targets

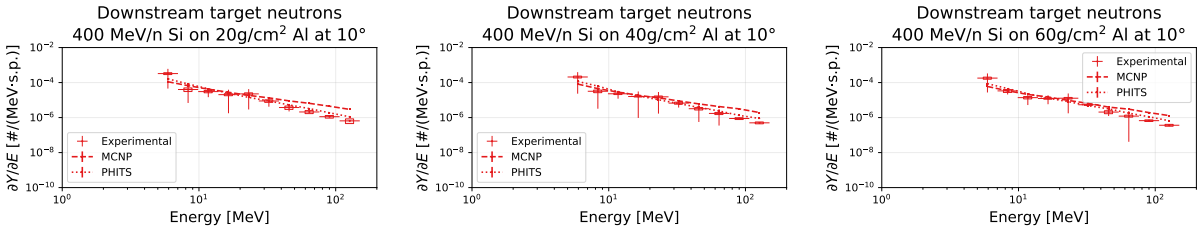


Figure C.69: Downstream target neutrons from 400 MeV/n Si incident on Al targets

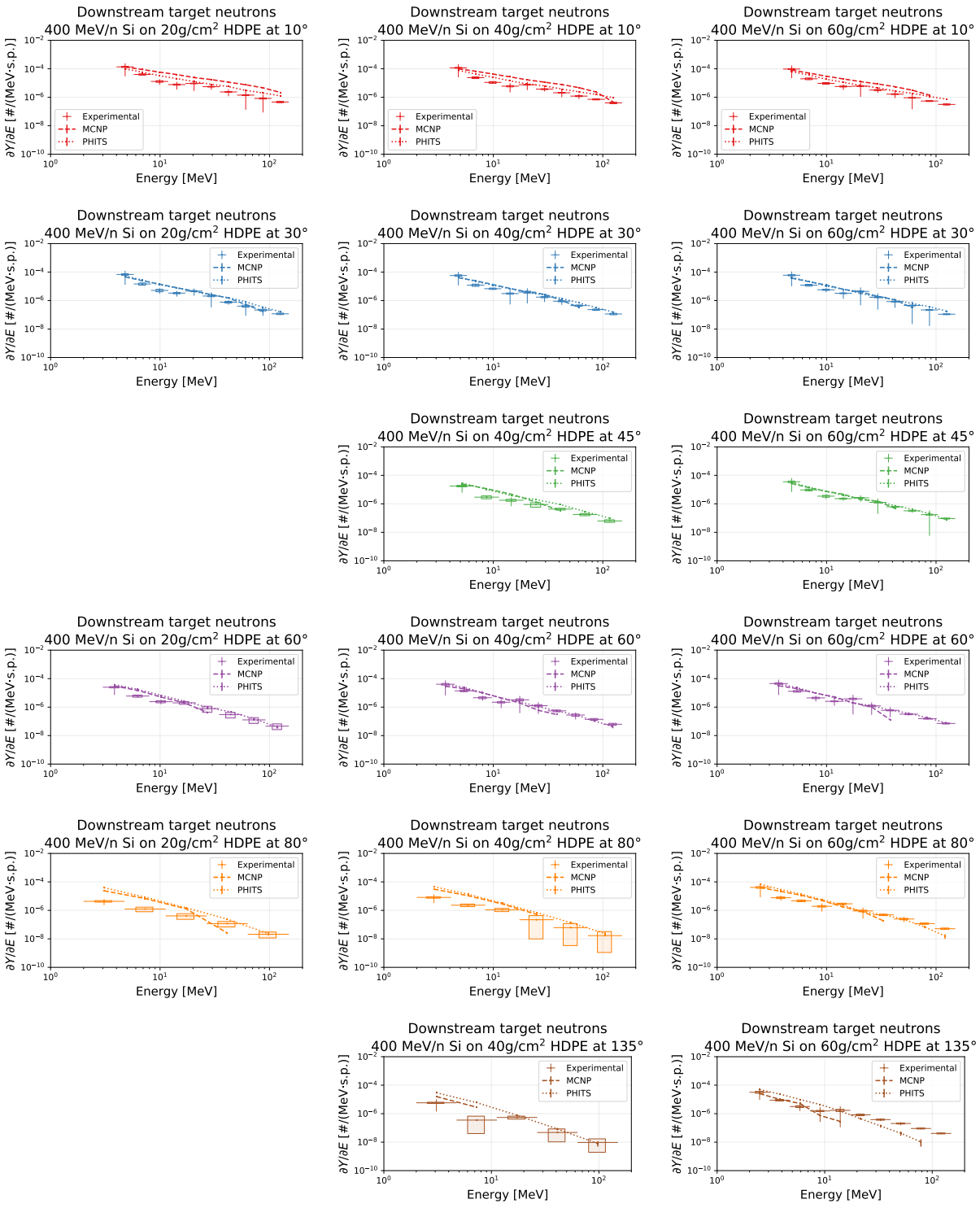


Figure C.70: Downstream target neutrons from 400 MeV/n Si incident on HDPE targets

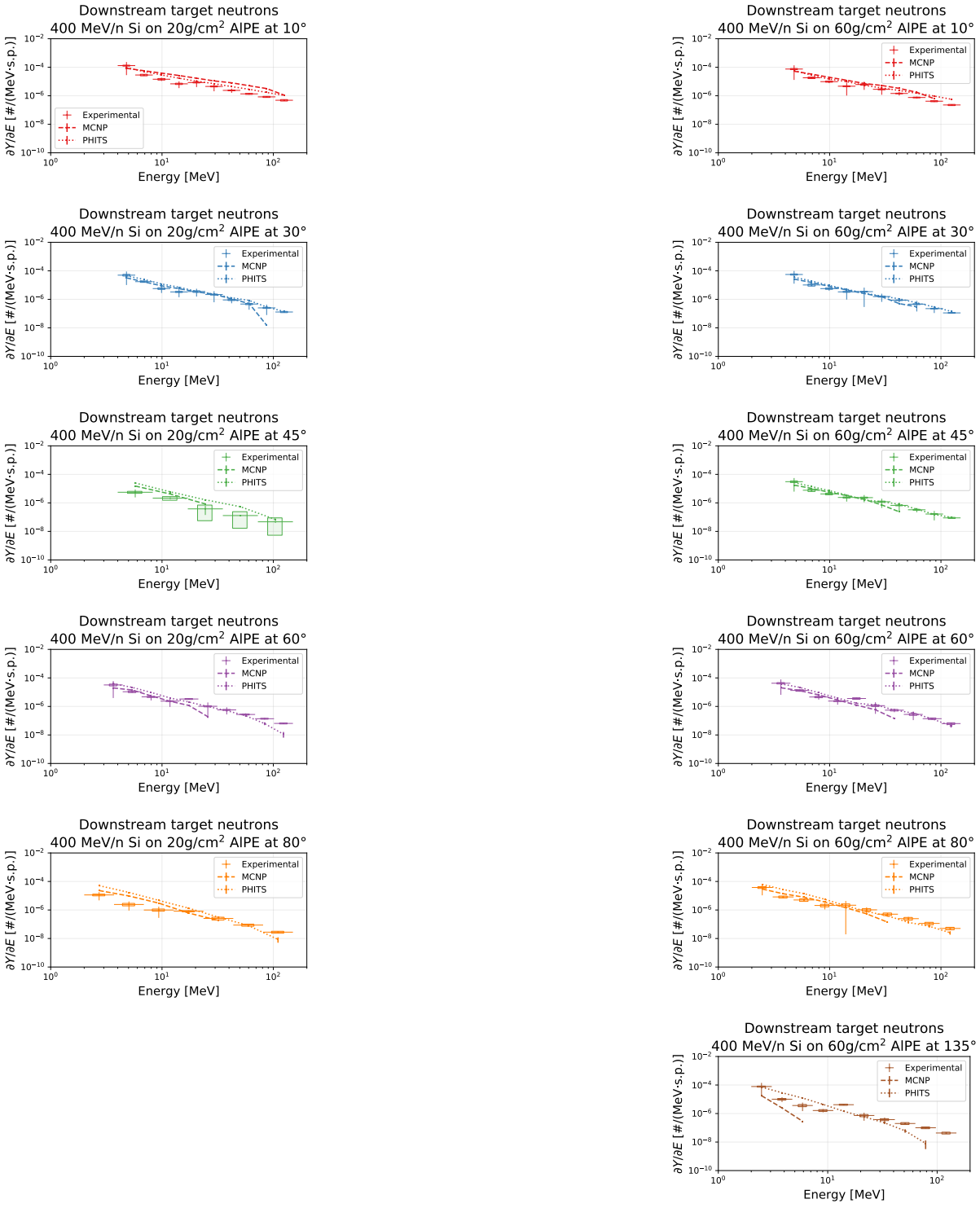


Figure C.71: Downstream target neutrons from 400 MeV/n Si incident on AlPE targets

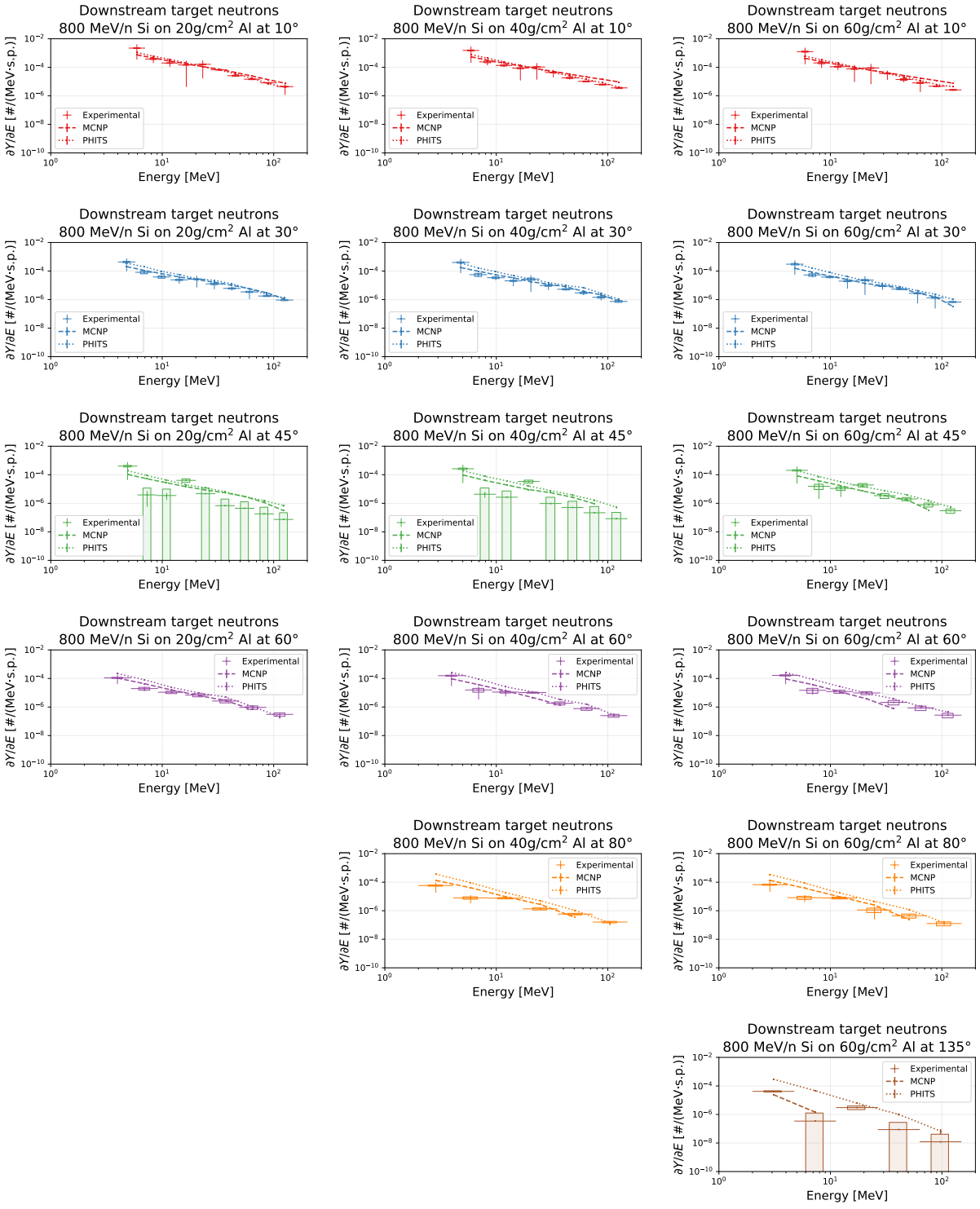


Figure C.72: Downstream target neutrons from 800 MeV/n Si incident on Al targets

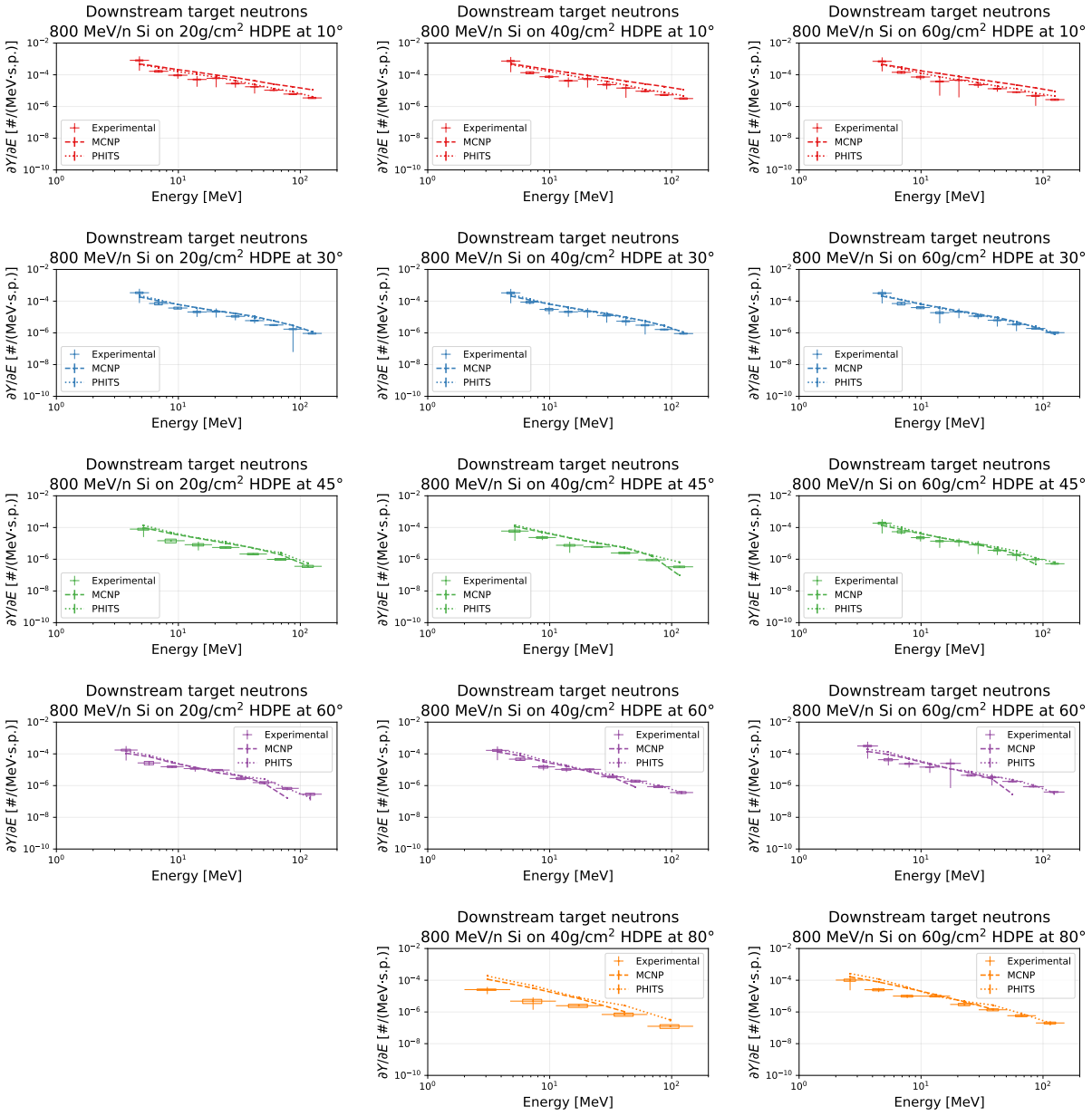


Figure C.73: Downstream target neutrons from 800 MeV/n Si incident on HDPE targets

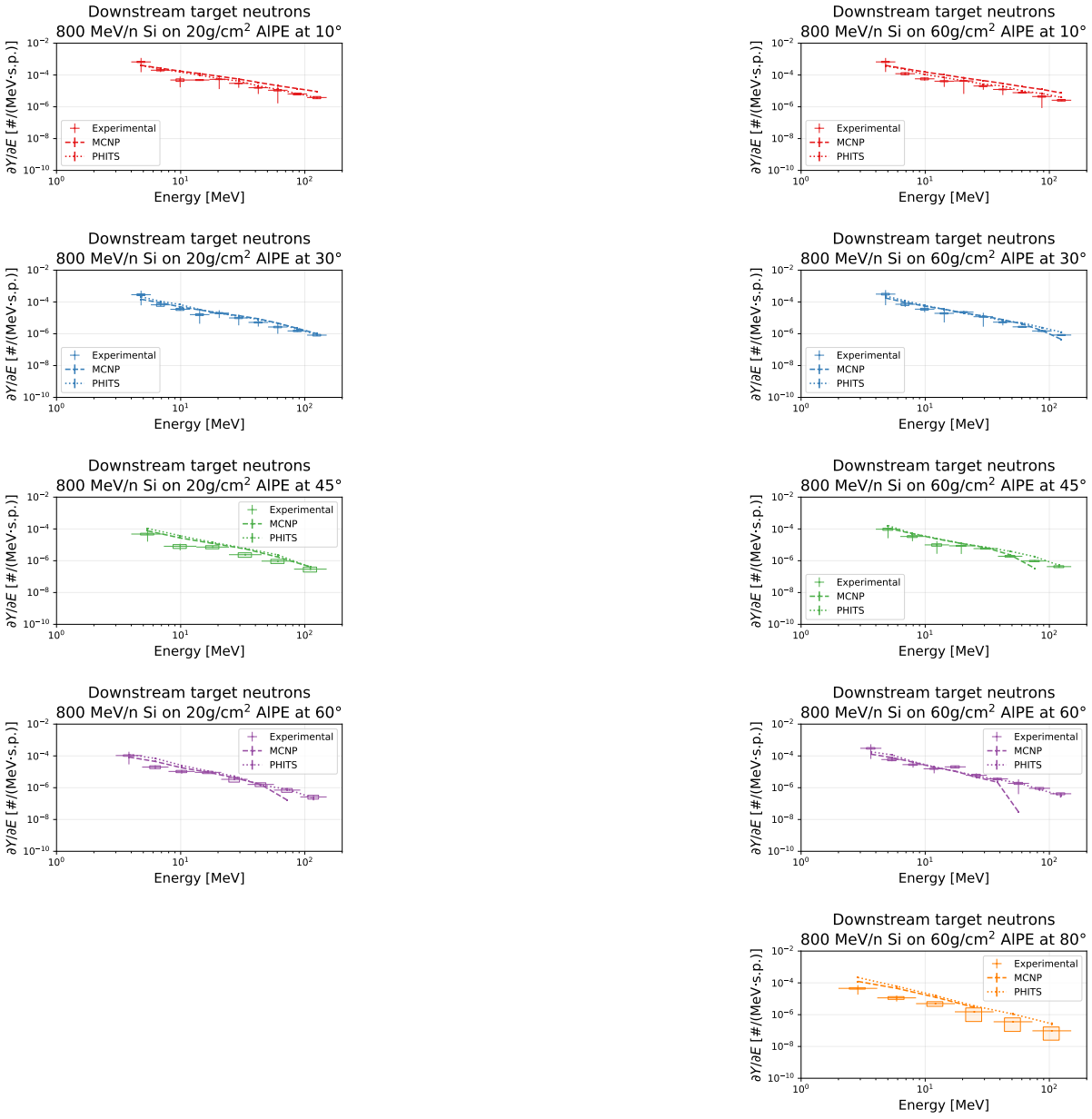


Figure C.74: Downstream target neutrons from 800 MeV/n Si incident on AlPE targets

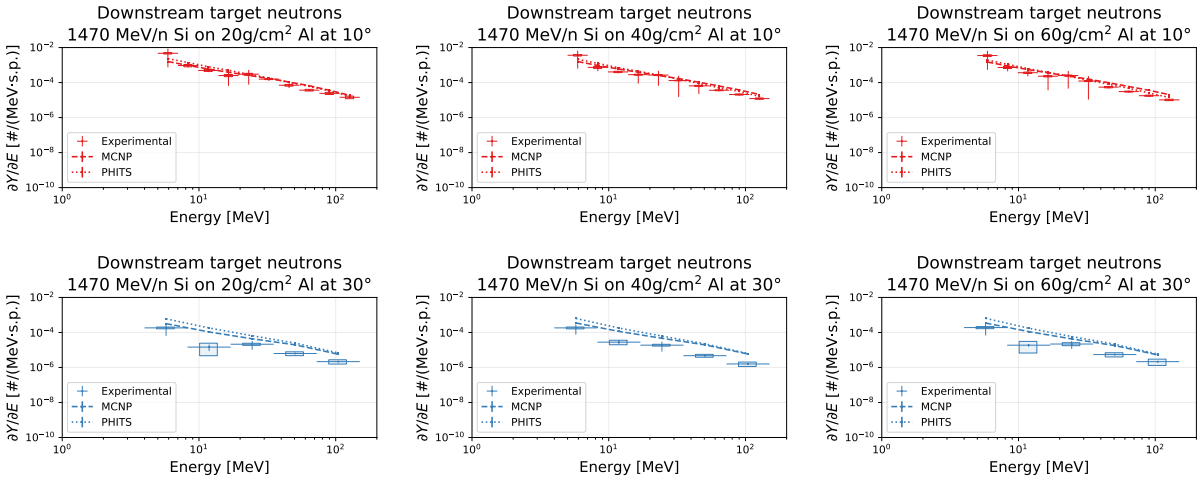


Figure C.75: Downstream target neutrons from 1470 MeV/n Si incident on Al targets

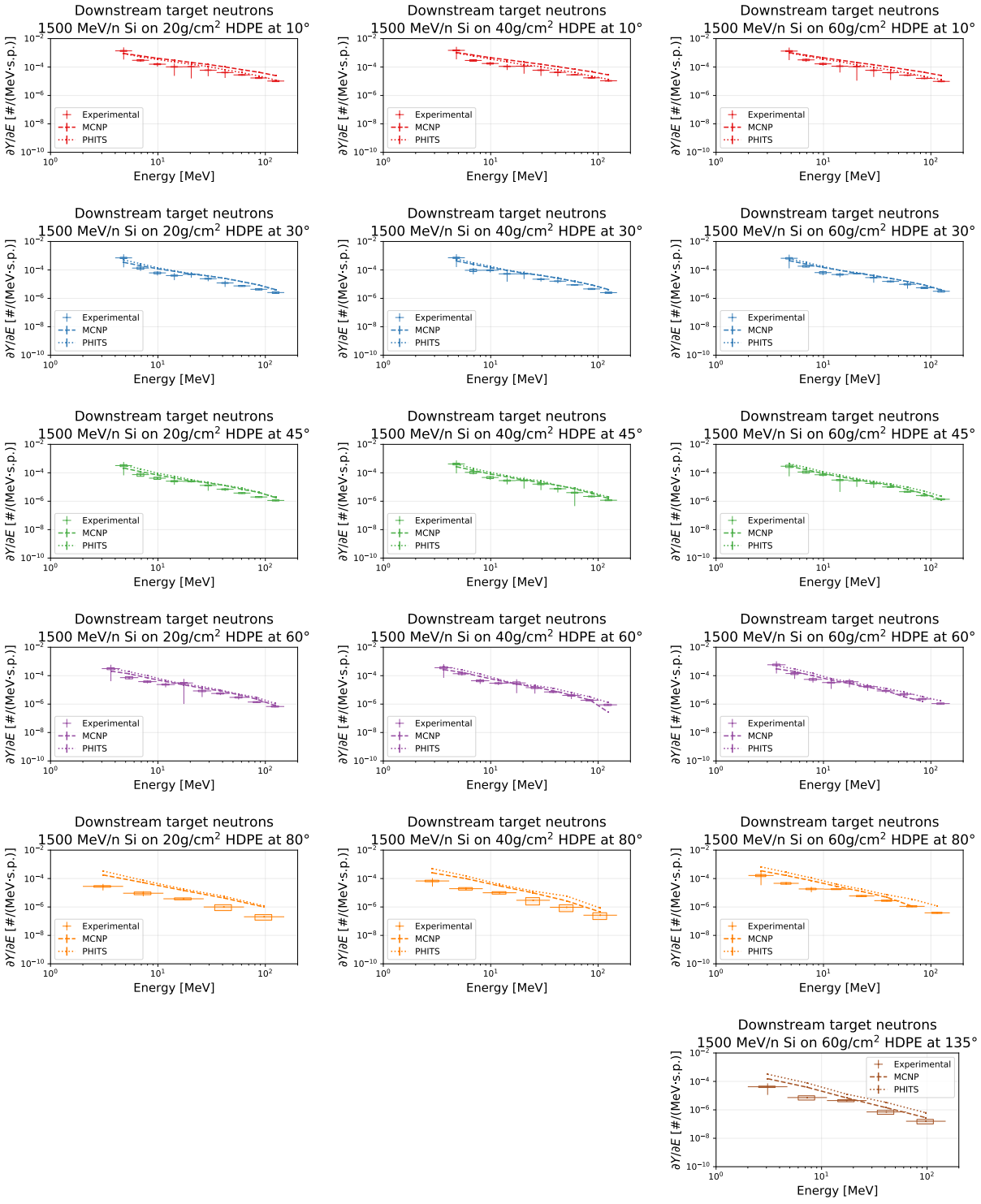


Figure C.76: Downstream target neutrons from 1500 MeV/n Si incident on HDPE targets

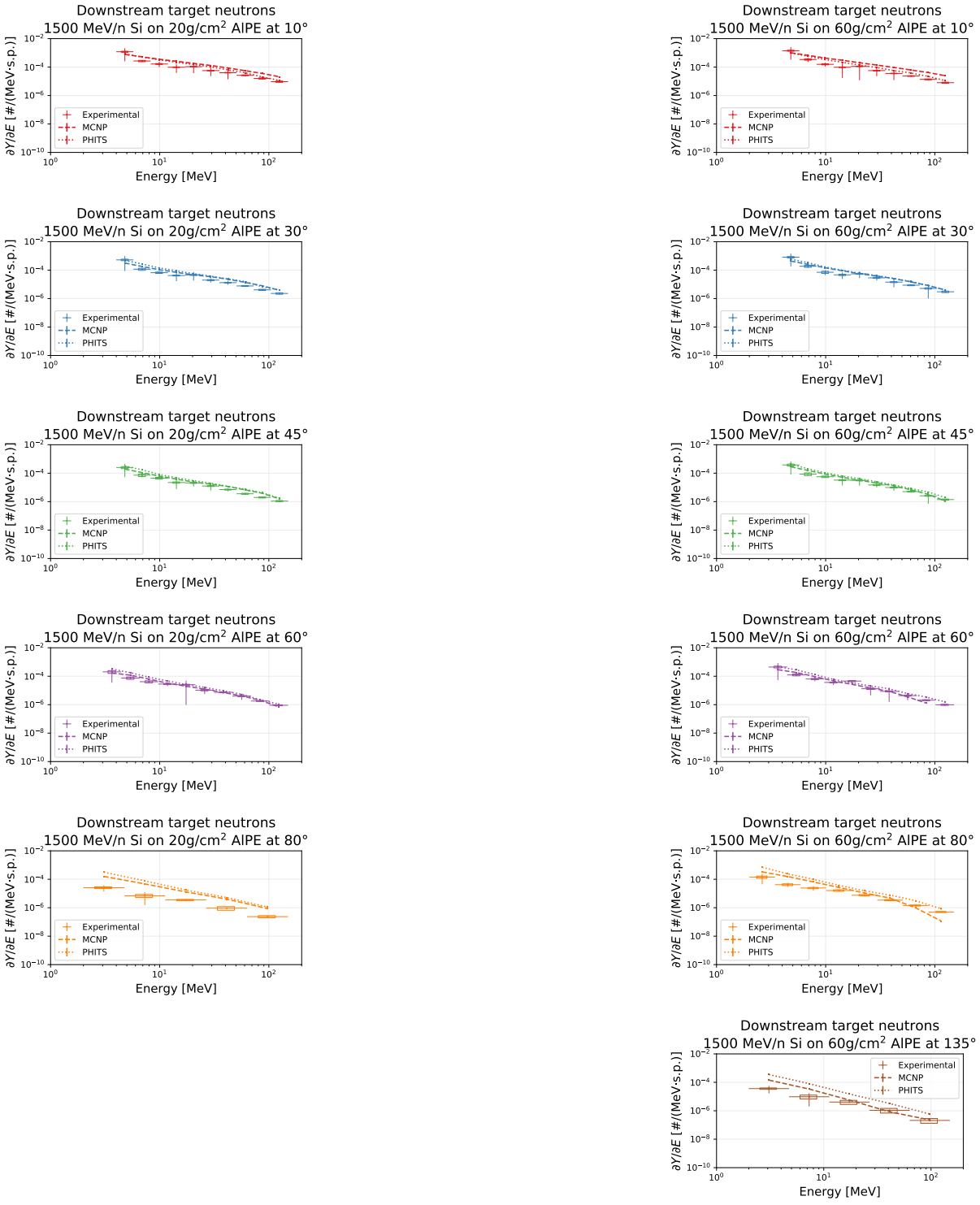


Figure C.77: Downstream target neutrons from 1500 MeV/n Si incident on AlPE targets

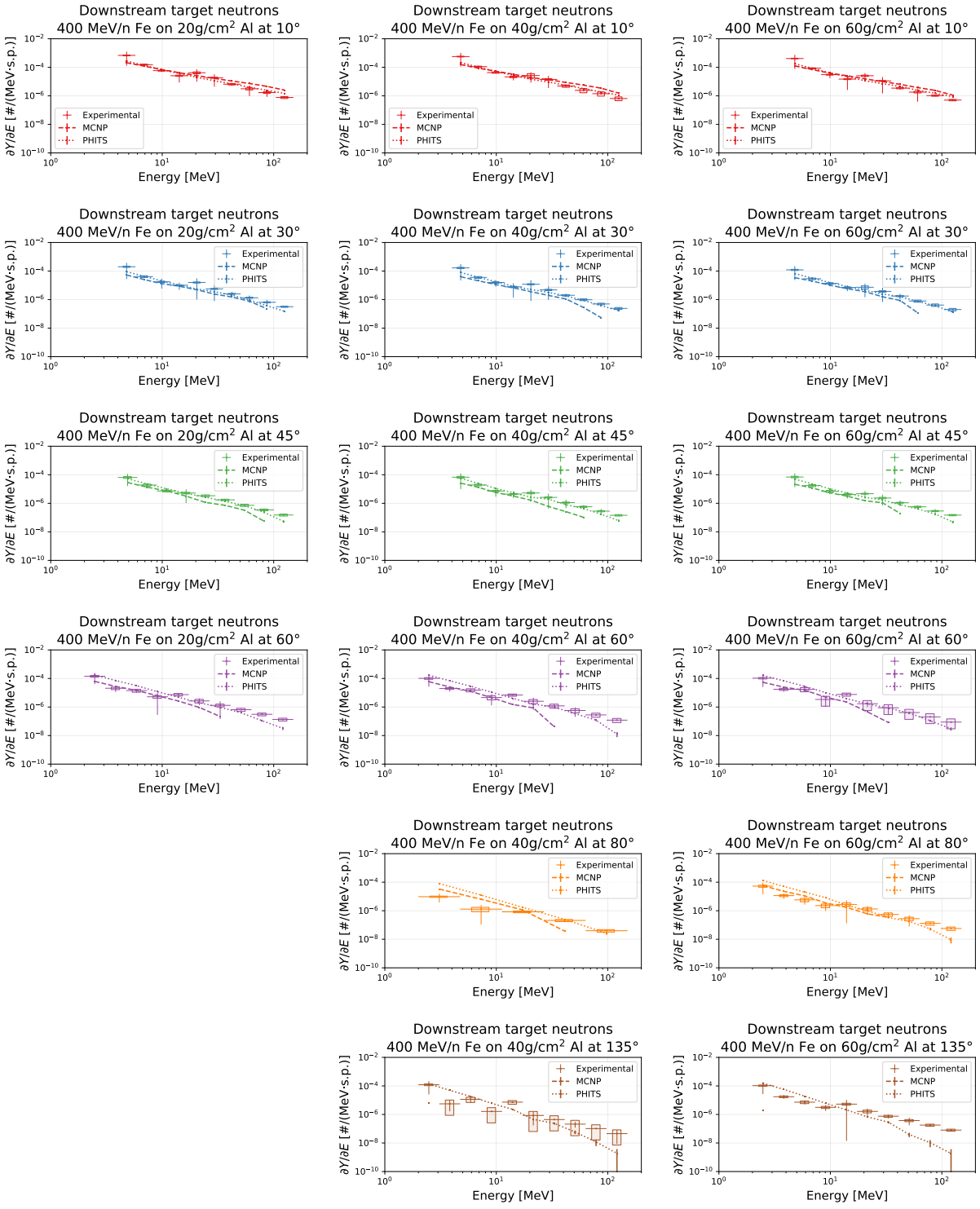


Figure C.78: Downstream target neutrons from 400 MeV/n Fe incident on Al targets

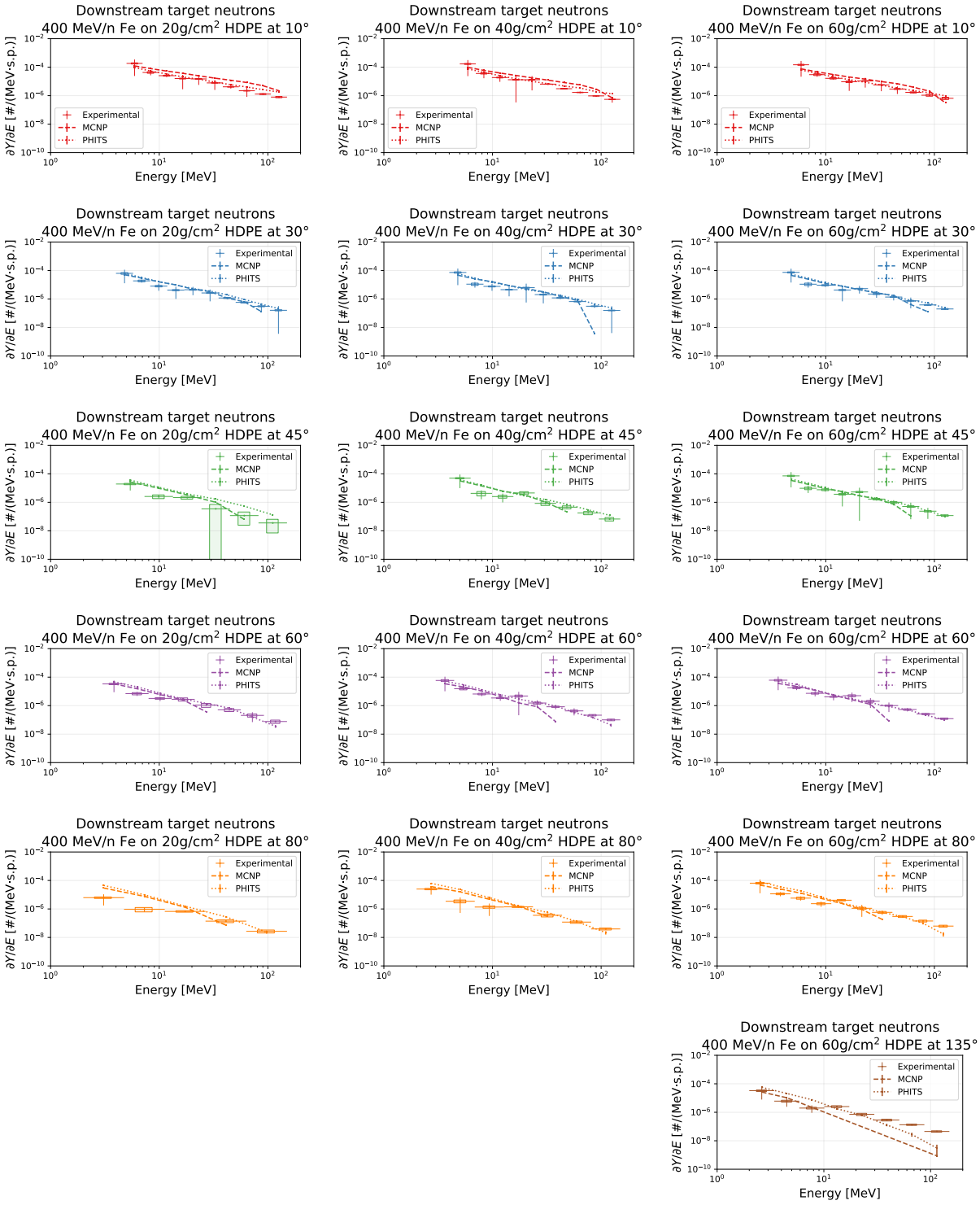


Figure C.79: Downstream target neutrons from 400 MeV/n Fe incident on HDPE targets

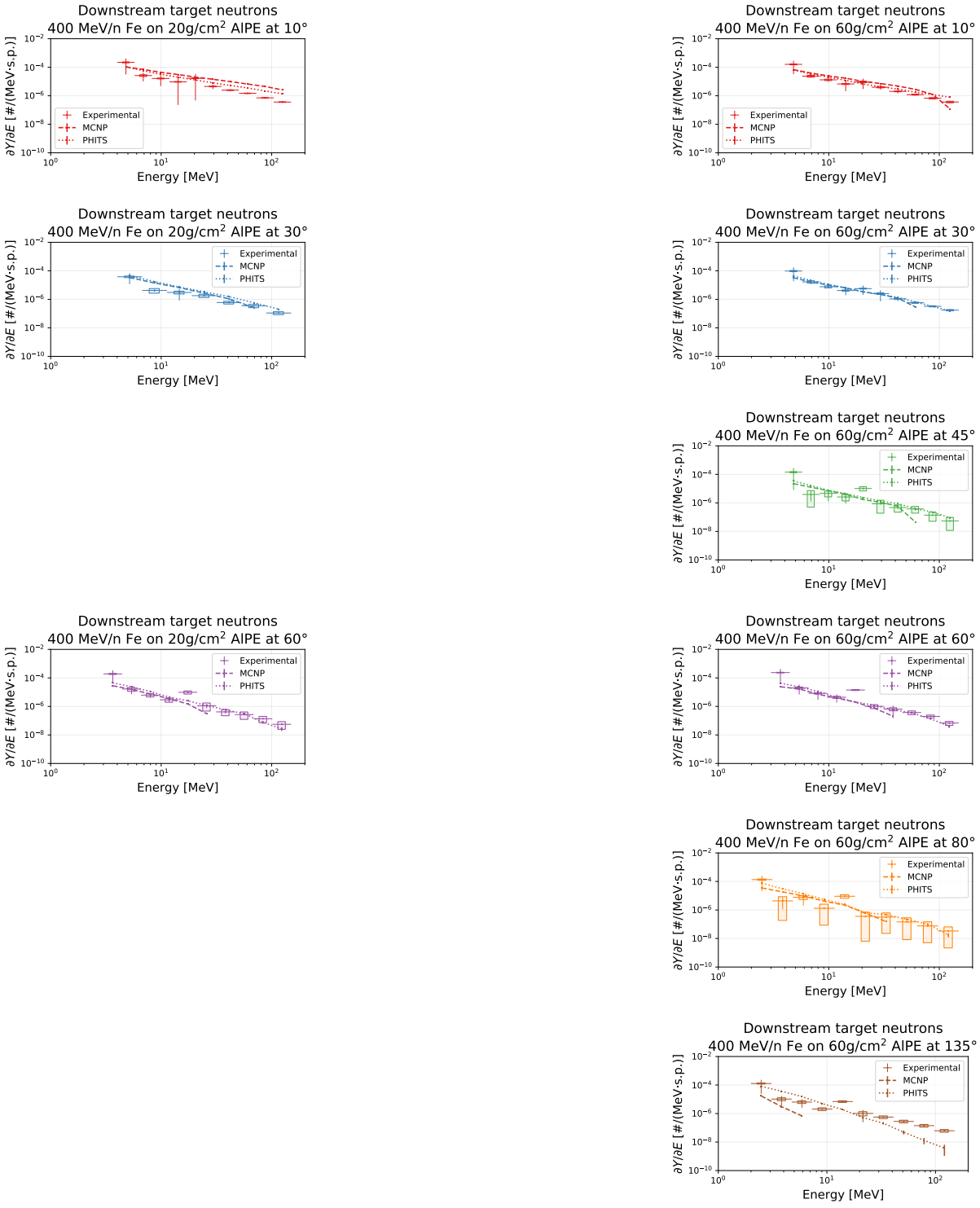


Figure C.80: Downstream target neutrons from 400 MeV/n Fe incident on AlPE targets

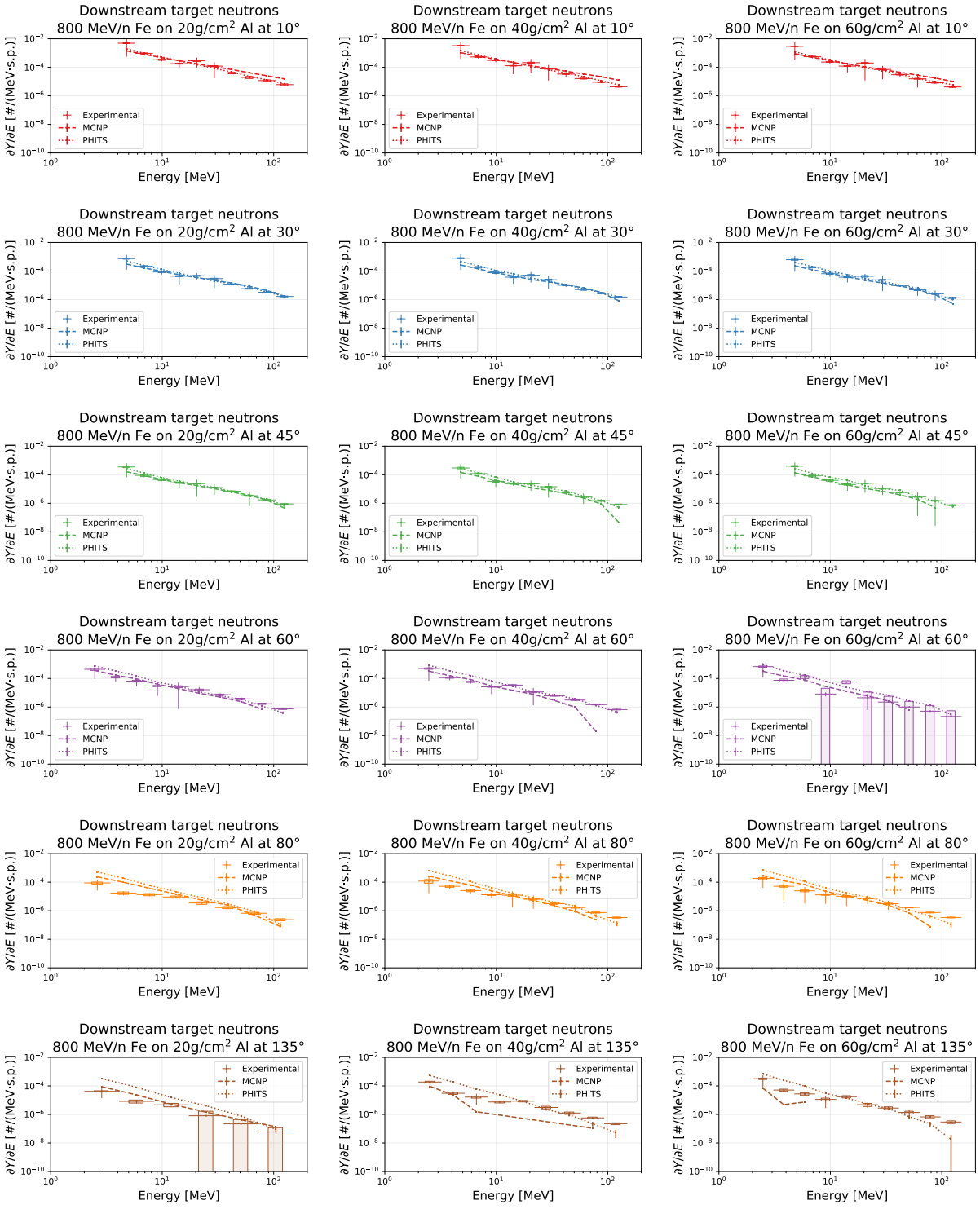


Figure C.81: Downstream target neutrons from 800 MeV/n Fe incident on Al targets

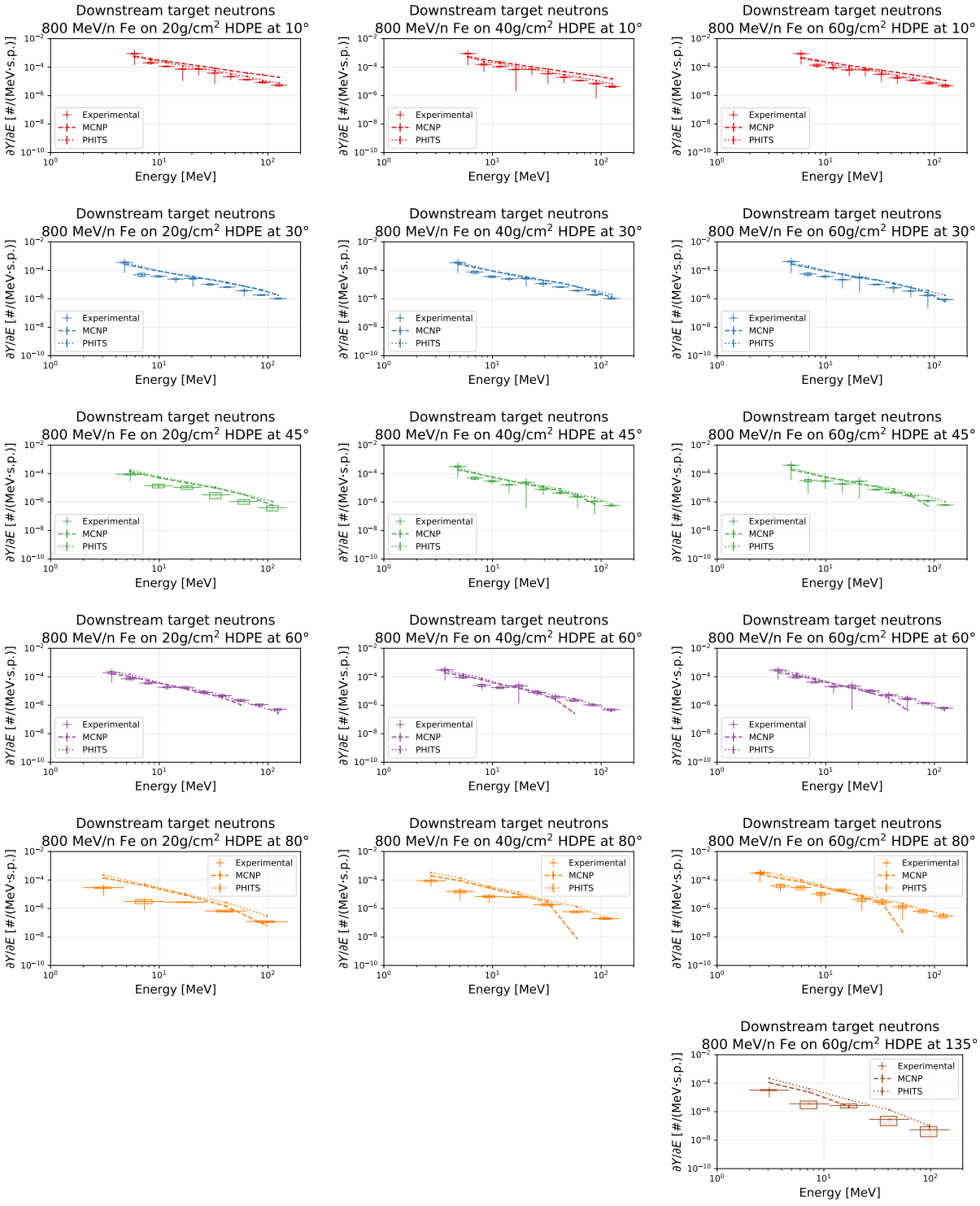


Figure C.82: Downstream target neutrons from 800 MeV/n Fe incident on HDPE targets

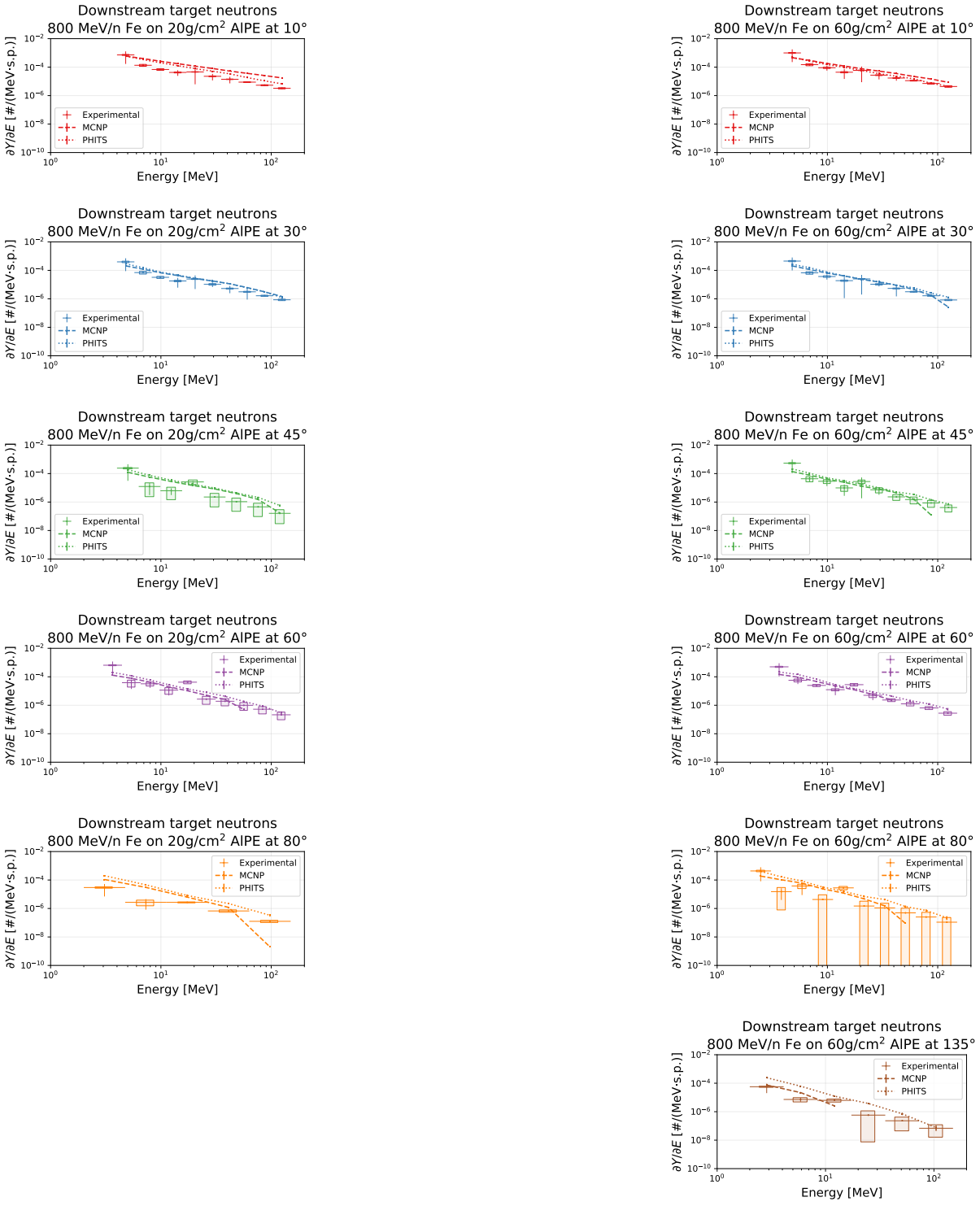
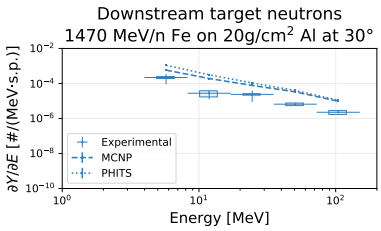


Figure C.83: Downstream target neutrons from 800 MeV/n Fe incident on AlPE targets



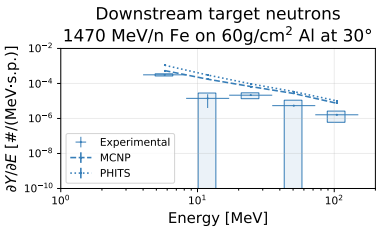


Figure C.84: Downstream target neutrons from 1470 MeV/n Fe incident on Al targets

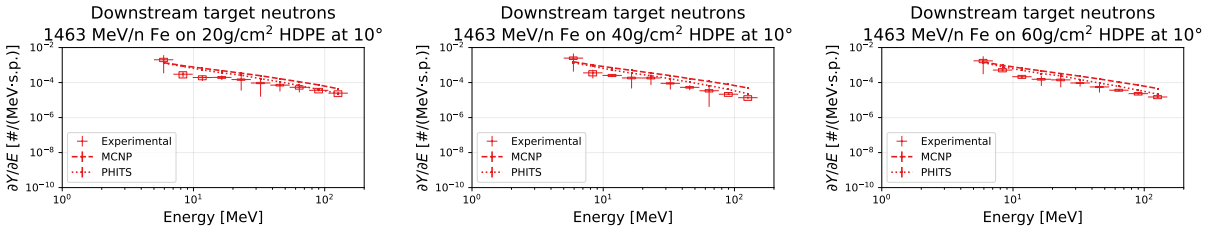


Figure C.85: Downstream target neutrons from 1463 MeV/n Fe incident on HDPE targets

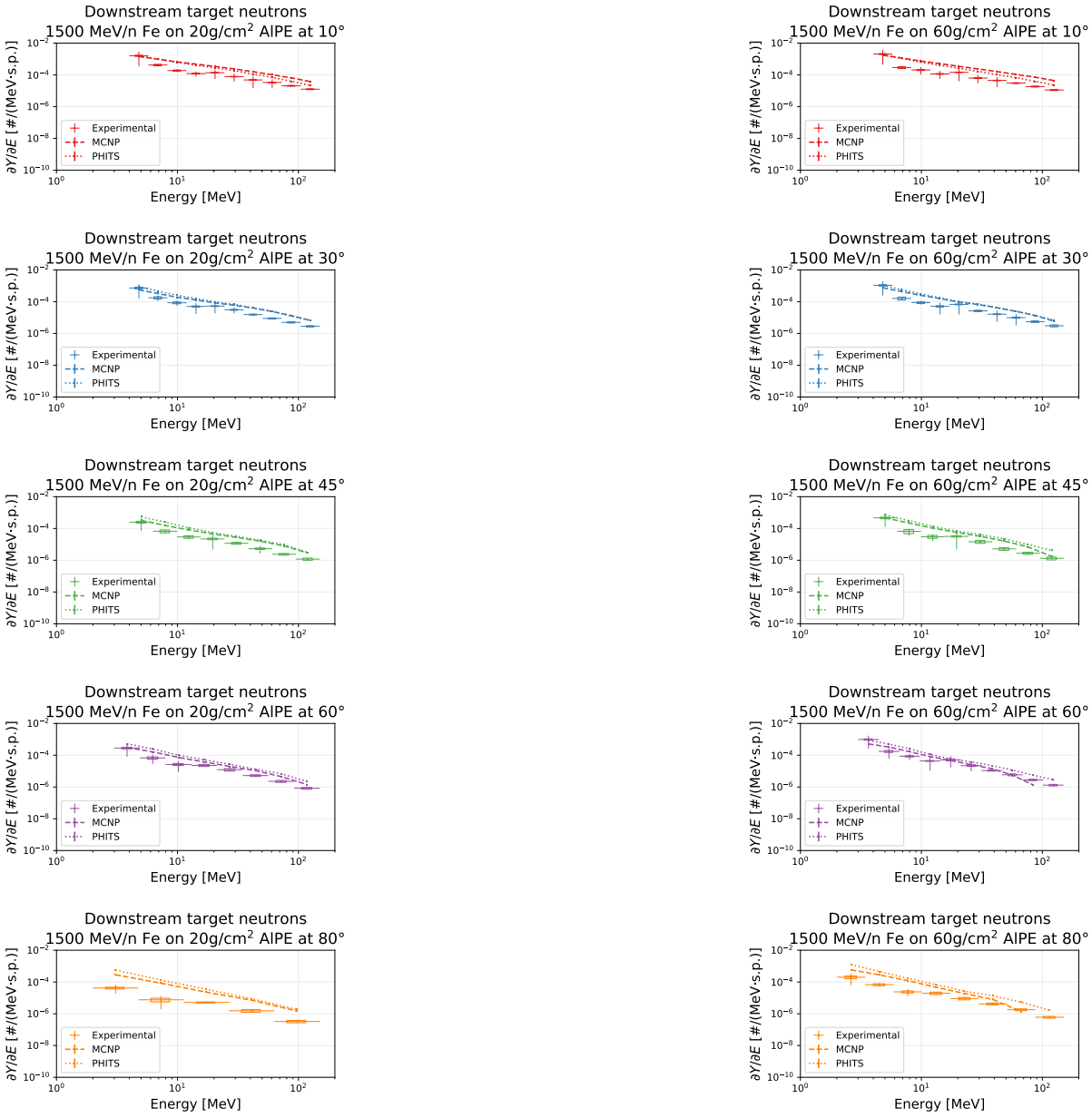


Figure C.86: Downstream target neutrons from 1500 MeV/n Fe incident on AlPE targets

Appendix D

Effective dose tables

This appendix features complete tables of all effective dose values calculated in this work.

D.1 Upstream target effective doses

This section contains effective dose tables for upstream target results only. They are normalized to solid angle, allowing for fair comparisons of dose as a function of detector angle. Note that the effective dose units are pSv.

Table D.1: Upstream target effective dose for H projectiles

E_{proj}	Target	z_{target}	Effective dose in $\left(\frac{pSv}{sr}\right) \cdot \left(\frac{cm^2}{sp}\right)$					
(MeV/n)	material	(g/cm^2)	10°	30°	45°	60°	80°	135°
400	Al	20	41.76 ± 1.03	21.75 ± 0.52	15.97 ± 0.36	7.92 ± 0.18	2.66 ± 0.08	5.11 ± 0.10
		40	73.23 ± 2.76	53.94 ± 1.31	28.79 ± 0.98	20.62 ± 0.62	6.95 ± 0.35	10.56 ± 0.28
		60	85.29 ± 2.92	60.54 ± 1.53	42.27 ± 1.14	23.66 ± 0.76	6.32 ± 0.37	15.81 ± 0.35
	HDPE	20	52.29 ± 1.56	19.36 ± 0.67	12.16 ± 0.44	3.00 ± 0.14	0.78 ± 0.05	0.81 ± 0.04
		40	77.15 ± 1.81	29.43 ± 0.87	14.08 ± 0.54	4.34 ± 0.18	1.59 ± 0.08	0.84 ± 0.04
		60	94.78 ± 1.66	32.60 ± 0.93	17.04 ± 0.52	3.54 ± 0.16	1.36 ± 0.08	1.03 ± 0.04
	AlPE	20	41.97 ± 1.19	19.89 ± 0.61	12.17 ± 0.42	4.80 ± 0.17	0.80 ± 0.05	3.20 ± 0.08
		60	70.18 ± 1.34	34.10 ± 0.82	16.85 ± 0.53	5.25 ± 0.20	1.59 ± 0.08	3.47 ± 0.08
800	Al	20	72.30 ± 4.14	29.39 ± 1.33	18.96 ± 1.01	19.24 ± 0.57	6.65 ± 0.30	6.49 ± 0.18
		40	104.50 ± 4.18	57.51 ± 1.51	35.66 ± 1.11	29.31 ± 0.69	8.23 ± 0.36	11.51 ± 0.27
		60	138.33 ± 3.65	72.02 ± 1.56	42.97 ± 1.21	33.67 ± 0.75	10.56 ± 0.39	14.56 ± 0.29
	HDPE	20	103.29 ± 2.72	24.03 ± 0.89	15.13 ± 0.58	2.90 ± 0.14	1.30 ± 0.08	1.36 ± 0.05
		40	153.58 ± 3.28	37.54 ± 1.21	22.21 ± 0.80	5.28 ± 0.22	1.66 ± 0.10	2.26 ± 0.09
		60	177.45 ± 3.35	43.01 ± 1.33	25.95 ± 0.90	6.73 ± 0.26	1.81 ± 0.11	2.12 ± 0.08
	AlPE	20	73.72 ± 2.21	23.59 ± 0.79	15.04 ± 0.50	5.42 ± 0.18	1.28 ± 0.06	4.07 ± 0.09
		60	146.38 ± 2.79	47.54 ± 1.21	26.12 ± 0.75	7.40 ± 0.26	2.42 ± 0.12	5.47 ± 0.13
2500	Al	20	85.94 ± 4.68	30.26 ± 1.34	20.63 ± 0.80	10.24 ± 0.30	5.24 ± 0.17	7.85 ± 0.17
		40	123.01 ± 5.27	63.88 ± 1.97	46.19 ± 1.39	21.02 ± 0.50	8.70 ± 0.24	13.92 ± 0.26
		60	478.04 ± 8.81	216.29 ± 4.34	174.53 ± 4.02	57.58 ± 1.33	25.75 ± 0.72	41.55 ± 0.84
	HDPE	20	64.06 ± 3.12	27.65 ± 1.06	20.56 ± 0.71	5.39 ± 0.20	3.17 ± 0.15	2.19 ± 0.06
		40	125.61 ± 3.99	54.23 ± 1.56	35.03 ± 1.16	8.39 ± 0.29	3.68 ± 0.13	3.68 ± 0.14
		60	140.43 ± 4.33	68.07 ± 1.92	47.30 ± 1.45	10.16 ± 0.37	4.25 ± 0.17	4.37 ± 0.13
	AlPE	20	68.36 ± 3.81	28.74 ± 1.22	23.00 ± 0.82	6.81 ± 0.27	2.10 ± 0.10	5.64 ± 0.13
		60	124.96 ± 5.70	67.66 ± 2.43	44.57 ± 1.54	9.89 ± 0.48	5.77 ± 0.24	9.23 ± 0.25

Table D.2: Upstream target effective dose for He projectiles

E_{proj}	Target	z_{target}	Effective dose in $\left(\frac{pSv}{sr}\right) \cdot \left(\frac{cm^2}{sp}\right)$					
(MeV/n)	material	(g/cm^2)	10°	30°	45°	60°	80°	135°
400	Al	20	243.23 ± 6.76	99.80 ± 2.34	56.96 ± 1.55	39.02 ± 1.06	12.64 ± 0.50	13.84 ± 0.30
		40	477.41 ± 7.95	151.76 ± 3.67	115.36 ± 2.62	72.84 ± 1.61	15.65 ± 0.79	26.40 ± 0.52
		60	549.35 ± 7.76	203.36 ± 3.83	119.54 ± 2.72	75.18 ± 1.72	16.79 ± 0.77	28.78 ± 0.56
	HDPE	20	292.92 ± 4.51	76.58 ± 1.80	45.49 ± 1.23	11.02 ± 0.37	2.65 ± 0.13	2.90 ± 0.11
		40	494.88 ± 5.75	118.75 ± 2.47	73.09 ± 1.71	13.27 ± 0.45	4.55 ± 0.19	2.91 ± 0.11
		60	603.78 ± 6.22	133.04 ± 2.66	73.42 ± 1.75	16.76 ± 0.54	5.57 ± 0.24	3.68 ± 0.12
	AlPE	20	262.84 ± 3.56	80.12 ± 1.63	46.37 ± 1.06	12.87 ± 0.38	2.99 ± 0.12	7.08 ± 0.15
		60	524.15 ± 4.75	146.15 ± 2.29	70.99 ± 1.52	17.67 ± 0.51	4.47 ± 0.20	8.65 ± 0.19
800	Al	20	193.86 ± 9.19	69.37 ± 2.92	61.79 ± 2.61	16.37 ± 0.65	10.76 ± 0.43	11.70 ± 0.38
		40	327.03 ± 12.17	158.96 ± 4.84	105.14 ± 3.65	34.15 ± 1.09	11.45 ± 0.47	22.59 ± 0.61
		60	515.72 ± 13.24	201.43 ± 5.40	146.23 ± 4.54	37.80 ± 1.24	14.20 ± 0.53	31.16 ± 0.83
	HDPE	20	502.17 ± 9.97	102.54 ± 3.62	64.35 ± 2.25	11.58 ± 0.53	6.12 ± 0.31	5.03 ± 0.18
		40	815.15 ± 12.89	189.46 ± 5.27	109.97 ± 3.37	17.80 ± 0.80	9.81 ± 0.44	6.35 ± 0.24
		60	941.18 ± 14.28	234.11 ± 6.10	132.32 ± 3.98	24.97 ± 0.99	12.42 ± 0.53	7.27 ± 0.28
	AlPE	20	364.28 ± 5.77	92.35 ± 2.16	55.26 ± 1.41	14.95 ± 0.46	3.95 ± 0.16	9.87 ± 0.21
		60	768.38 ± 8.77	199.00 ± 3.98	105.21 ± 2.62	27.06 ± 0.86	8.99 ± 0.33	15.32 ± 0.45
1500	Al	20	135.91 ± 7.49	103.63 ± 3.85	82.69 ± 2.95	20.60 ± 0.84	14.53 ± 0.52	16.82 ± 0.44
		40	301.62 ± 13.66	191.78 ± 6.50	174.66 ± 4.47	47.58 ± 1.42	17.39 ± 0.66	36.32 ± 0.79
		60	446.34 ± 15.15	257.51 ± 7.56	240.78 ± 5.78	69.56 ± 1.95	27.90 ± 1.02	47.87 ± 1.01
	HDPE	20	115.43 ± 8.20	111.50 ± 4.10	73.23 ± 2.81	11.52 ± 0.63	8.99 ± 0.40	4.57 ± 0.20
		40	243.56 ± 12.77	185.70 ± 5.96	111.28 ± 4.34	19.07 ± 0.88	13.94 ± 0.62	8.01 ± 0.31
		60	349.58 ± 13.61	233.85 ± 7.36	133.10 ± 4.46	26.28 ± 1.19	11.01 ± 0.53	8.93 ± 0.32
	AlPE	20	275.99 ± 6.88	113.17 ± 3.23	63.34 ± 1.92	15.94 ± 0.60	6.22 ± 0.27	12.67 ± 0.30
		60	598.09 ± 13.76	251.67 ± 6.43	131.25 ± 3.77	29.46 ± 1.17	14.28 ± 0.55	20.26 ± 0.59

Table D.3: Upstream target effective dose for C projectiles

E_{proj}	Target	z_{target}	Effective dose in $\left(\frac{pSv}{sr}\right) \cdot \left(\frac{cm^2}{sp}\right)$					
(MeV/n)	material	(g/cm^2)	10°	30°	45°	60°	80°	135°
400	Al	20	657.25 ± 8.50	177.87 ± 3.41	109.59 ± 2.47	34.24 ± 0.84	15.72 ± 0.44	16.27 ± 0.35
		40	968.02 ± 8.83	244.89 ± 3.77	155.37 ± 2.80	54.74 ± 1.14	14.78 ± 0.42	28.43 ± 0.47
		60	923.10 ± 7.34	252.17 ± 3.36	161.30 ± 2.55	45.65 ± 0.91	16.18 ± 0.47	34.86 ± 0.54
	HDPE	20	822.53 ± 9.60	212.29 ± 4.18	107.24 ± 2.67	27.43 ± 0.90	6.12 ± 0.29	5.66 ± 0.21
		40	1002.48 ± 8.95	271.53 ± 4.25	134.81 ± 2.82	33.86 ± 0.91	9.83 ± 0.37	7.13 ± 0.23
		60	961.97 ± 6.90	255.67 ± 3.33	116.37 ± 2.17	32.39 ± 0.80	11.17 ± 0.34	9.03 ± 0.26
	AlPE	20	702.01 ± 8.45	200.35 ± 3.76	112.72 ± 2.56	30.45 ± 0.87	5.77 ± 0.26	13.47 ± 0.35
		60	906.15 ± 6.53	240.30 ± 3.18	110.27 ± 2.09	31.59 ± 0.75	9.59 ± 0.32	16.21 ± 0.30
800	Al	20	446.35 ± 13.46	208.44 ± 5.31	153.60 ± 3.89	34.95 ± 1.07	21.65 ± 0.62	22.79 ± 0.47
		40	1028.30 ± 17.73	406.52 ± 7.81	290.18 ± 5.92	82.32 ± 1.89	27.71 ± 0.80	51.69 ± 0.98
		60	1381.68 ± 19.26	545.51 ± 9.21	404.44 ± 7.23	115.25 ± 2.38	34.56 ± 1.03	67.69 ± 1.29
	HDPE	20	1187.97 ± 17.07	242.29 ± 6.14	145.86 ± 3.82	28.84 ± 1.18	2.38 ± 0.22	9.44 ± 0.30
		40	1603.67 ± 21.03	427.99 ± 8.99	242.99 ± 5.87	57.66 ± 1.89	31.18 ± 0.90	13.73 ± 0.44
		60	1749.60 ± 21.28	546.04 ± 10.32	290.66 ± 6.42	66.26 ± 2.08	40.12 ± 1.12	13.82 ± 0.42
	AlPE	20	1004.55 ± 14.84	224.37 ± 5.60	134.46 ± 3.47	32.92 ± 1.21	13.70 ± 0.47	17.98 ± 0.43
		60	1697.22 ± 21.31	527.42 ± 9.90	283.72 ± 6.43	63.93 ± 2.09	45.43 ± 1.17	25.84 ± 0.68
1500	Al	20	364.44 ± 21.34	199.03 ± 7.84	186.60 ± 6.36	35.45 ± 1.40	41.92 ± 1.70	37.70 ± 1.12
		40	732.46 ± 30.57	387.42 ± 12.39	343.24 ± 9.71	79.09 ± 2.70	39.90 ± 1.37	67.76 ± 1.47
		60	1045.21 ± 36.13	639.89 ± 17.07	467.46 ± 11.90	127.29 ± 3.60	51.87 ± 1.73	101.30 ± 2.41
	HDPE	20	1359.57 ± 42.35	226.96 ± 11.20	156.05 ± 8.06	32.28 ± 2.47	14.88 ± 1.23	12.55 ± 0.88
		40	2159.73 ± 57.79	421.64 ± 19.52	296.56 ± 13.20	67.31 ± 3.74	17.36 ± 1.30	20.92 ± 1.21
		60	2587.83 ± 69.21	557.03 ± 26.75	376.98 ± 15.91	85.01 ± 4.41	38.80 ± 2.35	16.96 ± 0.91
	AlPE	20	1000.72 ± 32.67	273.83 ± 12.12	159.21 ± 7.57	37.08 ± 2.36	13.05 ± 0.92	21.23 ± 0.84
		60	2487.74 ± 67.85	605.97 ± 25.40	385.28 ± 16.38	81.39 ± 4.29	34.77 ± 2.19	36.14 ± 1.50

Table D.4: Upstream target effective dose for Si projectiles

E_{proj}	Target	z_{target}	Effective dose in $\left(\frac{pSv}{sr}\right) \cdot \left(\frac{cm^2}{sp}\right)$					
(MeV/n)	material	(g/cm^2)	10°	30°	45°	60°	80°	135°
400	Al	20	1077.30 ± 20.12	252.97 ± 7.60	148.26 ± 4.89	47.45 ± 1.78	16.93 ± 0.75	20.84 ± 0.62
		40	1143.74 ± 16.89	274.25 ± 7.12	179.04 ± 5.05	52.07 ± 1.65	15.21 ± 0.63	36.52 ± 0.81
		60	1136.72 ± 16.85	296.54 ± 7.59	183.90 ± 5.41	57.08 ± 1.80	13.46 ± 0.63	46.72 ± 1.03
	HDPE	20	1193.20 ± 10.51	256.25 ± 4.31	123.18 ± 2.56	38.90 ± 1.02	5.72 ± 0.25	11.00 ± 0.35
		40	1190.03 ± 8.80	286.73 ± 3.85	126.07 ± 2.33	31.30 ± 0.83	10.91 ± 0.34	10.26 ± 0.25
		60	1072.19 ± 6.87	250.82 ± 3.25	122.92 ± 2.19	33.67 ± 0.75	10.77 ± 0.31	10.19 ± 0.21
	AlPE	20	1064.85 ± 10.01	259.16 ± 4.47	137.25 ± 2.69	45.72 ± 1.23	9.10 ± 0.33	22.44 ± 0.48
		60	920.68 ± 6.02	252.92 ± 3.09	106.89 ± 2.03	29.98 ± 0.68	10.42 ± 0.31	23.48 ± 0.34
800	Al	20	1114.64 ± 35.42	430.42 ± 14.60	282.23 ± 9.74	68.12 ± 2.74	34.77 ± 1.42	38.15 ± 1.19
		40	2248.50 ± 44.60	750.34 ± 19.54	499.25 ± 13.68	141.45 ± 4.23	45.31 ± 1.82	80.96 ± 2.00
		60	2684.11 ± 45.64	912.10 ± 21.31	605.18 ± 15.37	183.53 ± 4.98	51.97 ± 2.01	101.80 ± 2.38
	HDPE	20	1787.03 ± 34.76	474.29 ± 13.75	308.97 ± 8.57	63.92 ± 2.55	21.48 ± 0.91	14.98 ± 0.60
		40	2796.83 ± 40.54	835.44 ± 17.64	457.87 ± 11.38	108.77 ± 3.62	34.96 ± 1.43	27.17 ± 1.01
		60	3265.80 ± 41.27	981.41 ± 19.03	479.10 ± 12.38	124.05 ± 4.27	36.41 ± 1.44	35.84 ± 1.52
	AlPE	20	1357.21 ± 30.20	448.74 ± 12.49	272.06 ± 8.19	61.76 ± 2.54	15.80 ± 0.85	30.48 ± 0.92
		60	3049.73 ± 38.56	868.59 ± 17.97	456.70 ± 11.76	118.22 ± 3.92	42.56 ± 1.55	45.15 ± 1.23
1500	Al	20	487.09 ± 57.55	389.88 ± 23.17	296.16 ± 16.54	67.58 ± 5.06	26.75 ± 1.74	46.44 ± 2.27
		40	948.79 ± 54.38	690.70 ± 35.53	531.21 ± 25.95	145.99 ± 7.34	83.61 ± 4.39	122.95 ± 4.98
		60	2097.72 ± 104.07	1282.52 ± 53.54	886.86 ± 35.76	233.34 ± 9.70	85.05 ± 4.43	168.91 ± 6.34
	HDPE	20	1369.67 ± 41.69	561.76 ± 21.32	325.46 ± 11.82	46.55 ± 2.86	21.94 ± 1.24	24.70 ± 1.17
		40	2795.25 ± 62.28	1013.45 ± 29.38	532.89 ± 17.06	96.72 ± 4.56	49.00 ± 2.19	30.86 ± 1.27
		60	3485.02 ± 71.57	1263.64 ± 33.25	698.87 ± 20.50	117.24 ± 5.40	65.95 ± 2.83	47.06 ± 2.06
	AlPE	20	1727.35 ± 40.04	504.17 ± 17.93	270.60 ± 10.67	40.26 ± 2.34	29.38 ± 1.29	42.34 ± 1.37
		60	4191.08 ± 73.58	1199.07 ± 33.78	653.71 ± 20.12	120.14 ± 5.56	64.82 ± 2.61	54.26 ± 1.81

Table D.5: Upstream target effective dose for Fe projectiles

E_{proj}	Target	z_{target}	Effective dose in $\left(\frac{pSv}{sr}\right) \cdot \left(\frac{cm^2}{sp}\right)$					
(MeV/n)	material	(g/cm^2)	10°	30°	45°	60°	80°	135°
400	Al	20	2105.29 ± 18.46	444.68 ± 7.65	257.25 ± 5.20	130.40 ± 3.14	35.22 ± 1.57	50.89 ± 0.95
		40	2022.45 ± 15.16	484.37 ± 6.47	287.42 ± 4.50	147.38 ± 2.76	35.64 ± 1.24	71.73 ± 0.96
		60	1701.90 ± 10.67	459.44 ± 4.83	258.86 ± 3.47	122.96 ± 2.08	34.76 ± 1.08	76.66 ± 0.79
	HDPE	20	2079.83 ± 15.79	280.64 ± 5.33	156.88 ± 3.54	32.40 ± 1.03	9.24 ± 0.49	7.70 ± 0.24
		40	2177.58 ± 14.97	335.41 ± 5.48	172.06 ± 3.66	33.45 ± 0.98	10.05 ± 0.40	11.87 ± 0.34
		60	2057.73 ± 12.25	341.85 ± 4.96	179.51 ± 3.21	39.47 ± 1.09	15.42 ± 0.49	13.31 ± 0.32
	AlPE	20	1475.26 ± 13.75	299.03 ± 5.49	142.98 ± 3.46	42.53 ± 1.27	9.38 ± 0.39	22.66 ± 0.51
		60	1581.58 ± 11.25	323.25 ± 5.06	161.69 ± 3.28	46.69 ± 1.26	17.19 ± 0.54	30.25 ± 0.47
800	Al	20	3866.67 ± 70.69	1268.38 ± 25.41	659.19 ± 16.34	340.98 ± 11.07	127.77 ± 4.72	120.72 ± 2.61
		40	5181.52 ± 58.67	1817.40 ± 26.27	1041.96 ± 17.55	566.15 ± 10.70	161.16 ± 4.96	223.47 ± 3.16
		60	4991.57 ± 51.02	1985.71 ± 23.73	1186.30 ± 16.72	576.67 ± 10.56	175.19 ± 4.92	283.11 ± 3.33
	HDPE	20	3742.66 ± 52.84	712.77 ± 18.24	392.98 ± 10.58	62.52 ± 2.83	30.01 ± 1.36	24.91 ± 0.99
		40	4674.62 ± 54.81	1056.68 ± 21.94	591.15 ± 14.65	91.85 ± 3.45	36.92 ± 1.47	31.45 ± 1.18
		60	5496.92 ± 56.35	1196.91 ± 22.89	638.14 ± 14.60	115.25 ± 3.69	52.16 ± 1.96	36.20 ± 1.22
	AlPE	20	3011.91 ± 40.76	873.49 ± 18.04	457.16 ± 11.00	66.32 ± 3.17	45.53 ± 1.63	52.33 ± 1.43
		60	3804.21 ± 48.78	1057.70 ± 21.00	451.61 ± 12.15	155.06 ± 4.27	30.57 ± 1.42	43.09 ± 1.12
1500	Al	20	811.51 ± 62.72	701.73 ± 48.32	581.03 ± 38.77	16.66 ± 2.08	101.00 ± 8.17	69.45 ± 4.76
		40	738.82 ± 61.78	1552.30 ± 82.03	1225.51 ± 61.29	97.06 ± 7.30	122.64 ± 8.50	160.51 ± 7.49
		60	1993.38 ± 154.51	2175.66 ± 98.90	1535.22 ± 69.15	289.47 ± 18.04	124.73 ± 8.44	238.88 ± 10.36
	HDPE	20	1040.22 ± 97.55	654.21 ± 40.66	515.81 ± 32.47	32.24 ± 3.66	26.88 ± 2.13	25.29 ± 2.53
		40	2590.58 ± 159.26	1444.01 ± 69.04	766.84 ± 43.19	112.22 ± 8.71	33.57 ± 2.72	54.33 ± 5.15
		60	4440.26 ± 185.68	1424.18 ± 71.05	1240.17 ± 56.12	133.60 ± 11.75	132.41 ± 10.95	50.07 ± 3.37
	AlPE	20	498.10 ± 37.66	641.83 ± 27.60	343.05 ± 15.53	60.49 ± 3.62	33.02 ± 1.96	47.32 ± 1.75
		60	2741.37 ± 82.67	1642.10 ± 43.54	1000.16 ± 27.49	184.43 ± 8.77	104.49 ± 4.22	77.87 ± 2.38

D.2 Total effective doses (without solid angle normalization)

To compare the prominence of neutron effective dose from the upstream target versus the effective dose from the downstream target (plus everywhere else), the solid angle normalization of the upstream target results can be undone. The tables featured in this section allow for comparison of the significance of each of these contributions. Note that the effective dose units are nSv.

Table D.6: Total effective dose for H projectiles at 10°

E_{proj} (MeV/n)	Target material	z_{target} (g/cm^2)	Effective dose in $\left(\frac{nSv \cdot cm^2}{s.p.}\right)$		
			Upstream target	Downstream target	Total
400	Al	20	56.23 ± 1.39	45.89 ± 1.42	102.12 ± 1.99
		40	98.07 ± 3.70	125.30 ± 7.93	223.37 ± 8.75
		60	114.22 ± 3.91	51.85 ± 4.09	166.08 ± 5.66
	HDPE	20	69.69 ± 2.08	46.55 ± 2.33	116.24 ± 3.12
		40	101.74 ± 2.39	38.81 ± 2.34	140.56 ± 3.35
		60	123.21 ± 2.16	20.67 ± 1.41	143.87 ± 2.57
	AlPE	20	56.51 ± 1.61	36.89 ± 1.59	93.40 ± 2.26
		60	91.86 ± 1.75	18.27 ± 1.01	110.13 ± 2.02
800	Al	20	96.82 ± 5.55	368.15 ± 6.93	464.97 ± 8.88
		40	139.95 ± 5.60	-	139.95 ± 5.60
		60	185.26 ± 4.89	-	185.26 ± 4.89
	HDPE	20	137.67 ± 3.63	107.01 ± 3.85	244.69 ± 5.29
		40	202.84 ± 4.33	101.71 ± 3.96	304.55 ± 5.87
		60	230.66 ± 4.35	78.55 ± 2.61	309.20 ± 5.08
	AlPE	20	99.24 ± 2.98	84.52 ± 2.15	183.75 ± 3.67
		60	192.37 ± 3.66	70.38 ± 2.28	262.76 ± 4.31
2500	Al	20	114.88 ± 6.25	723.19 ± 10.62	838.07 ± 12.32
		40	164.63 ± 7.06	666.69 ± 11.19	831.32 ± 13.23
		60	640.07 ± 11.79	608.11 ± 10.54	1248.18 ± 15.82
	HDPE	20	85.94 ± 4.19	256.51 ± 4.18	342.45 ± 5.91
		40	168.31 ± 5.34	264.05 ± 4.37	432.36 ± 6.91
		60	186.54 ± 5.75	276.23 ± 5.44	462.77 ± 7.92
	AlPE	20	91.55 ± 5.11	199.82 ± 3.24	291.38 ± 6.05
		60	165.41 ± 7.55	205.51 ± 5.15	370.92 ± 9.14

Table D.7: Total effective dose for He projectiles at 10°

E_{proj} (MeV/n)	Target material	z_{target} (g/cm^2)	Effective dose in $\left(\frac{nSv \cdot cm^2}{s.p.}\right)$		
			Upstream target	Downstream target	Total
400	Al	20	325.75 ± 9.05	712.74 ± 16.79	1038.49 ± 19.08
		40	639.38 ± 10.65	555.32 ± 16.54	1194.70 ± 19.67
		60	735.72 ± 10.40	418.47 ± 13.45	1154.18 ± 17.00
	HDPE	20	388.71 ± 5.99	173.97 ± 6.56	562.68 ± 8.88
		40	644.98 ± 7.50	156.20 ± 5.80	801.17 ± 9.48
		60	767.09 ± 7.90	136.32 ± 6.35	903.41 ± 10.13
	AlPE	20	354.22 ± 4.80	152.24 ± 4.41	506.46 ± 6.51
		60	674.39 ± 6.11	113.28 ± 3.87	787.67 ± 7.24
800	Al	20	258.74 ± 12.27	1012.16 ± 30.40	1270.90 ± 32.78
		40	436.24 ± 16.23	922.11 ± 30.35	1358.35 ± 34.41
		60	685.39 ± 17.60	785.86 ± 26.72	1471.25 ± 32.00
	HDPE	20	667.93 ± 13.26	409.77 ± 12.06	1077.70 ± 17.92
		40	1070.73 ± 16.93	439.73 ± 16.22	1510.47 ± 23.44
		60	1209.18 ± 18.34	420.26 ± 17.21	1629.44 ± 25.15
	AlPE	20	491.56 ± 7.79	314.47 ± 6.00	806.03 ± 9.83
		60	1001.77 ± 11.44	293.59 ± 7.79	1295.36 ± 13.84
1500	Al	20	181.53 ± 10.01	1921.65 ± 30.71	2103.18 ± 32.29
		40	402.85 ± 18.24	1757.72 ± 31.67	2160.57 ± 36.54
		60	595.73 ± 20.22	1638.31 ± 33.20	2234.04 ± 38.87
	HDPE	20	154.75 ± 10.99	658.97 ± 20.24	813.72 ± 23.03
		40	325.21 ± 17.05	690.39 ± 23.60	1015.60 ± 29.11
		60	461.15 ± 17.96	679.53 ± 19.80	1140.68 ± 26.73
	AlPE	20	370.85 ± 9.25	512.39 ± 9.14	883.24 ± 13.00
		60	786.29 ± 18.09	552.68 ± 12.59	1338.97 ± 22.04

Table D.8: Total effective dose for C projectiles at 10°

E_{proj} (MeV/n)	Target material	z_{target} (g/cm^2)	Effective dose in $\left(\frac{nSv \cdot cm^2}{s.p.}\right)$		
			Upstream target	Downstream target	Total
400	Al	20	875.46 ± 11.32	732.02 ± 18.66	1607.48 ± 21.83
		40	1281.37 ± 11.69	371.51 ± 12.78	1652.88 ± 17.32
		60	1204.95 ± 9.58	272.14 ± 9.86	1477.09 ± 13.75
	HDPE	20	1088.93 ± 12.71	260.64 ± 9.95	1349.57 ± 16.14
		40	1283.45 ± 11.46	179.73 ± 7.48	1463.18 ± 13.69
		60	1172.23 ± 8.40	144.66 ± 5.13	1316.89 ± 9.85
	AlPE	20	941.60 ± 11.33	266.36 ± 8.97	1207.96 ± 14.46
		60	1117.83 ± 8.05	130.56 ± 4.69	1248.39 ± 9.32
800	Al	20	596.25 ± 17.98	2435.97 ± 39.55	3032.21 ± 43.44
		40	1372.90 ± 23.67	2044.13 ± 33.93	3417.04 ± 41.37
		60	1840.34 ± 25.66	1761.22 ± 31.74	3601.56 ± 40.82
	HDPE	20	1578.45 ± 22.68	765.95 ± 19.16	2344.40 ± 29.69
		40	2105.23 ± 27.61	757.64 ± 19.53	2862.87 ± 33.82
		60	2241.06 ± 27.26	717.96 ± 18.59	2959.02 ± 32.99
	AlPE	20	1355.03 ± 20.02	724.91 ± 17.73	2079.95 ± 26.74
		60	2210.75 ± 27.75	706.80 ± 20.14	2917.55 ± 34.29
1500	Al	20	486.93 ± 28.52	4161.85 ± 69.42	4648.79 ± 75.05
		40	979.67 ± 40.89	3808.89 ± 65.32	4788.56 ± 77.06
		60	1397.02 ± 48.29	3526.31 ± 71.46	4923.34 ± 86.25
	HDPE	20	1809.45 ± 56.36	1427.17 ± 52.52	3236.61 ± 77.04
		40	2835.48 ± 75.87	1611.85 ± 69.26	4447.33 ± 102.73
		60	3346.60 ± 89.50	1389.64 ± 58.18	4736.24 ± 106.75
	AlPE	20	1347.58 ± 44.00	1401.90 ± 43.56	2749.48 ± 61.91
		60	3245.17 ± 88.50	1326.33 ± 53.78	4571.50 ± 103.57

Table D.9: Total effective dose for Si projectiles at 10°

E_{proj} (MeV/n)	Target material	z_{target} (g/cm^2)	Effective dose in $\left(\frac{nSv \cdot cm^2}{s.p.}\right)$		
			Upstream target	Downstream target	Total
400	Al	20	1430.44 ± 26.71	480.27 ± 29.78	1910.71 ± 40.01
		40	1492.76 ± 22.04	340.87 ± 18.20	1833.63 ± 28.58
		60	1460.82 ± 21.65	277.33 ± 17.13	1738.15 ± 27.60
	HDPE	20	1557.74 ± 13.72	218.96 ± 7.45	1776.70 ± 15.61
		40	1476.80 ± 10.93	173.32 ± 5.73	1650.13 ± 12.34
		60	1261.98 ± 8.09	143.09 ± 4.75	1405.08 ± 9.38
	AlPE	20	1418.48 ± 13.34	201.04 ± 6.46	1619.53 ± 14.82
		60	1096.57 ± 7.16	122.76 ± 4.16	1219.32 ± 8.29
800	Al	20	1488.84 ± 47.31	3429.59 ± 89.34	4918.43 ± 101.09
		40	2996.82 ± 59.44	2302.29 ± 80.43	5299.11 ± 100.01
		60	3548.17 ± 60.33	1899.25 ± 72.72	5447.42 ± 94.49
	HDPE	20	2376.92 ± 46.24	1335.11 ± 37.68	3712.04 ± 59.64
		40	3644.58 ± 52.83	1158.22 ± 38.05	4802.80 ± 65.10
		60	4088.97 ± 51.68	1081.70 ± 34.57	5170.67 ± 62.17
	AlPE	20	1833.42 ± 40.79	1219.09 ± 38.92	3052.51 ± 56.38
		60	3880.68 ± 49.06	995.44 ± 34.44	4876.12 ± 59.94
1500	Al	20	651.59 ± 76.99	7643.82 ± 337.42	8295.41 ± 346.09
		40	1270.96 ± 72.84	6413.95 ± 248.32	7684.92 ± 258.79
		60	2811.13 ± 139.46	5917.39 ± 262.10	8728.53 ± 296.89
	HDPE	20	1828.28 ± 55.65	2664.38 ± 66.64	4492.67 ± 86.82
		40	3684.57 ± 82.09	2804.55 ± 69.71	6489.12 ± 107.70
		60	4500.87 ± 92.43	2654.22 ± 69.10	7155.08 ± 115.41
	AlPE	20	2329.83 ± 54.01	2501.05 ± 63.86	4830.87 ± 83.64
		60	5473.46 ± 96.09	2557.55 ± 68.96	8031.00 ± 118.28

Table D.10: Total effective dose for Fe projectiles at 10°

E_{proj} (MeV/n)	Target material	z_{target} (g/cm^2)	Effective dose in $\left(\frac{nSv \cdot cm^2}{s.p.}\right)$		
			Upstream target	Downstream target	Total
400	Al	20	2819.51 ± 24.72	857.04 ± 28.61	3676.55 ± 37.81
		40	2708.57 ± 20.30	660.08 ± 34.17	3368.65 ± 39.75
		60	2279.27 ± 14.29	503.83 ± 14.06	2783.10 ± 20.04
	HDPE	20	2669.52 ± 20.27	362.95 ± 12.29	3032.47 ± 23.70
		40	2649.57 ± 18.22	303.66 ± 8.82	2953.22 ± 20.24
		60	2374.13 ± 14.14	267.17 ± 9.63	2641.30 ± 17.11
	AlPE	20	1950.31 ± 18.18	271.16 ± 9.15	2221.47 ± 20.35
		60	1860.53 ± 13.24	202.61 ± 7.49	2063.14 ± 15.21
800	Al	20	5178.43 ± 94.67	5777.49 ± 167.58	10955.93 ± 192.48
		40	6939.35 ± 78.58	4030.29 ± 88.03	10969.64 ± 118.00
		60	6684.96 ± 68.32	3687.85 ± 80.47	10372.81 ± 105.56
	HDPE	20	4963.79 ± 70.08	1810.53 ± 54.02	6774.33 ± 88.48
		40	5923.83 ± 69.46	1674.85 ± 48.19	7598.68 ± 84.54
		60	6640.57 ± 68.08	1600.15 ± 61.62	8240.73 ± 91.82
	AlPE	20	4071.28 ± 55.10	1115.24 ± 35.97	5186.52 ± 65.81
		60	4691.82 ± 60.16	1426.18 ± 45.21	6118.00 ± 75.26
1500	Al	20	1088.22 ± 84.11	-	1088.22 ± 84.11
		40	994.72 ± 83.17	-	994.72 ± 83.17
		60	2682.11 ± 207.89	-	2682.11 ± 207.89
	HDPE	20	1399.92 ± 131.28	4677.28 ± 379.13	6077.20 ± 401.21
		40	3504.94 ± 215.47	4525.79 ± 312.93	8030.73 ± 379.94
		60	5844.98 ± 244.42	4084.48 ± 274.06	9929.46 ± 367.22
	AlPE	20	671.89 ± 50.80	3277.67 ± 86.57	3949.56 ± 100.37
		60	3700.96 ± 111.61	3289.26 ± 82.96	6990.22 ± 139.07

Table D.11: Total effective dose for H projectiles at 30°

E_{proj} (MeV/n)	Target material	z_{target} (g/cm^2)	Effective dose in $\left(\frac{nSv \cdot cm^2}{s.p.}\right)$		
			Upstream target	Downstream target	Total
400	Al	20	29.09 ± 0.69	11.82 ± 0.58	40.91 ± 0.90
		40	72.24 ± 1.76	-	72.24 ± 1.76
		60	81.07 ± 2.05	-	81.07 ± 2.05
	HDPE	20	25.99 ± 0.90	-	25.99 ± 0.90
		40	39.37 ± 1.16	-	39.37 ± 1.16
		60	42.84 ± 1.22	-	42.84 ± 1.22
	AlPE	20	26.64 ± 0.82	5.52 ± 0.46	32.16 ± 0.94
		60	44.82 ± 1.08	-	44.82 ± 1.08
800	Al	20	39.36 ± 1.79	-	39.36 ± 1.79
		40	77.02 ± 2.03	-	77.02 ± 2.03
		60	96.45 ± 2.09	-	96.45 ± 2.09
	HDPE	20	32.25 ± 1.20	29.25 ± 1.44	61.50 ± 1.87
		40	50.19 ± 1.62	29.39 ± 1.59	79.58 ± 2.27
		60	56.73 ± 1.75	33.54 ± 1.68	90.26 ± 2.43
	AlPE	20	31.56 ± 1.06	26.71 ± 1.18	58.27 ± 1.58
		60	62.57 ± 1.59	28.62 ± 1.47	91.19 ± 2.16
2500	Al	20	40.57 ± 1.80	121.52 ± 3.56	162.08 ± 3.99
		40	85.73 ± 2.64	117.57 ± 4.00	203.30 ± 4.79
		60	290.42 ± 5.83	111.77 ± 3.10	402.19 ± 6.60
	HDPE	20	37.22 ± 1.42	79.04 ± 2.78	116.26 ± 3.12
		40	73.08 ± 2.10	86.99 ± 2.60	160.07 ± 3.34
		60	90.97 ± 2.57	95.90 ± 2.89	186.87 ± 3.87
	AlPE	20	38.35 ± 1.63	72.91 ± 2.70	111.26 ± 3.15
		60	89.45 ± 3.21	92.29 ± 4.28	181.74 ± 5.35

Table D.12: Total effective dose for He projectiles at 30°

E_{proj} (MeV/n)	Target material	z_{target} (g/cm^2)	Effective dose in $\left(\frac{nSv \cdot cm^2}{s.p.}\right)$		
			Upstream target	Downstream target	Total
400	Al	20	133.66 ± 3.14	134.16 ± 3.65	267.82 ± 4.81
		40	203.24 ± 4.92	156.35 ± 10.14	359.60 ± 11.26
		60	272.35 ± 5.13	110.94 ± 6.16	383.28 ± 8.01
	HDPE	20	102.67 ± 2.42	46.17 ± 2.45	148.84 ± 3.44
		40	158.14 ± 3.29	40.45 ± 2.16	198.59 ± 3.94
		60	174.17 ± 3.49	42.07 ± 2.46	216.24 ± 4.27
	AlPE	20	107.35 ± 2.18	50.96 ± 2.60	158.31 ± 3.40
		60	191.16 ± 3.00	49.76 ± 2.59	240.92 ± 3.97
800	Al	20	92.90 ± 3.91	156.14 ± 7.76	249.04 ± 8.69
		40	212.92 ± 6.49	147.79 ± 8.26	360.71 ± 10.50
		60	269.54 ± 7.23	117.70 ± 6.99	387.24 ± 10.05
	HDPE	20	137.50 ± 4.85	121.82 ± 5.34	259.33 ± 7.21
		40	252.16 ± 7.01	146.24 ± 6.12	398.40 ± 9.31
		60	308.02 ± 8.02	143.72 ± 6.67	451.74 ± 10.43
	AlPE	20	123.63 ± 2.89	111.27 ± 4.09	234.91 ± 5.01
		60	261.59 ± 5.23	133.89 ± 5.48	395.48 ± 7.57
1500	Al	20	138.87 ± 5.16	271.74 ± 9.23	410.61 ± 10.57
		40	257.10 ± 8.71	293.13 ± 8.23	550.23 ± 11.99
		60	345.00 ± 10.13	326.06 ± 11.16	671.06 ± 15.07
	HDPE	20	149.67 ± 5.50	182.53 ± 6.84	332.20 ± 8.78
		40	248.49 ± 7.97	219.64 ± 8.95	468.13 ± 11.99
		60	309.59 ± 9.74	240.33 ± 9.51	549.91 ± 13.61
	AlPE	20	151.14 ± 4.31	188.92 ± 6.37	340.05 ± 7.69
		60	330.73 ± 8.44	247.01 ± 9.02	577.74 ± 12.35

Table D.13: Total effective dose for C projectiles at 30°

E_{proj} (MeV/n)	Target material	z_{target} (g/cm^2)	Effective dose in $\left(\frac{nSv \cdot cm^2}{s.p.}\right)$		
			Upstream target	Downstream target	Total
400	Al	20	238.26 ± 4.57	114.24 ± 4.95	352.50 ± 6.73
		40	327.32 ± 5.04	84.70 ± 5.46	412.02 ± 7.43
		60	333.80 ± 4.45	75.07 ± 5.67	408.87 ± 7.21
	HDPE	20	283.04 ± 5.57	84.67 ± 4.11	367.71 ± 6.92
		40	355.21 ± 5.56	82.78 ± 4.35	437.99 ± 7.06
		60	321.68 ± 4.19	79.24 ± 3.75	400.92 ± 5.62
	AlPE	20	268.48 ± 5.04	77.53 ± 4.09	346.01 ± 6.49
		60	304.36 ± 4.03	73.19 ± 3.87	377.55 ± 5.59
800	Al	20	279.30 ± 7.12	393.01 ± 12.59	672.31 ± 14.46
		40	545.50 ± 10.48	382.53 ± 13.24	928.03 ± 16.89
		60	731.85 ± 12.36	367.98 ± 13.88	1099.82 ± 18.58
	HDPE	20	323.48 ± 8.20	293.85 ± 11.26	617.33 ± 13.93
		40	571.10 ± 12.00	312.51 ± 12.86	883.61 ± 17.59
		60	720.44 ± 13.62	323.66 ± 12.15	1044.10 ± 18.25
	AlPE	20	300.83 ± 7.51	289.61 ± 10.94	590.44 ± 13.27
		60	700.31 ± 13.15	325.36 ± 14.03	1025.66 ± 19.23
1500	Al	20	266.76 ± 10.51	665.79 ± 21.14	932.55 ± 23.61
		40	519.91 ± 16.62	716.66 ± 21.08	1236.57 ± 26.84
		60	859.04 ± 22.92	727.89 ± 29.29	1586.94 ± 37.19
	HDPE	20	302.89 ± 14.94	434.65 ± 24.55	737.54 ± 28.74
		40	563.73 ± 26.10	423.33 ± 27.56	987.06 ± 37.96
		60	739.21 ± 35.50	493.78 ± 44.79	1233.00 ± 57.15
	AlPE	20	366.17 ± 16.20	516.41 ± 28.68	882.59 ± 32.94
		60	799.48 ± 33.51	504.46 ± 35.11	1303.93 ± 48.54

Table D.14: Total effective dose for Si projectiles at 30°

E_{proj} (MeV/n)	Target material	z_{target} (g/cm^2)	Effective dose in $\left(\frac{nSv \cdot cm^2}{s.p.}\right)$		
			Upstream target	Downstream target	Total
400	Al	20	338.11 ± 10.16	-	338.11 ± 10.16
		40	362.28 ± 9.40	-	362.28 ± 9.40
		60	387.57 ± 9.93	-	387.57 ± 9.93
	HDPE	20	337.74 ± 5.68	90.14 ± 5.17	427.88 ± 7.69
		40	364.42 ± 4.90	82.53 ± 4.48	446.95 ± 6.64
		60	305.88 ± 3.96	83.45 ± 3.44	389.33 ± 5.25
	AlPE	20	345.55 ± 5.96	83.24 ± 4.08	428.79 ± 7.22
		60	308.64 ± 3.77	76.94 ± 3.08	385.58 ± 4.87
800	Al	20	577.51 ± 19.59	589.04 ± 29.56	1166.54 ± 35.47
		40	1007.69 ± 26.24	515.88 ± 28.49	1523.57 ± 38.73
		60	1219.39 ± 28.49	451.18 ± 21.49	1670.57 ± 35.69
	HDPE	20	635.24 ± 18.41	504.97 ± 24.97	1140.21 ± 31.02
		40	1116.93 ± 23.58	509.20 ± 25.16	1626.13 ± 34.48
		60	1282.69 ± 24.88	500.95 ± 24.62	1783.64 ± 35.00
	AlPE	20	603.53 ± 16.80	440.76 ± 23.24	1044.29 ± 28.67
		60	1142.64 ± 23.64	481.33 ± 22.87	1623.97 ± 32.89
1500	Al	20	523.01 ± 31.08	567.76 ± 52.32	1090.76 ± 60.86
		40	928.29 ± 47.76	551.93 ± 43.73	1480.21 ± 64.76
		60	1726.29 ± 72.06	581.58 ± 64.86	2307.87 ± 96.95
	HDPE	20	752.95 ± 28.58	1055.90 ± 46.26	1808.84 ± 54.38
		40	1361.12 ± 39.46	1132.25 ± 42.45	2493.37 ± 57.96
		60	1695.29 ± 44.61	1186.37 ± 49.60	2881.66 ± 66.70
	AlPE	20	676.62 ± 24.07	937.67 ± 39.79	1614.29 ± 46.50
		60	1610.10 ± 45.36	1248.80 ± 55.34	2858.90 ± 71.56

Table D.15: Total effective dose for Fe projectiles at 30°

E_{proj} (MeV/n)	Target material	z_{target} (g/cm^2)	Effective dose in $\left(\frac{nSv \cdot cm^2}{s.p.}\right)$		
			Upstream target	Downstream target	Total
400	Al	20	595.54 ± 10.24	273.09 ± 11.67	868.62 ± 15.53
		40	648.70 ± 8.67	223.31 ± 10.27	872.01 ± 13.44
		60	615.31 ± 6.47	170.52 ± 8.47	785.83 ± 10.66
	HDPE	20	366.27 ± 6.96	103.46 ± 5.03	469.73 ± 8.58
		40	421.47 ± 6.88	105.40 ± 4.47	526.87 ± 8.21
		60	413.13 ± 5.99	109.19 ± 4.02	522.32 ± 7.22
	AlPE	20	396.18 ± 7.27	65.07 ± 5.45	461.25 ± 9.09
		60	390.81 ± 6.11	120.65 ± 5.85	511.46 ± 8.46
800	Al	20	1698.68 ± 34.03	1138.99 ± 37.22	2837.67 ± 50.44
		40	2433.95 ± 35.19	1086.63 ± 42.78	3520.58 ± 55.39
		60	2659.37 ± 31.78	952.29 ± 35.15	3611.65 ± 47.38
	HDPE	20	961.13 ± 24.60	530.11 ± 24.64	1491.24 ± 34.82
		40	1389.21 ± 28.85	552.38 ± 25.65	1941.59 ± 38.60
		60	1528.17 ± 29.22	562.17 ± 21.80	2090.34 ± 36.46
	AlPE	20	1178.70 ± 24.35	520.81 ± 27.73	1699.51 ± 36.90
		60	1350.17 ± 26.81	554.56 ± 24.95	1904.73 ± 36.62
1500	Al	20	942.13 ± 64.87	675.18 ± 55.31	1617.31 ± 85.25
		40	2089.78 ± 110.44	-	2089.78 ± 110.44
		60	2935.53 ± 133.44	701.87 ± 121.04	3637.40 ± 180.16
	HDPE	20	885.77 ± 55.05	-	885.77 ± 55.05
		40	1971.25 ± 94.25	-	1971.25 ± 94.25
		60	1929.91 ± 96.27	-	1929.91 ± 96.27
	AlPE	20	863.25 ± 37.12	1225.26 ± 55.40	2088.50 ± 66.69
		60	2227.04 ± 59.05	1439.00 ± 66.31	3666.03 ± 88.79

Table D.16: Total effective dose for H projectiles at 45°

E_{proj} (MeV/n)	Target material	z_{target} (g/cm^2)	Effective dose in $\left(\frac{nSv \cdot cm^2}{s.p.}\right)$		
			Upstream target	Downstream target	Total
400	Al	20	21.40 ± 0.48	-	21.40 ± 0.48
		40	38.55 ± 1.31	-	38.55 ± 1.31
		60	56.62 ± 1.52	-	56.62 ± 1.52
	HDPE	20	16.34 ± 0.59	-	16.34 ± 0.59
		40	18.85 ± 0.72	-	18.85 ± 0.72
		60	22.63 ± 0.69	-	22.63 ± 0.69
	AlPE	20	16.31 ± 0.56	-	16.31 ± 0.56
		60	22.31 ± 0.70	-	22.31 ± 0.70
800	Al	20	25.40 ± 1.35	-	25.40 ± 1.35
		40	47.76 ± 1.49	-	47.76 ± 1.49
		60	57.54 ± 1.62	-	57.54 ± 1.62
	HDPE	20	20.30 ± 0.78	16.37 ± 1.42	36.67 ± 1.62
		40	29.73 ± 1.07	19.51 ± 1.69	49.24 ± 2.00
		60	34.40 ± 1.20	19.25 ± 1.93	53.65 ± 2.28
	AlPE	20	20.16 ± 0.67	7.99 ± 0.75	28.14 ± 1.01
		60	34.55 ± 0.99	7.96 ± 0.81	42.52 ± 1.28
2500	Al	20	27.64 ± 1.07	82.80 ± 3.82	110.44 ± 3.97
		40	61.94 ± 1.86	108.16 ± 7.95	170.10 ± 8.16
		60	234.14 ± 5.39	87.19 ± 2.16	321.33 ± 5.81
	HDPE	20	27.65 ± 0.95	53.52 ± 1.59	81.17 ± 1.85
		40	47.14 ± 1.57	78.07 ± 3.48	125.21 ± 3.82
		60	63.25 ± 1.94	77.86 ± 3.81	141.11 ± 4.28
	AlPE	20	30.76 ± 1.10	35.22 ± 1.86	65.99 ± 2.16
		60	59.15 ± 2.05	54.93 ± 3.07	114.08 ± 3.69

Table D.17: Total effective dose for He projectiles at 45°

E_{proj} (MeV/n)	Target material	z_{target} (g/cm^2)	Effective dose in $\left(\frac{nSv \cdot cm^2}{s.p.}\right)$		
			Upstream target	Downstream target	Total
400	Al	20	76.28 ± 2.07	59.94 ± 2.71	136.22 ± 3.41
		40	154.50 ± 3.52	47.83 ± 3.69	202.33 ± 5.10
		60	160.10 ± 3.64	31.91 ± 5.98	192.01 ± 7.00
	HDPE	20	61.03 ± 1.65	21.37 ± 1.38	82.40 ± 2.15
		40	97.87 ± 2.29	14.23 ± 2.48	112.10 ± 3.37
		60	97.30 ± 2.31	17.38 ± 1.90	114.68 ± 2.99
	AlPE	20	62.17 ± 1.42	14.24 ± 0.83	76.41 ± 1.65
		60	93.84 ± 2.00	24.38 ± 1.40	118.22 ± 2.45
800	Al	20	82.74 ± 3.50	103.36 ± 4.05	186.10 ± 5.35
		40	140.82 ± 4.89	101.33 ± 8.89	242.16 ± 10.15
		60	195.77 ± 6.08	102.67 ± 16.49	298.44 ± 17.58
	HDPE	20	86.33 ± 3.01	64.85 ± 3.95	151.18 ± 4.97
		40	147.04 ± 4.51	78.95 ± 5.22	226.00 ± 6.90
		60	175.14 ± 5.27	103.29 ± 5.79	278.42 ± 7.83
	AlPE	20	74.06 ± 1.88	58.03 ± 2.80	132.09 ± 3.37
		60	139.09 ± 3.46	86.30 ± 4.31	225.40 ± 5.52
1500	Al	20	110.76 ± 3.95	201.03 ± 8.16	311.79 ± 9.06
		40	234.03 ± 5.99	213.74 ± 7.22	447.78 ± 9.38
		60	322.62 ± 7.74	201.56 ± 19.16	524.18 ± 20.66
	HDPE	20	98.30 ± 3.77	129.02 ± 6.48	227.32 ± 7.50
		40	149.09 ± 5.81	151.64 ± 7.64	300.73 ± 9.60
		60	176.87 ± 5.93	190.42 ± 9.97	367.29 ± 11.60
	AlPE	20	84.73 ± 2.57	98.87 ± 4.17	183.59 ± 4.90
		60	173.43 ± 4.98	136.05 ± 6.42	309.47 ± 8.13

Table D.18: Total effective dose for C projectiles at 45°

E_{proj} (MeV/n)	Target material	z_{target} (g/cm^2)	Effective dose in $\left(\frac{nSv \cdot cm^2}{s.p.}\right)$		
			Upstream target	Downstream target	Total
400	Al	20	146.82 ± 3.31	84.83 ± 3.66	231.65 ± 4.94
		40	208.02 ± 3.74	37.57 ± 4.39	245.60 ± 5.77
		60	214.42 ± 3.39	40.32 ± 3.01	254.74 ± 4.53
	HDPE	20	143.77 ± 3.59	33.55 ± 4.33	177.32 ± 5.62
		40	178.75 ± 3.74	36.47 ± 3.03	215.22 ± 4.81
		60	149.76 ± 2.79	63.07 ± 3.78	212.84 ± 4.70
	AlPE	20	151.38 ± 3.44	30.48 ± 3.65	181.85 ± 5.02
		60	142.31 ± 2.70	59.34 ± 3.34	201.65 ± 4.30
800	Al	20	205.76 ± 5.21	220.29 ± 6.41	426.05 ± 8.26
		40	389.27 ± 7.93	233.48 ± 8.07	622.75 ± 11.32
		60	542.75 ± 9.71	255.30 ± 8.98	798.05 ± 13.22
	HDPE	20	195.36 ± 5.12	157.55 ± 7.78	352.91 ± 9.31
		40	325.69 ± 7.87	177.62 ± 9.39	503.31 ± 12.25
		60	387.75 ± 8.57	207.65 ± 11.31	595.40 ± 14.19
	AlPE	20	180.42 ± 4.65	134.18 ± 6.62	314.60 ± 8.09
		60	378.87 ± 8.58	190.49 ± 10.08	569.36 ± 13.24
1500	Al	20	250.01 ± 8.52	377.28 ± 13.37	627.30 ± 15.86
		40	460.39 ± 13.02	441.56 ± 17.16	901.96 ± 21.54
		60	627.30 ± 15.96	483.27 ± 18.83	1110.57 ± 24.69
	HDPE	20	209.07 ± 10.79	-	209.07 ± 10.79
		40	398.00 ± 17.72	-	398.00 ± 17.72
		60	503.87 ± 21.27	-	503.87 ± 21.27
	AlPE	20	213.35 ± 10.14	-	213.35 ± 10.14
		60	512.72 ± 21.80	-	512.72 ± 21.80

Table D.19: Total effective dose for Si projectiles at 45°

E_{proj} (MeV/n)	Target material	z_{target} (g/cm^2)	Effective dose in $\left(\frac{nSv \cdot cm^2}{s.p.}\right)$		
			Upstream target	Downstream target	Total
400	Al	20	198.39 ± 6.55	-	198.39 ± 6.55
		40	237.52 ± 6.69	-	237.52 ± 6.69
		60	242.49 ± 7.13	-	242.49 ± 7.13
	HDPE	20	163.80 ± 3.41	-	163.80 ± 3.41
		40	163.43 ± 3.03	34.62 ± 2.69	198.05 ± 4.05
		60	154.59 ± 2.75	55.25 ± 2.64	209.85 ± 3.81
	AlPE	20	183.68 ± 3.59	19.20 ± 3.63	202.88 ± 5.11
		60	133.74 ± 2.54	51.66 ± 2.53	185.41 ± 3.58
800	Al	20	378.40 ± 13.05	360.53 ± 48.47	738.93 ± 50.20
		40	670.72 ± 18.38	305.59 ± 37.42	976.31 ± 41.69
		60	811.51 ± 20.61	286.05 ± 24.79	1097.56 ± 32.24
	HDPE	20	415.42 ± 11.52	170.65 ± 11.74	586.07 ± 16.45
		40	616.90 ± 15.33	169.72 ± 9.67	786.62 ± 18.12
		60	637.61 ± 16.48	313.82 ± 16.82	951.43 ± 23.55
	AlPE	20	366.00 ± 11.02	130.20 ± 12.21	496.20 ± 16.45
		60	608.54 ± 15.66	215.84 ± 12.07	824.37 ± 19.77
1500	Al	20	397.14 ± 22.18	-	397.14 ± 22.18
		40	713.49 ± 34.86	-	713.49 ± 34.86
		60	1192.55 ± 48.09	-	1192.55 ± 48.09
	HDPE	20	437.51 ± 15.89	546.84 ± 32.19	984.35 ± 35.90
		40	719.57 ± 23.03	661.50 ± 35.85	1381.07 ± 42.61
		60	942.79 ± 27.65	669.67 ± 35.09	1612.46 ± 44.67
	AlPE	20	363.66 ± 14.33	490.88 ± 26.33	854.53 ± 29.98
		60	882.42 ± 27.16	675.87 ± 34.75	1558.30 ± 44.10

Table D.20: Total effective dose for Fe projectiles at 45°

E_{proj} (MeV/n)	Target material	z_{target} (g/cm^2)	Effective dose in $\left(\frac{nSv \cdot cm^2}{s.p.}\right)$		
			Upstream target	Downstream target	Total
400	Al	20	344.52 ± 6.96	112.79 ± 6.82	457.31 ± 9.74
		40	384.93 ± 6.02	106.56 ± 5.72	491.49 ± 8.31
		60	346.67 ± 4.65	102.80 ± 5.20	449.47 ± 6.97
	HDPE	20	206.72 ± 4.67	37.56 ± 4.38	244.28 ± 6.40
		40	221.07 ± 4.71	68.77 ± 5.14	289.84 ± 6.97
		60	223.68 ± 3.99	94.44 ± 4.35	318.13 ± 5.91
	AlPE	20	190.31 ± 4.60	-	190.31 ± 4.60
		60	200.75 ± 4.07	123.76 ± 12.30	324.52 ± 12.95
800	Al	20	882.82 ± 21.89	568.54 ± 24.16	1451.37 ± 32.60
		40	1395.44 ± 23.50	536.69 ± 22.93	1932.14 ± 32.84
		60	1588.75 ± 22.39	548.69 ± 23.26	2137.43 ± 32.29
	HDPE	20	531.58 ± 14.31	206.98 ± 22.26	738.56 ± 26.47
		40	789.58 ± 19.57	418.81 ± 18.99	1208.39 ± 27.27
		60	835.48 ± 19.11	465.86 ± 17.55	1301.34 ± 25.95
	AlPE	20	617.57 ± 14.87	298.23 ± 40.11	915.80 ± 42.78
		60	589.71 ± 15.87	500.68 ± 40.05	1090.40 ± 43.08
1500	Al	20	779.54 ± 52.02	-	779.54 ± 52.02
		40	1647.68 ± 82.41	-	1647.68 ± 82.41
		60	2066.14 ± 93.07	-	2066.14 ± 93.07
	HDPE	20	696.91 ± 43.87	-	696.91 ± 43.87
		40	1042.92 ± 58.74	-	1042.92 ± 58.74
		60	1683.07 ± 76.17	-	1683.07 ± 76.17
	AlPE	20	461.72 ± 20.91	529.06 ± 33.10	990.78 ± 39.15
		60	1356.93 ± 37.30	724.47 ± 48.87	2081.40 ± 61.48

Table D.21: Total effective dose for H projectiles at 60°

E_{proj} (MeV/n)	Target material	z_{target} (g/cm^2)	Effective dose in $\left(\frac{nSv \cdot cm^2}{s.p.}\right)$		
			Upstream target	Downstream target	Total
400	Al	20	15.05 ± 0.34	2.79 ± 0.24	17.83 ± 0.42
		40	39.38 ± 1.18	-	39.38 ± 1.18
		60	45.18 ± 1.44	-	45.18 ± 1.44
	HDPE	20	5.75 ± 0.27	-	5.75 ± 0.27
		40	8.31 ± 0.34	-	8.31 ± 0.34
		60	6.74 ± 0.30	-	6.74 ± 0.30
	AlPE	20	9.13 ± 0.31	-	9.13 ± 0.31
		60	9.89 ± 0.37	-	9.89 ± 0.37
800	Al	20	36.74 ± 1.08	-	36.74 ± 1.08
		40	55.97 ± 1.32	-	55.97 ± 1.32
		60	64.29 ± 1.42	-	64.29 ± 1.42
	HDPE	20	5.55 ± 0.28	8.81 ± 0.85	14.36 ± 0.90
		40	10.10 ± 0.42	9.99 ± 0.92	20.09 ± 1.01
		60	12.78 ± 0.50	13.78 ± 0.78	26.57 ± 0.93
	AlPE	20	10.30 ± 0.35	4.74 ± 0.40	15.03 ± 0.53
		60	13.92 ± 0.49	13.32 ± 0.96	27.24 ± 1.08
2500	Al	20	19.56 ± 0.58	45.23 ± 2.01	64.79 ± 2.10
		40	40.17 ± 0.95	55.74 ± 2.64	95.91 ± 2.80
		60	110.06 ± 2.54	66.37 ± 2.65	176.43 ± 3.67
	HDPE	20	10.33 ± 0.39	35.97 ± 1.66	46.29 ± 1.70
		40	16.10 ± 0.56	46.42 ± 1.81	62.52 ± 1.89
		60	19.39 ± 0.70	60.49 ± 1.70	79.89 ± 1.84
	AlPE	20	12.93 ± 0.51	26.55 ± 1.26	39.49 ± 1.36
		60	18.65 ± 0.90	51.10 ± 2.87	69.75 ± 3.01

Table D.22: Total effective dose for He projectiles at 60°

E_{proj} (MeV/n)	Target material	z_{target} (g/cm^2)	Effective dose in $\left(\frac{nSv \cdot cm^2}{s.p.}\right)$		
			Upstream target	Downstream target	Total
400	Al	20	74.52 ± 2.03	31.58 ± 2.36	106.10 ± 3.11
		40	139.10 ± 3.07	34.47 ± 2.95	173.58 ± 4.26
		60	143.56 ± 3.29	40.30 ± 2.56	183.86 ± 4.17
	HDPE	20	21.10 ± 0.71	12.17 ± 1.56	33.27 ± 1.72
		40	25.41 ± 0.86	21.27 ± 1.32	46.68 ± 1.58
		60	31.85 ± 1.03	27.15 ± 1.82	59.00 ± 2.09
	AlPE	20	24.46 ± 0.72	18.44 ± 1.02	42.90 ± 1.25
		60	33.25 ± 0.97	33.81 ± 1.80	67.06 ± 2.04
800	Al	20	31.26 ± 1.24	30.84 ± 3.47	62.09 ± 3.69
		40	65.23 ± 2.09	37.32 ± 3.94	102.55 ± 4.46
		60	72.20 ± 2.36	58.28 ± 4.61	130.48 ± 5.18
	HDPE	20	22.18 ± 1.02	45.02 ± 2.38	67.20 ± 2.59
		40	34.06 ± 1.54	66.47 ± 3.54	100.53 ± 3.86
		60	47.42 ± 1.88	88.15 ± 4.76	135.58 ± 5.12
	AlPE	20	28.40 ± 0.87	44.56 ± 2.20	72.96 ± 2.36
		60	50.89 ± 1.62	71.74 ± 3.38	122.62 ± 3.75
1500	Al	20	39.34 ± 1.61	137.45 ± 6.62	176.79 ± 6.82
		40	90.90 ± 2.72	159.42 ± 8.36	250.32 ± 8.79
		60	132.88 ± 3.72	182.04 ± 8.16	314.92 ± 8.97
	HDPE	20	22.06 ± 1.20	87.72 ± 4.33	109.79 ± 4.50
		40	36.50 ± 1.68	113.74 ± 5.87	150.23 ± 6.10
		60	49.99 ± 2.26	144.54 ± 7.70	194.53 ± 8.02
	AlPE	20	30.26 ± 1.15	76.47 ± 3.32	106.72 ± 3.51
		60	55.34 ± 2.21	137.00 ± 6.15	192.34 ± 6.53

Table D.23: Total effective dose for C projectiles at 60°

E_{proj} (MeV/n)	Target material	z_{target} (g/cm^2)	Effective dose in $\left(\frac{nSv \cdot cm^2}{s.p.}\right)$		
			Upstream target	Downstream target	Total
400	Al	20	65.39 ± 1.61	62.36 ± 3.77	127.75 ± 4.10
		40	104.61 ± 2.17	61.45 ± 4.31	166.05 ± 4.83
		60	86.87 ± 1.73	58.56 ± 3.45	145.44 ± 3.85
	HDPE	20	52.23 ± 1.71	36.46 ± 3.32	88.69 ± 3.74
		40	64.12 ± 1.72	53.09 ± 2.82	117.21 ± 3.30
		60	60.12 ± 1.48	62.80 ± 2.89	122.93 ± 3.25
	AlPE	20	57.99 ± 1.66	44.51 ± 3.24	102.50 ± 3.64
		60	58.59 ± 1.39	64.01 ± 2.55	122.59 ± 2.90
800	Al	20	66.76 ± 2.04	172.60 ± 7.23	239.36 ± 7.51
		40	157.39 ± 3.60	211.23 ± 10.55	368.62 ± 11.15
		60	220.46 ± 4.55	226.09 ± 10.38	446.56 ± 11.34
	HDPE	20	54.88 ± 2.25	134.28 ± 6.51	189.16 ± 6.89
		40	109.93 ± 3.60	174.83 ± 9.07	284.76 ± 9.76
		60	125.97 ± 3.96	220.45 ± 8.32	346.42 ± 9.22
	AlPE	20	62.62 ± 2.30	122.95 ± 8.34	185.56 ± 8.66
		60	121.40 ± 3.98	205.04 ± 9.56	326.44 ± 10.35
1500	Al	20	67.71 ± 2.67	296.47 ± 13.67	364.18 ± 13.93
		40	151.25 ± 5.15	366.64 ± 16.72	517.89 ± 17.49
		60	243.55 ± 6.89	421.42 ± 21.45	664.96 ± 22.53
	HDPE	20	61.38 ± 4.69	-	61.38 ± 4.69
		40	128.26 ± 7.14	-	128.26 ± 7.14
		60	161.70 ± 8.39	172.90 ± 21.89	334.60 ± 23.44
	AlPE	20	70.48 ± 4.48	102.35 ± 9.60	172.83 ± 10.59
		60	154.33 ± 8.14	166.96 ± 17.40	321.30 ± 19.21

Table D.24: Total effective dose for Si projectiles at 60°

E_{proj} (MeV/n)	Target material	z_{target} (g/cm^2)	Effective dose in $\left(\frac{nSv \cdot cm^2}{s.p.}\right)$		
			Upstream target	Downstream target	Total
400	Al	20	90.62 ± 3.41	-	90.62 ± 3.41
		40	98.94 ± 3.13	-	98.94 ± 3.13
		60	108.15 ± 3.42	-	108.15 ± 3.42
	HDPE	20	73.73 ± 1.92	36.96 ± 3.08	110.69 ± 3.63
		40	58.34 ± 1.55	52.53 ± 2.93	110.87 ± 3.32
		60	61.48 ± 1.37	56.33 ± 2.51	117.81 ± 2.86
	AlPE	20	86.91 ± 2.35	47.36 ± 2.15	134.27 ± 3.18
		60	54.34 ± 1.24	53.66 ± 2.51	108.00 ± 2.80
800	Al	20	130.18 ± 5.23	186.66 ± 13.81	316.83 ± 14.77
		40	270.71 ± 8.10	215.02 ± 12.16	485.73 ± 14.61
		60	351.15 ± 9.53	222.26 ± 18.39	573.41 ± 20.72
	HDPE	20	121.99 ± 4.87	213.81 ± 11.80	335.80 ± 12.77
		40	208.22 ± 6.92	236.53 ± 13.15	444.75 ± 14.86
		60	235.93 ± 8.11	321.76 ± 13.67	557.69 ± 15.90
	AlPE	20	117.75 ± 4.84	160.79 ± 11.20	278.54 ± 12.20
		60	224.87 ± 7.46	329.07 ± 17.21	553.94 ± 18.76
1500	Al	20	129.13 ± 9.68	-	129.13 ± 9.68
		40	279.39 ± 14.04	-	279.39 ± 14.04
		60	446.88 ± 18.57	-	446.88 ± 18.57
	HDPE	20	88.80 ± 5.46	429.47 ± 22.62	518.27 ± 23.27
		40	185.30 ± 8.74	555.36 ± 31.46	740.66 ± 32.65
		60	224.55 ± 10.35	704.25 ± 37.55	928.80 ± 38.95
	AlPE	20	76.72 ± 4.46	422.85 ± 22.23	499.57 ± 22.67
		60	230.09 ± 10.65	653.87 ± 30.11	883.97 ± 31.93

Table D.25: Total effective dose for Fe projectiles at 60°

E_{proj} (MeV/n)	Target material	z_{target} (g/cm^2)	Effective dose in $\left(\frac{nSv \cdot cm^2}{s.p.}\right)$		
			Upstream target	Downstream target	Total
400	Al	20	249.00 ± 6.00	104.86 ± 7.42	353.86 ± 9.54
		40	281.42 ± 5.26	91.18 ± 6.89	372.60 ± 8.67
		60	234.80 ± 3.97	84.77 ± 9.32	319.57 ± 10.13
	HDPE	20	61.35 ± 1.96	50.64 ± 3.68	111.99 ± 4.17
		40	62.50 ± 1.83	73.43 ± 4.26	135.93 ± 4.64
		60	72.44 ± 2.00	83.05 ± 3.88	155.49 ± 4.37
	AlPE	20	80.50 ± 2.40	127.86 ± 9.81	208.36 ± 10.10
		60	83.90 ± 2.27	165.35 ± 6.18	249.25 ± 6.59
800	Al	20	651.13 ± 21.14	466.07 ± 22.76	1117.19 ± 31.07
		40	1081.11 ± 20.44	448.68 ± 16.28	1529.79 ± 26.13
		60	1101.20 ± 20.17	469.58 ± 55.18	1570.77 ± 58.75
	HDPE	20	120.49 ± 5.46	326.38 ± 18.97	446.87 ± 19.74
		40	176.31 ± 6.62	370.26 ± 22.51	546.57 ± 23.46
		60	219.01 ± 7.02	414.66 ± 23.92	633.67 ± 24.93
	AlPE	20	126.86 ± 6.07	459.12 ± 36.00	585.98 ± 36.51
		60	291.73 ± 8.03	391.18 ± 24.70	682.91 ± 25.97
1500	Al	20	31.86 ± 3.97	-	31.86 ± 3.97
		40	185.78 ± 13.97	-	185.78 ± 13.97
		60	554.74 ± 34.58	-	554.74 ± 34.58
	HDPE	20	61.96 ± 7.04	-	61.96 ± 7.04
		40	216.92 ± 16.84	-	216.92 ± 16.84
		60	258.09 ± 22.70	-	258.09 ± 22.70
	AlPE	20	115.49 ± 6.92	466.35 ± 25.23	581.83 ± 26.16
		60	354.96 ± 16.88	1005.26 ± 43.31	1360.22 ± 46.49

Table D.26: Total effective dose for H projectiles at 80°

E_{proj} (MeV/n)	Target material	z_{target} (g/cm^2)	Effective dose in $\left(\frac{nSv \cdot cm^2}{s.p.}\right)$		
			Upstream target	Downstream target	Total
400	Al	20	5.06 ± 0.15	-	5.06 ± 0.15
		40	13.28 ± 0.67	-	13.28 ± 0.67
		60	12.06 ± 0.71	-	12.06 ± 0.71
	HDPE	20	1.48 ± 0.09	-	1.48 ± 0.09
		40	3.04 ± 0.15	-	3.04 ± 0.15
		60	2.60 ± 0.16	-	2.60 ± 0.16
	AlPE	20	1.53 ± 0.10	-	1.53 ± 0.10
		60	3.01 ± 0.16	-	3.01 ± 0.16
800	Al	20	12.71 ± 0.57	-	12.71 ± 0.57
		40	15.72 ± 0.70	-	15.72 ± 0.70
		60	20.16 ± 0.75	-	20.16 ± 0.75
	HDPE	20	2.48 ± 0.15	-	2.48 ± 0.15
		40	3.17 ± 0.20	3.71 ± 0.46	6.88 ± 0.50
		60	3.44 ± 0.21	4.37 ± 0.94	7.82 ± 0.97
	AlPE	20	2.43 ± 0.12	-	2.43 ± 0.12
		60	4.59 ± 0.22	4.51 ± 0.47	9.10 ± 0.52
2500	Al	20	9.99 ± 0.33	22.52 ± 2.77	32.51 ± 2.79
		40	16.60 ± 0.46	25.28 ± 1.79	41.88 ± 1.85
		60	49.11 ± 1.37	31.94 ± 3.55	81.05 ± 3.80
	HDPE	20	6.05 ± 0.28	16.39 ± 1.45	22.44 ± 1.47
		40	7.02 ± 0.26	24.44 ± 1.09	31.46 ± 1.12
		60	8.11 ± 0.32	34.04 ± 3.52	42.15 ± 3.53
	AlPE	20	4.00 ± 0.19	8.65 ± 0.54	12.65 ± 0.58
		60	10.95 ± 0.46	16.22 ± 0.78	27.16 ± 0.90

Table D.27: Total effective dose for He projectiles at 80°

E_{proj} (MeV/n)	Target material	z_{target} (g/cm^2)	Effective dose in $\left(\frac{nSv \cdot cm^2}{s.p.}\right)$		
			Upstream target	Downstream target	Total
400	Al	20	24.15 ± 0.96	13.96 ± 1.04	38.10 ± 1.42
		40	29.89 ± 1.50	12.85 ± 1.25	42.74 ± 1.96
		60	32.07 ± 1.48	-	32.07 ± 1.48
	HDPE	20	5.05 ± 0.25	-	5.05 ± 0.25
		40	8.68 ± 0.36	-	8.68 ± 0.36
		60	10.62 ± 0.46	9.19 ± 1.45	19.81 ± 1.52
	AlPE	20	5.68 ± 0.23	-	5.68 ± 0.23
		60	8.48 ± 0.37	11.75 ± 0.73	20.23 ± 0.82
800	Al	20	20.51 ± 0.82	-	20.51 ± 0.82
		40	21.85 ± 0.89	-	21.85 ± 0.89
		60	27.08 ± 1.02	-	27.08 ± 1.02
	HDPE	20	11.67 ± 0.60	10.77 ± 1.57	22.44 ± 1.68
		40	18.71 ± 0.84	18.27 ± 2.51	36.98 ± 2.65
		60	23.66 ± 1.01	30.93 ± 1.93	54.59 ± 2.18
	AlPE	20	7.52 ± 0.31	17.33 ± 0.98	24.84 ± 1.03
		60	17.04 ± 0.63	40.30 ± 2.86	57.34 ± 2.93
1500	Al	20	27.71 ± 0.99	35.26 ± 1.73	62.97 ± 1.99
		40	33.18 ± 1.25	75.11 ± 5.11	108.29 ± 5.26
		60	53.21 ± 1.94	87.73 ± 6.26	140.94 ± 6.55
	HDPE	20	17.16 ± 0.77	17.41 ± 1.30	34.57 ± 1.51
		40	26.61 ± 1.18	44.97 ± 2.61	71.58 ± 2.86
		60	20.99 ± 1.02	82.93 ± 6.05	103.92 ± 6.13
	AlPE	20	11.82 ± 0.51	25.22 ± 1.56	37.05 ± 1.64
		60	27.07 ± 1.04	64.95 ± 3.84	92.01 ± 3.98

Table D.28: Total effective dose for C projectiles at 80°

E_{proj} (MeV/n)	Target material	z_{target} (g/cm^2)	Effective dose in $\left(\frac{nSv \cdot cm^2}{s.p.}\right)$		
			Upstream target	Downstream target	Total
400	Al	20	29.97 ± 0.84	10.23 ± 1.03	40.20 ± 1.33
		40	28.20 ± 0.80	15.41 ± 0.95	43.61 ± 1.24
		60	30.83 ± 0.89	21.01 ± 1.50	51.83 ± 1.74
	HDPE	20	11.65 ± 0.55	-	11.65 ± 0.55
		40	18.68 ± 0.70	10.76 ± 1.03	29.43 ± 1.25
		60	21.10 ± 0.64	34.00 ± 2.07	55.10 ± 2.17
	AlPE	20	10.97 ± 0.50	-	10.97 ± 0.50
		60	18.10 ± 0.60	33.63 ± 2.83	51.73 ± 2.89
800	Al	20	41.29 ± 1.18	69.89 ± 3.96	111.18 ± 4.13
		40	52.86 ± 1.52	91.40 ± 7.62	144.26 ± 7.77
		60	65.94 ± 1.97	112.28 ± 5.19	178.22 ± 5.55
	HDPE	20	4.52 ± 0.41	41.04 ± 2.43	45.57 ± 2.46
		40	59.33 ± 1.72	-	59.33 ± 1.72
		60	76.31 ± 2.13	-	76.31 ± 2.13
	AlPE	20	26.06 ± 0.90	-	26.06 ± 0.90
		60	86.35 ± 2.23	-	86.35 ± 2.23
1500	Al	20	79.95 ± 3.24	64.74 ± 3.85	144.69 ± 5.03
		40	76.14 ± 2.61	137.49 ± 6.35	213.62 ± 6.86
		60	98.99 ± 3.29	190.64 ± 25.95	289.63 ± 26.16
	HDPE	20	28.29 ± 2.34	-	28.29 ± 2.34
		40	33.05 ± 2.48	-	33.05 ± 2.48
		60	73.80 ± 4.47	-	73.80 ± 4.47
	AlPE	20	24.83 ± 1.74	-	24.83 ± 1.74
		60	66.09 ± 4.17	-	66.09 ± 4.17

Table D.29: Total effective dose for Si projectiles at 80°

E_{proj} (MeV/n)	Target material	z_{target} (g/cm^2)	Effective dose in $\left(\frac{nSv \cdot cm^2}{s.p.}\right)$		
			Upstream target	Downstream target	Total
400	Al	20	32.28 ± 1.43	-	32.28 ± 1.43
		40	28.97 ± 1.20	-	28.97 ± 1.20
		60	25.62 ± 1.21	-	25.62 ± 1.21
	HDPE	20	10.88 ± 0.48	9.98 ± 1.54	20.86 ± 1.61
		40	20.66 ± 0.65	13.24 ± 2.02	33.90 ± 2.12
		60	20.24 ± 0.58	35.82 ± 1.75	56.06 ± 1.84
	AlPE	20	17.30 ± 0.63	15.65 ± 1.01	32.95 ± 1.19
		60	19.54 ± 0.58	34.50 ± 2.30	54.04 ± 2.37
800	Al	20	66.32 ± 2.71	-	66.32 ± 2.71
		40	86.46 ± 3.47	84.38 ± 4.72	170.84 ± 5.86
		60	99.18 ± 3.84	85.51 ± 6.41	184.69 ± 7.47
	HDPE	20	40.87 ± 1.73	-	40.87 ± 1.73
		40	66.62 ± 2.72	54.03 ± 5.12	120.65 ± 5.80
		60	69.28 ± 2.75	125.84 ± 7.33	195.12 ± 7.83
	AlPE	20	30.06 ± 1.62	-	30.06 ± 1.62
		60	80.97 ± 2.95	70.26 ± 10.56	151.23 ± 10.96
1500	Al	20	51.02 ± 3.31	-	51.02 ± 3.31
		40	159.55 ± 8.38	-	159.55 ± 8.38
		60	162.34 ± 8.46	-	162.34 ± 8.46
	HDPE	20	41.77 ± 2.37	78.73 ± 8.76	120.50 ± 9.07
		40	93.36 ± 4.17	130.01 ± 15.73	223.37 ± 16.27
		60	125.63 ± 5.40	227.84 ± 11.62	353.46 ± 12.82
	AlPE	20	55.90 ± 2.46	71.10 ± 5.98	126.99 ± 6.47
		60	123.48 ± 4.97	240.44 ± 12.21	363.92 ± 13.18

Table D.30: Total effective dose for Fe projectiles at 80°

E_{proj} (MeV/n)	Target material	z_{target} (g/cm^2)	Effective dose in $\left(\frac{nSv \cdot cm^2}{s.p.}\right)$		
			Upstream target	Downstream target	Total
400	Al	20	67.26 ± 3.01	-	67.26 ± 3.01
		40	68.07 ± 2.37	17.82 ± 1.39	85.89 ± 2.74
		60	66.37 ± 2.05	43.55 ± 3.53	109.92 ± 4.08
	HDPE	20	17.59 ± 0.93	12.55 ± 1.03	30.14 ± 1.39
		40	19.05 ± 0.76	26.39 ± 1.61	45.44 ± 1.78
		60	29.12 ± 0.93	49.13 ± 2.55	78.25 ± 2.72
	AlPE	20	17.83 ± 0.74	-	17.83 ± 0.74
		60	32.18 ± 1.00	67.38 ± 7.38	99.56 ± 7.45
800	Al	20	243.98 ± 9.02	125.61 ± 8.26	369.59 ± 12.23
		40	307.74 ± 9.46	183.00 ± 11.18	490.74 ± 14.65
		60	334.54 ± 9.40	196.45 ± 9.17	530.99 ± 13.13
	HDPE	20	57.32 ± 2.60	53.62 ± 3.21	110.95 ± 4.14
		40	70.53 ± 2.82	113.75 ± 6.38	184.28 ± 6.97
		60	99.37 ± 3.73	223.74 ± 17.27	323.12 ± 17.67
	AlPE	20	86.67 ± 3.11	53.41 ± 3.83	140.07 ± 4.93
		60	57.98 ± 2.70	225.46 ± 26.19	283.44 ± 26.33
1500	Al	20	192.67 ± 15.59	-	192.67 ± 15.59
		40	234.06 ± 16.22	-	234.06 ± 16.22
		60	238.07 ± 16.11	-	238.07 ± 16.11
	HDPE	20	51.31 ± 4.07	-	51.31 ± 4.07
		40	64.21 ± 5.21	-	64.21 ± 5.21
		60	253.06 ± 20.93	-	253.06 ± 20.93
	AlPE	20	62.85 ± 3.73	103.55 ± 7.41	166.40 ± 8.30
		60	199.11 ± 8.04	305.62 ± 19.41	504.73 ± 21.01

Table D.31: Total effective dose for H projectiles at 135°

E_{proj} (MeV/n)	Target material	z_{target} (g/cm^2)	Effective dose in $\left(\frac{nSv \cdot cm^2}{s.p.}\right)$		
			Upstream target	Downstream target	Total
400	Al	20	14.93 ± 0.29	-	14.93 ± 0.29
		40	31.05 ± 0.83	-	31.05 ± 0.83
		60	46.49 ± 1.02	-	46.49 ± 1.02
	HDPE	20	2.34 ± 0.11	-	2.34 ± 0.11
		40	2.45 ± 0.12	-	2.45 ± 0.12
		60	3.01 ± 0.12	-	3.01 ± 0.12
	AlPE	20	9.38 ± 0.24	-	9.38 ± 0.24
		60	10.31 ± 0.25	-	10.31 ± 0.25
800	Al	20	19.09 ± 0.53	-	19.09 ± 0.53
		40	33.83 ± 0.80	-	33.83 ± 0.80
		60	42.81 ± 0.85	-	42.81 ± 0.85
	HDPE	20	3.94 ± 0.16	-	3.94 ± 0.16
		40	6.57 ± 0.26	-	6.57 ± 0.26
		60	6.21 ± 0.24	-	6.21 ± 0.24
	AlPE	20	11.90 ± 0.27	-	11.90 ± 0.27
		60	16.25 ± 0.37	-	16.25 ± 0.37
2500	Al	20	22.88 ± 0.50	12.32 ± 0.63	35.21 ± 0.81
		40	40.52 ± 0.77	26.04 ± 1.35	66.56 ± 1.55
		60	120.89 ± 2.43	32.42 ± 1.55	153.31 ± 2.88
	HDPE	20	6.34 ± 0.18	4.26 ± 0.53	10.60 ± 0.56
		40	10.64 ± 0.39	12.71 ± 0.65	23.35 ± 0.76
		60	12.71 ± 0.37	21.13 ± 1.16	33.84 ± 1.22
	AlPE	20	16.52 ± 0.38	4.31 ± 0.58	20.83 ± 0.69
		60	27.23 ± 0.74	10.40 ± 1.34	37.62 ± 1.54

Table D.32: Total effective dose for He projectiles at 135°

E_{proj} (MeV/n)	Target material	z_{target} (g/cm^2)	Effective dose in $\left(\frac{nSv \cdot cm^2}{s.p.}\right)$		
			Upstream target	Downstream target	Total
400	Al	20	40.70 ± 0.88	14.83 ± 1.00	55.53 ± 1.34
		40	77.62 ± 1.53	15.89 ± 1.66	93.51 ± 2.26
		60	84.61 ± 1.64	-	84.61 ± 1.64
	HDPE	20	8.40 ± 0.33	-	8.40 ± 0.33
		40	8.43 ± 0.32	-	8.43 ± 0.32
		60	10.79 ± 0.36	-	10.79 ± 0.36
	AlPE	20	20.73 ± 0.44	-	20.73 ± 0.44
		60	25.72 ± 0.55	5.98 ± 0.63	31.70 ± 0.84
800	Al	20	34.09 ± 1.12	-	34.09 ± 1.12
		40	65.78 ± 1.77	-	65.78 ± 1.77
		60	90.75 ± 2.42	-	90.75 ± 2.42
	HDPE	20	14.60 ± 0.53	-	14.60 ± 0.53
		40	18.43 ± 0.70	-	18.43 ± 0.70
		60	21.30 ± 0.82	-	21.30 ± 0.82
	AlPE	20	28.89 ± 0.63	5.63 ± 0.86	34.51 ± 1.07
		60	45.46 ± 1.33	20.17 ± 1.03	65.64 ± 1.68
1500	Al	20	49.02 ± 1.27	-	49.02 ± 1.27
		40	105.77 ± 2.31	-	105.77 ± 2.31
		60	139.36 ± 2.94	22.84 ± 2.58	162.20 ± 3.91
	HDPE	20	13.25 ± 0.59	-	13.25 ± 0.59
		40	23.24 ± 0.90	-	23.24 ± 0.90
		60	26.12 ± 0.95	-	26.12 ± 0.95
	AlPE	20	37.09 ± 0.87	12.64 ± 1.59	49.73 ± 1.81
		60	60.08 ± 1.74	31.97 ± 2.19	92.05 ± 2.80

Table D.33: Total effective dose for C projectiles at 135°

E_{proj} (MeV/n)	Target material	z_{target} (g/cm^2)	Effective dose in $\left(\frac{nSv \cdot cm^2}{s.p.}\right)$		
			Upstream target	Downstream target	Total
400	Al	20	47.39 ± 1.02	-	47.39 ± 1.02
		40	82.76 ± 1.37	10.59 ± 1.35	93.35 ± 1.93
		60	101.89 ± 1.58	28.98 ± 1.58	130.88 ± 2.23
	HDPE	20	16.54 ± 0.61	-	16.54 ± 0.61
		40	20.90 ± 0.66	-	20.90 ± 0.66
		60	27.05 ± 0.78	6.13 ± 1.38	33.18 ± 1.59
	AlPE	20	39.36 ± 1.04	-	39.36 ± 1.04
		60	48.68 ± 0.90	15.44 ± 1.08	64.12 ± 1.41
800	Al	20	66.39 ± 1.38	22.98 ± 2.43	89.36 ± 2.79
		40	150.39 ± 2.85	54.65 ± 3.14	205.04 ± 4.24
		60	196.78 ± 3.75	97.55 ± 6.75	294.33 ± 7.72
	HDPE	20	27.56 ± 0.88	-	27.56 ± 0.88
		40	39.96 ± 1.28	-	39.96 ± 1.28
		60	40.34 ± 1.23	22.76 ± 2.18	63.10 ± 2.50
	AlPE	20	52.52 ± 1.26	-	52.52 ± 1.26
		60	75.76 ± 2.01	34.58 ± 5.16	110.34 ± 5.54
1500	Al	20	109.79 ± 3.28	26.06 ± 3.29	135.85 ± 4.64
		40	197.10 ± 4.28	60.51 ± 5.61	257.60 ± 7.06
		60	294.44 ± 7.00	94.02 ± 5.48	388.47 ± 8.89
	HDPE	20	36.67 ± 2.57	-	36.67 ± 2.57
		40	60.91 ± 3.51	-	60.91 ± 3.51
		60	49.50 ± 2.65	-	49.50 ± 2.65
	AlPE	20	62.05 ± 2.46	-	62.05 ± 2.46
		60	105.98 ± 4.39	-	105.98 ± 4.39

Table D.34: Total effective dose for Si projectiles at 135°

E_{proj} (MeV/n)	Target material	z_{target} (g/cm^2)	Effective dose in $\left(\frac{nSv \cdot cm^2}{s.p.}\right)$		
			Upstream target	Downstream target	Total
400	Al	20	60.71 ± 1.82	-	60.71 ± 1.82
		40	106.90 ± 2.37	-	106.90 ± 2.37
		60	137.12 ± 3.02	-	137.12 ± 3.02
	HDPE	20	32.26 ± 1.02	-	32.26 ± 1.02
		40	30.59 ± 0.74	8.52 ± 1.17	39.11 ± 1.39
		60	31.03 ± 0.64	28.08 ± 1.55	59.12 ± 1.68
	AlPE	20	65.66 ± 1.40	-	65.66 ± 1.40
		60	72.07 ± 1.05	45.27 ± 2.07	117.35 ± 2.32
800	Al	20	111.07 ± 3.47	-	111.07 ± 3.47
		40	235.33 ± 5.82	-	235.33 ± 5.82
		60	295.89 ± 6.92	46.71 ± 6.42	342.60 ± 9.44
	HDPE	20	43.63 ± 1.75	-	43.63 ± 1.75
		40	78.78 ± 2.94	-	78.78 ± 2.94
		60	104.56 ± 4.42	-	104.56 ± 4.42
	AlPE	20	88.96 ± 2.67	-	88.96 ± 2.67
		60	131.98 ± 3.59	-	131.98 ± 3.59
1500	Al	20	135.19 ± 6.60	-	135.19 ± 6.60
		40	357.47 ± 14.49	-	357.47 ± 14.49
		60	490.52 ± 18.41	-	490.52 ± 18.41
	HDPE	20	71.94 ± 3.41	-	71.94 ± 3.41
		40	89.41 ± 3.67	-	89.41 ± 3.67
		60	136.20 ± 5.95	82.62 ± 8.19	218.82 ± 10.12
	AlPE	20	123.55 ± 4.00	-	123.55 ± 4.00
		60	157.31 ± 5.23	88.09 ± 11.41	245.39 ± 12.55

Table D.35: Total effective dose for Fe projectiles at 135°

E_{proj} (MeV/n)	Target material	z_{target} (g/cm^2)	Effective dose in $\left(\frac{nSv \cdot cm^2}{s.p.}\right)$		
			Upstream target	Downstream target	Total
400	Al	20	149.63 ± 2.80	-	149.63 ± 2.80
		40	210.89 ± 2.83	67.06 ± 8.33	277.95 ± 8.79
		60	225.39 ± 2.31	70.20 ± 3.92	295.60 ± 4.55
	HDPE	20	22.58 ± 0.71	-	22.58 ± 0.71
		40	35.17 ± 1.00	-	35.17 ± 1.00
		60	40.13 ± 0.95	32.15 ± 1.85	72.28 ± 2.08
	AlPE	20	66.54 ± 1.49	-	66.54 ± 1.49
		60	93.14 ± 1.45	69.42 ± 3.96	162.56 ± 4.21
800	Al	20	354.91 ± 7.67	55.96 ± 8.37	410.87 ± 11.36
		40	657.00 ± 9.28	160.63 ± 9.66	817.63 ± 13.39
		60	832.35 ± 9.79	228.72 ± 14.38	1061.07 ± 17.40
	HDPE	20	71.91 ± 2.86	-	71.91 ± 2.86
		40	90.86 ± 3.40	-	90.86 ± 3.40
		60	105.71 ± 3.57	49.85 ± 7.09	155.55 ± 7.94
	AlPE	20	152.53 ± 4.15	-	152.53 ± 4.15
		60	127.20 ± 3.31	65.84 ± 7.77	193.04 ± 8.45
1500	Al	20	202.12 ± 13.85	-	202.12 ± 13.85
		40	466.44 ± 21.78	-	466.44 ± 21.78
		60	693.24 ± 30.07	-	693.24 ± 30.07
	HDPE	20	73.03 ± 7.31	-	73.03 ± 7.31
		40	156.44 ± 14.84	-	156.44 ± 14.84
		60	143.86 ± 9.69	-	143.86 ± 9.69
	AlPE	20	137.94 ± 5.10	-	137.94 ± 5.10
		60	225.09 ± 6.89	-	225.09 ± 6.89

Appendix E

Data repository structure

This appendix outlines the structure of the data file repositories containing all of the results (measured and simulated) from the experimental campaign as initially discussed in Section 9.1.

Briefly put, the repository is structured as four main folders within a primary directory: `Thick-Target_measurements`, `Thick-Target_simulations`, `Deconvoluted_neutrons`, and, `Thick-Target_zero_degree_data`. These first two contain all experimentally measured and simulated results for off-axis neutrons and charged particles from the upstream target. The deconvoluted neutron folder contains all calculated and simulated results pertaining to the downstream target and room scattered neutrons with a separate README file within the folder detailing how that set of data differs from the upstream target data. The zero-degree data folder contains all calculated and PHITS simulated results for the select systems measured at zero degrees with NaI detectors (not discussed in this work). Regardless, all sets of data within these main folders share the same folder hierarchy and file naming convention as shown below.

```
- Projectile {SpeciesEnergy (in MeV or MeV/n)}:
- Target Material {Aluminum, Polyethylene, Combination_AlPE}:
- Upstream Target Thickness {20, 40, 60 (g/cm2)}:
- Secondary Particle:
- ${system}_${detector type}_${angle}deg_${SP}.txt
```

Where:

`${system}`

- Projectile-Target system designator
- constructed as: `${ion}${energy}_${material}${thickness}`
  - `${ion}` - projectile species `{h, he, c, si, fe}`
  - `${energy}` - reduced projectile energy `{4, 8, 15, 25}`
  - `${material}` - upstream target material `{al, pe, ap}`
  - `${thickness}` - upstream target thickness `{20, 40, 60}`

`${detector type}`

- `OLS`: for Organic Liquid Scintillator (colloquially referred to as Neutron Detector)
- `NaI`: for Sodium Iodide

`${angle}`

- The angle/detector position where this particular secondary particle yield energy spectrum was measured (for example: `10`, `30`, `45`, etc.).
- Sodium Iodide results have finer angular resolution than OLS. Decimals are replaced with a "p" (`12p7` for 12.7, for example).
- Zero degree measurements are at -2.7, 0, and 2.7 degrees which are denoted as `2p7lower`, `0`, and `2p7upper` respectively.

`${SP}`

- Secondary Particle symbol.
  - `N`: Neutron
  - `H`: Proton
  - `D`: Deuteron
  - `T`: Triton
  - `S`: Helium-3

- `A`: Helium-4
- `Fe`: Iron; measured during the zero degree measurements (800 MeV Fe on 20 g/cm^2 of aluminum; iron stops in subsequent thicknesses of Al.)
- `DCN`: Deconvoluted Neutron; only present in the separate directory for deconvoluted neutron results

Each file begins with a 13-line header block followed by rows of text for each data point consisting of ten columns of information for the upstream target-produced secondary particles as detailed in Table E.1 and eleven columns for the downstream target-produced neutrons as detailed in Table E.2.

Table E.1: Columns in upstream target secondary particle text files

Name	Units[1]	Meaning
KE_left	MeV	Left/lower bound of energy bin
KE_mid[2]	MeV	Bin midpoint (see [2])
KE_right	MeV	Right/upper bound of energy bin
Norm_Cts	#/(sp·MeV·sr)	Normalized yield
Y_stat	#/(sp·MeV·sr)	Statistical uncertainty of yield
Y_syst_tot	#/(sp·MeV·sr)	Total systematic uncertainty of yield
X_tot	MeV	Energy resolution uncertainty
Y_syst_solid_angle	#/(sp·MeV·sr)	Solid angle component of Y_syst_tot
Y_syst_efficiency	#/(sp·MeV·sr)	Efficiency correction component of Y_syst_tot
Y_syst_graphical	#/(sp·MeV·sr)	Graphical cut component of Y_syst_tot

[1] # = number of secondary particles, "sp" = source particle, and "sr" = steradians

[2] KE_mid's meaning is slightly across the different datasets
(flux-weighted average energy for OLS results and average bin flight time converted to energy for NaI results unless otherwise specified in the "Additional notes" row of each file.)

Table E.2: Columns in measured downstream target neutron text files

Name	Units[1]	Meaning
KE_left	MeV	Left/lower bound of energy bin
KE_mid[2]	MeV	Bin midpoint (see [2])
KE_right	MeV	Right/upper bound of energy bin
Norm_Cts	#/(sp·MeV)	Normalized yield
Y_stat	#/(sp·MeV)	Statistical uncertainty of yield
Y_syst_tot	#/(sp·MeV)	Total systematic uncertainty of yield
X_tot	MeV	Energy resolution uncertainty
Y_syst_GC	#/(sp·MeV)	Graphical cut component of Y_syst_tot
Y_syst_reg	#/(sp·MeV)	Regularization vs. NNLS component of Y_syst_tot
Y_syst_mu	#/(sp·MeV)	Impact of specific choice of μ component of Y_syst_tot
Y_syst_QMD	#/(sp·MeV)	Response matrix error component of Y_syst_tot

[1] # is number of particles and "sp" stands for source particle.

[2] KE_mid here is just a log-spaced average of the energy bin boundaries. These energy bins are exact and determined by the response matrix's structure.

Vita

Hunter Ratliff spent his childhood in Tullahoma, TN, though he attended elementary school at New Union Elementary in Manchester, TN. Afterward, he attended middle school and high school in Tullahoma. After graduating from Tullahoma High School in the spring of 2011, Hunter moved to Knoxville, TN to attend The University of Tennessee, Knoxville. He graduated with a B.S. in Nuclear Engineering with highest honors in May 2015 and gained experience in a summer internship at Oak Ridge National Laboratory prior to his senior year. After graduation, Hunter began graduate school where he completed his M.S. in Nuclear Engineering in December 2016. Throughout his time in graduate school, Hunter accumulated 400 hours of beam time experience at the NASA Space Radiation Laboratory on Brookhaven National Laboratory's campus.